

1999

# Integrated Photonics Research

Technical  
Digest

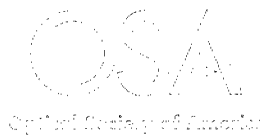
July 19-21, 1999

Fess Parker's Doubletree Resort  
Santa Barbara, California

Postconference Edition

20000306 095

Published by  
The Optical Society of America



DATC QUALITY INSURANCE

# REPORT DOCUMENTATION PAGE

*Form Approved  
OMB No. 0704-0188*

Public reporting burden for this collection of information is estimated to average 1 hour per response, including the time for reviewing instructions, searching data sources, gathering and maintaining the data needed, and completing and reviewing the collection of information. Send comments regarding burden estimate or any other aspect of this collection of information, including suggestions for reducing this burden to Washington Headquarters Service, Directorate for Information Operations and Reports, 1215 Jefferson Davis Highway, Suite 1204, Arlington, VA 22202-4302, and to the Office of Management and Budget, Paperwork Reduction Project (0704-0188) Washington, DC 20503.

**PLEASE DO NOT RETURN YOUR FORM TO THE ABOVE ADDRESS.**

1. REPORT DATE (DD-MM-YYYY)	2. REPORT DATE	3. DATES COVERED (From - To)		
29-02-2000	Final	June 1, 1999-May 30, 2000		
4. TITLE AND SUBTITLE		5a. CONTRACT NUMBER		
Organization of the 1999 Integrated Photonics Research Topical Meeting		5b. GRANT NUMBER N00014-99-1-0894		
		5c. PROGRAM ELEMENT NUMBER		
6. AUTHOR(S)		5d. PROJECT NUMBER		
John A. Thorner		5e. TASK NUMBER		
		5f. WORK UNIT NUMBER		
7. PERFORMING ORGANIZATION NAME(S) AND ADDRESS(ES)		8. PERFORMING ORGANIZATION REPORT NUMBER		
Optical Society of America 2010 Massachusetts Ave., NW Washington DC 20036				
9. SPONSORING/MONITORING AGENCY NAME(S) AND ADDRESS(ES)		10. SPONSOR/MONITOR'S ACRONYM(S)		
Office of Naval Research Program Officer Yoon S. Park ONR Code 312 Ballston Tower One 800 North Quincy Street Arlington VA 22217-5660		ONR		
		11. SPONSORING/MONITORING AGENCY REPORT NUMBER		
12. DISTRIBUTION AVAILABILITY STATEMENT				
Approved for public release Distribution unlimited ✓				
13. SUPPLEMENTARY NOTES				
14. ABSTRACT				
The 1999 Integrated Photonics Research Conference was one of the most important international conferences specializing in the science and technology of photonics. It provided an annual forum for the dissemination of new results involving all experimental and theoretical aspects of integrated photonic components. These included the design, simulation, fabrication, materials, characterization, packaging, and application of photonic devices as well as specific, timely and emerging topics which are represented by special symposia. IPR also provided a unique educational experience for students interested in photonic devices due to both its topical scope and its size. In scope, IPR was highly focused on issues relevant to photonic devices for use in communications, signal processing, and sensors, and thus provided an in-depth perspective on this field. The conference was large enough to provide comprehensive coverage of photonic device-related issues, ranging from materials to simulations to applications, while remaining sufficiently small to provide the informal atmosphere conductive technical interchanges.				
15. SUBJECT TERMS				
16. SECURITY CLASSIFICATION OF:		17. LIMITATION OF ABSTRACT	18. NUMBER OF PAGES	19a. NAME OF RESPONSIBLE PERSON
a. REPORT unclassified	b. ABSTRACT unclassified	c. THIS PAGE unclassified	unlimited	19b. TELEPHONE NUMBER (Include area code) 202/416-1464

# Integrated Photonics Research

## Technical Digest

July 19–21, 1999

**Fess Parker's Doubletree Resort**  
Santa Barbara, California

**Postconference Edition**

*Partial support provided by*  
**Office of Naval Research**

*Technically cosponsored by*  
**IEEE/Lasers and Electro-Optics Society**



*Sponsored by*  
**Optical Society of America**  
2010 Massachusetts Avenue, NW  
Washington, DC 20036-1023



Articles in this publication may be cited in other publications. To facilitate access to the original publication source, the following form for the citation is suggested:

Name of Author(s), "Title of Paper," in *Integrated Photonics Research*, OSA Technical Digest (Optical Society of America, Washington DC, 1999), pp. xx-xx.

Optical Society of America

ISBN

Conference Edition	1-55752-575-7
Postconference Edition	1-55752-586-2
1999 Technical Digest Series	1-55752-584-6

Library of Congress Catalogue Card Number

Conference Edition	98-89994
Postconference Edition	99-63509

Copyright © 1999, Optical Society of America

Individual readers of this digest and libraries acting for them are permitted to make fair use of the material in it, such as to copy an article for use in teaching or research, without payment of fee, provided that such copies are not sold. Copying for sale is subject to payment of copying fees. The code 1-55752-584-6/99/\$15.00 gives the per-article copying fee for each copy of the article made beyond the free copying permitted under Sections 107 and 108 of the U.S. Copyright Law. The fee should be paid through the Copyright Clearance Center, Inc., 21 Congress Street, Salem, MA 01970.

Permission is granted to quote excerpts from articles in this digest in scientific works with the customary acknowledgment of the source, including the author's name and the name of the digest, page, year, and name of the Society. Reproduction of figures and tables is likewise permitted in other articles and books provided that the same information is printed with them and notification is given to the Optical Society of America. In addition, the Optical Society may require that permission also be obtained from one of the authors. Address inquiries and notices to Director of Publications, Optical Society of America, 2010 Massachusetts Avenue, NW, Washington, DC 20036-1023. In the case of articles whose authors are employees of the United States Government or its contractors or grantees, the Optical Society of America recognizes the right of the United States Government to retain a nonexclusive, royalty free license to use the author's copyrighted article for United States Government purposes.

Printed in the U.S.A.

# Contents

<b>Agenda</b>	<b>v</b>
<b>RMA</b> Plenary Session	1
<b>RMB</b> WDM Devices: 1	7
<b>RMC</b> New Physics/Devices	23
<b>RMD</b> Waveguide Modeling	33
<b>RME</b> WDM Devices: 2	49
<b>RMF</b> Material and Characterization	63
<b>RMG</b> VCSEL Modeling	83
<b>RMH</b> Poster Session	91
<b>RTuA</b> WDM Devices: 3	125
<b>RTuB</b> Photonic Nanocircuits	145
<b>RTuC</b> IR, Mid-IR and THz Modeling	157
<b>RTuD</b> Integrated Optical Switches	173
<b>RTuE</b> PBG Structures and Devices	189
<b>RTuF</b> GaN Device Modeling	205
<b>RTuG</b> Active Devices	215
<b>RTuH</b> High-Q Resonators	231
<b>RTuI</b> Finite-Difference Modeling	241
<b>RTuJ</b> Optical Transmission and WDM Modeling	257
<b>RTuK</b> Waveguide Modulators	271
<b>RTuL</b> Mode Control	287
<b>JWA</b> Joint Session 1: Technologies for Optical Cross Connects	303
<b>RWA</b> WDM and TDM System Modeling	315
<b>RWB</b> Modulators and Receivers	325
<b>JWB</b> Joint Session 2: Optical Cross Connects	335
<b>RWC</b> Photonic Components System Modeling	351
<b>RWD</b> Integrated Devices	365
<b>Key to Authors and Presiders</b>	381

# Technical Program Committee

## Research Organizing Committee

Nadir Dagli, *General Chair, University of California, Santa Barbara, USA*  
Sujeet Chaudhuri, *Program Chair, University of Waterloo, Canada*  
Fred Heismann, *Program Chair, Qtera Corporation, USA*

## International Liaison Group Chairs

### Asia/Pacific Rim

Yasuo Kokubun, *Yokohama National University, Japan*

### Europe

Gunnar Arvidsson, *Institute of Optical Research, Sweden*

## OSA Technical Council Representative

Tso Yee Fan, *MIT Lincoln Laboratory, USA*

## Subcommittee I: Active and Compound Semiconductor Devices

S. Chandrasekhar, *Chair, Bell Laboratories, Lucent Technologies, USA*  
T.R. Ranganath, *Hewlett-Packard Laboratories, USA*  
Akihiko Kasukawa, *Furukawa Electric Company Ltd., Japan*  
Kazutoshi Kato, *NTT Opto-Electronics Laboratories, Japan*  
Jean-Francois Vinchant, *Alcatel Optronics, France*  
Claude Rolland, *Nortel Networks, Canada*  
M.K. Smit, *Delft University of Technology, The Netherlands*  
Julian Soole, *Bell Laboratories, Lucent Technologies, USA*

## Subcommittee II: Dielectric Waveguides and Waveguides Devices

Ramu V. Ramaswamy, *Chair, University of Florida, USA*  
Jaymin Amin, *Corning Inc., USA*  
Bahram Jalali, *University of California, Los Angeles, USA*  
Yasuo Kokubun, *Yokohama National University, Japan*  
Takashi Mizuochi, *Mitsubishi Electric Corporation, Japan*  
Kazuhiro Noguchi, *NTT Opto-Electronics Laboratory, Japan*  
Wolfgang Sohler, *University of Paderborn, Germany*  
William Steier, *University of Southern California, Los Angeles, USA*

## Subcommittee III: Modeling, Numerical Simulation and Theory

Joseph P. Donnelly, *Chair, MIT Lincoln Laboratory, USA*  
Shun-Lien Chuang, *University of Illinois, USA*  
Youngchul Chung, *Kwangwoon University, South Korea*  
Gregory Dente, *GCD Associates, USA*  
Wei Ping Huang, *University of Waterloo, Canada*  
Brent Little, *Massachusetts Institute of Technology, USA*  
Jerry Meyer, *Naval Research Laboratory, USA*  
Shuji Seki, *NTT Opto-Electronics Laboratory, Japan*  
K. Alan Shore, *University of Wales, UK*  
C. W. Weinert, *Heinrich-Hertz-Institute, Germany*  
Junji Yamauchi, *Hosei University, Japan*  
Richard W. Ziolkowski, *University of Arizona, USA*

## IPR Advisory Committee

Bob Deri, *Lawrence Livermore National Laboratories, USA*  
Anand Gopinath, *University of Minnesota, USA*  
David Smith, *Case Western Reserve University, USA*  
David Yevick, *Queen's University at Kingston, Canada*  
Jane Zucker, *Bell Laboratories, Lucent Technologies, USA*

# Agenda

■ Monday  
■ July 19, 1999

## Sierra Madre

8:00am–8:15am

### Opening Remarks

Nadir Dagli, *University of California, Santa Barbara, USA*

8:15am–10:30am

### RMA ■ Plenary Session

Nadir Dagli, *University of California, Santa Barbara, USA, Presider*

8:15am (Plenary)

**RMA1 ■ Fiber devices for ultrahigh-speed photonics**, Erich P. Ippen, *Massachusetts Institute of Technology, USA*. Erbium-doped fibers have enabled the development of new short-pulse sources and switches for future ultrahigh-speed technology. Recent progress in our laboratory on soliton lasers, optical ring memories, femtosecond stretched-pulse lasers, and nonlinear loop filters will be described. (p. 2)

9:00am (Plenary)

**RMA2 ■ Challenges and opportunities in photonic integration**, Meint K. Smit, *Delft Univ. of Technology, The Netherlands*. A review of progress in semiconductor-based photonic integrated circuits is given and the challenges and opportunities in photonic integration and photonic CAD are discussed. (p. 3)

9:45 am (Plenary)

**RMA3 ■ Transmission still, going networking and beyond**, Tetsuhiko Ikegami, *Univ. Aizu, Japan*; K. Okamoto, *NTT Photonics Laboratories, Japan*. Fiber technology and optoelectronics have moved up telecommunication to the most significant infrastructure in cooperation with information technology. In the electronic arena, integration of devices is a crucial condition for the application, however, photonic technology is running differently. Is it enough due to its versatility? The point will be reviewed and discussed. (p. 6)

## Grand Ballroom Foyer

10:30am–11:00am

Coffee Break

## Sierra Madre North

11:00am–12:30pm

### RMB ■ WDM Devices: 1

Meint K. Smit, *Delft University of Technology, The Netherlands, Presider*

11:00am (Invited)

**RMB1 ■ AOTF for optical ADM systems**, T. Nakazawa, M. Doi, S. Taniguchi, Y. Takasu, N. Hashimoto, M. Seino, *Fujitsu Laboratories Ltd., Japan*. We have developed highly integrated AOTFs by introducing a new film-loaded SAW guide and a new waveguide reflector. This enables a narrow bandwidth of 0.37 nm and a low sidelobe of -28 dB. (p. 8)

11:30am

**RMB2 ■ Optical add/drop multiplexing and WDM channel management using programmable holographic filters**, R.J. Mears, A.D. Cohen, M.C. Parker, C.R.S. Fludger, N.J. Jones, *Cambridge Univ., UK*. We report experimental demonstration of a 100-GHz-resolution dynamically reconfigurable optical add/drop multiplexer/channel manager. The device can control an arbitrary channel set and provide 'top hot' passbands. (p. 11)

11:45am

**RMB3 ■ Fabrication of compact wavelength add/drop filter circuits using a cross grid array vertically coupled to microring resonators**, Sai T. Chu, Wugen Pan, Taro Kaneko, Yasuo Kokubun, *Kanagawa Academy of Science & Technology, Japan*; Brent E. Little, *Massachusetts Institute of Technology, USA*. Compact eight-channel add/drop filter with nominal bandwidths of 1 nm and channel spacing of 5.7 nm using vertically coupled glass rings is fabricated onto an area of 1.75 mm x 50 µm. (p. 14)

NOON

**RMB4 ■ Multiwavelength lasers fabricated using selective-area chemical beam epitaxy**, Peter J. Harmsma, Meint K. Smit, Y. Siang Oei, *Delft Univ. of Technology, The Netherlands*; Maarten R. Leys, Coen A. Verschuren, Hilbert Vonk, *Eindhoven Univ. of Technology, The Netherlands*. Integration of SOAs and passive waveguide devices using selective-area chemical beam epitaxy has successfully been applied to the fabrication of extended-cavity lasers and multiwavelength lasers. (p. 17)

12:15pm

**RMB5 ■ Wavelength tuning characteristics of the grated coupler sampled reflector laser for wavelength switching applications**, Olga A. Lavrova, Daniel J. Blumenthal, *UC-Santa Barbara, USA*. We report on static tuning characteristics of the grated coupler sampled reflector semiconductor lasers. Results of a numerical simulation and experimental measurements are also presented. (p. 20)

## Sierra Madre South

11:00am–12:30pm

**RMC ■ New Physics/Devices**

Shun-Lien Chuang, *University of Illinois, Urbana-Champaign, USA, Presider*

11:00am (Invited)

**RMCI ■ Single photon turnstile device**, Y. Yamamoto, O. Benson, J. Kim, C. Santori, *Stanford Univ., USA*. A single photon turnstile device is proposed and demonstrated to produce single photon flow with a well-regulated time interval. A new device structure with an isolated single QD and monolithic microcavity will be discussed. (p. 24)

11:30am (Invited)

**RMC2 ■ Quantum interference in optoelectronics**, A. Imamoglu, H. Schmidt, D. Nikonov, *UC-Santa Barbara, USA*. The progress in absorption cancellation via coherent resonant tunneling induced Fano interference in semiconductor quantum wells is discussed. (p. 27)

NOON (Invited)

**RMCI ■ Optical and transport properties of superlattice quantum wires**, Jong Chang Yi, *Hong Ik Univ., South Korea*. The optical properties of superlattice quantum wires grown on vicinal substrates and patterned V-grooves are analyzed by using a Luttinger-Kohn Hamiltonian. The transport properties of 1DEG in electron waveguides are also self-consistently analyzed. (p. 30)

## Anacapa

11:00am–12:30pm

**RMD ■ Waveguide Modeling**

Anand Gopinath, *University of Minnesota, USA, Presider*

11:00am

**RMD1 ■ Time-domain solution of vector wave equations by Taylor expansion**, J.A. Fleck, Jr., *Lawrence Livermore National Laboratory, USA*. The fourth-order Taylor expansion method is generalized to the solution of Maxwell's vector equations in two space dimensions for the transverse electric case. (p. 34)

11:15am

**RMD2 ■ New finite-element vectorial formulation for beam propagation in anisotropic media**, Helder F. Pinheiro, H.E. Hernández-Figueroa, *Univ. Estadual de Campinas, Brazil*. A novel vectorial finite-element beam propagation method for anisotropic media is presented. Numerical results show excellent agreement with well-known theoretical results and experimental data. (p. 37)

11:30am (Invited)

**RMD3 ■ The impedance/admittance transformation—an efficient concept for the analysis of optical waveguide structures**, Reinhold Pregla, *Fern Univ., Denmark*. MoL-algorithms for analysis of planar optical devices are described. The algorithms are based on generalized transmission-line equations for transverse fields and impedance/admittance transformation. (p. 40)

NOON

**RMD4 ■ WKB analysis of bend losses in optical waveguides**, W. Berglund, A. Gopinath, *Univ. Minnesota, USA*. A more complete WKB analysis of bend losses is given for a circularly curved optical waveguide. Using the WKB approximation with a conformal transformation of a curved optical waveguide, is shown to give more accurate bend loss results. (p. 43)

12:15pm

**RMD5 ■ Characterization of ultrashort low-loss waveguide bends for compact photonic integrated circuits**, M. Rajarajan, B.M.A. Rahman, K.T.V. Grattan, *City Univ., UK*; S.S.A. Obayya, H.A. El-Mikati, *Mansoura Univ., Egypt*. An accurate calculation of the radiation loss, and maximization of transmission and minimization of reflection losses, of an optical bend is analyzed using vectorial approaches. (p. 46)

12:30pm–2:00pm

Lunch (on your own)

## Sierra Madre North

2:00pm–3:30pm

**RME ■ WDM Devices: 2**

Rick D. Clayton, *Nortel Networks, Canada, Presider*

2:00pm

**RME1 ■ Tunable distributed Bragg reflector laser-electroabsorption modulator based on the identical active layer integration approach**, A. Ramdane, D. Meichenin, *France Telecom, France*; E. Vergnol, H. Sik, A. Ougazzaden, *Opto+, France*. We report on the monolithic integration of a high-performance distributed Bragg reflector multiple quantum well laser-electroabsorption modulator at 1.55  $\mu\text{m}$  using the same MQW active layer for the three optical functions involved in this device. (p. 50)

**2:15pm**

**RME2 ■ Monolithic integration of a widely tunable laser and an electroabsorption modulator,** Beck Mason, Greg A. Fish, Steven P. DenBaars, Larry A. Coldren, *UC-Santa Barbara, USA.* We report on the integration of a sampled-grating distributed Bragg reflector laser with a Franz-Keldysh modulator. The modulator is capable of >22 dB of extinction, with a -4.0 V bias, over the entire 41-nm tuning range of the laser. (p. 53)

**2:30pm (Invited)**

**RME3 ■ Frequency stabilized tunable laser technology,** Michel Cyr, *Nortel Networks, Canada.* This paper describes two approaches for achieving frequency stabilized laser module with 7 and 18 channels tunability capability on a 100-GHz spacing. Discussion on the evolution of the technology of 36 channels will be made. (p. 56)

**3:00pm (Invited)**

**RME4 ■ Wideband WDM application of electroabsorption modulator-integrated DFB lasers,** Hiroaki Takeuchi, *NTT Photonics Laboratories, Japan.* Electroabsorption (EA) modulator-integrated distributed feedback (DFB) lasers operating in wide wavelength range, from 1530 nm to 1610 nm, are described from the point of wideband wavelength-division multiplexing (WDM) application. Polarization-independent EA modulators as optical gates are also reviewed. (p. 59)

## Sierra Madre South

---

**2:00pm–3:30pm**

### **RMF ■ Material and Characterization**

Bill Steier, *University of Southern California, USA, Presider*

**2:00pm**

**RMF1 ■ Large second-order optical nonlinearity in Ge-doped SiO<sub>2</sub> thin films,** Jabri Khaled, Takumi Fujiwara, Akira J. Ikushima, *Toyota Technological Institute, Japan.* Large second-order optical nonlinearity with *d* coefficient as high as  $12.5 \pm 0.6 \text{ pm/V}$  has been induced by UV-poling in Ge-doped SiO<sub>2</sub> thin films. Long decay time-constant of more than seven years has been achieved by loading the films in hydrogen prior to UV-poling. (p. 64)

**2:15pm**

**RMF2 ■ Alkali bismuth gallate glasses for 1.3-μm optical amplifiers,** S.Q. Man, E.Y.B. Pun, P.S. Chung, *City Univ. Hong Kong, Hong Kong.* Alkali bismuth gallate glass as suitable host for rare-earth praseodymium operating at 1.3-μm wavelength is demonstrated. The optical properties of these glasses were characterized. (p. 67)

**2:30pm**

**RMF3 ■ Spatial hole burning in second-order excitation probability distribution for densely erbium-doped fibers,** Sten Helmfrid, Dan Bremberg, Bozena Jaskorzynska, *Royal Institute of Technology, Sweden;* Jacob Philipsen, *Technical Univ. Denmark, Denmark.* The upconversion rate in densely erbium-doped fibers is investigated and explained in terms of spatial hole burning in the second-order distribution function of excitation energy. (p. 70)

**2:45pm**

**RMF4 ■ Method for characterization of clustering and homogeneous upconversion in Er-doped waveguides,** Marcin Swillo, Dan Bremberg, Bozena Jaskorzynska, Sten Helmfrid, *Royal Institute of Technology, Sweden;* Jacob L. Philipsen, *Technical Univ. Denmark, Denmark.* We propose and demonstrate a method for estimating a portion of unexcitable, clustered ions, and for characterizing the homogeneous upconversion in Er-doped waveguides. (p. 73)

**3:00pm**

**RMF5 ■ Optical isolation based on nonreciprocal phase shift in a Mach-Zehnder interferometer,** J. Fujita, M. Levy, R.U. Ahmad, R.M. Osgood, Jr., *Columbia Univ., USA;* M. Randles, *Litton Airtron SYNOPTICS, USA;* C. Gutierrez, R. Villareal, *Southwest Texas State Univ., USA.* We demonstrate 45° nonreciprocal phase shift in an integrated-optic YIG-waveguide structure; its suitability for use in a Mach-Zehnder-based isolator is via a hybrid isolation measurement. (p. 76)

**3:15pm**

**RMF6 ■ Temperature-insensitive glass microring resonator add/drop filters by means of a polymer overlay,** S.T. Chu, W. Pan, S. Sato, *Kanagawa Academy of Science and Technology, Japan;* Y. Kokubun, *Kanagawa Academy of Science and Technology and Yokohama National Univ., Japan;* B.E. Little, *Massachusetts Institute of Technology, USA;* S. Suzuki, *Yokohama National Univ., Japan.* The temperature dependence of the resonant wavelength of glass microring resonator channel dropping filters is reduced to -0.0025 nm/°C over the range of 25°C to 55°C by the use of a PMMA-TFMA polymer cover layer. (p. 79)

## Anacapa

---

**2:00pm–3:15pm**

### **RMG ■ VCSEL Modeling**

K. Alan Shore, *University of Wales, UK, Presider*

**2:00pm (Invited)**

**RMG1 ■ Quantum dots for GaAs-based long-wavelength edge-emitting and VCSELs,** D.G. Deppe, D.L. Huffaker, Z. Zou, S. Csutak, *Univ. Texas at Austin, USA.* InGaAs/GaAs quantum dots are described for edge-emitting lasers and vertical-cavity surface-emitting lasers (VCSELs) that operate in the 1.0 μm to 1.3 μm wavelength range. (p. 84)

**2:30pm (Invited)**

**RMG2 ■ Modeling and simulation of transverse-mode dynamics of VCSELs**, C.Z. Ning, P.M. Goorjian, *NASA Ames Research Center, USA*. We show how to incorporate microscopic gain model and arbitrary gain and index guidings into a space-time resolved model to simulate transverse-mode dynamics of vertical-cavity surface-emitting lasers (VCSELs). (p. 87)

**3:00pm**

**RMG3 ■ Split-step time-domain dynamic modeling of complex-coupled distributed feedback laser diodes**, Byoung-Sung Kim, Youngchul Chung, *Kwangwoon Univ., South Korea*. Complex-coupled distributed feedback laser diodes are modeled by novel split-step time-domain model, which is shown to be much more accurate and efficient than conventional methods. (p. 88)

## **Grand Ballroom Foyer**

---

**3:30pm–5:30pm**

**RMH ■ Poster Session**

**RMH1 ■ Local normal mode model for PHASAR-based wavelength-division multiplexing devices**, Michael Rivera, *Corning Inc., USA*. Phasars are modeled using local normal mode theory. A qualitative model for the waveguide array between the free propagation regions is developed to understand the impact of fundamental processing issues that contribute to nonadjacent channel cross talk. The fundamental principles of this model, its limitations, and some examples are laid out. (p. 92)

**RMH2 ■ Transverse-mode dynamics of VCSELs under current modulation**, Peter M. Goorjian, C.Z. Ning, *NASA Ames Research Center, USA*. The effects of transverse-mode dynamics on current modulation of vertical-cavity surface-emitting lasers (VCSELs) are investigated by solving an approximation to the Maxwell Semiconductor Block equations. (p. 95)

**RMH3 ■ Interdiffused InGaAsP/InP quantum well lasers**, L. Zhan, E.Y.B. Pun, K.S. Chan, H.P. Ho, *City Univ. Hong Kong, Hong Kong*. The optical gain of interdiffused InGaAsP/InP quantum well structures is calculated numerically including the effects of electrostatic deformation and density-dependent optical dephasing time. (p. 98)

**RMH4 ■ Propagating beam analysis based on the finite-difference formula for a general position of interfaces**, Junji Yamauchi, Shu Nakamura, Hisamatsu Nakano, *Hosei Univ., Japan*. A modified finite-difference formula is applied to the eigenmode and propagating beam analyses. Discretization error is reduced in tilted and tapered rib waveguides. (p. 101)

**RMH5 ■ Pade approximation analysis of reflection at optical waveguide facets**, Hatem El-Refaei, David Yevick, *Queen's Univ., Canada*; Ian Betty, *Nortel Networks, Canada*. We analyze, for the first time to our knowledge, the reflection problem from the interface between two arbitrary, lossless, and isotropic transverse refractive-index distributions  $n_a(x,y)$  and  $n_b(x-y)$  using stable and accurate modified Pade approximation methods. (p. 104)

**RMH6 ■ Noise in semiconductor cascade lasers**, F. Rana, S.G. Patterson, R.J. Ram, *Massachusetts Institute of Technology, USA*. A comprehensive model for noise in semiconductor series cascade lasers and parallel laser arrays is presented, and performance of cascade lasers in RF photonic links is discussed. (p. 107)

**RMH7 ■ Feedback regimes in a coupled cavity multimode laser diode model**, Iestyn Pierce, Paul S. Spencer, Paul Rees, K. Alan Shore, *Univ. Wales, UK*. We present a multimode coupled cavity model of laser operation with feedback. Feedback regimes are observed and compared with results from single-mode models. (p. 110)

**RMH8 ■ The single-mode condition for rib waveguides, revised**, R. Hauffe, U. Siebel, K. Petermann, *Technical Univ. Berlin, Germany*; C. Kostrzewa, *Siemens AG, Germany*. The single-mode condition usually defined by cutoff needs to be modified for practical rib waveguide designs in integrated optics. Modified design rules are presented. (p. 112)

**RMH9 ■ Efficiency analysis of quantum well lasers using PIC3D**, Joachim Piprek, Patrick Abraham, John E. Bowers, *UC–Santa Barbara, USA*. Using commercial software, we extract the contribution of lateral leakage, vertical leakage, and quantum well recombination losses to the differential internal efficiency from measurements at different temperatures. (p. 115)

**RMH10 ■ Variation of defect-mode transmission in a two-dimensional photonic bandgap crystal**, K.B. Chung, *Hong Ik Univ., South Korea*. This paper presents the numerically computed transmission characteristics of various defects with different size, shape, and permittivity in a finite-size two-dimensional photonic bandgap crystal. (p. 118)

**RMH11 ■ Optical waveguiding and steering in an active semiconductor slab structure**, Xuesong Dong, Patrick LiKamWa, *CREOL, Univ. Central Florida, USA*; John Loehr, Ron Kaspi, *Wright-Patterson AFB, USA*. We present experimental results of current-controlled beam guiding and steering in an active GaAs/AlGaAs slab waveguide based on electrically injected carrier-induced refractive index change. (p. 121)

## **Plaza del Sol**

---

**6:00pm–7:30pm**

**Reception**

■ Tuesday  
■ July 20, 1999

## Sierra Madre North

8:30am–10:00am

### RTuA ■ WDM Devices: 3

Bahram Jalali, *University of California, Los Angeles, USA*, Presider

8:30am

**RTuA1 ■ An all-pass filter for tunable dispersion and dispersion slope compensation**, C.K. Madsen, G. Lenz, A.J. Bruce, M.A. Cappuzzo, L.T. Gomez, R.E. Scotti, *Bell Laboratories, Lucent Technologies, USA*. A completely tunable all-pass filter is presented, capable of dispersion slope compensation. A 20-GHz channel spacing filter was demonstrated using  $\Delta = 2\%$  Ge-doped silica waveguides. (p. 126)

8:45am

**RTuA2 ■ A novel two-in-one arrayed waveguide grating MUX/DEMUX**, Hyoun-Soo Kim, Yeong-Gyu Lee, Dongkyoon Han, Hyung-Seung Song, *Samsung Electronics Co., Ltd., Korea*. We propose and demonstrate a novel TIO (two-in-one) AWG, which operates in both directions, simultaneously, and which will reduce the number of devices used in wavelength-division multiplexed systems by half. The proposed TIO AWG has two extra ports, one on each end of the AWG, designated to be either the input or the output depending on the desired function. (p. 129)

9:00am

**RTuA3 ■ Improvements in the yield of arrayed waveguide demultiplexers by the use of transition offsets**, Stephen Day, James Whiteaway, Alan Fielding, *Nortel Networks, UK*. The beam propagation method has been used to study the variable wavelength slope within the passband of AWG components and to design improved components. Experimental results show excellent correlation with predictions from modeling. (p. 132)

9:15am

**RTuA4 ■ An infinite impulse response multichannel frequency selector**, C.K. Madsen, *Bell Laboratories, Lucent Technologies, USA*. In this paper, an architecture and design algorithm is presented for an infinite impulse response (IIR) filter based on optical all-pass filters. (p. 135)

9:30am

**RTuA5 ■ Wavelength- and polarization-insensitive integrated directional couplers using Mach-Zehnder structures**, Thomas E. Murphy, Brent E. Little, Henry I. Smith, *Massachusetts Institute of Technology, USA*. We describe the design, fabrication, and measurement of a class of robust integrated directional couplers, which exhibit insensitivity to polarization, wavelength, and fabrication parameters. (p. 138)

9:45am

**RTuA6 ■ An integrated power splitter with ultralow loss**, Jong Sool Jeong, Byueng-Su Yoo, Kyung-Sook Hyun, *ETRI, South Korea*. We propose a phase grating integrated power splitter with high coupling efficiency. It is also found that ultra-low loss power splitting can be achieved without tapering the output waveguides. (p. 141)

## Sierra Madre South

8:30am–10:00am

### RTuB ■ Photonic Nanocircuits

Richard W. Ziolkowski, *University of Arizona, USA*; Brent E. Little, *Massachusetts Institute of Technology, USA*, Presiders

8:30am (Invited)

**RTuB1 ■ Photonic nanostructures and resonators**, Hermann A. Haus, *Massachusetts Institute of Technology, USA*. The exceptional characteristics of high-index contrast waveguide structures will be discussed. High-quality waveguide bends, crossings, and resonator structures for wavelength-division multiplexing applications will be described. (p. 146)

9:00am (Invited)

**RTuB2 ■ Ultrasmall and ultra-low-threshold microdisk injection lasers with evanescent coupled elements**, Toshihiko Baba, *Yokohama National Univ., Japan*. Recent progress on microdisk injection lasers are reported. Size reduction, room-temperature cw lasing with microampere order threshold, and some applications investigated are presented. (p. 149)

9:30am

**RTuB3 ■ Design and analysis of nonlinear microring resonators for third-order harmonic generation**, Vien Van, *Univ. Waterloo, Canada*; Brent E. Little, *Massachusetts Institute of Technology, USA*. The design of a nonlinear, high-Q microring resonator for third-order harmonic frequency generation is presented, accompanied by finite-difference time-domain analysis of the device's performance. (p. 151)

9:45am

**RTuB4 ■ Cascade coupled microring resonators for spectral cleanup and shaping in add/drop filters**, Brent E. Little, *Massachusetts Institute of Technology, USA*; Sai Tak Chu, Wugen Pan, *Kanagawa Academy of Science and Technology, Japan*; Taro Kaneko, Yasuo Kokubun, *Kanagawa Academy of Science and Technology and Yokohama National Univ., Japan*. Multiple microring resonators coupled in cascade and coupled in series are realized for the purpose of spectrum cleanup and spectral shaping. Fabricated devices consist of glass ring resonators 10  $\mu\text{m}$  to 25  $\mu\text{m}$  in radius and with Qs of 1,500 to 15,000. (p. 154)

## Anacapa

---

8:30am–10:15am

### RTuC ■ IR, Mid-IR, and THz Modeling

Dennis Deppe, *University of Texas at Austin, USA, Presider*

8:30am

**RTuC1 ■ Coherent pump-probe interactions and terahertz intersubband gain in semiconductor quantum wells**, Ansheng Liu, C.Z. Ning, *NASA Ames Research Center, USA*. Terahertz gain due to intersubband transitions in optically pumped semiconductor quantum wells is calculated nonperturbatively. We show that coherent pump-probe interactions contribute significantly to the THz gain. (p. 158)

8:45am

**RTuC2 ■ Optically pumped type II interband terahertz lasers**, I. Vurgaftman, J.R. Meyer, *Naval Research Laboratory, USA*. We demonstrate that in the terahertz spectral region, optically pumped type II interband lasers are expected to have longer lifetimes, higher optical gains, and lower internal losses than intersubband cascade lasers. (p. 161)

9:00am (Invited)

**RTuC3 ■ Electronic structure engineering of mid-infrared lasers**, Michael E. Flatte, J.T. Olesberg, T.F. Boggess, T.C. Hasenberg, *Univ. Iowa, USA*; C.H. Grein, *Univ. Illinois at Chicago, USA*. Mid-infrared heterostructures have remarkably flexible optoelectronic properties due to the large band offsets among three nearly-lattice-matched binary semiconductors. Some successes and further possibilities for engineering these properties for lasers will be presented. (p. 164)

9:30am (Invited)

**RTuC4 ■ Carrier transport in GaInP laser structures**, Peter Blood, Catherine Molloy, Scott Wood, *Cardiff Univ., UK*. We have directly observed electron leakage in AlGaInP lasers, determined the relative contributions of drift and diffusion, and studied the impact on modulation response. (p. 167)

10:00am

**RTuC5 ■ Optical properties of active semiconductor waveguides for integrated photonics device modeling**, Valery I. Tolstikhin, *Optiwave Corp., Canada*. A physics-based model for optical properties of the active semiconductor devices has been developed, which is applied to the analysis of free-carrier effects in a typical InP-based integrated photonics structure. (p. 170)

## Grand Ballroom Foyer

---

10:00am–10:30am

Coffee Break

## Sierra Madre North

---

10:30am–NOON

### RTuD ■ Integrated Optical Switches

Jaymin Amin, *Corning Inc., USA, Presider*

10:30am

**RTuD1 ■ Polarization-independent InP-based space switch with double-etched waveguide structure**, D.H.P. Maat, F.H. Groen, H. van Brug, H.J. Frankena, C.G.P. Herben, *Delft Univ. of Technology, The Netherlands*; B.H.P. Dorren, *Eindhoven Univ. of Technology, The Netherlands*. Application of a double-etch technique to MZI-switches leads to 25% reduction of switch length, crosstalk performance is not affected, and insertion loss is higher by 1 dB. (p. 174)

10:45am

**RTuD2 ■ Polymeric 1 x 3 thermo-optic switch**, Tae-Won Oh, Sang-Yung Shin, *Korea Advanced Institute of Science and Technology, South Korea*. We demonstrate a polymeric 1 x 3 thermo-optic switch, which has a simple structure as a basic switching unit. The measured cross talk is >20 dB. (p. 177)

11:00am

**RTuD3 ■ MEMS two-dimensional scanning mirror for dynamic alignment in optical interconnect**, Guo-Dung J. Su, Wibool Piyawattanametha, Raphael Rollier, Li Fan, Ming C. Wu, *UC-Los Angeles, USA*. We report on a micro-electro-mechanical systems (MEMS) two-dimensional scanning mirror for active optical alignment and dynamic tracking of alignment in free-space optical interconnect. Experimentally, a 400  $\mu\text{m} \times 400 \mu\text{m}$  scanning mirror with  $\pm 5.7^\circ$  scanning angles has been successfully demonstrated. (p. 180)

11:15am

**RTuD4 ■ Polymeric tunable optical attenuator for dynamic channel power regulation in WDM systems**, Sang-Shin Lee, Yong-Sung Jin, Yung-Sung Son, *LG Corporate Institute of Technology, Korea*; Jae-Hoon Jung, Ki-Woon Na, *LG Information & Communications, Ltd., South Korea*. A tunable optical attenuator was fabricated using polymeric devices with an asymmetric branching waveguide, and was used to demonstrate dynamic channel power regulation within 0.4 dB in wavelength-division multiplexing (WDM) systems. (p. 183)

11:30am (Invited)

**RTuD5 ■ Silica-based thermo-optic switch with layered wiring patterns**, Mikitaka Itoh, Masayuki Okuno, Takashi Goh, Kazuyuki Moriwaki, Yasuji Ohmori, Akira Hir meno, *NTT Photonics Laboratories, Japan*. We demonstrate a thermo-optic switch with double-layered wiring, which is necessary for the realization of densely integrated large-scale thermo-optic switches. (p. 186)

## Sierra Madre South

---

10:30am–12:15pm

### RTuE ■ PBG Structures and Devices

Richard W. Ziolkowski, *University of Arizona, USA*; Brent E. Little, *Massachusetts Institute of Technology, USA*, Presiders

10:30am (Invited)

**RTuE1 ■ Photonic microstructures: a key approach for high-density integrated optoelectronics**, R.M. De La Rue, C.J.M. Smith, C.D.W. Wilkinson, T.F. Krauss, *Univ. Glasgow, UK*; H. Benisty, C. Weisbuch, D. Labilloy, *Ecole Polytechnique, France*; R. Houdré, M. Illegems, U. Oesterle, *Ecole Polytechnique Fédérale Lausanne, Switzerland*. Photonic microstructure technology now being developed enables a wide range of compact devices to be integrated within conventional epitaxial III-V semiconductor waveguide structures. (p. 190)

11:00am

**RTuE2 ■ FDTD analysis of PBG waveguide power splitters and switches for integrated optics applications**, Richard W. Ziolkowski, *Univ. Arizona, USA*; Masahiro Tanaka, *Gifu Univ., Japan*. A waveguide Y power splitter and an associated defect switch formed in a triangular PBG structure appropriate for integrated optics applications was designed successfully with a finite-difference time-domain (FDTD) simulator. (p. 194)

11:15am

**RTuE3 ■ Observation of light propagation in photonic crystal optical waveguides with bends**, Toshihiko Baba, Naoyuki Fukaya, Jun Yonekura, *Yokohama National Univ., Japan*. We observed the light propagation in two-dimensional photonic crystal waveguides with bends. Wavelength and polarization dependence was observed at a wavelength of 1.47–1.60 microns. (p. 197)

11:30am (Invited)

**RTuE4 ■ Electromagnetic bandgap structures: advances in computational techniques**, Yahya Rahmat-Samii, *UC-Los Angeles, USA*. Electromagnetic bandgap structures (the counterpart of the optical photonic bandgaps, PBG) are synthesized two-dimensional or three-dimensional multilayered periodic structures that effectively prevent the propagation of electromagnetic waves in a specified band of frequency. (p. 200)

NOON

**RTuE5 ■ FDTD modeling of complex integrated optics structures**, Stoyan Tanev, Dazeng Feng, Velko P. Tzolov, Z. Jan Jakubczyk, *Optiwave Corp., Canada*. We demonstrate the ability of the finite-difference time-domain (FDTD) method to model a complex integrated optics structure—a focusing waveguide grating coupler integrated with a two-dimensional photonic crystal mirror and a micro Fresnel lens. (p. 202)

## Anacapa

---

10:30am–11:45am

### RTuF ■ GaN Device Modeling

Shuji Seki, *NTT, Japan*, Presider

10:30am (Invited)

**RTuF1 ■ Many-body theory of gain in InGaN and GaN quantum well lasers**, W.W. Chow, *Sandia National Laboratories, USA*. This paper describes a III-V nitride quantum well laser theory based on the semiconductor Bloch equations, with collisions treated at the level of quantum kinetic equations. Application of the theory to investigate laser threshold will be discussed. (p. 206)

11:00am (Invited)

**RTuF2 ■ Piezoelectric and spontaneous polarization effects in nitride heterostructure optoelectronics**, Jasprit Singh, Hongtao Jiang, Yifei Zhang, *Univ. Michigan, USA*. Properties of heterostructures based on III-V nitrides (InN, GaN, and AlN) are dramatically influenced by spontaneous polarization effects and strain-induced piezoelectric effects. These effects can produce built-in electric fields of  $\sim 10^6$  V/cm and introduce sheet charges of  $\sim 10^{13}$  cm $^{-3}$ . Consequences of these effects will be discussed. (p. 209)

11:30am

**RTuF3 ■ Analysis of excitons in gallium nitride-based quantum wells under valence band mixing, strain, and piezoelectric field**, C. Bulutay, N. Dagli, A. Imamoğlu, *UC-Santa Barbara, USA*. A coupled variational and finite element approach is used to analyze excitons in gallium nitride-based quantum wells. Binding energy, oscillator strength, and the absorption spectra are presented. (p. 212)

NOON–1:30pm

Lunch Break (on your own)

## Sierra Madre North

---

1:30pm–3:00pm

### RTuG ■ Active Devices

Ramu V. Ramaswamy, *University of Florida, USA*, Presider

1:30pm

**RTuG1 ■ Bidirectional optical module based on a GoS hybrid integration for access network applications**, Maurizio Lenzi, Massimo Magliocco, Lucio Cibinetto, *Italtel S.p.A., Italy*. We developed a bidirectional optical module in glass on silicon technology, including both active (transmitter and receiver) and passive (wavelength-division multiplexing) functionality. (p. 216)

1:45pm

**RTuG2 ■ Second-harmonic generation in 10- $\mu\text{m}$ -thick single-crystal  $z$ -cut  $\text{LiNbO}_3$  films obtained by epitaxial lift-off**, A.M. Radojevic, M. Levy, R.M. Osgood, Jr., *Columbia Univ., USA*; A. Kumar, H. Bakhrus, *SUNY-Albany, USA*. Single-crystal microns-thick  $z$ -cut  $\text{LiNbO}_3$  films obtained by epitaxial lift-off are used for efficient temperature phase-matched frequency doubling at a wavelength of 1.55  $\mu\text{m}$ . (p. 219)

2:00pm (Invited)

**RTuG3 ■ High-speed Er-doped  $\text{LiNbO}_3$  waveguide lasers**, Hubertus Suche, *Univ. Paderborn, Germany*. The actual status of electro-optically mode-locked and Q-switched Ti:Er: $\text{LiNbO}_3$  waveguide lasers is reviewed. Single supermode harmonic mode-locking up to 10 GHz, repetition rate doubling, and Q-switched operation with pulse peak powers up to 2.5 kW are discussed. (p. 222)

2:30pm

**RTuG4 ■ Optimized Si-on- $\text{LiNbO}_3$  waveguide reflectors with low loss and record-high reflectance**, Hao Feng, Robert F. Tavlykaev, Ramu V. Ramaswamy, *Univ. of Florida, USA*. A 6.5-mm-long reflector in Si-on- $\text{LiNbO}_3$  at 1.5  $\mu\text{m}$  with reflectance of 88% and 4.3A bandwidth is realized in conformance with theory. (p. 225)

2:45pm

**RTuG5 ■ Proposal of DFB lasers with refractive-index modulated upper cladding layer of the grating for reducing spatial hole burning effect**, Hong-Seok Lee, Byoung-Ho Lee, *Seoul National Univ., South Korea*; Hong-Kuk Kim, Boo-Gyun Kim, *Soongsil Univ., South Korea*. A new structure of distributed feedback (DFB) laser with effective quarter wavelength phase shift and the effect of distributed coupling is proposed to reduce the spatial hole burning effect. (p. 228)

## Sierra Madre South

---

1:30pm–3:15pm

**RTuH ■ High-Q Resonators**

Richard W. Ziolkowski, *University of Arizona, USA, Presider*

1:30pm (Invited)

**RTuH1 ■ In-plane photonic crystal microcavities for high-Q optical resonators**, Axel Scherer, *California Institute of Technology, USA*. Abstract not available. (p. 232)

2:00pm (Invited)

**RTuH2 ■ Coupling, Q-factor, and integration aspects of microsphere applications**, V.S. Ilchenko, X.S. Yao, L. Maleki, *California Institute of Technology, USA*. The report addresses state-of-the-art in Q, theory and practice of near-field coupling, recent fiber pigtailing demonstration with microspheres, and integration prospects with planar waveguides. (p. 233)

2:30pm (Invited)

**RTuH3 ■ Coupling of excited molecules and nanocrystals with photonic atoms (microspheres) and photonic molecules**, S. Arnold, N.L. Goddard, *Polytechnic Univ., USA*. Photonic atoms act as meso-optic high-Q resonators. Emission studies of nanoscopic “antennae” coupled to photonic atoms and photonic molecules (coupled photonic atoms) provide a possible harbinger for molecular design of microcavity devices. (p. 236)

3:00pm

**RTuH4 ■ Novel techniques for whispering-gallery-mode excitation in silica microspheres**, J.P. Laine, B.E. Little, D. Lim, H.A. Haus, *Massachusetts Institute of Technology, USA*. ARROW waveguide structures and etched fiber tapers are proposed as methods for coupling light into the high-Q modes of dielectric spherical resonators. (p. 238)

## Anacapa

---

1:30pm–3:00pm

**RTuI ■ Finite-Difference Modeling**

Yongchul Chung, *Kwangwoon University, South Korea, Presider*

1:30pm (Invited)

**RTuI1 ■ High-accuracy finite-difference equations for simulation of photonic structures**, G. Ronald Hadley, *Sandia National Laboratories, USA*. We present the derivation of sixth-order accurate finite-difference representations of the Helmholtz Equation and use them to compute highly accurate vector eigenmode solutions. (p. 242)

2:00pm

**RTuI2 ■ Stability condition of the nonlinear FDTD method for optical device simulation**, Vien Van, Sujeev K. Chaudhuri, *Univ. Waterloo, Canada*. We present a stability analysis of the nonlinear finite-difference time-domain (FDTD) method for optical device simulation. Numerical results for second- and third-order optical nonlinearities will be discussed. (p. 244)

2:15pm

**RTuI3 ■ Extended finite-difference time domain beam propagation methods**, Jun Shibayama, Tomokazu Takahashi, Junji Yamauchi, Hisamatsu Nakano, *Hosei Univ., Japan*. Efficient time-domain beam propagation methods are developed. The Douglas scheme is employed for a slab waveguide. Cylindrical coordinates are introduced for a fiber grating. (p. 247)

**2:30pm**

**RTuI4 ■ N-space staircase-free FDTD formulation for arbitrary material distributions: numerical investigations of a focusing grating coupler in dielectric waveguides**, Kim Dridi, *Technical Univ. Denmark, Denmark*; Jan S. Hesthaven, *Brown Univ., USA*. Stable and accurate finite-difference time-domain (FDTD) schemes are developed for arbitrary geometries with multiple materials. Numerical investigations of a focusing grating coupler are presented. (p. 250)

**2:45pm**

**RTuI5 ■ Modeling of thin dielectric layers in finite-difference schemes**, Stefan F. Helfert, Reinhold Pregla, *Fern Univ. Germany*. The modification of the finite-difference scheme due to thin dielectric layers is described. Starting with analytical formulas, the required equations are derived. (p. 253)

## **Grand Ballroom Foyer**

---

**3:00pm–3:30pm**

**Coffee Break**

## **Sierra Madre North**

---

**3:30pm–5:00pm**

### **RTuJ ■ Optical Transmission and WDM Modeling**

Carl M. Weinert, *Heinrich-Hertz Institute, Germany*, Presider

**3:30pm (Invited)**

**RTuJ1 ■ New approaches to modeling high-data-rate optical fiber transmission**, C.R. Menyuk, *Univ. Maryland–Baltimore County, USA*. Accurate modeling has become crucial for designing high-data-rate optical fiber transmission systems. New approaches aimed at meeting this need are described. (p. 258)

**4:00pm (Invited)**

**RTuJ2 ■ Wavelength-domain simulation: an efficient technique for the design of multiwavelength optical networks**, I. Roudas, N. Antoniades, R.E. Wagner, *Corning Inc., USA*; D.H. Richards, J.L. Jackel, *Telcordia Technologies, USA*. This paper reviews a simplified computer representation for the optical signals and network components in the optical transport layer of multiwavelength optical networks. This representation can be used for efficient steady-state and transient power-budget computations. (p. 261)

**4:30pm**

**RTuJ3 ■ Dynamic dispersion compensation using a parabolic phase-apertured active arrayed-waveguide grating**, Michael C. Parker, *Fujitsu Telecom Europe Ltd., UK*; Stuart D. Walker, *Univ. Essex, UK*. We simulate dynamic dispersion compensation of up to  $\pm 3100$  ps/nm using a combination of trapezoidal and parabolic-profiled active regions in the Fourier plane of an arrayed-waveguide grating. (p. 264)

**4:45pm**

**RTuJ4 ■ Active arrayed-waveguide gratings for equalization and wavelength-division multiplexed channel management**, A. Yiptong, R.J. Mears, *Cambridge Univ., UK*; M.C. Parker, *Fujitsu Telecom Europe Ltd., UK*. We present simulation results demonstrating active arrayed-waveguide gratings functioning as high-resolution (100-GHz) dynamic spectral equalizers and optical add/drop multiplexers, based on holographic Fourier techniques. (p. 267)

## **Sierra Madre South**

---

**3:30pm–5:00pm**

### **RTuK ■ Waveguide Modulators**

Wolfgang Sohler, *University GH Paderborn, Germany*, Presider

**3:30pm**

**RTuK1 ■ Linearized optical directional coupler modulators**, Chanin Laliew, Xiaobo Zhang, Anand Gopinath, *Univ. Minnesota, USA*. Optical directional coupler modulators with high linearity in their response function have been designed, fabricated, and tested. The results show low-harmonic distortion levels, which indicates that the modulators exhibit highly linear behavior as desired. (p. 272)

**3:45pm**

**RTuK2 ■ Integrated optical AC voltage sensor fabricated on LiNbO<sub>3</sub> platform**, Tadashi Ichikawa, Manabu Kagami, Hiroshi Ito, *Toyota Central R&D Laboratories Inc., Japan*. An integrated optical AC voltage sensor fabricated on an LiNbO<sub>3</sub> platform using a laser ablation technique. Detected sensitivities were 0.2 mV at frequency from 6 Hz to 1 GHz. (p. 275)

**4:00pm**

**RTuK3 ■ Enhancement of electro-optic effect in stoichiometric LiNbO<sub>3</sub>**, Takumi Fujiwara, Akira J. Ikushima, *Toyota Technological Institute, Japan*; Yasunori Furukawa, Kenji Kitamura, *National Institute for Research in Inorganic Materials, Japan*. Electro-optic effect ( $r_{33}$ ) in stoichiometric lithium niobate (LiNbO<sub>3</sub>) crystals has been found to be at least 20% larger than that of LiNbO<sub>3</sub> with congruent composition. (p. 278)

**4:15pm**

**RTuK4 ■ High-power single-mode LiTaO<sub>3</sub> waveguides with improved temporal stability**, D.B. Maring, R.F. Tavlykaev, R.V. Ramaswamy, *Univ. Florida, USA*; S.M. Kostritskii, *Kemerovo State Univ., Russia*. Single-mode proton-exchanged waveguides in LiTaO<sub>3</sub> at 1.55  $\mu$ m with photorefractive resistance far superior to that in LiNbO<sub>3</sub> and improved temporal stability are demonstrated. (p. 281)

**4:30pm (Invited)**

**RTuK5 ■ High-speed LiNbO<sub>3</sub> modulators for telecommunications**, Rangaraj Madabhushi, NEC Corp., Japan. We present ultrahigh-speed Ti:LiNbO<sub>3</sub> optical modulators for telecommunication applications, with very low microwave attenuation and low driving voltage structures. We confirmed the capabilities of these modulators at 40-Gbit/s applications through wave form measurements. (p. 284)

## Anacapa

---

**3:30pm–5:00pm**

**RTuL ■ Mode Control**

Yoshi Nakano, Tokyo Institute of Technology, Japan, Presider

**3:30pm (Invited)**

**RTuL1 ■ Hierarchical modeling of semiconductor distributed feedback laser diodes**, Xun Li, Wei-Ping Huang, Univ. Waterloo, Canada. Modeling and simulation of the advanced laser diodes is usually difficult and time-consuming due to the complexity of their material and geometrical properties and the physical processes involved in the operation. We have developed a hierarchical model that divides the simulation into several levels in order to achieve a good balance between the accuracy and the efficiency. An overview of this model, the related simulation tools, the calculated results, and the comparisons will be presented. (p. 288)

**4:00pm**

**RTuL2 ■ An iterative bidirectional beam propagation method for multi-interface reflective photonic devices**, H. Rao, R. Scarmozzino, M.J. Steel, R.M. Osgood, Jr., Columbia Univ., USA. We provide a brief review of the formulation and then demonstrate the capability of the approach in simulating photonic bandgap (PBG) structures through an example. We only consider two-dimensional TE cases, although in principle the formulation can be extended to TM and even three-dimensional problems. (p. 291)

**4:15pm**

**RTuL3 ■ Large-signal regime nearly-degenerate four-wave mixing in multisection laser diodes**, J.M. Tang, K.A. Shore, Univ. Wales, UK. Nearly-degenerate four-wave mixing behaviors depend significantly on probe injection into either facet of a multisection laser diode. Carrier diffusion and pump depletion are important in determining the processes. (p. 294)

**4:30pm**

**RTuL4 ■ Fundamental cavity mode of a spot-size converted Fabry–Perot semiconductor laser**, G. Hugh Song, Kwangju Institute of Science and Technology, Korea; Jeong K. Ji, Ahn Goo Choo, Samsung Advanced Institute of Technology, Korea. The fundamental cavity mode of a spot-size converted Fabry–Perot semiconductor laser is analyzed based on coupled local-mode theory. The analysis gives a new guideline on the design of spot-size converter integrated semiconductor lasers. (p. 297)

**4:45pm**

**RTuL5 ■ Transmission, reflection, alignment tolerance, and far-field profiles of spot-size converters**, B.M.A. Rahman, M. Rajarajan, P.K. Arasaratnam, K.T.V. Grattan, City Univ., London, UK; T. Wongcharoen, Univ. Bangkok, Thailand; M. Meyer, Univ. Dortmund, Germany. Improved transmission, with reduced reflection coefficients, and relaxed alignment tolerances, coupled with narrower far-field profiles, are shown for both tapered and uniform guided-wave spot-size converters. (p. 300)

**5:00pm–5:30pm**

**Refreshment Break**

## Sierra Madre

---

**5:30pm–**

**Postdeadline Paper Session**

Fred Heismann, Qtera Corporation, USA, Presider

■ Wednesday  
■ July 21, 1999

## San Rafael

---

8:45am–10:15am

### JWA ■ Joint Session 1 (IPR & PS): Technologies for Optical Cross Connects

Julian B. Soole, *Bell Laboratories, Lucent Technologies, USA, Presider*

8:45am

**JWA1 ■ Micromachined scalable fiber-optic switch,** Paul Hagelin, Uma Krishnamoorthy, Carl Arft, Jonathan Heritage, Olav Solgaard, *UC-Davis, USA*. We demonstrate a scalable single-mode optical fiber switch architecture using surface-micromachined mirrors. The switch has –4.2 dB insertion loss and –50 dB cross talk. (p. 304)

9:00am

**JWA2 ■ A robust, low cross talk, InGaAsP/InP total-internal-reflection switch for optical cross-connect applications,** Ian Betty, Roghieh Rousina-Webb, *Nortel Networks, Canada; Chi Wu, California Institute of Technology, USA*. We report a robust, total-internal-reflection switch designed for a novel, compact, and scalable cross-connect architecture. Bar-state loss <0.5 dB with cross talk >20 dB is achieved. (p. 307)

9:15am (Invited)

**JWA3 ■ Monolithically integrated wavelength-selective cross connects,** C.R. Doerr, *Bell Laboratories, Lucent Technologies, USA*. Integrated wavelength-selective cross connects (WSCs), also called wavelength-selective switches, can serve as wavelength add/drops in the field or as elements in large central-office cross connects. The simplest WSC is a two-line by two-line version, and it can have a switch for each wavelength in either a bar or cross state between the lines. We first describe some reported WSCs and then discuss some architectures for the latter application. (p. 310)

9:45am (Invited)

**JWA4 ■ Silicon micromachines for lightwave networks,** David Bishop, *Bell Laboratories, Lucent Technologies, USA*. Silicon micromechanics is an emerging field, which is beginning to impact almost every area of science and technology. In areas as diverse as the chemical, automotive, aeronautical, cellular, and optical communications industries, silicon micromachines are becoming the solution of choice for many problems. In my talk, I will describe what they are, how they are built, and will show how they have the potential to revolutionize lightwave systems. (p. 313)

## Sierra Madre North

---

8:45am–10:00am

### RWA ■ WDM and TDM System Modeling

Curtis R. Menyuk, *University of Maryland, Baltimore County, USA, Presider*

8:45am (Invited)

**RWA1 ■ High-speed optical transmission,** John D. Moores, *MIT Lincoln Laboratory, USA*. Examples of modeling digital optical data transmission using split-step Fourier numerical simulation code are presented. Topics include ultrafast time-division multiplexed transmission both near zero dispersion and using dispersion management, all-optical regeneration, and higher-order dispersion compensation. (p. 316)

9:15am (Invited)

**RWA2 ■ Modeling of high-bit-rate time-division multiplexed and wavelength-division multiplexed systems,** Dirk Breuer, *Virtual Photonics Inc., Germany; Klaus Petermann, TU Berlin, Germany*. With the increasing complexity of optical systems, simulations provide a powerful technique to understand performance of optical systems, to develop upgrade strategies, and to evaluate new technologies. Different applications for the use of simulations will be discussed. (p. 318)

9:45am

**RWA3 ■ Degradation of optical signals caused by optoelectronic transponders in networks: modeling and measurement,** C.M. Weinert, L. Molle, *Heinrich-Hertz-Institut für Nachrichtentechnik Berlin GmbH, Germany*. An analytical expression for the bit error rate which includes the effects of timing jitter in optoelectronic transponders is proposed and tested by experiment. (p. 321)

## Anacapa

---

8:45am–10:15am

### RWB ■ Modulators and Receivers

S. Chandrasekhar, *Bell Laboratories, Lucent Technologies, USA, Presider*

8:45am (Invited)

**RWB1 ■ Electroabsorption modulators for ultrafast optical demultiplexing,** D.G. Moodie, P.J. Cannard, C.W. Ford, J. Reed, A.D. Ellis, R.T. Moore, I.D. Phillips, *BT Laboratories, UK*. A detailed characterization of low polarization sensitivity buried heterostructure electroabsorption modulators is described. Their short switching window capability equips them for 100-Gbit/s demultiplexing. (p. 326)

**9:15am**

**RWB2 ■ Novel substrate removed Mach-Zehnder GaAs/AlGaAs electro-optic modulators**, S.R. Sakamoto, A. Jackson, N. Dagli, *UC-Santa Barbara, USA*. A novel GaAs/AlGaAs electro-optic modulator utilizing push-pull metal electrodes was fabricated using substrate removal techniques and polymer integration. The scheme enables significant drive voltage reduction over previous designs and should enable ultrahigh-speed operation. (p. 329)

**9:30am (Invited)**

**RWB3 ■ Monolithic OEIC photoreceivers for 40 Gbit/s and beyond**, Heinz-Gunter Bach, *Heinrich-Hertz-Institut fuer Nachrichtentechnik Berlin GmbH, Germany*. 40-Gbit/s photoreceiver OEICs for 1.55- $\mu$ m time-division multiplexed system applications are described. The OEICs comprise side-illuminated or waveguide-integrated photodiodes. The amplifiers are based on the traveling-wave concept. OEIC packaging into pig-tailed modules is addressed. (p. 332)

## **Grand Ballroom Foyer**

---

**10:00am–10:45am**

**Coffee Break**

## **San Rafael**

---

**10:45am–12:45pm**

**JWB ■ Joint Session 2 (IPR & PS): Optical Cross Connects**

David Cotter, *BT Laboratories, UK*, Presider

**10:45am (Invited)**

**JWB1 ■ Progress in optical cross connects for circuit-switched applications**, J.E. Fouquet, *Hewlett-Packard Laboratories, USA*. Current optical cross-connect switches utilize a wide range of technologies. Total internal reflection switches, with  $\leq 0.15$  dB transmission insertion loss and  $-70$  dB cross talk per crosspoint, enable compact, high-port-count arrays with 1 msec switching times. (p. 336)

**11:15am**

**JWB2 ■ Monolithic InP optical cross connects: 4 x 4 and beyond**, Gregory A. Fish, B. Mason, Larry A. Coldren, Steven P. DenBaars, *UC-Santa Barbara, USA*. Results of 4 x 4 monolithic InP-based optical cross connects are discussed along with methods for improving the performance to allow larger arrays ( $\sim 16 \times 16$ ) to be fabricated. (p. 339)

**11:30am**

**JWB3 ■ Optoelectronic switching in semiconductor waveguides incorporating a resonant tunneling diode**, J.M.L. Figueiredo, *Univ. Glasgow, UK and Univ. Porto, Portugal*; A.R. Boyd, C.R. Stanley, C.N. Ironside, *Univ. Glasgow, UK*; A.M.P. Leiter, *Univ. Porto, Portugal*.

Electroabsorption modulators consisting of unipolar optical waveguides incorporating resonant tunneling diodes showed wide bandwidth (up to 20 GHz) and large modulation depth ( $> 10$  dB) at 900 nm and 1550 nm. (p. 342)

**11:45am (Invited)**

**JWB4 ■ MEMS for optical switching**, Lih Y. Lin, Evan L. Goldstein, *AT&T Labs-Research, USA*. Microelectromechanical systems (MEMS) have quite recently emerged as a promising route to large-scale optical switching in wavelength-division multiplexing networks. We describe the status and promise of this nascent technology in its various emergent forms. (p. 345)

**12:15pm (Invited)**

**JWB5 ■ IP over optical networks: transport and routing**, E. Radius, *Signal Transport Systems, The Netherlands*. European telecommunication operators investigate the integration of internet protocol (IP) and wavelength-division multiplexed networking. Intermediate results of the EURESCOM P918 project are presented. (p. 348)

## **Sierra Madre North**

---

**10:45am–12:15pm**

**RWC ■ Photonic Components System Modeling**

Joe Donnelly, *MIT Lincoln Laboratory, USA*, Presider

**10:45am (Invited)**

**RWC1 ■ Integrated photonic device and systems simulator using multiple signal formats**, Arthur Lowery, Rod Vance, *Virtual Photonics Inc., Australia*; Olaf Lenzmann, Dirk Breuer, Igor Koltchanov, *Virtual Photonics Inc., Germany*. We present a photonic systems simulator, which applies the most efficient signal representation to each part of the system, to achieve both efficiency and accuracy. (p. 352)

**11:15am (Invited)**

**RWC2 ■ Modeling of all-optical functional devices for signal processing: 3R regenerators**, Hans-Peter Nolting, *Heinrich-Hertz-Institute Berlin GmbH, Germany*. Modeling of all-optical signal processing on device and circuit level (wavelength conversion, full 3R signal regeneration at 20 Gbit/s) will be described and discussed. (p. 355)

**11:45am**

**RWC3 ■ Modeling of new grating designs for self-pulsating distributed feedback lasers**, M. Radziunas, H.J. Wuensche, *Humboldt Univ. Berlin, Germany*; B. Sartorius, H.-P. Nolting, O. Brox, D. Hoffmann, *Heinrich-Hertz-Institute fuer Nachrichtentechnik Berlin GmbH, Germany*; K. Schneider, *Weierstraß-Institut für Angewandte Analysis und Stochastik Berlin, Germany*. Self-pulsating devices for high-bit-rate optical clock recovery are optimized by using detuned gratings, tapered reflectors, and a gain section with quarter-wave shift. (p. 358)

**NOON**

**RWC4 ■ Modeling of lasers with wavelength-dependent feedback**, Ping Chieh Koh, *Cambridge Univ., UK*. We present a time-domain method capable of predicting characteristics of lasers with wavelength-dependent feedback. This method is in agreement with experimental results. (p. 361)

## Anacapa

---

**10:45am–12:15pm**

### **RWD ■ Integrated Devices**

T.R. Ranganath, *Hewlett-Packard Laboratories, USA*, Presider

**10:45am (Invited)**

**RWD1 ■ Uncooled and low-cost plastic module for high-bit-rate applications**, Jean-Louis Nicque, *Alcatel Optronics, France*. We report results for 2.5 Gbits/s intra-office transmissions with a new product family. A novel technological approach uses a spot-size laser, edge-illuminated detector, Si board, clip-on fiber, and plastic package. (p. 366)

**11:15am**

**RWD2 ■ Gain and switching measurements of the side-injection light-controlled bistable laser diode**, S.I. Pegg, M.J. Adams, *Univ. Essex, UK*. The parabolic switching power spectra measured for the side-injection light-controlled bistable laser has been explained highly accurately by both experimentally and theoretically determined gain spectra. (p. 369)

**11:30am**

**RWD3 ■ Novel ultralow voltage expanded-mode modulator monolithically integrated with a laser using single-epitaxial growth**, S.S. Saini, P.J.S. Heim, R. Grover, M. Dagenais, *Univ. Maryland–College Park, USA*; F.G. Johnson, D.R. Stone, *Laboratory for Physical Sciences, USA*; H. Shen, J. Pamulapati, W. Zhou, *Army Research Laboratory, USA*. We propose and demonstrate a novel ultralow voltage expanded-mode modulator monolithically integrated with a laser in single epitaxial-growth. Greater than 20 dB modulation was achieved with <1 V of bias. The device also had an expanded mode for ease of coupling to a single-mode fiber. (p. 372)

**11:45am**

**RWD4 ■ Compact 1.55-μm spot-size converters for photonic integrated circuits**, Gregory A. Fish, B. Mason, Larry A. Coldren, Steven P. DenBaars, *UC–Santa Barbara, USA*. A short 1.55-μm optical spot-size converter created using selective-area etching is presented. Results from spot-size converted ridge lasers indicate low conversion loss and high coupling efficiency to lensed fibers. (p. 375)

**NOON**

**RWD5 ■ All-active InGaAsP/InP optical tapered amplifier 1 × N power splitters**, S.S. Choi, W.D. Goodhue, *MIT Lincoln Laboratory and Univ. Massachusetts–Lowell, USA*; J.P. Donnelly, S.H. Groves, R.E. Reeder, R.J. Bailey, P.J. Taylor, *MIT Lincoln Laboratory, USA*. Tapered amplifier power splitters in which the signal is amplified during the splitting process have been fabricated. Gains in each output guide of a 1 × 8 splitter of 3.5 dB to 9.5 dB have been obtained at 1302 nm on initial devices. (p. 378)

## Anacapa

---

**12:15pm–12:30pm**

### **Closing Remarks**

Fred Heismann, *Qtera Corporation, USA*

## Sierra Madre North

---

**12:15pm–12:30pm**

### **Closing Remarks**

Sujeet Chaudhuri, *University of Waterloo, Canada*

**Integrated Photonics Research**

# **Plenary Session**

**Monday, July 19, 1999**

**Nadir Dagli, University of California, Santa Barbara, USA**  
Presider

**RMA**  
**8:15am–10:30am**  
Sierra Madre

## FIBER DEVICES FOR ULTRA-HIGHSPEED PHOTONICS

Erich P. Ippen

Department of Electrical Engineering and Computer Science

Department of Physics

Research Laboratory of Electronics

Massachusetts Institute of Technology

Cambridge, MA 02139

Erbium-doped fibers have enabled the development of new short-pulse sources and switches for future ultrahigh-speed technology. Recent progress in our laboratory on soliton lasers, optical ring memories, femtosecond stretched-pulse lasers, and nonlinear loop filters will be described.

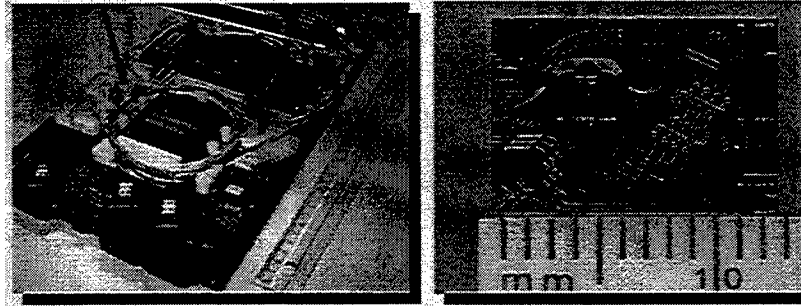
## Challenges and opportunities in Photonic Integration

M.K. Smit

Delft University of Technology, Faculty ITS, Photonic Integrated Circuits Group,  
PO Box 5031, NL-2600 GA, Delft, The Netherlands.  
Tel: +31 15 278 1752, fax: +31 15 278 4046, email: smit@its.tudelft.nl

**Introduction.** Photonic Integration leads to a drastic reduction in dimensions of complex optical devices. Fig. 1 shows a 2x2 crossconnect realized in today's most compact fiber-based technology, the device is slightly larger than a laptop. The picture at the right shows a similar device integrated on an InP chip smaller than 1 cm<sup>2</sup>! A probably even greater advantage is the reduction of packaging cost: the left device contains twenty fiber-chip connections, integration reduces this number to four! For more complex circuits the advantage becomes even more pronounced.

A factor hampering the break-through of Photonic Integration has been the large variety of devices and device concepts used in photonic engineering, which complicates their integration, and the lack of a large-scale market justifying the investments in developing complex Photonic Integrated Circuits. WDM-technology is rapidly changing this situation. For the key functions in WDM-systems, multiplexing and demultiplexing, there is a planar device, the phased-array demultiplexer or PHASAR [1] (also called AWG or WGR), which is very suitable for integration with other devices like amplifiers and switches. Most of the functions required in WDM-systems can be composed from PHASAR's, switches and amplifiers, and a market for complex integrated devices like multiwavelength lasers, reconfigurable add-drop multiplexers and crossconnects is rapidly evolving. In this paper a review will be given of progress in the field of semiconductor-based Photonic Integrated Circuits (PIC's) for WDM-applications, and the role of Photonic Integration and Photonic CAD in supporting the increasing device complexity required in today's and tomorrow's network applications will be discussed.



**Compact fibre-based 4-channel  
2x2 crossconnect module**  
(Telefonica I&D, Madrid)

**Photonic Integrated 4-channel  
2x2 crossconnect chip**  
(Delft University of Technology)

*Figure 1 Reduction of volume and cost through Photonic Integration*

**Integrated WDM receivers.** Figure 2 shows an 8-channel WDM-receiver module containing a PHASAR-demultiplexer integrated with 8 detector diodes on a chip of 3x4 mm<sup>2</sup>, which has been packaged with 8 front-end amplifiers in a standard 14-pins butterfly package [2]. The photograph illustrates the potential of photonic integration in reducing the volume of optical modules. The integration can be pushed even further by monolithic integration of the amplifiers. This has first been demonstrated by Chandrasekhar et al. [3], who realized an 8x2.5 Gb/s MW-receiver with integrated Heterojunction Bipolar Transistor (HBT) preamplifiers. The main challenge in developing WDM receiver modules is in reducing crosstalk at high frequencies and in reducing module cost so far as to be competitive with hybrid solutions.

**Integrated WDM lasers.** Integrated multiwavelength lasers have been realized by combining a DFB-laser array (with a linear frequency spacing) with a power combiner on a single chip. Using a power combiner for multiplexing the different wavelengths in a single fiber is a tolerant method but it introduces a loss of  $10 \log N$  dB,  $N$  being the number of wavelength channels. An elegant solution to this problem is the integration of a broadband optical amplifier array with a multiplexer in a Fabry-Perot cavity. If one of the amplifiers is excited the device will start lasing at the passband maximum

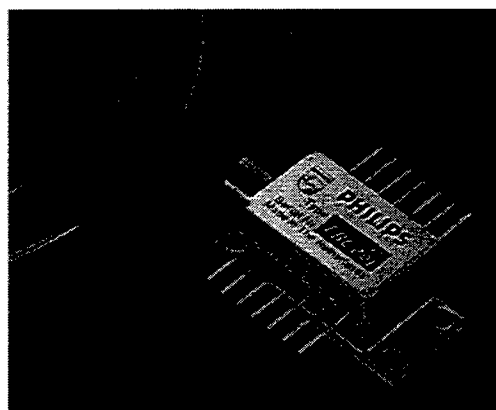


*Figure 2 8x620 Mb/s WDM-receiver chip packaged with 8 frontend amplifiers in a 14-pins butterfly package.*

of the multiplexer channel to which it is connected. All Semiconductor Optical Amplifiers (SOA's) can be operated and (intensity) modulated simultaneously, in principle. An important advantage of this component is that the wavelength channels are automatically tuned to the passbands of the multiplexer and that they are coupled to a single output port with low loss. Single-mode operation with <1 MHz linewidth, >50 dB Side Mode Suppression Ratio and more than 1 mW output power in a single mode fiber has been reported [4]. Modulation speed is limited due to the large cavity length. Error free transmission at 2.5 Gb/s data rate of 16 channels with two interspersed 8-channel multiwavelength lasers has been demonstrated over 627 km, however, using external MZ-modulators [5].

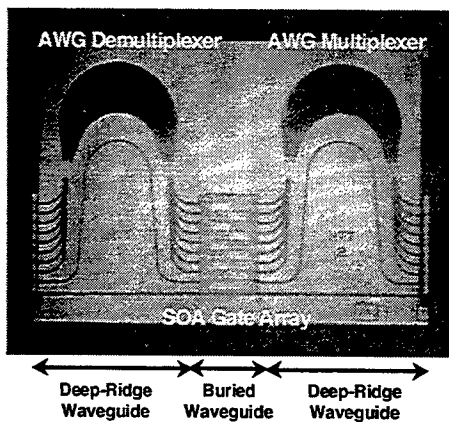


**Figure 3** Microscope photograph of a monolithically integrated 8-channel WDM channel selector (from [6]).

that can drop a fixed wavelength out of a multiplex on a fiber link or add a signal at the same wavelength, to crossconnects that can crossconnect individual wavelengths from a number of input fibers independently to a number of output fibers. Fig. 1 (right) shows a 4-channel 2x2-crossconnect device with dimensions 9x12 mm<sup>2</sup>, realized on InP-substrate [9]. Crosstalk figures of semiconductor-based crossconnects are still insufficient for system applications, but subject to steady improvement.

**Photonic Integration philosophy.** Except for the WDM receivers all devices discussed above can be realized by a combination of PHASAR's, optical amplifiers and switches. As the optical switches can be realized in the form of SOA-based gate-switches almost any function can be realized by a combination of PHASAR's and integrated SOA's, so the integration of a high-quality passive waveguides structure with sufficient resolution to realize low-loss PHASAR's, with high quality SOA's with a low reflectivity at the junctions between the active and the passive waveguide sections, is considered as a key technology for realization of advanced PIC's.

In addition to PHASAR's and SOA's pin-type waveguide phase-modulators are promising as a third elementary component. They introduce little additional complexity to passive waveguide structures and in combination with MMI-couplers, compact and fabrication tolerant couplers which can be realized in the same process as PHASAR's, they can be used to form Mach-Zehnder Interferometer switches. Although MZI-switches take considerably more space and have a poorer on-off ratio, they have some important advantages over SOA's: they have very low power consumption, they do not add ASE-noise and they are potentially very fast: equipped with travelling wave electrodes they can be operated at speeds of tens of GHz. As power dissipation and speed will become an important issue in advanced PIC's MZI-switches and modulators are expected to constitute an important addition to SOA-based switches.

A major problem for the development of Photonic Integration technology are the large investments required to make integration cost-competitive, which are usually prohibitive if a hybrid or micro-optic solution is possible. Photonic Integration technology should, therefore, focus on devices which provide important additional or exclusive functionality as compared to a hybrid approach, such as multiwavelength lasers and add-drop multiplexers with zero-loss-between-fibers. Such devices are promising as commercial vehicles for developing an integration technology which will turn out to be capable of realizing an ever larger variety of devices at steadily decreasing costs.

**Photonic Computer Aided Design.** With the increasing circuit complexity computer aided design tools become increasingly important. Most commercially available design software for full-circuit design and analysis

**WDM channel selectors and equalizers.** With the technology for integration of optical amplifiers with passive demultiplexers, a variety of functions can be realized. Fig. 5 shows a WDM channel selector realized by NTT [6], consisting of a demultiplexer and a multiplexer with a SOA gate array in between, that can pass or block each of the 8 wavelengths applied to the input demultiplexer. The device operates with zero-loss between fibers for the transmitted channels at an amplifier current of 70 mA and an extinction of 40 dB for unwanted channels. A 4-channel device realized by Alcatel [7] shows 3 dB loss between fibers for 30 mA amplifier current in the on state and an extinction of 50 dB for unwanted signals. Lucent recently reported a comparable device for use as dynamic power equalizer [8].

**Wavelength selective routers and switches.** Most WDM systems today are used in point-to-point links. The next step is the introduction of WDM routing and switching into the network. This requires wavelength selective routers and switches, ranging from simple add-drop multiplexers (ADM's),

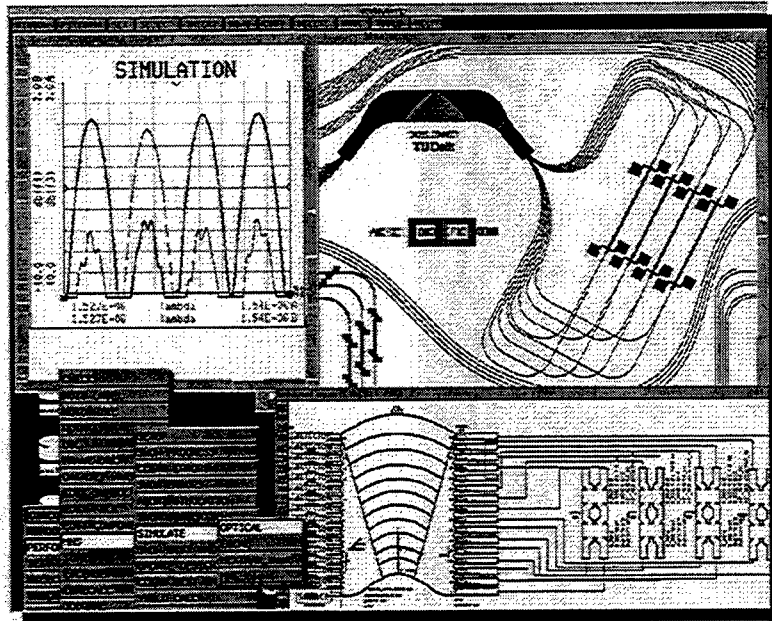


**Figure 4** Screenshot of Photonic CAD-tool based on HP's MDS, showing the symbolic circuit description (lower right), the simulation result (upper left) and the mask layout (upper right) of the chip shown in Fig. 1. On the symbolic circuit page the symbols for a 16x16 PHASAR and 4 MZ- switches can be distinguished.

not extend the analysis down to a chip design level, however. We are developing a Photonic CAD-tool for chip design, including mask-layout, based on a professional CAD-tool for microwave circuits using a scattering matrix approach [10] (see fig. 4). An approach like this will be necessary to master the complexity involved in advanced Photonic Integrated Circuits.

**Conclusions.** Semiconductor-based Photonic Integrated Circuits are rapidly gaining performance. In the coming years they will play an increasingly important role in providing the functionality required in advanced WDM-networks in a compact form and at steadily decreasing costs.

**Acknowledgements.** Support from ACTS-project AC332 APEX and the Dutch ministry of Economic Affairs (IOP "Electro-Optics") is gratefully acknowledged.

## References

- /1/ M.K. Smit and C. Van Dam, "PHASAR-based WDM devices: principles, design and applications", J. of Sel. Topics in Quantum. Electron., Vol. 2, No. 2, pp. 236-250, June 1996.
- /2/ A.A.M. Staring et al., "Packaged PHASAR-based wavelength demultiplexer with integrated detectors", Proc. 23rd European Conf. on Opt. Comm. ECOC '97, 22-25 Sept. 1997, Edinburgh, UK, Vol. 3, pp. 75-78.
- /3/ S. Chandrasekhar et al., "Monolithic eight-wavelength demultiplexed receiver for dense WDM applications", IEEE Photon. Technol. Lett., Vol. 7, No. 11, pp. 1342-1344, Nov. 1995.
- /4/ C.R. Doerr et al., "Wavelength selectable laser with inherent wavelength and single-mode stability", IEEE Photon. Technol. Lett., Vol. 9, No. 11, pp. 1430-1432, Nov. 1997.
- /5/ R. Monnard et al., "16-channel 50 GHz channel spacing long-haul transmitter for DWDM systems", Electron. Lett., Vol. 34, No. 8, pp. 765-767, April 1998.
- /6/ H. Ishii et al., "Monolithically integrated WDM channel selectors on InP Substrates", Proc. 24th Eur. Conf. on Opt. Comm. ECOC'98, 20-24 Sept. 1998, Madrid, Spain, pp. 329-330.
- /7/ R. Mestric et al., "Four-channel wavelength selector monolithically integrated on InP", Electron. Lett., Vol. 34, No. 19, pp. 1841-1843, Sept. 1998.
- /8/ C.R. Doerr et al., "Integrated WDM dynamic power equaliser with potentially low insertion loss", IEEE Photon. Technol. Lett., Vol. 10, No. 10, pp. 1443-1445, Oct. 1998.
- /9/ C.G.P. Herben et al., "A Compact Integrated InP-Based Single-PHASAR Optical Crossconnect," IEEE Photon. Technol. Lett., vol. 10, no. 5, May 1998, pp. 678-680.
- /10/ X.J.M. Leijtens, P. Le Lourec, M.K. Smit, "S-matrix oriented CAD-tool for simulating complex integrated optical circuits", J. of Sel. Topics in Quantum. Electron., Vol. 2, No. 2, pp. 257-262, June 1996.

of Photonic Integrated Circuits is based on Beam-Propagation Methods. They start from a circuit description on layout level. A drawback of BPM-methods is that they cannot handle light propagating at large off-axis angles and that they are unidirectional (no reflections, no loops or rings). Further they are less suitable for analyzing propagation through long waveguide sections (interconnections, phase shifters etc.).

A more powerful approach uses a mixed-mode analysis starting from a symbolic circuit description in which the response of the individual components is described by a matrix and the full circuit response is calculated with matrix algebra. The matrices of the different components can be computed using BPM-methods or other methods, for each component the most suitable computation method can be selected. This matrix approach is common in circuit and system analysis programs, at present these programs do

## Transmission Still, Going Networking and Beyond

Tetsuhiko Ikegami  
The University of Aizu, Japan  
Ikegami@u-aizu.ac.jp

K. Okamoto  
NTT Photonics Laboratories, Japan

Fiber technology and optoelectronics have moved up telecommunication to the most significant infrastructure in cooperation with information technology. In the electronic arena, integration of devices is a crucial condition for the application, however, photonic technology is running differently. Is it enough due to its versatility? The point will be reviewed and discussed.

**Integrated Photonics Research**

# **WDM Devices: 1**

**Monday, July 19, 1999**

**Meint K. Smit, Delft University of Technology, The Netherlands**  
Presider

**RMB**  
**11:00am–12:30pm**  
Sierra Madre North

## AOTF for Optical ADM Systems

T. Nakazawa, M. Doi, S. Taniguchi, Y. Takasu, N. Hashimoto and M. Seino

Fujitsu Laboratories Ltd.

10-1 Morinosato-Wakamiya, Atsugi 243-0197, Japan

Phone : +81-462-50-8220

Fax : +81-462-48-5194

E-mail: tdnaka@flab.fujitsu.co.jp

### 1. Introduction

Acousto-optic tunable filters (AOTFs) using TE/TM mode conversion are beneficial for use as optical add/drop multiplexers (OADM) in wavelength division multiplexed (WDM) systems because of their multichannel selectivity and wide tuning range. However there remains some problems to be solved, before AOTFs can be commercially practical for OADM. The most serious of these problems are achieving a narrow bandwidth with a low sidelobe. In this paper, I would like to discuss how to resolve these problems from the component level.

### 2. Film-loaded SAW guide

In AOTF, a technique for guiding SAW is indispensable. We developed a film-loaded guide as a new SAW guide<sup>1-3)</sup> (Fig.1). As compared with conventional SAW guides, i.e. Ti-deep diffused guide, our film-loaded guide has advantages as follows:

#### (1)Easy to fabricate

SAW guide can be fabricated easily by patterning an optical material such as SiO<sub>2</sub>.

#### (2)Controllability of SAW velocity

The velocity of SAW can be controlled by doping metal materials such as InSn. For 0-60 wt%-density, the velocity differences between the film-loaded part and the other part are 0.5-2.2%. This value is very large, compared with 0.5% of the Ti-diffused guide.

#### (3)Suitable for integration

The film can be set freely on optical waveguides as shown in the cross-sectional view (Fig.1). Furthermore, the large difference in velocity can confine the SAW power in a narrow region of 40 μm width compared with the width for the conventional method.

### 3. Integrated AOTF

In order to apply AOTF to 0.8nm channel-spaced systems, a narrow bandwidth must be achieved. The bandwidth can be decreased by making the tip length longer. But this method is limited by wafer size. On the other hand, a multi-stage method can also reduce the bandwidth according to the number of stages. However, even with this method, as long as conventional tandem integration is used, the SAW interaction length must be short and ultimately the bandwidth cannot be reduced.

The folded multistage structure we proposed can eliminate this restriction.

### 3-1 Waveguide reflector

We developed a waveguide reflector based on the principle of two-mode interference. Basically this configuration is similar to PBS as shown in Fig.2. So the splitting ratio changes against parameters of structure. We found that both TE and TM light are guided to the same port P2, by adjusting the angle  $\theta$  and the length  $L_c$ . By cutting the center line and forming a reflecting film on the cut face, this device can be used as a mirror. This reflector has the following advantages: (1)It can be fabricated simultaneously with waveguides and PBSs in a Ti-diffusion process. (2)The reflecting characteristics are not sensitive to cut position. The tolerance for obtaining a -20 dB-splitting ratio is 40  $\mu\text{m}$ . This value is wide enough to fabricate.

### 3-2 Multistage AOTF

Fig.3 shows our proposed folded multi-stage AOTF. Basically, polarization-independent AOTFs are located side-by-side with each connected by a waveguide reflector at the end-face of the tip. This produces a multistage while keeping the long interaction length of the SAW guide for both the drop and through signals. In the configuration shown in Fig.3, the drop and through signals pass through triple-stages to different ports. Using this structure, additional multistages can be integrated easily.

Fig.4 shows the transmission characteristics at the drop port. The sidelobe of -28 dB was measured. A 3 dB bandwidth of 0.37 nm was obtained. This value is narrow enough for the application of this device to 0.8 nm spaced WDM systems.

A good extinction ratio for the drop of 37 dB can also be obtained at the Thru port. It is presumed that the measured extinction ratio is limited by the precision of the setup. Furthermore, there is practically no crosstalk of the add light to the drop port due to the spatial separation between the add and drop sections.

The total insertion loss from fiber to fiber is 9 dB. This AOTF is driven by an RF signal of ~170 MHz and requires only 15 mW of total power.

## 4. Conclusion

We developed a narrowband low-crosstalk tunable filter that features multistages located side-by-side and comprised of film-loaded waveguide and optical waveguide reflectors. Since a film-loaded waveguide can effectively confine SAW power to a narrow region, the AOTFs can be located close together. The polarization-independent waveguide reflectors that connect the AOTFs can be fabricated by Ti-diffusion process. These new techniques enable the integration of AOTFs while maintaining a long interaction length on one tip.

## References

- 1) M. Seino et al., "Low Sidelobe and Low Insertion Loss Ti:LiNbO<sub>3</sub> AOTF", LEOS'97, PD.
- 2) T. Nakazawa et al., "Ti:LiNbO<sub>3</sub> AOTF for 0.8nm Channel-Spaced WDM", OFC'98, PD1
- 3) M. Seino et al., "Tunable add/drop filters using LiNbO<sub>3</sub>", IPR'98, IMG3

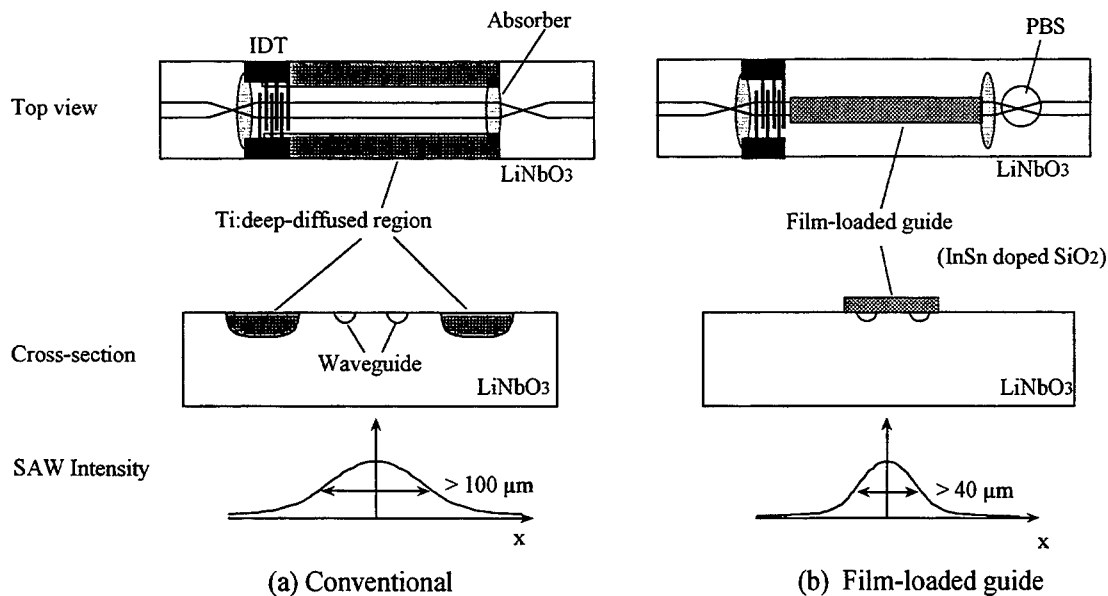


Fig. 1. SAW guide

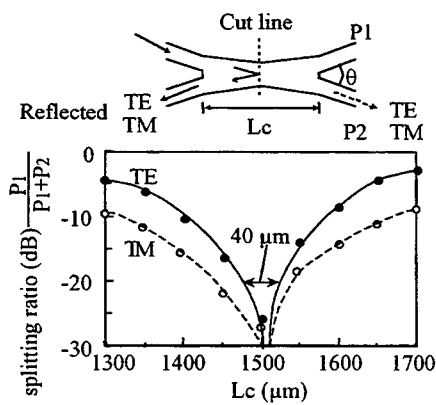


Fig.2. Waveguide reflector

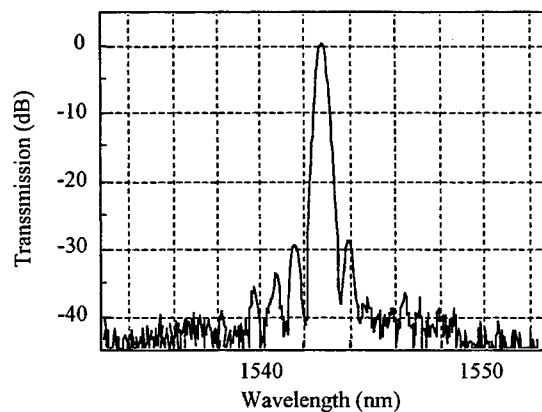


Fig.4. Filter characteristics

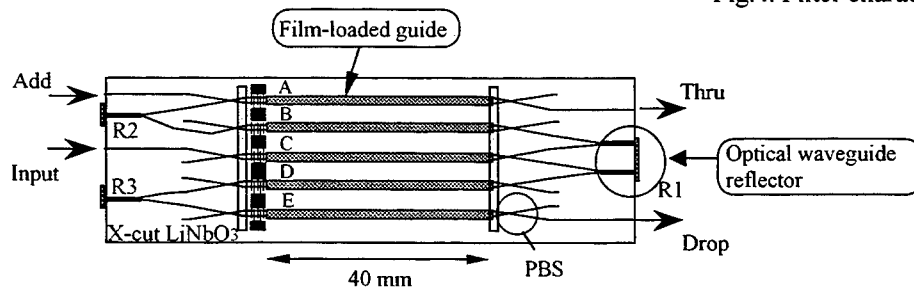


Fig.3. Multistage AOTF

## OADM and WDM channel management using programmable holographic filters

R. J. Mears, A. D. Cohen, M. C. Parker, C. R. S. Fludger and N. J. Jones

CUED: Cambridge University Engineering Department, Trumpington Street, Cambridge, CB2 1PZ, UK, Tel. +44 1223 332784, Fax +44 1223 332662. Work performed whilst authors at CUED. Adam Cohen is now at JDS FITEL Inc., 3000 Merivale Rd., Nepean, Ontario, K2C 3H1, Canada, Tel. (613) 727 1304, Fax (613) 823 4986. Mike Parker is now at Fujitsu Telecommunications Europe Ltd. Research, Northgate House, St Peter's St., Colchester, Essex, CO1 1HH, UK, Tel. +44 1206 363007, Fax +44 1223 336009. Chris Fludger is now at Nortel Networks, London Road, Harlow, Essex, CM17 9NA, UK, Tel. +44 1279 429531, Fax +44 1279 403325.

### Introduction

The deployment of the EDFA in WDM systems has to date required passive spectral gain equalisation/flattening. Dynamically reconfigurable multi-channel equalising add-drop elements have been identified as key components in future wavelength-switched networks [1]. Broadband spectral equalisation has recently been demonstrated using an arrayed waveguide grating demux plus thermo-optic phase shift array in one arm of an interferometer [2]. This technique presents a number of advantages, including ease of integration and low loss, but once fabricated it manages a fixed channel set. Technologies that provide the equalisation of an arbitrary channel set on a channel-by-channel basis, in tandem with add-drop functionality, include the acousto-optic tunable filter (AOTF) [3] and the technology described herein, the programmable holographic filter (PHF) [4]. Although the AOTF-based technology is relatively well developed, the achievement of 100-GHz resolution entails a design of increased complexity. By contrast, the PHF attains such resolution by means of straightforward optimisation of filter design parameters, and is intrinsically polarisation-insensitive. The PHF provides the additional benefits of inter-channel ASE suppression and arbitrary spectral shaping (e.g. 'top-hat' functions) [5] of the filter passband.

### Dynamic Spectral Equalisation

The facility to provide dynamic holographic spectral equalisation of WDM channels (e.g. to compensate for EDFA gain tilt and/or fluctuations in individual channel powers) has already been demonstrated [4]. The PHF consists of a 4f free-space relay between cleaved single-mode fibres, in the collimated beam of which relay is disposed a pixellated programmable binary phase grating, generated by dynamic frame transfer to a ferroelectric liquid crystal spatial light modulator (FLC-SLM), and a fixed diffraction grating of smaller line-pair width. The FLC-SLM consists of 128 x 128 pixels on a 165- $\mu\text{m}$  pitch with inter-pixel dead space of 15  $\mu\text{m}$ , however in this application the device is simply used to display 1-D frames. A typical result obtained by deploying an 18- $\mu\text{m}$ -pitch transmissive fixed grating in a linear architecture was the compression of 8 x 500-GHz-spaced WDM channels with an input dynamic range of 9.5 dB to within 0.75 dB [5]. In addition, the PHF provided inter-channel ASE suppression >15dB and attenuation of the 1.53- $\mu\text{m}$  gain peak by > 20 dB.

### Enhanced resolution OADM and equaliser

The experimental configuration is similar to that previously described [4]. The key modification is the adoption of a folded architecture to accommodate a 3.3- $\mu\text{m}$ -pitch reflective blazed grating in place of the original 18- $\mu\text{m}$ -pitch transmissive grating. The tuning resolution – corresponding to unit increments in the hologram spatial frequency parameter (see below) – is thus reduced to 27.5 GHz, multiples of which are very close to matching the ITU grid spacing. A further investigation has successfully demonstrated the deployment of a VGA-resolution nematic liquid crystal device, also operated in binary phase mode, establishing the versatility of the holographic technique. Fig. 1 shows results for 8 x ~100-GHz-spaced channels equalised and with a single channel (#4) suppressed. The input dynamic range of 3 dB over the ~7-nm wavelength range is equalised to less than 1.5 dB. A variety of holograms were pre-calculated and loaded into the SLM memory to give arbitrary power control and/or suppression (i.e. dropping) of the various channels. Inter-channel ASE suppression was designed to be consistently greater than 15 dB and dropped channel suppression approximately 19 dB; these figures represent limitations of the low resolution SLM (binary phase quantisation errors) but can be much improved by deploying a higher resolution device with more pixels. The facility to drop multiple channels has also been demonstrated – this is described in the next section.

### Extension to OADM functionality

The ability to suppress and/or fine tune the optical power of the various channels enables a simple extension to the demonstration of a WDM OADM. The VGA nematic device was used in this experiment. Fig. 2 shows the basic functionality: the concept is for WDM channels to be dropped and added via a regenerator and interface unit which would perform reception and transmission at different WDM wavelengths. The overall management and allocation of wavelength channels is made in association with the management layer. At the optical level the channels are boosted and equalised by the PHF unit in conjunction with an optical amplifier. The WDM OADM can also provide suppression of channels prior to insertion of the added channels (for example to suppress recirculating inserted channels and also to suppress dropped channels if broadcast is not required).

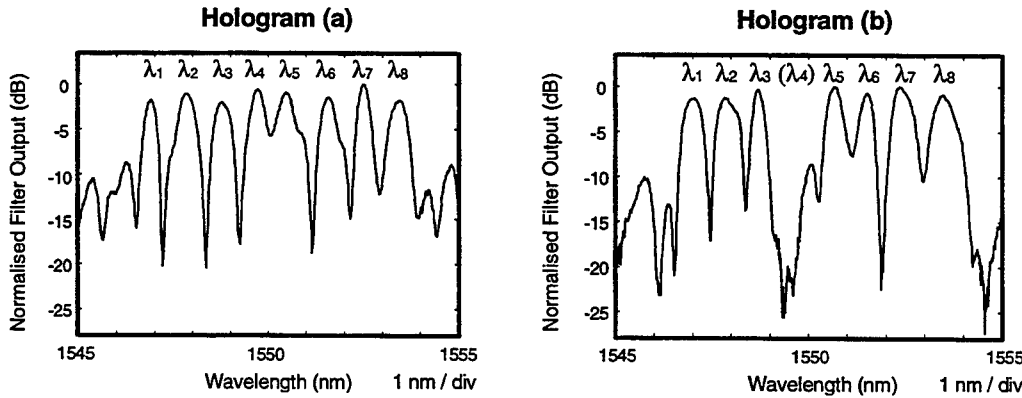


**Figure 1** Management of 8 x 100-GHz-spaced channels using PHF: (a) all eight channels equalised; (b) channel #4 suppressed/dropped

For the purpose of the demonstration, three ITU source lasers,  $\lambda = 1550.1$  (ch #1), 1557.4 (ch #7) and 1558.2 nm (ch #8), were multiplexed. Channel power supervision was performed with a single 10:90 tap splitter, and supervisory data (wavelength tags) were added using a spread-spectrum technique. Since the tags were added at the sources at known power levels the system could detect which wavelengths were present and determine their power levels by DSP cross-correlation. This technique allowed a > 20-dB dynamic range in channel power detection with a single tap. The PC-controlled PHF unit could be configured to 'drop' (i.e. suppress) any combination of the input wavelengths, as would be required in the full OADM unit prior to addition of locally generated wavelengths.

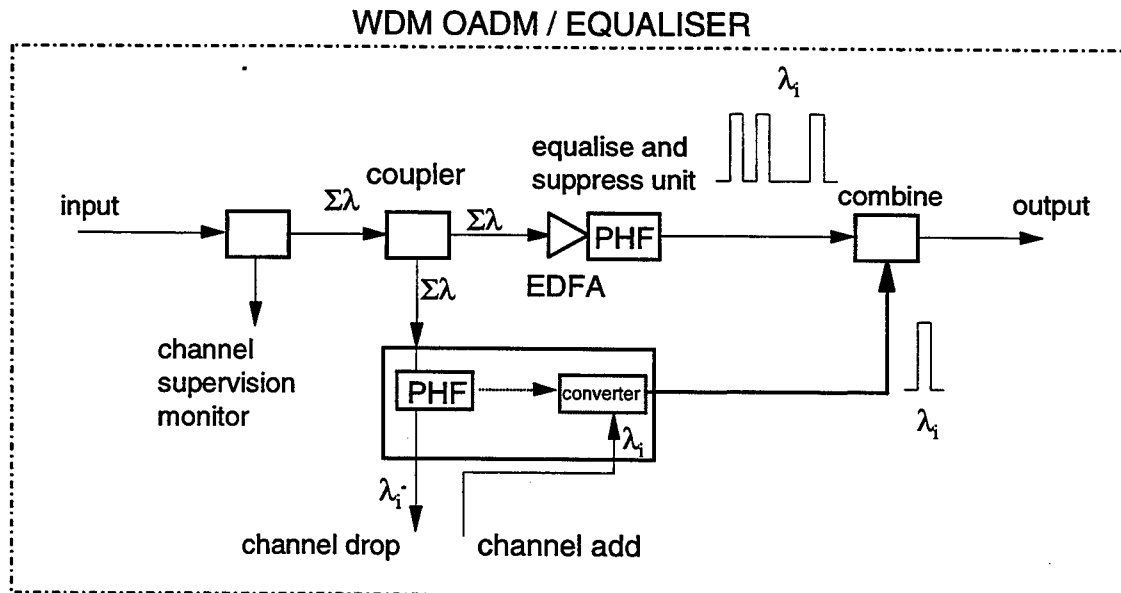


**Figure 2** Extension of PHF equaliser to OADM

Single channel selection was achieved with > 30-dB suppression of other channels, both adjacent and non-adjacent. When selecting 2 of the 3 channels the suppression was > 20dB; improved performance would be obtained by further iterations of the design algorithm (see below). Additional results will be shown at the meeting.

### Hologram design, PHF scalability and further WDM-OADM development

Design calculations were based on the following equation (derived by consideration of summed first-order diffraction angles):

$$\tan^{-1}\left(\frac{x}{f}\right) \cong \sin^{-1}\left(\frac{\lambda}{d}\right) + \frac{n\lambda}{ND} - \Psi \quad (1)$$

where  $\lambda$  is the filter wavelength,  $x$  the displacement of the output fibre from the optical axis,  $f = 96.1$  mm the focal length of the collimating/focussing lenses,  $N = 128$  the 1-D hologram pixel count,  $D$  the SLM pixel pitch and  $d \sim 3.3 \mu\text{m}$  the period of the fixed grating.  $\Psi$  is the inclination of the grating normal to the input optical axis. The hologram spatial frequency parameters,  $n$ , lie in the range  $0-N/2$  and typically take integer values. A set of  $n$  having  $\Delta n = 4$  increments were input to a simulated annealing algorithm adapted to give multiple, arbitrary-amplitude passbands, in order to demonstrate various pass/drop permutations of eight channels. The holograms generated and displayed thus had mixed spatial frequency. Control of  $C$  channels incurs an excess filter loss of  $10\log_{10}C$ , or  $10\log_{10}3C$  for flattened passbands, but at the high channel counts anticipated in next-generation systems the incremental penalty would be small.

In the OADM application, steering of dropped channel(s) to separate output port(s) is feasible by solving for spatial frequency parameters  $n$  with the respective wavelength  $\lambda$  and an increment to  $x$  substituted into Eqn. (1). Simulations show that the resultant high spatial frequency components produce satisfactory holograms if the increment in  $x$  is set to  $\sim 125 \mu\text{m}$  (representing fibres in adjacent v-grooves), but that superior performance would be achieved if the outputs were to be more closely spaced, e.g.  $\sim 15-20 \mu\text{m}$  in, for example, a pigtailed waveguide concentrator.

With an optimised electronic drive scheme, device reconfiguration for a ferroelectric LC device can be of the order of a few microseconds [6], however the larger switching angle of the binary phase operated devices are likely to result in switching times of the order of  $100 \mu\text{s}$ . Although the nematic device responds on the millisecond time-scale, this is not inconsistent with potential management times for a large multiwavelength network. The LC modulator is inherently polarisation-insensitive such that the PHF incurs negligible PDL given the deployment of a suitably optimised fixed diffraction grating. The results presented above were achieved using a relatively small number of pixels (128-pixel 1-D SLM). Devices with both smaller pixel pitch and much higher numbers of pixels have been experimentally demonstrated.

### Conclusion

In this paper we have demonstrated the use of a programmable holographic filter for dynamic EDFA gain equalisation and active equalisation/OADM management of WDM channels spaced by approximately 100 GHz. This technology has direct applications in future switched WDM networks and is also scalable to both higher channel count and reduced channel spacing, e.g. 50 GHz or less, over the extended EDFA window.

### References

- 1) A. E. Willner, "Systems Issues for WDM Components", *IEEE-LEOS Summer Topical Meeting on WDM Components Technology*, pp. 5-6, August 1997.
- 2) C. R. Doerr, P. Schiffer, L. W. Stulz, M. Capuzzo, E. Laskowski, A. Paunescu, L. Gomez and J. Gates, "Compact integrated dynamic wavelength equalizer", *Proc. OFC '99*, PD30, February 1999.
- 3) S. H. Huang, A. E. Willner, Z. Bao and D. A. Smith, "Experimental Demonstration of Active Equalization and ASE Suppression of Three 2.5-Gb/s WDM-Network Channels over 2500 km Using AOTF as Transmission Filters", *IEEE Photonics Technology Letters*, 9, (3), pp. 389-391, 1997.
- 4) M. C. Parker, A. D. Cohen and R. J. Mears, "Dynamic Holographic Spectral Equalization for WDM", *IEEE Photonics Technology Letters*, 9, (4), pp. 529-531, 1997.
- 5) A. D. Cohen and R. J. Mears, "Dynamic Holographic Eight-Channel Spectral Equalizer for WDM", *IEEE-LEOS Summer Topical Meeting on WDM Components Technology*, pp. 46-47, August 1997.
- 6) M. A. Handschy, K. M. Johnson, G. Model and L. A. Pagano-Stauffer, "Electro-optic applications of ferroelectric liquid crystals to optical computing", *Ferroelectrics*, 85, pp. 279-289, 1988.

## Fabrication of compact wavelength add/drop filter circuits using a cross grid array vertically coupled to microring resonators

Sai T. Chu<sup>1</sup>, Brent E. Little<sup>2</sup>, Wugen Pan<sup>1</sup>, Taro Kaneko<sup>1</sup>, and Yasuo Kokubun<sup>1</sup>

<sup>1</sup>Kanagawa Academy of Sci. & Tech., KSP E308, 3-2-1 Sakato, Takatsu, Kawasaki, Japan 213-0012

Email: sai@maxwell.uwaterloo.ca

<sup>2</sup>Research Laboratory of Electronics, Massachusetts Institute of Technology, Cambridge, MA 02139

Microring resonator devices have two important attributes as a key new technology for future optical communications: functionality and compactness. Functionality refers to the fact that a wide range of desirable filter characteristics can be synthesized by coupling multiple rings<sup>1</sup>. Compactness refers the fact that ring resonators with radii less than  $25 \mu\text{m}$  can lead to large scale integration of devices. In this technology, vertically coupled microring resonators<sup>2-4</sup> (VCMRRs) have proven to be a versatile means of implementing high quality WDM components. Of particular advantage in the vertical structure is that the bus waveguide layer is independent of the ring resonator layer. Each layer can therefore be optimized independently. If the index contrast of the buried bus waveguides can be made sufficiently low, then the waveguides can cross through each other with little scattering loss or cross-talk. The entire two dimensional surface of the chip then becomes readily accessible for device integration with packing densities limited only by the very small dimensions of the rings. In this paper we demonstrate a simple, practical, 8 channel add/drop filter using microring resonators coupled to buried channel waveguides that cross through each other with less than -30 dB of cross-talk.

The 8 channel VCMRR add/drop filter is depicted schematically in Figs. 1(a)-(c). Fig. 1(a) shows the basic filter element. It consists of an input bus waveguide and an add/drop waveguide that are crossed at right angles. A vertically coupled ring resonator serves as the wavelength selective cross-connect at each node. The ring is integrated on the top layer and suffers negligible bending loss as a result of the high index contrast air cladding. This basic element allows flexible connection for the construction of complex circuits. A schematic of the cross section in the coupling region is shown in Fig. 1(b). The ring and bus

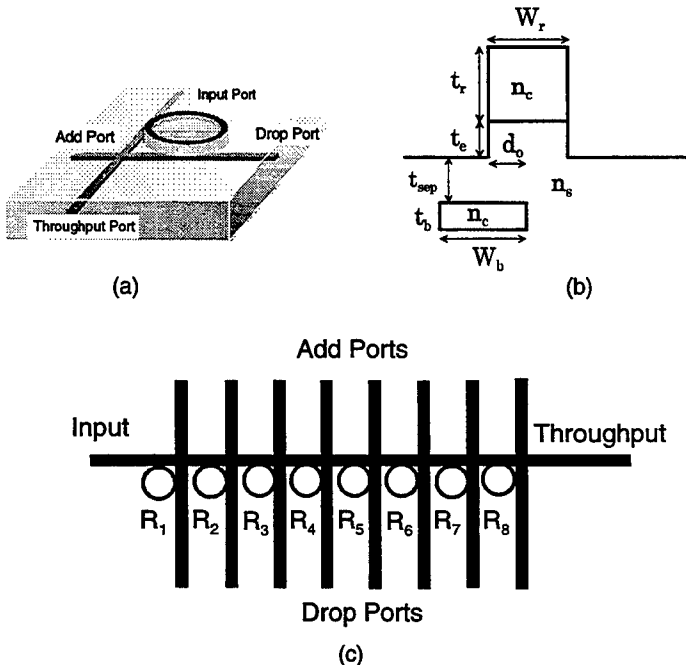


Fig 1. (a) Perspective view of the single channel VCMRR add/drop filter. (b) Cross-sectional view of the structure in the coupling region. (c) Layout of the 8 channel add/drop filter.

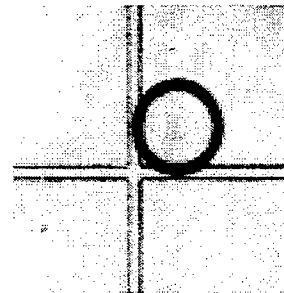


Fig 2. Microscope image of a single filter element. The waveguide parameters are  $W_r=1.5 \mu\text{m}$ ,  $W_b=2.0 \mu\text{m}$ ,  $t_r=1.5 \mu\text{m}$ ,  $t_e=0.25 \mu\text{m}$ ,  $t_{sep}=0.35 \mu\text{m}$ ,  $t_b=0.5 \mu\text{m}$ ,  $d_o=1.5 \mu\text{m}$ ,  $n_c=1.6532$ ,  $n_s=1.4508$ ,  $R=10 \mu\text{m}$  and air as superstrate.

waveguide cores are composed of the compound glass  $Ta_2O_5/SiO_2$ , with the ratio of  $Ta_2O_5$  to  $SiO_2$  (17:83) mol % chosen to give an index of 1.6532.  $SiO_2$  is used for the cladding and buffer layers. Details of the fabrication can be found in Ref. [3]. Fig. 1(c) shows how 8 cross-grid VCMRR elements are connected in parallel to form the multi-channel add/drop filter. Different add/drop wavelengths can be selected by varying the radius of each ring. In the fabricated device,  $R_1$  has a radius of  $10.35\ \mu m$ , while the remaining rings decrease in radius by increments of  $50\ nm$ . The adjacent ports are separated by  $250\ \mu m$  so that the 1<sup>st</sup> and the 8<sup>th</sup> ports are separated by  $1.75\ mm$ . All device parameters are depicted in the figure captions. A microscope image of the VCMRR node is shown in Fig. 2. The simplicity of the add/drop device is evident.

In the measurement setup, a tunable laser diode (Anritsu MG9638A) with a tunable wavelength range of  $1.50\ \mu m$  to  $1.58\ \mu m$  was used as the light source. The laser output is linearly polarized and a polarization maintaining fiber was used to launch the light into the bus waveguide. The power at the output of the device was coupled into a small spot size fiber ( $\approx 4\ \mu m$ ) to cut down on the noise due to scattering, and the filter response was measured with an optical spectrum analyzer (Anritsu MS9710B). The measured TE and TM filter responses from the first drop port are shown in Fig. 3. The wavelength range spans four resonant peaks. The FWHMs of the peaks, from shortest to longest wavelengths, are  $0.53\ nm$ ,  $0.63\ nm$ ,  $0.64\ nm$  and  $0.71\ nm$  for the TE response, and  $0.92\ nm$ ,  $1.00\ nm$ ,  $1.06\ nm$ , and  $1.16\ nm$  for the TM response. The corresponding microring resonator loaded Q factors are approximately  $Q_L^{TE} = 2500$  and  $Q_L^{TM} = 1500$ . The average FSR is  $20.1\ nm$  for the TE spectrum, and  $20.2\ nm$  for the TM spectrum, centered near the wavelength of  $1.54\ \mu m$ . The peaks all exhibit the classical single-pole Lorentzian shape, except at the nulls where there is noise due to the floor of the detector, as well as some polarization mixing. The polarization cross-talk levels are between  $-15\ dB$  to  $-20\ dB$ , and they are slightly higher for the TE polarization. It is believed that the polarization mixing occurs due to both the imperfect control of the input polarization direction, as well as polarization coupling at the input and crossing junction. Cross-talk might be reduced with better junction design and fabrication techniques.

The complete TM filter responses of all 8 drop ports are shown in Fig. 4. The resonant peaks at each drop port are distinctly observable. In all cases the response increases towards larger wavelengths due to better input coupling, as well as stronger bus-ring coupling. A change in ring radius results in a change in resonant wavelength. With a total change in radius from the first to eighth ring of  $0.35\ \mu m$ , the resonant spectra shifts by  $39.74\ nm$  for the TM polarization, yielding approximately a  $5.7\ nm$  channel spacing per  $50\ nm$  change in ring radius. Smaller incremental changes in ring radius yield smaller channel spacings, and thus multichannel filter design is a simple endeavor using ring resonators. Finer tuning of the channel spacing can also be achieved by changing the widths of the

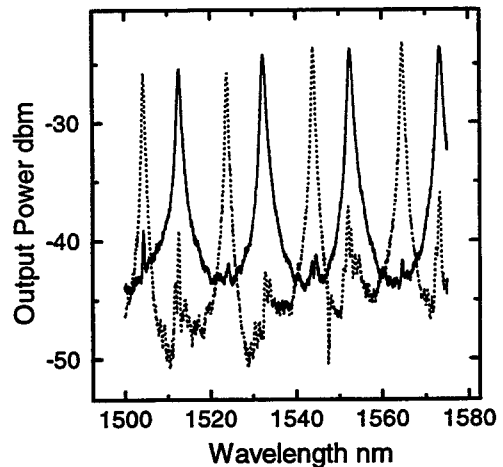


Fig 3. Measured TE (dotted) and TM (solid) filter responses from drop port 1, with  $R=10.35\mu m$ .

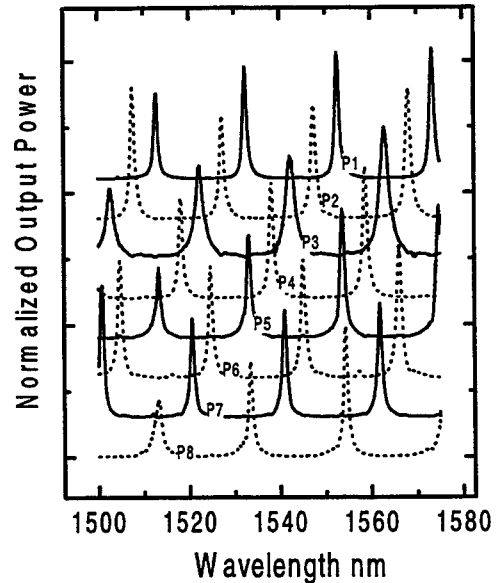


Fig 4. Normalized TM filter responses from all the drop ports.

waveguides, which induce changes in the propagation constants.

In the design of the proposed filter structure, a major concern was the scattering induced cross-talk at the junctions. Although numerical simulations predicted that cross-talk values of less than  $-40 \text{ dB}$  per junction could be achieved theoretically, higher levels of cross-talk were expected due to sidewall roughness and imperfect corners in the fabricated devices. In order to determine the signal to noise ratio of these devices, the cross-grid shown in the inset of Fig. 5 was used.

It consists of two cross-grid nodes, one containing a ring resonator and one without any resonator. The device parameters are the same as in Fig. 1, except that  $R = 20 \mu\text{m}$ ,  $t_{sep} = 0.3$ , and  $t_e = 0.1 \mu\text{m}$ . Fig. 5 highlights the absolute measured responses at the indicated ports, where the top curve shows the channel dropping response, while the bottom curve shows the junction scattering induced cross-talk. The signal to noise ratio is the ratio of the channel drop peaks ( $\approx -20 \text{ dBm}$ ) to the junction scattered baseline power ( $\approx -52 \text{ dBm}$ ). The signal to noise ratio is thus below  $-30 \text{ dB}$ , and can be made smaller by using lower index contrast bus waveguides and by improving the fabrication quality of the junction.

In conclusion, a simple 8 channel add/drop filter incorporating microring resonators vertically coupled to buried waveguides on a cross-grid array was demonstrated. The buried waveguides form an array, crossing through each other at right angles. The low index contrast of the buried waveguides leads to less than  $-30 \text{ dB}$  scattering induced cross-talk at the junctions. The optical channel bandwidths observed were approximately  $1 \text{ nm}$ , and might easily be reduced by decreasing the interaction strength of the ring with the bus waveguides, for example, by increasing the vertical buffer thickness, or displacing the rings laterally away from the buried guides. The observed channel spacings were approximately  $5.7 \text{ nm}$ , and might be reduced by making the incremental changes in ring radii smaller. Because of the topography of the cross-grid, the low index contrast buried waveguides do not need to be bent in order to access the complete surface of the chip. Device density is limited only by the ring dimensions, and one can envision densities approaching  $10^5 \text{ devices/cm}^2$  using  $10 \mu\text{m}$  radius rings.

#### REFERENCES

- [1] B. E. Little, S. T. Chu, H. A. Haus, J. Foresi, and J.-P. Laine, Micro-ring resonator channel dropping filters, *IEEE J. Lightwave Tech.*, vol. 15, pp. 998-1005, 1997.
- [2] S. Suzuki, K. Shuto, and Y. Hibino, Integrated optic ring resonators with two stacked layers of silica waveguides on Si, *IEEE Photonic. Tech. Lett.*, vol. 4, pp. 1256-1258, 1992.
- [3] B. E. Little, S. T. Chu, W. Pan, D. Ripin, T. Kaneko, Y. Kokubun, E. Ippen Vertically coupled glass microring resonator channel dropping filters, *IEEE Photonic. Tech. Lett.*, vol. 11, pp. 215-217, 1999.
- [4] D. V. Tishinin, I. Kim, A. E. Bond, and P. D. Dapkus, in *LEOS 11<sup>th</sup> Annual meeting*, Institute of Electrical and Electronics Engineers, New York, 1998, paper TuK5.

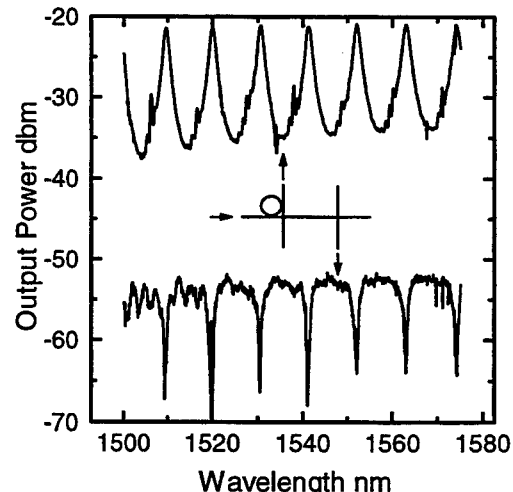


Fig 5. Measured junction cross-talk levels of the layout shown in the inset. The top curve is the measured response at the drop port of the filter and the bottom curve is the measured response from the waveguide junction.

# Multi Wavelength Lasers fabricated using Selective Area Chemical Beam Epitaxy

Peter J. Harmsma, Meint K. Smit and Y. Siang Oei

COBRA Inter-University Research Institute, Delft University of Technology, Faculty of Information

Technology and Systems, P.O. Box 5031, 2600 GA Delft, The Netherlands.

Phone: +31 15 2784950 Fax: +31 15 2784046

e-mail: [P.Harmsma@et.tudelft.nl](mailto:P.Harmsma@et.tudelft.nl)

Maarten R. Leys, Coen A. Verschuren and Hilbert Vonk

COBRA Inter-University Research Institute, Eindhoven University of Technology, Department of Physics, P.O. Box 513, 5600 MB Eindhoven, The Netherlands

## Introduction

Fabrication of complex Photonic Integrated Circuits (PICs) requires the integration of Semiconductor Optical Amplifiers (SOAs) and Passive Waveguide Devices (PWDs) on a single substrate. Integrated SOAs can compensate for device losses and fiber-chip coupling losses in PICs such as Optical Cross Connects (OXC)s [1]. Furthermore, integrated SOAs are key building blocks for wavelength convertors [2], gate switches [3] and on-chip light sources [2,4]. We present the application of a Selective Area Chemical Beam Epitaxy regrowth step [5,6] for the integration of SOAs and PWDs. Fabrication and characterization of extended cavity lasers having transparent waveguides on both sides, as well as 4-channel Multi Wavelength Lasers (MWL) will be presented.

## Device Fabrication

For the definition of active and passive areas we have used a Selective Area Chemical Beam Epitaxy (SA-CBE) regrowth step. This technology enables the fabrication of butt joints between arbitrary layer stacks, where coupling losses can be as low as 0.1 dB/interface [6]. First fabrication step was the epitaxial growth of the layer stack for the SOAs using MOVPE. This layer stack consisted of an InP buffer layer, a 550 nm Q(1.25) film layer, a MQW active layer (5 x 4.5 nm InGaAs well, 4 x 10 nm Q(1.25) barrier), a 1200 nm InP cladding and a highly p-doped InGaAs contact layer. A 100 nm SiN<sub>x</sub> layer was deposited using Plasma Enhanced Chemical Vapor Deposition (PE-CVD), and was removed at the regions to be regrown. Using the SiN<sub>x</sub> layer as a mask, the InGaAs top layer and the InP cladding were removed at these regions using selective wet chemical etching. The MQW active layer was successively removed using Reactive Ion Etching (RIE). In the following SA-CBE regrowth step, the etched trenches were refilled with an undoped InP cladding layer as described in ref. [6] (fig. 1). The resulting butt joint interfaces are shown in fig. 2 for two different crystallographic orientations. Excellent connection between original and regrown layer stacks was obtained. Perfect area selectivity of the regrowth is proven by the absence of material deposition on the SiN<sub>x</sub> layer.

SOA ridges and PWDs were defined in their appropriate regions using one single lithography- and RIE etching step. SOAs were passivated with a new 200 nm PE-CVD SiN<sub>x</sub> layer, contact openings were etched on top of the SOAs. After planarization using photosensitive polyimide and subsequent metallization and annealing, samples were cleaved and Indium soldered on top of a temperature controlled Cu-holder for characterization.

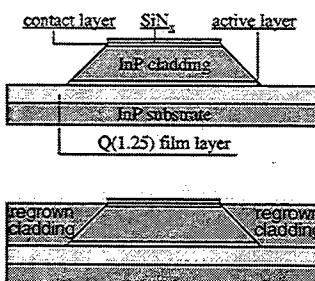


*Fig. 1: definition of active and passive areas using SA-CBE.*

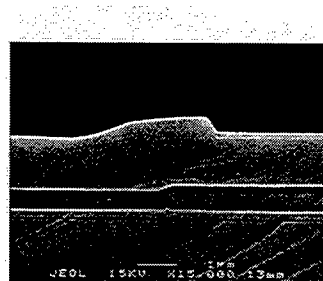


*Fig. 2a: butt joint interface, view on (011) plane,*

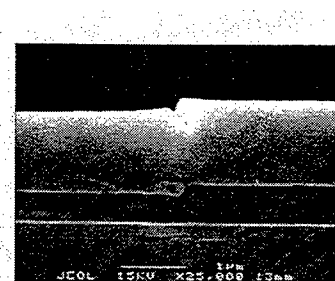


*Fig. 2b: butt joint interface, view on (011) plane.*

### Measurement results

SOAs of various lengths with transparent waveguides on both sides were characterized as extended cavity lasers. Devices with as-cleaved facets showed stable CW laser operation at a wavelength of 1.56  $\mu\text{m}$ . For an SOA length of 1000  $\mu\text{m}$  the threshold current was 71 mA. Without applying any bias current, systematic Fabry-Perot loss measurements on integrated SOAs with lengths of 10 to 100  $\mu\text{m}$  were performed. From these measurements, butt joint coupling losses of 0.25 and 0.45 dB/interface were deduced for the butt joint interfaces corresponding to fig. 2a and 2b respectively. For the Multi Wavelength Lasers (MWLs) the active section length was 1500  $\mu\text{m}$ , butt joint interfaces were as shown in fig. 2b. Fig. 4 shows a photograph of two 4-channel MWLs, labeled A and B, each MWL containing a PHASAR and 4 SOAs. Design channel spacing and Free Spectral Range (FSR) of the PHASARS were 3.2 nm (400 GHz) and 8 times 3.2 nm = 25.6 nm respectively. The central wavelengths of devices A and B differ by 4 times the channel spacing = 12.6 nm. In this way, at least one of the MWLs will have all its channels lasing in adjacent wavelengths (in one PHASAR order), irrespective of the position of the gain peak. PHASAR losses were 3 – 4 dB, as was deduced from measurements of ASE spectra at the individual outputs 1...4 and at the common outputs A and B (fig. 5). For pulsed operation, both MWLs operated in one order of the PHASAR. For CW operation, the gain spectrum is shifted to the longer wavelengths, and channels 1 and 2 of MWL A were shifted to a lower order. CW spectra of all channels are shown in fig. 5 at a current of 150 mA and a temperature of 20°C, threshold currents of the MWLs ranged from 125 to 140 mA. The ‘bumps’ in the spectra at the shorter wavelength side of each peak were caused by TM ASE, as was verified by inserting a polarizer in the optical path. The position of these bumps corresponds to the TE/TM shift of the polarization dependent PHASARS.

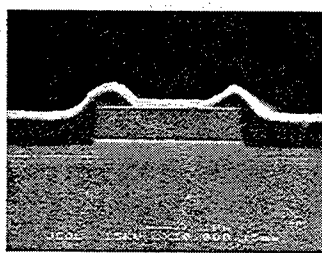


*Fig. 3: SEM photograph of SOA cross section.*

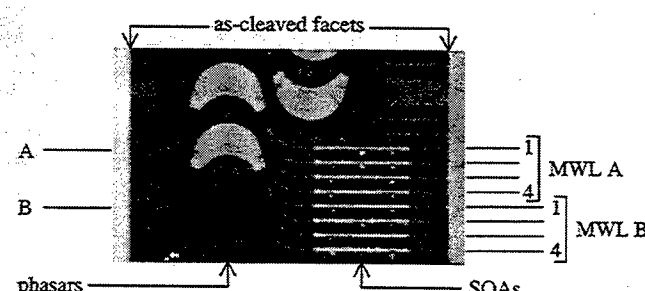


*Fig. 4: optical photograph of two 4-channel multi wavelength lasers.*

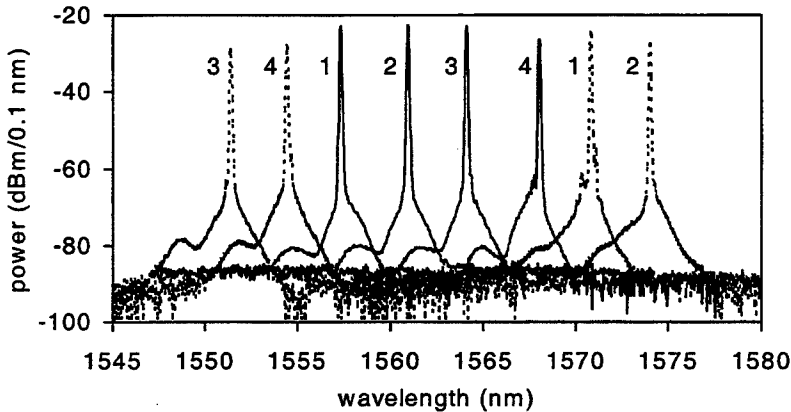


Fig. 5:Laser spectrum of MWL A (dashed) and MWL B (solid), 150 mA, 20 °C

### Conclusions

We have applied a Selective Area Chemical Beam Epitaxy regrowth step for the definition of active and passive regions on a single chip. Excellent butt joint interface morphology and area selectivity of the regrowth was demonstrated. Butt joint coupling losses were 0.25 and 0.45 dB/interface, depending on crystal orientation. SOAs, transparent waveguides and PHASARS were fabricated in their appropriate regions. Extended cavity lasers with transparent waveguides on both sides showed stable CW laser operation at 1.56 μm. Using SA-CBE, we have successfully fabricated 4-channel Multi Wavelength Lasers consisting of SOAs integrated with PHASARS. Therefore, we believe that SA-CBE is compatible with the fabrication of complex Photonic Integrated Circuits such as Add Drop Multiplexers and Optical Cross Connects.

### References

- [1] C.G.P. Herben, C.G.M. Vreeburg, D.H.P. Maat, X.J.M. Leijtens, Y.S. Oei, F.H. Groen, J.W. Pedersen and M.K. Smit, "A Compact Integrated InP-Based Single-PHASAR Optical Crossconnect", IEEE Photon. Technol. Lett., Vol. 10, No. 5, pp. 678-680, 1998.
- [2] L.H. Spiekman, U. Koren, M.D. Chien, B.I. Miller, J.M. Wiesenfeld and J.S. Perino, "All-Optical Mach-Zehnder Wavelength Converter with Monolithically Integrated DFB Probe Source", IEEE Photon. Technol. Lett., Vol. 9, No. 10, pp. 1349-1351, 1997.
- [3] H. Ishii, H. Sanjoh, M. Kohtoku, S. Oku, Y. Kadota, Y. Yoshikuni, Y. Kondo and K. Kishi, "Monolithically Integrated WDM Channel Selectors on InP Substrates", Proc. ECOC Madrid, pp. 329-330, 1998.
- [4] C.R. Doerr, C.H. Joyner, L.W. Stulz and J.C. Centanni, "Wavelength Selectable Laser With Inherent Wavelength and Single-Mode Stability", IEEE Photon. Technol. Lett., Vol. 9, No. 11, pp. 1430-1432, 1998.
- [5] E. Vergnol, F. Devaux, D. Jahan and A. Carencio, "Fully integrated millimetric single-sideband lightwave source", Electronics Letters, Vol. 33, No. 23, pp. 1961-1963, 1997.
- [6] C.A. Verschuren, P.J. Harmsma, Y.S. Oei, M.R. Leys, H. Vonk and J.H. Wolter, "Butt-coupling loss of 0.1 dB/interface in InP/InGaAs MQW waveguide-waveguide structures grown by selective area chemical beam epitaxy" J. Cryst. Growth 188, pp 288-294, 1998.

## Wavelength Tuning Characteristics of the Grated Coupler Sampled Reflector Laser for Wavelength Switching Applications

Olga A. Lavrova, Daniel J. Blumenthal

Department of Electrical and Computer Engineering  
 University of California at Santa Barbara, Santa Barbara, CA 93106  
 Phone: (805) 893 5616      Fax: (805) 893 5705  
 e-mail: [olavrova@engineering.ucsb.edu](mailto:olavrova@engineering.ucsb.edu)

Wavelength Division Multiplexing (WDM) technologies are developing and gaining rapid acceptance in modern optical networking. Grated Coupler Sampled Reflector (GCSR) semiconductor lasers show great promise for implementation in future DWD communication systems as a broadly tunable transmitter. Tuning ranges of 70 –100 nm [1-3] are possible with these devices, which means potential availability of 150-100 standard ITU channels with just one device. Previous studies [4] has also shown that GCSR lasers are capable of a fast (on the order of nanosecond) switching between lasing modes. In this paper we report on an analytic numerical model of the GCSR laser. To the best of the authors' knowledge, such a model of the GCSR has not been reported so far. Simulation results are compared with experimental ones.

The GCSR laser is a four section device (Fig. 1(a)) where one section is responsible for gain, and three other sections (Coupler, Phase and Reflector) provide wide wavelength tunability of the device. Superimposed optical spectra of operation at 42 standard ITU channels (50 GHz spacing) is shown in the Fig. 1(b).

We have developed a numerical analytic model, based on the coupled-mode theory and transmission matrix formalism, which describes output characteristics (spectral selectivity of a lasing mode, SMSR, etc.) of the GCSR in a wide tuning range. Peak lasing wavelength as a function of coupler and reflector currents is shown in the Figure 2(a). 2-Dimensional projection of the same surface is plotted in the Figure 2(b). Coarse tuning of the lasing wavelength is realised by changing only Coupler current – peak wavelength is tuned in steps corresponding to Samples Reflector comb spacing (2.-.5 nm). Fine tuning is realised by changing Reflector current

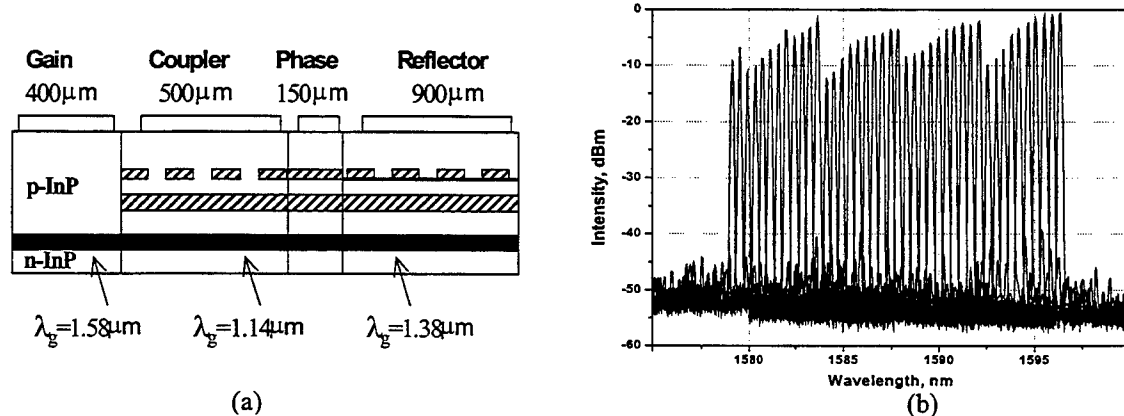


Figure 1: (a) Schematic structure of the Grated Coupler Sampled Reflector (GCSR) laser and  
 (b) Superimposed optical spectra of 42 ITU channels spaced 50 GHz apart

– peak wavelength is changed “quasi-continuously” with jumps corresponding to longitudinal mode spacing of the GCSR laser cavity (0.2-0.4 nm). Truly continuous tuning of the lasing wavelength is realised by simultaneous changes of all three (coupler, reflector and phase) currents (not shown in the figure for clarity). From the simulation we can also see that some wavelengths are impossible to obtain or can only be obtained with a poor SMSR. This happens when the Sampled Reflector and Grated Coupler transmission spectra have poor or no overlap. The insets in the Figure 2 explain the situation.

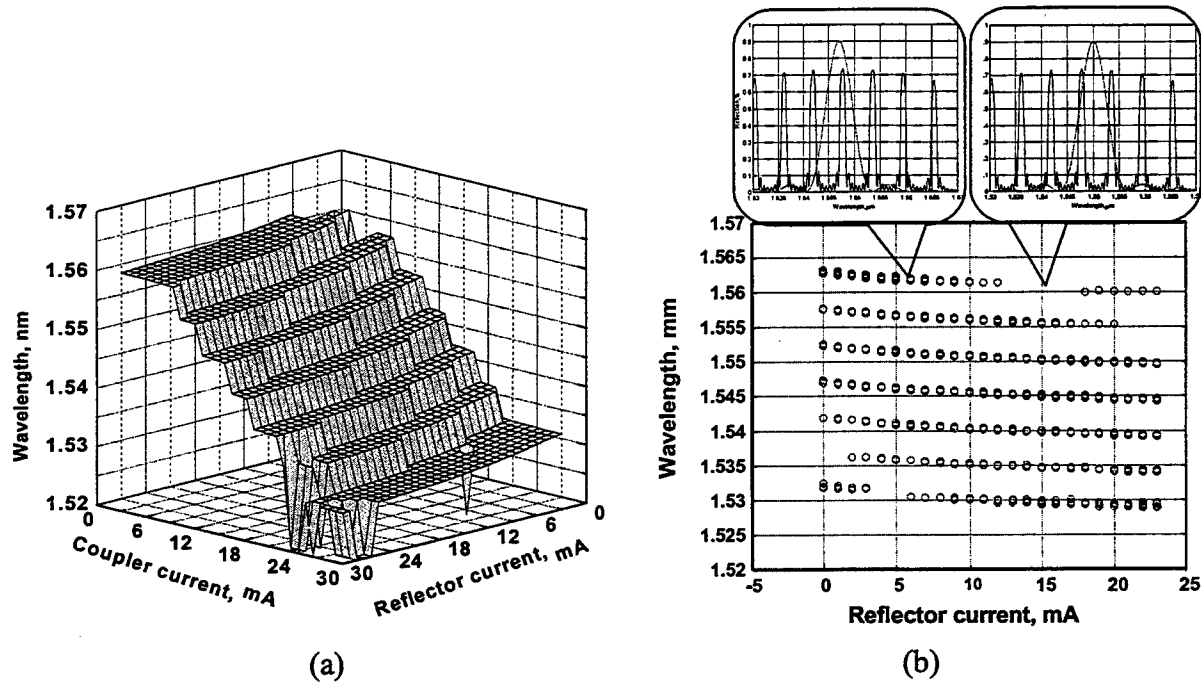


Figure2: (a) Simulation of the map of lasing wavelength versus coupler and reflector currents for a GCSR laser.

(b) Simulation of the tuning curves of a GCSR laser as a function of reflector current for a number of coupler currents

Accurate analytical model of the GCSR gives us a powerful tool to analyse performance of the device. Therefore, it becomes possible to determine the triplets of currents into the tuning sections to obtain lasing at a desired wavelength (standard ITU frequency grid) without a routine manual searching for each of these channels (that may take as long as few days).

To verify results of the simulation, we have performed a systematic experimental measurements of a wavelength tuning of the GCSR laser. For that, mapping of the peak lasing wavelength, power and Side Mode Suppression Ratio (SMSR) in a wide range of coupler and reflector currents was carried out. A typical map of the lasing wavelength and its 2-Dimensional projection are shown in Figs. 3 (a) and (b) correspondingly. Plateaus, corresponding to coupler current tuning, and long continuous regions, corresponding to reflector current tuning, can be clearly seen. We can also observe drop off of some the lasing wavelengths, similar to the case in our simulation. (The simulation was carried out for a device parameters, different from the ones of the device in the Fig. 2, so wavelength to drop are different in each case.)

In summary, we have presented analytical model, describing static tuning and wavelength selectivity mechanisms in the GCSR laser. Providing GCSR structure and parameters are known, static tuning characteristics (such as lasing wavelength, SMSR) can be accurately simulated in a wide range of tuning currents, and wavelength instability regions can be predicted. Further work will include development of the dynamic tuning model that will allow us describing fast switching between lasing modes and determine the ultimate limits switching times. Experimental measurements of the switching times will be carried out and compared with results of the simulation.

This work was supported by funding from the Naval Research Laboratory under the Grant N00014-97-1-G024

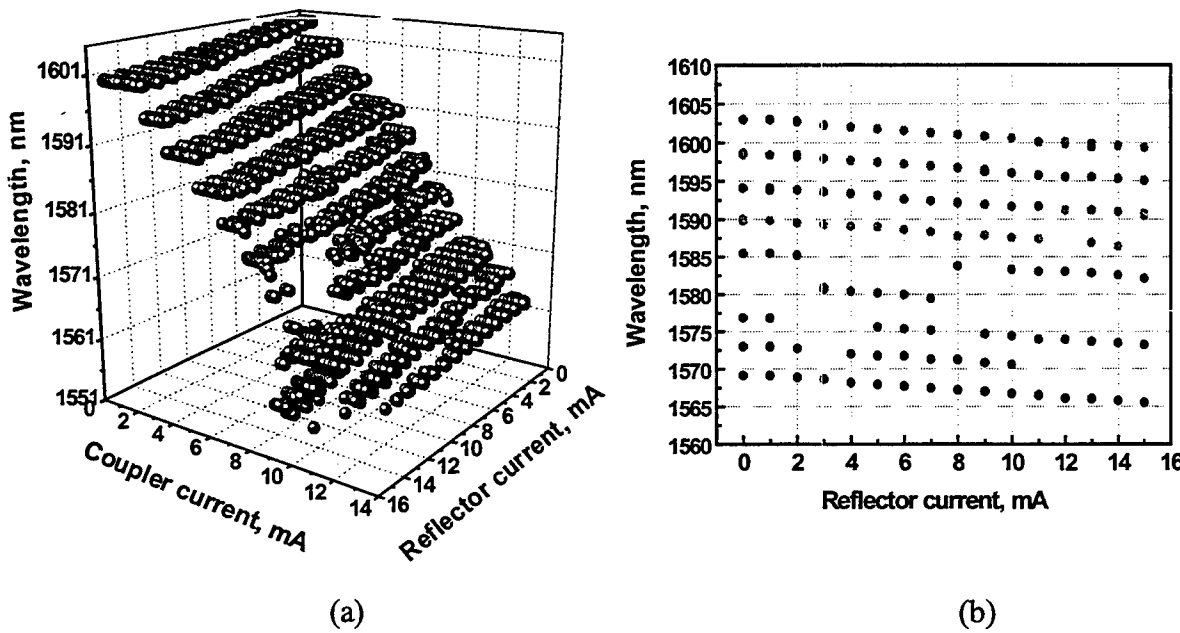


Figure. 3: (a) Measured map of lasing wavelength versus coupler and reflector currents for a GCSR laser.  
 (b) Measured tuning curves of a GCSR laser as a function of reflector current for a number of coupler currents

#### References:

- [1] P.-J. Rigole et al. "State-of-the art: widely tunable lasers", SPIE Vol. 3001, p.382
- [2] P.-J. Rigole et al. "114-nm wavelength tuning range of a vertical grating assisted codirectional coupler laser with a super structure grating distributed Bragg reflector", IEEE Photonics Technology Letters, vol. 7, July 1995
- [3] P.-J. Rigole et al. "Wavelength coverage over 67 nm with a GCSR laser. Tuning characteristics and switching speed", 15<sup>th</sup> IEEE Int. Semiconductor Laser Conference, paper W1.1, Haifa, Israel, October 1996
- [4] P.-J. Rigole et al. "Fast wavelength switching in a widely tunable GCSR laser using a pulse pre-distortion technique", OFC'97, paper WL63, Feb. 1997

**Integrated Photonics Research**

# New Physics/Devices

**Monday, July 19, 1999**

**Shun-Lien Chuang, University of Illinois, Urbana-Champaign, USA**  
Presider

**RMC**  
**11:00am–12:30pm**  
Sierra Madre South

## Single Photon Turnstile Device

O. Benson, J. Kim, C. Santori, and Y. Yamamoto

*ICORP Quantum Entanglement Project*

*Edward L. Ginzton Laboratory, Stanford University*

*Stanford, CA 94305-4085*

A single photon turnstile device utilizes simultaneous Coulomb blockade for electrons and holes in a mesoscopic double barrier p-n junction [1]. Figure 1 (a) shows a schematic of the energy levels of our GaAs/AlGaAs structure [2]. It consists of three quantum wells (QW) sandwiched between n-type and p-type layers grown by MBE. The lateral size of the device is reduced to increase the single charging energy. The electron resonant tunnel condition into an electron sub-band in the central QW is satisfied at a certain bias voltage. When the electron tunnels, the Coulomb repulsive interaction between electrons shifts the electron sub-band energy to above the Fermi level of the n-side QW, so further electron tunneling is inhibited. Then, the bias voltage is increased to the hole resonant tunneling condition and a single hole tunnels. By modulating the bias voltage between the electron and hole resonant tunneling conditions, we can inject a single electron and a single hole into the central QW periodically. If the tunnel time and the radiative recombination time of an electron-hole pair are much shorter than the pulse duration, one and only one photon is emitted for every modulation period.

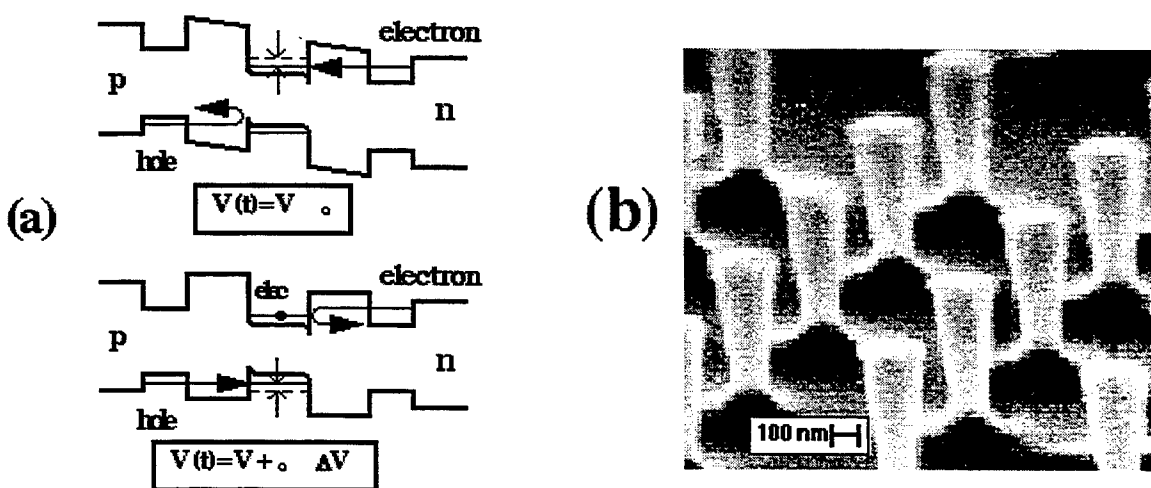


**Figure 1:** (a) Energy level structure and (b) SEM picture of the device.

The device was installed in a dilution refrigerator and was biased with a DC and AC voltage source. A DC current flowing through the device was measured as a function of DC bias voltage with a square wave AC modulation voltage. Figure 2 (a) shows the measured current through the device as a function of AC modulation frequency, with three different DC bias voltages. The measured current was in close agreement with the relation  $I = ef$ ,  $I = 2ef$ , and  $I = 3ef$  (solid lines). In Figure 2 (b) we evaluate the slope  $I/f$  from the current vs. frequency curves and plot it as a function of the DC bias voltage. We find that the slope increases discretely.

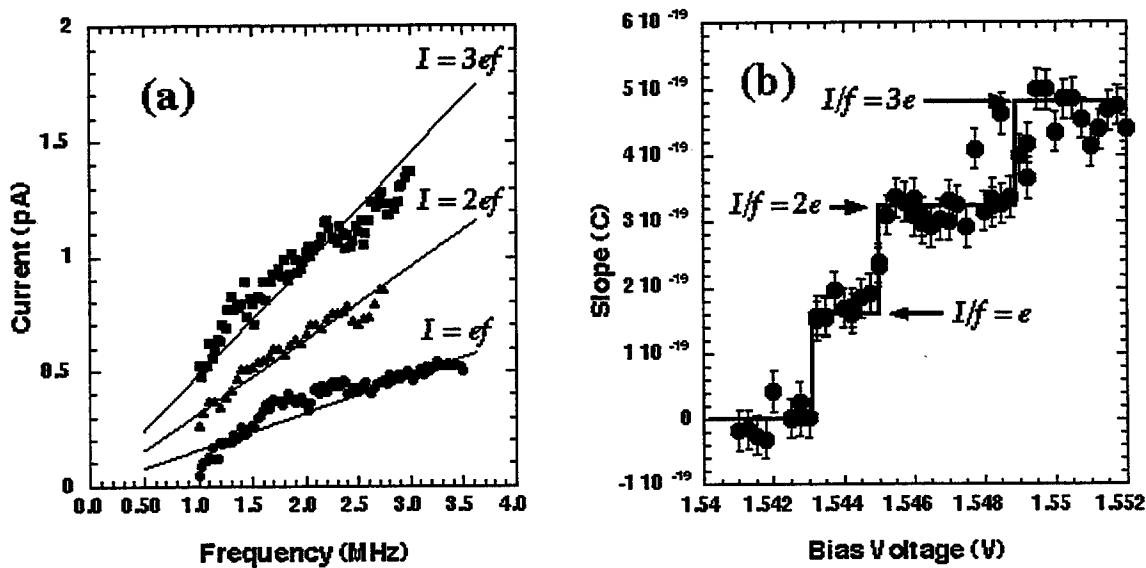


**Figure 2:** (a) Current frequency dependence and (b) slope  $I/f$  vs. bias voltage.

The locking of the current at multiples of the modulation frequency suggests that the charge transfer through the device is strongly correlated with the external modulation signal. At the first current plateau, at  $I = ef$ , a single electron and a single hole are injected into the central QW per modulation period. At the second current plateau, two electrons and two holes are injected into the central QW per modulation period, resulting in two photon emission. This multiple charge operation becomes possible because of relatively broad inhomogeneous linewidths of the n-side and p-side QWs.

We detected the emitted photons from this device and measured the time delay from the rising edge of the modulation input to the photon detection event at the first current plateau ( $I = ef$ ) and second current plateau ( $I=2ef$ ). The histograms of the measured time delay is shown in Fig. 3 (a) and (c) together with Monte-Carlo numerical simulations (b) and (d). The fact that the photon

emission probability decreases during the on-pulse duration is a unique signature that the number of holes injected during an on-pulse is restricted to either one or two due to the Coulomb blockade effect. Figure 3 (e) shows the experimental result on a larger area device at a higher temperature of 4 K, where Coulomb blockade effect is absent. In this case, the resulting photon emission probability increases monotonically. This result is well-reproduced by the simulation Fig. 3 (f).

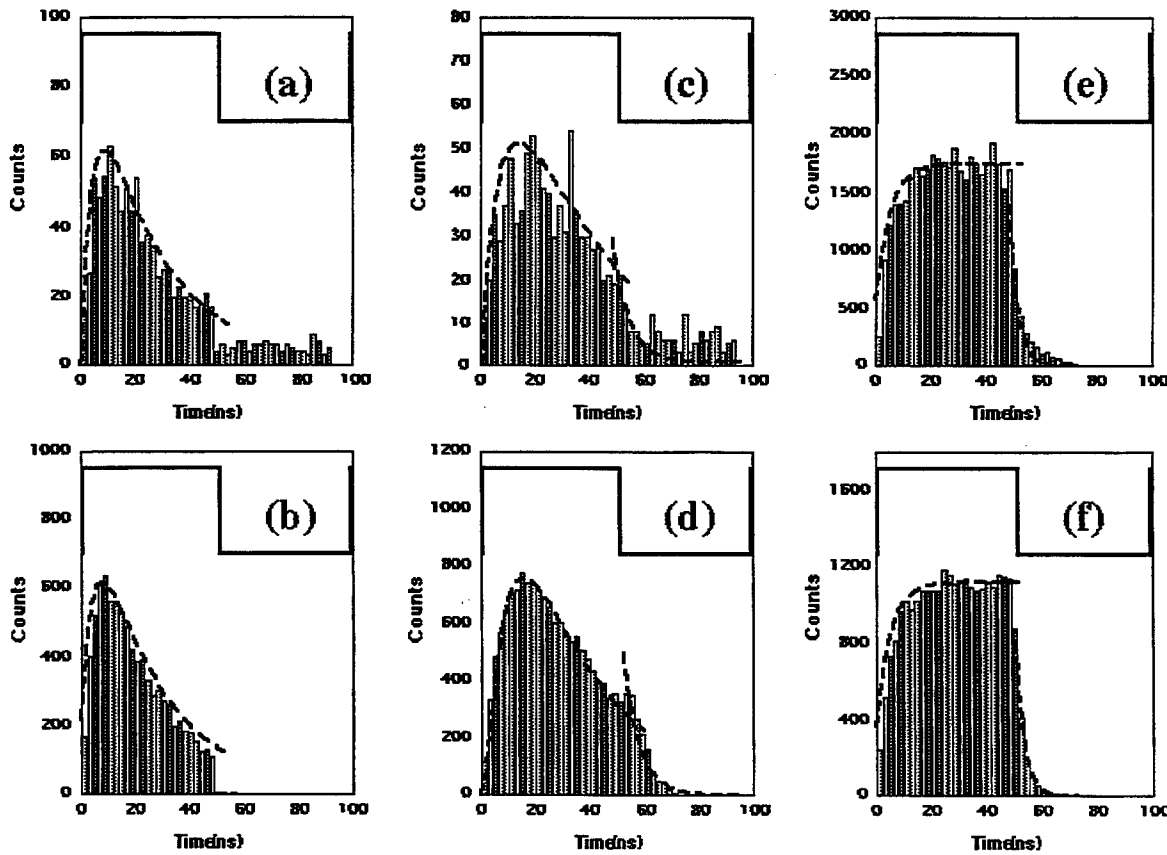


**Figure 3:** Photon emission characteristics.

The experimental results reported here provide evidence for the generation of heralded single photons (and n-photons) where the time interval between single photons is regulated to beyond the Poisson limit. A new device structure with an isolated single quantum dot and a monolithic microcavity will allow an improved operation and will be discussed as well.

[1] A. Imamoglu & Y. Yamamoto, Phys. Rev. Lett. **72**, 210-213 (1994).

[2] J. Kim, O. Benson, H. Kan, and Y. Yamamoto, Nature **397**, 500-503 (1999).

## Quantum interference in optoelectronics

A. Imamoglu, H. Schmidt, and D. Nikonov

The progress in absorption cancellation via coherent resonant tunneling induced Fano interference in semiconductor quantum wells is discussed.

### Introduction

Many interesting phenomena in optics such as electromagnetically induced transparency (EIT) [1] and lasers without population inversion (LWI) originate from atomic coherence and interference of radiative processes. One common feature is Fano interference where two decay processes from two different states interfere due to coupling of these states to the same reservoir. This interference occurs even though the processes are irreversible. After the successful observation of these phenomena in atomic media, it is natural to investigate the possibility of extending them to semiconductor materials where practical applications in optoelectronic devices can be pursued[2]. Despite possibility of designing optical properties using *bandgap engineering* to enhance quantum interference effects, semiconductors suffer from ultrafast dephasing processes that severely limit the observability of quantum coherence effects. In addition, many-body interactions between electrons (and holes) play a crucial role in determining the dynamics.

We have recently succeeded in demonstrating *tunneling induced transparency* (TIT) in intersubband transitions of double quantum-well (QW) structures [3]. Unlike their atomic counterparts, QW experiments do not require the presence of a strong coherent laser field to induce Fano interference; instead, resonant tunneling between two subbands provide the coherent coupling.

A rigorous theory of quantum interference effects in semiconductors requires the inclusion of many-body effects in connection with relaxation and subband dispersion. We have extended the semiconductor Bloch equations to include quantum interference effects and utilized this technique to analyze the possibility of observing TIT in a wide range of semiconductor systems [4]. In particular, we found that TIT can be observed using interband excitonic transitions.

### Tunneling induced transparency

The band structure of the generic double QW structure that exhibits TIT is shown in Figure 1. The subband  $|2\rangle$  of the shallow well is resonant with the upper subband  $|3\rangle$  of the deep well: coherent resonant tunneling between these two subbands (with strength  $\Omega_c$ ) creates two delocalized subbands that are the counterparts of atomic dressed states created by a coherent laser field. The absorption of the electrons in subband  $|1\rangle$  is monitored using Fourier transform infrared (FTIR) spectroscopy. The applied gate voltage is used to tune the subbands  $|2\rangle$  and  $|3\rangle$  in and out of resonance. The dominant broadening mechanism for this structure is incoherent tunneling of electrons (at rate  $\Gamma_3$ ) from subband  $|3\rangle$  to the collector region.

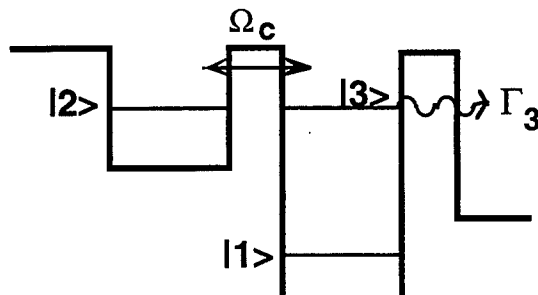


Figure 1: The band diagram of a double quantum-well structure that exhibits quantum interference.

Absorption profile obtained for a GaAs/AlGaAs double QW structure similar to that of Fig.1 is shown in Figure2: We note that the peaks in the doublet structure are asymmetric and cannot be fitted without taking into account quantum interference effects. Conversely, the absorption in between the two peaks is more than 50% smaller what it would have been, had the interference effects been absent (dashed line in Fig.2) [3]. For comparison, we have also plotted the best fit to the experimental results obtained by density matrix calculations that include quantum interference terms (solid line). This experimental demonstration of tunneling induced Fano interference, which we have termed TIT, has been later reproduced by other groups.

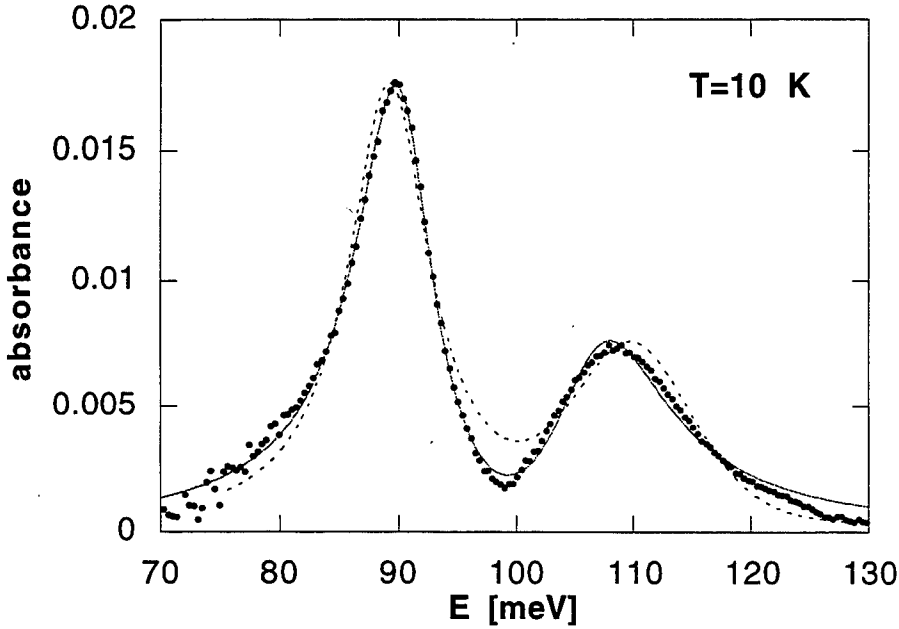


Figure 2: The absorption profile of the double quantum well structure obtained by Fourier transform infrared spectroscopy. The dots correspond to the experimental data. The solid and dotted lines correspond to the best fits obtained with and without taking into account quantum interference terms, respectively.

As we discussed earlier, the existence of quantum interference effects even in intersubband transitions (which most closely resemble atomic transitions) is somewhat surprising given the presence of strong electron-electron interactions and relatively large inhomogeneous broadening due to band non-parabolicity. We have recently carried out calculations of the absorptive and emissive properties of multi-subband QW structures that exhibit quantum interference effects, by generalizing semiconductor Bloch equations [4]. Our results showed that the principal effect of interactions is to shift the absorption line due to the so-called *depolarization* effect and to eliminate the effects of inhomogeneous broadening by creating collective excitations that carry practically all of the oscillator strength of the electron gas (Figure 3). In other words, quantum interference effects in semiconductors is observable due to the presence of Coulomb interactions, and the interfering transitions are collective in nature.

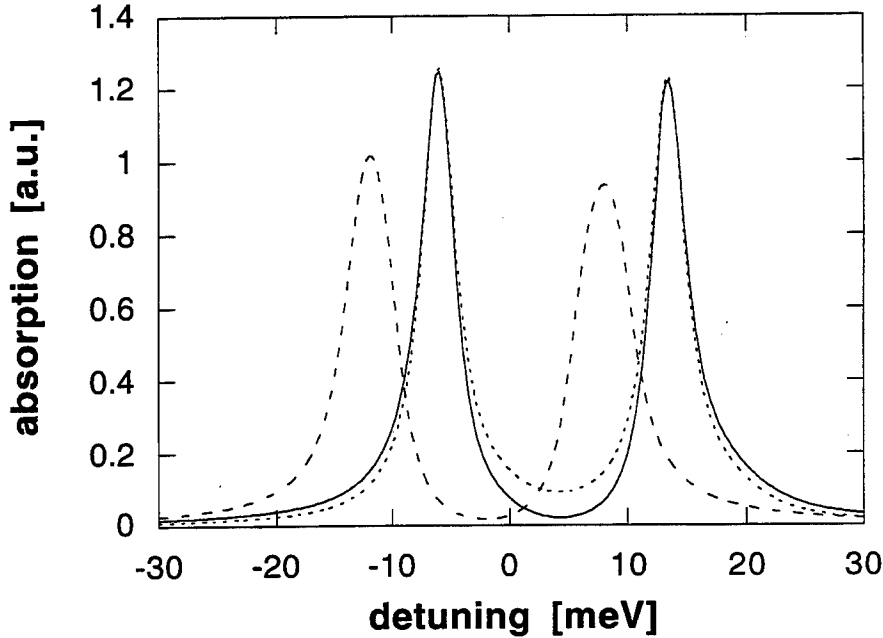


Figure 3: The absorption profile of the double quantum well structure calculated using semiconductor Bloch equations. The solid-curve takes into account both band nonparabolicity, quantum interference, and Coulomb interactions. The dashed line is the single-particle result whereas the dotted curve shows the profile when Coulomb interactions are not taken into account, whereas nonparabolicity and quantum interference effects are.

### Conclusion

Absorption presents a fundamental limitation to practically all optical devices. Therefore, the demonstration of resonant absorption reduction by an induced destructive quantum interference has implications for a wide variety of optoelectronic devices. The most important question from the optoelectronics point-of-view is the applicability of these techniques to actual devices such as lasers and nonlinear frequency converters. In atomic systems it has been shown experimentally that destructive quantum interference in absorption is accompanied by a constructive quantum interference in emission, which lead to the realization of a laser that operates without population inversion. It is also well known that nonlinear susceptibilities can also exhibit constructive interference, giving rise to large improvements in conversion efficiency. Most of these results appear to be applicable to semiconductor devices; however significant technological challenges need to be met.

### References

- [1] S. E. Harris, Phys. Today **50**, 36-42 (1997).
- [2] A. Imamoglu and R. J. Ram, Opt. Lett. **19**, 1744 (1994).
- [3] H. Schmidt, K. Campman, A. Gossard, and A. Imamoglu, App. Phys. Lett. **70**, 3455 (1997).
- [4] D. Nikonov, A. Imamoglu, L. Butov, and H. Schmidt, Phys. Rev. Lett. **79**, 4366 (1997).

## Optical and transport properties of superlattice quantum wires

Jong Chang Yi

School of Electronics and Electrical Engineering, Hong Ik University

Sangsu 72-1, Mapo, Seoul, 121-791, Korea

Tel: 82-2-320-1484 Fax:82-2-320-1119 E-mail:wave@wow.hongik.ac.kr

Despite the potential advantages of the quantum wire for the optoelectronic device applications, there has been a wide skepticism on its practical feasibility. Although the experimental samples and devices incorporating the quantum wire as the active media have shown great progresses since it was first reported[1], they still show little improvement compared to the quantum well counterparts in view of the practical device applications. Seemingly good one dimensional nanostructure devices have shown no true quantum wire-like characteristics such as the larger temperature coefficient, smaller threshold current, or larger resonance frequency[2-3] when they serve as the active region in semiconductor diode lasers. The apparent problems are mainly due to the difficulties in controlling their nanostructure hetero-interfaces and material homogeneity. Since the best prescription may come from a precise diagnosis, the state-of-the art one dimensional nanostructures[4-6] will be investigated in this paper to get insights of what is going on inside the practical quantum wires. Necessary theoretical and numerical methods developed for a more efficient and systematic analysis will be introduced. The possible benefits in the optical and electrical properties one can obtain from the practical quantum wire devices will be quantitatively assessed, together with the detrimental conditions and requirements to be met.

Firstly, a numerical method has been applied to the analysis of the optical properties of lateral superlattice quantum wire arrays grown on vicinal substrates known as the serpentine superlattices(SSLs) as shown in Figure 1. In the modeling, the aluminum composition in the AlGaAs SSL is assumed to vary sinusoidally between  $x_b$  and  $x_w$  along the horizontal line A-A'. For the analysis of the valence band intermixing effects, the 4 band Luttinger-Kohn Hamiltonian is used[7] and the linewidth of the gaussian lineshape function was used as a fitting parameter to simultaneously fit the gain curves for TE and TM modes. To show the validity of the numerical tools developed, the theoretical calculations for gain and injection current levels are compared to the experimental data as shown in Figure 2, where they agree well. Further analysis results revealed that the aluminum segregation between  $x_b$  and  $x_w$  is only 7% and the linewidth is approximately 7 meV.

In addition, the said method has also been applied to the analysis of lateral quantum wires grown on patterned V-grooves[6] and laterally strained quantum wires[5]. The laterally strained quantum wire arrays have shown a strong polarization anisotropy in threshold current up to 77K and are very promising for the polarization dependence control in optoelectronic devices. The quantum wire lasers grown on patterned V-grooves have

shown a reduced threshold current density at room temperature. Such promising devices will be analyzed to see whether such an improvement is due to the quantum wire effect, and how much one can expect.

The second part of this paper is focused on the transport properties of 1D nanostructure. The ultimate reduction of the scattering in 1D system will result in ballistic transport along the quantum wires. Such coherent wavelike transport properties have presented new device concepts for quantum interference devices[8]. Most current 1D-transport structures, however, have quasi-one-dimensional structures. The carriers are not confined by lateral hetero-structures but by a spatial variation of electrostatic potential, which is controlled by remotely attached electrodes. The analysis of such structures thus requires a self-consistent solution of Poisson's and Schrödinger's equations, since the flat band approximation is no longer valid. In this paper, a new approach to the self-consistent solution of these equations is described by using another finite-element method. The convergence rate is accelerated by using Newton-Raphson method[9]. This numerical technique is applied to analyze the band structures of the split-gate electron waveguides. Figure 3 shows good agreement between experimental data and theory, which has been obtained with an accurate modeling of the surface states and the charge densities.

- [1] P. M. Petroff, A. C. Gossard, R. A. Logan and W. Wiegmann, *Appl. Phys. Lett.*, vol. 41, pp. 635-638 (1982).
- [2] Y. Arakawa and H. Sakaki, *Appl. Phys. Lett.*, vol. 40, 939-941 (1982).
- [3] Y. Arakawa, K. Vahala, and A. Yariv, *Surface Science*, vol. 174, pp. 155-162 (1986).
- [4] S. Y. Hu, M. S. Miller, D. B. Young, J. C. Yi, D. Leonard, A. C. Gossard, P. M. Petroff, L. A. Coldren, and N. Dagli, *Appl. Phys. Lett.*, vol. 63, pp. 2015-2017 (1993).
- [5] K. Y. Cheng, E. M. Stellini, P. J. Pearah, A. C. Chen, A. M. Moy, and K. C. Hsieh, *International Electron Device Meeting '92*, pp. 875-878 (1992).
- [6] T. Toda and Y. Nakano, to be presented at *InP Related Material '99* (1999).
- [7] J. C. Yi and N. Dagli, *IEEE J. Quantum Electronics*, vol. 31, pp. 208-218 (1995).
- [8] N. Dagli, G. Snider, J. Waldman, and E. Hu, "An electron wave directional coupler and its analysis," *J. Appl. Phys.*, vol. 69, pp. 1047-1051, (1991).
- [9] J. C. Yi, M. Thomas and N. Dagli, *IPR '94*, paper FD2, (1994).

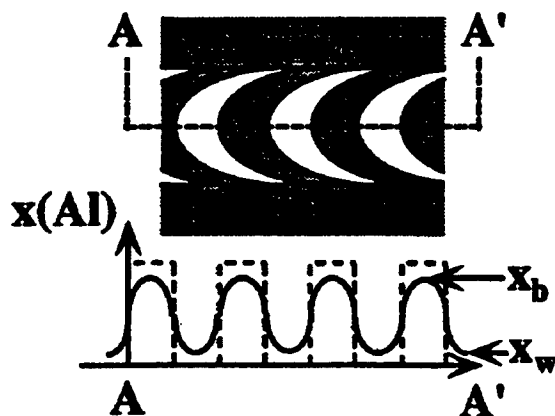


Figure 1. Cross sectional profile of  $\text{Al}_x\text{Ga}_{1-x}\text{As}$  serpentine superlattice(SSL) quantum

wires. Aluminum composition along the horizontal line A-A' is assumed to vary sinusoidally between  $x_b$  and  $x_w$ .

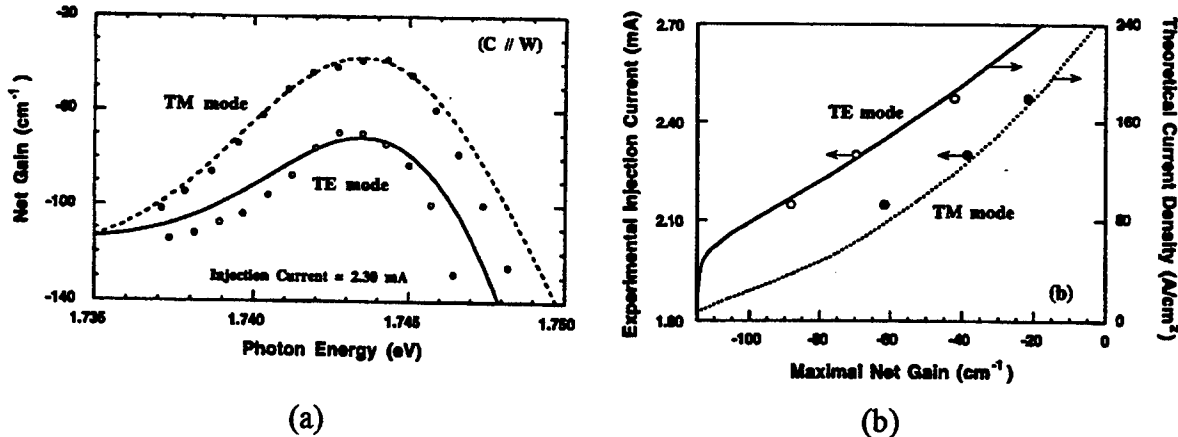


Figure 2. (a) TE and TM gain spectra of SSL QWR LD at 1.4K with the injection current of 2.30mA. (b) Experimental injection current(circles) and theoretical current densities(lines) as a function of the maximal net gain for TE and TM modes.

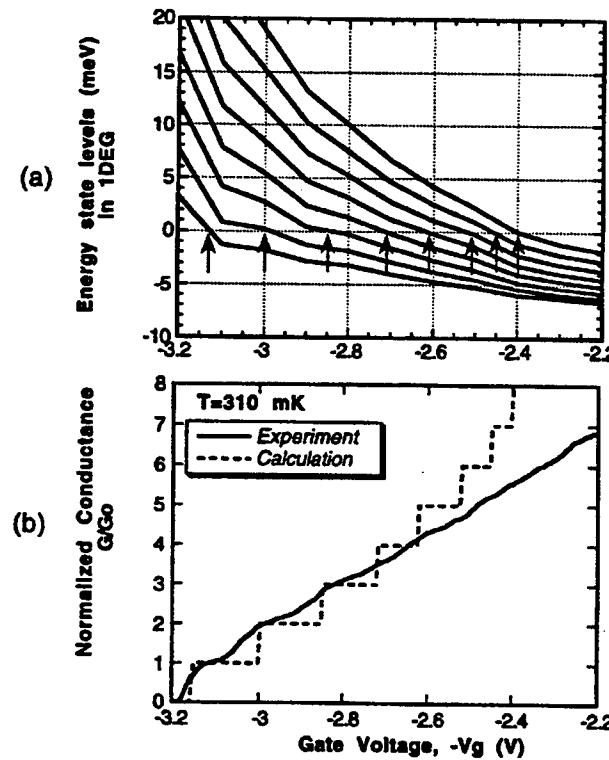


Figure 3. (a) Variation of eigen energy levels in split gate electron waveguide. The arrows indicate where the energy levels cross over the fermi level. (b) Its measured and calculated conductance at 310 mK. They agree well for the first 3 steps. Measured steps for the higher subbands are smeared due to the scattering.

**Integrated Photonics Research**

# **Waveguide Modeling**

**Monday, July 19, 1999**

**Anand Gopinath, University of Minnesota, USA**  
Presider

**RMD**  
**11:00am–12:30pm**  
Anacapa

## Time-domain solution of vector wave equations by Taylor expansion

**J. A. Fleck, Jr.**, Lawrence Livermore National Laboratory, 312 Remington Loop, Danville, CA 94526, (925) 743 1758

In a recent publication we have described a method for solving a general class of wave equations by Taylor expansion.<sup>1</sup> The method is based on expanding the field  $E(\mathbf{r}, t)$  and its time-derivative  $\partial E(\mathbf{r}, t) / \partial t$  as Taylor series in  $t$ . Using the governing wave equation one can express the Taylor series coefficients in terms of spatial derivatives of the field. Termination of the expansion at a given order of  $t$  provides an explicit algorithm for advancing the field numerically in time over increments  $\Delta t$  by numerical evaluation of spatial derivatives of the field available at the end of the previous time step. The Taylor series method is typically applied to fourth order in time but can be readily generalized to higher orders. The widely prevalent finite-difference time-domain (FDTD) method, on the other hand, as usually applied, is second order accurate in time and space and is much more difficult to generalize to higher orders.<sup>2-3</sup> A further advantage of the Taylor series method is that  $E(\mathbf{r}, t)$  and  $\partial E(\mathbf{r}, t) / \partial t$  are both evaluated at points on the same spatial grid and time scale. The FDTD method, in contrast, operates with the field variables  $E$  and  $H$  expressed on staggered spatial grids and time scales. One of the main advantages of time-domain methods over steady-state methods is the ease and accuracy of treating scattering and reflections. For treating monochromatic radiation it is customary to employ cw boundary conditions, wherein the field at some boundary is assigned a sinusoidal variation in time or a sinusoidal variation with perhaps a slowly varying envelope. We report here how the Taylor expansion method can be applied with cw boundary conditions by including a suitable source term in the wave equation. We also report the application of the method to full-vector field calculations for the TE polarization in two space dimensions.

We begin by writing the scalar wave equation with a source term as

$$\frac{\partial^2 E}{\partial t^2} - p^2 E = S(\mathbf{r}, t), \quad (1)$$

where the operator  $p^2$  is defined by

$$p^2 = \frac{c^2}{n^2} \nabla^2, \quad (2)$$

and the index of refraction  $n(\mathbf{r})$  is a continuous function of position, which, however, can vary rapidly in the neighborhood of material interfaces. The behavior of steep changes in refractive index at material interfaces can be modeled effectively using super-Lorentz distributions.<sup>1</sup> Without specifying the source term explicitly, we express the solution to Eq. (1) for  $t \geq 0$  as

$$E(t) = \cosh(pt)E(0) + \frac{1}{p} \sinh(pt)E'(0) - \frac{f(\mathbf{r})}{\omega^2} \sin \omega t, \quad (3)$$

where  $E'(t) = \partial E(\mathbf{r}, t) / \partial t$ . The first two right hand terms represent the solution to (1) without the source. An equation for  $E'(t)$  is obtained by differentiating Eq. (3) with respect to time, or

$$E'(t) = p \sinh(pt)E(0) + \cosh(pt)E'(0) - \frac{f(\mathbf{r})}{\omega} \cos \omega t. \quad (4)$$

The appearance of the square root operator in Eqs. (3) and (4) poses no difficulty because the application of the formal solution involves Taylor series expansions, wherein only even powers of  $p$  appear. If we now expand Eqs. (3) and (4) to fourth order about  $t_0 = t^n = n\Delta t$ , but evaluate without approximation the source terms at time  $t = t^{n+1} = (n+1)\Delta t$ , Eqs. (3) and (4) become

$$\begin{aligned} E(t^{n+1}) &= E(t^n) + E'(t^n)\Delta t + \frac{1}{2}p^2E(t^n)\Delta t^2 + \frac{1}{6}p^2E'(t^n)\Delta t^3 \\ &\quad + \frac{1}{24}p^4E(t^n)\Delta t^4 - \frac{f(\mathbf{r})}{\omega^2}\sin\omega t^{n+1}, \end{aligned} \quad (5)$$

$$\begin{aligned} E'(t^{n+1}) &= E'(t^n) + p^2E(t^n)\Delta t + \frac{1}{2}p^2E'(t^n)\Delta t^2 + \frac{1}{6}p^4E(t^n)\Delta t^3 \\ &\quad + \frac{1}{24}p^4E'(t^n)\Delta t^4 - \frac{f(\mathbf{r})}{\omega}\cos\omega t^{n+1}, \end{aligned} \quad (6)$$

which represent the algorithm for marching the field in time. Spatial derivatives can be evaluated using FFT's. The desired form for the source function  $f(\mathbf{r})$  in two dimensions is

$$f(x, y) = A \sum_{n=1}^{N_s} \delta(x - x_n) \delta(y - y_n), \quad (7)$$

where  $x_n$  and  $y_n$  refer to grid coordinates. The source (7) represents a uniformly illuminated aperture parallel to the  $y$ -axis and intersecting the  $x$ -axis at  $x = x_n$ .

For the TE polarization in two space dimensions one can write  $E(x, y, t) = E_z(x, y, t)$ .

Since  $\partial E_z(x, y, t) / \partial t$  is already determined by the marching process,  $H_x$  and  $H_y$  can be determined, when desired or convenient, by the curl equation  $n^2 \partial E_z / \partial t = \partial H_y / \partial x - \partial H_x / \partial y$  and the divergence relation  $\partial H_x / \partial x + \partial H_y / \partial y = 0$ , which combine to give

$$\nabla^2 H_x = -\frac{\partial}{\partial y} \left[ n^2(x, y) \frac{\partial E_z}{\partial t} \right], \quad \nabla^2 H_y = \frac{\partial}{\partial x} \left[ n^2(x, y) \frac{\partial E_z}{\partial t} \right]. \quad (8)$$

Equations (8) are Poisson equations which are easily solved using FFT's.

Figures (1a)-(1d) show the results of applying the concepts described above on a 64x64 grid. Pictured are instantaneous gray-scale contour plots of  $E_z$ , Fig.(1a), the transverse magnetic field,  $H_y$ , Fig.(1b), the longitudinal magnetic field  $H_x$ , Fig.(1c), and a vector plot of the Poynting vector  $\mathbf{E} \times \mathbf{H}$ , following 100 integration steps. The refracting structure is a cylinder with  $n = 2$  in a surrounding medium with  $n = 1$ . The source is confined to the interior of the cylinder on the plane  $x = 0$ . The time-step is chosen so that  $c\Delta t = \Delta x / 2$ . The value of  $\omega$  in Eqs. (5) and (6) is chosen so that the period of oscillation is  $T = 16\Delta t$ . It is seen that the wavelength in the higher index medium is half that in the lower index medium, as it should be.

1. J. A. Fleck, Jr., J. Opt. Soc. Am. **15**, 2182-2198 (1998).
2. K. S. Yee, IEEE Trans. Antennas Propag. **AP-14**, 302-307 (1966).
3. A. Taflove, Wave Motion **10**, 547-582 (1988).

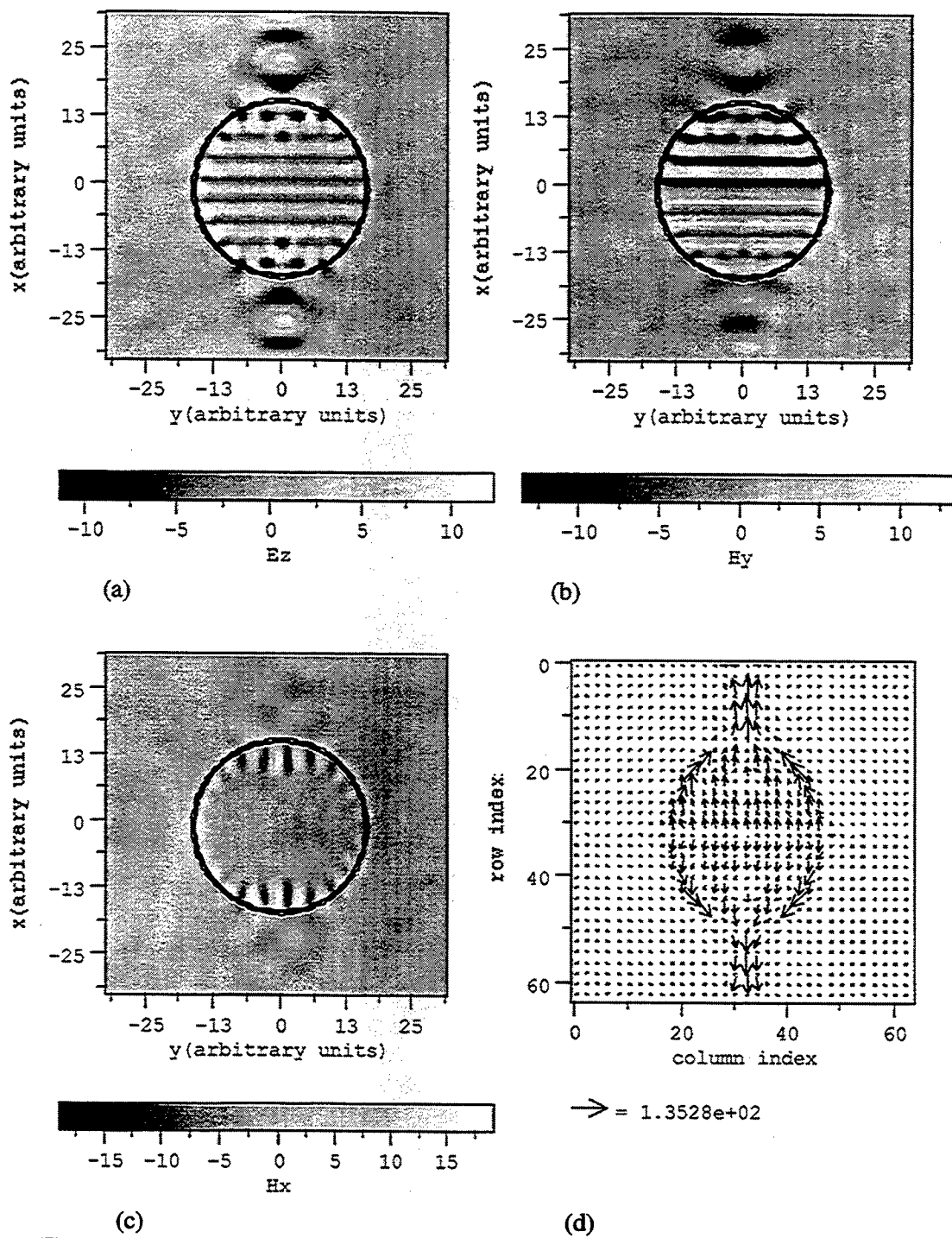


Fig. 1. Vector propagation of TE polarization through lens-like system, consisting of cylinder with  $n = 2$ , embedded in medium with  $n = 1$ . The cw source is located along diameter. Field components are (a)  $E_z$ , (b)  $H_y$ , and (c)  $H_x$ . Poynting vector plot, showing some radiation being totally internally reflected from the edge of the cylinder, is shown in (d).

# NEW FINITE ELEMENT VECTORIAL FORMULATION FOR BEAM PROPAGATION IN ANISOTROPIC MEDIA

Helder F. Pinheiro and H. E. Hernández-Figueroa

Universidade Estadual de Campinas, Faculdade de Eng. Elétrica e de Computação, Dept. de Microonda e Óptica.

Av. Albert Einstein, Nº 400, 13083-970 Campinas – SP, Brazil

Tels. +55-19-7883735 and +55-19-7883704, Fax. +55-19-2891895

E-mails: holder@dmo.fee.unicamp.br and hugo@dmo.fee.unicamp.br

## 1. INTRODUCTION

The beam propagation method (BPM) is one of most powerful numerical technique to analyze the propagation of electromagnetic fields in fibers and integrated optics devices [1]. Vectorial formulations are essential because they consider the vector nature of the electromagnetic fields. So that, it is possible to take into account the polarization dependence and mutual coupling between fields components due to material and geometric effects. Vectorial and semi-vectorial approaches were developed using finite difference or FFT algorithms [2]. Recently, a work reported by Zoboli et al. [2] presented a vectorial propagation scheme based on the finite element method for anisotropic medium. Nodal elements were used and the three components of the magnetic field  $\mathbf{H}$  were considered. The magnetic field is adopted instead of the electric one because the former is continuous at dielectric interfaces. Our method, although based on nodal finite elements, solves instead the vectorial wave equation in terms of the transverse components, reducing computational efforts and resources by roughly 50%. The elimination of the axial component is obtained by using the magnetic field divergence condition,  $\nabla \cdot \mathbf{H} = 0$ , which guarantees the complete elimination of spurious modes. In addition, this formulation is optimized by the use of adaptive mesh refinement and efficient sparse techniques to solve the resultant complex matrix equations.

## 2. FORMULATION

By combining the double curl equation for the magnetic field  $\mathbf{H}$  and the divergence condition  $\nabla \cdot \mathbf{H} = 0$ , the following vectorial wave equation involving only the  $\mathbf{H}$  transverse components is obtained:

$$\mathbf{u}_z \times \tilde{\mathbf{k}}_{0t} \nabla_t \times \left( \nabla_t \cdot \frac{\partial \mathbf{h}_t}{\partial z} \mathbf{u}_z \right) + \tilde{\mathbf{k}}_{1t} \frac{\partial \mathbf{h}_t}{\partial z} \mathbf{u}_z + \nabla_t \times \tilde{\mathbf{k}}_{zz} \nabla_t \times \mathbf{h}_t + \mathbf{u}_z \times \tilde{\mathbf{k}}_{2t} \nabla_t \times (\nabla_t \cdot \mathbf{h}_t \mathbf{u}_z) - (k_0^2 + \gamma^2 \tilde{\mathbf{k}}_{3t}) \mathbf{h}_t = 0 \quad (1)$$

Here,  $\mathbf{H}(x, y, z) = \mathbf{h}(x, y, z)e^{-jk_0\beta_z z}$ , where  $\beta_z$  is the reference propagation constant and  $\mathbf{h}(x, y, z) = \mathbf{h}_t \hat{\mathbf{u}}_t + \mathbf{h}_z \hat{\mathbf{u}}_z$  and  $e^{-jk_0\beta_z z}$  are the slow (envelope) and fast variation terms of the propagating wave, respectively. In addition, by applying the paraxial approximation, the following terms were neglected:  $|2k_0\beta_z |\partial \mathbf{h}_t / \partial z| \rangle |\partial^2 \mathbf{h}_t / \partial z^2|$ ,

$\partial \mathbf{h}_z^2 / \partial^2 z$  and  $\partial \mathbf{h}_z / \partial z$ . The other parameters in (1) are:  $\gamma = jk_0\beta_z$ ,  $k_{zz} = \hat{a}_{zz}^{-1}$ ,

$$\begin{aligned} \tilde{\mathbf{k}}_t &= \begin{bmatrix} k_{xx} & k_{xy} \\ k_{yx} & k_{yy} \end{bmatrix} = \tilde{a}_t^{-1}, & \tilde{\mathbf{k}}_{0t} &= \gamma^{-1} \tilde{\mathbf{k}}_t, & \tilde{\mathbf{k}}_{2t} &= \tilde{a}^{-1} \frac{\partial \tilde{\mathbf{k}}_t}{\partial z} - \tilde{\mathbf{k}}_t, \\ \tilde{\mathbf{k}}_w &= \begin{bmatrix} -k_{yy} & k_{yx} \\ k_{xy} & -k_{xx} \end{bmatrix}, & \tilde{\mathbf{k}}_{1t} &= \frac{\partial \tilde{\mathbf{k}}_w}{\partial z} - 2\tilde{a} \tilde{\mathbf{k}}_w, & \tilde{\mathbf{k}}_{3t} &= \tilde{a}^{-1} \frac{\partial \tilde{\mathbf{k}}_w}{\partial z} - \tilde{\mathbf{k}}_w \end{aligned}$$

The  $\tilde{a}_t^{-1}$  is an arbitrary tensor  $2 \times 2$  given by  $\tilde{a}_t = \hat{a}_{xx} \mathbf{u}_x \mathbf{u}_x + \hat{a}_{xy} \mathbf{u}_x \mathbf{u}_y + \hat{a}_{yx} \mathbf{u}_y \mathbf{u}_x + \hat{a}_{yy} \mathbf{u}_y \mathbf{u}_y$ .

Next, applying the Galerkin method to equation (1) the following equivalent integral equation is obtained:

$$\begin{aligned} & - \int_{\Omega} \left( \nabla_t \cdot \frac{\partial \mathbf{h}_t}{\partial z} \mathbf{u}_z \right) \left( \nabla_t \times \tilde{\mathbf{k}}_{0t}^T (\mathbf{u}_z \times \mathbf{w}_t) \right) d\Omega - \int_{\partial\Omega} \left( \nabla_t \cdot \frac{\partial \mathbf{h}_t}{\partial z} \right) \cdot (\mathbf{u}_z \times \tilde{\mathbf{k}}_{0t}^T (\mathbf{u} \times \mathbf{w}_t)) \cdot \mathbf{n} d\ell + \\ & + \int_U \tilde{\mathbf{k}}_{1t} \frac{\partial \mathbf{h}_t}{\partial z} \cdot \mathbf{w}_t dU + \int_{\Omega} \mathbf{k}_{zz} (\nabla_t \times \mathbf{h}_t) (\nabla_t \times \mathbf{w}_t) d\Omega + \int_{\partial\Omega} \mathbf{k}_{zz} (\nabla_t \times \mathbf{h}_t) \cdot (\mathbf{w}_t \times \mathbf{n}) d\ell - \\ & - \int_{\Omega} \left( \nabla_t \cdot \frac{\partial \mathbf{h}_t}{\partial z} \mathbf{u}_z \right) \left( \nabla_t \times \tilde{\mathbf{k}}_{2t}^T (\mathbf{u}_z \times \mathbf{w}_t) \right) d\Omega - \int_{\partial\Omega} \left( \nabla_t \cdot \frac{\partial \mathbf{h}_t}{\partial z} \right) \cdot (\mathbf{u}_z \times \tilde{\mathbf{k}}_{2t}^T (\mathbf{u} \times \mathbf{w}_t)) \cdot \mathbf{n} d\ell + \\ & + \int_{\Omega} (k_0^2 + \gamma^2 \tilde{\mathbf{k}}_{3t}) \mathbf{h}_t \cdot \mathbf{w}_t d\Omega = 0 \end{aligned} \quad (2)$$

$\forall w_i$  and  $h_i \in H^{(1)}(\Omega)$  where  $\Omega$  represents the waveguide transverse section domain, the  $H^{(1)}(\Omega)$  is a subspace of the Hilbert space  $H^{(2)}(\Omega)$ , whose function-elements and their first derivatives are square integrable in the Lebesgue sense, and  $\partial\Omega$  includes all material interfaces in  $\Omega$  and an artificial closed curve chosen to separate the guiding (interior) region from the infinitely extended (exterior) region. The contribution of the second line integral in (2) is zero for the interior of the domain and when  $\partial\Omega$  coincides with perfect electric walls (PECs) or perfect magnetic walls (PMCs). It is also noticed that the contributions of the first and third line integrals in (2) are zero when  $\partial\Omega$  coincides with PMCs. On the other hand, when  $\partial\Omega$  coincides with PECs, these integrals vanishes only if the contiguous dielectrics (to the PECs) are diagonally anisotropic. Otherwise, the line integrals do not vanish in general over  $\partial\Omega$ , and consequently their contributions must be taken into account in the formulation. Now expanding the components  $h_x(x, y, z)$  e  $h_y(x, y, z)$  in terms of the base functions  $\psi_i(x, y)$ , with expansion coefficients  $h_{xj}$  and  $h_{yj}$ , which are the fields values in the nodal points of the elements, the following differential equation is obtained:

$$[A] \frac{\partial \{h_t\}(z)}{\partial z} \{h_t\}(z) = [B] \{h_t\}(z), \quad (3)$$

where  $[A]$  and  $[B]$  are sparse, symmetric matrices of order  $2n_p \times 2n_p$  and  $N_p$  the number of nodal unknowns linked to the partitioned cross-section (mesh). The column vector  $\{h_t\}(z)$  contains the unknown values of  $h_t$ . Finally, applying the Crank-Nicolson scheme to equation (3), the following matrix system  $([A] - \Delta z \theta [B]) \{h_t\}_{[n]} = ([A] + \Delta z (1 - \theta) [B]) \{h_t\}_{[n-1]}$  is obtained, where  $\Delta z$  is the increment in  $z$  given at each step along the propagation and  $\theta$  is introduced to control the stability of the method.

### 3. RESULTS

To validate our numerical technique we analyzed the evolution of the state-of-polarization (SOP) of a wave propagation in a high-birefringent fiber. This kind of fiber has been used in coherent optical systems communication and in interferometric sensors such as gyroscopes [6]. We considered a fiber, according to Fig.3a, with radius equal to  $1.1\mu\text{m}$  and with the electric permittivity tensor elements given by  $\epsilon_{xx}=2.16$ ,  $\epsilon_{yy}=\epsilon_{zz}=2.162099384$  for the core and  $\epsilon_t=2.1257$  for the cladding. The fiber was excited by launching an input field with  $H_x=0$  and a gaussian  $H_y$  distribution  $H_y = A \cdot \text{Exp}(-\frac{(x^2 + y^2)}{2\sigma^2})$ , where  $\sigma$  and  $A$  represents the spot size and the amplitude, respectively, see Fig. 2(a). The  $H_z$  component was computed by using Maxwell equations.

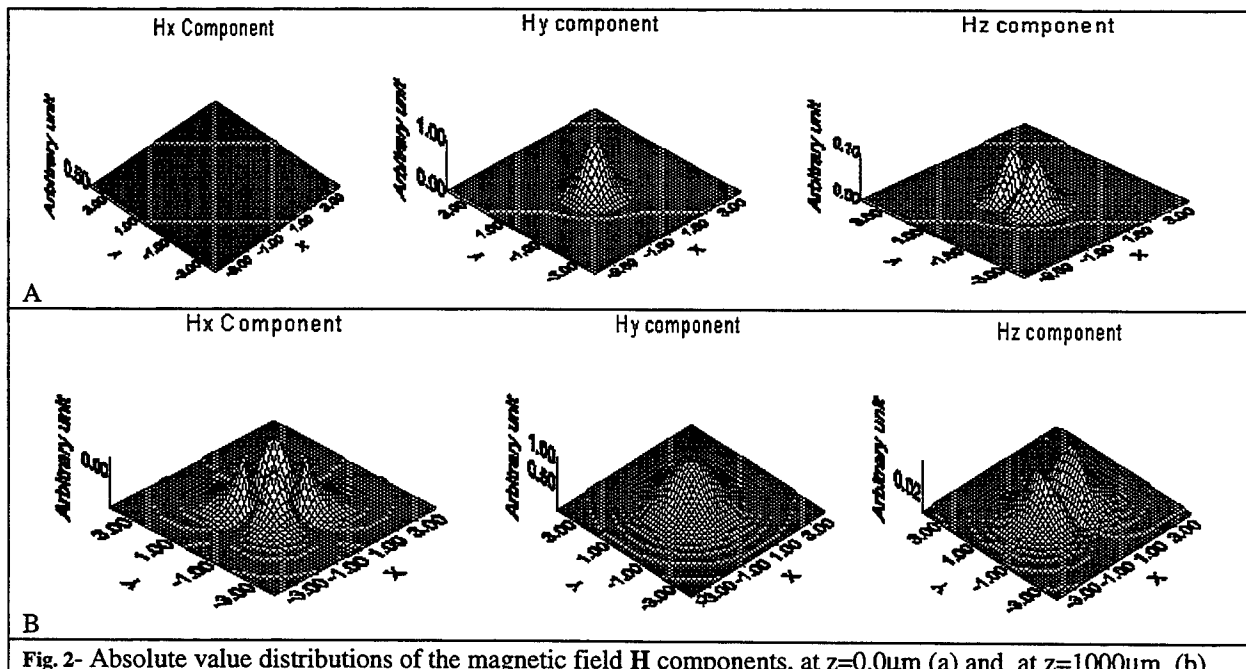
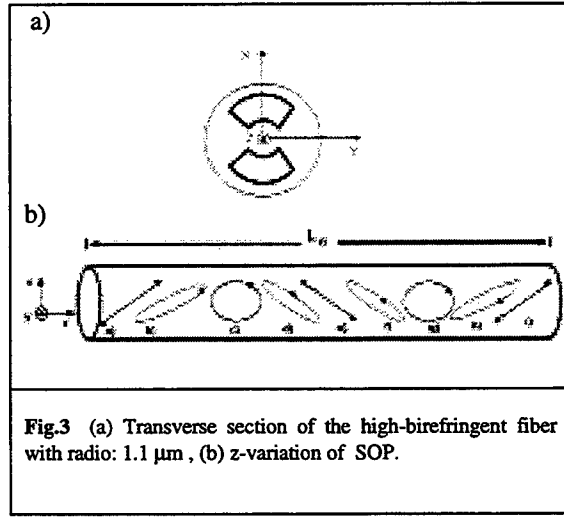
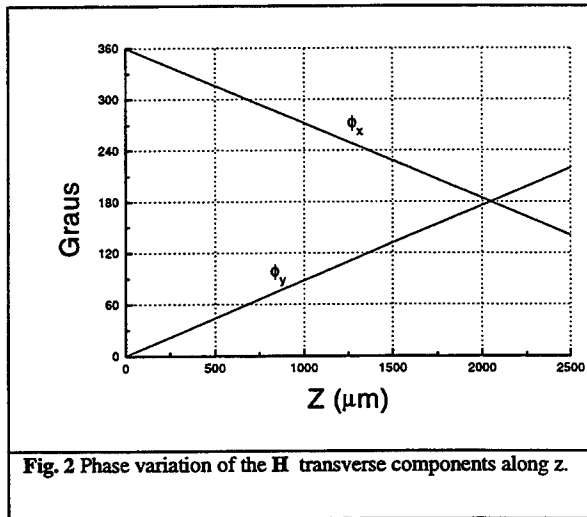


Fig. 2- Absolute value distributions of the magnetic field  $H$  components, at  $z=0.0\mu\text{m}$  (a) and at  $z=1000\mu\text{m}$  (b).

It is assumed  $\sigma=0.55\mu\text{m}$ ,  $\theta=0.55$ , the wavelength  $\lambda=0.829\mu\text{m}$ ,  $\Delta z=0.1\mu\text{m}$  and  $\beta_z = n_{\text{eff}} = 1.461223961$ . Fig. 2(b) shows the computed field after a propagation length of approximately  $1000\mu\text{m}$ . As theoretically expected, this

result perfectly agrees with the fundamental mode distribution  $HE_{11}^y$ , computed by solving the modal equation, obtained from (1) by imposing  $\frac{\partial}{\partial z} = 0$  [3].

To verify the polarization effect in anisotropic medium, the fiber was excited with a linear combination of the polarization modes  $HE_{11}^x$  and  $HE_{11}^y$  which were evaluated by means of the modal equation obtained from (1). Their effective indexes are  $n_{eff1}=1.461223961$  and  $n_{eff2}=1.4608187976$ . We assume  $\lambda=0.829\mu m$ ,  $\Delta z=0.1\mu m$  and  $\beta_{ref}=(n_{eff1}+n_{eff2})/2$  for the reference index refraction. Fig. 3 shows the phase variations  $\phi_x$  and  $\phi_y$  which represent the wave phase fronts of the polarization modes  $HE_{11}^x$  and  $HE_{11}^y$ . Due to the chosen  $\beta_{ref}$  the crossing point of the straight lines corresponds to the phase difference  $\delta\phi=\phi_x-\phi_y=2\pi$  and this happens at  $z=2,047\mu m$ . The beat length, computed by  $L_B=\lambda/(|n_{eff1}-n_{eff2}|)$ , is  $2,046\mu m$ . This agrees well with the experimental value:  $2,060\mu m$ , given in [4].. On the other hand, the SOP evolution is calculated by using the amplitude and phase of the  $H$  transverse components computed at several lengths along a beat length, in conjunction with the well-known expression:  $h_t(z,t)=u_x|h_x|\cos(\omega t-\phi_x(z))+u_y|h_y|\cos(\omega t-\phi_y(z))$ . Here  $u_x$  and  $u_y$  are the unitary vectors in the high-birefringence fiber axes direction. The results are shown in Fig. 4, where is clearly observed a cyclic distribution for the SOP, as expected.



As a conclusion, an efficient and rigorous finite-element vectorial approach for beam propagation in anisotropic media has been presented. This formulation effectively takes into account the polarization dependence and the field components coupling. The numerical results presented for high-birefringence optical fibers, show excellent agreement with well known theoretical results and experimental data.

The authors would like to thank the Brazilian Agency CNPq, for their financial support, and A. P. L. Barbero for helpful and enlightening discussions.

## REFERENCES

- [1] Reinhard März, "Integrated Optics Design and Modeling". Boston/London, Artech House, 1994.
- [2] E. Montanari, S. Selleri, L. Vincetti, and M. Zoboli, "Finite-element formulation for full-vectorial propagation analysis in three-dimensional optical waveguides", *IEEE Photon. Technol. Lett.*, vol.9, pp. 1244-1246, Sep.1997
- [3] H. E. Hernández-Figueroa, F. A. Fernández, Y. Lu, and J. B. Davies, "Vectorial Finite Element Modeling of 2D leaky waveguides", *IEEE Trans. on Magnetics*, vol 33, pp. 1710-1713, May 1995
- [4] A. P. L. Barbero, "Characterization System for Optical Circuits Based on Highly Birefringent Fibers", M.Sc. Thesis, ITA, São José dos Campos, SP, 1995 (in Portuguese).

## The impedance/admittance transformation – an efficient concept for the analysis of optical waveguide structures

Reinhold Pregla

FernUniversität, D-58084 Hagen, Germany - E-mail: R.Pregla@FernUni-Hagen.de

**Introduction:** Integrated optical structures can in general be described as concatenations of various quasi planar waveguide sections (see example in Fig. 1). Even sections with no special guiding properties can be incorporated into this model. The sections in these devices mostly are very long compared with the cross section dimensions. The analysis cannot be performed in one step for the whole structure because of these characteristics. Therefore, BPM algorithms are the most used procedures for the analysis. However, in each of the waveguide sections the light propagation can also be described by modes: propagation and evanescent ones. At the transition from one waveguide section to the next one the tangential field has to be matched. This can also be done by superposition of the mode fields. In this contribution a concept will be proposed allowing a very efficient analysis. To calculate the eigenmodes of the sections generalized transmission-line-equations for the transverse field components (or the tangential field components of the layers in 2D eigenmode solver case) are developed. The solution is obtained by the method of lines (MoL) [1], that means by discretization in the cross section and analytical solution

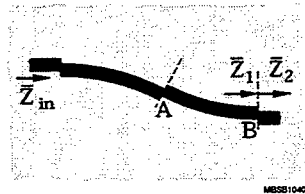


Fig. 1: S-bend structure

Using the field transformation equations and the impedances at the section or layer transitions all the fields can be calculated stepwise from input to output. The generalized forms of the equations take anisotropic material parameters into account. A mode solver with anisotropic material is described in [4].

**Theory - Basic equations:** In this section we would like to develop equations similar to the well known transmission line equations for coupled transmission lines. This will be done for curved waveguide sections in cylindrical coordinates for propagation in  $\phi$ -direction. The case of straight sections in Cartesian coordinates can be obtained from these equations. We assume the material parameters  $\nu = \epsilon, \mu$  as tensors

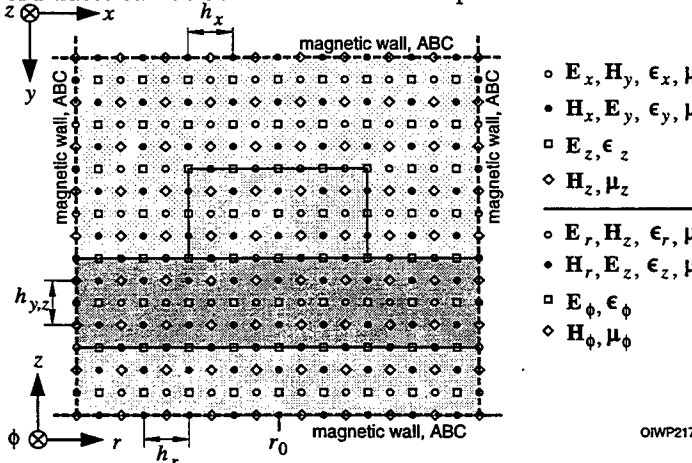


Fig. 2: Cross section of a general planar optical waveguide section with discretization points

of the following form

$$\vec{\nu}_r = \text{diag}(\nu_{rr}, \nu_{r\phi}, \nu_{rz}) \quad (1)$$

The propagation takes place in  $\phi$ -direction. Therefore the material parameters should be functions of  $r$  and  $z$  only. There should be no parameter variation in  $\phi$ -direction in the section under consideration. Otherwise the section must be subdivided in suitable subsections.

From Ampere's law and the law of induction we obtain the following two coupled equation systems

$$\frac{\partial}{\partial \phi} \begin{bmatrix} -\tilde{H}_z \\ \tilde{H}_r \end{bmatrix} = -j \begin{bmatrix} R_E^\phi \\ R_H^\phi \end{bmatrix} \begin{bmatrix} E_r \\ E_z \end{bmatrix} \quad \begin{bmatrix} R_E^\phi \\ R_H^\phi \end{bmatrix} = \begin{bmatrix} D_{\bar{z}}\mu_{r\phi}^{-1}\bar{r}D_{\bar{z}} + \epsilon_{rr}\bar{r} & -D_{\bar{z}}\mu_{r\phi}^{-1}\bar{r}D_{\bar{r}} \\ -D_{\bar{r}}\mu_{r\phi}^{-1}\bar{r}D_{\bar{z}} & D_{\bar{r}}\mu_{r\phi}^{-1}\bar{r}D_{\bar{r}} + \epsilon_{rz}\bar{r} \end{bmatrix} \quad (2)$$

$$\frac{\partial}{\partial \phi} \begin{bmatrix} E_r \\ E_z \end{bmatrix} = -j \begin{bmatrix} R_E^\phi \\ R_H^\phi \end{bmatrix} \begin{bmatrix} -H_z \\ H_r \end{bmatrix} \quad \begin{bmatrix} R_E^\phi \\ R_H^\phi \end{bmatrix} = \begin{bmatrix} D_{\bar{r}}\epsilon_{r\phi}^{-1}\bar{r}D_{\bar{r}} + \mu_{rz}\bar{r} & D_{\bar{r}}\epsilon_{r\phi}^{-1}\bar{r}D_{\bar{z}} \\ D_{\bar{z}}\epsilon_{r\phi}^{-1}\bar{r}D_{\bar{r}} & D_{\bar{z}}\epsilon_{r\phi}^{-1}\bar{r}D_{\bar{z}} + \mu_{rr}\bar{r} \end{bmatrix} \quad (3)$$

$D_{\bar{r}, \bar{z}}$  are abbreviations for  $\partial/\partial\bar{r}, \bar{z}$ . The coordinates  $\bar{r}, \bar{z}$  and quantities  $\bar{r}_o, \bar{h}_v (v = x, y, z, r)$  are normalized with the free space wave number  $k_o$  (e.g.  $\bar{r} = k_o r$ ). The magnetic field components are always normalized with the free space wave impedance  $\eta_o (\tilde{H} = \eta_o H)$ .

**Discretization and characteristics of the matrices:** The fields and the field equation will be discretized in the cross section. Fig. 2 shows a cross section of a planar waveguide with the adequate (four different) discretization point systems. The field components are collected in column vectors and written in boldface letters. The collection is made in vertical direction upwards (downwards for Cartesian coordinates  $x, y$ ) and from left to right. The material parameters and the radii are discretized analogous and collected in diagonal matrices. Matrices in general will be written with boldface italic letters. Now, the vectors of the discretized field components will be combined into supervectors in the following way:

$$\hat{\mathbf{E}} = [\hat{\mathbf{E}}_r^t, \hat{\mathbf{E}}_z^t]^t \quad \hat{\mathbf{H}} = [-\hat{\mathbf{H}}_z^t, \hat{\mathbf{H}}_r^t]^t \quad \left( \hat{\mathbf{E}} = [\hat{\mathbf{E}}_x^t, \hat{\mathbf{E}}_y^t]^t \quad \hat{\mathbf{H}} = [\hat{\mathbf{H}}_y^t, -\hat{\mathbf{H}}_x^t]^t \right) \quad (4)$$

The inner product of these supervectors can be used to describe the transported power. The difference operators  $\hat{D}$  for the whole cross section can be constructed from the difference operators  $D_{\bar{r}, \bar{z}} (D_{\bar{x}, \bar{y}})$  in  $r$  and  $z$  ( $x$  and  $y$ ) direction, respectively, with the help of Kronecker products ( $\otimes$ ). Using the cross section of Fig. 2 as example we obtain the difference operators:  $\hat{D}_{\bar{z}}^{o,*} = I_r^{o,*} \otimes D_z^{o,*}$  and  $\hat{D}_{\bar{r}}^{o,*} = D_r^{o,*} \otimes I_z^{o,*}$  ( $\hat{D}_{\bar{y}}^{o,*} = I_z^{o,*} \otimes D_y^{o,*}$  and  $\hat{D}_{\bar{x}}^{o,*} = D_x^{o,*} \otimes I_y^{o,*}$ ). All difference operators are divided by the corresponding discretization distance  $\bar{h}_v$ . Now the equations (2) and (3) can be written in discretized form.

$$\frac{d}{du} \hat{\mathbf{H}} = -j \hat{\mathbf{R}}_E^u \hat{\mathbf{E}} \quad \hat{\mathbf{R}}_E^\phi = \begin{bmatrix} \hat{\epsilon}_r \hat{r}_n^o - \hat{D}_r^{ot} \hat{\mu}_\phi^{-1} \hat{r}_n^o \hat{D}_z^o & + \hat{D}_z^{ot} \hat{\mu}_\phi^{-1} \hat{r}_n^o \hat{D}_r^o \\ \hat{D}_r^{ot} \hat{\mu}_\phi^{-1} \hat{r}_n^o \hat{D}_z^o & \hat{\epsilon}_z \hat{r}_n^o - \hat{D}_r^{ot} \hat{\mu}_\phi^{-1} \hat{r}_n^o \hat{D}_r^o \end{bmatrix} \quad (5)$$

$$\frac{d}{du} \hat{\mathbf{E}} = -j \hat{\mathbf{R}}_H^u \hat{\mathbf{H}} \quad \hat{\mathbf{R}}_H^\phi = \begin{bmatrix} \hat{\mu}_z \hat{r}_n^o - \hat{D}_r^{ot} \hat{\epsilon}_\phi^{-1} \hat{r}_n^o \hat{D}_r^o & - \hat{D}_r^{ot} \hat{\epsilon}_\phi^{-1} \hat{r}_n^o \hat{D}_z^o \\ - \hat{D}_z^{ot} \hat{\epsilon}_\phi^{-1} \hat{r}_n^o \hat{D}_r^o & \hat{\mu}_r \hat{r}_n^o - \hat{D}_z^{ot} \hat{\epsilon}_\phi^{-1} \hat{r}_n^o \hat{D}_z^o \end{bmatrix} \quad (6)$$

where  $u = \phi, \bar{u} = \bar{r}_o \phi$  in the cylindrical case and  $u = z, \bar{u} = \bar{z}$  in the Cartesian case,  $\bar{r}_n = \bar{r}/\bar{r}_o$ . The matrices  $\hat{\mathbf{R}}^z$  for the Cartesian case are obtained from  $\hat{\mathbf{R}}^\phi$  by the following substitution:  $\hat{D}_z \rightarrow \hat{D}_y$ ,  $\hat{D}_r \rightarrow \hat{D}_x$ ,  $\hat{\epsilon}_r \rightarrow \hat{\epsilon}_x$ ,  $\hat{\epsilon}_z \rightarrow \hat{\epsilon}_y$  and  $\bar{r}_n = 1$ . In case of electric or magnetic boundary walls but not for ABCs [2,II] the matrices  $\hat{\mathbf{R}}$  are symmetric because the relations  $\hat{\mathbf{R}}_{E,H} = \hat{\mathbf{R}}_{E,H}^t$  hold. Analogous equations can also be obtained for propagation in the other coordinate directions. In the following we will treat the symmetric case. Combining eqs. (5) and (6) we obtain the well known wave equations for vectorial field:

$$\frac{d^2}{du^2} \hat{\mathbf{H}} - \hat{Q}_H \hat{\mathbf{H}} = 0 \quad \frac{d^2}{du^2} \hat{\mathbf{E}} - \hat{Q}_E \hat{\mathbf{E}} = 0 \quad \frac{d^2}{du^2} \hat{\mathbf{H}} - \hat{\Gamma}_H^2 \hat{\mathbf{H}} = 0 \quad \frac{d^2}{du^2} \hat{\mathbf{E}} - \hat{\Gamma}_E^2 \hat{\mathbf{E}} = 0 \quad (7)$$

where the transformation to  $\hat{\mathbf{H}} = \hat{T}_H \hat{\mathbf{H}}$  and  $\hat{\mathbf{E}} = \hat{T}_E \hat{\mathbf{E}}$  was introduced. The matrices  $\hat{Q}_E = -\hat{\mathbf{R}}_E \hat{\mathbf{R}}_E$  and  $\hat{Q}_H = -\hat{\mathbf{R}}_H \hat{\mathbf{R}}_H$  are transposed to each other:  $\hat{Q}_H = \hat{Q}_E^t$ . Therefore, the eigenvalues and the eigenvector or modal matrices  $\hat{T}_{E,H}$  are related by:

$$\hat{T}_H^{-1} \hat{Q}_H \hat{T}_H = \hat{\Gamma}_H^2 \quad \hat{T}_E^{-1} \hat{Q}_E \hat{T}_E = \hat{\Gamma}_E^2 \quad \hat{\Gamma}_E^2 = \hat{\Gamma}_H^2 = \hat{\Gamma}^2 \quad \hat{T}_E^t = \hat{T}_H^{-1} \quad \hat{T}_H^t = \hat{T}_E^{-1} \quad (8)$$

From the general solution ( $\hat{\mathbf{F}} = \hat{\mathbf{E}}, \hat{\mathbf{H}}$ ):  $\hat{\mathbf{F}} = e^{-\hat{\Gamma}u} \mathbf{A} + e^{-\hat{\Gamma}u} \mathbf{B}$  we obtain for the relation of the fields in two cross sections A and B of a homogeneous section layer at distance  $d$  ( $\bar{d} = k_0 d$ )

$$\frac{d}{du} \begin{bmatrix} \hat{\mathbf{F}}_A \\ \hat{\mathbf{F}}_B \end{bmatrix} = \begin{bmatrix} -\hat{\gamma} & \hat{\alpha} \\ -\hat{\alpha} & \hat{\gamma} \end{bmatrix} \begin{bmatrix} \hat{\mathbf{F}}_A \\ \hat{\mathbf{F}}_B \end{bmatrix} \quad \begin{aligned} \hat{\alpha} &= \hat{\Gamma} / \sinh(\hat{\Gamma}\bar{d}) \\ \hat{\gamma} &= \hat{\Gamma} / \tanh(\hat{\Gamma}\bar{d}) \end{aligned} \quad (9)$$

A further relation between the eigenvector matrices of  $\hat{Q}_E$  and  $\hat{Q}_H$  comes from the fact that  $\hat{Q}_E$  and  $\hat{Q}_H$  are products of the matrices  $\hat{\mathbf{R}}_H$  and  $\hat{\mathbf{R}}_E$  with interchanged order. Therefore, we obtain the following relationship between these two transformation or modal matrices

$$\hat{T}_E = \hat{\mathbf{R}}_H \hat{T}_H \hat{\beta}_H^{-1} \quad \hat{T}_H = \hat{\mathbf{R}}_E \hat{T}_E \hat{\beta}_E^{-1} \quad \rightarrow \quad \hat{\beta}_E = \hat{T}_E^t \hat{\mathbf{R}}_E \hat{T}_E \quad \hat{\beta}_H = \hat{T}_H^t \hat{\mathbf{R}}_H \hat{T}_H \quad (10)$$

Because generally the amplitudes of the eigenvectors can be chosen arbitrarily, we have introduced the (diagonal) matrices  $\beta_{E,H}^{-1}$  for normalization. This product must result in  $\beta_E \beta_H = \hat{\beta}^2 = -\hat{\Gamma}^2$ . To determine  $\hat{\beta}_E$  and  $\hat{\beta}_H$  we have introduced the last relations in eq. (8) into the equations on the left side of the arrow in eq. (10). The transformed eqs. (5) and (6) can now be written as

$$\frac{d}{du} \hat{\bar{E}} = -j\hat{\beta}_H \hat{\bar{H}} \quad \frac{d}{du} \hat{\bar{H}} = -j\hat{\beta}_E \hat{\bar{E}} \quad (11)$$

**Field and impedance/admittance transformation:** Introducing eq. (11) into eq. (9) finally results in the field transformation equation (short circuit matrix parameter type)

$$\begin{bmatrix} \hat{\bar{H}}_A \\ -\hat{\bar{H}}_B \end{bmatrix} = \begin{bmatrix} \bar{y}_1 & \bar{y}_2 \\ \bar{y}_2 & \bar{y}_1 \end{bmatrix} \begin{bmatrix} \hat{\bar{E}}_A \\ \hat{\bar{E}}_B \end{bmatrix} \quad \begin{aligned} \bar{y}_1 &= \widehat{\bar{Y}}_0 / \tanh(\hat{\Gamma}d) & \widehat{\bar{Y}}_0 &= \sqrt{\hat{\beta}_E \hat{\beta}_H^{-1}} \\ \bar{y}_2 &= -\widehat{\bar{Y}}_0 / \sinh(\hat{\Gamma}d) & \widehat{\bar{Z}}_0 &= \sqrt{\hat{\beta}_H \hat{\beta}_E^{-1}} \end{aligned} \quad (12)$$

The wave impedance  $\widehat{\bar{Z}}_0$  and wave admittance  $\widehat{\bar{Y}}_0$  are defined from the first part of the general solution (forward propagating fields) and eq. (11). The inversion can easily be performed and results in the open circuit matrix parameter type (with matrices  $\bar{z}_{1,2}$ ). In case of ABCs [2,II] analogous equations may be obtained by introduction one of the adequate eq.(5) or (6) into eq. (9). This equation must then be transformed with the same transformation matrix as  $\hat{\bar{F}}$  in eq. (9). The procedure for the 2D case and isotropic material is presented in [3]. A mode solver for anisotropic material is described in [4]. Defining admittances/impedances matrices at cross sections A and B according to

$$\hat{\bar{Y}}_{A,B} = \widehat{\bar{Y}}_{A,B} \hat{\bar{E}}_{A,B} \quad \hat{\bar{E}}_{A,B} = \widehat{\bar{Z}}_{A,B} \hat{\bar{H}}_{A,B} \quad (13)$$

results in the admittance/impedance transformation formulas

$$\widehat{\bar{Y}}_A = \widehat{\bar{y}}_1 - \widehat{\bar{y}}_2 \left( \widehat{\bar{y}}_1 + \widehat{\bar{Y}}_B \right)^{-1} \widehat{\bar{y}}_2 \quad \widehat{\bar{Z}}_A = \widehat{\bar{z}}_1 - \widehat{\bar{z}}_2 \left( \widehat{\bar{z}}_1 + \widehat{\bar{Z}}_B \right)^{-1} \widehat{\bar{z}}_2 \quad (14)$$

At concatenations or layer interfaces the admittance/impedance transformation from section(layer) 2 to section(layer) 1 is given by

$$\widehat{\bar{Z}}_{B1} = \hat{T}_{E1}^{-1c} \left( \hat{T}_{H2}^c \widehat{\bar{Y}}_{A2} \hat{T}_{E2}^{-1c} \right)^{-1} \hat{T}_{H1}^c \quad (15)$$

The superscript c marks the common part of the transformation matrices in case of different cross sections [10].

**Numerical results:** The described algorithms improve the procedures and open new possibilities. However, they do not have an influence on the numerical results. A lot of numerical results have been obtained with the classical procedures. Dispersion diagrams for eigenmodes are e.g. reported in [5]-[9]. A comparison with other mode solvers is given in [11]. Concatenations of straight and the analysis of curved waveguides and the analysis of periodic structures are described in [2][3][12][13].

## References

- [1] R. Pregla and W. Pascher, "The Method of Lines", in T. Itoh, (editor), *Numerical Techniques for Microwave and Millimeter Wave Passive Structures*, J. Wiley Publ., New York, 1989, pp. 381-446.
- [2] W.P. Huang (ed), "Methods for Modeling and Simulation of Guided-Wave Optoelectronic Devices: Part I: Modes ...; II: Waves ...", PIER 10 and 11, EMW Publishing, Cambridge/USA 1995
- [3] G. Guekos (ed), "Photonic Devices for Telecommunications", Springer, Berlin 1998.
- [4] R. Pregla, *AEÜ*, Vol. 52, No. 2 (1998), pp. 94-98 and Vol. 53, No. 1 (1999), p. 32.
- [5] U. Rogge and R. Pregla, *J. Opt. Soc. Am. B*, Vol. 8, No. 2, February, 1991, pp. 459-463.
- [6] U. Rogge and R. Pregla, *J. Lightwave Technol.*, Vol. 11, No. 12, December, 1993, pp. 2015-2020.
- [7] R. Pregla, *Electromagnetics*, 15 (1995), pp. 441-456
- [8] R. Pregla, *J. Lightwave Technol.*, Vol. 14, No. 4, April, 1996, pp. 634-639.
- [9] R. Pregla, *Latsis Symposium*, Zürich, 1995, pp. 216-229.
- [10] R. Pregla, *AEÜ*, Vol. 50, No. 5 (Sept. 1996), pp. 293-300.
- [11] C. Vassallo, *Optical and Quantum Electronics*, Vol. 29, No. 2 (Febr. 1997), pp. 95-114.
- [12] S. Helfert, and R. Pregla, *J. of Lightwave Technology*, Vol. 16, No. 9 (Sept. 1998), pp. 1694-1702.
- [13] S. Helfert, *Optical and Quantum Electronics*, vol. 30(1998), pp. 359-368.

## WKB Analysis of Bend Losses in Optical Waveguides

W. Berglund, A. Gopinath

Department of Electrical and Computer Engineering, University of Minnesota, 200 Union St. SE  
Minneapolis, MN 55455

Tel (612) 625-1002, Fax: (612) 625-4583, E-mail: [berglund@ece.umn.edu](mailto:berglund@ece.umn.edu)

### Introduction

A number of methods have been devised for the analysis of losses that occur in curved optical waveguide structures. Heiblum and Harris[1] found that conformally transforming a curved waveguide into a straight structure was a powerful and insightful method of analysis for curved waveguide loss. Using the effective index method in the waveguides vertical direction, a two dimensional analysis of the conformally transformed index can be carried out. In their paper they broke up the transformed region into a series of constant index steps and applied a quantitative geometrical WKB approximation to determine the curvature and transition losses in these guides due to the leaky mode structure of the transformed index. In this paper we carry out a more complete WKB analysis of the transformed structure along the lines of analysis by Janta[2], and Gedeon[3]. They found that comparing the calculated mode spectrum by the WKB method for a number of monotonic varying indexes, with the results of numerical calculations showed agreement within 0.03- 0.15 percent. This paper shows a modification of Heiblum-Harris analysis, using the WKB method of [2,3] shows excellent agreement with experimentally measured waveguide losses, and with other computational intensive methods such as the method of lines (Mol) [4], scalar finite-element (SFEM)[5], and vector finite-difference method [6].

### Theory

A curved planar ridge waveguide structure can be modeled by the effective index method as a curved slab guide. The problem can then be resolved into a two dimensional case by finding the scalar wave equations for both the TE and TM modes for a curved slab guide. The fields can be constructed from two scalar potentials  $\phi^{TE}$  and  $\phi^{TM}$  which correspond to TE and TM waves [4], such that

$$\bar{E} = -j\omega\mu_0\nabla \times (\phi^{TE}\hat{x}) + \frac{1}{n^2}\nabla \times \nabla \times (\phi^{TM}\hat{x}) \quad (1)$$

$$\bar{H} = \nabla \times \nabla \times (\phi^{TE}\hat{x}) + j\omega\epsilon_0 n^2 \nabla \times (\phi^{TM}\hat{x})$$

From the slab geometry all derivatives in the z coordinate are taken to be zero,  $n(x)$  is the effective step index of the two dimensional structure. The scalar potentials then satisfy the following two-dimensional equations.

$$\nabla_z^2 \phi^{TE} + k_0^2 n^2 \phi^{TE} = 0 \quad (2)$$

$$\nabla_z \cdot \left( \frac{1}{n^2} \nabla_z \phi^{TM} \right) + k_0^2 \phi^{TM} = 0$$

By using the invariance properties of the Lagrangian that these scalar equations can be derived from, we can then find the scalar field equations for the circular guide when it is conformally mapped into a straight section.

Using the following conformal transformation

$$w = u + jv = R_2 \ln\left(\frac{(x+jy)}{R_2}\right) \quad (3), \quad R_2 = \text{OuterRadius of Curvature}$$

A Jacobian term from the transformation modifies the effective index of the guide along the u axis.

$$J = \frac{\partial(x, y)}{\partial(u, v)} = \left| \frac{dz}{dw} \right|^2 = \exp\left(\frac{2u}{R_2}\right) \quad (4)$$

Giving the resulting equations and boundary conditions at a point  $u=u_0$  where  $n(u)$  is discontinuous.

Where  $\phi(u, v) = \phi(u) \exp(-j\beta v)$  (5)

TE Case : (6)

$$\frac{d^2 \phi^{TE}}{du^2} + (k_0^2 n^2 \exp(\frac{2u}{R_2}) - \beta^2) \phi^{TE} = 0 \quad (6a)$$

$$\begin{cases} \phi_I^{TE}(u_0) = \phi_{II}^{TE}(u_0) \\ \frac{d\phi_I^{TE}(u_0)}{du} = \frac{d\phi_{II}^{TE}(u_0)}{du} \end{cases} \quad b.c. \quad (6b)$$

$$TM \text{ Case} : \frac{d}{du} \left( \frac{1}{n^2} \frac{d\phi^{TM}}{du} \right) + (k_0^2 \exp(\frac{2u}{R_2}) - \frac{\beta^2}{n^2}) \phi^{TM} = 0 \quad (7a)$$

$$\begin{cases} \phi_I^{TM}(u_0) = \phi_{II}^{TM}(u_0) \\ \frac{1}{n_I^2} \frac{d\phi_I^{TM}(u_0)}{du} = \frac{1}{n_{II}^2} \frac{d\phi_{II}^{TM}(u_0)}{du} \end{cases} \quad b.c. \quad (7b)$$

WKB Analysis: Fig. 1 illustrates how the step index change of the curved slab guide is modified under the conformal transformation. Using the equations and boundary conditions derived for the scalar fields under the conformal transformation (6,7), one can determine the eigenvalue condition for  $\beta$  by the WKB Method. Because of the leaky nature of the modified index for  $u > c$  the eigenvalue condition for  $\beta$  will have both real and imaginary parts. The imaginary part of  $\beta$  gives the loss due to curvature; transition losses can be determined by the mode mismatch of the fields, at junctions between the straight and curved sections of waveguide.

The WKB approximation for the transformed index is good everywhere [6] except for very small values for the radius of curvature  $R_2$ , which corresponds to very high loss, and for very large values of the  $u$  coordinate. At step discontinuities of the index at points a and b in Fig. 1, a plane wave treatment of the WKB fields in the neighborhood of the point is used [2]. This approximation with the boundary conditions from (6,7), the WKB connection formula [6] at the turning points  $x_0$  and  $c$ , and with the proper radiative boundary conditions for the fields; results in the following eigenvalue condition for  $\beta$ .

$$\text{Let } \beta = k_0 n_3, \quad R_1 = \text{Inner Radius}, \quad R_2 = \text{Outer Radius} \quad \text{Let } S = \begin{cases} 1 & \text{TE Modes} \\ (\frac{n_2}{n_1})^2 & \text{TM Modes} \end{cases} \quad (9)$$

$$\text{Let } I_{xy} = \int_x^y k(u) du \quad \text{and } k(u) = k_0 \sqrt{\left| n^2(u) \exp(\frac{2u}{R_2}) - n_3^2 \right|} \quad (10)$$

$$\tan(\tilde{I}_{II} - \phi_1) = S \frac{(n_3^2 - n_1^2)}{(n_2^2 - n_3^2)} \frac{(1 + \frac{j}{2} \exp(-2I_{bc}))}{(1 - \frac{j}{2} \exp(-2I_{bc}))} \quad - \text{WKB Eigenvalue Condition} \quad (11)$$

$$\tilde{I}_{II} = \begin{cases} I_{ab} \\ I_{-xb} \end{cases} \quad (12) \quad \text{and } \phi_1 = \begin{cases} \tan^{-1} \left[ S \frac{(n_3^2 - n_1^2) (\frac{R_1}{R_2})^2}{(n_2^2 (\frac{R_1}{R_2})^2 - n_3^2)} \right] & \text{for } n_3 \leq \frac{R_1}{R_2} n_2 \\ \frac{\pi}{4} + \tan^{-1} \left[ \frac{1}{2} \frac{S - \chi}{S + \chi} \exp(-2I_{ax}) \right] & \text{for } n_3 > \frac{R_1}{R_2} n_2 \end{cases} \quad (13)$$

$$\text{where } \chi = \frac{(n_3^2 - n_2^2) (\frac{R_1}{R_2})^2}{R_2} / (n_3^2 - n_1^2) (\frac{R_1}{R_2})^2$$

### Results

The main difference of the eigenvalue condition given in (11), from the results given in [1] is in the imaginary loss term. An expansion of eigenvalue condition given in (11) in terms of the tunneling integral  $I_{bc}$  (10) gives a smaller attenuation term than from [1], by a factor of one half. The phase condition (13) for the whispering gallery case is more complete ( $n_3 > n_2 (R_2/R_1)$ ), accounting for effects of the buried inner boundary at  $u=a$  for the curved guide.

The eigenvalues from (11) can be determined by graphical means by computer programs such as Mathematica. WKB fields have singularities at turning points, however one can interpolate the fields across these points to perform transition loss calculations. Comparison of bend losses found from the WKB eigenvalue condition (11) with experimental data [7,8] and other theoretical methods [3,4,5] shows good agreement. Fig.2 illustrates better agreement for (11) than [1] with the experimental results [3,7] for the bend loss values from a curved GaAs/AlGaAs ridge guide.

### Conclusion

A WKB analysis of losses from curved waveguide by conformal transformation shows excellent agreement with experimental and other numerical methods, better than what has been presented previously by this method. A relatively simple graphical method can be used to determine the roots for the eigenvalue condition for  $\beta$ , and the WKB fields can be interpolated to allow overlap integral calculations for transition losses and offset.

### References

- [1] M. Heiblum and J.H. Harris, "Analysis of curved waveguides by conformal transformation," IEEE J. Quantum Electron., vol. QE-11, pp. 75-83, 1975.
- [2] J. Janta and J. Ctyroky, "On The Accuracy of WKB Analysis of TE and TM Modes in Planar Graded-Index Waveguides," Optics Comm. Vol. 25, pp. 49-52, 1978.
- [3] J. Gu, P. Besse, and H. Melchior, "Novel Method for Analysis of Curved Optical Rib-Waveguides," Electron. Lett., vol. 25, pp. 278-280, 1989.
- [4] T. Yamamoto and M. Koshiba, "Numerical Analysis of Curvature Loss in Optical Waveguides by Finite-Element Method," J. Lightwave Technol., vol. 11, pp. 1579-1583, 1993.
- [5] S. Kim and A. Gopinath, "Vector Analysis of Optical Dielectric Waveguide Bends using Finite-Difference Method," J. Lightwave Technol., vol. 14, pp. 2085-2092.
- [6] D. Bohm, "Quantum Theory," Prentice-Hall, 1951.
- [7] R. Deri, E. Kapon, and L. Schiavone, "Bend Losses in GaAs/AlGaAs Optical Waveguides," Electron. Lett., vol. 23, pp. 845-847, 1987.
- [8] M. Austin, "GaAs/GaAlAs Curved Rib Waveguides," , IEEE J. Quantum Electron., vol. QE-18, pp. 795-799, 1982.

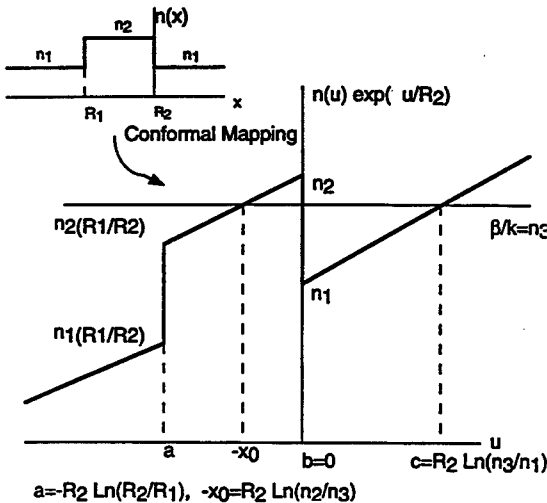


Figure 1. Conformal Transformation of Curved Step Index

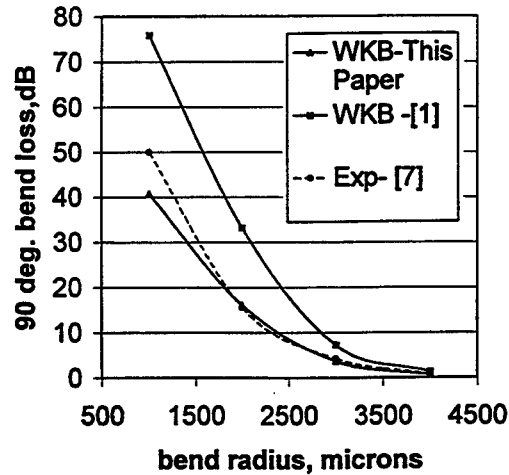


Figure 2. Comparison of Bend Loss [1,7]

## Characterization of ultra-short low-loss waveguide bends for compact Photonic Integrated Circuits

M. Rajarajan, S.S.A. Obayya<sup>1</sup>, B.M.A. Rahman, K.T.V. Grattan, and H.A. El-Mikati<sup>1</sup>

Department of Electrical, Electronic and Information Engineering

City University, London EC1V 0HB, UK

Tel : +44-171-477-8123 Fax : +44-171-477-8568, Email : B.M.A.Rahman@city.ac.uk

<sup>1</sup> Department of Electrical Communications, Mansoura University, Egypt.

### 1.0 Introduction

Devices incorporating small radius bends (or corners) are essential to achieve higher packaging density of optical components in Photonic Integrated Circuits (PICs) to improve their functionality. To achieve their mass production at a reduced cost, the device size is a key parameter and sharp bends or cornered or angled sections are most important in that they dramatically affect the PIC dimensions. However, on the other hand, the waveguide bends and corners are inherently lossy, and sharper bends and weaker confinement will increase the overall loss. Such waveguide bends are widely used in arrayed waveguide filters [1], optical delay lines [2], and also to interconnect photonic devices within a PIC. Early work concerning bends in optical waveguides [3] was in devices using Ti:LiNbO<sub>3</sub>. However, due to the low index contrast the modes are not well confined within the guide, hence it was found not suitable for the design of complex optical bends. An integrated optic format in semiconductor materials will allow the addition of optical switches, modulators, detectors, and lasers, and in principle a complete programmable network could be designed on a single chip. The overall bending loss is highly dependent on the waveguide parameters, particularly on the radius of curvature and the mode confinement, and as well confined modes suffer low-loss at corners and bends, this can be achieved by using a higher index contrast. It has been shown that in curved waveguide the mode shifts to the outer edge of the bend which also causes a field mismatch at the junction between a straight and bent waveguide, so a waveguide offset is necessary to improve the coupling between the sections. The radiation loss suffered in a bend can be reduced by increasing the modal confinement, particularly in the plane of the bending for example by deep etching or by increasing the index contrast of the materials used for the system. The radiation loss for TE and TM polarizations differ considerably and it will be shown in this study that the optimization parameters depend on the polarization state of the modes.

Although various semianalytical and numerical approaches have been developed to estimate the overall loss due to curved waveguides and the butt-coupling of such waveguides to straight waveguide sections, for realistic waveguides with irregular boundaries or non-vertical edges, many of these simple approaches may not be either applicable or accurate enough. In this paper, rigorous numerical approaches, based on vector techniques have been developed for the accurate analysis of such systems and results reported. The combination of the vector H-field finite element method (VFEM) [4], the conformal transformation [5], and the use of the vectorial finite element beam propagation (VFEBPM) method with the perfectly matched layers have been used to find the radiation leakage of the curved guides. The combination of the VFEM and the Least Squares Boundary Residual method (LSBR) has been used to find the coupling loss at the discontinuity interface. The LSBR method has also been used to calculate the reflection coefficients which have been neglected by most research workers.

### 2.0 Results of Analysis

The structure simulated in this study is shown as an inset in Fig. 1. A guiding layer, GaAs, is placed on thick layer, Al<sub>0.15</sub>Ga<sub>0.85</sub>As. At the wavelength considered, of 1.15 μm, the refractive indices of the GaAs and AlGaAs are 3.44 and 3.35 respectively. Figure 1 illustrates the radiation loss with the changing radius of curvature, where the solid line shows the results that have been obtained in this study by using the VFEBPM for the TE polarization. The dashed-dot line shows the experimental results of Austin [6], and the dotted line shows the results obtained by using the finite difference-based beam propagation method (FDBPM) [7], where the dotted line shows those from Gu *et al.*, using the method of lines (MOL) [8]. It can be seen from Figure 1 that conclusions using the MOL and FDBPM are similar. However, the results obtained in this study by using the finite element based BPM approach shows better agreement with the experimental results. At low loss values, most of the simple methods work reasonably well; however, at high loss values these simple methods suffer more due to the field moving away from the center of the guide and being affected by the boundary walls. In this study, the Perfectly Matched Layers (PML) approach has been used. The inset in Figure 2 is a similar structure to that of the inset in Figure 1. In this structure a well confined rib waveguide of width 3 μm and of height 0.4 μm is used. The guide and the substrate indices were taken as 3.5 and 3.17 at an operating wavelength of 1.55 μm. Figure 2 shows the radiation loss as a function of the bending radius for both the TE

and the TM polarizations from which it can be seen that the TE and the TM losses are very small up to a bending radius of 100 $\mu\text{m}$ . However at very low bending radius, R=50 $\mu\text{m}$ , the losses could be as high as 4.9 dB/90° for the TE polarization and 2.1 dB/90° for the TM polarization. It can also be noticed from Figure 2 that the TE has a larger loss than the TM polarization. The higher curvature loss of the quasi-TE mode, as compared to the quasi-TM mode is due to the weaker confinement of the quasi-TE mode, in the  $r$  direction, although it is better confined in the vertical  $y$  direction. The light intensity distributions in waveguides with 100 $\mu\text{m}$  bending radius and the intensity profile of the straight guide are shown in Figures 3a and 3b respectively. With the decrease in the radius of curvature, a distinct outward shift of the mode is seen which requires lateral shift and Figure 4 shows the coupling loss with the lateral offset for different values of bending radius where, the dashed, solid, and dotted lines indicate the coupling efficiency and the reflection coefficients for the 200 $\mu\text{m}$ , 150 $\mu\text{m}$  and 100 $\mu\text{m}$  radii respectively. It can be observed that for R=200 $\mu\text{m}$ , without any waveguide offset coupling efficiency, the efficiency is 88%, and this value increases to a maximum value of 96.6% when a +0.5 $\mu\text{m}$  offset is introduced. On the other hand, it can be observed that for R=100 $\mu\text{m}$ , without any offset coupling efficiency is only 62%, but this value increases to its maximum value of 90% with an offset of 0.75 $\mu\text{m}$ . This shows that for sharper bends an offset is essential to improve the coupling efficiency. When the bending radius is 200 $\mu\text{m}$ , the reflection coefficient is smaller compared to the case when the radius is 100 $\mu\text{m}$  as the bend is reasonably sharp and the wave reflects back more. It is also possible to improve power coupling by using different waveguide widths. Figure 5 shows the power coupling efficiency as a function of the width of the straight guide for two different radii without any offsets. In this case the width of the bent guide was 3 $\mu\text{m}$ . It can be seen from this that for a 150 $\mu\text{m}$  bending radius, the maximum coupling occurs at W<sub>2</sub>=3.5 $\mu\text{m}$ . However, when the bending radius is 100 $\mu\text{m}$  the maximum coupling occurs at W<sub>2</sub>=4 $\mu\text{m}$ . Since the field intensity for the smaller bends shifts more outward and hence a larger guide is needed. From Figure 5 it can also be seen that for R=100 $\mu\text{m}$ , a maximum coupling efficiency of 64.7% can be achieved. However, when R=150 $\mu\text{m}$ , this increases to around 80% and the reflection coefficients for R=100 $\mu\text{m}$  and R=150 $\mu\text{m}$  are also shown by the dotted lines in this figure. It can be seen that the reflection coefficients for the 100 $\mu\text{m}$  bend are larger than for the 150 $\mu\text{m}$  bend due to the high radiation loss for the 100 $\mu\text{m}$ . Figure 6 shows the transmission as a function of the lateral offset for different widths of the straight waveguide. It can be noticed from Figure 6 that when the width of the rib is 4 $\mu\text{m}$  the coupling is slightly lower than the other two cases. However, since the guide is reasonably wide a good coupling is achieved over a range of 2 $\mu\text{m}$ , but when the bend guide width is 3 $\mu\text{m}$  it can be seen that although the 2 $\mu\text{m}$  straight guide gives a slightly higher coupling efficiency, it has a very tight alignment tolerance. This arises as when the field is more confined in the guide it matches better with the bend field. However, shifting the field in the lateral direction moves the field profile of the straight guide reasonably far away from the bent field profile so the overlap of the two fields will result in a high mismatch. In Figure 6 the reflection coefficients are also plotted which again show a similar nature to the transmission coefficients. For example, if the optimal offset is applied, the transition loss of the bent with 100 $\mu\text{m}$  radius can be reduced by approximately 2dB.

### 3.0 Conclusions

It has been shown that the powerful vector approach used in this work gives more accurate results than the other available techniques for the simulation carried out. The LSBR method has been used to calculate the coupling efficiencies and also the reflection coefficients, which is an important parameter and has been estimated for the first time for the bend waveguides. In our result, it has also been shown that by applying optimal offsets at the junctions between the straight waveguide and the waveguide bend, and also using unequal guide widths the transition loss can be minimized.

- [1] M. Zirngibl *et al.*, *Electronics Letters*, pp. 201-202, 1993.
- [2] R. R. Hayes and D. Yap, *J.Lightwave Technol.*, pp. 523-527, 1993.
- [3] V. Ramaswamy and M D Divino, *Proc. CLEO*, Paper THP1, 1981.
- [4] B.M.A. Rahman and J.B. Davies, *IEEE J Lightwave Technol.*, pp.682-688, 1984.
- [5] M. Heiblum and J.H. Harris, *IEEE J. Quantum electron*, QE-11, pp75-83, 1975.
- [6] M.W Austin and P.G. Flavin, *J.Lightwave Technol.*, pp.236-240, 1983.
- [7] S. Kim and A. Gopinath, *J. Lightwave Technol.*, pp. 2085-2092, 1996.
- [8] Gu *et al.*, *IEEE J. Quantum Electron.*, QE-27 pp. 531-537, 1991.

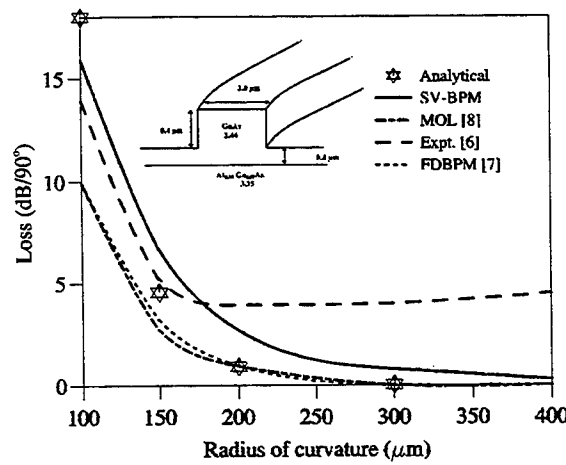


Fig. 1 Graph showing the radiation loss as a function of the radius of curvature

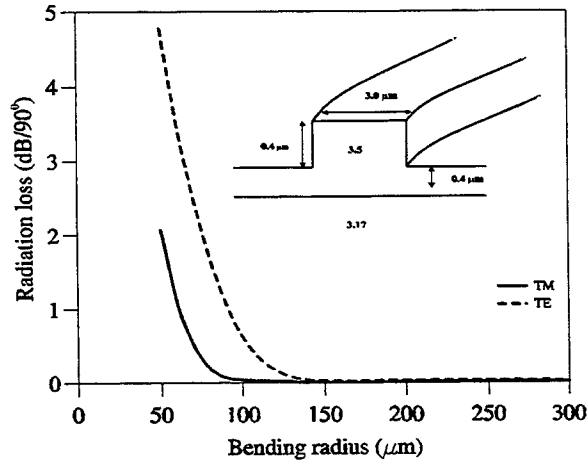


Fig. 2 Radiation loss as a function of the bending radius

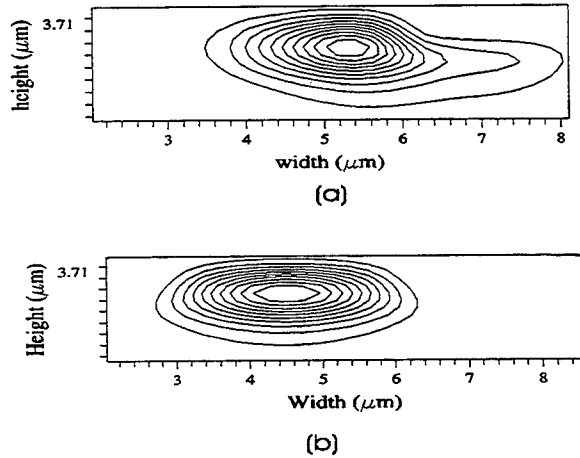


Fig. 3 (a)  $H_y$  field profile for a bending radius of  $100 \mu\text{m}$  (b)  $H_y$  field profile of the straight guide

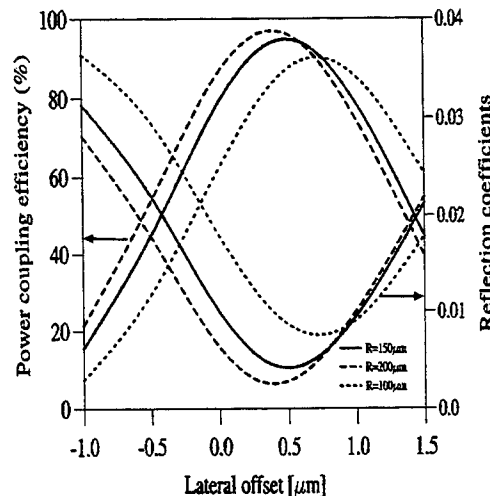


Fig. 4 Power coupling efficiency and reflection coefficients as a function of the lateral offset

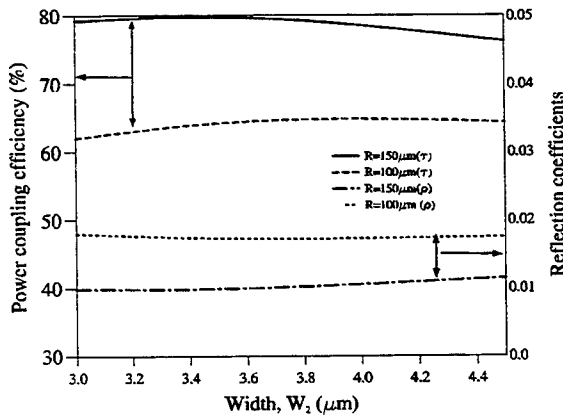


Fig. 5 Graph showing the power coupling and the reflection with the width of the straight guide,  $W_2$

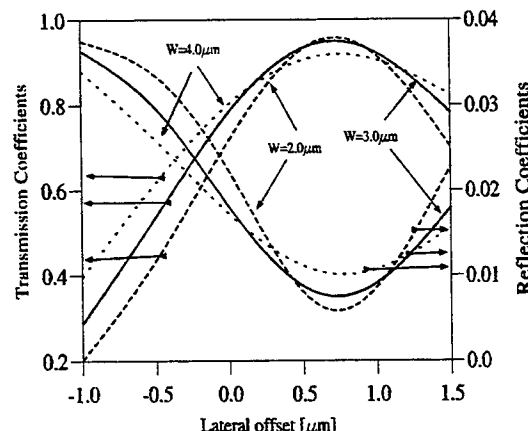


Fig. 6 Graph showing the transmission coefficients with the lateral offsets for different waveguide widths,  $W_2$

**Integrated Photonics Research**

# **WDM Devices: 2**

**Monday, July 19, 1999**

**Rick D. Clayton, Nortel Networks, Canada**  
Presider

**RME**  
**2:00pm–3:30pm**  
Sierra Madre North

**Tunable distributed Bragg reflector laser-electroabsorption modulator based on the identical active layer integration approach.**

**A Ramdane, D Meichenin, E Vergnol\*, H Sik\*, A Ougazzaden\***

France Telecom / BD / CNET / DTD / Laboratoire de Bagneux, URA 250

196 Avenue Henri-Ravéra, 92225 Bagneux Cedex, France Telecom

Tel : 33 1 42 31 78 24

Fax : 33 1 42 53 76 32

Email : [abderrahim.ramdane@cnet.francetelecom.fr](mailto:abderrahim.ramdane@cnet.francetelecom.fr)

\*Opto+

Groupement d'Intérêt Economique

Route de Nozay, F-91460 Marcoussis, France

## INTRODUCTION

Implementation of WDM architectures in fiber optic communication systems is now well under way and relies on advanced optoelectronic components. Tunable emitters are very attractive for the achievement of the precise wavelength combs required in these applications. Monolithically integrated DBR laser-Electro-Absorption (EA) modulators are further attracting considerable interest owing to their intrinsically low wavelength chirping in NRZ applications on standard fiber [1]. Additional advantages of these devices stem from their switching properties between the available channels for e.g. network reconfiguration at the emitter, or their use as spares for several single frequency (DFB-type) lasers.

DFB laser-modulator monolithic integration has been achieved with various approaches and we developed a very simple technique based on the use of the same active layer for the two optical functions, where wavelength compatibility is ensured by a small positive detuning of the DFB Bragg wavelength relative to that of the peak of the excitonic optical absorption spectrum [2]. The same method has been adapted to realize a tunable two-section DBR laser with a ~ 6 nm tuning range [3]. We also investigated the Selective Area Growth (SAG) technique to integrate a DBR laser and an EA modulator [4].

In the following we report on a three-section injection tunable DBR laser-EA modulator device using the same multiple quantum well (MQW) stack for the active, Bragg and modulator sections. A tuning range of ~ 5.2 nm with 12 channels is demonstrated together with an extinction ratio of 17 dB for a 2V driving voltage. The device further exhibits a 15 GHz bandwidth, compatible with high bit rate applications (>10 Gbit/s).

## DEVICE DESIGN AND FABRICATION

Fig. 1 shows a schematic view of the component with the same MQW structure for the amplifying, Bragg and modulator sections. This active layer is grown by atmospheric pressure MOCVD on an n+ InP substrate and consists of fourteen periods of 10 nm-thick compressively strained (+1%) InGaAsP wells and 10 nm-thick tensile strained (-1%) InGaAsP barriers ( $\lambda_{PL} = 1.18 \mu\text{m}$ ) embedded in between two 30 nm-thick lattice-matched InGaAsP confinement layers ( $\lambda_{PL} = 1.18 \mu\text{m}$ ). The peak photoluminescence wavelength of the stack is 1.50  $\mu\text{m}$ .

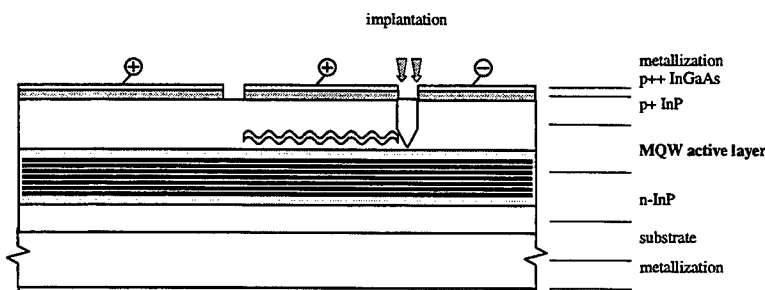


Fig 1: Schematic view of the 3-section integrated component.

The Bragg grating is first etched after holographic exposure, with a nominal Bragg wavelength corresponding to a  $\sim 55$  nm detuning, a trade-off for efficient modulation, low insertion loss and optimal chirping behaviour. The coupling coefficient and length of this section are such that  $KL \sim 1$  for optimal transmitted power in the modulator section while keeping a sufficiently high side mode suppression ratio (SMSR).

This is followed with a standard planar regrowth of p+ -InP confining layer and p++ -InGaAs contact layer over the whole wafer. A 2  $\mu\text{m}$ -wide ridge waveguide is achieved by dry and wet etching in the three sections, yielding very small modulator capacitance. An antireflection coating is finally deposited on the modulator facet.

#### DEVICE PERFORMANCES

Output powers up to 0 dBm have been coupled into a single mode fiber depending on the length of the modulator section for an active layer injection current of  $\sim 120$  mA. The spectral characteristics for a device of 500, 225 and 115  $\mu\text{m}$  lengths for the active, Bragg and modulator sections respectively are shown in Fig. 2. Single mode lasing at  $\sim 1555$  nm is obtained with an SMSR greater than 35 dB for the whole tuning range which, for this particular device, covers about 5.2 nm with 12 channels. This range has been limited by heating of the sample, and we measured up to 8 nm on other components.

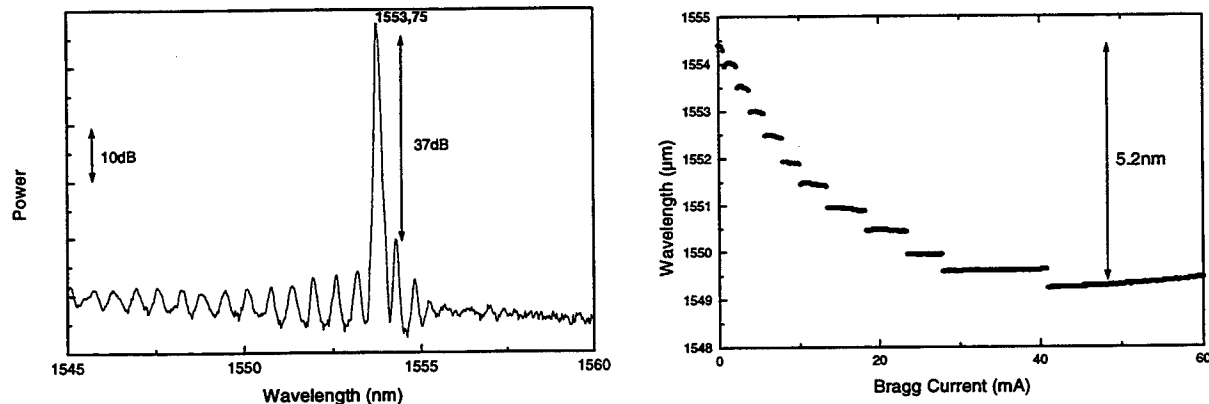


**Fig 2: Spectral characteristics of the integrated device.**

The modulation characteristic of this device is shown in Fig. 3 for the longest lasing wavelength. A 17 dB extinction ratio is recorded for a 2V swing, compatible with the active layer optimization for efficient quantum confined Stark effect.

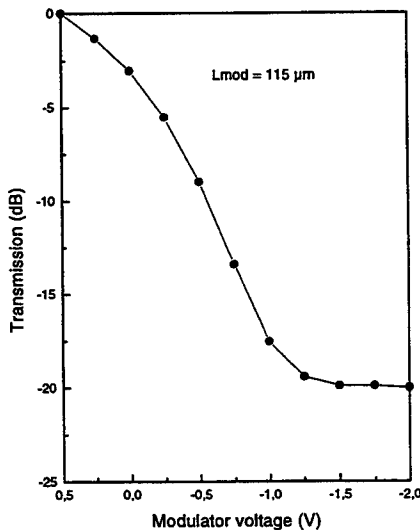


**Fig 3: Modulation characteristics.**

The small signal modulation shows a bandwidth of 15 GHz (Fig. 4), compatible with transmission experiments at rates >10 Gbit/s.

Full assessment of this run is still under way and in particular the chirping behaviour of these light sources at 2.5 and 10 Gbit/s will be presented at the conference.

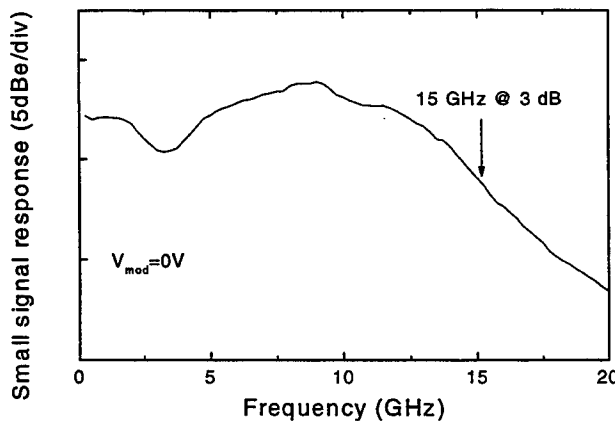


**Fig 4: Small signal frequency response.**

## CONCLUSION

We have demonstrated the monolithic integration of a DBR laser and EA modulator at  $1.5 \mu\text{m}$ , in a very simple manner, using the same MQW active layer for the three optical functions involved in this kind of device. A proper design of this active layer and wavelength compatibility yields high performance of the integrated light sources (up to 0 dBm coupled power, 5.2 nm tuning range, > 35 dB SMSR, 17 dB/2V modulation efficiency and 15 GHz bandwidth).

## References

- [1] K C Reichmann, P D Magill, U Koren, B I Miller, M Youg, M Newkirk, and D Chien  
IEEE Photonics Technology Letters, vol.5, pp1098-1100, 1993
- [2] A Ramdane, F Devaux, N Souli, D Delprat, and A Ougazzaden  
IEEE Journal of Selected Topics in Quantum Electronics, vol.2, pp 326-335, 1996
- [3] D Delprat, A Ramdane, A Ougazzaden, and M Carré  
Electronics Letters, vol.32, pp 2079-2080, 1996
- [4] P Legay, A Ramdane, D Delprat, A Ougazzaden, Y Sorel, and M Morvan  
*Proceedings International Conference on Integrated Photonic Research IPR'98*, Victoria (Canada), May 1998

## Monolithic integration of a widely tunable laser and an electro-absorption modulator

Beck Mason, Greg A. Fish, Steven P. DenBaars, Larry A. Coldren

Electrical and Computer Engineering Department, University of California, Santa Barbara, Santa Barbara, California, 93103, Tel: (805)-893-8465 Fax: (805)-893-4500, mason@ece.ucsb.edu

Widely tunable lasers are essential components for a wide variety of wavelength division multiplexing (WDM) and packet switching network architectures. The three most successful types of widely tunable lasers are the super structure grating distributed Bragg reflector laser (SSGDBR)<sup>[1]</sup>, the grating assisted co-directional coupler with sampled grating reflector laser (GCSR)<sup>[2]</sup>, and the sampled grating DBR laser (SGDBR). These devices are capable of greater than 40 nm quasi-continuous tuning ranges. Making them attractive as replacement sources in long haul DWDM communication systems. The large optical cavities in these devices limit their direct modulation bandwidth to between 3 and 4 GHz<sup>[3]</sup>. For data transmission applications these lasers must typically be operated with an extinction ratio penalty in order to ensure wavelength stability. They can also have fairly large chirp parameters for wavelengths which are detuned significantly from the band edge of the active region. External modulators have the potential to provide a higher bandwidth and lower chirp for data transmission applications. However external modulators increase the cost and complexity of a transmitter and can have significant insertion losses. To overcome this we have developed a widely tunable laser with a monolithically integrated a modulator Figure 1.

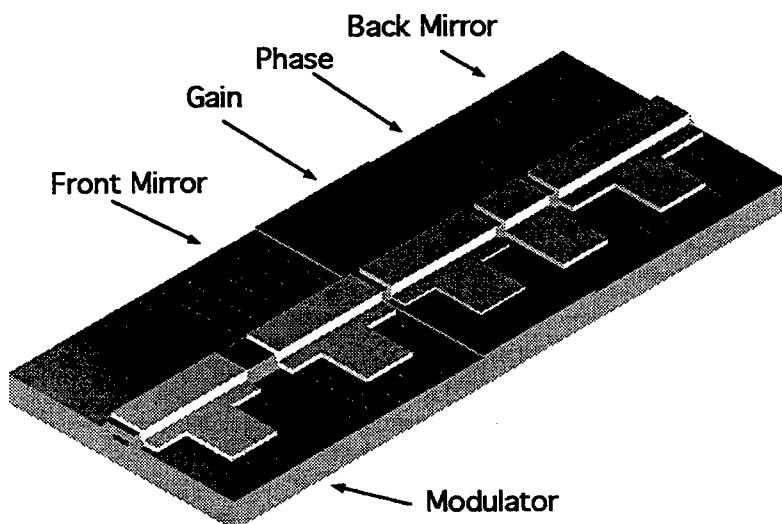


**Figure 1** Schematic of sampled grating DBR with integrated EA modulator

The laser has four separate sections: a 450  $\mu\text{m}$  long gain section, a 150  $\mu\text{m}$  long phase section, and two sampled grating mirrors. The multi-quantum well active region for the laser is grown on top the waveguide, separated by a thin InP stop etch layer. The quantum wells are removed in the tuning and modulator sections with a selective wet etchant prior

to the capping regrowth. The waveguide layer is 400 nm thick and has a bandgap of 0.87 eV. This low bandgap waveguide provides high index shift for the tuning sections of the laser at low carrier densities. The Bragg wavelength shift is on the order of 9.3 nm for a current density of only  $2 \text{ kA/cm}^2$  in the tuning sections. The 250  $\mu\text{m}$  long modulator section has the same waveguide structure as the tuning sections.

Electrical isolation between the different laser sections and between the laser and the modulator is achieved by removing the InGaAs contact layer and proton implanting. This implant is also used for lateral current confinement in the buried ridge stripe. The laser sections are separated by 10  $\mu\text{m}$  long implants and the modulator is isolated from the laser with a 50  $\mu\text{m}$  long implanted section. After implantation the sample is annealed at 410°C for 45 seconds to reduce the optical loss from the implant. It is important to keep the annealing temperature below 430°C to maintain the electrical isolation between the sections.

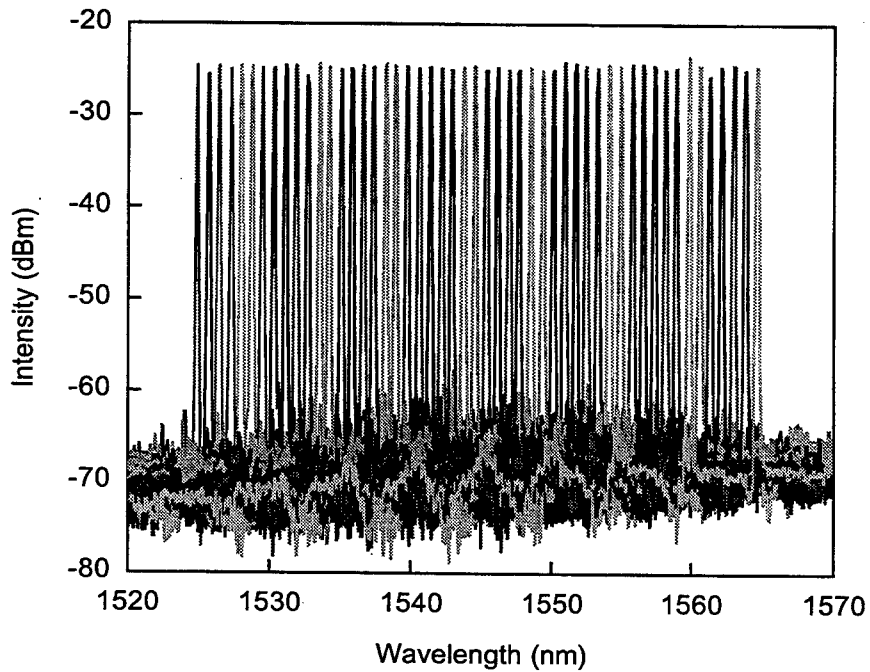


**Figure 2**      Laser spectra showing 51 channels spaced at 100 GHz over a 40 nm range.

The threshold current for the laser was 20 mA and the output power was 1.2 mW at 75 mA. The laser had a tuning range of 41 nm enabling it to reach 51 different ITU grid wavelength channels spaced at 100 GHz (Figure 2). The maximum tuning currents for the front and back mirrors were 20.5 and 23.5 mA respectively. The current density required in the mirrors was  $1500 \text{ A/cm}^2$  for an effective index shift of -0.01. This corresponded to a wavelength shift of 4.7 nm giving the laser a tuning enhancement factor of 8.7, based on the ratio of the wavelength coverage to index tuning.

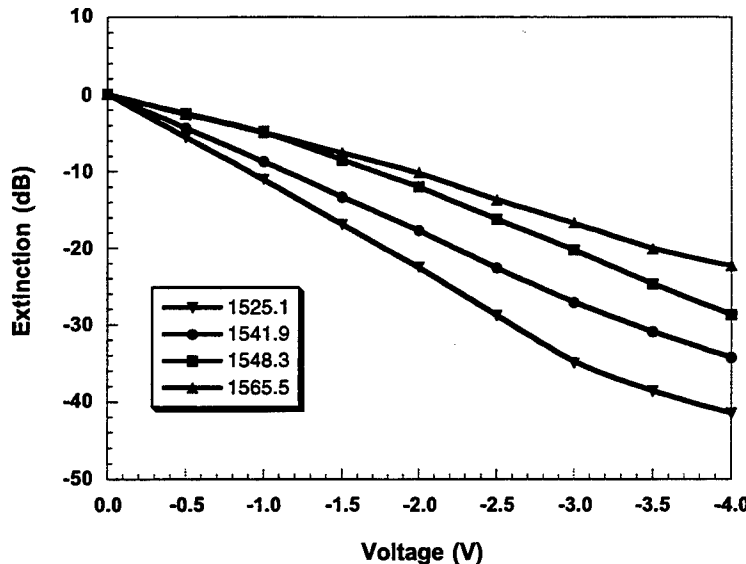


**Figure 3** Extinction ratio vs. applied voltage for four different wavelengths.

The extinction ratio of the modulator as a function of reverse bias voltage is shown in Figure 3 for four different wavelengths that span the tuning range of the laser. The absorption increases monotonically for all four channels from 0.0 to -4.0V. The maximum extinction was 41.5 dB for 1525 nm at -4.0 V and the minimum was 22.3 dB at 1565.5 nm. There was no observable change in the wavelength of the output light over the entire range of bias voltages indicating sufficient electrical isolation of the laser and modulator sections. We have successfully demonstrated the integration of a widely tunable laser with an electro-absorption modulator by using an offset quantum well structure with a low bandgap waveguide.

*This work was funded by a grant from the Office of Naval Research.*

## References

- [1] H. Ishii, H. Tanobe, F. Kano, Y. Tohmori, Y. Kondo, Y. Yoshikuni, "Quasicontinuous wavelength tuning in super-structure-grating (SSG) DBR lasers," *IEEE Journal of Quantum Electronics*, vol.32, (no.3), March 1996, p.433-41
- [2] M. Oberg, S. Nilsson, K. Streubel, J. Wallin, L. Backbom, T. Klinga, T., "74 nm wavelength tuning range of an InGaAsP/InP vertical grating assisted codirectional coupler laser with rear sampled grating reflector", *IEEE Photonics Technology Letters*, vol.5, (no.7), July 1993. p.735-7
- [3] C. Ougier, A. Talneau, F. Delorme, Y. Raffle, J. Landreau, D. Mathoorasing, "Sampled-grating DBR lasers with 80 addressable wavelengths over 33 nm for 2.5 Gbit/s WDM applications," *Electronics Letters*, vol.32, (no.17), Aug. 1996, p.1592-3

# FREQUENCY STABILIZED TUNABLE LASER TECHNOLOGY

Michel Cyr ([mcyr@nortelnetworks.com](mailto:mcyr@nortelnetworks.com))

Nortel Networks, Advanced Technology Lab, P.O. Box 3511, Station C, Ottawa, Ontario, Canada K1Y 4H7

*Abstract: This paper describe two approaches for achieving frequency stabilized laser module with 7 and 18 channels tunability capability on a 100 GHz spacing. Discussion on the evolution of the technology to 36 channels will be made.*

## Introduction

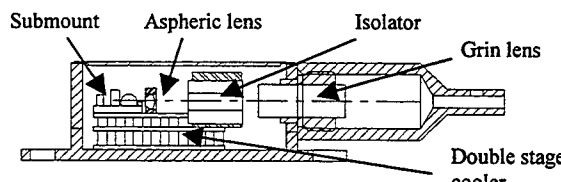
In Dense Wavelength Division Multiplexing (DWDM), system planners are increasingly looking for new sparing strategies, transmitter inventory reduction and frequency agile transmitters to name a few. One approach to answer this requirement is a tunable laser. DFB lasers are well-behaved and characterized. Furthermore, extensive reliability studies have been made on them. By tuning the temperature of a high power DFB one can achieve continuous tuning with a small change in power. To increase the tuning range cascaded DFB present an attractive solution for tuning over 18 channels on the 100 GHz grid. This technology could be push further by integrating multiple rows of cascaded devices merge into a single output by a combiner. This would extend the tuning range to 36 channels and beyond.

In this paper, we will describe a high power CW DFB ( $> +12 \text{ dBm}$  over all channels) laser module temperature tuned over seven 100GHz channels. To ensure stability, a frequency stabilization scheme is incorporated to the device. A second laser module incorporating a 3 sections cascaded DFB laser will be describe. Means of integrated frequency stabilization scheme will be discuss. Finally, we will open a door on extending the technology.

## High Power DFB

Our implementation is based on a high power DFB laser, mounted on a double-stage thermo-electric cooler for frequency tuning. The submount temperature range required for tuning the device is  $-10$  to  $+50^\circ\text{C}$ . The  $+50^\circ\text{C}$  limit is established to minimize laser degradation over life. A double-stage cooler is used to keep the laser at constant temperature over a 0 to  $70^\circ\text{C}$  module case temperature.

Figure 1: Module Side view

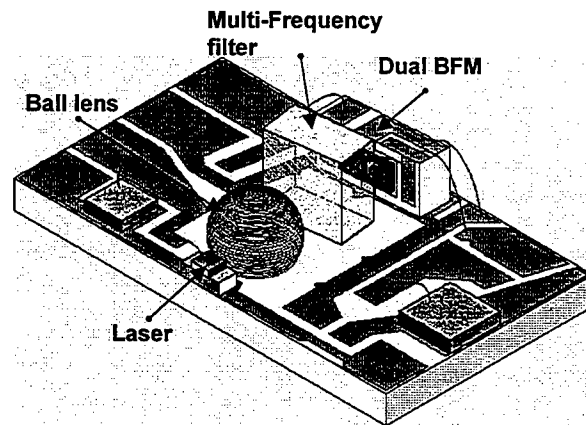


The front-facet optical train is composed of an aspheric lens, a semi-double isolator and a grin lens. Polarization maintaining fiber allows for use with an external modulator. All the required components are fitted in a 14 pin butterfly package.

Coarse tuning is made with temperature but long-term frequency stabilization is achieved with current. Our previously reported frequency stabilization scheme is used in the module /1/. This scheme uses a ball lens for beam control, an etalon filter as frequency discriminator and a dual photodetector.

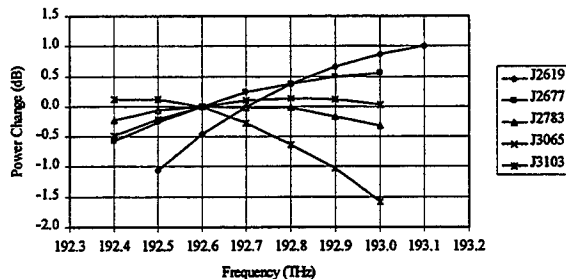
To allow for multi-frequency stabilization the etalon filter needs to be different from the all thin films technology used in the previous version. The filter structure is changed for a solid etalon made of a fused silica spacer with dielectric coating mirrors. Mirror reflectivity is around 60% in order to have an appropriate filter bandwidth. Fused silica is chosen for its good thermal expansion characteristics. The refraction index thermal coefficient of fused silica is causing the  $-1.2 \text{ GHz}/^\circ\text{C}$  frequency shift. The physical implementation is illustrated in figure 2.

Figure 2: Wavelength stabilized laser submount

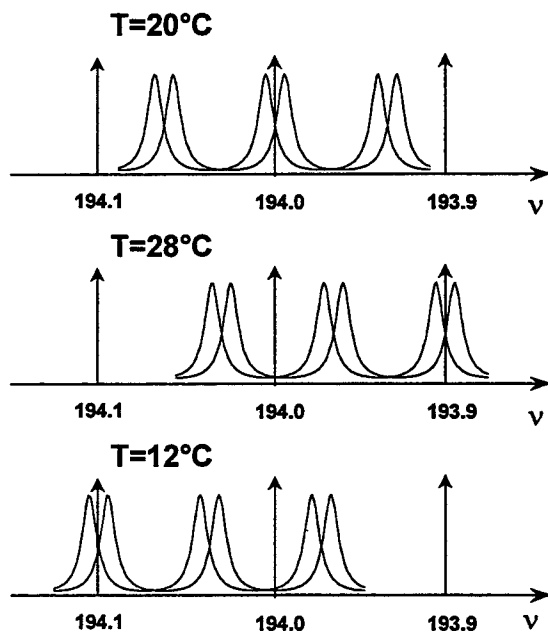


## Power stability results

Fiber output power was measured at each channel with the frequency stabilization mechanism engaged. The power variation can be explained by two mechanisms competing against each other: laser chip power change with temperature and optical train mechanical movement over temperature. The results obtained show a  $+1/-1.5 \text{ dB}$  power stability over the full operating range (figure 3).

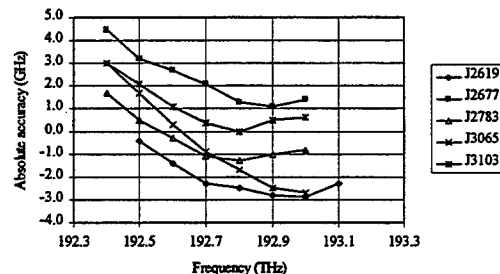
**Figure 3: Power stability results****Wavelength stabilization results**

As noted earlier, the multi-frequency etalon filter used in the stabilization scheme has a temperature coefficient of  $-1.2 \text{ GHz}/^\circ\text{C}$ . This filter is sitting on the laser submount so it sees a potential temperature between  $-10$  and  $+50$   $^\circ\text{C}$ . This would introduce a 75 GHz uncertainty on the wavelength stability, which is unacceptable. To solve this problem, a thermal compensation scheme is used on the filter. The filter is designed in such a way that the free spectral range is around 88 GHz instead of exactly 100 GHz.

**Figure 4: Temperature coefficient compensation**

In figure 4, we illustrated the principle behind the thermal compensation. It shows how the comb shifts to intersect the previous or the next ITU frequency. The comb of the two photodetectors currents over frequency is drawn at three different temperatures, which correspond to 100 GHz steps in laser frequency. With the temperature change the comb of etalon transmission peaks is shifted toward higher or lower frequency depending on a decrease or increase of temperature. This compensation allows accurate frequency stabilization on the ITU grid.

Results from 5 modules are presented in figure 5. The absolute frequency accuracy is within  $\pm 5$  GHz over 7 channels on the 100 GHz grid. Frequency accuracy at start of life can be improved by electronic means. The gain of one photodetector can be adjusted to improve the frequency accuracy. In that case the total variation, over the channel would be down to  $\pm 2.5$  GHz. One could implement a variable gain adjustment stored in memory for each channel to improve further the frequency accuracy.

**Figure 5: Wavelength stabilization results****General performance**

Other measurement results are presented in table 1.

**Table 1: general performance**

Description	Results
RIN	$<-140 \text{ dB/Hz}$
SMSR	$> 40 \text{ dB}$
Linewidth	$< 4 \text{ MHz}$
Fiber Power (nominal)	13 dBm

**Cascaded DFB**

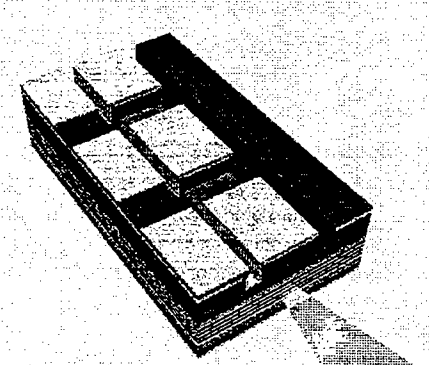
In an effort to extend the tuning range while keeping the mode stability of a DFB laser, a cascaded three-section DFB laser was design. The three sections grating-cascaded strongly-gain-coupled (SGC) DFB laser is tunable over 18 channels on 100 GHz spacing.

The laser used is a standard ridge waveguide DFB laser with a ridge width of 2  $\mu\text{m}$ . The laser cavity is approximatively 750  $\mu\text{m}$  long, and is divided equally into three sections through the metalization process. One unique feature of this structure is its three uniform gratings cascaded along the cavity. The three gratings were written by electron-beam lithography, with the Bragg wavelengths shifted by about 5nm relative to each other. The active region of the laser consisted of six QWs with a 1% compressive strain and an asymmetric P-side and n-side SCH structure to maximize the gain-coupling. A schematic of the laser chip is drawn in figure 6. /2/-/3/

Module assembly of the laser chip is realized in a similar manner as previously describe in figure 1. The tuning mechanism is temperature. An excursion of 50  $^\circ\text{C}$  and a selection of the section will allow a tuning of 18 channels on 100 GHz.

The laser module can easily be controlled by current and temperature. In order for the device to operate properly, any previous section need to be at transparency. This is achieved around the threshold point. A higher than threshold current could be used to amplify the power of the back and middle section but care must be taken for isolation between the main mode 5nm apart. A practical number would be 30 dB isolation. To cover 18 channels at 100 GHz spacing, a simple matrix of three currents, one per section, and one temperature for each points can be built. The section current is adjusted to have uniform power over the full frequency range. A constant current method could be also used. In this method, the current settings are fixed for each section and only the temperature is varied. With this method, a power variation of 3 dB could be observed over the full frequency range, see figure 7.

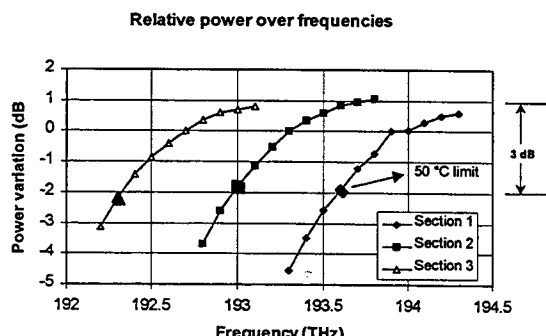
**Figure 6: Laser chip schematic**



#### Integrated frequency locking

The integrated frequency scheme described earlier in this document can not be used with the three section device. The etalon filter would sit on the same submount as the laser but this time the thermal compensation is not possible. The thermal compensation can be used with only one variable, in the previous case temperature. For the three section device there are two variables: temperature and operating section. To minimize the complexity of the integration, a temperature insensitive etalon need to be developed. One way to achieve this is by using an air spaced etalon specially designed. In this etalon the spacer is made of ultra low thermal expansion material. Mirrors of proper reflectivity are optically contact to the spacer. The reflectivity is chosen to have a reasonable capture range on the frequency locking.

**Figure 7:**



Some results of a laser module are presented in the previous and following figures. One can observe that the power variation on a constant current operation is less than 3 dB over the frequency range. Linewidth and RIN measurement are shown below.

**Figure 8:**  
**Linewidth vs Frequency**

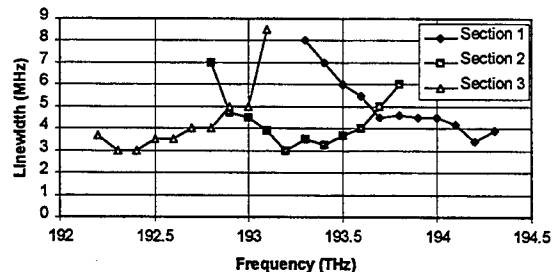
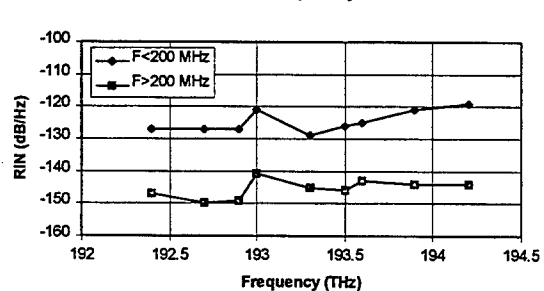


**Figure 9:**  
**RIN vs Frequency**



Future development for this device will look at how to increase the power and extend the tuning range. For higher power, an integrated SOA is an attractive solution. The tuning range can be extended by combining multiple devices together. For example, two rows of three lasers could be merged by a combiner into a single output for a frequency coverage of 36 channels at 100 GHz spacing.

#### Conclusion

In conclusion, we have demonstrated two approaches to frequency stabilized tunable laser. A high power DFB and a strongly gain coupled coolerless (-40°C ~ +85°C) DFB lasers," OECC'98, Chiba, Japan, 1998.

#### References

- /1/ B. Villeneuve, H.B. Kim, M. Cyr, D. Gariépy, A Compact Wavelength Stabilization Scheme for Telecommunication Transmitters, LEOS summers topical meetings 98, Montreal, August 1997, paper WD2.
- /2/ J. Hong, T. Makino, C. Blauu, R. Moore, S. Jatar and S. Dzioba, "Strongly gain-coupled coolerless (-40°C ~ +85°C) DFB lasers," OECC'98, Chiba, Japan, 1998.
- /3/ J. Hong, C. Dreze, F. Shepherd, D. Pollex, A. Fekete, C. Rogers and B. Baulcomb, "Compact WDM laser arrays with integrated BFM arrays for 4- simultaneous 100km fiber transmission with direct modulation @ 2.5Gb/s," ICAPT'98, Ottawa, Canada, 1998.

## Wide-band WDM application of electroabsorption modulator integrated DFB lasers

Hiroaki Takeuchi

NTT Photonics Laboratories

Morinosato Wakamiya, Atsugi-shi, Kanagawa, 243-01 Japan

Tel. +81 462 40 2835, Fax. +81 462 40 3186, e-mail takeuchi@aecl.ntt.co.jp

### **1. Introduction**

Very large capacity optical transmission technology, in the order of a Tbit/s, is required for next-generation multimedia networks. A high-density wavelength division multiplexing (DWDM) system is one of the best solutions for this purpose. Recently, flat-gain wavelength range of fiber amplifiers has rapidly been extended, it covers L-band (1570 nm-1610 nm) as well as C- or M-band (1530 nm-1570 nm) [1], [2]. Thus, wider range DWDM systems covering C(M)-band and L-band are ready for practical use. In addition, we can eliminate the four-wave mixing effect in a dispersion-shifted fiber when we use the wavelength in the L-band. Under these circumstances, we have developed 10-Gbit/s electroabsorption (EA) modulator integrated distributed feedback (DFB) lasers that operate in the C(M)- (1530 nm-1570 nm) and L-band (1570 nm-1610 nm). The fabricated device had a small power-penalty of 1.5 dB for 10-Gbit/s NRZ data after 40-km transmission along a standard single-mode fiber (SMF). We also confirmed penalty-free transmission of 2.5-Gbit/s NRZ signal over a 400-km SMF.

A polarization independent EA modulator plays a key role in a wavelength conversion system[3] and an optical switching system[4], because of its advantage of high-speed modulation, polarization independence, high saturation power level and low power consumption. I will summarize our developed EA modulators from the viewpoint of their WDM application.

### **2. EA modulator integrated DFB laser**

The schematic of the fabricated EA modulator integrated DFB laser is shown in Fig. 1. We integrated an MQW EA modulator and a DFB laser by a butt-joint technique[5]. These two devices were buried with Fe-doped InP material to get the high power of the laser and high-speed operation of the modulator. The length of the DFB laser and the EA modulator were 450  $\mu\text{m}$  and 225  $\mu\text{m}$ . We developed EA modulator integrated DFB lasers operating at 10 Gbit/s over a wide wavelength range from 1530 to 1600 nm. The averaged side-mode suppression ratio was more than 40 dB. The static and dynamic extinction ratios were around 15 dB and 10 dB at peak-to-peak driving voltage of 2 V. We conducted transmission experiments by applying 2.5-Gbit/s and 10-Gbit/s NRZ data streams (PN:2<sup>23</sup>-1) to the EA modulator integrated DFB laser module. Standard SMFs with zero dispersion wavelength of 1.3  $\mu\text{m}$  were used in the experiments. The EA modulator was driven by 2.0-V peak-to-peak signals, and it was biased at -1.5 V in both cases. Figure 2(a) and (b) show the bit error rate (BER) curves before and after transmission over 400 km at 2.5 Gbit/s and 40 km at 10 Gbit/s, respectively. Penalty-free transmission was achieved at 2.5 Gbit/s and a power-penalty of 1.5 dB at  $10^{-9}$  was obtained at 10 Gbit/s. The 10-Gbit/s eye diagram that

was obtained by using baseband filter after 40-km SMF transmission is inserted in Fig. 2(b). The full-width at 20 dB-down from the peak of the output spectra under 10 Gbit/s operation was about 37 GHz, which is narrow enough for the DWDM systems with 100-GHz channel spacings. These outstanding performance of the EA modulator integrated DFB laser proves its high-potential as a compact lightsource in a WDM system.

### 3. Polarization independent EA modulator

The polarization dependent loss (PDL) is expressed by the following equation.

$$PDL = 10/\ln 10(-\Gamma_{TE}\alpha_{TE} + \Gamma_{TM}\alpha_{TM})L \dots (1)$$

Here,  $\Gamma$  is the optical confinement coefficient,  $\alpha$  is the optical absorption coefficient, and  $L$  is the length of the modulator. The  $\alpha_{TE}$  and  $\alpha_{TM}$  are absorption by the electron to heavy-hole transition (E1-HH1) and the electron to light-hole transition (E1-LH1). We can design the energy levels of HH1 and LH1 by adjusting the strain of the well. After careful design considering the well strain and the optical confinement coefficients, we achieved polarization independent InGaAlAs/InAlAs EA modulator[6] as shown in Fig. 3. The average optical switching time was around 50 ps, which was 1/20 of that of a semiconductor optical amplifier (SOA) gate. The wavelength dependence of the EA modulator was examined as shown in Fig. 4. Polarization independent operation was kept at the input wavelength from 1550 to 1570 nm. The insertion loss increased only by 1.5 dB from 1570 to 1550 nm. We confirmed that polarization independent EA modulators had sufficient performance as high-speed optical gates against signals with wide wavelength.

### 4. Summary

We have developed a 10-Gbit/s EA modulator integrated DFB laser operating at 1530 nm-1600 nm in C(M)- and L-band for wide-band WDM systems. A power-penalty of 1.5 dB for 10-Gbit/s NRZ signal was achieved with standard SMF transmission over 40 km, and 2.5-Gbit/s penalty-free transmission over 400-km SMF was also demonstrated. We also developed polarization independent EA modulators. It has a potential as a high-speed optical gate utilized in various kind of WDM systems.

### [References]

- [1] B. Clesca, "Flat-gain amplifiers and transmission in WDM networks," Tech. Dig. OAA'96, FA1, pp. 54 - 57, 1996
- [2] H. Masuda, S. Kawai, K. Suzuki, and K. Aida, "Wide-band WDM transmission using erbium-doped fluoride fiber and Raman amplifiers," Tech. Dig. OAA'98, MD2, pp. 58 - 61, 1998
- [3] M. Teshima, T. Kawai, N. Sakaida, H. Ishii, and M. Koga, "Demonstration of virtual wavelength path cross-connect," ECOC'97, vol. 3, pp. 59-62, 1997
- [4] T. Okagawa, T. Matsunaga, and K. Habara, "Composite optical/electrical buffer configuration for photonic ATM switching systems," Electron. Lett., vol. 33, pp. 1398-1400, 1997
- [5] H. Takeuchi, K. Tsuzuki, K. Sato, M. Yamamoto, Y. Itaya, A. Sano, M. Yoneyama, and T. Otsuji, "NRZ operation at 40 Gb/s of a compact module containing an MQW electromodulator integrated with a DFB laser," IEEE Photon. Technol. Lett., vol. 9, pp. 572-574, 1997
- [6] K. Wakita, I. Kotaka, K. Yoshino, S. Kondo, and Y. Noguchi, "Polarization-independent electroabsorption modulators using strain-compensated InGaAs-InAlAs MQW structures," IEEE Photon. Technol. Lett., vol. 7, pp. 1418-1420, 1995

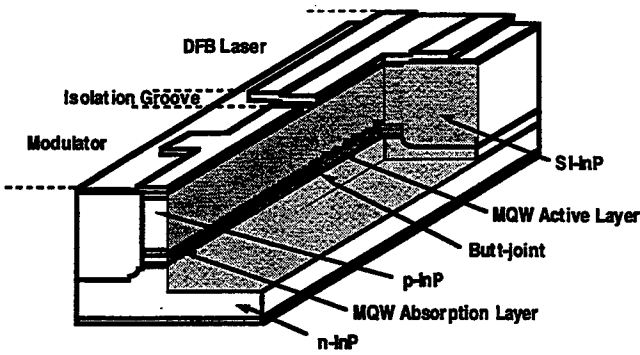


**Fig. 1 Schematic view of EA modulator integrated DFB laser**

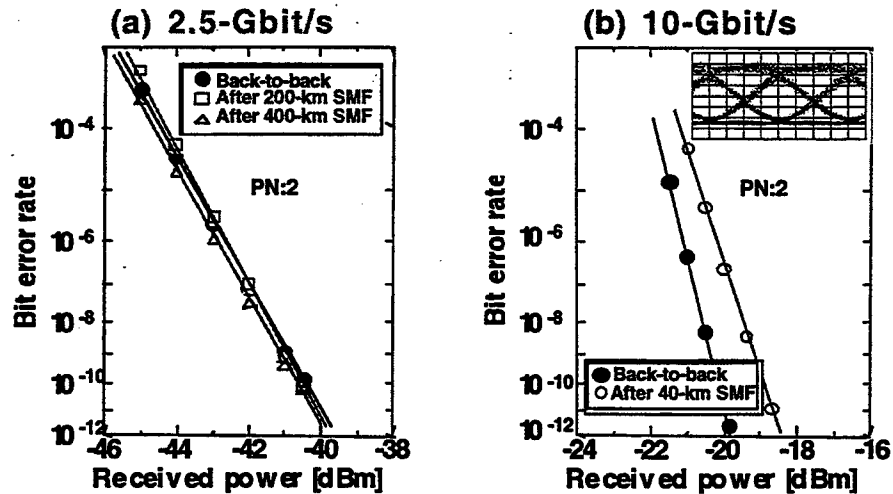


**Fig. 2 Bit-error-rate curves at 2.5 Gbit/s(a) and 10 Gbit/s(b)**

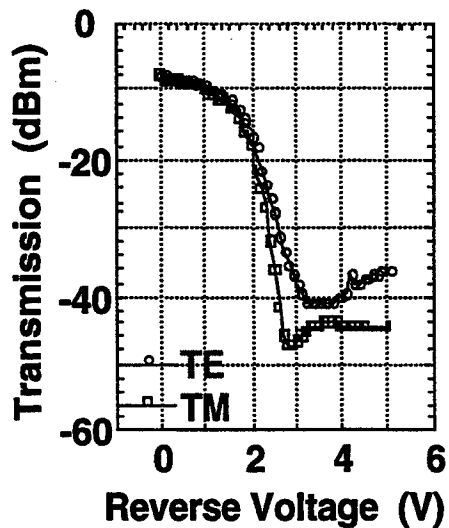


**Fig. 3 Polarization independent operation of EA modulator**

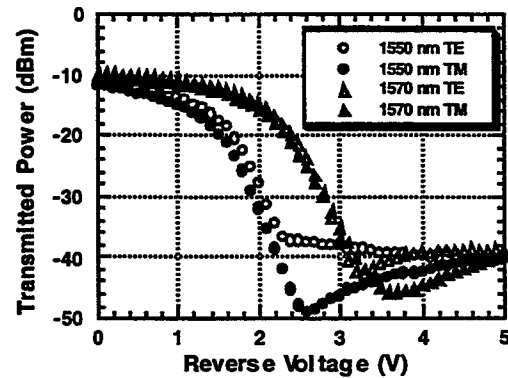


**Fig. 4 Wavelength dependence of EA extinction curves**



**Integrated Photonics Research**

# **Material and Characterization**

**Monday, July 19, 1999**

**Bill Steier, University of Southern California, USA**  
Presider

**RMF**  
**2:00pm–3:30pm**  
Sierra Madre South

## Large second-order optical nonlinearity in Ge-doped SiO<sub>2</sub> thin films

Jabri Khaled, Takumi Fujiwara, Akira J. Ikushima

Research Center for Advanced Photonic Technology,

Toyota Technological Institute, Hisakata, Tempaku, Nagoya 468-8511, Japan

Tel: +81-52-809-1882

Fax:+81-52-809-1882

### I. Introduction

Development of photonic devices such as optical switch and modulator requires materials with large enough second-order optical nonlinearity. Compared to nonlinear crystals, glass has advantages of being transparent over a wide wavelength range, ability to be shaped in desired forms such as fibers, and easy connectivity to transmission network and more, although glasses possess the inversion symmetry that deprives them from the second-order optical nonlinearity.

Several years ago, second harmonic generation was reported in glasses <sup>1-2</sup>. Since then, extensive work has been carried out for developing novel glasses with large enough second-order optical nonlinearity <sup>1-4</sup>. Recently, Fujiwara et al. <sup>5</sup> have discovered in their pioneer work that an appreciable electro-optic effect can be induced in Ge-doped silica fiber if they are subject to poling under UV-irradiation. This technique, so called the UV-poling, seems to be very promising for obtaining novel photonic glasses with second-order optical nonlinearity to be comparable or even beyond that of crystals. The UV-poling technique, however, has not been applied to thin films yet, which is inevitable for active devices with waveguides.

In the present study we report on the second-order optical nonlinearity induced by the same technique in Ge-doped SiO<sub>2</sub> thin films. Effects of oxygen flow content during sputtering, vacuum annealing and loading in hydrogen on the second-order nonlinearity are dealt with.

### II. Experimental procedure

Thin films are prepared by rf-sputter at room temperature in controlled Ar/O<sub>2</sub> gas flow. Ar flow content was fixed at 3 cm<sup>3</sup>/min, and O<sub>2</sub> flow content was varied in the range from 0 to 5 cm<sup>3</sup>/min. Polycrystalline targets of 20 and 50 mole% GeO<sub>2</sub> added SiO<sub>2</sub> with a grade of 99.99% were selected for the present study. Silica thin films with a thickness larger than 1 μm were prepared. Measurements of refractive indices of the films were performed by an ellipsometer.

In UV-poling, thin film samples were irradiated by a pulsed ArF laser of 6.4 eV as photon energy. The irradiation was carried out with an energy density of 100 mJ/cm<sup>2</sup> per pulse and a pulse repetition of 10 pulses/sec. The total number of shots was fixed at 10<sup>4</sup>. Poling electric field strength was chosen to be 10<sup>5</sup> V/cm.

Maker fringe technique using a Q-switched Nd:YAG laser with a fundamental wavelength of 1.06 μm was used to measure induced SHG. Y-cut quartz with  $d_{33}=0.5$  pm/V was used as a reference for estimating the absolute values of  $d$  coefficient.

### III. Results and discussions

#### A. Second-order optical nonlinearity in thin films

Figure 1 shows change of nonlinear coefficient,  $d$ , for 20% and 50% GeO<sub>2</sub> containing thin

films with changing oxygen mass flow content . In both cases,  $d$ 's clearly depend on the oxygen flow content during sputtering. Maximum values at 1 cm<sup>3</sup>/min are 3.3 and 8.7pm/V for 20% and 50%GeO<sub>2</sub> samples, respectively.

Figure 2 is plots of the refractive indices, measured at 1.06  $\mu$ m, in silica thin films with 20 mole% Ge as functions of oxygen flow content. Here, the behaviors before and after the UV-poling are shown, and the change of refractive index induced by UV-poling at 1cm<sup>3</sup>/min is of the order of 10<sup>-2</sup>. This value is 1.5 magnitude larger than the value,  $4.5 \times 10^{-5}$ , reported with UV-poled bulk samples<sup>6</sup>.

Nishii et al.<sup>7</sup> reported an increase of absorption coefficient by annealing in a vacuum. Simmons et al.<sup>8</sup> reported that a variety of photosensitive defects are induced by heat treating of as-grown germanosilicate sol-gel films in a reduced atmosphere.

Intending to further improve the second-order optical nonlinearity of thin films, the as-deposited samples underwent an annealing in a vacuum prior to UV-poling. As a result,  $d$  coefficient has been increased from 8.7pm/V to 9.3, 10.7 and 12.5pm/V after the treatment for 1, 12 and 24h durations, respectively. To our best knowledge, this is the first report of such high values of nonlinear coefficient  $d$  with thin films.

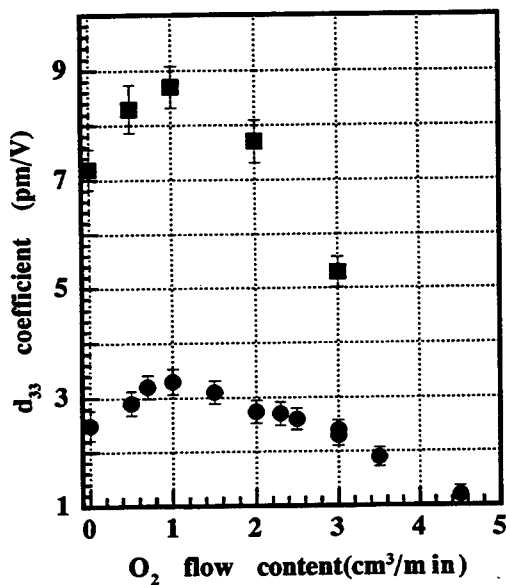


Fig. 1:  $d_{33}$  plots vs  $O_2$  flow content.

- Silica thin films with 20 mole% GeO<sub>2</sub>,
- Silica thin films with 50 mole% GeO<sub>2</sub>

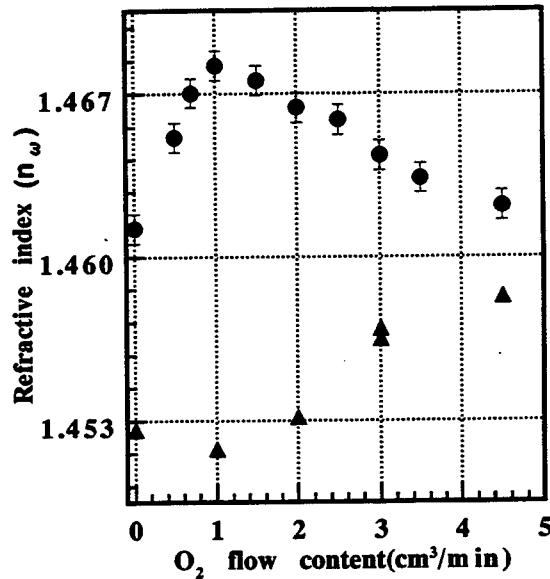


Fig. 2: Refractive indices vs  $O_2$  flow content.

- ▲ before UV-poling,
- after UV-poling

## B. Decay of second-order optical nonlinearity

Another key property is the decay of second-order nonlinearity. Figure 3 shows the relative values of  $d(t)/d(0)$  versus time, where  $d(t)$  is  $d$  coefficient as a function of time,  $t$ , after the nonlinearity was induced. The decay time constant,  $\tau$ , for thin films was found to be short and around several months.

This is very much shorter than the corresponding value, 280 days, with bulk samples<sup>9</sup>.

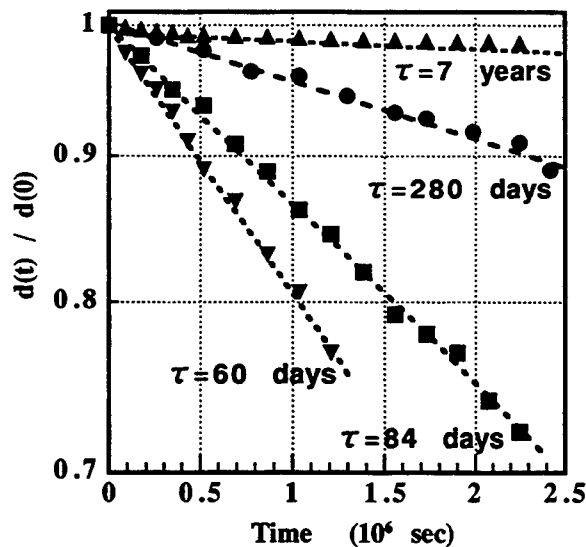
Several authors<sup>10-12</sup> have reported an improvement of photosensitivity of bulk samples by hydrogen loading.

Figure 3 shows the decay of  $d$  coefficient with our hydrogen loaded films, where the sample

was 50 mole% GeO<sub>2</sub> added thin film preannealed in vacuum at 500°C for 12h and then left at room temperature in hydrogen gas at 85 atm for 45 days. The decay time constant has increased to approximately 7 years.

#### IV. Summary

UV-poling technique has been used to study second-order optical nonlinearity in rf sputtered Ge-doped SiO<sub>2</sub> thin films. This technique induces second-order nonlinearity in all sputtered thin films. The optical nonlinearity depends on oxygen flow content with an optimum condition at 1 cm<sup>3</sup>/min. Vacuum annealing improves the matter and the *d* coefficient as high as 12.5 pm/V was obtained. UV-poling induces a positive change of the order of 10<sup>2</sup> in the refractive indices, much larger than bulk samples treated by the same technique. Loading in H<sub>2</sub> at high pressure prior to UV-poling, makes the decay or degradation time much longer up to approximately 7 years.



**Fig.3: Decay of *d* coefficient as function of time.** ● bulk sample,  
 ■ 20 mole % Ge added silica films,  
 ▼ 50 mole% Ge added silica films,  
 ▲ 50 mole% Ge added silica films loaded  
 in H<sub>2</sub> gas.

#### References

- <sup>1</sup> Y. Sasaki and Y. Ohmori, *Appl. Phys. Lett.* **39**, 466 (1981).
- <sup>2</sup> U. Osterberg and W. Margulis, *Opt. Lett.* **11**, 516 (1986).
- <sup>3</sup> T. Hirama, H. Muto, O. Sugihara and N. Okamoto, *Opt. Rev.* **3**, 17 (1996)
- <sup>4</sup> R. A. Meyers, N. Mukherjee and S.R.J. Brueck, *Opt. Lett.* **16**, 1732 (1991).
- <sup>5</sup> T. Fujiwara, D. Wong, Y. Zhao, S. Flemming, S. Poole and M. Sceats, *Electron. Lett.* **31**, 573 (1995)
- <sup>6</sup> R. M. Atkins, V. Mizrahi and T. Erdogan, *Electron. Lett.* **29**, 3858 (1993).
- <sup>7</sup> J. Nishii, H. Yamanaka, H. Hosono and K. Kawazoe, *Appl. Phys. Lett.* **64**, 282 (1994).
- <sup>8</sup> K. D. Simmons, G. I. Stegeman, B. G. Potter Jr. and J. H. Simmons, *J. Non-Cryst. Solids* **179**, 254 (1994).
- <sup>9</sup> T. Fujiwara, M. Takahashi and A. J. Ikushima, *Electron. Lett.* **33**, 980 (1997).
- <sup>10</sup> A. J. Ikushima and T. Fujiwara, *J. Nonlinear Optic.* *in press*.
- <sup>11</sup> M. Takahashi, T. Fujiwara, T. Kawachi and A. J. Ikushima, *Appl. Phys. Lett.* **72**, 1287 (1998).
- <sup>12</sup> B. Malo, J. Albert, F. Biodeau, T. Kitagaewa, D. Johnson, K. Hill, K. Hattori, Y. Hibino and S. Gujrathi, *Appl. Phys. Lett.* **65**, 394 (1994).

## Alkali bismuth gallate glasses for 1.3 $\mu\text{m}$ planar optical amplifiers

S. Q. Man, E.Y.B. Pun, and P.S. Chung

Department of Electronic Engineering, City University of Hong Kong, Tat Chee Avenue,  
Kowloon, Hong Kong

Tel no : (852) 2788 8609, Fax no : (852) 2788 7791, E-mail : [eeeybpun@cityu.edu.hk](mailto:eeeybpun@cityu.edu.hk)

At present, there are three principal rare earth candidates for 1.3  $\mu\text{m}$  optical amplifiers: neodymium ( $\text{Nd}^{3+}$ ), praseodymium ( $\text{Pr}^{3+}$ ) and dysprosium ( $\text{Dy}^{3+}$ ).  $\text{Pr}^{3+}$  is the most likely ion to be used in an efficient optical amplifier for the 1.3  $\mu\text{m}$  telecommunication window, and amplification has been demonstrated in  $\text{Pr}^{3+}$ -doped fluoride glass fibers [1,2]. Unfortunately, the intrinsic phonon spectra of these fluoride hosts limit the quantum efficiency to low values. In order to improve the performance of a  $\text{Pr}^{3+}$  doped amplifier, it is essential to use a host with a smaller maximum phonon energy, so that the multiphonon relaxation rate is reduced. Sulfide glasses and chloro-fluoride glasses with lower phonon energies have been extensively studied to tentatively improve the gain coefficient of 1.3  $\mu\text{m}$  amplifiers [3,4].

In this paper, we propose and investigate  $\text{Pr}^{3+}$  doped alkali bismuth gallate ( $\text{K}_2\text{O}-\text{Bi}_2\text{O}_3-\text{Ga}_2\text{O}_3$  glasses) [5] for 1.3  $\mu\text{m}$  optical amplifiers. The optical properties of these glasses were characterised. Ion-exchanged optical waveguides were fabricated, and fluorescence at 1.3  $\mu\text{m}$  wavelength was observed. The quantum efficiency is also estimated.

$\text{K}_2\text{O}-\text{Bi}_2\text{O}_3-\text{Ga}_2\text{O}_3$  glass sample used in this work has the following molar composition: 5%  $\text{K}_2\text{O}$ , 70%  $\text{Bi}_2\text{O}_3$  and 25%  $\text{Ga}_2\text{O}_3$ .  $\text{Pr}_6\text{O}_{11}$  was added to the starting powders to prepare glasses doped with 0.1 wt%, 0.5 wt% and 1 wt%  $\text{Pr}^{3+}$ . The glass powders were melted at  $1200\text{--}1300^\circ\text{C}$  in a platinum crucible using an electrically heated furnace. The glasses were subsequently annealed at lower temperatures, and then sliced and polished to dimensions  $20\times 20\times 2$  mm.

The Raman spectrum of undoped  $\text{K}_2\text{O}-\text{Bi}_2\text{O}_3-\text{Ga}_2\text{O}_3$  glasses is shown in Fig.1. The Raman spectrum shows two strong peaks at  $134\text{ cm}^{-1}$  and  $381\text{ cm}^{-1}$ , and a weak peak at  $660\text{ cm}^{-1}$ . Because the  $660\text{cm}^{-1}$  band is very weak, the maximum phonon energy of these glasses can be considered as  $381\text{cm}^{-1}$ . The absorption spectrum of 1.0wt%  $\text{Pr}^{3+}$  doped glasses is shown in Fig.2. The Judd-Ofelt analysis is carried out based upon the measured oscillator strengths of the absorption bands, and the intensity parameters  $\Omega_t$ , determined by using a

least-squares fitting approach, are found to be  $\Omega_2 = 4.4 \times 10^{-20} \text{ cm}^2$ ,  $\Omega_4 = 8.9 \times 10^{-20} \text{ cm}^2$ , and  $\Omega_6 = 4.1 \times 10^{-20} \text{ cm}^2$ .

The fluorescence spectrum of the  ${}^1\text{G}_4 \rightarrow {}^3\text{H}_5$  transition in 0.5 wt%  $\text{Pr}^{3+}$  doped glasses is shown in Fig. 3. The peak appears at  $1.34 \mu\text{m}$ , and is shifted to the longer wavelength comparing to ZBLAN and  $\text{PbO-Bi}_2\text{O}_3-\text{Ga}_2\text{O}_3$  glasses. The bandwidth of the transition is  $\sim 120 \text{ nm}$ . This is considerably larger than those of fluoride and chalcogenide glasses. Ion-exchanged optical waveguides were fabricated using mixed melts of  $\text{RbNO}_3:\text{Ba}(\text{NO}_3)_2$ , and similar fluorescence spectrum was also obtained in the waveguides. The stimulated emission cross-section of  ${}^1\text{G}_4 \rightarrow {}^3\text{H}_5$  is  $0.75 \times 10^{-20} \text{ cm}^2$  which is larger than that of fluoride glasses. The quantum efficiency is defined as  $\eta = \tau_{\text{meas}} / \tau_{\text{rad}}$  [6]. The lifetime of 0.1 wt%  $\text{Pr}^{3+}$  doped glasses is measured to be  $\sim 78 \mu\text{s}$ , and the radiative quantum efficiency is estimated to be 17.4%. This value is larger than that in fluoride glasses, but less than that in chalcogenide glasses.

In conclusion,  $\text{Pr}^{3+}$  doped  $\text{K}_2\text{O-Bi}_2\text{O}_3-\text{Ga}_2\text{O}_3$  glasses have been fabricated and characterized. The Raman scattering, the optical absorption, and the fluorescence properties of these glasses are studied. Optical waveguides were fabricated using the ion-exchange process. For the  ${}^1\text{G}_4 \rightarrow {}^3\text{H}_5$  transition the peak appears at  $1.34 \mu\text{m}$  with a bandwidth of  $\sim 120 \text{ nm}$ . The lifetime of the  $\text{Pr}^{3+}: {}^1\text{G}_4$  level is measured to be  $\sim 78 \mu\text{s}$ , and the quantum efficiency is  $\sim 17.4\%$  which is larger than that in fluoride glasses. From our data, it appears that  $\text{Pr}^{3+}$  doped  $\text{K}_2\text{O-Bi}_2\text{O}_3-\text{Ga}_2\text{O}_3$  glasses are promising materials for lasers and optical amplifiers operating in the  $1.3 \mu\text{m}$  telecommunication window.

This work is supported by a Competitive Earmarked Research Grant, Research Grant Council, and the Croucher Foundation.

#### References :

- [1] Y. Miyajima, T. Sugawa, and Y. Fukasaku, Electron. Lett., 27, 1706 (1991).
- [2] Y. Nishida, T. Kanamori, Y. Ohishi, M. Yamada, K. Kobayashi, and S. Sudo, IEEE Photonics Technol. Lett., 9, 318 (1997).
- [3] M. A. Newhouse, R. F. Bartholomew, B. G. Aitken, L. J. Button and N. F. Borrelli, IEEE Photon. Technol. Lett., 6, 191 (1994).
- [4] K. Wei, D. P. Machewirth, J. Wenzel, E. Snitzer, and G. H. Sigel, Jr., J. Non-Cryst. Solids, 182, 257 (1995).
- [5] J. C. Lapp, Am. Ceram. Soc. Bull., 71, 1543 (1992).
- [6] R.R. Jacobs and M.J. Weber, IEEE J. Quantum Electron., 12, 102 (1976).

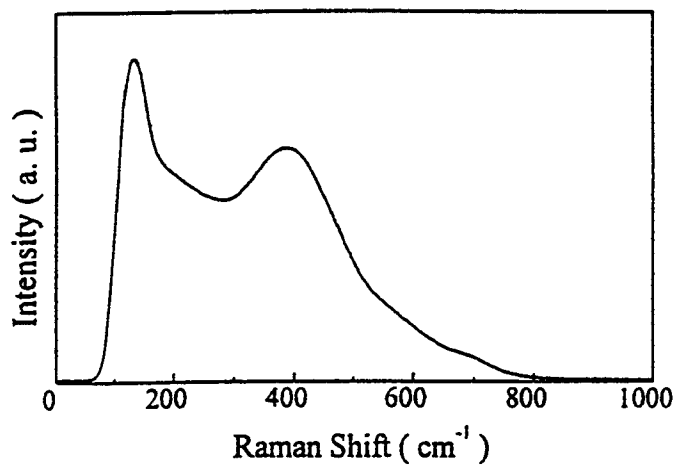


Fig.1 Polarized Raman spectrum of undoped  $\text{K}_2\text{O}-\text{Bi}_2\text{O}_3-\text{Ga}_2\text{O}_3$  glasses.

Fig. 2 Absorption spectrum of 1.0 wt%  $\text{Pr}^{3+}$  doped  $\text{K}_2\text{O}-\text{Bi}_2\text{O}_3-\text{Ga}_2\text{O}_3$  glasses.

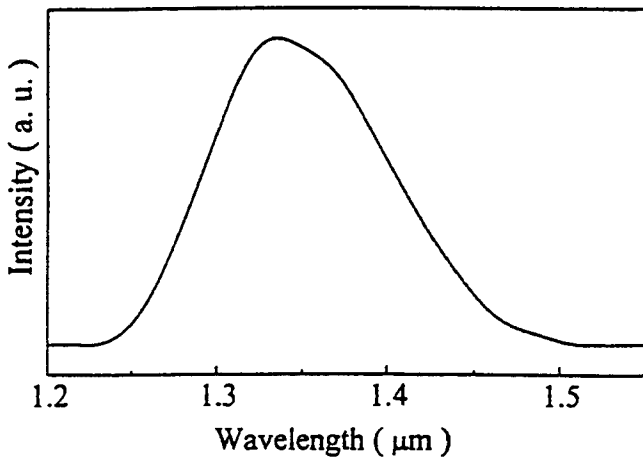
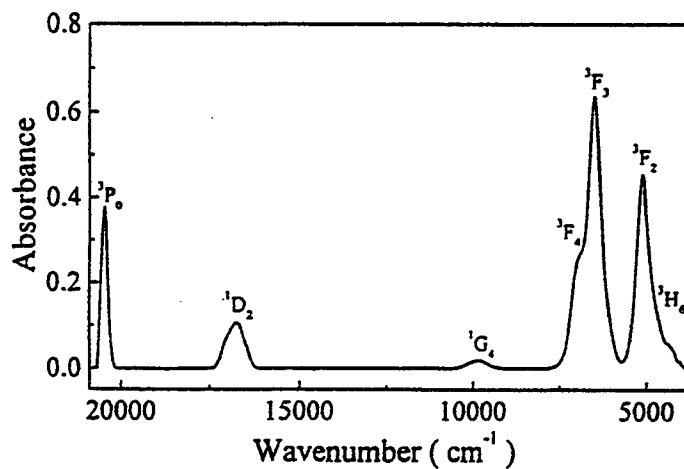


Fig. 3 Fluorescence spectrum of  $^1\text{G}_4 \rightarrow ^3\text{H}_5$  transition in 0.5 wt%  $\text{Pr}^{3+}$  doped  $\text{K}_2\text{O}-\text{Bi}_2\text{O}_3-\text{Ga}_2\text{O}_3$  glasses.

## Spatial holeburning in second-order excitation probability distribution for densely erbium-doped fibres

S. Helmfrid, D. Bremberg, and B. Jaskorzynska

Laboratory of Photonics and Microwave Engineering, Department of Electronics  
Royal Institute of Technology, Electrum 229, S-16440 Kista, Sweden  
srh@ele.kth.se, db@ele.kth.se, bj@ele.kth.se

J. L. Philipsen

COM Center, Bldg. 349, Technical University of Denmark, DK-2800 Lyngby, Denmark  
jp@com.emi.dtu.dk

### Introduction

Concentration-dependent quenching effects due to ion-ion interaction are known to degrade the performance of erbium-doped fibre and waveguide amplifiers. The quenching of erbium ions is caused by an energy transfer upconversion process, so-called homogeneous upconversion (HUC), in which the energy from one excited ion is transferred to an excited neighbour and then lost to phonons in the host material. Homogeneous upconversion is often studied by measuring the fluorescence decay from the metastable level after switch-off of the pump beam. In case of strong ion-ion interaction, the effective de-excitation rate is a function of the instantaneous degree of excitation and the decay curves show a strong deviation from the ideal exponential shape. It has usually been assumed that the interacting erbium ions are in the so-called kinetic limit [1,2]. This means that the migration of the excitation energy among the ions is so fast that any gradients in the excitation probability are rapidly smeared out and, therefore, all ions have the same probability of being excited.

Recently, it has been experimentally demonstrated that the kinetic approximation is not valid for erbium [3, 4]. A finite migration will in general reduce the upconversion rate, as it takes a finite time to transport energy to ions that have been quenched. This causes a negative correlation in the excitation probability of closely located ions. It turns out that the upconversion rate in the non-kinetic regime is not only a function of the degree of excitation, but is influenced by all processes that re-distribute the excitation energy among the erbium ions. For instance, if an amplifier is operated at the same degree of excitation but with a strong signal and an elevated pump power to compensate for the increased stimulated emission, it will have a higher upconversion than in the case with no input signal. Hence, we should be able to see different decay curves after switching the pump and signal off for different initial values of the power levels, even if the initial degree of excitation is the same.

The negative correlation of excitation probability, which causes the difference in the decay curves, can also be explained in terms of spatial holeburning in the second-order probability distribution of the excitation energy [3]. When the re-distribution of excitation energy is slow, the second-order spatial probability distribution for simultaneous excitation of two closely located ions decreases, as there is no process to compensate for the fast upconversion. In this paper, we communicate the first study of such spatial holeburning in erbium-doped fibres. The cw distribution functions and the temporal evolution during decay are evaluated and compared to experimental data. The time to smooth out differences in the spatial holeburning is studied as function of erbium concentration and it is concluded that upconversion and not migration is the driving force in the equalisation process.

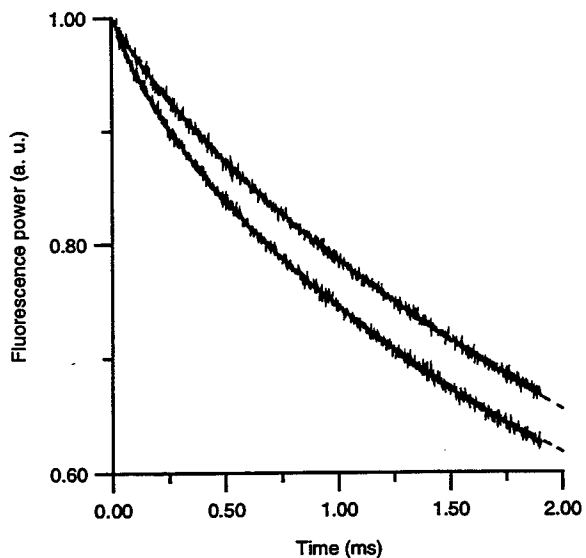


*Fig. 1. Decay of fluorescence from erbium-doped fibre after switch-off of pump and signal beams.*

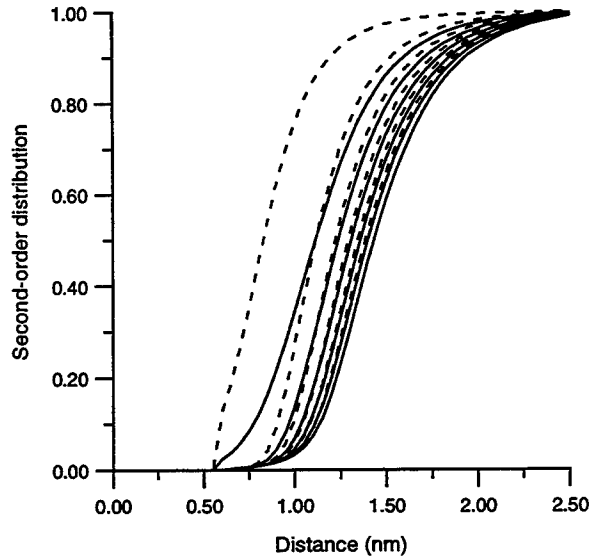


*Fig. 2. Evolution of the normalised second-order distribution function of excitation energy. (The minimum distance between ions is 0.59 nm.)*

### Theoretical model and comparison with decay curves

To evaluate the upconversion rate and the second-order spatial distribution function of excitation energy, we used the model presented in Ref. 3. The probability per squared unit volume of finding two excited ions at time  $t$  and distance  $r$  is  $f^{**}(r,t)$ , the probability of finding one excited ion and one ion in the ground state is  $f^{*0}(r,t)$  and the probability of finding two ions in the ground state  $f^0(r,t)$ . The time evolution of these joint probability distributions is described by a set of differential equations. The solution of the differential equations can then be used to evaluate the observables. In Fig. 1, we compare experimental decay curves of the 1.5  $\mu\text{m}$  fluorescence with the corresponding theoretical values. In the upper solid curve, the fibre was pumped with 10 mW radiation of wavelength 980 nm. In the lower solid curve, a signal of 8.6 mW at 1530 nm was added and the pump power was increased to 30 mW. The dashed curves show the theoretical predictions. The agreement is excellent, although parameters such as pump rate and signal emission rate in the simulation were fitted rather than evaluated from experimental data.

### Evolution of the spatial holeburning

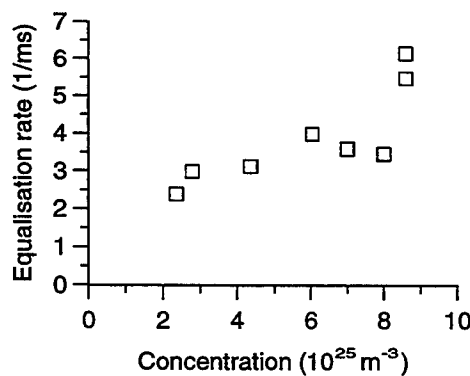
In the following, we will focus our interest on  $f^{**}$ . In the kinetic limit, this function takes on the value  $n_2(t)^2$ , where  $n_2$  is the average number of excited erbium ions per unit volume. Hence the normalised function  $f^{**}/n_2(t)^2$  will be unity in the kinetic limit and less than unity for inter-ion distances where spatial holeburning has been induced by the upconversion process. In Fig. 2, we show the calculated values of the normalised function  $f^{**}$  for the decay measurement that was described above. The solid curves in the figure correspond to the decay with only a pump beam before switch off and the dashed curves to the decay with both pump and signal before switch off. The time step between each curve is 500  $\mu\text{s}$ . At time  $t = 0$ , the two leftmost curves in the figure, the distribution function is in steady state. The spatial holeburning is much smaller for the dashed curve, owing to the energy re-distribution induced by the signal and elevated pump beams.

After switch off, the decay corresponding to the dashed curves in Fig. 2 is much faster than for the solid curves, as there are excited ions at much closer distances in the dashed curves

and there is no additional re-distribution process that can maintain this large excitation at short range. At  $t = 2.5$  ms, the two rightmost curves, the distribution functions are almost identical. In Fig. 1, there is a rapid initial increase in the ratio between the fluorescence curves when closely located ions interact. (It is more natural to study the logarithm of the ratio between the two curves, rather than the difference, as the magnitude of the fluorescence signals is rapidly decaying.) The growth of the ratio is getting slower as these ions are getting depleted, and finally, after 3.3 ms, it will reverse sign as the holeburning in the two cases is equally large but the curve with faster initial decay now has a lower degree of excitation. The equalisation of the decay rates is clearly a non-exponential process, but we will still use the 1/e-time of the maximum difference to characterise the typical time scale. In Fig. 1, this value is 420  $\mu$ s. It is significantly smaller than the inverse cw upconversion rate at full inversion with only a pump beam present (2 ms), but much smaller than the typical migration time (50  $\mu$ s) [4]. This illustrates the fact that the equalisation of the decay rates is caused by fast upconversion of closely located ions, rather than any migration process.

To further investigate the spatial holeburning process, we measured the equalisation time for fibres with different concentration. In Fig. 3, we show the inverse time as function of erbium concentration. Theoretical simulations show that this relation should be almost linear, because all ions are closer and all exchange processes are faster for higher concentrations. Within the measurement error, we have good agreement.

*Fig. 3. Equalisation rate as function of concentration*



## Conclusions

In conclusion we have investigated spatial holeburning in the second-order spatial distribution function of excitation energy in erbium-doped fibres. We have shown that the theoretical model from Ref. 3 correctly describes fluorescence decay curves. We have studied how the decay rates in different curves become equalised and shown that the driving force in this process is the fast depletion of regions with low spatial holeburning. Hence the time constant for the process is shorter than the typical average upconversion time but longer than the migration time. The fibres were supplied by Lucent Technologies Denmark.

## References

1. J. Nilsson, P. Blixt, B. Jaskorzynska, and J. Babonas, "Evaluation of parasitic upconversion mechanisms in Er<sup>3+</sup>-doped silica-glass fibers by analysis of fluorescence at 980 nm," *J. Lightwave Technol.*, 1995, **13**, (3), pp. 341-349
2. J. L. Philipsen and A. Bjarklev, "Monte Carlo simulations of homogeneous upconversion in erbium-doped silica glasses", *IEEE J. Quantum Electron.*, 1997, **33**, (5), pp. 845-854
3. J. Philipsen et al., "Observation of strongly non-quadratic homogeneous upconversion in Er<sup>3+</sup>-doped silica fibres and reevaluation of the degree of clustering", submitted to *IEEE J. Quantum Electron*
4. D. Bremberg et al., "Observation of energy-distribution-dependent homogeneous upconversion in erbium-doped silica glass fibres", submitted to *Electron. Lett.*

# Method for characterization of clustering and homogeneous upconversion in Er-doped waveguides

**Marcin Swillo, Dan Bremerg, Bozena Jaskorzynska, Sten Helmfrid**

Royal Institute of Technology, Department of Electronics, Electrum 229, S-164 40 Kista, Sweden

Tel: +46 8 752 12 19 Fax: +46 8 752 12 40 E-mail: [bj@ele.kth.se](mailto:bj@ele.kth.se)

**Jacob L. Philipsen**

COM Center, Bldg. 349, Technical University of Denmark, DK-2800 Lyngby, Denmark

Tel.: +45 45 25 37 71 Fax: +45 45 93 65 81 E-mail: [jp@com.dtu.dk](mailto:jp@com.dtu.dk)

## Introduction

Parasitic energy transfer between excited ions [1-4] have been widely recognized as gain limiting factor in high-concentration rare-earth doped amplifiers. The effect of homogeneous upconversion (HUC), when the energy is transferred between non-clustered ions, is unavoidable but can be counteracted by increasing pump powers. In clustered ions, however, the effect often called pair induced quenching (PIQ), can totally quench the gain in a three level system. Since clustering can be minimized by choice of the host material and the doping technology it is important to be able to characterize a degree of clustering in newly fabricated samples. For optimizing design of rare-earth doped devices it is also important to characterize HUC in a simple waveguide.

In this paper we propose a method for measuring the portion of unexcitable, clustered ions, and for measuring characteristics of HUC in erbium-doped waveguides. The method is based on analysis of decay curves for the fluorescence from the metastable ( $1.5\mu\text{m}$ ) and the upconverted (980nm) levels. It enables us to separate the HUC and the PIQ contribution to the 980nm fluorescence.

It should be pointed out that the theoretical model that we use does not assume any particular form of the HUC rate. In most of the models used so far, the HUC rate is assumed to be a linear function of the population  $N_2$  of the metastable level. In [1] this assumption has been questioned and we have earlier observed [2] a non linear dependence of the HUC on  $N_2$ . The nonlinear HUC characteristics are also obtained from the present measurements.

## Theory

To describe the decay of the populations in a metastable ( $N_2$ ) and the upconversion ( $N_3$ ) levels we use an approach similar to [3]. However, also upconversion between singly excited clusters and excited isolated ions, are included in our model.

$$\frac{dN_2}{dt} = -\frac{N_2}{\tau_2} - 2W_c N_2 + \left(1 - \frac{1}{m}\right) \frac{N_3}{\tau_3}, \quad \frac{dN_3}{dt} = -\frac{N_3}{\tau_3} + W_c N_2; \quad (1)$$

$$\text{Initial condition: } \frac{N_3(0)}{\tau_3} = (k-1)RN_2^P(0) + W_c(0)N_2(0)$$

where:  $\tau_i$  is a spontaneous decay time from level i,  $R$  is the pump rate at  $1.48\mu\text{m}$ ,  $W_c = f(N_2, R)$  is the homogeneous upconversion rate,  $1/m$  is a branching ratio (usually ca 1/1000) between the radiative and nonradiative decay of  $N_3$ , and  $k$  is an average number of ions in a cluster.  $N_2^P$  is the metastable population of clustered ions only. Because of the very fast energy transfer between ions in a doubly excited cluster the model assumes that only one ion in a cluster can be in an excited state. Pumping of a singly excited cluster results in an almost immediate upconversion process. This can be described as effective pumping of the level 3 and is represented by the first term in the initial condition for  $N_3$ .

In terms of the measured fluorescence powers  $P_i$  Eqs.1 can be expressed as:

$$\begin{aligned} \frac{dP_2}{dt} &= -\frac{P_2}{\tau_2} - \alpha_2 F, & 2 \frac{dP_3}{dt} &= -\frac{P_3}{\tau_3} + \alpha_3 F; \\ \frac{P_3(0)}{\tau_3} &= \alpha_3 [(k-1)RN_2^P(0) + W_c(0)N_2(0)] \end{aligned} \quad (2)$$

where:  $1/m$  has been neglected,  $P_2 \equiv P_{1.5} = \alpha_2 N_2$ ,  $P_3 \equiv P_{980} = \alpha_3 N_3$ ,  $F \equiv [2W_c N_2 - N_3 / \tau_3]$

From the measured decay curves  $P_2(t)$  and  $P_3(t)$  we find  $\alpha_2 F(t)$  and  $\alpha_3 F(t)$ . The scaling factor  $\gamma \equiv \alpha_2 / \alpha_3$  is determined by dividing  $\alpha_2 F(t)$  by  $\alpha_3 F(t)$ . The decay of the HUC in the units of  $P_3$  is found as

$$\alpha_3 W_c N_2 = 1/2 [\alpha_3 F + P_3 / \tau_3] \quad (3)$$

From the boundary condition (2) divided by the measured  $P_2(0)$  we obtain:

$$\tilde{\rho} \equiv \tau_3 R (k-1) N_2^P(0) / N_2(0) = \gamma [P_3(0) - \alpha_3 W_c(0) N_2(0) \tau_3] / P_2(0) \quad (4)$$

Dividing Eq.3 by  $P_2$  gives the decay of the HUC rate in absolute units (1/s):

$$W_c = \gamma (\alpha_3 F + P_3 / \tau_3) / (2P_2) \quad (5)$$

In particular,  $W_c(0)$  is a value of the HUC rate for a steady state at a given pump rate  $R$ .

$(1+\varepsilon)R$ , where  $\varepsilon$  is a ratio of the emission to the absorption cross-section, is found from the steady state equation for  $N_2$  using the measured values of  $N_2(0)$ ,  $W_c(0)$ , and  $\tau_2$ . From Eqs.4 we can now find  $(k-1)N_2^P/N_2$ , i.e. a ratio of unexcitable Er-ions in singly excited clusters to all excited ions, which is an important figure of merit for characterizing the influence of clusters on the gain reduction. For large pump rates ( $W_c/R \ll 1$ ,  $\tau_2 R \gg 1$ ) and small emission cross-sections ( $\varepsilon \ll k$ ) we can also estimate a ratio  $\rho$  of unexcitable (unbleachable [4]) ions from all clusters to all ions that can be excited:

$$\tilde{\rho} / [\tau_3 (1+\varepsilon) R] \approx [(k-1)N_2^P / k] / [N_o^S + N_o^P / k] \equiv \rho, \quad (6)$$

### Experimental results

The measurements were done on two fibers (manufactured by Lucent Technologies Denmark) of different Er-concentration. The decay of fluorescence at 1.5  $\mu\text{m}$  and 980 nm were measured with detectors placed transverse to the fibers. In order to find  $\alpha_i F(t)$  Eqs.2 were solved by integration over a time interval  $\Delta t$  for each time point with a sampling step  $dt$ . The result for the fiber with a higher Er-concentration,  $\Delta t=600\mu\text{s}$  and  $dt=2\mu\text{s}$  are shown in Fig.1. The curves in Fig.1 have been fitted to each other and the resulting scaling ratio  $\gamma$  was found as an average over a large time interval as it is shown in Fig.2.

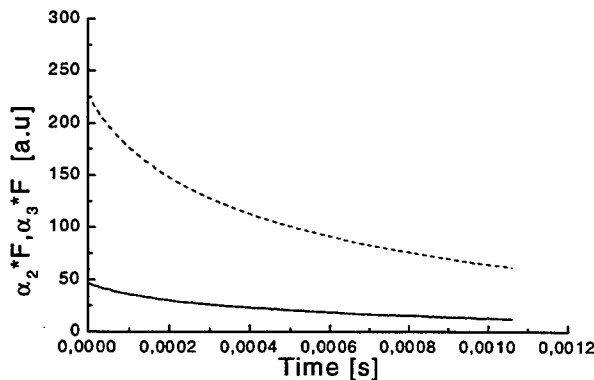


**Fig. 1** Fig.1  $F=2W_c N_2 - N_3 / \tau_3$  obtained from the decay of 1530nm (solid line) and 980nm (dashed line) fluorescence measured in different units.

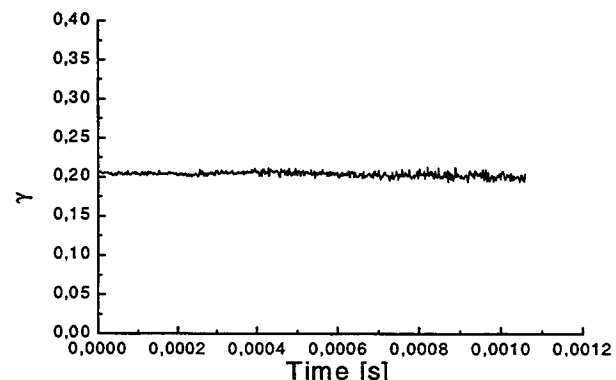


**Fig. 2** Ratio  $\gamma$  between the units of the curves in Fig.1.

The HUC was calculated from decay of fluorescence at 980 nm by integration Eqs.2 over time intervals  $\Delta t=4\mu s$  with a time step  $dt=0.2 \mu s$ . In Fig.3 we plotted  $\tilde{\rho}$  given by Eq.4 as a function of  $(1+\varepsilon)R$  for both fibers. The linear characteristics confirm validity of the model. From the slopes of the curves we obtained the ratios of the unexcitable to the excitable Er ions shown in the table below:

	Er-concentration	$\tilde{\rho}/[\tau_3(1+\varepsilon)R] \approx \rho$	Wc(t=0)
Fiber 1	$8.0 \cdot 10^{25} [\text{ions/m}^3]$	$0.16 \pm 0.02$	$1.8 \cdot 10^3 [\text{s}^{-1}]$ at $(1+\varepsilon) \cdot R = 1.25 \cdot 10^4 [\text{s}^{-1}]$
Fiber 2	$6.0 \cdot 10^{25} [\text{ions/m}^3]$	$0.072 \pm 0.012$	$1.2 \cdot 10^3 [\text{s}^{-1}]$ at $(1+\varepsilon) \cdot R = 1.65 \cdot 10^4 [\text{s}^{-1}]$

As expected, both the portion of unexcitable Er-ions and the HUC rate increase with increasing Er-concentration.

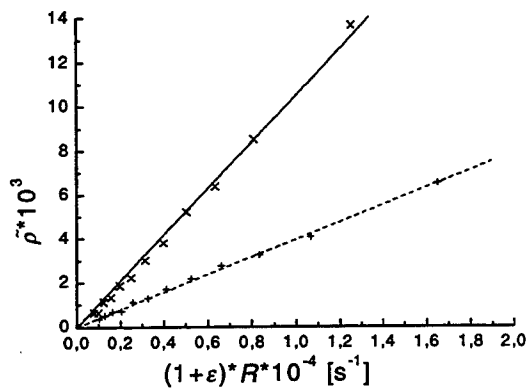


Fig. 3 Ratio  $\tilde{\rho} = \tau_3 R(k-1) N_2^P(0)/N_2$  measured for the fibers with the higher (solid line) and the lower (dashed line) Er-concentration for a varying pump rate.

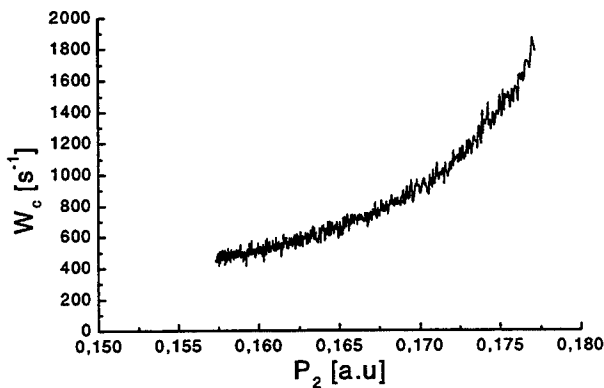


Fig. 4 Upconversion rate as a function of  $1.5\mu\text{m}$  fluorescence power ( $\propto N_2$ ).

In order to test a commonly made assumption that  $W_c$  is a linear function of  $N_2$  we plotted in Fig.4  $W_c$  vs  $P_2 \propto N_2$ . We can see that  $W_c$  shows a clearly nonlinear dependence on  $N_2$ , which confirms the hypothesis of [1] and our earlier observation [2].

### Conclusions

We proposed and demonstrated a method for determination of a ratio of unexcitable, clustered ions to the ions that can be excited, as well as of the rate of the homogeneous upconversion in Er-doped waveguides. We characterized two fibers with different Er-concentrations and found that the effect of both clustering and HUC increase with increasing Er-concentration.

The method demonstrated for Er-doped fibers is directly applicable for Er-doped planar waveguides.

### References

1. Jacob L. Philipsen, and Anders Bjarklev, "Monte Carlo Simulations of Homogeneous Upconversion in Erbium-Doped Silica Glasses", IEEE J. Quantum Electron **33**, 845-854, (1997).
2. J. Philipsen, J. Broeng, A. Bjarklev, S. Helmfrid, D. Bremberg, B. Jaskorzynska, and B. Palsdottir, "Observation of strongly non-quadratic homogeneous upconversion in Er-doped silica fibres and reevaluation of the degree of clustering", submitted to IEEE J. Quantum Electron.
3. E. Delevaque, T. Georges, M. Monerie, P. Lamouler, and J-F. Bayon, "Modelling of Pair-Induced Quenching in Erbium-Doped Silica Fibers", IEEE Photonics Technol. Lett. **5**, 73-75, (1993).
4. C. C. Ye, B. Jaskorzynska, S. Helmfrid, and P.-Y. Fonjallaz, "Nondestructive method for measuring the degree of cluster-induced quenching in  $\text{Er}^{3+}$ -doped waveguides and fibers", Applied Optics **37**, 6362-6365 (1998).

## Optical Isolation Based on Nonreciprocal Phase Shift in a Mach-Zehnder Interferometer

J. Fujita, M. Levy, R. U. Ahmad, and R. M. Osgood, Jr.

Microelectronics Sciences Laboratories, Columbia University

530 West 120<sup>th</sup> St. Rm. 1001 M/C 8903 New York, NY 10027

Tel (212) 854-8042 Fax (212) 860-6182 Email: [juni@cumsl.ctr.columbia.edu](mailto:juni@cumsl.ctr.columbia.edu)

M. Randles

Litton Airtron SYNOPTICS

1201 Continental Blvd. Charlotte, NC 28273

C. Gutierrez and R. Villareal

Southwest Texas State University, Physics Dept. NSB 280

601 University Dr. San Marcos, TX 78666

While optical isolators are an important component in optical fiber telecommunications, they are commercially available only in bulk form; an integrated version of these devices is desirable to reduce device size and costs. Integrated isolators utilizing Faraday rotation<sup>1,2</sup> and TM-to-radiation mode-conversion<sup>3</sup> have been demonstrated, with extinction ratios close to 30dB. However, these devices require tight birefringence control or maximum mode conversion to achieve high performance. The use of a Mach-Zehnder interferometric design based on the magneto-optic nonreciprocal phase shift offers the possibilities of obviating these problems.<sup>4-6</sup> When transverse magnetic fields are applied to a magneto-optical material such as YIG, the dielectric permittivity tensor couples the transverse and longitudinal components of the propagating wave. This leads to a difference in forward and backward propagation constants, or nonreciprocal phase shift in TM modes for a given length of waveguide. By choosing a nonreciprocal phase shift of  $\pm 90^\circ$  and a reciprocal phase shift of  $90^\circ$  between the two arms of the Mach-Zehnder interferometer, a constructive and destructive interference for the forward and backward direction can be obtained.<sup>4-6</sup> This type of isolator does not require birefringence minimization or mode matching, thus relaxing design tolerances. It also avoids the need for integrated polarizers, which are required for devices using Faraday rotation. Okamura *et al* have observed nonreciprocal phase shifts in the Mach-Zehnder configuration at  $\lambda=1.15\mu\text{m}$ ,<sup>7</sup> but did not study its isolation performance because of the small nonreciprocal phase shift, i.e.  $\sim 7.5^\circ$  per arm.

This report describes the design of a much larger nonreciprocal phase shift and its use in a hybrid isolator based on a Mach-Zehnder waveguide/fiber interferometer to investigate isolation performance. The experimental results from the isolator, operating at  $\lambda=1.55\mu\text{m}$ , confirm that a high performance isolator can be obtained by using the nonreciprocal phase shift with a Mach-Zehnder interferometric design.

A bismuth-and lutetium- substituted iron garnet epitaxial film on a [111] oriented GGG is used for this experiment. This garnet layer has a composition of  $\text{Bi}_{1.3}\text{Lu}_{1.7}\text{Fe}_{4.4}\text{Ga}_{0.6}\text{O}_{12}$  and TE and TM refractive indices of 2.2434 and 2.2425 at a wavelength of  $1.55\mu\text{m}$ . Magnetic measurements carried out via vibrating sample magnetometry (VSM) show that its easy axis is in-plane along the <110> direction with a required field to saturate its magnetization of  $\sim 3\text{Oe}$ .

Rib waveguides for the garnet samples are fabricated by the following procedure: First, chromium is patterned on  $1.0\mu\text{m}$ -thick BiLu-IG samples. Si ions are then implanted in the sample at 160keV, in order to create a thin damage layer near the top surface. This damage layer is removed by subsequent wet etching in phosphoric acid,<sup>8</sup> and the Cr mask stripped off with ceric ammonium nitrate. BiLu-IG waveguide heights of 0.50 to  $1.00\mu\text{m}$  are obtained, depending on the thicknesses of the Cr mask. The waveguides are patterned with easy magnetization axis oriented transversely to the propagation

direction. For our optical setup, these rib waveguides are measured to have an 8.5-10dB coupling and Fresnel loss at facet and 10dB/cm absorption loss, a typical value for garnet waveguide.

The optical configuration to measure the phase shift and isolation performance is depicted in Fig. 1. The lower arm of a fiber Mach-Zehnder interferometer is coupled into the BiLu-IG waveguide. A spatial light filter is inserted after the BiLu-IG waveguide to prevent spurious coupling of unguided light into the output fiber. For the upper arm, a small gap is created to both balance the power and control the phase difference between the two interferometer arms. Two electromagnets are positioned to generate an AC transverse magnetic field with frequency of ~100Hz to simulate magnetization in the forward and backward propagation directions.

Measurements are made with BiLu-IG waveguides having heights of 0.50 $\mu\text{m}$ , 0.72, 0.80, 1.00 $\mu\text{m}$  and lengths ranging from 2.5 to 8.1mm are used in this study. TM light of better than 30dB polarization purity is coupled into the waveguides, and a relative phase difference of nearly 90° between the arms is obtained by adjusting the optical path length in one of the arms. The measured amplitude of the modulation is then translated into nonreciprocal phase shift by comparing the modulated amplitude with total output power.

For each waveguide height, at least two different sample lengths are used to measure nonreciprocal phase shifts. Given these data, the difference in forward and backward propagation constant,  $\Delta\beta$  ( $=|\beta_{\text{forward}}| - |\beta_{\text{backward}}|$ ), is calculated by taking the ratio of measured nonreciprocal phase shift and its length. The  $\Delta\beta$  for each sample is plotted in Fig. 2. The waveguide height dependence on  $\Delta\beta$  for an off-diagonal dielectric permittivity tensor of  $\epsilon_{xz}=0.00085$  is theoretically calculated by solving a dispersion relation for the sample geometry, and is also included in the figure. The experimental results for  $\Delta\beta$  are found to agree well with the theoretical plot. Measurements using a TE input into BiLu-IG are also performed and show no significant nonreciprocal phase shift, as expected.

The largest nonreciprocal phase shift (45°) is measured with a 3.5mm-long waveguide with 0.5 $\mu\text{m}$  height and is thus used to measure isolation performance. In order to observe a maximum extinction ratio, the phase difference for backward propagation is adjusted to ~180°. Fine tuning the reciprocal phase difference within a few degrees is achieved by adjusting the optical path lengths of the two arms with a differential micrometer stage. With this procedure, a maximum extinction ratio of 11dB is obtained with a power imbalance between the two arms of <0.05dB. The full ±90° nonreciprocal phase shift required for optimal isolation can be achieved with higher specific-Faraday rotation material. A more optimized waveguide geometry can bring the extinction ratio >20dB, according to the measurements.

In summary, a study to characterize BiLu-IG samples in a hybrid Mach-Zehnder waveguide/fiber interferometer configuration has shown 45° nonreciprocal phase shift. The isolator functionality based on this nonreciprocal phase shift has an 11dB extinction ratio. These results show that a fully integrated version of this Mach-Zehnder waveguide is feasible.

## References

1. M. Levy, R.M. Osgood, Jr., H. Hegde, F.J. Cadieu, R. Wolfe, V.J. Fratello, IEEE Photon. Tech. Lett., vol. 8, pp.903-5 (1996).
2. N. Sugimoto, H. Terui, A. Tate, Y. Katoh, Y. Yamada, A. Sugita, A. Shibukawa, and Y. Inoue, IEEE J. Lightwave Tech., vol.14, pp.2537-46 (1996).
3. T. Shintaku, Appl. Phys. Lett., vol. 73, pp.1946-8 (1998).
4. M. Levy, M.H. Hu, R. Scarmozzino, R.M. Osgood, Jr., IEEE Lasers and Electro-Optics Society 1996 Annual Meeting, vol.2, pp.232-3 (1996).
5. N. Bahlmann, M. Lohmeyer, M. Wallenhorst, H. Dotsch, P. Hertel, MRS 1998 Spring Meeting, M2.2, P234 (1998).
6. T. Mizumoto, S. Mashimo, T. Ida, Y. Naito, IEEE Trans. Magnetics, vol.29, pp.3417-9 (1993).
7. Y. Okamura, H. Inuzuka, T. Kikuchi, S. Yamamoto, J. Lightwave Tech., vol. LT-4, pp.711-4 (1986).
8. M. Levy, R.M. Osgood, Jr., A. Kumar, H. Bakrhu, Appl. Phys. Lett., vol. 71, p.2617-9 (1997).

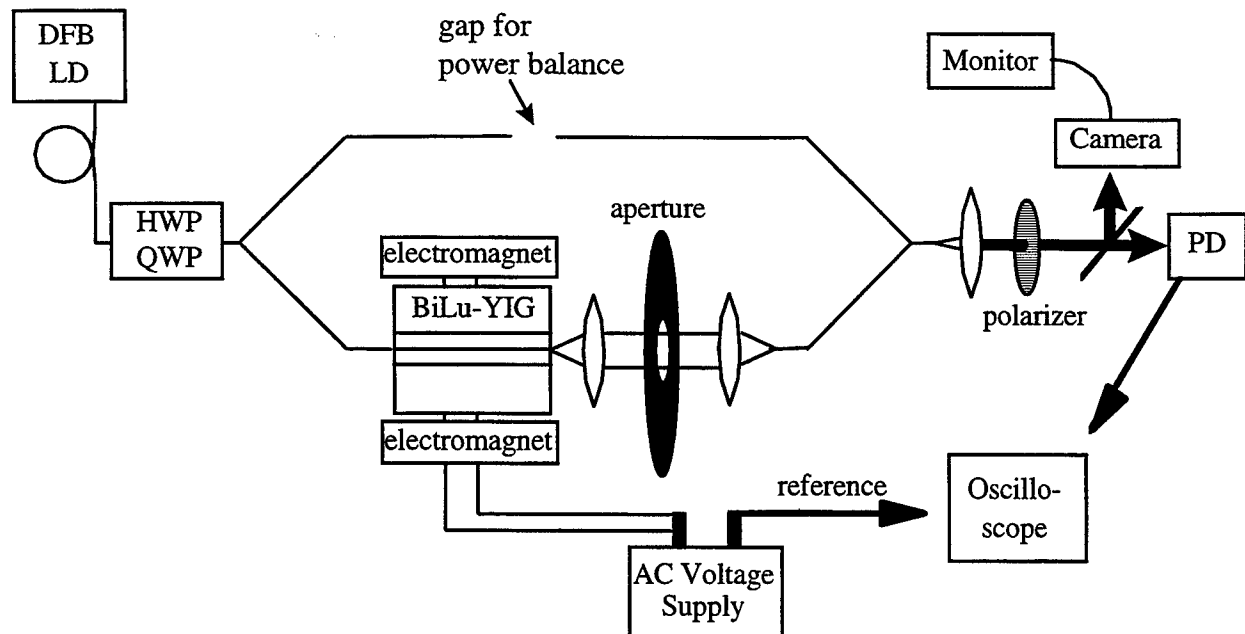


Fig. 1: Experimental setup for nonreciprocal-phase-shift and extinction-ratio measurements

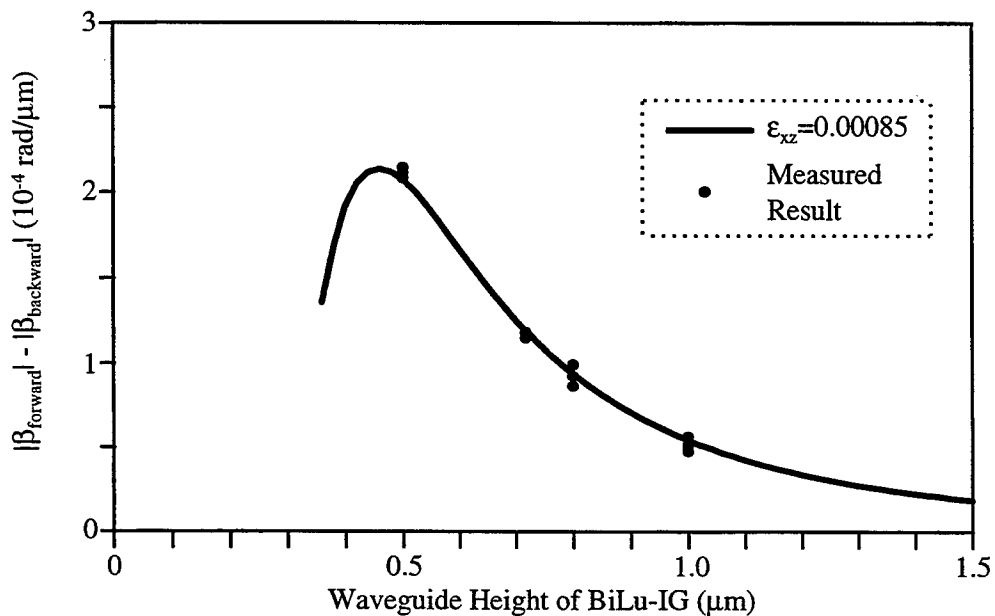


Fig. 2: Observed  $\Delta\beta$ 's for BiLu-IG waveguides

## Temperature Insensitive Glass Microring Resonator Add/Drop Filters by Means of a Polymer Overlay

Sai T. Chu, *Member, IEEE*, Wugen Pan, Shuichi Suzuki, Brent E. Little, *Member, IEEE*,  
Shinya Sato, and Yasuo Kokubun, *Member, IEEE*

S. T. Chu, W. Pan, S. Sato, and Y. Kokubun are with the Kanagawa Academy of Science and Technology, KSP E308, 3-2-1 Sakato, Takatsu, Kawasaki, Japan 213-0012. Email: [sai@maxwell.uwaterloo.ca](mailto:sai@maxwell.uwaterloo.ca)

B. E. Little is with the Research Laboratory of Electronics, Massachusetts Institute of Technology Cambridge, MA 02139

S. Suzuki and Y. Kokubun are also with the Yokohama National University, Department of Electrical & Computer Engineering, 79-5 Tokiwadai, Hodogaya-ku, Yokohama, Japan 240-8501

Compact and highly wavelength selective microring resonator add/drop filters [1-4] are attractive building blocks for dense integration of WDM components. We have recently demonstrated a vertically coupled microring resonator (VCMRR) add/drop filter [4], with the advantage of having the bus waveguides and resonators located in two separate layers. The ring and waveguides can therefore each be optimized separately. Using similar technology, a cross-grid array of rings gives an 8 channel add/drop filter with a compact device size of 1.75 mm by 50  $\mu\text{m}$  [5]. The ring waveguide is in the top layer, and has the advantage of easy access for wavelength tuning or trimming [6]. In passive add/drop filter applications, temperature dependence of the device is an important issue. This is especially true of narrow band filters, where a slight change of the material composition due to the ambient environment can shift the center wavelength outside the pass-band of interest [7]. In this talk, temperature induced resonance shift of the air-clad VCMRR add/drop filter is first measured to determine its temperature dependence. We then propose and demonstrate a method to compensate this temperature dependence by putting an overlay of polymer (PMMA-PFMA) on top of the ring resonator.

The VCMRR add/drop filter used in this work is depicted schematically in Fig. 1. Fig. 1(a) shows the cross sectional view of the VCMRR. It consists of a strip waveguide ring vertically coupled to a pair of buried channel waveguides. Fig.1(b) shows the top-down view of the fabricated device, where the output bus consists of an 180° bend with a 50  $\mu\text{m}$  bend radius to direct the output signal in the forward propagation direction. The ring and bus waveguide cores are composed of the compound glass  $\text{Ta}_2\text{O}_5/\text{SiO}_2$  [17:83] mol % chosen to give an index of 1.6532.  $\text{SiO}_2$  is used for the cladding and buffer layers. The device configuration is similar to Ref [4] except for the lower index waveguide cores for better input/output coupling and the

ring waveguide is over-etched to increase the Q factor of the resonator. Details of the fabrication can be found in Ref. [4]. All device parameters are depicted in the figure caption.

In the measurement setup, the sample was placed on a heater stage with a thermo-coupler on top of the sample to monitor the device temperature. The locations of two output resonant peaks  $\lambda_0$  were measured at each sampling temperature to determine the temperature dependence of the filter. Fig. 2 shows the measured filter TM responses of the microring resonator filter with  $R=19 \mu\text{m}$  at three sampled temperatures. As can be seen, the resonant peaks shifted to the longer wavelength side with temperature increase due to the positive value of  $d\text{n}/dT$  of  $\text{Ta}_2\text{O}_5/\text{SiO}_2$ . A linear dependence between  $\lambda_0$  and T was observed within the measured range and the measured resonance shift  $d\lambda_0/dT$  was  $0.01375 \text{ nm}^\circ\text{C}$ .

In order to compensate for the temperature dependence of the VCMRR add/drop filter, a material that has a negative value of  $d\text{n}/dT$  is needed in the composition of the filter. This can be accomplished with a polymer as the overlay [8]. To investigate the effectiveness of the proposed compensation method, a layer of co-polymer (PMMA-TFMA  $n=1.440$  at 1550 nm room temperature) was deposited onto the VCMRR filter. Except for  $h_r=1.0 \mu\text{m}$ ,  $h_g=0.7 \mu\text{m}$  and  $t=0.5 \mu\text{m}$ , the waveguide parameters of the VCMRR were the same as in Fig. 1. The index of the waveguide cores was increased to  $n=1.7852$  by an increase of the  $\text{Ta}_2\text{O}_5$  composition to mol. 30% to maintain the high index contrast for the resonator. The  $d\lambda_0/dT$  of three VCMRR add/drop filters with  $R=14$ ,  $19$ , and  $24 \mu\text{m}$  with FWHM 0.85, 0.59 and 0.39 nm, respectively, were measured. Again, the locations of two or more resonance peaks

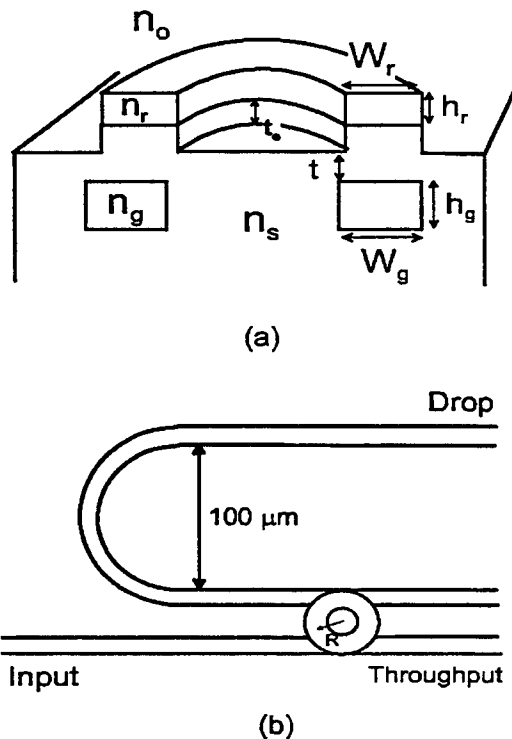


Fig. 1 Vertically coupled micro-ring resonator add/drop filter. (a) Cross sectional view. (b) Top-down view with  $W_r=1.5 \mu\text{m}$ ,  $W_g=1.5 \mu\text{m}$ ,  $h_r=1.5 \mu\text{m}$ ,  $h_g=0.7 \mu\text{m}$ ,  $t_e=0.3 \mu\text{m}$ ,  $t=0.4 \mu\text{m}$ ,  $n_r=n_g=1.6532$ ,  $n_s=1.4508$ , and  $n_o=1$ .

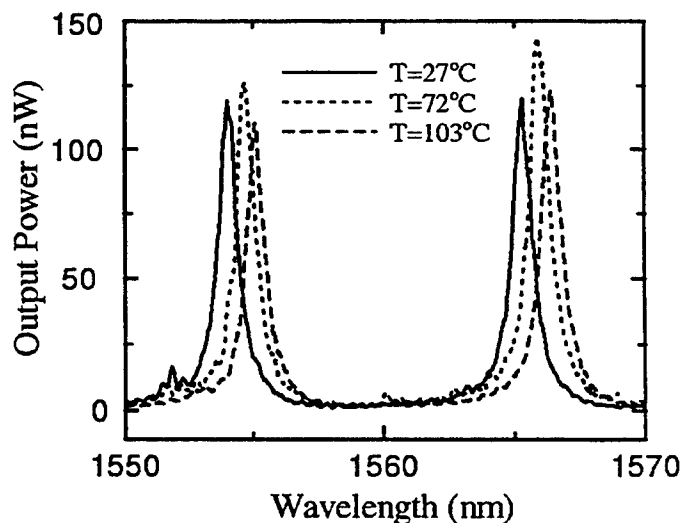


Fig. 2. Measured TM spectra of the air-clad micro-ring add/drop filter at three different sampled temperatures.

were traced at the sampled temperatures and Fig. 3 shows the nominal resonance peak shift  $\Delta\lambda_0$  as a function of temperature. The results show that in the low temperature region, the application of a polymer overlay has successfully reduced the temperature dependence  $d\lambda_0/dT$  to  $-0.0025 \text{ nm}^\circ\text{C}$ , approximately one fifth of the initial value. However, at temperature above  $55^\circ\text{C}$   $d\lambda_0/dT$  was increased to  $-0.030 \text{ nm}^\circ\text{C}$ . The large change of  $d\lambda_0/dT$  at around  $55^\circ\text{C}$  is due mainly to the low glass-transition temperature of the PMMA-TFMA mixture ( $T_g = 80^\circ\text{C}$ ). Since the transition process of the polymer can occur before the temperature reaches the glass-transition, as a result the value of  $dn/dT$  of the polymer changes as  $T$  approaches  $T_g$ . In general, polymer with a higher  $T_g$  value will therefore be needed for temperature independent operation at above  $55^\circ\text{C}$ .

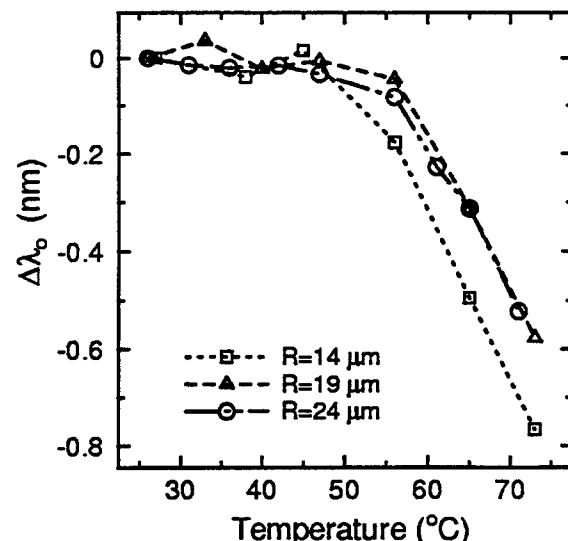


Fig. 3 Plot of the resonant wavelength shifts as a function of temperature for the PMMA-TFMA covered VCMRR filter. The waveguide parameters are the same as in Figure 1, except for  $h_r=1.0 \mu\text{m}$ ,  $h_g=0.5 \mu\text{m}$ ,  $t_e=0 \mu\text{m}$ ,  $t=0.5 \mu\text{m}$ , and  $n_r=n_g=1.7852$ .

- [1] S. Suzuki, K. Shuto, and Y. Hibino, IEEE Photon. Tech. Lett. 4, 1256 (1992).
- [2] D. Rafizadeh, J. P. Zhang, S. C. Hagness, A. Taflove, K. A. Stair, S. T. Ho, and R. C. Tiberio, Opt. Lett. 22, 1244 (1997).
- [3] B. E. Little, J. Foresi, H. A. Haus, E. P. Ippen, and W. Greene, and S. T. Chu, IEEE Photon. Tech. Lett. 10 549 (1998).
- [4] B. E. Little, S. T. Chu, W. Pan, D. Ripin, T. Kaneko, Y. Kokubun, E. Ippen, IEEE Photon. Tech. Lett. 11, 215 (1999).
- [5] S. T. Chu, W. Pan, S. Sato, T. Kaneko, Y. Kokubun, and B. E. Little, "A n 8 channel add/drop filter using vertically coupled microring resonators over a cross grid," *to be published in IEEE Photon. Tech. Lett., June 1999.*
- [6] S. T. Chu, W. Pan, S. Sato, T. Kaneko, Y. Kokubun, and B. E. Little, "Wavelength trimming of a microring resonator filters by means of a UV sensitive polymer overlay", *to be published in IEEE Photon. Tech. Lett., June 1999.*
- [7] D. Rafizadeh, J. P. Zhang, S. C. Hagness, A. Taflove, K. A. Stair, and S. T. Ho, LEOS 10<sup>th</sup> annual meeting, paper WT2, 1997.
- [8] Y. Kokubun, S. Yoneda, and S. Matsuura, IEICE Trans. Electron. E-81-C, 1187 (1998).



**Integrated Photonics Research**

# **VCSEL Modeling**

**Monday, July 19, 1999**

**K. Alan Shore, University of Wales, UK**  
Presider

**RMG**  
**2:00pm–3:15pm**  
Anacapa

## Quantum Dots for GaAs-Based Long Wavelength Edge-Emitting and Vertical-Cavity Surface-Emitting Lasers

D.G. Deppe, D.L. Huffaker, Z. Zou, and S. Csutak

Microelectronics Research Center  
Department of Electrical and Computer Engineering  
The University of Texas at Austin, Austin, Texas 78712  
Ph: (512) 471-4960, Fax: (512) 471-8575, E-mail: deppe@mail.utexas.edu

InGaAs/GaAs quantum dots (QDs) are very promising for extending the lasing wavelength of GaAs-based devices, including vertical-cavity surface-emitting lasers (VCSELs), edge-emitting lasers, and microcavity light emitting diodes, into the 1.0  $\mu\text{m}$  to 1.3  $\mu\text{m}$  wavelength range. Initial demonstrations already show that room temperature lasing at these longer wavelengths is possible [1]-[3], and that spontaneous lifetime control is possible with small apertures [4]. Problems to contend with, however, are that the optical gain in a single layer ensemble of QDs is much less than for a single quantum well, in large part due to inhomogeneous broadening, and that nonradiative recombination is at present greater in the QDs. The results of these effects are that room temperature operation can suffer from an increased threshold and decreased efficiency. At the same time, an advantage of the QDs for very small oxide apertures is in improving the emission efficiency, due to the electron-hole confinement at small dimensions.

In this talk we will present both modeling work and experimental data characterizing the QD light emission in lasers and microcavity light emitters. The QD electronic density of states is well modeled by a 2-dimensional harmonic oscillator potential. Assuming that the energy levels have Gaussian widths due to the inhomogeneous broadening caused by the different dot sizes, and that a spin degeneracy of two exists for each energy level, the functional form can be given by

$$\rho_{red}(\hbar\omega) = 2\sqrt{\frac{\ln(2)}{\pi}} \frac{n_{QD}}{(\hbar\Delta\omega/2)} \sum_{m=0}^{\infty} (m+1) \exp\left\{-\ln(2)\frac{[\omega - (\omega_g + m\omega_o)]^2}{(\Delta\omega/2)^2}\right\}. \quad (1)$$

In (1)  $m$  is an integer characterizing each energy level of a 2-dimensional harmonic oscillator,  $\omega$  is the transition frequency,  $\hbar\omega_o$  is the energy level separation where  $\hbar$  is Planck's constant divided by  $2\pi$ ,  $\hbar\omega_g$  is the transition energy for the ground state emission,  $\Delta\omega$  is the full-width at half-maximum, and  $n_{QD}$  is the quantum dot density per unit area.

For VCSELs, this density of states can be used to predict the required cavity reflectivity needed for threshold under the typical assumption that the round trip gain must balance the cavity loss. The threshold condition for ground state lasing can then be expressed as

$$\ln\left(\frac{1}{\sqrt{R_T R_B}}\right) = \sqrt{\frac{\ln(2)}{\pi}} \frac{8\pi^2 c^2}{n^2 \omega_g^2 \tau_{sp} \Delta\omega} n_{QD}, \quad (2)$$

where  $c/n$  is the speed of light in the cavity,  $\tau_{sp}$  is the spontaneous lifetime of a QD exciton, and  $R_T$  is the top (upper) mirror reflectivity and  $R_B$  is the bottom mirror reflectivity. We have studied QD active layers with  $n_{QD} \approx 5 \times 10^{10} \text{ cm}^{-2}$  per layer,  $\omega_o = 1.76 \times 10^{15} \text{ rad/sec}$ ,  $\hbar\Delta\omega \approx 76 \text{ meV}$ , and  $\tau_{sp}$  is measured under non-resonant excitation at low temperature to be  $\sim 800 \text{ psec}$ . For a three-stack QD active layer, and assuming  $\tau_{sp} = 800 \text{ psec}$  and  $c/n = 9 \times 10^7 \text{ m/sec}$ , we find that  $\sqrt{R_T R_B} \geq 0.9983$  must be achieved for lasing threshold. However, it's not clear that the nonresonant excitation gives the true Einstein A coefficient, as some evidence exists that resonant excitation can give shorter lifetimes due to superradiance [5]. For this reason we have compared experimental cavity Q's in oxide-confined VCSELs with calculated values to extract reflectivities and compare these with Eq. (2). The calculated mirror reflectivity for our VCSELs are  $\sqrt{R_T R_B} = 0.99978$ , well above that needed from the estimate of the maximum QD gain assuming  $\tau_{sp} = 800 \text{ psec}$ . However, the calculated spectral full-width at half-maximum is  $0.2 \text{ \AA}$ , and gives an extremely high quality factor for the cavity of  $Q = 50,000$ . We estimate our experimental linewidths to be  $\sim 2.9 \text{ \AA}$  for a  $10 \mu\text{m}$  aperture, and the resulting  $Q$  is  $\sim 3660$ . If we approximate that the experimental effective cavity length is the same as that of the idealized cavity, the experimental reflectivity products can be estimated to be  $\sqrt{R_T R_B} \approx 0.9970$ , and we must have  $\tau_{sp} \approx 400 \text{ psec}$  for threshold. This range is within what Kurtenbach et al. measured for resonantly pumped InP/In<sub>0.48</sub>Ga<sub>0.52</sub>P QDs [5], and considerably shorter than our own measurements for

nonresonant pumping. Calculations will also be compared with experimental results on single layer  $1.3 \mu\text{m}$  QD edge-emitting lasers.

For very small apertures, lifetime control (the Purcell effect) of the spontaneous emission becomes possible, an effect we have measured using the QDs [4], [6]. For an aperture size of  $1 \mu\text{m}$  diameter we find that the spontaneous emission rate is enhanced by a factor of 2.3 on resonance with the cavity mode. Modulation in the spontaneous emission rate versus wavelength corresponds to different transverse modes of the dielectric aperture for different aperture sizes. The spontaneous emission is also sensitive to the spatial position of the QD within an aperture, and simple approximation of Gaussian modes allows predictions of the true enhancement for QDs placed at the aperture center. We will present an analytical model of the spontaneous rate enhancement, and that predicts spatial hole burning effects.

### *References*

- [1] D.L. Huffaker, H. Deng, and D.G. Deppe, "1.15  $\mu\text{m}$  Wavelength Oxide-Confined Quantum Dot Vertical-Cavity Surface-Emitting Laser," *IEEE Phot. Tech. Lett.* 10, 185-187 (February, 1998).
- [2] D.L. Huffaker, G. Park, Z. Zou, O.B. Shchekin, and D.G. Deppe, "1.3  $\mu\text{m}$  Room Temperature GaAs-Based Quantum Dot Laser," *Appl. Phys. Lett.* 73, 2564-2565 (2 November, 1998).
- [3] D.G. Deppe, D.L. Huffaker, S. Csutak, Z. Zou, G. Park, and O.B. Shchekin, "Spontaneous Emission and Threshold Characteristics of 1.3  $\mu\text{m}$  InGaAs/GaAs Quantum Dot GaAs-Based Lasers," *IEEE J. Quant. Electron.*, submitted for publication.
- [4] L.A. Graham, D.L. Huffaker, and D.G. Deppe, "Spontaneous Lifetime Control in a Native-Oxide-Apertured-Microcavity," *Appl. Phys. Lett.* 74, (26 April, 1999).
- [5] A. Kurtenbach, W.W. Ruhle, and K. Eberl, "Intrinsic Radiative Lifetimes of InP/InGaP Quantum Dots," *Solid State Comm.* 96, 265 (1995).
- [6] L.A. Graham, D.L. Huffaker, S.M. Cuzak, Q. Deng, and D.G. Deppe, "Spontaneous Lifetime Control For Quantum Dot Light Emitters in Dielectrically-Apertured Fabry-Perot Microcavities," *J. Appl. Phys.*, (15 March, 1999).

## Modeling and Simulation of Transverse Mode Dynamics of VCSELs

C. Z. Ning and P.M. Goorjian

NASA Ames Research Center, M/S N229-1, Moffett Field, CA 94035

Tel.: (650) 604 3983, Fax: (650) 604 5244; Email: cning@nas.nasa.gov

Spatial profiles and dynamical evolution of transverse modes in VCSELs are important for many applications including optical storage and fiber couplings. The issue of space-time dynamics in VCSELs is also important because VCSELs offer a unique system with a large Fresnel number which allows more complex spatial pattern to develop. In the theoretical modeling and numerical simulation of large-area VCSELs, there are two major issues to resolve. The first is how to incorporate gain and index model into simulation and the second is how to incorporate gain and index guiding profiles and how to solve the transverse modes which are very often dynamically evolving.

In our modeling, the first issue is resolved by parameterizing optical gain and refractive index as functions of wavelength and carrier density [1]. Such parameterized gain and refractive index allow us to deal with arbitrary nonlinear gain and index profiles and any number of transverse modes in any location of gain spectra. This procedure leads to the introduction of a set of effective partial differential equations for large-area VCSELs, called effective Bloch equations (EBEs). To these EBEs, we then add the gain and index guiding profiles that are determined by laser design, for example, by oxidation profiles. These EBEs with the appropriate guiding profiles are then directly solved in space and time domain using the finite-difference method. The solution of these equations provide time evolution of arbitrary transverse mode profiles in a natural way without assuming type and number of transverse modes *a priori*.

Using the above approach, we have studied transverse mode dynamics of VCSELs of different shapes (for example, ring and disk shapes) and sizes with different gain and/or index guidings [2]. Simulation is carried out for devices with and without index guiding at different pumping levels. We show that index guided VCSELs involve more transverse modes

than purely gain-guided devices at the same pumping level. Both time-resolved and time-averaged near field patterns over different time scales are investigated. Complicated spatial and temporal dynamical behaviors occur at higher pumping levels that include azimuthal rotating waves and intensity oscillations due to dynamical competition between modes of the same order and those of different orders. Finally the influence of transverse mode dynamics on modulation speed is also investigated by adding a time-periodic component to the pumping current for both cases with and without index guidings.

### References

1. C.Z. Ning, R.A. Indik, J.V. Moloney, "Effective Bloch equations for semiconductor lasers and amplifiers", IEEE J. Quant. Electr., **33**, pp. 1543-1550, (1997)
2. C.Z. Ning and P.M. Goorjian, "Microscopic Modeling and Simulation of Transverse Mode Dynamics of Vertical-Cavity Surface-Emitting Lasers", to appear in Special Issue on Spatial and Polarization Dynamics of Semiconductor Lasers, J. Opt. Soc. Am., B (1999).

## Split-Step Time-Domain Dynamic Modeling of Complex-Coupled Distributed-Feedback Laser Diodes

Byoung-Sung Kim and Youngchul Chung

Dept. of Electronic Communications Eng., Kwangwoon University, Seoul, Korea 139-701  
Tel) +82-2-940-5138 Fax) +82-2-941-7855 E-mail) bskim@explore.kwangwoon.ac.kr

**Abstract:** Complex-coupled distributed-feedback laser diodes are modeled by novel split-step time-domain model, which is shown to be much more accurate and efficient than conventional methods.

The large-signal time-domain dynamic model has been used in analyzing the dynamic characteristics and the internal properties of the photonic devices, such as DFB/DBR laser diodes. The dynamic model is based on the time-dependent coupled-wave equations and photon-carrier rate equation. The finite difference approximation has been usually used to solve the time-dependent coupled-wave equations numerically [1,2]. But, the conventional methods have the inherent excess error resulted from the non-power conserving discretization.

In this paper, a novel method to improve the accuracy and efficiency is proposed, in which the time-dependent coupled-wave equations are implemented using split-step algorithm. It is demonstrated through the analysis of complex-coupled distributed-feedback laser diodes that this method is much more accurate, efficient, and stable compared with the conventional methods.

The electrical fields in the waveguide can be divided into the forward wave and reverse wave by the propagating direction, and they are governed by the following time-dependent coupled-wave equations:

$$\frac{1}{c_g} \frac{\partial F(z,t)}{\partial t} + \frac{\partial F(z,t)}{\partial z} = (G - i\delta)F(z,t) + i(\kappa_i + i\kappa_g)R(z,t) + S_f \quad (1a)$$

$$\frac{1}{c_g} \frac{\partial R(z,t)}{\partial t} - \frac{\partial R(z,t)}{\partial z} = (G - i\delta)R(z,t) + i(\kappa_i^* - i\kappa_g^*)F(z,t) + S_r \quad (1b)$$

where,  $F(z,t)$  and  $R(z,t)$  represent the forward and reverse waves propagating along the longitudinal direction, respectively.  $c_g$  is the group velocity, which is assumed to be constant over the frequencies of interest,  $\delta$  is the detuning factor which means how much the operating wavelength is deviated from the Bragg condition, and  $G$  is the field gain including the waveguide loss. The spontaneous noises coupled into the forward and reverse fields are given as  $S_f$  and  $S_r$ , respectively.  $\kappa_i$  and  $\kappa_g$  are index- and gain-coupling coefficients respectively, and can be written as [3]

$$\kappa_i = \kappa_{i,0} - Q\alpha_m \Delta N \frac{g_N}{2(1+\varepsilon P)} \quad (2a)$$

$$\kappa_g = \kappa_{g,0} + Q\Delta N \frac{g_N}{2(1+\varepsilon P)} \quad (2b)$$

here,  $\kappa_{i,0}$  and  $\kappa_{g,0}$  are index- and gain-coupling coefficients near the threshold.  $\alpha_m$  is the material linewidth enhancement factor,  $g_N$  is the differential gain, and  $\Delta N$  is the change of carrier density.  $Q$  is the carrier scattering parameter, and has the value of 0 ~ 1 depending on details of the grating structure.

The time-dependent coupled-wave equations can be numerically solved by dividing the device into a number of small subsections with equal length of  $\Delta z (= c_g \Delta t)$ , as shown in Figure 1, and adopting a split-step algorithm [4]. That is, the time-dependent coupled-wave equations

are solved with two split steps. As the first step, the numerical solution of the partial differential equations related to the gain and detuning factors is given by

$$\begin{bmatrix} F(z + \Delta z, t) \\ R(z, t) \end{bmatrix} = \begin{bmatrix} \exp\{(G - i\delta)\Delta z\} & 0 \\ 0 & \exp\{(G - i\delta)\Delta z\} \end{bmatrix} \begin{bmatrix} F(z, t - \Delta t) \\ R(z + \Delta z, t - \Delta t) \end{bmatrix} \quad (3)$$

When the field gain is 0, the absolute value of the determinant of a  $2 \times 2$  matrix in equation (3) becomes equal to 1. This means that a  $2 \times 2$  matrix in equation (3) maintains the power-conservation condition. And the numerical solution of the partial differential equations relating to the backward couplings can be solved by diagonalizing the array of coupling elements contrary to the Crank-Nicholson scheme in [4]. Its processes are finding its eigenvalues, taking its exponential, and transforming it into a proper matrix. Then, the numerical solution can be written as

$$\begin{bmatrix} F(z + \Delta z, t) \\ R(z, t) \end{bmatrix} = \begin{bmatrix} \cos(\gamma\Delta z) & i\sin(\gamma\Delta z) \\ i\sin(\gamma\Delta z) & \cos(\gamma\Delta z) \end{bmatrix} \begin{bmatrix} F(z, t) \\ R(z + \Delta z, t) \end{bmatrix} \quad (4)$$

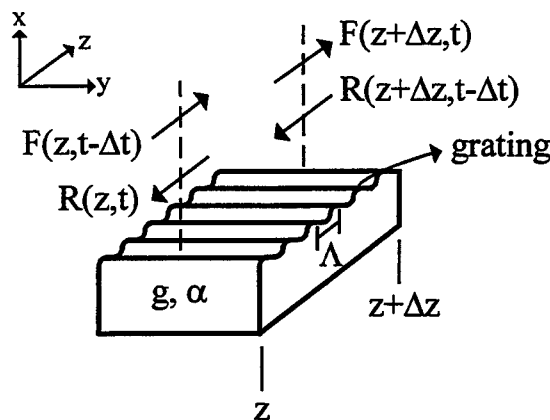
where  $\gamma = [(\kappa_i + i\kappa_g)(\kappa_i^* - i\kappa_g^*)]^{1/2}$ . It can be easily shown that the equation (4) is unconditionally stable algorithm.

Figure 2 shows the comparison of optical output powers calculated by conventional methods [1,2] and the proposed method. The considered device is the complex-coupled DFB laser diode. The device parameters are as follows: longitudinal length 600  $\mu\text{m}$ , differential gain  $2.5 \times 10^{-16} \text{ cm}^2$ , confinement factor 0.3, waveguide width 2  $\mu\text{m}$ , thickness of the active layer 0.2  $\mu\text{m}$ , transparency carrier density  $1.8 \times 10^{18} \text{ cm}^{-3}$ , linewidth enhancement factor 5, waveguide loss 40  $\text{cm}^{-1}$ , group refractive index 4, carrier lifetime 10 ns, and gain saturation coefficient  $3 \times 10^{-17} \text{ cm}^3$ . The index- and gain-coupling coefficients close to the threshold are  $\pm 30 \text{ cm}^{-1}$  and  $20 \text{ cm}^{-1}$ . The injection current into gain region is 80 mA. The spontaneous emission noises are generated from a Gaussian distributed random number generator. After the lasing is stabilized, the optical output powers from a facet are recorded neglecting the spontaneous emission noise. As shown in Figure 2, the proposed method shows the stability independent of the number of subsections, while the conventional methods have the large dependence on the number of subsections.

Figure 3 compares the AM responses of in- and anti-phase complex-coupled DFB laser diodes, calculated by the proposed method. It can be seen that the bandwidth of an anti-phase complex-coupled DFB laser diode is wider than that of an in-phase device. In an anti-phase complex-coupled DFB laser diode, since the coupling coefficient increases with the carrier injection, the threshold current decreases and then the photon density in the cavity increases until the gain is saturated. The relaxation oscillation frequency, thus, increases. On the other hand, an in-phase complex-coupled DFB laser diode has the decreased coupling coefficient with the carrier injection.

In summary, complex-coupled DFB laser diodes are modeled by novel split-step time-domain model, which is demonstrated to be much more accurate and efficient than conventional methods. And it is shown that the anti-phase complex-coupled DFB laser diode has the wider bandwidth than the in-phase device.

- [1] L. M. Zhang, S. F. Yu, M. C. Nowell, D. D. Marcenac, J. E. Carroll, and R. G. S. Plumb, *IEEE J. Quantum Electron.*, vol. 30, pp. 1389-1395, 1994.
- [2] B. S. Kim, J. K. Kim, Y. Chung, and S. H. Kim, *IEEE Photon. Tech. Lett.*, vol. 10, pp. 39-41, 1998.
- [3] L. Olofsson and T. G. Brown, *IEEE J. Quantum Electron.*, vol. 28, pp. 1450-1458, 1992.
- [4] B. S. Kim and Y. Chung, *Electron. Lett.*, vol. 35, pp. 84-85., 1999.



**Fig. 1.** Schematic view of a subsection in corrugated waveguide

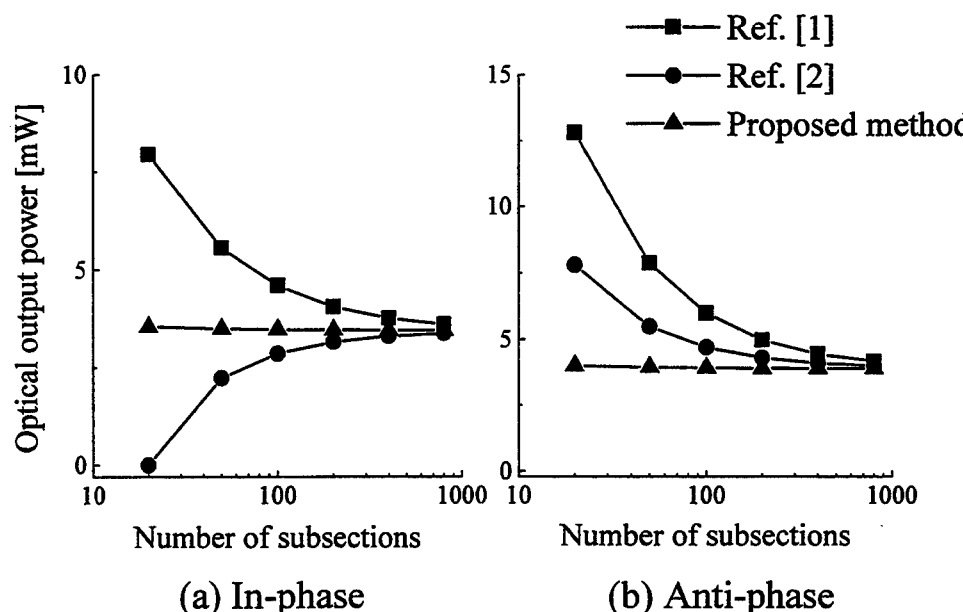


**Fig. 2.** Comparison of optical output powers between the conventional methods [1,2] and proposed method, under same conditions. (a) In-phase complex coupling:  $\kappa_{i,0} = 30 \text{ cm}^{-1}$  and  $\kappa_{g,0} = 20 \text{ cm}^{-1}$ . (b) Anti-phase complex coupling:  $\kappa_{i,0} = -30 \text{ cm}^{-1}$  and  $\kappa_{g,0} = 20 \text{ cm}^{-1}$ .

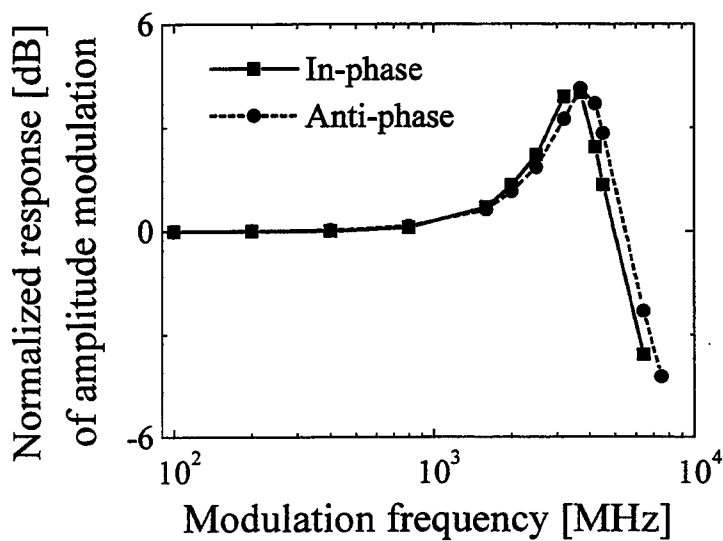


**Fig. 3.** AM(amplitude modulation responses of complex-coupled DFB laser diodes.



**Integrated Photonics Research**

# **Poster Session**

**Monday, July 19, 1999**

**RMH**

**3:30pm–5:30pm**

**Grand Ballroom Foyer**

## Local Normal Mode Model for PHASAR-based WDM devices

Michael Rivera

Corning Incorporated, SP-TD-01-2, Corning, NY 14831, USA ,Tel: 1(607) 974-5069/ Fax: 1(607)974-3405

### **Introduction:**

Wavelength multiplexers and demultiplexers based on optical phased arrays are devices that have great potential for deployment in the photonics industry. Unfortunately, efforts in developing silica-based PHASAR devices can meet with processing issues that contribute to non-adjacent channel crosstalk. This crosstalk is one of the fundamental limitations to the industrial specifications required for commercial deployment.

Current problems focus on the deformation of the silica-based step-index waveguides after a protective silica overlay is placed on the etched channels. A diffusion process takes place that contributes to the deformation, thus affecting the array's physical and material parameters. The problem thus involves an array of waveguides with arbitrary index and physical parameters that vary longitudinally.

For this paper, a propagation model is developed using the local normal modes of the non-varying sections of the array to qualitatively understand the effects of process variations in the array. Each waveguide will be individually characterized using a model for a one-dimensional diffused index distribution. Approximations to these waveguides are introduced to gain insight into the problem. Some simple results will be shown to demonstrate the robustness of the model and the physical behavior of the waveguide array. Finally, some conclusions are drawn from the observed behavior. The working theory for PHASAR devices can be found in Smit [1] and van Dam [2]. A schematic of a phasar is illustrated in Figure 1.

### **Description of the Model:**

To model waveguides of different lengths an idealized slab model for the waveguides with longitudinally invariant, but individually characterized waveguide parameters is used as a first approximation. Also, the waveguides are assumed to be straight, thus departing from the usual curved design that is used. The physical layout of this model is shown in Figure 2.

The model based on Local Normal Mode (LNM) Theory uses the local modes of the waveguide array at each  $z$ -invariant stage, i.e., where the array does not change longitudinally, and the overlap of these modes with the incident field  $\phi(x)$  is used to determine the propagated field in each section. Specifically, the modes can be found by using any one dimensional mode solver that will determine both the propagation constants,  $\beta_i$ , and modal fields,  $f_i(x)$ 's—the properly normalized and orthogonalized set of complete guiding modes. The overlap of the incident field with the modes for the array is accomplished by determining the complex amplitude coefficients  $a_i$ 's that will best reproduce the coupled field at the incident plane [3]. After propagation through a distance  $z_i$  for a non-varying section of the array the individual fields are added together to determine the total propagated field, this total field becomes the incident field for the next  $z$ -invariant section. This is illustrated in the following expression:

$$\tilde{\phi}_-(^{(M)})(x) = \sum_i a_i^{(M)} f_i^{(M)}(x) \exp(-j\beta_i^{(M)} z_i).$$

Since the waveguides are of different lengths we must determine the modes of each new section and propagate the field to the next  $z$ -invariant section. The distance  $z_i$  is equal to  $L_0$  or  $\Delta L$ . Where  $j = \sqrt{-1}$  and we have defined  $\tilde{\phi}_-(^{(M)})(x)$  as the field after propagating through  $M$  waveguides in the array and just before coupling to the remaining  $(M-1)$  waveguides. The remaining parameters with superscript  $(M)$ , namely  $a_i$  and  $f_i$ , pertain to the array of  $M$  waveguides. Here  $N \geq M$  and the field is not normalized. The output field for the  $K$ th individual waveguide  $\phi_K(x)$  is found by subtracting the remaining field from the incident field. Hence, the total output field is given by:

$$\phi_{total}(x) = \sum_{M=2}^N \left\{ \tilde{\phi}_-(^{(M)})(x) - \tilde{\phi}_+^{(M-1)}(x) \right\} + \tilde{\phi}_-^{(1)}(x) = \sum_{K=1}^N \phi_K(x).$$

Knowing the total output field allows us to finally determine the diffracted (Fraunhofer) pattern at the other end of the second Free Propagation Region (FPR). The diffracted field is as follows [4]:

$$\Phi(x) = \frac{\exp(jkz_{12})}{j\lambda z_{12}} \exp\left[\frac{j\pi(x^2 + y^2)}{\lambda z_{12}}\right] \Im \left\{ \phi_{total}(x) \right\} \Big|_{\xi=x/\lambda z_{12}}$$

where  $\Phi(x)$  is the diffracted field and  $\Im \{ \cdot \}$  is the one dimensional Fourier Transform of the quantity in the curly brackets evaluated at the spatial frequency coordinate  $\xi = x/\lambda z_{12}$ .

The results of a one dimensional diffusion model [5,6] are incorporated to produce the desired dimensions given the diffusion characteristics of each individual waveguide. This model follows the one dimensional diffusion equation,  $\partial C/\partial t = D \partial^2 C/\partial x^2$ , where  $D$  is a constant diffusion coefficient. If we assume that the index of the medium is proportional to the dopant concentration and the substrate index  $n_s$  is the base index of the host medium, we can obtain a final expression for the index of a diffused slab waveguide.

$$n(x) = n_s + \frac{\Delta n}{2} \left\{ \operatorname{erf} \left[ \frac{h+x}{2\sqrt{D\tau}} \right] + \operatorname{erf} \left[ \frac{h-x}{2\sqrt{D\tau}} \right] \right\},$$

Where  $\operatorname{erf}$  is notation for the Error Function,  $h$  is the width of the waveguide and  $\tau$  is a characteristic diffusion time for the particular waveguide of interest. The peak index is  $n_f = n_s + \Delta n$  for  $\tau=0$ , a waveguide with no diffusion.

### Results:

Examples are given to illustrate the capabilities and robustness of this model. We will use a small number of waveguides but this will be enough to illustrate the principles behind the physics of phased arrays and help us obtain a qualitative picture of the effects of process variability. The parameters used are  $\lambda_c = 1.55 \mu\text{m}$ ,  $n_s = 1.454$ ,  $D\tau = 0.01$ ,  $\Delta\lambda = 0.01 \mu\text{m}$ ,  $R = 4300.00 \mu\text{m}$ ,  $L_0 = N' 2\pi/\beta_{\text{eff}}$ ,  $\Delta L = n' 2\pi/\beta_{\text{eff}}$ ,  $N' = 7000$ ,  $n' = 11$ ,  $w_{\text{ideal}} = 6 \mu\text{m}$  and  $\Delta s = 18 \mu\text{m}$ . The initial field profile is gaussian of arbitrary height  $A$ , proportional to the square root of the total power, and width  $\sigma = 100.0 \mu\text{m}$ . Recall that this is qualitative model and does not represent all the features of a true phasar design. The discussion in reference [1] states that the number of waveguides involved will determine the free spectral range (FSR), the spectral window available around  $\lambda_c$  for the device, and the differential length  $\Delta L$  for each waveguide needed to separate the channels. Also, the channel spacing determines the dispersion, which is the spatial shift required at the image plane to separate the channels. These parameters are also critical in fixing the diffracted widths on the receiver plane. Hence, a true phasar design is not implemented here. With this in mind, a qualitative picture is shown of the output characteristics.

In example #1, the diffracted fields, i.e., the far fields, on the receiver waveguides for the ideal array case for channels  $\lambda_c$ ,  $\lambda_c \pm \Delta\lambda$  are shown in Figure 3(a). In example #2 we introduce a defective waveguide into the array ( $D\tau = 1.00$ ) to find the resulting output field at the image plane, Figure 3(b). With a defective waveguide the field at the image plane experiences a lateral shift and some increased noise which may account for an increased crosstalk in the designs. Recall that this a systematic error effectively introducing a phase delay at the output aperture, hence a shift in the far field pattern. We will see that these types of errors are just as much a factor on the lateral shift as on the resulting crosstalk.

In example #3 we altered the shapes of the waveguides in the phased array arbitrarily ( $D\tau = 0.01, 0.25$  and  $0.50$  for 2, 4, and 4 waveguides, respectively) and observed the resulting field patterns at image plane. The field at the output is essentially somewhat unpredictable and erratic. The resulting gaussian envelope that was characteristic of the ideal waveguide array output is would be no longer distinguishable. In Figure 3(c) an increased noise floor is apparent thus suggesting a link with the adjacent and non-adjacent channel crosstalk and the waveguide characteristics. This approach assists in understanding which parameters, whether index or length and/or width of the waveguide, are most likely to introduce increased crosstalk. In addition, the shift in the field output is due to erratic but systematic errors on the phase of the output fields of the individual waveguides.

For the last example (Figure 4) the number of waveguides in the array was increased to 15 and 19 waveguides, respectively; the result is a decreased noise floor. This is due to the fact that the entire gaussian input field was resolved by the array. It is well known that a wider gaussian input and a larger number of waveguides would also reduce the crosstalk considerably.

### Conclusions:

A qualitative LNM model for a phased array of waveguides, an essential component for WDM devices, is developed to understand impact of process variability on the output field and its corresponding far field pattern on the image plane of the receiver waveguides. The results show deviations from ideal behavior for a small number (11) waveguides. Specifically, if there is only one defective waveguide there is a lateral shift in the image plane and an increase in the noise floor. With several defective waveguides a lateral shift also results and there is a larger increase in the noise floor. For ideal arrays of 11, 15 and 19 waveguides a corresponding decrease in the noise floor results with increase in the number of waveguides. This is due to the fact that the entire extent of the gaussian input completely captured by the array. The types of errors encountered here were systematic so that the results are of a cumulative nature rather than from random errors. It may be inferred that the position (lateral shift) would not be affected greatly by random errors although the noise floor, and thus adjacent and non-adjacent channel crosstalk, can increase considerably.

### Acknowledgments:

I would like to thank James S. Sutherland of Corning Incorporated for providing answers to all of my questions in regard to modeling PHASARs.

### References:

- [1] Smit, M. K. and C. van Dam, "PHASAR-based WDM-devices: principles, design and applications", *IEEE Journal of Selected Topics in Quantum Electronics*, 2, June 1996, pp. 236-250.
- [2] van Dam, C., *InP-based polarisation independent wavelength demultiplexers*, Ph.D. Dissertation, Delft University of Technology, 1997.
- [3] Yariv, A., *Quantum Electronics*, Chapter 1, 3<sup>rd</sup> Edition, John Wiley and Sons, 1989.
- [4] Gaskill, J.D., *Linear Systems, Fourier Transforms, and Optics*, Chapter 10, Wiley, 1978.
- [5] Crank, J., *Mathematics of Diffusion*, Chapter 2, Oxford University Press, 1957.
- [6] Jost, W., *Diffusion*, Chapter 1, Sections IV-V, p-16-25, Revised Edition, Academic Press, 1960.

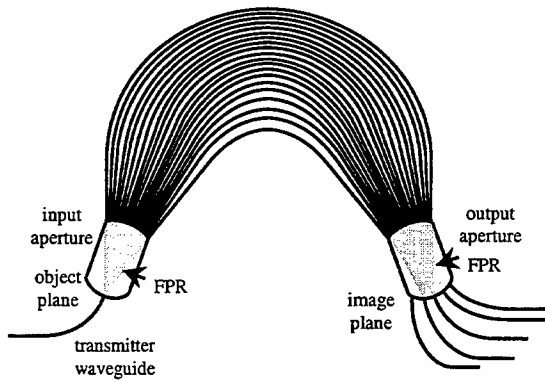


Fig. 1: Schematic of a phased array device.

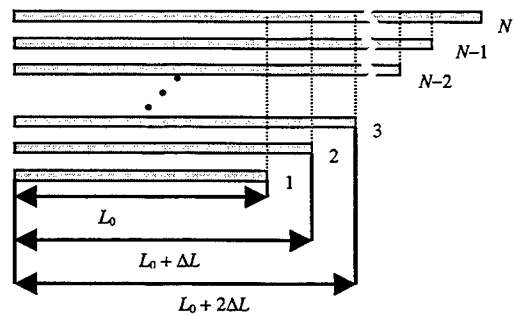


Fig. 2: Representation of a waveguide array.

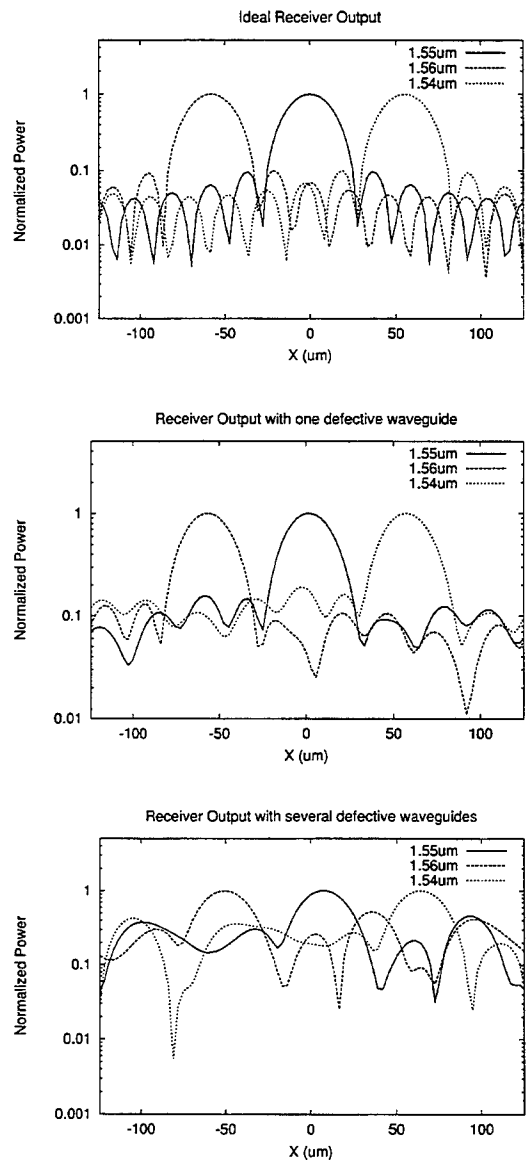


Fig 3. Receiver output for 11 waveguides. (a) ideal case, (b) one defective waveguide and (c) several defective waveguides.

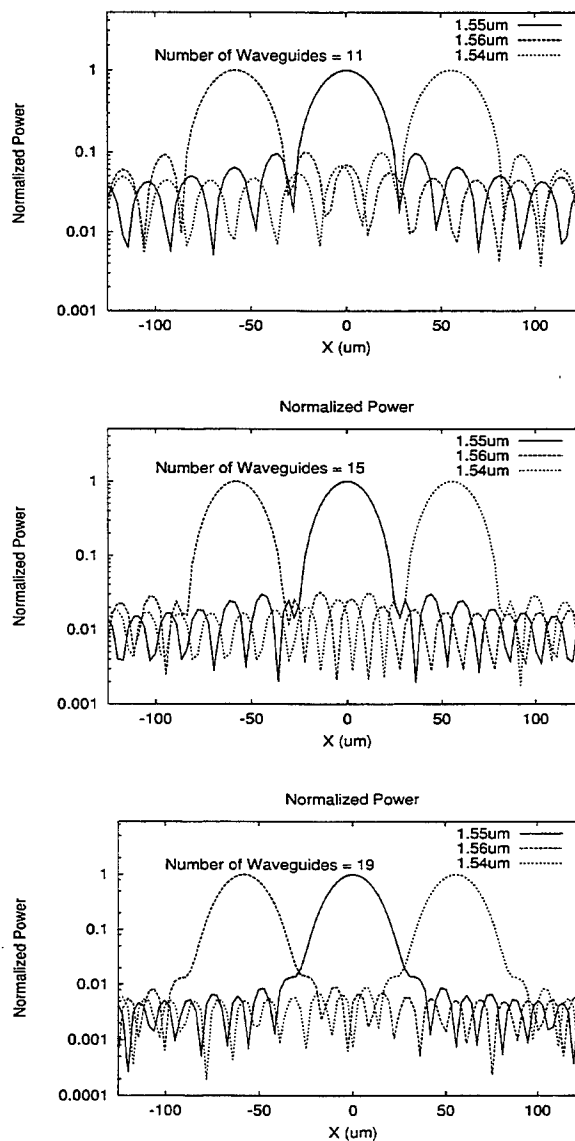


Fig 4. Receiver output for increasing waveguide number. (a) 11, (b) 15 and (c) 19 waveguides, respectively.

## Transverse Mode Dynamics of VCSELs Under Current Modulation

**Peter M. Goorjian**

NASA Ames Research Center, M.S. T27A-2, Moffett Field, CA 94035-1000  
Phone: (650) 604-5547, Fax: (650) 604-4377, Email: goorjian@nas.nasa.gov

**C. Z. Ning**

NASA Ames Research Center, M.S. T27A-1, Moffett Field, CA 94035-1000  
Phone: (650) 604-3983, Fax: (650) 604-3957, Email: cning@nas.nasa.gov

### 1. INTRODUCTION

In this paper, an approximation to the Maxwell-Semiconductor Bloch equations is used to model the transverse mode dynamics of vertical-cavity surface-emitting lasers (VCSELs), under current modulation. VCSELs, under current modulation, are important for many applications, such as optical interconnects and optical data storages. In many applications, high beam quality or high output powers or both are critical requirements. To help the design and optimization of VCSELs for such applications, it is essential to have a simulation model that includes the time evolution of the transverse space dependence of the beam.

Here, the transverse mode dynamics of VCSELs<sup>1-3</sup> are modeled by an approximation to the Maxwell-Semiconductor Bloch equations.<sup>4,5</sup> The time-evolution of the spatial profiles of the laser and carrier density is obtained by solving the coupled partial differential equations that govern their evolution by a finite-difference algorithm. The algorithm is fairly general; it can handle devices of any shape, which are either gain or index guided or both. Also there is no a priori assumption about the type or number of modes. The physical modeling includes the nonlinear carrier dependence of the optical gain and refractive index and dispersion effects on the gain and the refractive index are also included. The modeling of the optical susceptibility is based on first-principles and includes device details such as the quantum well structures, and also includes many-body effects. Temporal dynamics as fast as on a picosecond scale can be resolved. This bottom-up approach uses measured material parameters and quantum well structure parameters, with the number of free parameters minimized. In these simulations, the VCSELs are based on InGaAs/GaAs quantum well structures.

Earlier work<sup>1-3</sup> has calculated the transverse mode dynamics of VCSELs under steady currents. VCSELs have been studied under different pumping levels, and that had different active region shapes and sizes with and without index guiding. In this paper, the effects of transverse mode dynamics of VCSEL on modulation are investigated. Typically laser modulation is modeled by the single-mode rate equations. Our previous simulation results have shown interesting spatio-temporal dynamics at DC bias. Such dynamical behaviors will influence the modulation bandwidth and the beam quality under current modulation. Simulation results for different levels of DC and AC currents will be shown. The effects of index and gain guiding on the modulation will be studied in detail.

## 2. GOVERNING EQUATIONS

After assuming a fixed mode profile along the longitudinal direction in VC-SELS, the resulting Maxwell-Effective Bloch Equations model is given by the following equations.<sup>4,5</sup>

$$\frac{n_g}{c} \frac{\partial E}{\partial t} = \frac{i}{2K} \nabla_{\perp}^2 E - \kappa E + \frac{iK\Gamma}{2\epsilon_0\epsilon_b} P + \frac{i\delta n(x,y)}{n_b} KE \quad (1)$$

$$\frac{\partial N}{\partial t} = \nabla_{\perp} D_N \nabla_{\perp} N - \gamma_n N + \frac{\eta J(x,y,t)}{e} + \frac{L\Gamma}{2} \frac{i}{4\hbar} (P^* E - PE^*) \quad (2)$$

$$P = P_0 + P_1 \quad (3)$$

$$P_0 = \epsilon_0 \epsilon_b \chi_0(N) E \quad (4)$$

$$\frac{dP_1}{dt} = -\Gamma_1(N) P_1 + i(\omega_c - \omega_1(N)) P_1 - i\epsilon_0 \epsilon_b A_1(N) E \quad (5)$$

$$J(x,y,t) = J_{DC}(x,y) + J_{AC}(x,y) \sin(2\pi\nu t) \quad (6)$$

Here  $E$  is the complex laser field envelope amplitude,  $N$  is the total carrier density,  $P_0$  and  $P_1$  are the effective material polarization functions that have been constructed from microscopic theory,<sup>4</sup> and  $J(x,y,t)$  is the modulated pumping current density. Many-body effects and quantum well structure information<sup>6</sup> are contained in the density dependent coefficients  $\chi_0(N)$ , the effective background susceptibility, with real and imaginary parts  $\chi_{0,r}(N)$  and  $\chi_{0,i}(N)$  respectively;  $\Gamma_1(N)$ , the gain bandwidth,  $\omega_1(N)$ , the detuning, and  $A_1(N)$ , the strength of the Lorentzian oscillator.

## 3. COMPUTED RESULTS

Initial calculations were performed at low DC pumping levels. Figure 1 shows the modulation response MR, where  $MR = 10\log_{10}(P(\omega_o))/(P(0))$  for two values of the AC current amplitude. Here,  $P(\omega_o)$  and  $(P(0))$  are the total power at the modulation frequency  $\omega_o$  and at DC respectively. The results for the larger amplitude AC current show the effects on the light output at the resonant frequency when the total current drops close to the threshold current during a cycle of modulation. These effects on the time histories of the laser output are shown in Figs. 2 and 3 for the two cases. At the higher AC current amplitude, the light output is deformed away from a simple harmonic response to the driving current frequency.

## REFERENCES

1. P.M. Goorjian, and C.Z. Ning, "Computational Modeling of Vertical-Cavity Surface-Emitting Lasers," Paper Thc15, Nonlinear Optics Topical Meeting, Kauai, HI, August 9-14, 1998.

2. P.M. Goorjian, and C.Z. Ning, "Simulation of Transverse Modes in Vertical-Cavity Surface-Emitting Lasers," 1998 Annual Meeting of the Optical Society of America, Baltimore, MD, October 5-9, 1998.
3. P.M. Goorjian, and C.Z. Ning, "Transverse Mode Dynamics of VCSELs through Space-Time Simulation," Paper 3625-45, Integrated Optoelectronic Devices, Photonics West, 1999, (SPIE), San Jose, CA, January 23-29, 1999.
4. C.Z. Ning, R.A. Indik and J.V. Moloney, "Effective Bloch-equations for semiconductor lasers and amplifiers," IEEE J. Quan. Electron. **33**, 1543 (1997).
5. T. Rossler, R. A. Indik, G. K. Harkness, J. V. Moloney, C. Z. Ning, "Modeling the interplay of thermal effects and transverse mode behavior in native-oxide-confined vertical-cavity surface-emitting lasers," Phys. Rev. A, **58**, 3279(1998)
6. J.V. Moloney, R.A. Indik and C.Z. Ning, "Full space-time simulation for high brightness semiconductor lasers," IEEE Photon. Tech. Lett., **9**, 731(1997).

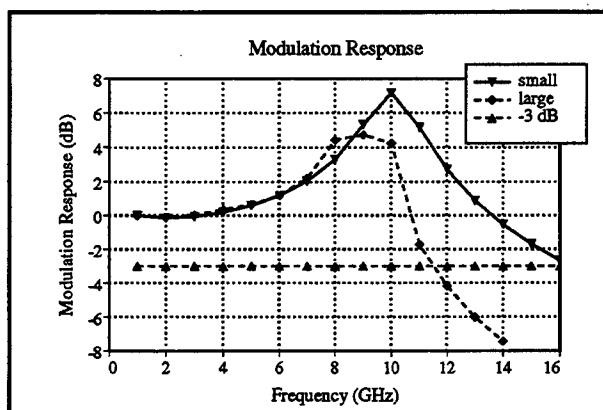


Fig. 1. Modulation Response MR

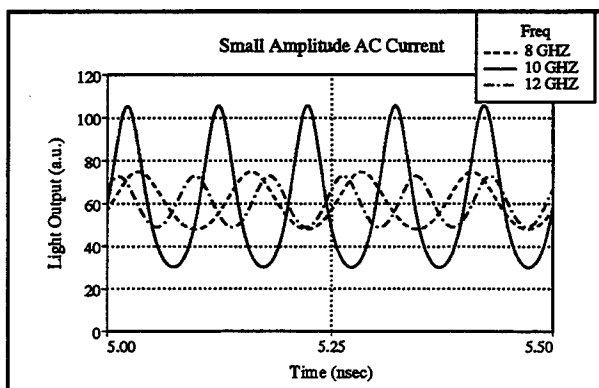


Fig. 2. Small AC Current Modulation

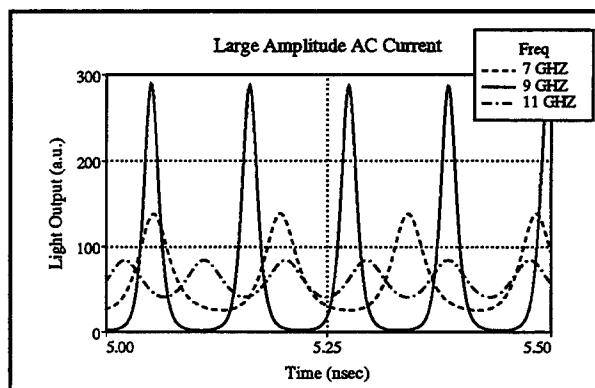


Fig. 3. Large AC Current Modulation

## Interdiffused InGaAsP/InP quantum well lasers

L. Zhan and E.Y.B. Pun

Department of Electronic Engineering, City University of Hong Kong, Kowloon, Hong Kong

K.S.Chan and H.P. Ho

Department of Physics and Materials Science, City University of Hong Kong, Kowloon,  
Hong Kong

Tel No: 27887814, Fax No: 27887830, E-mail: [apkschan@cityu.edu.hk](mailto:apkschan@cityu.edu.hk)

Several studies have reported that strained quantum well (QW) lasers show improvement in performances including lower threshold currents, higher differential gains, and wider frequency modulation bandwidths as compared to unstrained QW lasers. The InGaAsP/InP strained QWs have been widely studied for long wavelength applications. Apart from tuning the strain, interdiffusion of constituent atoms is a versatile technique to modify the bandstructure, and the diffusion rates depend on lattice distortion, impurities, defects and the process temperatures. Using this technique, the QW composition profiles, the confinement potentials and the device performances can be modified as a result of the diffusion of constituent atoms. Three categories of interdiffusion of InGaAsP/InP can occur for a quaternary material system: group-III only interdiffusion (Ga and Al), group-V only interdiffusion (As and P), and both group-III and group-V sublattices diffusion. Interdiffusion of InGaAsP/InP has been reported by Cao et al [1].

This paper presents a theoretical study of the effects of interdiffusion in an InGaAsP/InP single QW structure. The effects of interdiffusion on the strains, the splitting of the HH and LH subbands and the optical gains of the QW laser are calculated based on a multi-band k•p model including valance band-mixing. In InGaAsP/InP quantum well it is important to include the electrostatic potentials due to the spill over of carriers in the separate-confinement heterostructure layer. Owing to the change in carrier density as a result of the change in confinement potential, it is also important to consider the effects of a density-dependent optical dephasing time on the gain spectrum. In the present work the characteristics of the QW laser is analysed in details including the effects mentioned, in order to assess the application potential of the interdiffusion technique in photonic integration.

The group-III and group-V interdiffusion processes are modeled using the Fick's Law. The interdiffusion of the Al and Ga atoms is characterized by a diffusion length  $L_d^{III}$ ,

which is defined as  $L_d^{III} = \sqrt{D^{III}t}$ , where  $D^{III}$  is the diffusion coefficient of group-III atoms and  $t$  is the diffusion time. The interdiffusion of As and P atoms is characterized in much the same way by the diffusion length  $L_d^V$ . The structure to be modeled consists of an active layer of  $In_{0.98}Ga_{0.02}As_{0.48}P_{0.52}$  sandwiched between two thick  $In_{0.88}Ga_{0.12}As_{0.25}P_{0.75}$  barriers. The thickness of the active layer is 60Å and the barrier layer is 1000Å.

To calculate the electron and hole wave functions in QW, we use the effective mass approximation. The valence band mixing effects is included using the Luttinger-Kohn Hamiltonian. In this work, the effective Hamiltonian approach described in Chan [2] is used to solve the Luttinger-Kohn Hamiltonian to obtain the valence subband structure.

Owing to the small barrier heights in InGaAsP/InP QWs, the carriers in the QW can easily spill over to the barrier layer. Since electrons and holes have different effective masses, the hole and electron densities in the wells are not the same, and lead to an electrostatic deformation potential. The electrostatic deformation potential can be found by solving the Poisson's equation. The deformation potential has a strong effect on the number of carriers in the well and, as a result, can affect the optical dephasing time. In the present work, the density dependence of the optical dephasing time is obtained from the intrasubband scattering rates for the electrons and holes due to carrier-carrier and carrier-phonon interactions using fully dynamic random phase approximation [3]. In Fig 1, we show the confinement potentials with and without the deformation potential. With the deformation potential, electron confinement is increased and hole confinement is decreased. In Fig. 2, we show the peak gain as a function of the radiative current with and without the deformation potential. Including the deformation potential can decrease the peak gain by about 30% and therefore is important in determining the laser characteristics. Assuming a threshold gain of  $1200\text{cm}^{-1}$ , we can shift the peak gain wavelength by increasing  $L_d$  from 0Å to 20Å with an increase in the radiative current by 30%. The corresponding change in photon energy is about 100meV.

This work is supported by a Competitive Earmarked Research Grant, Research Grant Council, Hong Kong, and a Strategic Research Grant, City University of Hong Kong.

## REFERENCES

- [1] N Cao et al, Appl. Phys. Lett. **70**, 3419 (1997)
- [2] K.S.Chan, J. Phys. C **19**, L125 (1986)
- [3] S Seki et al, IEEE JST Quantum Electron. **1**, 264, (1996).

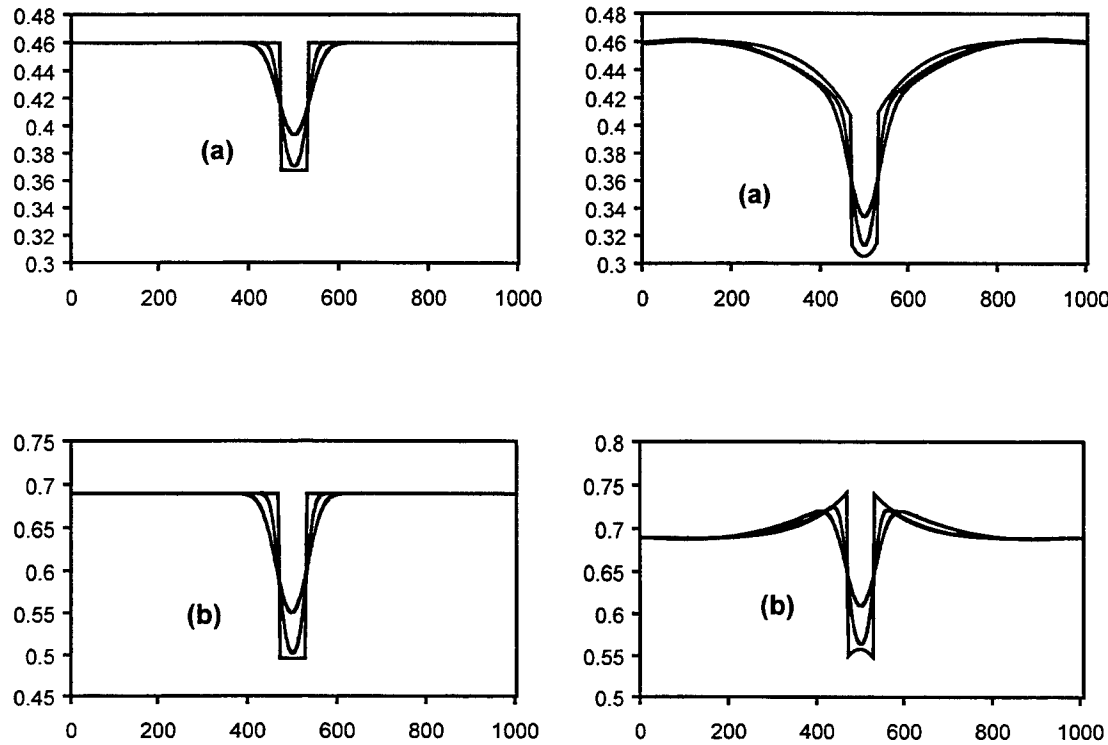


Fig 1. The confinement potentials for (a) electrons and (b) heavy holes; left figure: without electrostatic deformation; right figure: with electrostatic deformation. Both group III and V atoms are interdiffused with the same rates.  $L_d=0\text{\AA}$ ,  $10\text{\AA}$ ,  $20\text{\AA}$

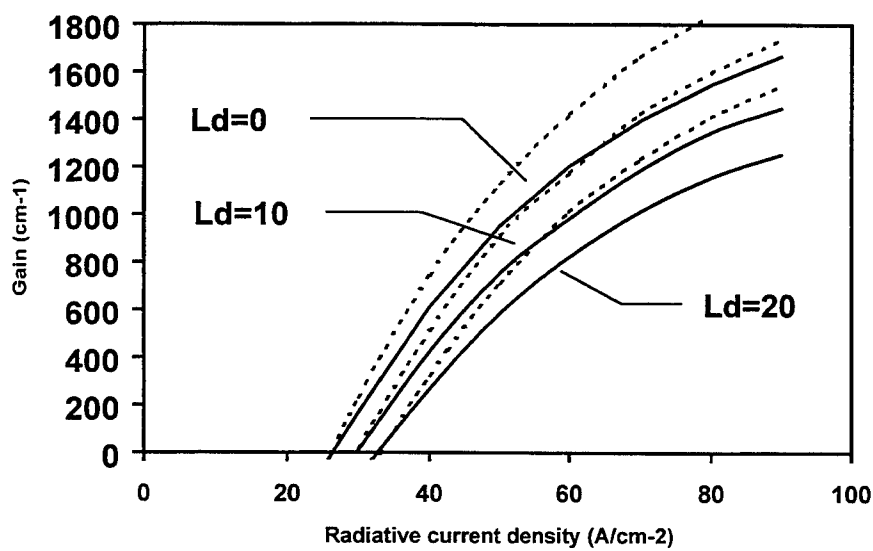


Fig. 2 The peak gain versus radiative current for  $L_d=0, 10, 20 \text{\AA}$ .

# Propagating beam analysis based on the finite-difference formula for a general position of interfaces

Junji Yamauchi, Shu Nakamura, and Hisamatsu Nakano

College of Engineering, Hosei University

3-7-2 Kajino-cho, Koganei, Tokyo 184 Japan

Phone: +81-42-387-6190, Fax: +81-42-387-6381, e-mail: j.yma@k.hosei.ac.jp

## 1 Introduction

It is imperative to reduce the discretization error in the propagating beam analysis of step-index optical waveguides. There are two techniques to tackle this problem.

One is to use a modified grid adaptive to the waveguide geometry. An oblique [1], a more advanced bi-oblique [2] and a tapered [3] coordinate have been developed and tested in the finite-difference beam-propagation method. A tapered grid approach based on cylindrical coordinates has been used in the method of lines [4].

The other is to use a finite-difference (FD) formula that allows a general position of interfaces. The latter technique has an advantage over the modified grid approach in that the connection between different coordinates is not needed, and that inherent error caused by a nonuniform grid is completely eliminated. It should be noted, however, that few attempts have been made in this respect. Recently, we have derived a modified FD formula [5][6] by advancing Vassallo's pioneer work [7][8].

In this paper, we present some applications of the modified FD formula to the semivector analysis of optical waveguides, and demonstrate the effectiveness of the present technique. After brief explanation of the modified FD formula, we discuss the difference between the E-field and H-field formulations, and clarify the advantage of the H-field formulation in terms of the stability of the eigenmode analysis of a rib waveguide. In the propagating beam analysis, a tilted and a tapered rib waveguide are treated. The field profile and the guided-mode power at the output are compared with those obtained in the conventional staircase approximation.

## 2 Finite-difference formula and eigenmode analysis

We consider a rib waveguide shown in Fig.1. Suppose that a discontinuity is located between  $i$  and  $i+1$  and the interface is at distance  $\xi_x \Delta x$  (with  $0 < \xi_x < 1$ ) from point  $i$ . Using Taylor-series expansions of the magnetic field near the discontinuity and the boundary conditions at the interface, we get the following modified FD formula that allows a general position of interfaces:

$$\frac{\partial^2 \phi_i}{\partial x^2} = \frac{a\phi_{i-1} + b\phi_i + c\phi_{i+1}}{d\Delta x^2} + e \frac{\Delta x}{3} \frac{\partial^3 \phi_i}{\partial x^3} + O(\Delta x^2) \quad (1)$$

where  $a = 1 + (\theta - 1)(1 - \xi_x) + m\Delta x^2\Gamma$ ,  $b = -2 - (\theta - 1)(1 - \xi_x) - m\Delta x^2(1 + \Gamma)$ ,  $c = 1$ ,  $d = 1 + 0.5(\theta - 1)(1 - \xi_x)(2\xi_x + 1) + 0.5m\Delta x^2\Gamma$ , and  $e = -(\theta - 1)\xi_x(1 - \xi_x)(2\xi_x - 1)/d$ , in which  $k$  is the free-space wavenumber.  $m$  and  $\Gamma$  are defined in [5]. The coefficient  $\theta = n_{i+1}^2/n_i^2$  must be unity when the normal component is treated. Eq.(1) is also used for the second derivative with respect to  $y$ . In this paper,  $\xi_y$  for the  $y$  direction is fixed to be 0.5. In other words, we deal with the waveguide whose configuration changes only in the  $x$ - $z$  plane. A formula similar to Eq.(1) can also be derived for the E field. It should be noted, however, that the formula based on the H field has some advantages, as will be seen in the following.

The first-order term in Eq.(1) is neglected in this analysis. It should be noted that the coefficient  $e$  vanishes for  $\theta = 1$ . This means that Eq.(1) is exactly second-order accurate as long as the normal component is treated. Strictly speaking, Eq.(1) does not ensure second-order accuracy for the tangential component ( $\theta \neq 1$ ). Fortunately, we can find that the effect of the

first-order term is small in the rib waveguide, so that a dramatic improvement in accuracy is achieved by the use of Eq.(1) even for  $\theta \neq 1$ .

We investigate the dependence of numerical results on the position of interface. Fig.2 shows the normalized propagation constant  $B = (n_{eff}^2 - n_s^2)/(n_{gl}^2 - n_s^2)$  as a function of  $\xi_x$ . A wavelength of  $\lambda = 1.15\mu m$  is used. The transverse sampling width is fixed to be  $\Delta (= \Delta x = \Delta y) = 0.025\mu m$ , and the total number of sampling points is taken to be  $N_x \times N_y = 320 \times 180$ . The imaginary-distance procedure is used with a unit amplitude field as a starting field. For comparison, the data obtained by the E-field formulation are also presented. The data for both the quasi-TE and quasi-TM modes are shown. It is found that the results from the H field are insensitive to the location of the interface regardless of the mode, while the results from the E field are sensitive to the position in the quasi-TE mode. The dependency of the E-field results on the interface position is probably due to the fact that the E field becomes singular at the lower corner. This fact has already been suggested by Vassallo [7], but he has not noticed that the dependency can be almost eliminated by the use of the H field [9].

### 3 Propagating beam analysis

Since superiority of the H-field formulation is demonstrated, the present H-field formulation is applied to propagating beam analyses of z-dependent structures. We first study the propagating beam in a tilted rib waveguide. The waveguide whose configuration parameters are identical to those in Fig.1 is tilted by an angle  $\theta$ . Fig. 3 shows the guided-mode power as a function of the propagation distance. The quasi-TE mode is tested, and the tilt angle is typically chosen to be 1 degree. The computational parameters are chosen to be  $\Delta = 0.05\mu m$  and  $\Delta z \simeq 0.072\mu m$ . Ideally, the guided-mode power should be unity regardless of the propagation distance. It is clearly shown that the present scheme maintains a unit value of the guided-mode power. In contrast, the conventional staircase approximation ( $\xi_x$  is fixed to be 0.5) results in gradual deterioration with increase in the propagation distance.

We next consider the case of a tapered rib waveguide. The rib width is tapered from  $3\mu m$  to  $2\mu m$ , as shown in the inset of Fig.4. Calculation is made under the condition that  $\Delta x = \Delta y$  and  $\Delta z = 0.05\mu m$ . Other configuration and computational parameters are the same as those used in Fig.3. Fig.4 shows the guided-mode power at the output as a function of transverse sampling width  $\Delta$ . For comparison, the data obtained from the staircase approximation are also shown. It is revealed that the present technique shows rapid convergence behavior.

Fig.5 illustrates the output field profiles for  $\Delta = 0.1\mu m$ . Appreciable numerical noise is found for the staircase approximation. It is worth mentioning that the use of the present technique greatly contributes to reduction in numerical noise.

### 4 Conclusions

A modified finite-difference formula that allows a general position of interfaces has been applied to the semivector analysis of rib waveguides with particular emphasis on reducing the discretization error. First, the eigenmode analysis is made to demonstrate that the numerical results are almost independent of the interface position. Next, propagating beams in a tilted and a tapered waveguide are calculated. Numerical results clearly show reduction in numerical noise of the field profile and faster convergence as a function of transverse sampling width.

### References

- [1] J. Yamauchi et al., OSA/IEEE Integr. Photon. Res., pp.19-21, 1994.
- [2] P. Sewell et al., J. Lightwave Technol., vol.15, no.4, pp.688-696, 1996.
- [3] P. Sewell et al., Electron. Lett., vol.32, no.11, pp.1025-1026, 1996.
- [4] S. Helfert and R. Pregla, Opt. and Quantum Electron., vol.27, pp.943-950, 1995.
- [5] J. Yamauchi et al., IEEE Photon. Tech. Lett., vol.9, no.7, pp.961-963, 1997.
- [6] J. Yamauchi et al., IEEE Photon. Tech. Lett., vol.10, no.8, pp.1127-1129, 1998.
- [7] C. Vassallo, Proc. ECOC'92, pp.565-568, 1992.
- [8] C. Vassallo, Proc. IEE part J, vol.139, no.2, pp.137-142, 1992.
- [9] C. Vassallo, J. Opt. Soc. Amer. A, vol.14, no.12, pp.3273-3284, 1997.

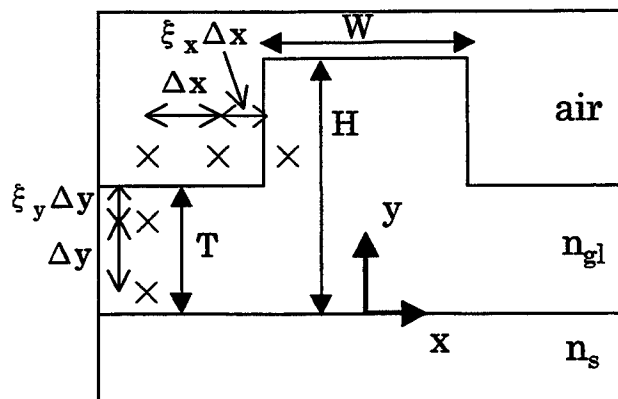


Fig.1 Rib waveguide geometry:

$W = 3.0\mu\text{m}$ ,  $H = 1.0\mu\text{m}$ ,  $T = 0.5\mu\text{m}$   
 $n_{\text{gl}} = 3.44$ ,  $n_s = 3.40$ .

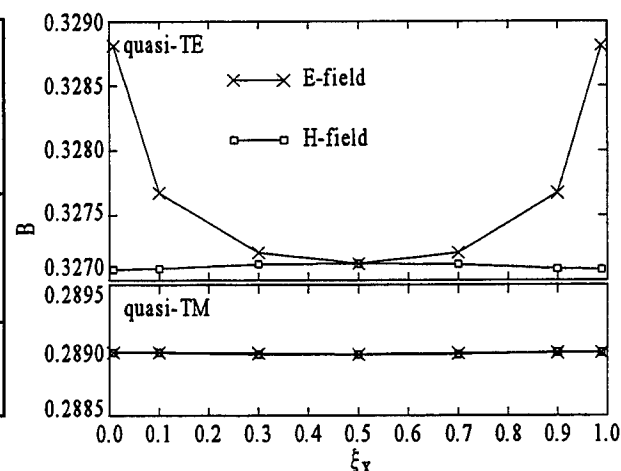
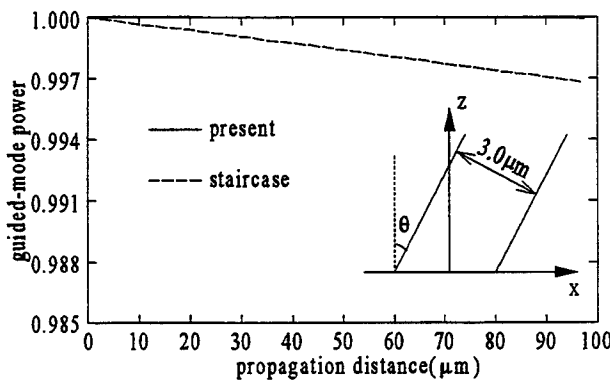
Fig.2 Normalized propagation constant B as a function of  $\xi_x$ .

Fig.3 Guided-mode power as a function of propagation distance (quasi-TE).

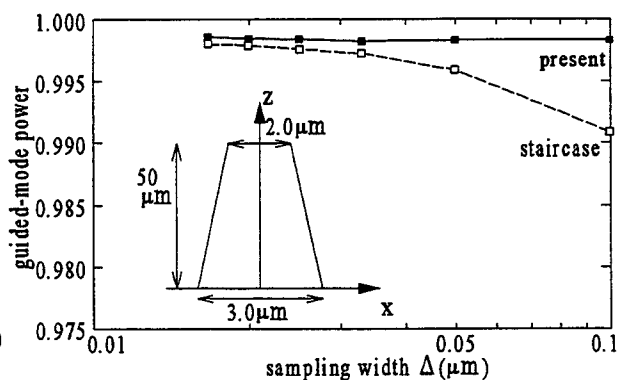
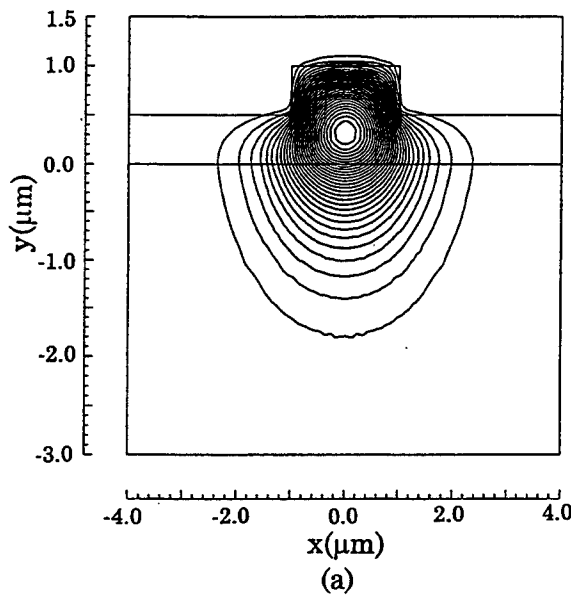
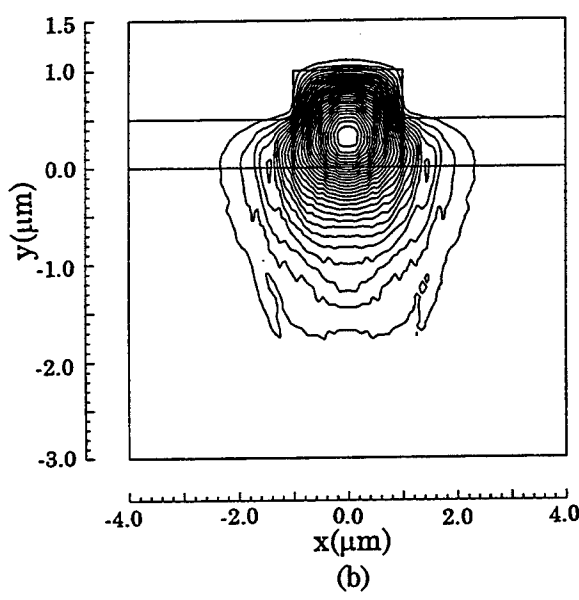


Fig.4 Convergence behavior of the guided-mode power (quasi-TE).

Fig.5 Field profiles observed at the output of the tapered rib waveguide:  
(a) present scheme, (b) staircase approximation ( $\xi_x = 0.5$ )

# Pade approximation analysis of reflection at optical waveguide facets

Hatem El-Refaei, David Yevick

Department of Electrical & Computer Engineering, Queen's University, Kingston, K7L 3N6, Canada.

Phone: 01-613-765-5430, Fax: 01-613-765-2471, e-mail: hrefaei@nortelnetworks.com

Ian Betty

Nortel Networks, Advanced Technology Lab, Box 3511 Station C, Ottawa, Canada, K1Y 4H7

## Introduction :

Stable, accurate, and fast numerical procedures are often required to estimate power reflection in integrated optical components and devices. Numerous methods have been proposed to analyze reflection effects. The most straightforward approach, which requires knowledge of all eigenvalues and eigenvectors of the characteristic matrix representation of the reflection operator [1], is highly time consuming and memory intensive. Alternatively, the square root operator of the characteristic matrix can be expanded in Taylor series [4] or Pade approximation [6] around a reference point. A further performance improvement using Pade approximation can be realized by inserting a fictitious layer [2] with a refractive index equal to the average of the refractive indices along both sides of the interface, and then developing an iterative solution for the reflection operator at the interfaces between this fictitious layer and the input and output media [3]. However the results of the Pade approximation tend to fluctuate markedly with changes in the calculation parameters. This behavior results from the fact that evanescent modes are assigned real eigenvalues by the standard Pade approximation of the square root operator, leading to a vanishing denominator in the evaluation of the reflection operator. Here we examine two methods for restoring the stability of such a calculation. The first method is based on a simple modification of the continued fraction representation of the Pade approximation yielding complex Pade primes [5] while the second directly rotates the branch-cut of the square root operator in the complex plane [7]. In this paper we analyze for the first time the reflection problem from the interface between two arbitrary, lossless, and isotropic transverse refractive index distributions,  $n_a(x,y)$  and  $n_b(x,y)$  using stable and accurate modified Pade approximation methods.

## Theoretical approach :

To calculate the reflected field, we begin with the Helmholtz wave equation, solve for the forward and backward field components of  $E_y$ , and match these field components and their derivatives on either side of the interface. This results in the reflected field component  $E_{yr}$  that can be written in terms of the incident field component  $E_{yi}$  as [3],

$$E_{yr} = \frac{L_a - L_b}{L_a + L_b} E_{yi} \quad (1) \quad \text{with} \quad L_m = \sqrt{1 + \frac{\nabla_t^2 + k_o^2(n_m^2(x,y) - n_{0m}^2)}{k_o^2 n_{0m}^2}} \quad , m = a \text{ or } b \quad (2)$$

where  $k_o$  is the vacuum wave vector,  $\nabla_t^2 = \partial^2/\partial x^2 + \partial^2/\partial y^2$ , and  $n_m(x,y)$  and  $n_{0m}$  are the index distribution and the reference refractive index for the  $m$ th region respectively.

To calculate the square root of the characteristic operator we use the  $[n/n]$  diagonal Pade approximant of the function  $g(x) = \sqrt{1+x}$  given by [5],

$$g_n(x) = \prod_{j=1}^n \frac{1 + c_j^{(n)}x}{1 + b_j^{(n)}x} \quad (3)$$

where  $b^{(n)}$  and  $c^{(n)}$  are known as the Pade primes. Until now, the real Pade primes [6] -- generated from matching constraints on the first  $2n$  derivatives of the square root function -- have been used for the optical facet reflection problem [1][4]. However the real Pade primes do not yield a valid approximation for  $g(x)$  when  $x < -1$  [6].

Improving the stability of the real Pade approximation of  $g(x)$  is achieved by replacing two of the accuracy constraints with stability constraints to obtain complex Pade primes that guarantee a positive imaginary part of  $g_n(x)$ .

for  $x < -1$  [6]. However, the difficulty associated with calculating these complex Pade primes led Lu [5] to introduce a more robust calculation method where the complex Pade primes  $b^{(n)}$  and  $c^{(n)}$  are given by the zeros of the functions

$$F(z) = \sum_{j=1}^n \frac{\sin^2(2j\theta)}{z - \cos^2(j\theta)} + (2n+1)\left(1 - \frac{2i}{\beta}\right) \quad (4) \quad \text{and} \quad G(z) = \sum_{j=1}^n \frac{\sin^2(2j\theta)}{z - \sin^2(j\theta)} + (2n+1)\left(1 - \frac{2i}{\beta}\right) \quad (5)$$

respectively, with  $\theta = \pi/(2n+1)$ ,  $i = \sqrt{-1}$ , and  $\beta$  is an arbitrary positive real number. Newton's method can then be applied for  $n$  different initial guesses to calculate the  $n$  Pade primes with a computation time of  $O(n^2)$ .

An alternative procedure for improving the stability of the Pade approximation of  $g(x)$  involves rotating the original real axis branch-cut by an angle  $\alpha$  [7]. Thus  $g(x)$  becomes

$$g(x) = e^{ia/2} \sqrt{1 + [(1+x)e^{-ia} - 1]} \quad (5)$$

Such a rotation of the branch-cut maps the  $x < -1$  real axis into the positive imaginary half-space, restoring the stability of the square-root operator.

### Results :

We now present results for the reflection at an optical waveguide facet using procedures involving both real and complex Pade primes. In both cases, we additionally examined the effects of rotating the branch-cut. In particular, we examined the reflection of the  $TE_0$  mode of a symmetric three layer slab waveguide terminated by a uniform semi-infinite medium, as shown in figure (1).

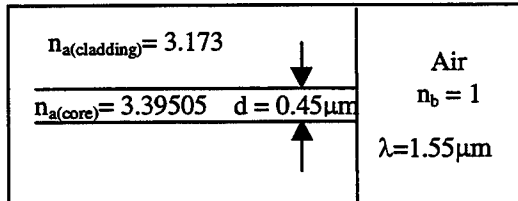


Figure (1)  
Problem description

Figures (2) and (3) show the reflected power calculated with real and complex Pade primes respectively as a function of Pade order and branch-cut rotation angle. The calculation window consisted of 128 points covering a  $6\mu\text{m}$  space. Figures (4-7) show the numerical stability of the calculated reflected power using real unrotated, real rotated ( $90^\circ$ ), complex unrotated, and complex rotated ( $90^\circ$ ) Pade primes respectively (all at Pade order 10) as a function of the calculation window width and number of grid points. The calculation window varies from  $5\mu\text{m}$  to  $20\mu\text{m}$  in  $1\mu\text{m}$  steps, while the number of points in the window varies from 100 to 400 with 20 point steps. For all complex Pade prime calculations  $\beta=1$ .

For real Pade primes without branch-cut rotation, Figures (2-7) reveal the large instability in the calculated reflected power as the calculation parameters vary. They also show that the solution stability is greatly improved through complex Pade primes without rotation. In addition, a stable solution is realized with either real or complex Pade primes after branch-cut rotation. Clearly, the higher the rotation degree, the lower the Pade order at which the results converge.

### Conclusions :

We have shown that the numerical instability of reflected power calculations performed using a standard real Pade approximation expressions for the components of the reflection operator can be largely eliminated. We have examined two realizations, one based on a modified continued fraction expansion to obtain complex Pade primes and the second on a direct rotation of the original branch-cut. Either procedure leads to large improvements in the stability of the calculated reflected coefficient. We believe that these results will enable numerically efficient bi-directional beam propagation algorithms that will be applicable to a variety of integrated optical devices.

### Reference :

- [1] Yih-Peng Chiou and Huan-Chun Chang; IEEE Photonics Technology Letters, Vol. 9, No. 7, pp. 964-966, July 1997.
- [2] J. Xu, Devid Yevick, and Michel Gallant; J. Opt. Soc. Am. A, Vol. 12, No. 4, pp. 725-728, April 1995.
- [3] Chunlin Yu and Devid Yevick; J. Opt. Soc. Am. A, Vol. 14, No. 7, pp. 1448-1450, July 1997.
- [4] Chenglin Xu, et al.; Integrated Photonics Research Proceeding, pp. 20-22, March 30-April 1, 1998.
- [5] Ya Yan Lu; Applied Numerical Mathematics, Vol. 27, pp. 141-154, 1998.
- [6] Michael D. Collins; J. Acoust. Soc. Am., Vol. 93, No. 4, Pt. 1, pp. 1815-1824, April 1993.
- [7] Fausto A. Milinazzo, Cedric A. Zala, and Gary H. Brooke; J. Acoust. Soc. Am., Vol. 101, No. 2, pp. 760-766, February 1997.

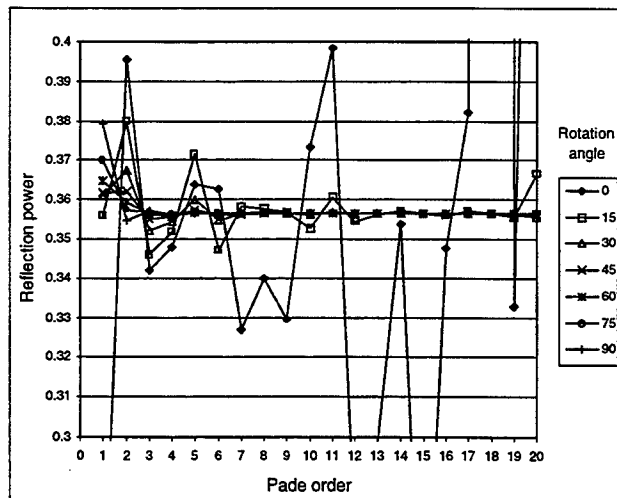


Fig. (2) Reflected power using real Pade primes. The only point greater than 1 is at Pade order 18, its value is 4.66.

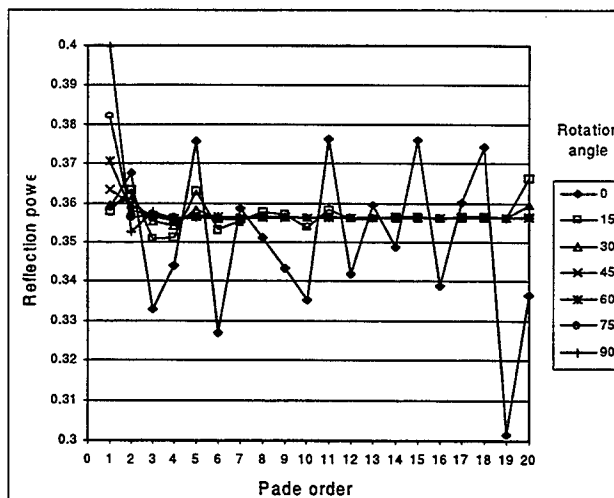


Fig. (3) Reflected power using complex Pade primes.

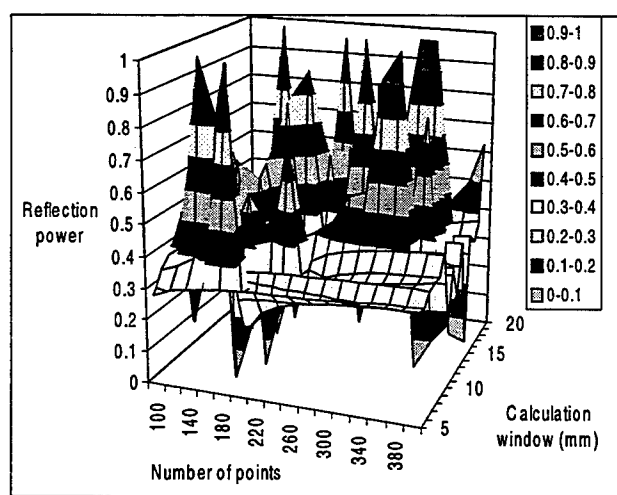


Fig. (4) Reflected power using real unrotated Pade primes. Seven maximum peaks have values larger than 1, the highest value is 17.66.

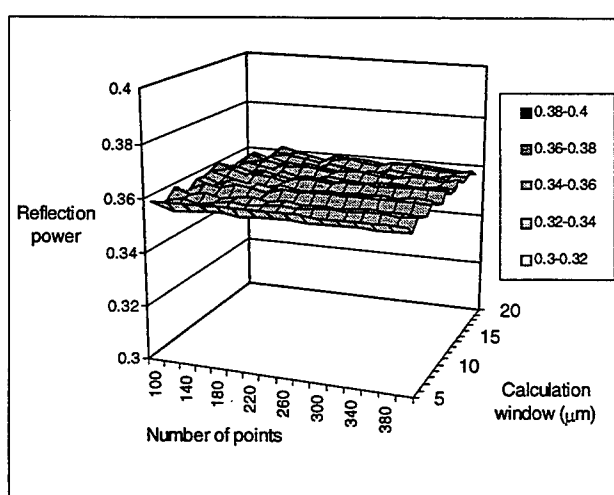


Fig. (5) Reflected power using real rotated (90°) Pade primes.

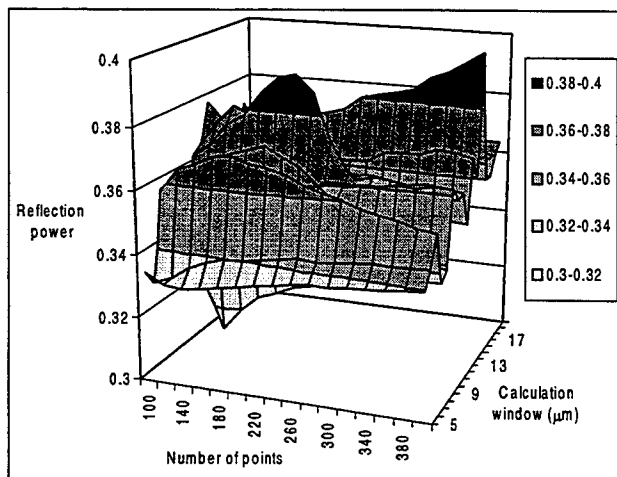


Fig. (6) Reflected power using complex unrotated Pade primes.

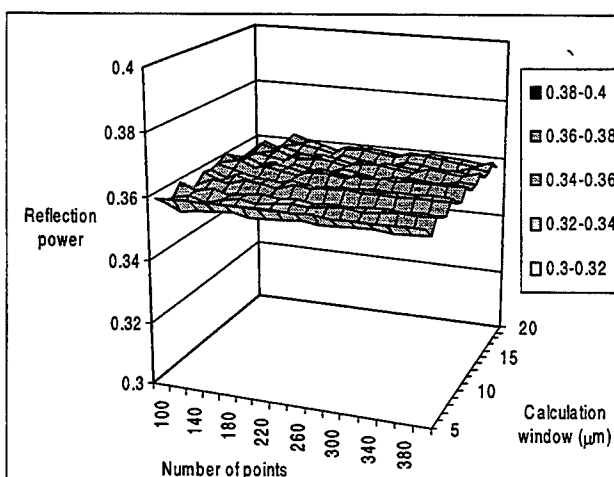


Fig. (7) Reflected power using complex rotated (90°) Pade primes.

# Integrated Photonics Research

## Noise in Semiconductor Cascade Lasers

F. Rana, S. G. Patterson, R. J. Ram

MIT Research Laboratory for Electronics, 77 Massachusetts Av., Room 26-457, Cambridge, MA 02139  
farhan@mit.edu

Semiconductor cascade lasers are capable of producing multiple photons for each injected electron. Slope efficiency of cascade laser devices can therefore be made in excess of the fundamental limit  $\hbar\omega/e$ .

These laser devices may play a very important role in RF photonic links since link gain increases as the square of the laser slope efficiency [1, 2, 3]. In addition, cascade lasers have higher series resistances and can be better impedance matched to the driving electronic circuit. There have been several recent demonstrations of cascade lasers [1-7] and the various implementation schemes reported include inter-connect coupled cascade lasers [1, 2, 3], bipolar interband cascade lasers [4, 5, 6] and unipolar intersubband cascade lasers [7].

A comprehensive noise model for semiconductor cascade lasers will be presented in this paper. While cascade lasers have been receiving increased attention from experimentalists, so far very few theoretical models have appeared in literature. Work that has been reported on noise in cascaded PN junctions includes references [8-11] but most of them present experimental work. Devices, which will be focused upon in this paper, are shown schematically in fig. 1. Inter-connect coupled cascade lasers (either integrated or discrete) fall in categories A and B, and bipolar cascade lasers and unipolar intersubband lasers belong to category A. Parallel laser arrays will also be examined (category C). Coupled Langevin rate equations are used to describe fluctuations in carrier density, photon number and electrical current. In a cascade laser gain stages are all electronically coupled and fluctuations in carrier density and, therefore, rate of photon generation are strongly correlated among different gain sections. Any noise model must take into account these correlations, which, in turn, depend sensitively on the external circuit in which the laser device is embedded. For example, in the device shown in category B in fig.1, a photon emission event in one section of the cascade will cause the carrier population to fall below the average value in that section. A relaxation current will flow in the external circuit and will tend to increase the photon generation rate in other sections of the device. As a result, photon number fluctuations will get positively

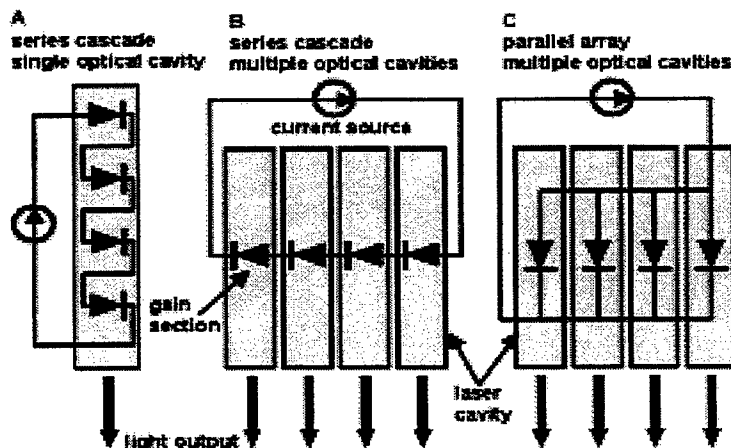


Fig.1 Different types of semiconductor cascade lasers. Category A have multiple gain sections in series inside a single optical cavity. Category B have separate lasers connected in series. Category C is a parallel array of lasers.

correlated in different sections of the device even in the absence of external thermal noise sources from circuit resistances. The noise model presented in this paper fully accounts for such correlations in carrier population and photon number and it agrees well with the experimental results presented in references [8,9].

Effect of noise on important laser parameters, such as relative intensity noise (RIN) and signal to noise ratio (SNR) for direct RF laser modulation, will be examined and scaling of various device figures of merit with the number N of cascaded sections will be discussed. Performance of different cascade lasers in RF photonic links will also be evaluated. Fig. 2 shows evolution of the low frequency RIN in inter-connect coupled cascade lasers with bias current. For multiple optical guides it is assumed that optical power from all guides is collected when the noise is measured. The DC power supply is assumed to be a noiseless current source inductively coupled to the laser devices. A  $0.98\mu\text{m}$  InGaAs laser, with a cavity length of  $250\mu\text{m}$  and differential resistance of  $4\Omega$ , has been used for these calculations. Fig. 2 shows that RIN scales down with the increase in number of sections (N) in the multi-guide cascade and in the parallel array. It remains largely unchanged for the single guide cascade device. Fig. 3 shows the variation in RF signal to noise ratio (SNR) in these devices with N when they are biased much above threshold. RF modulation is achieved by capacitively coupling laser devices to a noiseless RF voltage source with a  $50\Omega$  series resistor. The SNR has a maximum value for both the single guide cascade and the multi-guide cascade lasers. Although, maximum value of SNR for both devices is about the same, single guide cascade devices attain this value for much smaller values of N. SNR of parallel array always decreases with increase in N. In fig. 2 and fig. 3 the length of laser cavity has been kept the same for all devices.

Design methodologies for realizing optimal devices for RF optical links will also be discussed in this paper. Various design tradeoffs exist and cascade devices can be tailored to meet specific applications. Recently we have fabricated inter-connect coupled cascade lasers and the first room temperature CW bipolar cascade laser [1,6]. Experimental results from noise measurements on these lasers will be presented and compared with the theoretical model.

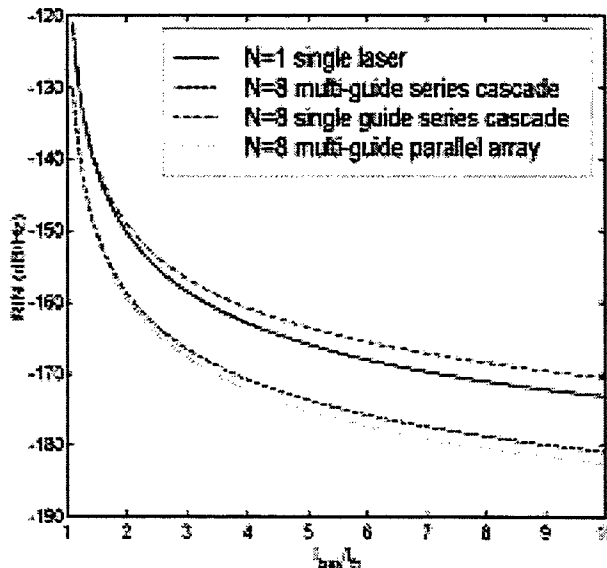


Fig. 2 Low frequency (1 GHz) relative intensity noise (RIN) in cascade laser devices as a function of bias. The power supply is assumed to be noise free. T=300K.

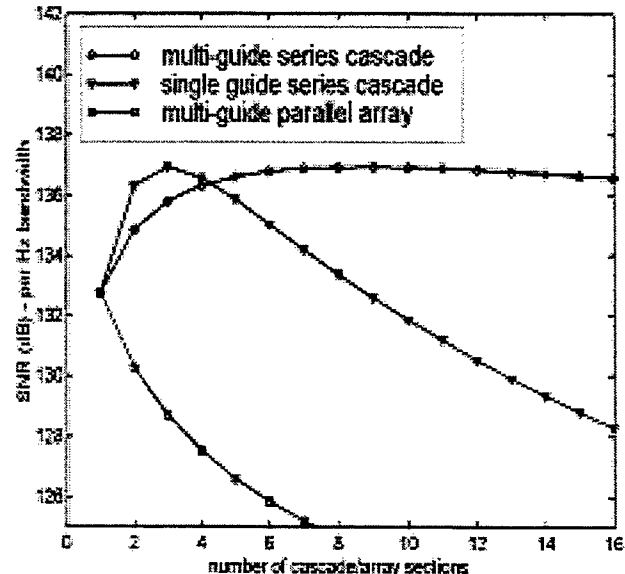


Fig. 3 Signal to noise ratio (SNR) as a function of number of cascade/array sections (signal frequency is 1 GHz and input signal power is  $1\mu\text{W}$ ). The power supply is assumed to be noise free. T=300K.

## References:

1. C. Cox, H. Roussell, R. J. Ram, R. J. Helkey, "Broadband, directly modulated analog fiber link with positive intrinsic gain and reduced noise figure," International Topical Meeting on Microwave Photonics, Princeton, October 1998.
2. S.G. Ayling, D. R. Wight, M. B. Allenson, K. P. Hilton, G.W. Smith: "Intrinsically matched 50 Ohm laser arrays with greater than 100% quantum efficiencies for optically coupled transistors and low loss fibre optic links," SPIE Photonics West '98, Optoelectronics '98: Laser Diode Applications IV; Conf. No. 3285B-Paper 36.
3. S.G. Ayling, D. R. Wight, M. B. Allenson, K. P. Hilton, G.W. Smith: "Novel integrated laser devices with greatly enhanced quantum efficiency and intrinsic RF matching for low loss, broad band opto-microwave applications," Microwave Photonics '98, October 1998.
4. J. P. van der Ziel, W. T. Tsang, "Integrated multi-layer GaAs lasers separated by tunnel junctions," App. Phys. Lett., 1982, **41**, (6), pp. 499-501.
5. J. Ch. Garcia, E. Rosencher, Ph. Collot, N. Luarent, J. Guyaux, B. Vinter, J. Nagle: "Epitaxially stacked lasers with Esaki junctions: A bipolar cascade laser," App. Phys. Lett., 1997, **71**, 26, pp. 3752-3754.
6. S. G. Patterson, G. S. Petrich, R. J. Ram, L. A. Kolodzjieski, "Room temperature, continuous wave operation of a bipolar quantum cascade laser," Elect. Lett. (accepted for publication, March 1999).
7. J. Faist, A. Tredicucci, F. Capasso, C. Sirtori, "High-power continuous-wave quantum cascade lasers," IEEE J. Quantum Electronics, Feb. 1998, **34**, pp.336-43.
8. E. Goobar, A. Karlsson, G. Bjork, P-J. Rigole, "Quantum correlated light beams and Sub-Poissonian electrical partition noise in parallel and series coupled semiconductor light emitters," Phys. Rev. Lett., Jan. 1993, **70**, pp. 437-440.
9. P. J. Edwards, G. H. Pollard, "Quantum noise correlated operation of electrically coupled semiconductor light emitters," Phys. Rev. Lett., Sep. 1992, **69**, pp. 1757-1760.
10. G. Bjork, "Generation of intensity correlated twin beams using series coupled semiconductor lasers," Phy. Rev. A, June 1992, **45**, pp. 8259-8267.
11. Y. Yamamoto, H. A. Haus, "Effect of electrical partition noise on squeezing in semiconductor lasers," Phys. Rev. A, 1992, **45**, pp. 6596-6504.

## Feedback regimes in a coupled cavity multimode laser diode model

Iestyn Pierce, Paul S. Spencer, Paul Rees and K. Alan Shore

University of Wales, Bangor,

School of Electronic Engineering and Computer Systems,  
Bangor, Gwynedd LL57 1UT

United Kingdom

tel: +44 1248 382715

fax: +44 1248 361429

email: iestyn@sees.bangor.ac.uk

The vulnerability of semiconductor lasers to unintentional reflections has been known almost from their inception. Semiconductor lasers exposed to external optical feedback have been found to exhibit a wide variety of behaviour. In particular dramatic spectral broadening has been observed over a large range of feedback levels. This phenomenon, commonly referred to as coherence collapse, [1], has been found to be a consequence of chaotic dynamics. Experimentally, back reflections of the order of  $10^{-4}$  of the emitted power have been found to be sufficient to induce coherence collapse. Typically the lasers linewidth broadens from a few MHz to a several tens of GHz [2]. This vulnerability places severe demands on the optical isolation required for applications that need narrow linewidth operation.

For low feedback regimes of operation the standard Lang-Kobayashi rate equations, [3], have been found to successfully describe the behaviour of laser diodes. An alternative method for modelling optical feedback in laser diodes can be obtained using an iterative approach based on a travelling wave description, [4]. In both these approaches the laser diode's active region is described using the alpha-factor and linear gain to approximate the dynamical evolution of the complex susceptibility. This approach is justified when considering single mode operation, but becomes questionable when multimode dynamics are being considered. The formalism to overcome this difficulty, namely a many body theory of the optical susceptibility, has been known for some time, but the complexity of the theory has limited its use.

The limitations of present theoretical models have led to the situation that the experimental work, which in general has been undertaken using multimode semiconductor lasers, has been analysed using single mode models. This mis-match has resulted in some heated debate in the literature about the validity of such theoretical interpretations of the experimental data.

The model presented in this paper views the system as a coupled-cavity problem, and self-consistently calculates the optical susceptibility [5] and the longitudinal modes of the cavity. The optical susceptibility is calculated over the full wavelength-range of the expected optical cavity modes and includes many-body effects [6]. Tkach and Chraplyvy, [7], classified the types of behaviour observed, as the feedback strength was increased, into five regimes of operation. The validity of our approach has been tested by simulating the dynamics of each of these five regimes. As an example figure 1 shows a typical spectral mode distribution for a solitary laser operating just above threshold. The effect of optical feedback on the spectral distribution can be seen in figure 2, where an external reflectivity of  $r_{ext} = -28\text{dB}$  and external cavity round-trip time of  $\tau_{ext} = 24\text{ps}$ , were assumed, corresponding to the coherence collapse regime. The model has also been used to analyse devices that show feedback insensitive behaviour.

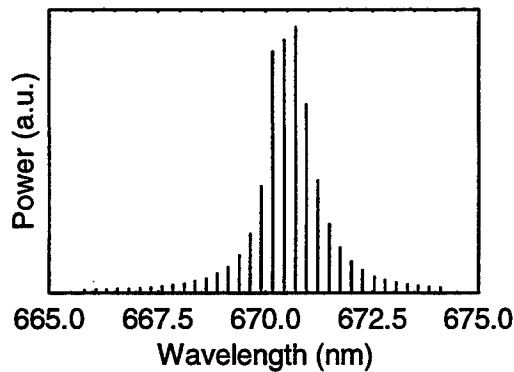


Figure 1: Longitudinal mode distribution of a typical Fabry-Perot laser diode operating just above threshold

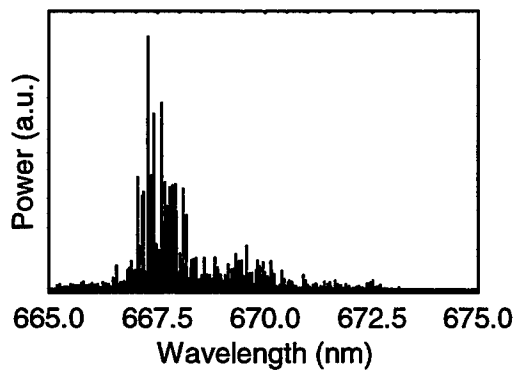


Figure 2: Longitudinal mode distribution of a Fabry-Perot laser diode operating just above threshold and subject to an external optical reflector,  $r_{ext} = -28\text{dB}$ , with external cavity round-trip time  $\tau_{ext} = 24\text{ps}$ .

## References

- [1] D.Lenstra, B.H.Verbeek, and A.J.den Boef, "Coherence collapse in single mode semiconductor lasers due to feedback", IEEE J. Quant. Elec., **QE-21**, 674-679, (1985).
- [2] P. Besnard, B. Meziane, and G.M.Stephan "Feedback phenomena in a semiconductor laser induced by distant reflectors", IEEE J. Quant. Elec., **QE-29**, 1271-1284, (1993).
- [3] R.Lang and K.Kobayashi, "External optical feedback effects on semiconductor injection laser properties", IEEE J. Quant. Elec., **QE-16**, 347-355, (1980).
- [4] P.S.Spencer, Claudio.R.Mirasso and K.A.Shore, "Effect of strong feedback on VCSELs", IEEE Phot. Tech. Lett. **10**, 191-193, (1998).
- [5] A.Egan, M.Harley-Stead, P.Rees, S.Lynch, P.McEvoy, J.O'Gorman and J.Hegarty, "All-Optical Synchronization Of Self-Pulsating Laser Diodes", Appl. Phys. Lett. **68**, 3534-3536, (1996).
- [6] H.Haug and S.W.Koch, "Quantum theory of the optical and electrical properties of semiconductors", World Scientific, Singapore, (1990).
- [7] R.W.Tkach and A.R.Chraplyvy, "Regimes of Feedback Effects in  $1.5\mu\text{m}$  Distributed Feedback Lasers", IEEE J. Lightwave Technol., **LT-4**, 1655, (1986).

# The Single Mode Condition for Rib Waveguides, Revised

R. Hauffe, U. Siebel, K. Petermann

Technical University of Berlin, Einsteinufer 25, 10587 Berlin, Germany

Tel.: +49 30 314 22628, FAX: +49 30 314 24626, e-mail: hauffe@sun6hft.ee.tu-berlin.de

C. Kostrzewa

Siemens AG, Hofmannstr. 51, 81359 München, Germany

Tel.: +49 89 722 35287, Fax: +49 89 722 48046, e-mail: carsten.kostrzewa@icn.siemens.de

## Introduction

In integrated optics the single mode rib waveguide (Fig. 1) is one of the most important basic waveguide structures that allows an arbitrary high refractive index contrast between core and cladding despite large cross sections for mode matching to single mode fibers. Very important for the proper functioning of devices based on this waveguide concept, like digital optical switches and filters, is the single mode behavior.

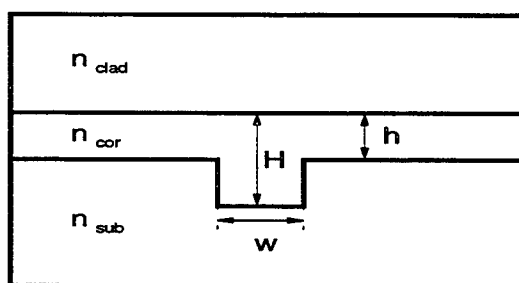


Fig. 1: Schematic of a rib waveguide

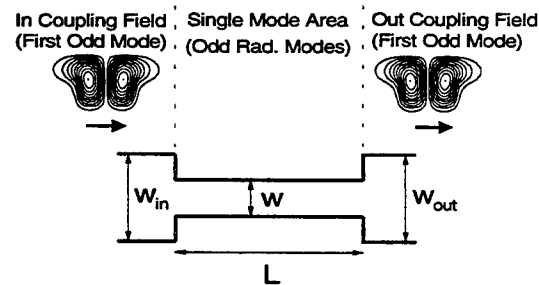


Fig. 2: Top view of the simulated rib waveguide structure

Usually the cutoff of the second order mode is used as a criterion for single mode behavior [1, 2]. For practical purposes this is however not always accurate because for every waveguide close to cutoff imperfections like crossings or slightly off axis coupling by fibers lead to excitation of dominantly uneven radiation modes with low wave numbers transversal to the waveguide (high propagation constants  $\beta$ ) which results in a very slow power divergence from the waveguide. This is of course also true for slab and strip waveguides but less critical as will be shown.

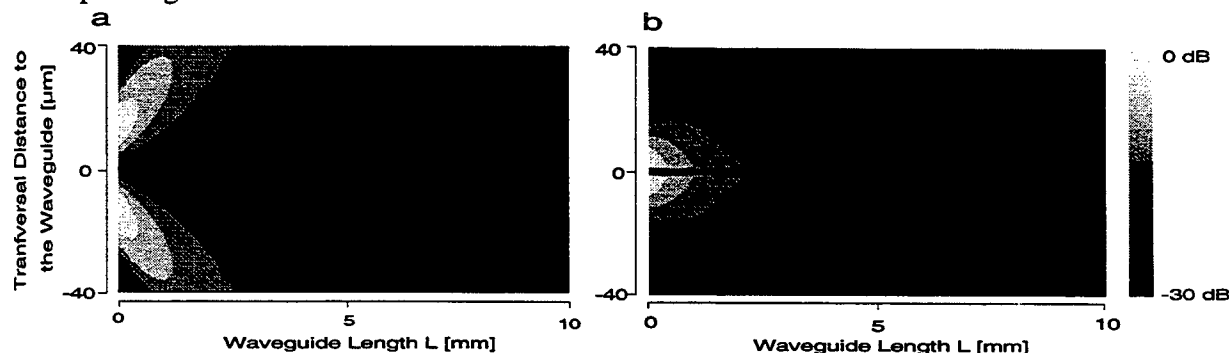


Fig. 3: Normalized intensity plot in dB alongside a single mode waveguide far from cutoff of the first odd mode (Fig. 3.a with  $w/w_c=0.7$ ) and close to cutoff of the first odd mode (Fig. 3.b with  $w/w_c=0.98$ ) after excitation by an uneven field distribution at  $L=0$ .

Figure 3 illustrates how the power of an uneven exciting field distribution holds much longer on to the strong guiding single mode waveguide (Fig. 3.b) in comparison to a weak guiding waveguide (Fig. 3.a). To allow the power to diverge from the waveguide a straight waveguide section needs to be introduced between devices which needs space that is a crucial design criterion in integrated optics and not readily available. This trade-off between guidance of the rib waveguide and device length is investigated here.

### Calculations and Results

We will concentrate on waveguides with  $h/H \geq 0.5$  to insure single mode behavior in the vertical direction [3]. The cutoff condition for the second order mode in horizontal direction is calculated numerically via a full vectoriel 3D mode solver (FIMMWAVE) based on the film mode matching method due to Sudbo [4]. Quasi TE and TM modes were treated separately and lead to similar results. In the following we therefore refer to quasi TE modes. Also possible are analytical approximations like the effective index method [6] or more sophisticated and accurate methods as proposed in [1, 5]. Figure 4 shows the results of the different calculations for low  $h/H$  (but  $h/H > 0.5$ ) ratios ensuring good horizontal guidance for a given width  $w$ . The lines mark the upper limit of  $w/H$  for single mode waveguides referring to the cutoff condition. Obviously the EIM is very inaccurate but leads to best results in comparison to experimental data as shown by P. Pogossian in [2]. This seemingly contradiction is resolved in the following.

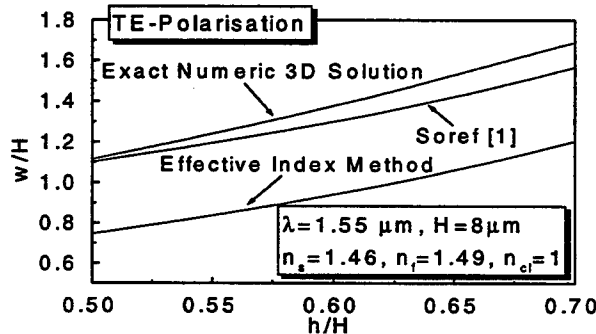


Fig. 4: Different horizontal cutoff conditions for a rib waveguide

As shown in Figure 2 the simulation setup includes a single mode area of variable length  $L$  and variable rib width  $w$ . In and out coupling of this region was done with the first odd mode of a rib guide just below cutoff of the third mode that is symbolized by the wider ribs in the in and out coupling regions. This special uneven field distribution is chosen to allow for normalization of the results. In principle every uneven distribution could be used. The light propagation in the single mode region was calculated by a 3D BPM (Optiwave 2.0) program for small  $h/H$  ratios ( $0.5 < h/H < 0.6$ ) and also for slab waveguides, expanding the exciting field in terms of uneven radiation modes. The second calculation also models rib waveguides with  $h/H \rightarrow 1$ . The results are shown in figure 5. The width  $w$  is chosen as a parameter for plots of the out coupling power into the first uneven mode over the length  $L$  of the waveguide in normalized form. At the width  $w_c$  the cutoff of the second mode is reached and it becomes guided. Comparing the results for the slab and rib guide it can be noticed that the rib width needs to be designed significantly further below cutoff in comparison to the slab for the same decrease in power in the uneven mode after a certain length. If we choose a certain power level e.g. -20dB of the in coupling power it becomes obvious that after a threshold value of the width  $w$  is reached the necessary length  $L$  for the given power level raises rapidly (figure 6).

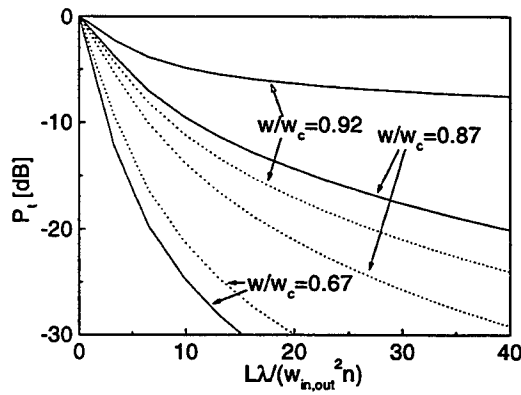


Fig. 5: Power in the first odd mode after a single mode region of length  $L$  for a strong guiding rib waveguide with  $h/H=0.5$  (solid lines) and a slab waveguide (dotted lines)

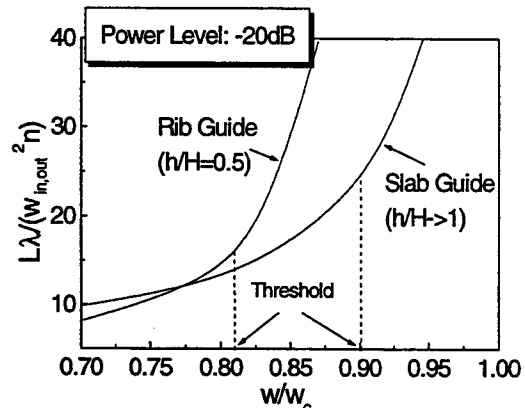


Fig. 6: Length for a power drop to -20dB in the out coupled odd mode over the ratio of  $w/w_c$

This threshold value (defined by the maximum curvature of graphs in figure 6) falls with falling  $h/H$  and reaches a value of  $w/w_c=0.81$  at  $h/H=0.5$ . The upper limit for slab guides ( $h/H \rightarrow 1$ ) lies at  $w/w_c=0.9$ . This is also physically plausible as in deep ribs the light is strongly bound by the rib borders and in shallow ribs only an effective refractive index change is responsible for light confinement.

### Example

To illustrate the results given above some special parameters are chosen ( $n_{cor}=1.49$ ,  $n_{sub}=1.46$ ,  $n_{clad}=1$ ,  $H=8\mu m$ ,  $h/H=0.5$  and  $\lambda=1.55\mu m$ ). These values correspond to a polymer rib waveguide on a  $SiO_2$  substrate with air cladding. If we choose the width 0.899 times the cutoff width a length of over 15mm is necessary for a power decrease to -20dB in the odd out coupling mode. At a  $w/w_c$  ratio of 0.87 this length drops to 9.1mm and for  $w/w_c=0.78$  only 2.7mm are necessary.

### Conclusion

In practical designs of strongly guiding rib waveguides the cutoff condition must be very carefully applied as a single mode condition. As a rule of thumb the rib width  $w$  should be chosen as 0.81 (for  $h/H=0.5$ ) times the cutoff width of the first uneven mode to get moderate lengths for sufficient radiation power divergence from the waveguides proximity.

- [1] R. A. Soref, J. Schmidtchen and K. Petermann, "Large Single Mode Rib Waveguides in GeSi-Si and Si-on-SiO<sub>2</sub>", IEEE Journal of Quantum Electronics, Vol. 27, No. 8, August 1991
- [2] S. P. Pogossian, L. Vescan and A. Vonsovici, "The Single Mode Condition for Semiconductor Rib Waveguides with Large Cross Sections", Journal of Lightwave Technology, Vol. 16, No. 10, October 1998
- [3] E. A. J. Marcatili, „Slab-coupled waveguides, „Bell Syst. Tech. J., vol. 53, pp. 645-674, Apr. 1974
- [4] A. S. Subdo, "Numerically stable formulation of the transverse resonance method for vector mode field calculations in dielectric waveguides", IEEE Phot. Tech. Lett. Vol. 5, 1993
- [5] K. Petermann, "Properties of optical rib guides with large cross sections", Archiv für Elektronik und Übertragungstechnik, (Germany), vol. 30, pp. 139-140, 1976
- [6] V. Ramaswamy, "Strip loaded film waveguides", Bell. Syst. Tech. J., vol. 53, 1974

# Efficiency Analysis of Quantum Well Lasers using PICS3D

Joachim Piprek, Patrick Abraham, and John E. Bowers

Electrical and Computer Engineering Department

University of California, Santa Barbara, CA 93106-9560

Phone: 805-893-4051, Fax: 805-893-5440, E-mail: piprek@ece.ucsb.edu

The performance of multi-quantum well (MQW) laser diodes is often limited by loss mechanisms. Only the fraction  $\eta_i$  of carriers injected above threshold generates stimulated photons. The rest is lost in carrier leakage or non-stimulated recombination within the active region (Shockley-Read-Hall recombination, spontaneous recombination, or Auger recombination). Only the fraction  $\eta_o$  of stimulated photons ends up in the emitted laser beam. Both the internal differential efficiency  $\eta_i$  and the optical efficiency  $\eta_o$  determine the measured slope efficiency  $\eta_d = \eta_i \eta_o$  of the power vs. current  $P(I)$  characteristic. The different carrier loss mechanisms are hard to distinguish by experimental methods. However, it is of great importance for laser optimization to identify the mechanisms that limit the performance of actual devices. We demonstrate such an analysis of measurements using quasi three-dimensional (3D) numerical laser simulation.

Laser simulation codes have been developed by several research groups and commercial laser software has entered the market. PICS3D [1] is one of the most advanced packages in this field. It self-consistently combines two-dimensional carrier transport, wave guiding, and gain calculations with a longitudinal mode solver. Using commercial software has the advantage that results can be reproduced and extended by other researchers.

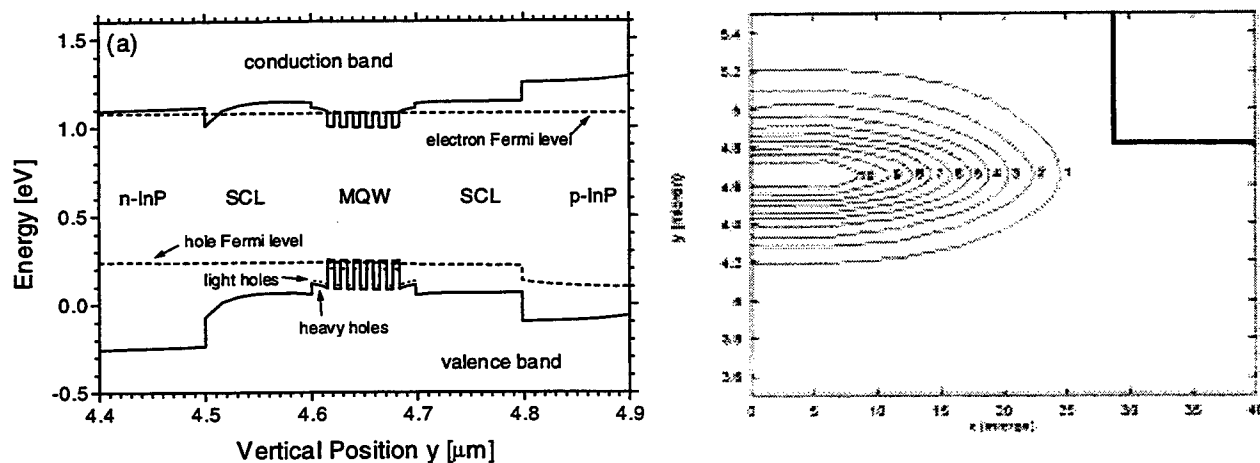


Fig. 1: (a) Energy band diagram of the active region. (b) Normalized wave intensity at the laser facet ( $y$  – vertical position,  $x$  – lateral distance from  $y$ -axis).

In this paper, we focus on the analysis of loss mechanisms in  $1.55\mu\text{m}$  InGaAsP/InP ridge-waveguide laser diodes (Fig. 1). The laser structures are grown by metalorganic vapor phase epitaxy. The MQW

active region consists of six compressively strained (1%)  $\text{In}_{0.76}\text{Ga}_{0.24}\text{As}_{0.79}\text{P}_{0.21}$  quantum wells and  $\text{In}_{0.71}\text{Ga}_{0.29}\text{As}_{0.55}\text{P}_{0.45}$  barriers. The MQW stack is sandwiched between 100nm thick InGaAsP separate confinement layers (SCLs). Broad area ridge-waveguide lasers (57 $\mu\text{m}$  wide ridge) are processed with the p-ridge etched down to the SCL layer. Energy band diagram and wave intensity at the laser facet are shown in Fig. 1. Lasers with different cavity length are manufactured and characterized as-cleaved. Pulsed power vs. current  $P(I)$  measurements with different cavity lengths  $L$  and with different stage temperatures  $T$  are shown in Fig. 2 (dots).

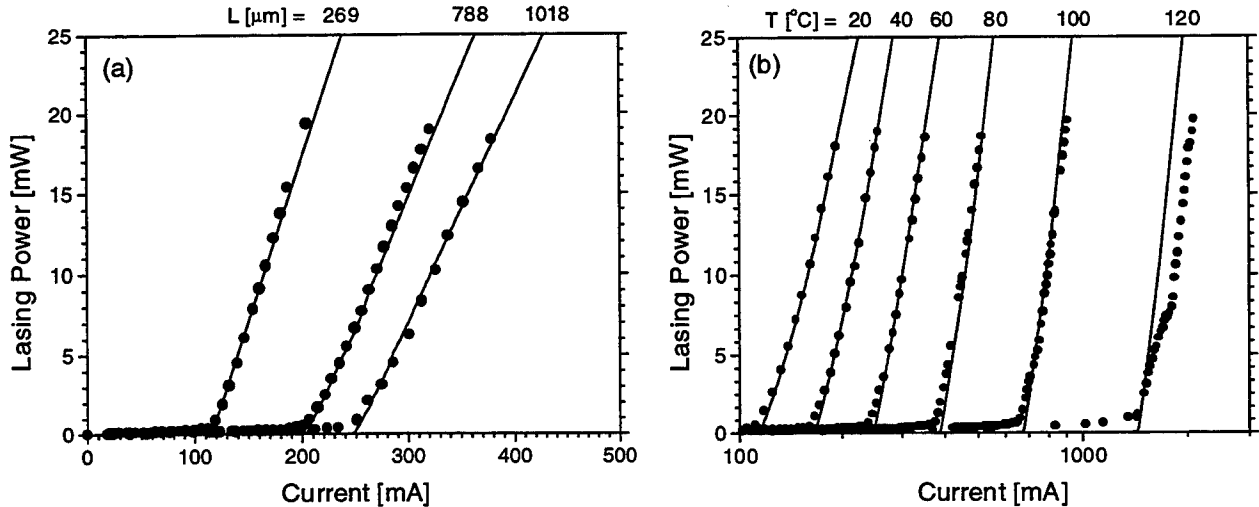


Fig. 2: Pulsed power vs. current characteristics (a) for various laser lengths  $L$  at  $T=20^\circ\text{C}$  and (b) for various stage temperatures  $T$  with  $L=269\mu\text{m}$ . Dots give measurements and lines give simulation results.

Linear fits to the inverse slope efficiencies  $1/\eta_d(L)$  from Fig. 2a are used to extract the internal differential efficiency  $\eta_i = 0.67$  and the internal optical absorption  $\alpha_i = 14\text{cm}^{-1}$ . Since both the loss parameters depend on the cavity length, this method may not give accurate results for short lasers. Measured temperature effects on threshold current  $I_{th}(T)$  and slope efficiency  $\eta_d(T)$  are often described by characteristic temperatures  $T_o$  and  $T_\eta$ , respectively. From Fig. 2b, we find that both parameters show a monotonic decrease with increasing temperature:  $T_o = 55\dots 20\text{K}$ ,  $T_\eta = 180\dots 30\text{K}$ . This simple analysis does not reveal the physical mechanisms behind all these parameters.

PICS3D includes models for all relevant loss mechanisms and a fit to measurements can usually be obtained by careful adjustment of material parameters. However, the correct balance of all physical mechanisms is only found when a variety of measurements is reproduced simultaneously using the same set of material parameters. For our lasers, Fig. 2 demonstrates an excellent agreement of simulation (lines) and experiment (dots). To achieve this, several key parameters had to be identified and adjusted. Internal optical losses are governed by the material parameter  $\kappa$  which gives the local absorption  $\kappa_p p + \kappa_n n$  as function of the local carrier densities ( $n$  – electrons,  $p$  – holes). This parameter includes free carrier absorption as well as intervalence band absorption (IVBA). Holes are assumed to dominate absorption and  $\kappa_p = 120 \times 10^{-18} \text{ cm}^2$  is obtained from the fit in Fig. 2a. This result is in good agreement with published absorption measurements [2]. Carrier losses are dominated by the Auger recombination

rate  $np(C_p p + C_n n)$  which is assumed to be governed by the conduction-hole-hole-split-off (CHHS) process. In good agreement with the literature, a room-temperature Auger parameter of  $C_p = 1.6 \times 10^{-28} \text{ cm}^6 \text{s}^{-1}$  is extracted with an Arrhenius-type temperature dependence (activation energy  $\Delta E_a = 60 \text{ meV}$ ).

Auger recombination is not only the strongest contribution to the threshold current  $I_{th}(T)$ , it also affects our differential internal efficiency  $\eta_i = \eta_s \eta_e \eta_r$  which can be separated into contributions from lateral spreading current ( $\eta_s$ ), vertical carrier escape from the active region ( $\eta_e$ ), and recombination losses within the active region ( $\eta_r$ ) [3]. Fig. 3a shows the calculated MQW electron density  $n(x,y)$  at the laser facet indicating lateral carrier leakage. An enhancement of recombination losses above threshold ( $\eta_r < 1$ ) is often neglected assuming QW carrier density clamping. We recently showed that increasing non-uniformity of the MQW carrier distribution yields enhanced Auger recombination above threshold causing  $\eta_r$  to limit the differential internal efficiency of our lasers [4]. At room temperature, we obtain  $\eta_e = 0.99$ ,  $\eta_s = 0.90$ , and  $\eta_r = 0.74$  giving  $\eta_i = 0.66$  which is in excellent agreement with the  $1/\eta_d(L)$  measurement. Temperature effects on carrier loss mechanisms are shown in Fig. 3b. Carrier spreading slightly declines due to the lower mobility at higher temperature. MQW recombination losses slightly increase but they loose their dominating role to vertical carrier leakage at about  $80^\circ\text{C}$ . The escape of electrons into the p-InP cladding layer dominates the strong reduction of the slope efficiency  $\eta_d(T)$  at higher temperatures.

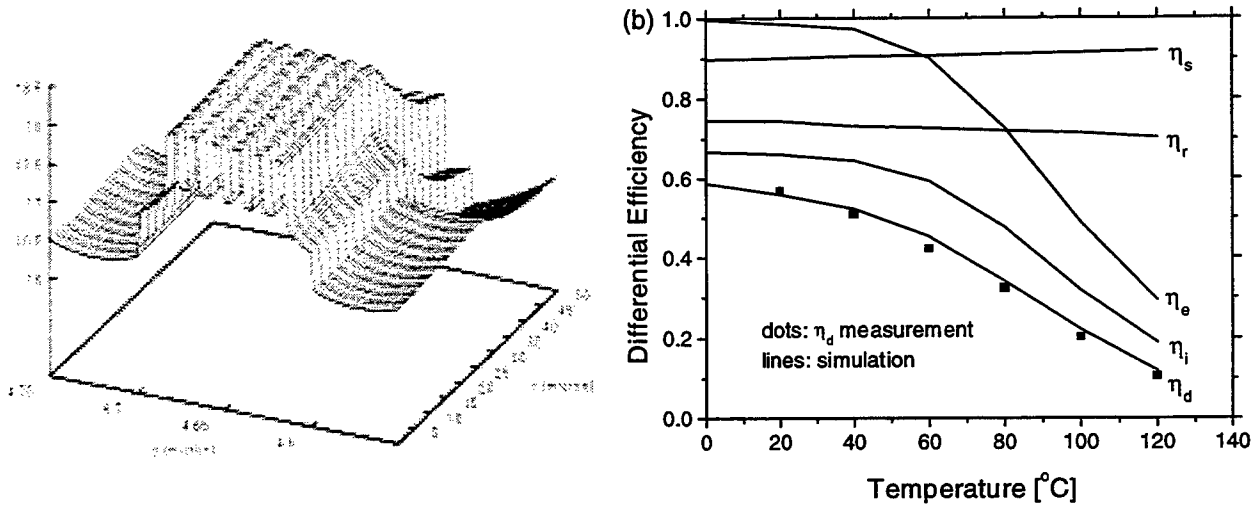


Fig. 3: (a) Logarithm of MQW electron density  $n(x,y)$  [ $\text{cm}^{-3}$ ] at laser facet (y – vertical position, x – lateral distance from y-axis). (b) Differential efficiencies vs. stage temperature (see text).

- [1] PIC3D 4.1.2 by Crosslight Software, Inc., 1998 (details are available at [www.crosslight.ca](http://www.crosslight.ca)).
- [2] I. Joindot and J. L. Beylat, Electr. Lett. **29**, 604 (1993).
- [3] P.M. Snowton and P. Blood, IEEE J. Sel. Top. Quant. Electr. **3**, 491 (1997).
- [4] J. Piprek, P. Abraham, and J. E. Bowers, Appl. Phys. Lett. **74**, 489 (1999).

# Variation of defect-mode transmission in a two-dimensional photonic bandgap crystal

**K. B. Chung**

School of Electronic and Electrical Engineering, Hong Ik University

72-1, Sangsu-dong, Mapo-gu, Seoul, 121-791, Korea

Tel: +82-2-320-1690, Fax: +82-2-320-1119, e-mail: kbchung@wow.hongik.ac.kr

## Introduction

Since they were proposed in 1987 [1], photonic bandgap crystals (PBCs) have attracted considerable attention [2]. The PBC is an artificially-generated periodic dielectric structure that has a photonic bandgap, a band of frequencies in which electromagnetic waves are prohibited from propagating. This concept is in analogy to an electronic bandgap in semiconductors. Within the frequency range of the photonic bandgap, all optical modes are absent, meaning that even spontaneous emission can be suppressed. If a defect is placed inside the PBC, a localized defect-induced electromagnetic mode emerges. The localized mode can accept stimulated emission, thereby allowing the possibility of the formation of a microcavity [3]-[5]. Another promising application is that a series of defects can act as a photonic waveguide [6], [7]. An electromagnetic wave whose frequency lies inside the bandgap can propagate only along the defects, because propagation is inhibited in other directions. By extending the idea of the photonic bandgap waveguide and the localized resonant mode, channel drop tunneling in two parallel waveguides [8] and waveguide intersections with no cross talk [9] were proposed. In both structures, defects with different size or dielectric constant are located in the waveguides to create resonant cavities. In this paper, we investigate the numerically-computed transmission characteristics of various defects with different size, shape, and permittivity in a finite-size two-dimensional photonic bandgap crystal.

## Modeling and Results

The transmission characteristics of the PBC with defects, considered in this work, are numerically computed by the finite-difference time-domain method [10]. Figure 1 shows the two-dimensional computational domain in which the PBC are located. The computational domain is divided into the total-field region and the scattered-field region, and an incident plane wave with a Gaussian envelope in time is given at the connecting interface between the two regions [10]. The incident wave propagates along the  $x$  direction, passes through the PBG, and the transmitted wave is observed as a function of time at the observation point. The outer boundary of the scattered-field region is truncated with the second-order Mur absorbing boundary condition. The photonic bandgap crystal is composed of cylinder rods on a square lattice in air. The radii and permittivity of the cylinders are  $0.2a$  ( $a$  is the lattice constant) and 11.56, respectively. The frequency spectrum of the transmitted wave is divided by that of the incident wave to give the transmission spectra shown in Figures 2 and 3.

When no defects are present inside the PBC, the bandgap ranges from  $0.25 (c/a)$  to  $0.42 (c/a)$  with  $c$  being the speed of light in free space. If one defect (a missing cylinder) is placed, the transmission exhibits a sharp peak around  $0.38 (c/a)$  [4]. This is due to the fact that the periodicity is broken and a localized resonant mode is formed around the defect. Figure 2 shows our computed result of two transmission peaks around  $0.37 (c/a)$  and  $0.39 (c/a)$  within the bandgap, when two empty defects are present as shown in the left figure. These peaks may be understood qualitatively by considering that the microcavities originating from the two defects are coupled together to form a large cavity with a different resonant frequency. If we

place a square defect of size  $0.4a$  and permittivity 11.56, as illustrated in Figure 2, we again obtain two peaks around  $0.39 (c/a)$  and  $0.40 (c/a)$ . It is not clear intuitively how these peaks are formed. We have computed the transmission characteristics of various defects with different size, shape, and permittivity. More computed results will be presented at the talk.

### **Summary**

We have presented the numerically-computed transmission characteristics of various defects with different size, shape, and permittivity in a finite-size two-dimensional photonic bandgap crystal. Particularly, we have found two transmission peaks within the bandgap for two separate empty defects and one square defect.

### **Acknowledgement**

This work was supported by the Korea Institute of Science and Technology as part of the Future Root Technology Research Program.

### **References**

- [1] E. Yablonovitch, "Inhibited spontaneous emission in solid-state physics and electronics," *Phys. Rev. Lett.* **58**, 2059-2062, 1987.
- [2] J. D. Joannopoulos, R. D. Meade, and J. N. Winn, *Photonic Crystals: Molding the Flow of Light*, Princeton University Press, Princeton, New Jersey, 1995.
- [3] E. Yablonovitch, T. J. Gmitter, R. D. Meade, A. M. Rappe, K. D. Brommer, and J. D. Joannopoulos, "Donor and acceptor modes in photonic band structure," *Phys. Rev. Lett.* **67**, 3380-3383, 1991.
- [4] P. R. Villeneuve, S. Fan, and J. D. Joannopoulos, "Microcavities in photonic crystals: Mode symmetry, tunability, and coupling efficiency," *Phys. Rev. B* **54**, 7837-7842, 1996.
- [5] G. Tayeb and D. Maystre, "Rigorous theoretical study of finite-size two-dimensional photonic crystals doped by microcavities," *J. Opt. Soc. Am. A* **14**, 3323-3332, 1997.
- [6] H. Benisty, "Modal analysis of optical guides with two-dimensional photonic band-gap boundaries," *J. Appl. Phys.* **79**, 7483-7492, 1996.
- [7] A. Mekis, J. C. Chen, I. Kurland, S. Fan, P. R. Villeneuve, and J. D. Joannopoulos, "High transmission through sharp bends in photonic crystal waveguides," *Phys. Rev. Lett.* **77**, 3787-3790, 1996.
- [8] S. Fan, P. R. Villeneuve, J. D. Joannopoulos, and H. A. Haus, "Channel drop tunneling through localized states," *Phys. Rev. Lett.* **80**, 960-963, 1998.
- [9] S. G. Johnson, C. Manolatou, S. Fan, P. R. Villeneuve, J. D. Joannopoulos, and H. A. Haus, "Elimination of cross talk in waveguide intersections," *Opt. Lett.* **23**, 1855-1857, 1998.
- [10] A. Taflove, *Computational Electrodynamics: The Finite-Difference Time-Domain Method*, Artech House, Boston, 1995.

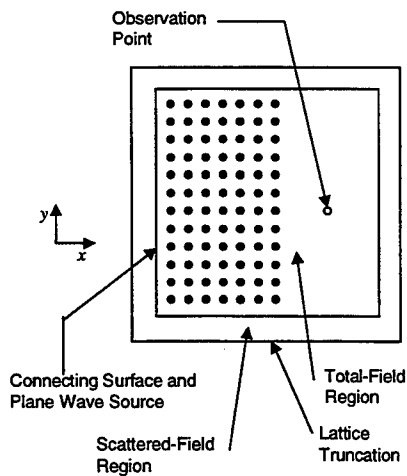


Figure 1 A 2D photonic bandgap crystal and the observation point for the transmitted wave in a 2D computational domain.

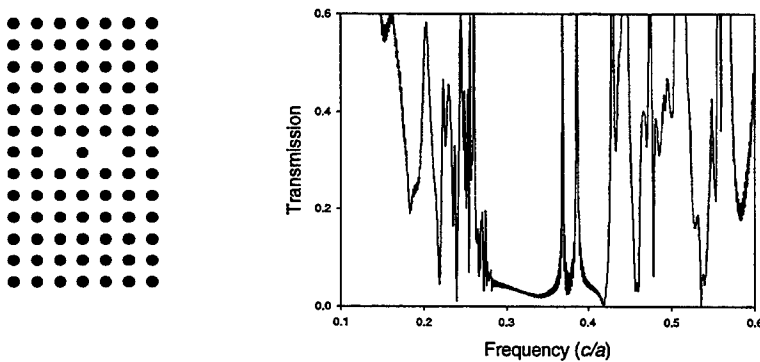


Figure 2 Two defect-mode transmission peaks when two empty defects are present inside the photonic bandgap crystal.

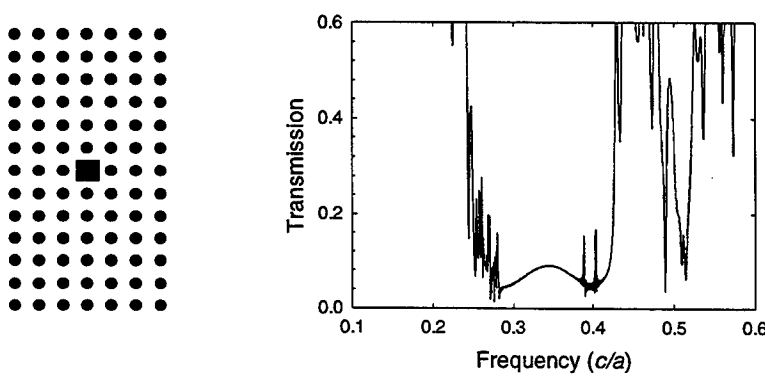


Figure 3 Two defect-mode transmission peaks when one square defect with the same permittivity is present inside the photonic bandgap crystal.

## Optical Waveguiding and Steering in an Active Semiconductor Slab Structure

Xuesong Dong, Patrick LiKamWa  
 School of Optics / CREOL  
 University of Central Florida  
 4000 Central Florida Blvd.  
 Orlando, FL 32816-2700  
 Tel: (407) 823-6861/ 823-6816,  
 Fax: (407) 823-6880

John Loehr, Ron Kaspi  
 Wright-Patterson AFB  
 AFRL/SNDD Bldg 620  
 2241 Avionics Circle  
 W-P AFB, OH 45433-7322

Optical beam steering has a wide range of potential applications in signal processing, optical memory, display, laser scanning, communication multiplexing and free space interconnection etc. In this paper, we present a new approach that achieves beam steering by making use of the refractive index dependence on charged carriers in semiconductors. A doped GaAs/AlGaAs semiconductor structure is used as an active slab waveguide base that is suitable for optical integrated circuits. Current injections are used to control, guide and steer an optical beam between two contact stripes. Strong lateral confinement and waveguiding was experimentally achieved at 100mA current injection and a continuously controlled motion of the output beam was obtained when a current imbalance caused the position of the waveguide to shift sideways.

Owing to the band-filling (Burstein-Moss) effect, the effective optical bandgap energy is increased and the absorption edge shifts toward higher energies when the density of electrons in the conduction band increases. Through the Kramers-Kronig's relationship, the refractive index of the semiconductor, at energies below the bandgap, will experience a decrease when the carrier density increases[1]. A schematic drawing of the device structure is shown in figure 1. When electrical currents are injected through the two contact stripes, the sideways spreading of the injected carriers (as a consequence of finite surface conductance) results in the formation of a narrow localized higher refractive index region bounded by the depressed refractive index regions on either side. Therefore, an electrically controllable single lateral mode channel waveguide is formed, which causes an optical beam launched through the input facet to be guided between the two stripes. By changing the balance of the currents injected through the two stripes, the position of the channel waveguide, and hence the output beam spot can be adjusted continuously between the stripes.

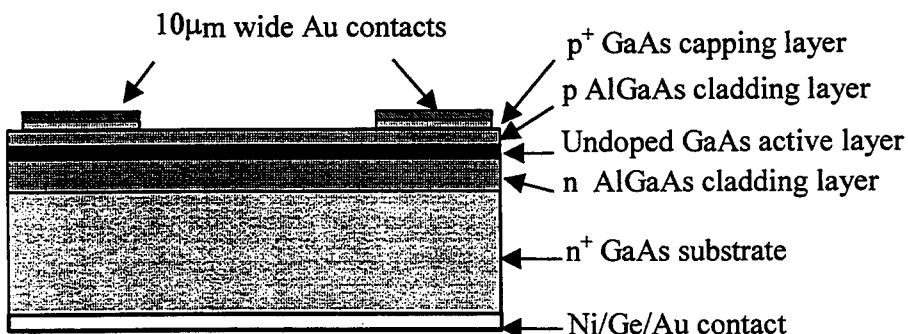


Figure 1. Schematic drawing of the active device structure.

The device structure shown in figure 1. is a standard double heterojunction GaAs/AlGaAs laser diode material consisting of a  $0.2\mu\text{m}$  thick GaAs active core sandwiched between  $\text{Al}_{0.2}\text{Ga}_{0.8}\text{As}$  cladding layers doped n-type and p-type respectively on a  $n^+$  substrate. Currents were injected via two gold stripes each  $10\mu\text{m}$  wide separated by a gap of  $19\mu\text{m}$ . In order to prevent lasing from taking place, the stripes were tilted by  $0.6^\circ$  from the normal to the cleaved facets thus avoiding optical feedback. The overall length of the device was  $710\mu\text{m}$ .

TM polarized light from a cw Ti:sapphire laser tuned to  $906\text{nm}$  was chopped by an acousto-optic modulator and then launched into the device using a laser objective lens ( $f = 4.5\text{mm}$ ) and the output facet was imaged onto a CCD camera using a X20 microscope objective lens. With very low current injection through the stripes, the light was only confined in the vertical direction and a slab mode was observed in GaAs layer. However, when equal currents of  $100\text{mA}$  were injected into each stripe, the output beam was shaped into an elliptical mode in the center of the channel between the stripes. Figure 2 shows the output beam with less than  $1\text{mA}$  and with  $125\text{mA}$  current injection respectively. In addition to the clear evidence of waveguiding and mode confinement, it was also observed that the output intensity increased by a factor of x30

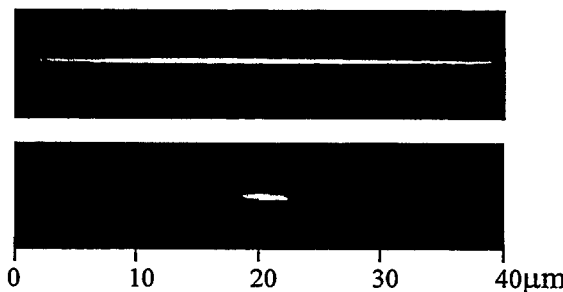


Figure 2. Near field output images.

Upper: Injected current is less than  $1\text{mA}$  on each contact stripe;  
Lower: Injected current is  $100\text{mA}$  on each contact stripe.

due to stimulated gain when the current flowing through each stripe was increased from  $1\text{mA}$  to  $125\text{mA}$ .

By offsetting the balance between the currents through the two stripes, the output spot was readily shifted continuously to either side. For instance, when more current was passed through the left stripe then the current spreads out more from that stripe causing a larger area of depressed refractive index that pushes the optical beam towards the right stripe. Figure 3 shows the effect of asymmetric current distribution between the stripes on the

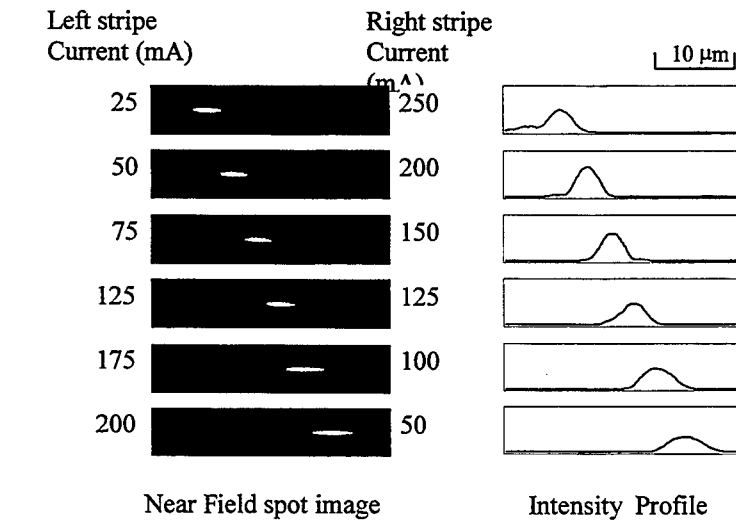


Figure 3. Near field output images with varying currents (left), output intensity profiles obtained with the different currents (right).

position of the output beam. A total shift of the guided spot of up to  $17\mu\text{m}$  at the output facet was recorded in our experiments. Figure 4 shows the measured shift of the spot position from the midpoint between the stripes versus the difference between currents flowing through the two stripes. Theoretical calculation of current spreading underneath the contact stripes[2,3] yields the carrier concentration profile between the stripes. The local minimum in the carrier concentration corresponds to the location of the waveguide. In these calculations, the following parameters were used; sheet conductance  $\sigma = 0.1 \text{ ohm}^{-1}$  and effective radiation recombination  $B_0 = 0.74 \times 10^{-10} \text{ cm}^3/\text{s}$ ). The predicted position of the waveguide is plotted as the solid line in figure 4.

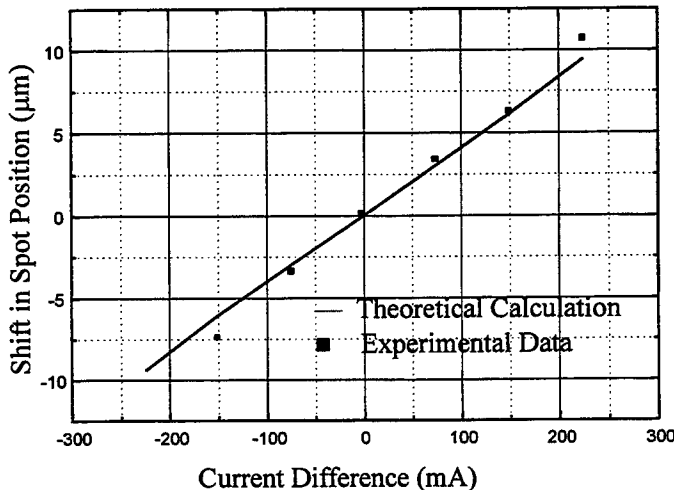


Figure 4. Shift of the near field output spot position as a function of the difference between the currents through the two stripes.

In conclusion, we have demonstrated a novel method of achieving optical beam steering in an active semiconductor slab waveguide structure using electrical injection through two contact stripes.

The work presented in this paper is funded in part by the US Army Research Office under contract/grant number DAAG55-97-1-0161.

#### REFERENCES:

1. Brian R. Bennett, Richard A. Soref, and Jesus A. Del Alamo, "Carrier-Induced Change in Refractive Index of InP, GaAs and InGaAsP" *IEEE J. Quantum Electronics*, vol. 26, no.1, pp 113-122, Jan.1990.
2. W.B. Joyce and S.H. Wemple, "Steady-State Junction-Current Distributions in Thin Resistive Films on Semiconductor Junctions (Solutions of  $\nabla^2V = \pm \exp(V)$ )", *J.Appl.Phys.* , vol.41, no.9, pp. 3818-3830, Aug.1970.
3. C. B. Su and R. Olshansky , "Carrier lifetime measurement for determination of recombination rates and doping levels of III-V semiconductor light sources" *Appl.Phys.Lett.* , vol.41, vo.9, pp 833-835, Nov.1982.



**Integrated Photonics Research**

# **WDM Devices: 3**

**Tuesday, July 20, 1999**

**Bahram Jalali, University of California, Los Angeles, USA**  
Presider

**RTuA**  
**8:30am–10:00am**  
Sierra Madre North

# An All-pass Filter for Tunable Dispersion and Dispersion Slope Compensation

C.K. Madsen, G. Lenz, A.J. Bruce, M.A. Cappuzzo, L.T. Gomez, and R.E. Scotti

Bell Laboratories, Lucent Technologies, 600 Mountain Ave., Murray Hill, NJ 07974

Tel: (908) 582-6095, FAX: (908) 582-4868, email: cmadsen@lucent.com

Chromatic dispersion compensation is critical for high speed lightwave systems. Reconfigurable optical networks introduce a need for tunable dispersion compensation since different routes may have different cumulative dispersions. Another application for tunable dispersion compensation arises because high speed nonlinear systems have an optimal dispersion that depends on the channel power [1]. Thus, fluctuations in the signal power require an adaptable dispersion compensating technique. While the preceding applications address single channel requirements, there is also a need for dispersion slope compensation due to the finite dispersion slope of optical fibers. In this case, different wavelengths have different cumulative dispersions at the receiver and a device capable of applying varying amounts of dispersion compensation to each channel is needed. Currently available compensating techniques involve fixed dispersion introduced by dispersion compensating fibers or chirped Bragg gratings. Recently, a compact, planar waveguide implementation of a multichannel, fixed dispersion compensating filter has been proposed and demonstrated based on the concept of all-pass filters [2,3]. In this paper, we describe a modified ring resonator all-pass filter that is completely tunable using phase shifters. By employing Vernier operation, we are also able to demonstrate a dispersion slope compensating device for the first time.

## Principle of Design:

The new all-pass filter architecture is shown in Fig. 1. The single coupler of previous ring resonator all-pass filters is replaced with a Mach-Zehnder Interferometer (MZI). The MZI is curved to minimize any increase in the feedback path length. The advantage is that a phase shifter can be used to tune the effective coupling  $\kappa_e$  for the feedback path, thus a completely tunable all-pass filter is easily realized with two phase shifters, one to set  $\kappa_e$  and one to tune the resonant wavelength. In the prior work [3], it was necessary to hit the design target for the coupling ratios very accurately. In this case, the tolerances on the couplers  $\kappa$  in the device are substantially relaxed. In Fig. 1b, the MZI path lengths are different by a length  $\Delta L = \pi d_{sep}$  where  $d_{sep}$  is the separation of the MZI arms. The MZI path length difference  $\Delta L$  is much smaller than the feedback path length. The asymmetric MZI allows the flexibility for designing wavelength dependent feedback coupling. The effective coupling for the asymmetric MZI is  $\kappa_e = 4\kappa(1-\kappa)\cos^2\left(\left[2\pi n_g \Delta L / \lambda + \phi_m\right] / 2\right)$ , which can be made equal to zero at a given wavelength by choosing  $\phi_m$  appropriately.

In Fig. 1c, the path lengths are made to be identical by crossing the waveguides. An advantage of the Fig. 1c architecture is that, even for a large  $\kappa_e$ , the individual coupling ratios  $\kappa$  can be small, thus helping to minimize the overall feedback path length. For dispersion compensation, a low finesse cavity is required, which translates to

large  $\kappa_e$ . When the MZI arms are crossed, as in Fig. 1c, the effective coupling is given by  $\kappa_e = 1 - 4\kappa(1-\kappa)\cos^2(\phi_m/2)$ . So, a proper choice of  $\phi_m$  allows  $\kappa_e$  up to 1 to be achieved.

### Experimental Results:

The architecture using the asymmetric MZI was implemented using silica-on-silicon planar waveguides. A core-to-cladding index contrast of 2% was obtained using Ge-doped waveguides. The core size was  $3.5 \mu\text{m}^2$  and the directional coupler lengths were  $477 \mu\text{m}$ . With this index difference, a minimum bend radius of 1.2 mm and a filter FSR of 20 GHz were achieved. The separation of the MZI arms was  $50 \mu\text{m}$ , resulting in a FSR of 1280 GHz for the asymmetric MZI. Thin film chromium heaters were deposited over sections of the ring and MZI for phase shifters. The minimum spacing between the MZI arms is dominated by the thermal isolation, since one arm must be heated relative to the other one.

The spectral magnitude and group delay response were measured for a single ring. A tunable external cavity laser was swept in 5 pm steps. The phase shift group delay technique, employing a  $\text{LiNbO}_3$  intensity modulator and a heterodyne lock-in detector, was used to measure both the magnitude and group delay. The results are shown in Fig. 2. The frequency response is plotted relative to a center wavelength of 1490 nm. The effective coupling ratio is a maximum at  $f-f_0=470 \text{ GHz}$  and decreases with increasing frequency through the region shown in Fig. 2. A good fit to the data was achieved using the theoretical model of an all-pass filter with the coupler replaced by the MZI. The fitted parameters for the roundtrip loss and coupling ratio were 1.2 dB and  $\kappa=0.43$ , respectively. To demonstrate the dispersion compensating capability of the device, a linear fit to the passband group delay for several channels was performed. The channel center frequencies are indicated by the vertical lines. For the extreme channels in Fig. 2, the dispersions were  $-378 \text{ ps/nm}$  over a 7.5 GHz passband and  $-3026 \text{ ps/nm}$  over a 3.4 GHz passband. As expected, the passband decreases for the larger dispersions. By using multiple stages, the passband width can be increased for a given dispersion [3]. The passband group delay ripple for the lowest and highest frequency channels was  $\pm 2 \text{ ps}$  and  $\pm 5 \text{ ps}$ , respectively.

In summary, two completely tunable all-pass filter architectures using phase shifters were presented. The ring resonator with the asymmetric MZI is the first demonstration of an all-pass filter capable of dispersion slope compensation. All-pass filters are also key elements in bandpass filters with flat passbands and large stopband rejections having a small number of filter stages [4,5]. Thus, tunable bandpass filters will also be realizable using the new all-pass filter architectures discussed in this paper.

### References:

1. B. Eggleton, J. Rogers, P. Westbrook, T. Strasser, T. Nielsen, P. Hansen and K. Dreyer, "Electrically tunable power efficient dispersion compensating fiber Bragg gratings for dynamic operation in nonlinear lightwave systems," Optical Fiber Communication Conference and the International Conference on Integrated Optics and Optical Fiber Communication. San Diego, CA, Feb. 23-26, 1999, PD27.
2. C. Madsen and G. Lenz, "Optical All-Pass Filters for Phase Response Design with Applications for Dispersion Compensation," *IEEE Photonics Technol. Lett.*, vol. 10, no. 7, pp. 994-996, 1998.
3. C. Madsen, G. Lenz, A. Bruce, M. Capuzzo, L. Gomez, T. Nielsen, L. Adams, and I. Brener, "An all-pass filter dispersion compensator using planar waveguide ring resonators," Optical Fiber Communication Conference and

the International Conference on Integrated Optics and Optical Fiber Communication. San Diego, CA, Feb. 23-26, 1999, p. FE6.

4. C. Madsen, "Efficient Architectures for Exactly Realizing Optical Filters with Optimum Bandpass Designs," *IEEE Photonics Technol. Lett.*, vol. 10, no. 8, pp. 1136-1138, 1998.
5. C. Madsen, "A multiport band selector with inherently low loss, flat passbands and low crosstalk," *IEEE Photon. Technol. Lett.*, vol. 10, no. 12, pp. 1766-1768, 1998.

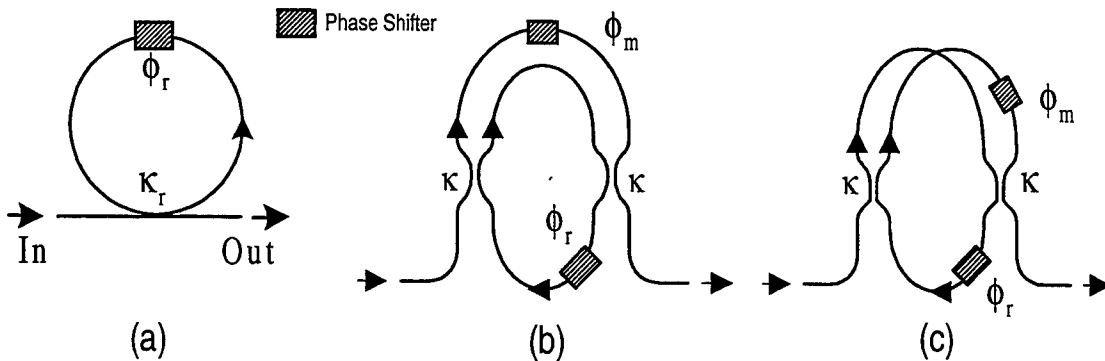


Fig. 1. (a) Ring resonator all-pass filter with a fixed coupling ratio, and fully tunable ring resonator all-pass filters with (a) an asymmetric MZI and (b) a symmetric MZI.

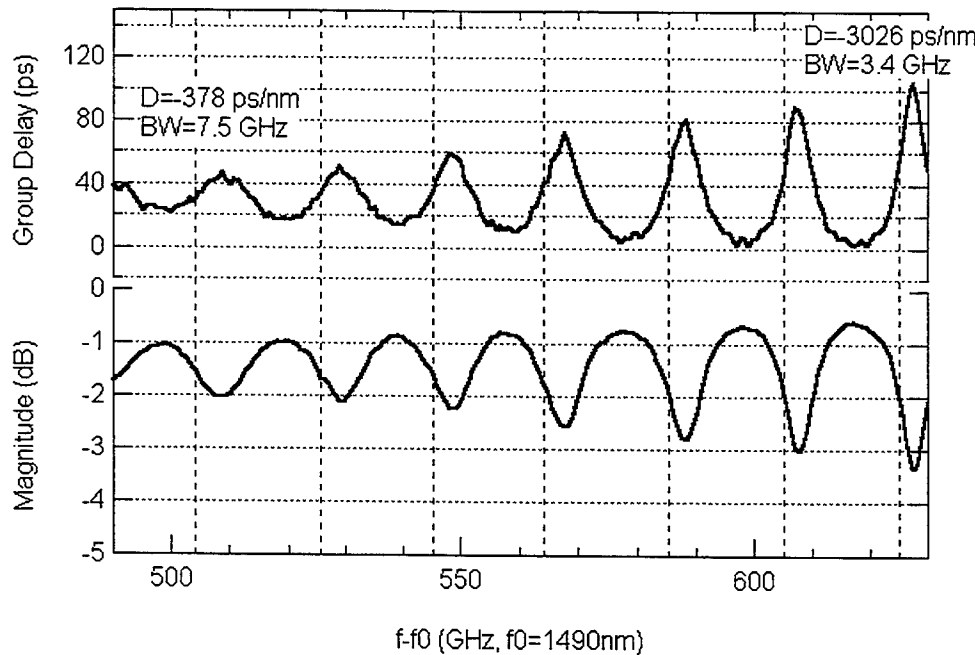


Fig. 2. Measured spectral response magnitude and group delay of a tunable all-pass filter with an asymmetric MZI. The dispersion and passband width (BW) are shown for the extreme channels.

# A Novel Two-in-One Arrayed Waveguide Grating Mux/Demux

Hyoun-Soo Kim, Yeong-Gyu Lee, Dongkyoon Han, and Hyung-Seung Song  
 Applied Optics Res. Group, Samsung Electronics Co., Ltd.  
 Suwon PO Box 105, Kyungki-Do, Rep. of Korea, 440-600  
 Tel) 82-331-280-9646, fax) 82-331-280-9639

## I. Introduction

Commercially available integrated-optic MUXes/DEMUXes are fabricated using the PLC(planar lightwave circuit) technology[1]. Unlike micro-optic and fiber-optic type MUX/DEMUXes[2], in which the cost of the devices increase super-linearly with increasing number of ports, the cost of integrated-optic AWGs increase sub-linearly since most of the cost arises during packaging. Therefore, the integrated-optic type WDM MUX/DEMUX, or AWG, seems more competent for application in multi-port WDM systems having 16 or more wavelength ports. In addition, the semiconductor processing technology used to fabricate integrated-optic AWGs makes it possible to reduce the cost by mass production.

In most WDM systems the MUX and DEMUX are used in pairs. A WDM system usually has two separate lines, a working line and a protection line. Since each line has a MUX for a transmitter and a DEMUX for a receiver, the system needs two MUXes and two DEMUXes. An ADM (Add-Drop Multiplexers) in a WDM node also requires a pair of AWGs for the add/drop operation and an additional pair for protection. Meanwhile, a conventional AWG can be used in either direction[3] but can only be dedicated to only one direction when actually used in the system. In this paper, we propose and demonstrate a novel TIO (two-in-one) AWG which operates in both directions, simultaneously, which will reduce the number of devices used in WDM systems by half. The proposed TIO AWG has two extra ports, one on each end of the AWG, designated to be either the input or the output depending on the desired function.

## II. Principle of Operation

For simplicity, we restrict our discussion to a TIO AWG used as a DEMUX. An 8 channel TIO AWG DEMUX has 9 ports on each side as illustrated in Fig. 1. The extra port at the center of the eight output ports is designated to be the input port for DEMUX operation in the opposite direction. Two sets, with each set consisting of an input port on one end and 8 output ports on the other end, can function independently so that both sets can be used as two DEMUXes, simultaneously.

A schematic of the mask layout is shown in Fig. 2. Equally separated 8 output waveguides are placed at one end of each star coupler. An extra waveguide is placed at the center in between the fourth and fifth waveguides. The distance between the input waveguide and its adjacent waveguides, the fourth and fifth waveguides, are kept far enough not only to avoid mode coupling at the vicinity of the star coupler, but also to ensure acceptable crosstalk levels. Optical signals launched through the center waveguide from one end of the AWG will be DEMUXed into the 8 output waveguides on the other end with corresponding wavelengths.

Although the principle of operation of a TIO AWG was explained for its DEMUX application only, it is important to note that the TIO AWG can also be utilized as a pair of MUXes or a MUX and DEMUX as a pair, operating simultaneously.

## III. Experiment

A silica based 8 channel TIO AWG with a waveguide cross-section of  $6.5\mu\text{m} \times 6.5\mu\text{m}$  and  $\Delta n=0.75\%$  was fabricated. Silica layers were deposited by FHD(Flame Hydrolysis Deposition) on a silicon wafer. The core layer was etched using an ICP(Inductively Coupled Plasma) system at an etching speed of 450nm/min[4]. After the overcladding layer was deposited, the wafer was diced and the end-faces were

polished. The polished chip was aligned and pigtailed with connectorized fiber blocks, and finally assembled for measurement as shown in Fig. 3.

The measured transmission spectra of the fabricated TIO AWG as DEMUXes in both directions are shown in Fig. 4. An HP8168F tunable laser source was used as the input light source and an HP86120B multi-wavelength meter along with a lightwave multi-meter were used to obtain accurate peak wavelengths and insertion loss at each channel. The results show that the peaks in the two spectra are almost matched and the wavelength differences between corresponding peaks are <0.05nm. Insertion losses were measured to be 5.2~7.1dB in one direction and 5.1~6.3dB in the opposite direction. Adjacent channel crosstalks between the center port and its adjacent ports were 20.4dB and 19.9dB. Adjacent channel crosstalks between the 8 remaining ports were measured between 19.9~24.5dB. The measured insertion losses and crosstalks can be further improved by optimizing the design and the fabrication process. Isolators may be used to eliminate the small amount of backward traveling light, caused by finite crosstalk when the TIO AWG is used as a MUX/MUX or a DEMUX/DEMUX.

As a final experiment, an ASE(amplified spontaneous emission) of an EDFA(Erbium Doped Fiber Amplifier) was launched into a center port, DEMUXed, looped-back, and MUXed into the other center port as illustrated in Fig. 5(a). The resulting spectrum is shown in Fig. 5(b). The big lobe at the center of the spectrum accounts for the light directly transmitted from the input center port to the output center port. The 8 peaks in the spectrum experienced two passes through the AWG resulting in a greater loss than the center peak.

#### IV. Conclusion

A novel TIO AWG was proposed for the first time. We fabricated an 8 channel TIO AWG and demonstrated simultaneous operation of two AWGs in a single chip. The TIO AWG uses the same fabrication process as the conventional AWGs so that there is virtually no added cost associated with the two-in-one feature. Measured characteristics clearly verified the concept of the proposed TIO AWG. Considering that the MUX and DEMUX are almost always used in pairs in WDM systems, we strongly believe that the TIO AWG will drastically reduce the total cost of MUXes and DEMUXes used in the systems as well as considerable savings in space and power consumption.

#### References

- [1] M. Kawachi, Opt. And Quantum Electron., vol. 22, pp. 391-416 (1990)
- [2] C. Huang, H. Luo, S. Xu, and P. Chen, in Conference on Optical Fiber Communication, 1999, Technical Digest Series, paper TuH2
- [3] W. Lin, H. Li, Y. J. Chen, M. Dagenais, and D. Stone, IEEE Photon. Technol. Lett., pp. 1501-1503 (1996)
- [4] S. Jung, H. Song, D. Kim, and H. S. Kim, Thin Solid Films, to be published

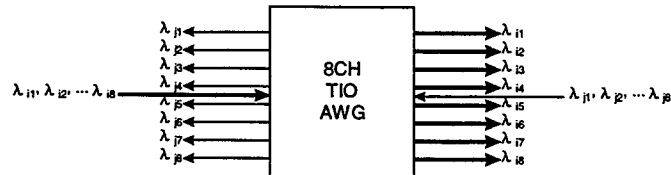


Fig. 1. Schematic concept of an 8 channel TIO AWG DEMUX/DEMUX

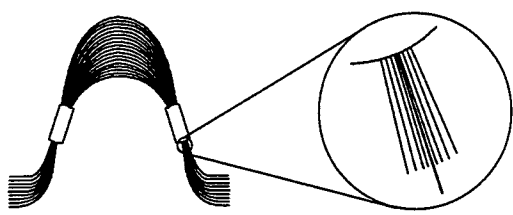


Fig. 2. Schematic mask layout of proposed TIO AWG

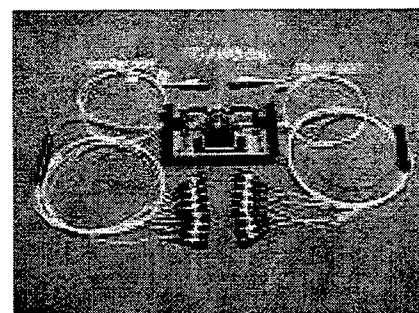
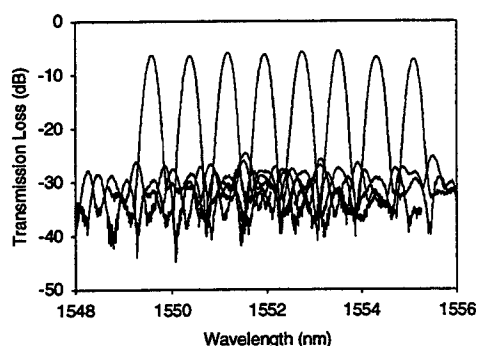
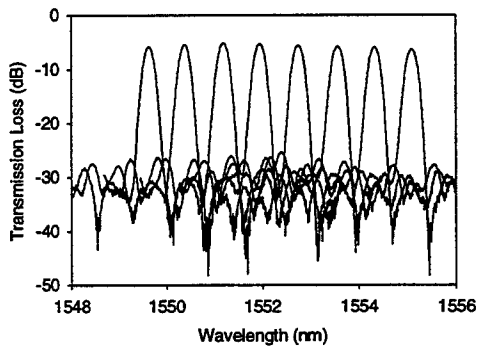


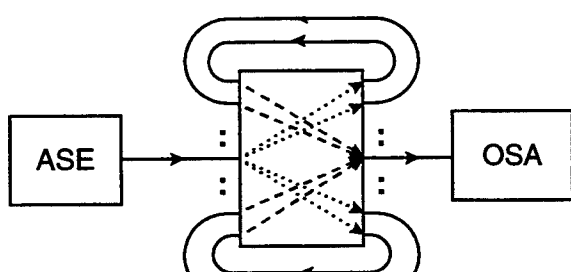
Fig 3. Photograph of the packaged TIO AWG



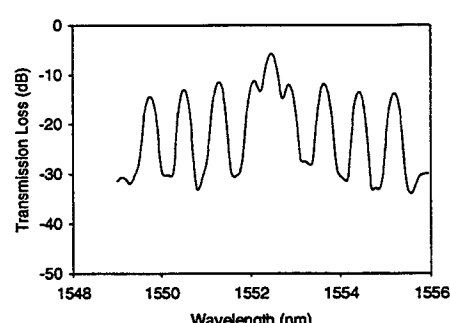
(a)



(b)

Fig. 4. (a) Transmission spectrum of TIO AWG using the left input  
(b) Transmission spectrum using the right input

(a)



(b)

Fig. 5. (a) Experimental setup for TIO AWG as a DEMUX/MUX pair  
(b) Output spectrum

# IMPROVEMENTS IN THE YIELD OF ARRAYED WAVEGUIDE DEMULTIPLEXERS BY THE USE OF TRANSITION OFFSETS

**Stephen Day, James Whiteaway and Alan Fielding**

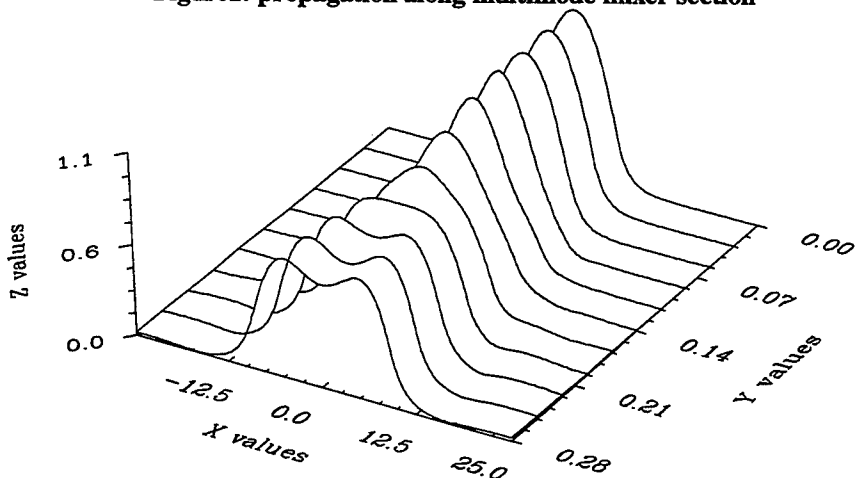
Nortel Networks, London Rd., Harlow, Essex, CM17 9NA, Tel (+44) 1279 402785

## ***Introduction***

The arrayed waveguide grating (AWG) demultiplexer is increasingly being used as the demultiplexer of choice in high density wavelength division multiplexed systems. In its simplest form as a 1 to N demultiplexer, the device consists of a single input channel waveguide, and N output waveguides which are inter-connected via two free space regions and an array of waveguides with a linearly varying path length. The channel spacing can be set as required by designing the array with an appropriate path length difference. The transmission response against wavelength shows a curve that is approximately gaussian in nature, with a figure of merit (FOM) between the 0.5 dB width and the 30 dB width of 0.14, independent of channel spacing. As system channel spacings continue to reduce, there is a need to increase the bandwidth figure of merit beyond that of a standard AWG. Various techniques have been proposed to increase the bandwidth FOM, such as parabolic horn, y junctions, multimode mixer and double pass<sup>1,2,3</sup>.

We have recently been developing 16 channel 100 GHz devices using multimode mixers as the passband broadening element. The components have been produced using silica on silicon technology with a 5.5  $\mu\text{m}$  by 7  $\mu\text{m}$  waveguide, a refractive index step  $\Delta n$  of 0.011 and 5 mm bend radii. In the multimode mixer, light is launched from the fundamental mode of an input waveguide into the fundamental and second order modes of a wider multimode waveguide. The fundamental and second order modes propagate along the wider mixer section with different phase velocities until they are in antiphase. At this point a double peaked distribution with a dip in the centre is formed, as shown in figure 1 which illustrates propagation along the mixer section.

**Figure1: propagation along multimode mixer section**



This double peaked distribution is transferred to the output waveguides by the two free space regions that expand and focus the distribution and the interconnecting waveguide array, which introduces a phase tilt. The overlap of the double peaked distribution with the fundamental mode of the output waveguide produces a wavelength flattened response, although with higher loss than the unflattened device. Using this approach the bandwidth FOM can be increased from 0.14 to 0.30 for a 2 dB loss penalty. We have successfully produced flattened devices based on this technique as illustrated in

figure 2a. However, a proportion of the devices we produced had a slope across the top of the transmission curve, an example of which is shown in figure 2b. A range of slopes was measured for similar devices, with both positive and negative values being observed.

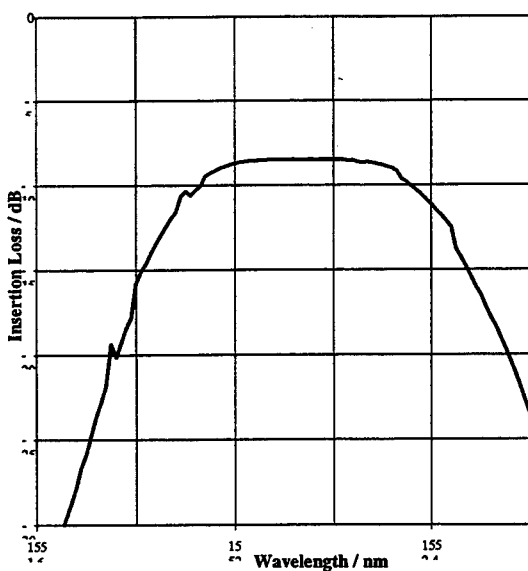


**Figure 2a**  
**Figure 2: passband flattened WDM's without slope and with slope across the response**

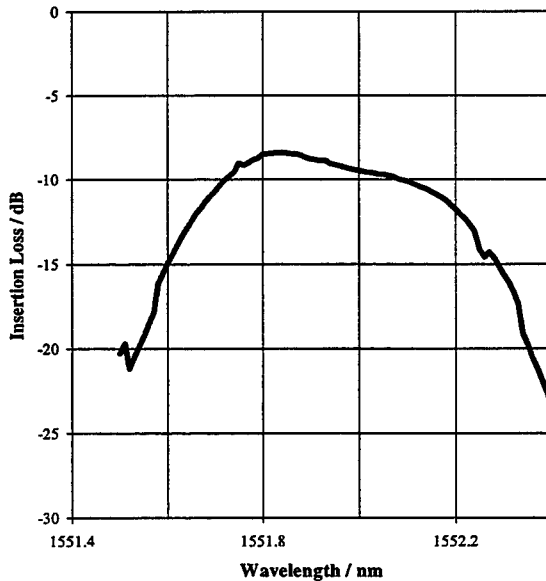


**Figure 2b**

To help to understand the origin of the slope, a device was sectioned at various points along its length so that the field distribution at that point could be imaged onto an infra red camera. Using this technique, it was observed that the tilted wavelength response was originating within the multimode mixer section. Having identified the region of the device which was causing the slope, beam propagation modelling was used to develop an understanding of the effect. In particular, we wanted to understand how both positive and negative slopes could be produced from nominally identical devices. A beam propagation model was set up to study the multimode mixer together with its curved input waveguide. The curved waveguide was represented by the use of a conformal transform.

From these simulations, it was observed that oscillations are set up at the transition from a straight waveguide to a curved waveguide. These oscillations propagate through to the multimode mixer section and cause some first order mode to be excited within the multimode mixer section. It is the presence of this first order mode which causes the output field of the multimode mixer to have a slope. Changing the waveguide width in the model showed that the oscillation period was very sensitive to waveguide width. A change in the oscillation period changes the distribution of the field launched into the multimode mixer, and consequently its output distribution, resulting in either positive or negative slopes across the passband.

Hence the modelling explained the reason for the slope across the passband. It also explained the sensitivity of the oscillation period to the waveguide parameters and therefore why it was possible to get a range of devices exhibiting both positive and negative slopes together with some devices with minimal slopes. The next step was to use the model to eliminate the oscillations and to design devices without slopes across their passbands. Four methods were considered :-

- Inserting sufficient straight waveguide after the curve to allow the oscillations to decay. It was found that even after 20 mm, little discernible decay in the oscillation had occurred.
- Reducing the waveguide width to prevent the transmission of higher order modes. It was not found possible to eliminate the oscillations using this approach.
- Increasing the radius of curvature to reduce oscillations. As the radius of curvature was increased then the oscillation amplitude reduced, however even at 20 mm bend radius oscillations were present.

d) Introducing a waveguide offset between the curved and the straight waveguides. The use of transition offsets was found to be the most effective method of eliminating the oscillations. As the offset increased from 0  $\mu\text{m}$  to 0.35  $\mu\text{m}$  the oscillations reduced to zero before increasing for greater offsets.

A test mask was designed which contained 26 AWG devices using offsets from 0  $\mu\text{m}$  to 0.5  $\mu\text{m}$ , the devices were designed to be 4 channel devices with a 400 GHz channel spacing to enable a large number of devices to be produced on a single 4 inch wafer. The devices were measured and the slope across the central portion of the passband was calculated in dB/nm.

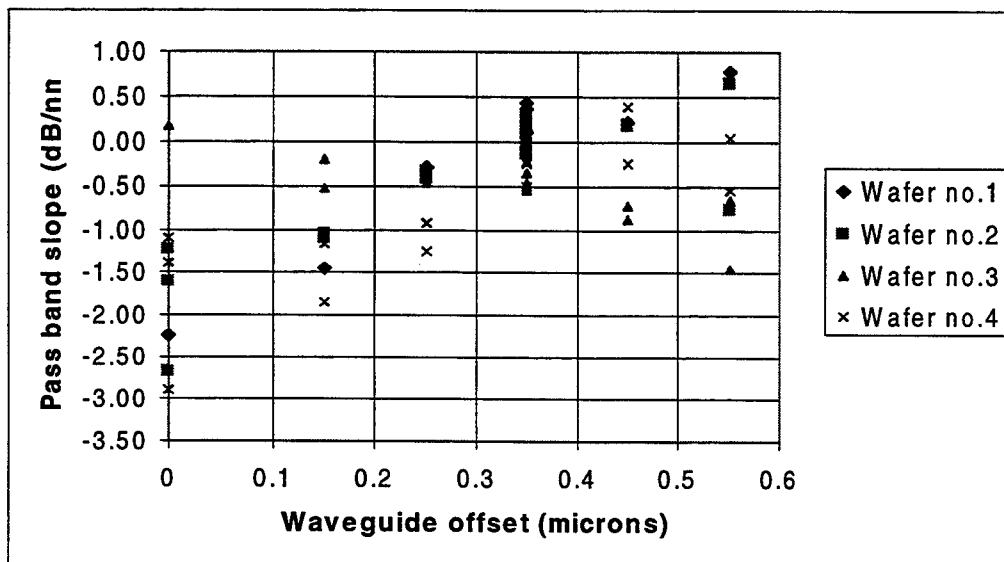


Figure 3: passband flatness of devices from test mask

Figure 3 shows the results of these measurements. From the results it can be seen that initially with zero offset there is a large spread in the magnitude of the slope, as predicted by the modelling. As the offset increases the spread in the slope magnitude reduces until 0.35  $\mu\text{m}$  offset, where there is very little spread and the slope is close to zero. This is again in good correlation with the model predictions. As the offset is increased further beyond 0.35  $\mu\text{m}$ , the spread in the measured slopes increases again. Hence by the use of transition offsets, we have been able to significantly improve the yield of arrayed waveguide devices with low slope across the passband.

### Conclusions

A model has been developed based on the beam propagation method, which explains the initial results of variable wavelength slope obtained on 16 channel bandpass flattened AWG components. The model has been further used to significantly understand the cause of slope within the passband. A test mask has been designed and devices produced. The test mask results show excellent correlation with model predictions and enable passband flattened components to be produced with a higher yield than was previously possible. These results are currently being applied to a range of devices including 50 GHz and 100 GHz AWG devices.

### References

- 1) K. Okamamoto et al, Flat spectral response arrayed waveguide grating multiplexer with parabolic waveguide horns; Electronics Letters 29 th August 1996 V32 n 18
- 2) J.B.D Soole et al; Use of multimode interference couplers to broaden the passband of dispersive integrated WDM filters; Integrated Photonics Research 96;April 1996 ;p44-46
- 3) G.H.B Thompson et al; An original low-loss and pass-band flattened silica on silicon planar wavelength demultiplexer; OFC 98; February 1998 ; p77

## An Infinite Impulse Response Multichannel Frequency Selector

C.K. Madsen

Bell Laboratories, Lucent Technologies, 600 Mountain Ave., Murray Hill, NJ 07974  
Tel: (908) 582-6095, FAX: (908) 582-4868, email: cmadsen@lucent.com

Optical add/drop filters for dense WDM systems must satisfy strict requirements on the passband flatness so that many filters can be cascaded in the system without reducing the passband width. In addition, the filters must meet tight requirements on crosstalk. The crosstalk may result from leakage of adjacent or nonadjacent channels into the output for a particular channel. A greater concern is leakage of a dropped channel into the through path that may interfere with an added channel at the same wavelength later in the system. A periodic filter capable of selecting multiple channels within one Free Spectral Range (FSR) that are not necessarily adjacent is discussed in this paper. Previously, a selector with a transversal filter structure with feedforward paths was demonstrated [1], so the selector had a finite impulse response (FIR). The major drawback was the achievable crosstalk for a given number of filter stages and channels. In this paper, an architecture and design algorithm is presented for an infinite impulse response (IIR) filter based on optical all-pass filters [2]. Traveling (rings) or standing wave (like a Fabry-Perot cavity) feedback paths may be used to implement the all-pass filters. Micro-cavity rings [3,4] will enable the ring architectures to achieve FSRs suitable for bandpass filter applications in current WDM systems.

Previous work showed that single-passband (per FSR) elliptic, Chebyshev and Butterworth designs can be implemented using optical all-pass filters in a Mach-Zehnder interferometer (MZI) [5]. The design capability is now extended to allow multiple passbands per FSR so that several wavelengths, not necessarily adjacent, can be selected for adding or dropping in a similar fashion to the FIR frequency selector. The IIR multi-wavelength selector uses two all-pass filters,  $A_1(\omega)$  and  $A_2(\omega)$ , to construct two bandpass functions,  $H_1(\omega)$  and  $H_2(\omega)$ , as shown in Fig. 1. Each function is represented in the Z-domain as a ratio of polynomials as follows:

$$H_1(z) = \frac{N_1(z)}{D(z)} \quad \text{and} \quad H_2(z) = \frac{N_2(z)}{D(z)} \quad (1)$$

$$A_1(z) = \frac{D_1^R(z)}{D_1(z)} \quad \text{and} \quad A_2(z) = \frac{D_2^R(z)}{D_2(z)} \quad (2)$$

where  $D(z)=D_1(z)D_2(z)$  and the superscript R denotes the reverse polynomial. The frequency response is found by evaluating (1) and (2) at  $z = e^{j\omega T}$ , where the unit delay T is related to the nominal feedback path length L and group index  $n_g$  by  $T = c / n_g L$ . The numerator polynomials  $N_1(z)$  and  $N_2(z)$  were previously assumed [5] to have either even or odd symmetry. We now remove the symmetry requirement so that multiple passbands can be obtained. The decomposition into all-pass functions is written as follows:

$$H_1(z) = \frac{1}{2} [A_1(z) + A_2(z)] \quad \text{and} \quad H_2(z) = \frac{e^{-j\phi}}{2} [A_1(z) - A_2(z)] \quad (3)$$

The new phase term  $\phi$  is discussed below. Given a desired  $H_1(\omega)$  response, the  $H_2(\omega)$  response can be found from power conservation, i.e.  $|H_1(\omega)|^2 + |H_2(\omega)|^2 = 1$ . A simple way to determine  $H_1(z)$  and  $H_2(z)$  is by finding suitable zeros. If we multiply the power conservation relationship by  $|D(\omega)|^2$  and divide by  $|N_1(\omega)|^2$ , we obtain [6]:

$$1 + \frac{|N_2(\omega)|^2}{|N_1(\omega)|^2} = \frac{|D(\omega)|^2}{|N_1(\omega)|^2} = \frac{1}{|H_1(\omega)|^2} \quad (4)$$

In the Z-domain,  $K(z) = N_2(z)/N_1(z)$  is called the characteristic function. By evaluating  $K(z)$  on the unit circle, the magnitude response  $|H_1(\omega)|^2$  is defined. Similarly, dividing by  $|N_2(\omega)|^2$  instead of  $|N_1(\omega)|^2$ , the magnitude response  $|H_2(\omega)|^2$  is obtained. The characteristic function for  $H_2(\omega)$  is  $1/K(z)$ . Thus, the characteristic function, which is defined solely by the zeros of the numerator polynomials, defines the magnitude responses for both  $H_1(\omega)$  and  $H_2(\omega)$ .

As an example, a 16<sup>th</sup>-order filter was designed to drop channels 2, 3 and 5 out of 8 channels distributed evenly across the FSR. Since 100% transmission is desired for the passband frequencies of one response, the zeros of the opposite response were located on the unit circle across the respective stopbands for an initial guess. The solution was refined by numerical optimization to yield the spectral responses shown in Fig. 2. For comparison, the response for a 16<sup>th</sup>-order FIR filter was also calculated and optimized. The target was to achieve a 30 dB stopband rejection assuming a channel width equal to 30% of the channel spacing. The channel widths are indicated by the shaded regions. For the drop-response, the IIR selector exhibits a much flatter, wider passband and significantly better rejection. For the through-response, the FIR filter offers very little rejection, which limits its use as a multichannel add/drop filter. The IIR selector's through-channel response, on the other hand, yields good rejection.

Once satisfactory zeros are identified, the design algorithm is completed by finding  $D(z)$ ,  $A_1(z)$  and  $A_2(z)$ . The design parameters for an optical ring (or cavity) implementation are obtained from the all-pass responses. It is important to note that only the magnitudes of  $H_1(\omega)$  and  $H_2(\omega)$  are determined by Eq. (4), leaving a constant phase for each response undetermined. Since only the relative phase is important, let  $\phi$  represent the phase difference so that the all-pass functions are now defined as follows:

$$A_1(z) = H_1(z) + e^{j\phi} H_2(z) \quad \text{and} \quad A_2(z) = H_1(z) - e^{j\phi} H_2(z) \quad (5)$$

From [5], we know that if  $N_2(z)$  has odd order and symmetry,  $\phi=0$ . If it has even order and symmetry, then  $\phi=\pi/2$ . For the general case, we must determine  $\phi$ . Setting  $|A_1(\omega)| = |A_2(\omega)| = 1$  at an arbitrary frequency, say  $z=1$ , results in  $|N_1(1) + e^{j\phi} N_2(1)| = |N_1(1) - e^{j\phi} N_2(1)|$ . Let the phase of  $N_1(1)$  and  $N_2(1)$  be represented by  $\eta_1$  and  $\eta_2$ , then  $\phi$  is given by

$$\phi = \eta_1 - \eta_2 + \frac{\pi}{2}(2m+1) \quad (6)$$

where  $m$  is an integer. The roots of the denominator polynomials can now be determined by multiplying the relationships in (5) by  $D(z)$  to obtain

$$N_1(z) + e^{j\phi} N_2(z) = D_1^R(z) D_2(z) \quad (7)$$

$$N_1(z) - e^{j\phi} N_2(z) = D_1(z) D_2^R(z) \quad (8)$$

For Eq. (7), the minimum-phase roots are used to define  $D_2(z)$  and the maximum phase roots to define  $D_1^R(z)$ . A scale factor is then determined for  $N_1(z)$  and  $N_2(z)$  to make  $|H_1(\omega)|^2 + |H_2(\omega)|^2 = 1$ . The denominator of  $A_1(z)$  and  $A_2(z)$  are fully defined as well as the roots of the numerators. There is, however, a constant phase  $\alpha$  that must be determined. The phase is found by evaluating (5) at a particular frequency, for example  $z=1$ .

$$e^{j\alpha} A_1(1) = e^{j\alpha} \frac{D_1^R(1)}{D_1(1)} = \frac{N_1(1)}{D(1)} + e^{j\phi} \frac{N_2(1)}{D(1)} \quad (9)$$

$$e^{-j\alpha} A_2(1) = e^{-j\alpha} \frac{D_2^R(1)}{D_2(1)} = \frac{N_1(1)}{D(1)} - e^{j\phi} \frac{N_2(1)}{D(1)} \quad (10)$$

The relative phase between the MZI arms is  $2\alpha$ . The coupling (or reflection strengths for the cavity design) and phases for each all-pass filter are then determined as discussed in [2]. In our example, the all-pass filters have different orders,  $A_1(z)$  is ninth-order while  $A_2(z)$  is seventh-order.

In summary, an all-pass filter decomposition algorithm was defined for the design of multiple-passband filters. Two phase terms,  $\phi$  and  $\alpha$ , were added over the single-passband algorithm, and the characteristic function was introduced. The resulting IIR multichannel frequency selector has substantially better passband flatness and stopband rejection than is possible with an FIR filter having the same number of stages.

**References:**

1. K. Sasayama, M. Okuno, and K. Habara, "Photonic FDM Multichannel Selector Using Coherent Optical Transversal Filter," *J. Lightw. Technol.*, vol. 12, no. 4, pp. 664-669, 1994.
2. C. Madsen and G. Lenz, "Optical All-Pass Filters for Phase Response Design with Applications for Dispersion Compensation," *IEEE Photonics Technol. Lett.*, vol. 10, no. 7, pp. 994-996, 1998.
3. J. Foresi, B. Little, G. Steinmeyer, E. Thoen, S. Chu, H. Haus, E. Ippen, L. Kimerling, and W. Greene, "Si/SiO<sub>2</sub> micro-ring resonator optical add/drop filters," CLEO Conf. Baltimore, MD, May 18-23, 1997, pp. CPD22-2.
4. D. Rafizadeh, J. Zhang, S. Hagness, A. Taflove, K. Stair, and S. Ho, "Nanofabricated waveguide-coupled 1.5-  
um microcavity ring and disk resonators with high Q and 21.6-nm free spectral range," CLEO Conf. Baltimore,  
MD, May 18-23, 1997, pp. CPD23-2.
5. C. Madsen, "Efficient Architectures for Exactly Realizing Optical Filters with Optimum Bandpass Designs," *IEEE Photonics Technol. Lett.*, vol. 10, no. 8, pp. 1136-1138, 1998.
6. A. Willson and H. Orchard, "Insights into digital filters made as the sum of two all-pass functions," *IEEE Trans. Circuits and Systems*, vol. 42, no. 3, pp. 129-137, 1995.

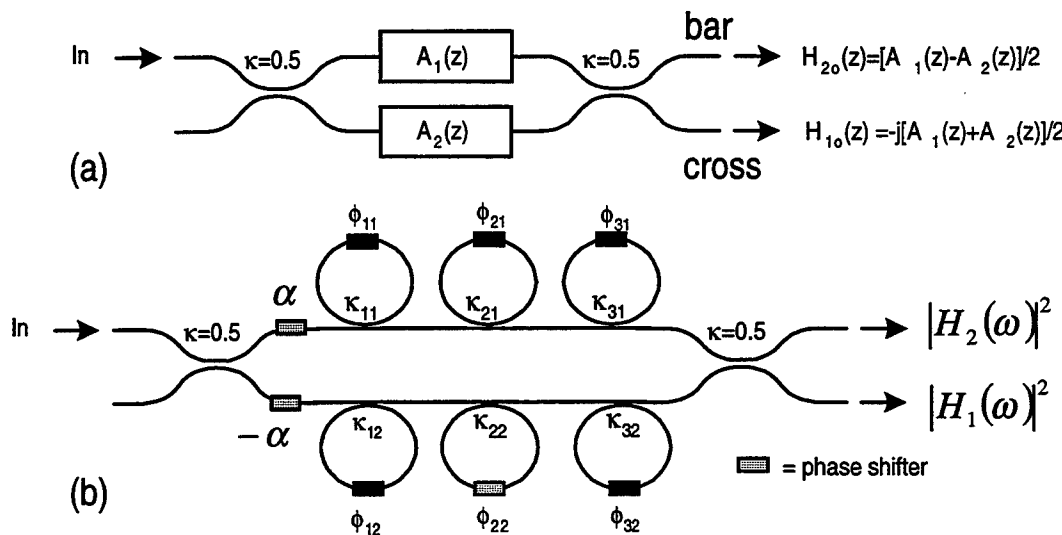


**Fig. 1.** (a) A general bandpass filter architecture using all-pass filter decomposition and (b) a specific sixth-order architecture implemented with a cascade of single-stage ring resonators in each MZI arm.

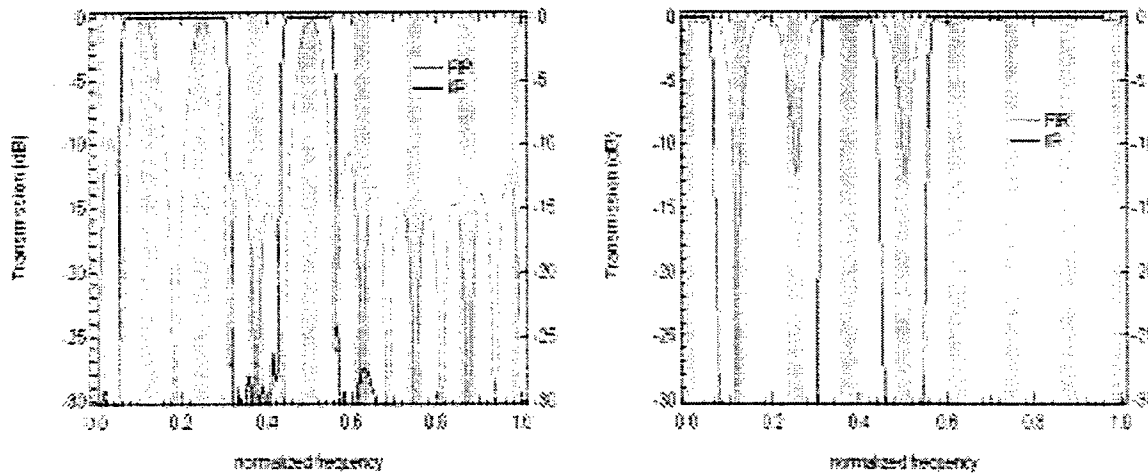


**Fig. 2.** Power complementary responses for an add/drop filter comparing the FIR and IIR responses.

# Wavelength- and Polarization-Insensitive Integrated Directional Couplers using Mach-Zehnder Structures

Thomas E. Murphy, Brent E. Little, and Henry I. Smith

Research Laboratory of Electronics, Department of Electrical Engineering and Computer Science  
Massachusetts Institute of Technology, Cambridge, MA 02139 USA

<b>tem@mit.edu</b>	<b>belittle@mit.edu</b>	<b>hismith@nano.mit.edu</b>
ph: (617) 253-0213	ph: (617) 253-8524	ph: (617) 253-6865
fax: (617) 253-8509	fax (617) 253-9611	fax: (617) 253-8509

## INTRODUCTION

Directional couplers are essential components in a wide variety of important devices, including modulators, switches, and Bragg-grating add/drop filters [1,2]. For many of these applications, it is important that the directional coupler provide the desired power splitting ratio, independent of wavelength or polarization. Broadband performance is especially important in wavelength division multiplexing systems, where a constant splitting ratio must be maintained for all wavelength channels. Using conventional couplers, it is often impossible to achieve broadband polarization-insensitive performance, especially in planar integrated devices.

In this work we describe the design, fabrication, and measurement of a class of integrated directional couplers which provide wavelength-, polarization-, and fabrication-insensitive performance.

Others have recognized that wavelength-insensitive couplers can be realized by cascading two conventional couplers in a Mach-Zehnder configuration [3,4]. Using numerical optimization techniques in combination with empirically determined wavelength-dependence data, researchers at NTT have employed this technique to build broadband 20% couplers [3].

In contrast, this paper offers simple, analytical design rules for building such cascaded couplers with arbitrary splitting ratios. We apply these rules to the particularly important case where 50% splitting is required [1,2]. By directly comparing the performance to that of a similarly-constructed conventional coupler, we demonstrate that these simple analytical design rules yield devices which are not only wavelength-insensitive, but also polarization-insensitive and fabrication-insensitive. Specifically, our couplers achieve near-50% power splitting over a 120 nm bandwidth, for both polarizations. Furthermore, our measurements indicate that the devices are robust to fabrication deviations and material uncertainties.

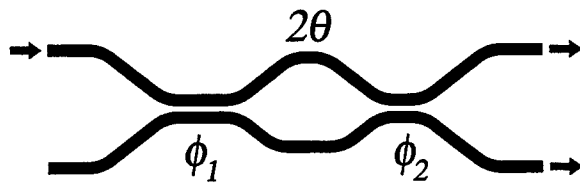


**Fig. 1.** Structure of the parameter-insensitive coupler: two non-identical conventional couplers separated by a relative phase shift  $2\theta$ .

## DESIGN

The structure of the insensitive coupler is depicted schematically in Fig. 1. The device consists of two conventional directional couplers, cascaded in a Mach-Zehnder configuration, with a relative phase shift introduced between them. The device achieves insensitive performance in the following manner: a fractional change in wavelength (or polarization, refractive index, waveguide size, etc.) tends to affect each directional coupler in the same way. The relative phase shift between the two couplers causes these deviations to balance each other such that the resulting power splitting ratio remains unchanged.

The splitting ratio at the output of the device can be expressed in terms of three dimensionless quantities,  $\phi_1$ ,  $\phi_2$ , and  $2\theta$  [3,5]:

$$S = \cos^2 \theta \sin^2(\phi_1 + \phi_2) + \sin^2 \theta \sin^2(\phi_1 - \phi_2). \quad (1)$$

$\phi_1$  and  $\phi_2$  represent, respectively, the total integrated coupling of the two constituent directional couplers, and  $2\theta$  is the relative phase shift which separates them. Each of these parameters depends implicitly upon wavelength, polarization, etc.. As we describe in a previous work [5], insensitive performance is achieved by choosing these three

parameters in the following way:

$$\phi_1 = \frac{3\pi}{8} \left(1 + \frac{1}{N}\right), \quad \phi_2 = \frac{3\pi}{8} \left(1 - \frac{1}{N}\right) \quad (2)$$

$$\cos^2 \theta = \sin \left(\frac{3\pi}{2N}\right) \left[N + \sin \left(\frac{3\pi}{2N}\right)\right]^{-1} \quad (3)$$

where  $N$  is a dimensionless real parameter larger than 3.  $N$  can be chosen to give any desired splitting ratio as described in (1). In the case where 50% splitting is required,  $N = 3$  and the solutions are particularly simple:  $\phi_1 = \pi/2$ ,  $\phi_2 = \pi/4$ , and  $\theta = \pi/3$ .

Knowing the three quantities  $\phi_1$ ,  $\phi_2$ , and  $2\theta$ , we then designed a waveguide device to nominally achieve the desired accumulated coupling factors and phase shift. We began by selecting a suitable waveguide geometry and material system. Based upon vendor-supplied information about the refractive indices at  $\lambda = 1.55 \mu\text{m}$ , we designed waveguide geometry to yield efficient coupling to an optical fiber. Using coupled mode theory, we calculated the waveguide coupling as a function of separation, and with this information we designed the two directional couplers. The phase shift  $2\theta$  is achieved by making one arm of the interferometer slightly longer than the other. For all calculations, we used a free-space wavelength of  $1.55 \mu\text{m}$ . Fig. 2 illustrates the important design parameters.

#### FABRICATION

It is important to point out that we did not include a range of coupling lengths ( $\phi_1$  and  $\phi_2$ ), waveguide separations, or waveguide widths on our optical mask. Instead, we used only our best estimate for these parameters based upon the calculations described above. After all, the purpose of the device is to compensate for any deviations from the nominal design. However, we did include a range of phase shifts ( $\theta$ ) above and below the nominal design. The optical photomask was written with e-beam lithography, using a relatively coarse (and therefore economical) pixel size of  $0.12 \mu\text{m}$ . The patterns were carefully placed to insure that each device does not cross an e-beam field boundary, which could introduce spurious phase shifts. For comparison, we included in our design a set of conventional directional couplers, designed to achieve 50% splitting ratios at  $\lambda = 1.55 \mu\text{m}$ .

The device is fabricated using commercially available Ge-doped  $\text{SiO}_2$  planar waveguides, with a core to clad refractive index contrast of 0.3%. Initially, a  $1 \mu\text{m}$ -thick silicon layer is sputter-deposited over the substrate. We then use deep UV optical contact photolithography to transfer the waveguide patterns from a mask to the substrate. The

silicon layer is patterned by reactive ion etching in  $\text{Cl}_2$ . The waveguides are then etched to a depth of  $6.8 \mu\text{m}$  by reactive-ion etching in  $\text{CHF}_3$ , using the silicon layer as a hard mask. A final layer of cladding is then deposited over the structure.

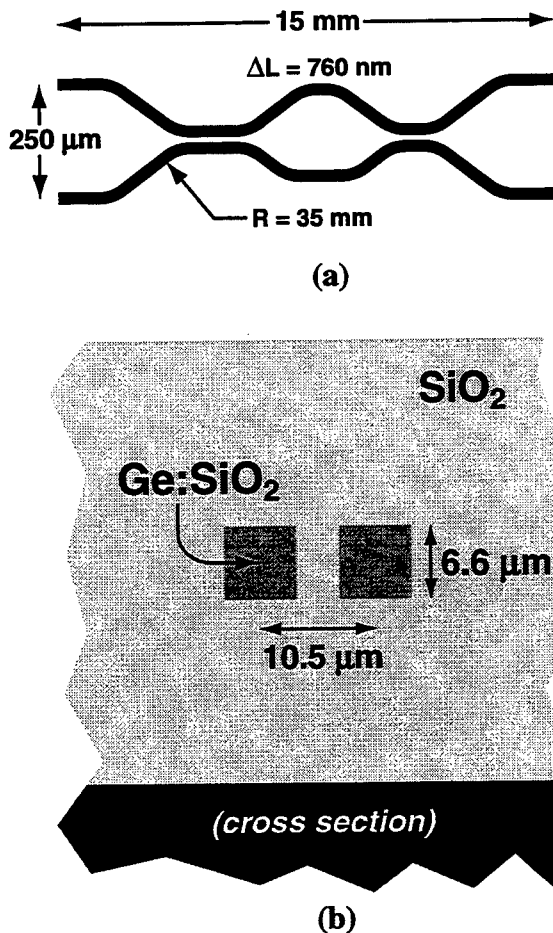


Fig. 2. (a) Diagram (not drawn to scale) of the cascaded direction couplers, indicating important dimensions. (b) Cross-sectional diagram illustrating waveguide geometry at point of closest separation.

#### MEASUREMENT

To prepare the samples for measurement, we polished the input facet normal to the waveguides to allow butt-coupling from a cleaved fiber. We polished the output facet at 10 degrees from the normal to prevent unwanted reflections. We measured the performance of the couplers using an external cavity tunable diode laser. Light from the laser was sent into one port of the device through a single-mode fiber, using an index-matching gel to improve the coupling efficiency. At the output facet, the light

emerging from either waveguide was separately imaged onto a power meter.

For a representative device, the total insertion loss (including fiber-coupling loss, bending loss, and intrinsic waveguide loss) was approximately 1.0 dB.

Fig. 3 plots the splitting ratio vs. wavelength for a conventional directional coupler and for an improved insensitive coupler. Notice that the conventional coupler achieves a splitting ratio which is uniformly higher than the nominal value of 50%. We attribute this discrepancy to (i) uncertainty in the material indices of refraction used in our calculations, and (ii) structural and material deviations from the nominal design which may occur during the various fabrication steps. In principle, this bias can be removed by performing a more exhaustive empirical investigation of the material properties and by carefully controlling and characterizing each step of the fabrication process. However, in addition to this offset, the conventional coupler exhibits a sloped wavelength dependence which is characteristic of directional couplers and cannot be flattened without using a completely different design.

The conventional coupler also exhibits significant polarization dependence: the splitting ratio is consistently higher for TM- than for TE-polarized light at all of the wavelengths measured. We attribute this difference to material birefringence in the deposited oxide films.

In spite of this polarization dependence, and the apparent uncertainty in material and fabrication parameters, the cascaded Mach-Zehnder coupler achieves a splitting ratio between 45 and 50% (within 5% of the targeted value) over the entire wavelength range from 1475 – 1595 nm (spanning 120 nm), with negligible polarization dependence.

### CONCLUSIONS

Based upon simple design rules, we have constructed a set of cascaded Mach-Zehnder couplers which are insensitive to wavelength, polarization, and other material and structural parameters. In spite of relatively large uncertainties in the materials and fabrication, these devices show remarkably low wavelength and polarization dependence. By more carefully controlling and characterizing the materials and fabrication, we believe that we can bring these devices closer to the nominal design, which should further improve their performance.

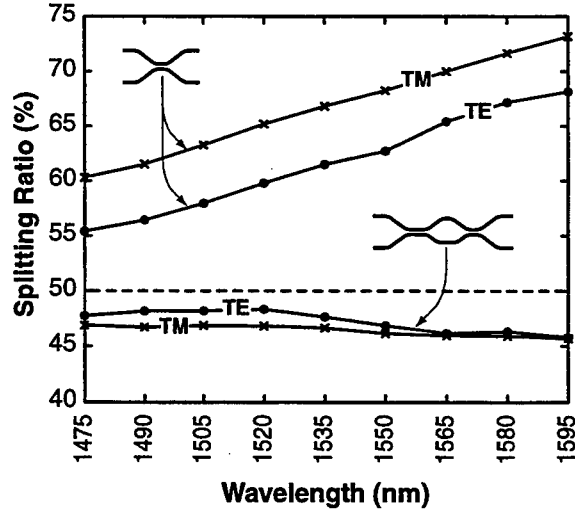


**Fig. 3.** Measured power splitting ratio vs. wavelength for two devices: the upper two curves represent the measured splitting ratio for a conventional coupler (TE and TM polarizations), and the lower two curves correspond to the parameter-insensitive Mach-Zehnder coupler.

### REFERENCES

- [1] T. Erdogan, T. A. Strasser, M. A. Milbrodt, E. J. Laskowski, C. H. Henry, and G. E. Kohnke, “Integrated-optical Mach-Zehnder add-drop filter fabricated by a single UV-induced grating exposure”, *Applied Optics*, **36** (30), 7838–7845 (1997).
- [2] F. Bilodeau, D. C. Johnson, S. Theriault, B. Malo, J. Albert, and K. O. Hill, “An all-fiber dense-wavelength-division multiplexer/demultiplexer using photoimprinted Bragg gratings”, *IEEE Photonics Technology Letters*, **7**, 388–390 (1997).
- [3] K. Jinguji, N. Takato, A. Sugita, and M. Kawachi, “Mach-Zehnder interferometer type optical waveguide coupler with wavelength-flattened coupling ratio”, *Electronics Letters*, **26**, 1326–1327 (1990).
- [4] F. Gonthier, D. Ricard, S. Lacroix, and J. Bures, “Wavelength-flattened  $2 \times 2$  splitters made of identical single-mode fibers”, *Optics Letters*, **16**, 1201–1203 (1991).
- [5] B. E. Little and T. E. Murphy, “Design Rules for Maximally Flat Wavelength-Insensitive Optical Power Dividers Using Mach-Zehnder Structures”, *IEEE Photonics Technology Letters*, **9**, 1607–1609 (1997).

## An integrated power splitter with ultra-low loss

Jong Sool Jeong, Byueng-Su Yoo, and Kyung-Sook Hyun

Telecommunication Basic Research Lab., ETRI, Yusong P.O.Box 106, Taejon, 305-600, Korea  
jeong@etri.re.kr, bsyoo@etri.re.kr, kshyun@etri.re.kr

Low-loss power splitting is important for optical signal distribution in high-capacity local-area networks [1]. The typical power splitters have the output tapered waveguides in order to enhance the splitting efficiency [2]. However, the lightwaves are still leaked into the free-space region between the tapered waveguides and then the leaky lightwaves are fractionally returned. Moreover, the implementation of the tapered waveguides demands the elaborate patterning and etching skills in the fabrication in order to fulfill the sharp edges [3].

In this work, we propose a power splitter integrated with a phase grating, which can greatly reduce the leaky and returned lightwaves without tapering the output waveguides. The integrated power splitter can achieve the high coupling efficiency with ultra-low losses, which is rigorously described by the finite-difference time-domain (FDTD) method.

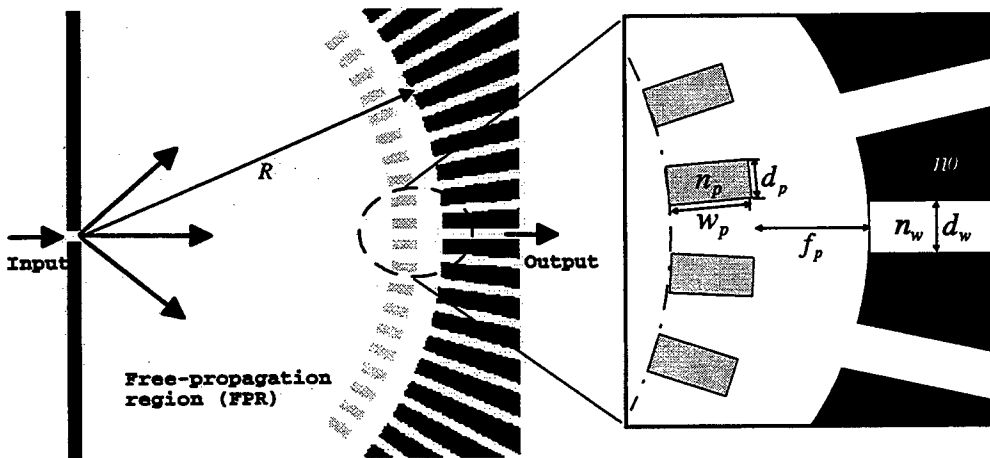
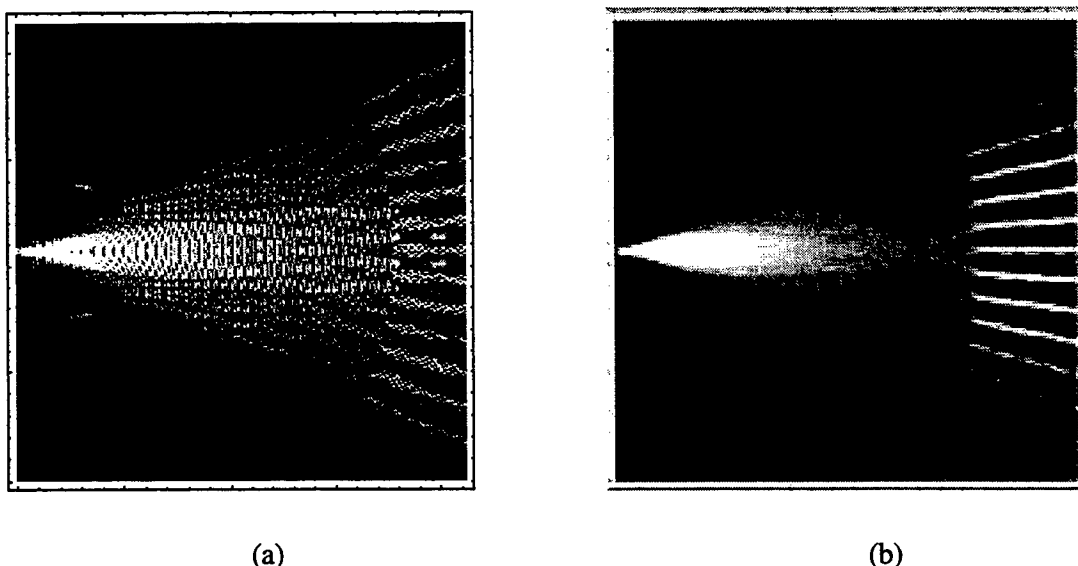


Fig. 1. Geometry of the  $1 \times N$  power splitter.

Figure 1 shows the configuration of the  $1 \times N$  power splitter, which consists of the input/output waveguides and the free-propagation region (FPR) integrated with the phase grating. The geometry parameters used in calculation are as follows: the material indices of  $n_w=3.315$ ,  $n_p=3.0$ ,  $n_0=1.0$ , the waveguide widths of  $d_w=1.0 \mu\text{m}$ , the grating length and width of  $w_p=2.5 \mu\text{m}$  and  $d_p=0.9 \mu\text{m}$ , the focal length of  $f_p=1.5 \mu\text{m}$ , and the FSR length of  $R=35.0 \mu\text{m}$ .

We analyze the characteristics of the power splitter by using the FDTD method with the grid size of  $\Delta x = \Delta z = 0.04 \mu\text{m}$  and the time step of  $\Delta t = 0.5(\Delta z/c)$  for the excitation of the fundamental TE mode with a carrier wavelength of  $\lambda = 1.55 \mu\text{m}$ . Figure 2 shows the density plot of the steady-state electric field intensity for two power splitters: (a) without the phase grating and (b) with the phase grating, respectively. In Fig. 2(a), the power splitter without the phase grating shows the large leaky lightwaves at the free-space region between the output waveguides. The leaky lightwaves are fractionally reflected at the interfaces between the waveguide and the free space, resulting in the interference and the return loss. In the phase grating-integrated power splitter, the lightwaves are



**Fig. 2.** Density plot of steady-state electric field intensity for two power splitters : (a) without the phase grating and (b) with the phase grating.

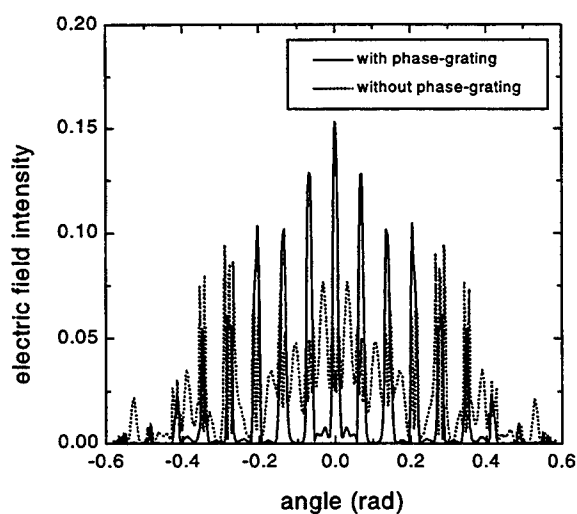


Fig. 3. Comparison of the power characteristics at the location of 40  $\mu\text{m}$  radius for two power splitters.

concentrated within the output waveguides, as shown in Fig. 2(b). Accordingly, the phase grating can greatly reduce the coupling losses such as the leakage and reflections.

Figure 3 shows the comparison of the power splitting characteristics at the location of  $40 \mu\text{m}$  radius for two power splitters. It should be noted that the integrated power splitter can efficiently split the lightwaves with very small leakage but the power splitter without phase grating shows large leaky lightwaves.

Figure 4 shows the spectral responses of the coupling efficiency at the location of  $40 \mu\text{m}$  from the input waveguide for two power splitters. The coupling efficiency is defined as the ratio of power coupled into the central output waveguide from the input waveguide. The coupling efficiency is about  $-4.4 \text{ dB}$  with variation of  $\pm 0.12 \text{ dB}$  and gradually increases with increase of the wavelength for the

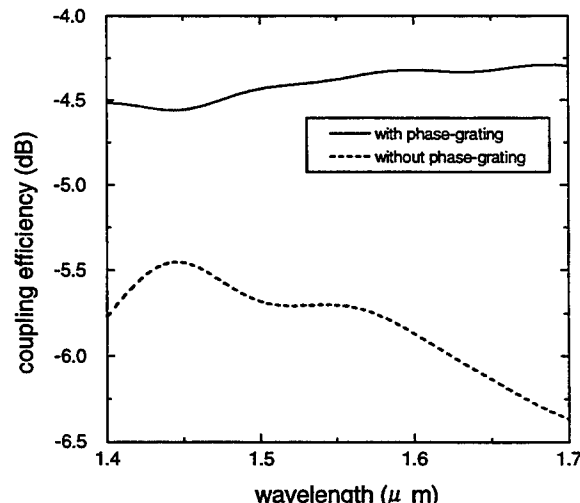
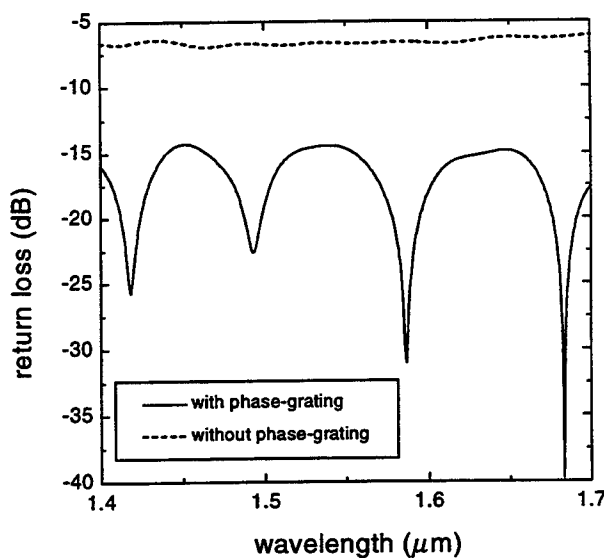


Fig. 4. Spectral responses of the coupling efficiency at the location of  $40 \mu\text{m}$  from the input waveguide for two power splitters.



reduced less than about  $-15$  dB, which is mostly arisen by the effective index difference of  $\Delta n = 0.315$  between the waveguide and the phase grating. In the design parameters, the index difference can be much smaller than  $\Delta n = 0.315$ .

Fig. 5. Spectral responses of the return losses in the cross section of the input waveguide for two power splitters.

In the structure of the power splitter having the InGaAsP ( $\lambda_g = 1.3 \mu\text{m}$ ) waveguide layer of  $0.6 \mu\text{m}$  thickness and the InP clad layer of  $0.3 \mu\text{m}$  thickness, the index difference is about  $\Delta n = 0.04$  with the phase grating of the  $20 \mu\text{m}$  length. The phase grating can readily be fabricated by etching the InP clad layer of  $0.3 \mu\text{m}$  thickness. Therefore, the return loss can be much lower than  $-15$  dB in the practical power splitter with the phase grating.

In conclusion, we have proposed the power splitter integrated with the phase grating. The FDTD modeling shows that highly efficient power splitting with ultra-low losses can be achieved without tapering the output waveguides. It has been found that the coupling efficiency increases more than about  $1.5$  dB and the return loss decreases more than  $8.5$  dB in comparison with the power splitter without the phase grating.

1. D. B. Keck, A. J. Morrow, D. A. Nolan, and D. A. Thompson, *J. Lightwave Technol.*, **7**, 1623-1633 (1989).
2. H. Takahashi, K. Okamoto, and Y. Ohmori, *IEEE Photon. Technol. Lett.*, **5**, 58-60 (1993).
3. P. D. Trinh, S. Yegnanarayanan, and B. Jalali, *IEEE Photon. Technol. Lett.*, **8**, 794-796 (1996).

integrated power splitter. In the phase splitter without the phase grating, however, the coupling efficiency is about  $-5.9$  dB with variation of about  $\pm 0.5$  dB and rapidly decreases with increase of the wavelength. Therefore, the integrated power splitter can enhance the splitting efficiency higher than about  $1.5$  dB.

Figure 5 shows the spectral responses of the return losses in the cross section of the input waveguide for two power splitters. The results are obtained from the Fast Fourier transforms (FFT's) of the measured powers with the time domain formulation. In the power splitter without the phase grating, the return loss is about  $-6.5$  dB over the wavelength range of  $300$  nm. In integrating the phase grating, however, the return loss is



**Integrated Photonics Research**

# **Photonic Nanocircuits**

**Tuesday, July 20, 1999**

**Richard W. Ziolkowski, University of Arizona, USA;  
Brent E. Little, Massachusetts Institute of Technology, USA  
Presiders**

**RTuB**  
**8:30am–10:00am**  
Sierra Madre South

## Photonic Nanostructures and Resonators

Hermann A. Haus

Department of Electrical Engineering and Computer Science

Research Laboratory of Electronics

Massachusetts Institute of Technology

Cambridge, MA 02139 USA

Tel: (617) 253-2585; Fax: (617) 253-9611; Email: haus@mit.edu

Photonic bandgap (PBG) structures permit low loss and low reflection bends and spatially well confined resonances with low radiation loss. The challenges posed by fabrication of such structures are daunting. Simpler structures that are more easily fabricated may fill a niche that is competitive in performance with some of the PBG structures. The high index contrast structures described in this talk may hold this promise.

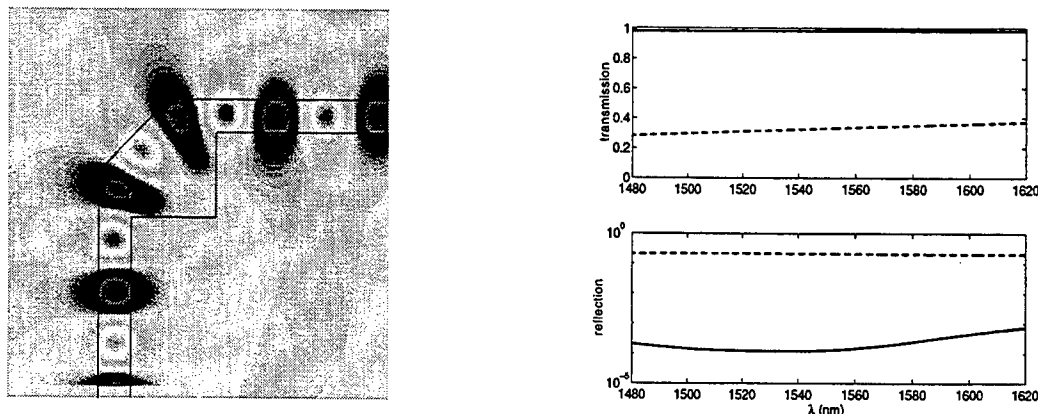


Figure 1. (a) A waveguide bend with the electric field pattern. (b) Its transmission and reflection characteristics (solid line) compared with those of a simple right angle bend (dashed line).

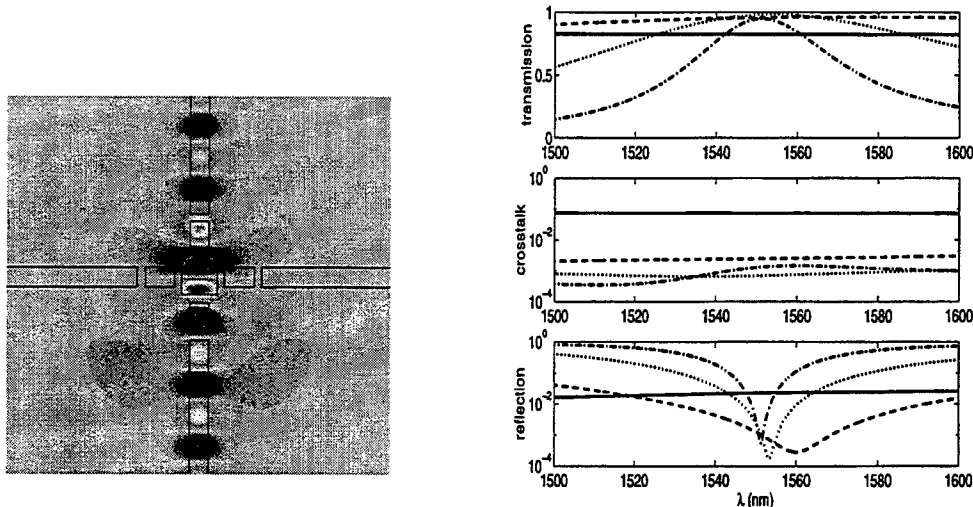


Figure 2. (a) A waveguide crossing with the electric field pattern. (b) Its characteristics for different number of cuts. Simple cross, solid line; one cut, dashed line; two cuts, dotted line; three cuts, dash-dotted.

Figure 1a shows the electric field distribution in a waveguide bend in a high index contrast waveguide (3/1). The characteristic performance is shown in Figure 1b and compared with that of a simple rectangular bend. The transmission and reflection characteristics of the optimized bend are spectacularly better than those of the simple bend. The principle of the design rests on treating the region connecting the two waveguides as a low-Q resonator, with a modal shape that minimizes radiation. When this condition is met, the propagation through the bend is reflection free as it is for a symmetric resonator at resonance.

The same principle of the passage through a resonator can be used to optimize a waveguide crossing. The optimized structure is tuned via cut-out sections in the waveguides. Figure 2a shows the electric field in such a crossing and Figure 2b compares its performance with a straightforward waveguide cross.

It is possible to design resonators with corners, as in Figure 1, while suppressing radiation from such a resonator. The radiation Q of such a resonator can be made high. As an illustration of the use of such resonators, we show in Figure 3 the electric field pattern of a channel dropping filter designed through the use of two such resonators in cascade. Through selective excitation of the symmetric and antisymmetric mode pair of the total resonant structure, one may achieve full power transfer from one waveguide to the other. Full transfer is achieved at resonance, if the coupling between the resonators and the coupling between the waveguides and the resonators is properly adjusted. Combinations of pairs of resonators can be used to design filter characteristics with increased off-resonance roll-off.

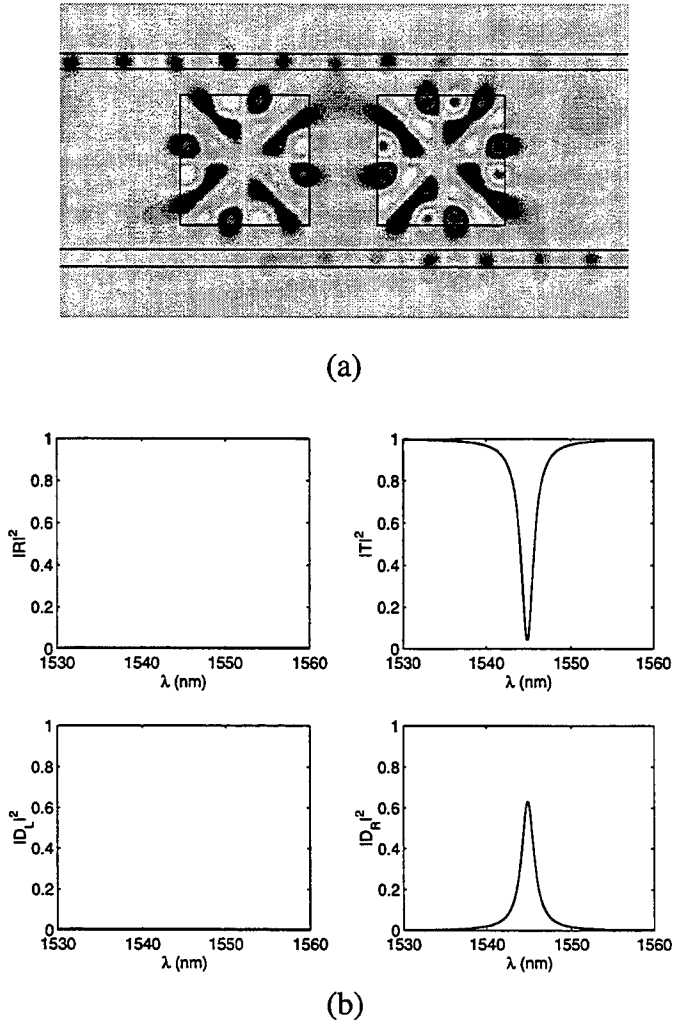


Figure 3. (a) Channel dropping filter with electric field pattern. (b) The response of the filter.

This paper is based on work by Dr. Shanhui Fan, Christina Manolatou, Steven G. Johnson, and Mohammad J. Khan, all at MIT.

# Ultra-Small and Ultra-Low-Threshold Microdisk Injection Lasers with Evanescent Coupled Elements

Toshihiko Baba

Yokohama National University, Division of Electrical and Computer Engineering  
79-5 Tokiwadai, Hodogayaku, Yokohama 240-8501, Japan  
Phone +81-45-339-4258, Fax +81-45-338-1157, E-Mail baba@dnj.ynu.ac.jp

**Abstract** — Recent progress on microdisk injection lasers are reported. Size reduction, room temperature cw lasing with microampere order threshold, and some applications investigated are presented.

## 1. Introduction

Microdisk lasers[1-3] are very unique in many respects. The simple geometry allows the easy fabrication and size reduction with maintaining the strong confinement of a whispering gallery (WG) mode as a laser mode. In this study, the low threshold lasing and the spontaneous emission control have been investigated for injection devices. A problem of this laser is the difficulty of light extraction. The evanescent coupling of microdisk elements has been studied to solve this problem and to apply them to a functional integrated photonics. An active near field probe directly utilizing this laser as a probe tip has been proposed and demonstrated.

## 2. Lasing Characteristics

Fig. 1 shows the smallest injection laser[4]. It was a microdisk fabricated into a GaInAsP/InP compressively-strained MQW GRIN-SCH wafer by using a ECR dry etching and a selective wet etching. The thickness and diameter were 0.2 and 2  $\mu\text{m}$ , respectively, and the effective cavity volume was 0.4  $\mu\text{m}^3$ . The room temperature pulsed lasing was obtained at  $\lambda = 1.56 \mu\text{m}$ . The first room temperature cw operation was achieved in a 3- $\mu\text{m}$ -diameter device with a record low threshold current of 150  $\mu\text{A}$ [5], as shown in Fig. 2. Key issues to improve the performance are the efficient carrier diffusion from post claddings to the disk edge, the reduction of the scattering loss of the WG mode at the disk edge, and the reduction of the thermal resistance of typically 10<sup>5</sup> K/W[6]. The nonradiative recombination at disk surfaces was found to be negligible. The spontaneous emission factor was evaluated to be 0.006 – 0.03 for 3- $\mu\text{m}$ -diameter devices by using the curve fitting method. It depends on the detuning of the WG mode against the spontaneous emission peak.

## 3. Evanescent Coupled Elements

The evanescent field of the WG mode spreads to the air. The optical coupling of WG mode lasers and straight waveguides through the evanescent field has been studied by many groups. This study discusses the coupling and butt-joint of circular or fan-shaped microdisks used as lasers, resonators,

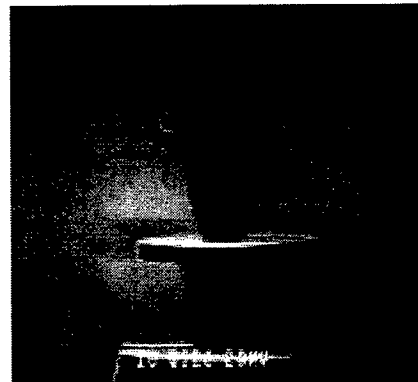


Fig. 1 Fabricated GaInAsP/InP microdisk injection laser. Disk diameter was 2  $\mu\text{m}$ .

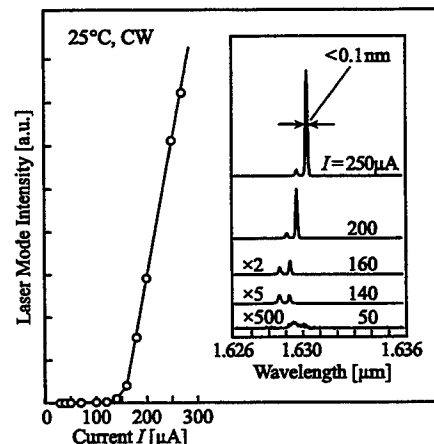


Fig. 2 Room temperature cw lasing characteristics.

waveguides, etc. Fig. 3 shows an example of FDTD simulations[7]. When the distance between a microdisk laser and a fan-shaped waveguide is less than 0.3  $\mu\text{m}$ , over 70 % laser light is extracted from two ends of fan-shaped microdisk waveguides. When microdisk waveguides are butt-joined with an overlap width of 0.5  $\mu\text{m}$ , the waveguide loss can be as low as 0.1 dB. By combining these elements, mode size converter, tunable filter, multiplexer, and other various functional devices and circuits will be synthesized. Such coupling distance and joint width were controlled using absolutely the same process as that for microdisk lasers.

#### 4. Near Field Probe Action

The evanescent field of the WG mode exponentially decays from the disk edge. If a nanometer object is put close to the disk, the evanescent field is scattered and the laser characteristic is modulated. The near field probe based on this principle, as shown in Fig. 4, has been proposed and the spatial resolution has been theoretically estimated[8]. Longitudinal and lateral resolutions are determined by the decay length of the evanescent field to be  $<0.07\lambda$  and  $0.17\lambda$ , respectively. Almost the same or rather superior lateral resolution of 190 nm was experimentally observed by moving a metal needle across the microdisk[9]. Advantages of this probe are the ease of array integration, which allows the high speed parallel probing, and a high S/N originated from the unification of the light source and the sensing head.

#### 5. Conclusion

The injection lasing of microdisk lasers is amazingly easy for the ultra-small cavity. The establishment of the integration technology of microdisk elements and the exploitation of suitable applications are key issues to realize the ultra-high-density integrated photonics with sophisticated functions.

**Acknowledgments** — The author would like to thank Prof. Y. Kokubun, Yokohama National University, and Prof. K. Iga, Associate Prof. F. Koyama, and Dr. T. Miyamoto, Tokyo Institute of Technology, for encouragement and discussion. This work was partly supported by Japan Society for Promotion of Science, Research for the Future, #JSPS-RFTF 97P00103.

#### References

- [1] S. L. McCall, A. F. J. Levi, R. E. Slusher, et.al., *Appl. Phys. Lett.* **60**, 289-291, 1992.
- [2] A. F. J. Levi, R. E. Slusher, S. L. McCall, T. Tanbun-Ek, et.al., *Electron. Lett.* **28**, 1010-1012, 1992.
- [3] T. Baba, *IEEE J. Selected Topics in Quantum Electron.* **3**, 808-830, 1997.
- [4] T. Baba, M. Fujita, A. Sakai, M. Kihara and R. Watanabe, *IEEE Photon. Technol. Lett.* **9**, 878-880, 1997.
- [5] M. Fujita, K. Inoshita and T. Baba, *Electron. Lett.* **25**, 278-279, 1998.
- [6] M. Fujita, A. Sakai and T. Baba, *IEEE J. Selected Topics in Quantum Electron.*, submitted in 1998.
- [7] A. Sakai and T. Baba, *IEEE/OSA J. Lightwave Technol.*, submitted in 1998.
- [8] A. Sakai, H. Yamada, M. Fujita and T. Baba, *Jpn. J. Appl. Phys.* **37**, 517-521, 1998.
- [9] H. Yamada, A. Sakai, M. Fujita and T. Baba, *Electron. Lett.* **27**, 222-223, 1999.

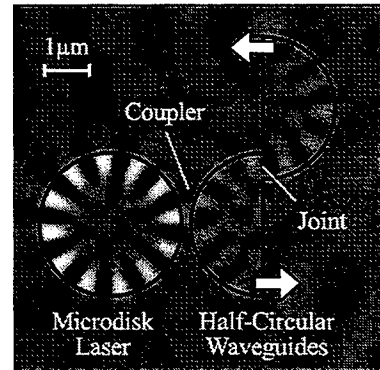


Fig. 3 Simulated field distribution in microdisk laser and microdisk waveguide. Finite difference time domain (FDTD) method was used.

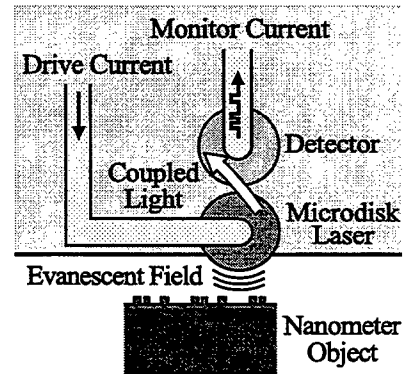


Fig. 4 Schematic of microdisk near field probe.

## Design and Analysis of Nonlinear Microring Resonators for Third-order Harmonic Generation

Vien Van<sup>1</sup> and Brent E. Little<sup>2</sup>

<sup>1</sup> Department of Electrical and Computer Engineering  
University of Waterloo, Waterloo, Ontario, Canada N2L 3G1  
Tel. (519) 885-1211, ext. 6597, Fax. (519) 746-3077

Email: [vvan@uwaterloo.ca](mailto:vvan@uwaterloo.ca)

<sup>2</sup> Department of Electrical Engineering and Computer Science  
Massachusetts Institute of Technology, Cambridge, MA 02139

Tel. (617) 253-8524, Fax. (617) 253-9611

Email: [belittle@MIT.edu](mailto:belittle@MIT.edu)

### 1. Introduction

Optical ring resonators are useful devices for wavelength filtering, multiplexing and demultiplexing [1–3]. Recent fabrication advances have made it possible to realize high index contrast microrings with strong mode confinement and negligible bending loss, leading to resonators having theoretical quality factors  $Q$  in the order of  $10^4$  [2]. Since the ratio of the input field amplitude to the field amplitude inside the ring is inversely proportional to the coupling coefficient between the straight waveguide and the ring, the field stored in the ring of high- $Q$  resonators can be one to two orders of magnitude higher than the input field. It is obvious that with such an intense field circulating in the ring, a slight nonlinearity in the material can induce large nonlinear effects, making the resonator ideal for nonlinear mixing processes. Here we are particularly interested in third-order harmonic generation whereby a material having third-order optical nonlinearity illuminated with two waves at frequencies  $\omega_1$  and  $\omega_2$  radiates a third wave at frequency  $2\omega_1 - \omega_2$ . In this paper, we present the design and finite-difference time-domain analysis of a nonlinear microring resonator for use as a frequency mixing device.

### 2. The Nonlinear Optical Microring Resonator

Consider the standard single-ring resonator evanescently coupled to two straight waveguides serving as input and output, as shown in Figure 1. The core index of the straight waveguides is  $n_1$ , which is assumed to be linear, while the ring waveguide has third-order nonlinearity characterized by susceptibility coefficient  $\chi^{(3)}$ , so that its relative permittivity is given by

$$\epsilon_r = n_1^2 + \chi^{(3)} |\mathbf{E}|^2, \quad (1)$$

where  $\mathbf{E}$  is the total electric field impinging on the material. A pump beam at frequency  $\omega_1$  and an input signal at frequency  $\omega_2$  are coupled into the ring via the input waveguide. Both  $\omega_1$  and  $\omega_2$  are chosen to be resonance frequencies of the ring, which are given by

$$\omega = M \frac{c}{n_{eff} R}, \quad (2)$$

where  $M$  is an integer, and  $n_{\text{eff}}$  and  $R$  are the effective core index and radius, respectively. Third-order mixing generates a new wave at  $\omega_3 = 2\omega_1 - \omega_2$ , which is also at resonance since

$$\omega_3 = 2\omega_2 - \omega_1 \approx (2M_2 - M_1) \frac{c}{n_{\text{eff}} R}. \quad (3)$$

In the above we have assumed that the frequencies  $\omega_1$ ,  $\omega_2$  and  $\omega_3$  are close enough to each other so that the waveguide dispersion is small.

Third-order nonlinearity causes the effective index  $n_{\text{eff}}$  of a nonlinear waveguide to be slightly larger than that of an identical linear waveguide. Consequently, the resonances of a nonlinear ring are slightly shifted toward longer wavelengths compared to those of a linear ring. This self-phase modulation effect is especially amplified in a microring mixer, where the pump beam, whose amplitude is usually much larger than the signal beams, provides a constant bias intensity level in the ring which causes the effective indices seen by the signal waves to increase. Figure 2 compares the FDTD-simulated power spectra at port 3 of linear and nonlinear microrings. The resonators have physical parameters  $n_0 = 1$ ,  $n_1 = 3$ ,  $d = 0.2\mu\text{m}$ ,  $g = 0.2\mu\text{m}$ ,  $R_1 = 0.9\mu\text{m}$  and  $R_2 = 1.1\mu\text{m}$ . For the nonlinear ring, the susceptibility  $\chi^{(3)}$  is  $1 \times 10^{-10}\text{m}^2/\text{V}^2$  and the ring is biased by a pump beam at  $1.368\mu\text{m}$  having an amplitude of  $4 \times 10^4\text{V/m}$ . It is seen from the plot that the nonlinear resonance peaks are shifted to the right with respect to the linear peaks. For example, the resonance corresponding to  $M = 14$  occurs at  $1.196\mu\text{m}$  for the linear ring but is shifted to  $1.211\mu\text{m}$  for the nonlinear ring. Another resonance peak, corresponding to  $M = 16$  (not shown in Figure 2), is shifted from  $1.361\mu\text{m}$  to  $1.368\mu\text{m}$  when nonlinearity is introduced into the ring.

In designing the nonlinear microring mixer, the shifts in the resonance peaks due to self-phase modulation must be taken into account to ensure that the pump beam and signal beams are sustained in the ring by resonance. Also, a high- $Q$  resonator is desirable in order to achieve a large field in the ring without requiring a strong pump beam at the input. In the numerical example above, we choose the pump beam wavelength to be  $1.368\mu\text{m}$  and the input signal beam to be  $1.211\mu\text{m}$ . Figure 3 shows the spectrum of the electric field magnitude at port 3. Third-order mixing generates a signal at  $1.574\mu\text{m}$  in the ring, which is partly coupled out into the output waveguide as seen in the spectrum at port 3, and partly coupled back into the input waveguide to exit at port 2.

### 3. Conclusions

The design and FDTD analysis of a nonlinear microring resonator for third-order harmonic generation is presented. Along with the design concerns for high quality factor and wide free-spectral range of a linear ring resonator, the nonlinear effect of self-phase modulation on the resonances also needs to be taken into account. The nonlinear microring mixer has the advantage that due to resonance, a high-intensity pump beam can be achieved in the ring without requiring a strong beam at the input. In addition, very narrow output wavelength channels can be realized by increasing the quality factor of the microring resonator.

## References

- [1] Chin, M.K. and Ho, S.T., "Design and modeling of waveguide-coupled single-mode microring resonators", *J. Lightwave Technology*, vol. 16, no. 8, pp. 1433–1446, Aug. 1998.
- [2] Little, B.E., Chu, S.T., Haus, H.A., Foresi, J. and Laine, J.-P., "Microring resonator channel dropping filters", *J. Lightwave Technology*, vol. 15, no. 6, pp. 998–1005, June 1997.
- [3] Little, B.E., Foresi, J.S., Steinmeyer, G., Thoen, E.R., Chu, S.T., Haus, H.A., Ippen, E.P., Kimerling, L.C. and Greene, W., "Ultra-compact Si-SiO<sub>2</sub> microring resonator optical channel dropping filters", *IEEE Photonics Technology Letters*, vol. 10, no. 4, pp. 549–551, April 1998.
- [4] Hagness, S.C., Rafizadeh, D., Ho, S.T. and Taflove, A., "FDTD microcavity simulations: design and experimental realization of waveguide-coupled single-mode ring and whispering-gallery-mode disk resonators", *J. Lightwave Technology*, vol. 15, pp. 2154–2165, 1997.

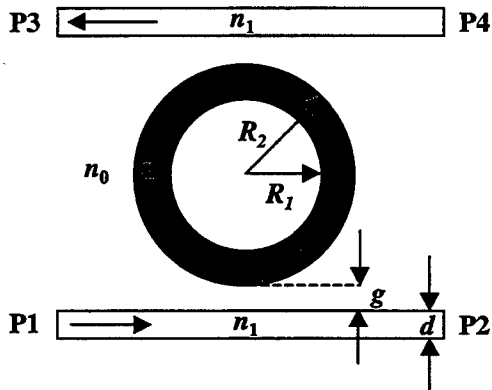


Figure 1. Structure of a nonlinear microring resonator.

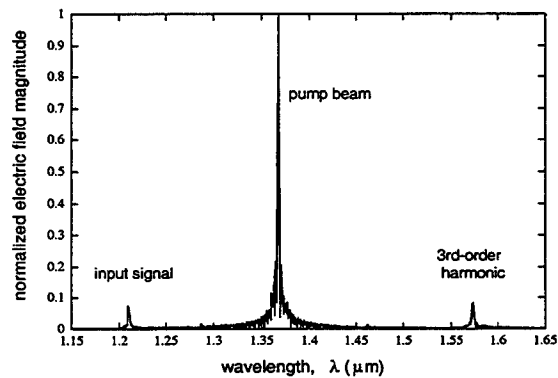


Figure 3. Electric field spectra at port 3 of the nonlinear microring resonator showing the generation of third-order harmonic at  $\lambda_3 = 1.574\mu\text{m}$ . The field is normalized with respect to the pump beam amplitude.

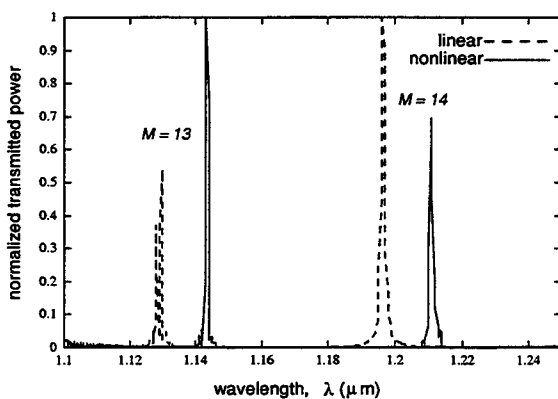


Figure 2. Normalized power spectra at port 3 of linear and nonlinear microring resonators showing the resonance shift due to the nonlinear effect of self-phase modulation.

## Cascade Coupled Microring Resonators for Spectral Cleanup and Shaping in Add/Drop Filters

Brent E. Little<sup>1</sup>, Sai Tak Chu, Wugen Pan, Taro Kaneko<sup>2</sup>, and Yasuo Kokubun<sup>2</sup>

Kanagawa Academy of Science and Technology, KSP E 308, 3-2-1 Sakato, Takatsu, Kawasaki, Japan  
213-0012.

Email: belittle@mit.edu

<sup>1</sup> Research Laboratory of Electronics, Massachusetts Institute of Technology, Cambridge MA 02139, and the Laboratory for Physical Sciences, University of Maryland, College Park MD 20742.

<sup>2</sup> Also with the Department of Electrical Engineering & Computer Engineering, Yokohama National University, 79-5 Tokiwadai, Hodogaya-ku, Yokohama, Japan 240-8501.

Wavelength filters and switches based on microring resonators<sup>[1,2]</sup> are of considerable interest because they offer performance that is superior to other wavelength selective mechanisms while offering dimensions that are two or three orders of magnitude smaller than conventional devices. Recently, microring resonators 3  $\mu\text{m}$  to 25  $\mu\text{m}$  in radius have been realized in various material systems<sup>[3-6]</sup>. Packed closely together, integration densities approaching  $10^5$  devices/cm<sup>2</sup> can be envisioned. Complex circuits involving several resonators per node for improved performance can be employed without concern for chip space. In this talk, we discuss and demonstrate the use of additional resonators for the purpose of spectrum cleanup and spectral passband shaping in WDM filters.

Recently, the Cross-Grid Array<sup>[6]</sup> of microring resonators vertically coupled above low index contrast buried waveguides was developed as a scalable architecture for building complex optical circuits. The buried waveguides are laid out on a grid pattern, and cross through each other at points of intersection. A Cross-Grid node consisting of a single ring over a pair of crossing waveguides is depicted schematically in Fig. 1a. The cross-grid node is a four port device having an input, throughput, add, and drop port as labeled. An optical signal launched at the input port will interact with the ring and exit the drop port at the resonant wavelengths, or the throughput port at off resonant wavelengths. The cross sectional waveguide geometry of the ring and buried waveguide near their point of mutual interaction is depicted in Fig. 1b. The ring and bus waveguides were fabricated from the compound glass Ta<sub>2</sub>O<sub>5</sub>/SiO<sub>2</sub>, with the ratio of Ta<sub>2</sub>O<sub>5</sub> to SiO<sub>2</sub> adjusted to achieve an index of 1.539. The cladding material is pure SiO<sub>2</sub>. Other device parameters are listed in the figure caption. Fabrication and measurement details of similar devices can be found in Refs. [5] and [6]. Figure 1c shows two rings coupled in parallel. The rings occupy diagonal positions on the cross-grid node.

Figure 2 shows a 2x2 cross-grid array serving as a single add/drop node. At three of the junctions, identical ring resonators are vertically coupled over pairs of crossing waveguides. Although the single cross-grid vertically coupled microring resonator (VCMRR) filter in Fig. 1a can serve as an add/drop node, the configuration in Fig. 2 can enhance the signal to noise ratios of the throughput and drop ports significantly. The added complexity consumes negligible real estate. Ring resonators R<sub>1</sub>, R<sub>2</sub>, and R<sub>3</sub> are all designed to select wavelength channel  $\lambda_1$ . Resonator R<sub>1</sub> is the first channel dropping filter along the input bus waveguide. R<sub>2</sub> re-routes  $\lambda_1$  to the drop port and simultaneously increases the out-of-band signal rejection. R<sub>2</sub> therefore, cleans up the drop port spectrum. Signal power at  $\lambda_1$  that leaks past the first resonator R<sub>1</sub> is dropped a second time by R<sub>3</sub>. R<sub>3</sub> therefore, cleans up the throughput spectrum. The add port is cross connected to the bus waveguide by R<sub>3</sub>. The add port does not have any leakage path to the drop port. Although the intersection of two waveguides leads to scattering induced cross-talk, cross-talk

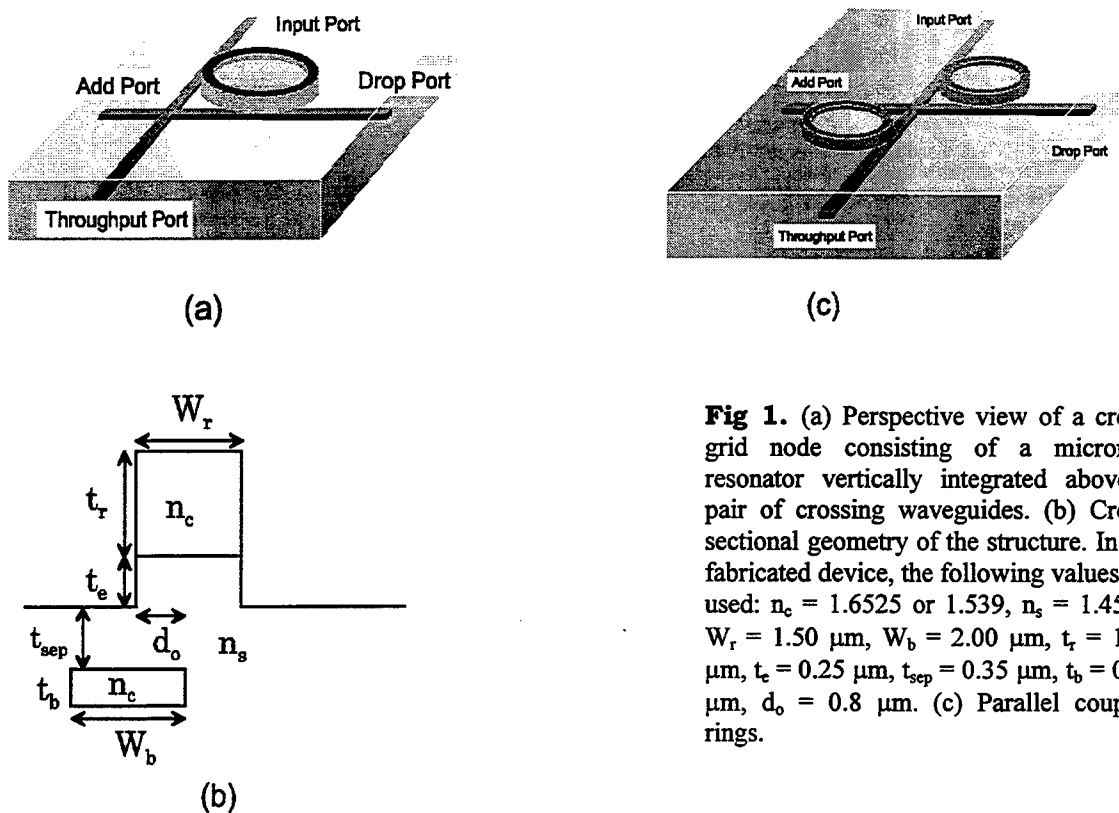


**Fig 1.** (a) Perspective view of a cross-grid node consisting of a microring resonator vertically integrated above a pair of crossing waveguides. (b) Cross-sectional geometry of the structure. In the fabricated device, the following values are used:  $n_c = 1.6525$  or  $1.539$ ,  $n_s = 1.4508$ ,  $W_r = 1.50 \mu\text{m}$ ,  $W_b = 2.00 \mu\text{m}$ ,  $t_r = 1.50 \mu\text{m}$ ,  $t_c = 0.25 \mu\text{m}$ ,  $t_{sep} = 0.35 \mu\text{m}$ ,  $t_b = 0.50 \mu\text{m}$ ,  $d_o = 0.8 \mu\text{m}$ . (c) Parallel coupled rings.

that reaches the drop port in the node of Fig. 2 must be scattered by two consecutive junctions. Cross-talk at a single junction was measured to be less than  $-30 \text{ dB}^{[6]}$ , and therefore cross-talk observed at the drop port of Fig. 2 would in practice be less than  $-60 \text{ dB}$ . Thus the add/drop node depicted in Fig. 2 reduces all cross-talk values to second order when compare with a node consisting of a single add/drop filter. Figure 3a compares the experimental drop port response for a single ring and a cascaded pair of rings. Note that the out of band signal rejection increases significantly.

The response of each individual node might be improved by using multiple rings as shown in Fig. 1c. The measured response of the double ring configuration of Fig. 1c is shown in Fig. 3b. Due to fabrication tolerances there are slight deviations in radii which lead to shifts of the resonant wavelengths. If individual resonant linewidths overlap, box-like spectra can be observed, as shown by the peaks labeled A, B and C. There is another requirement for achieving box-like response in parallel coupled rings, which entails spacing the rings appropriately such that there is the proper phase delay between them (peak labeled E). The required phase delay is  $\pi/2 + 2\pi N$ , where

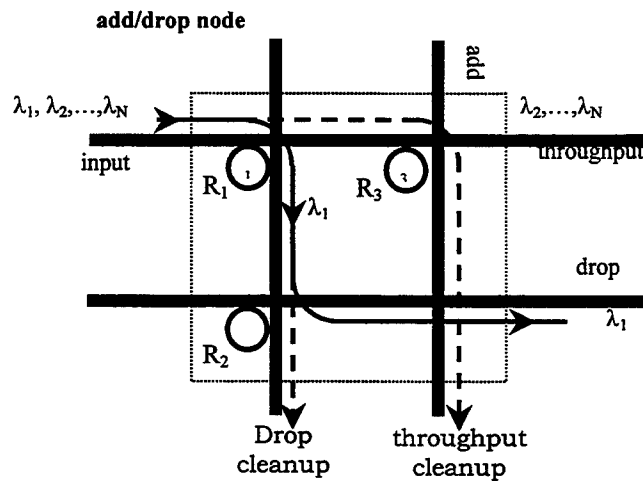


**Fig 2.** An Add/Drop node using a  $2 \times 2$  cross-grid array and three microring resonators to reduce the output port cross-talk values to second order.

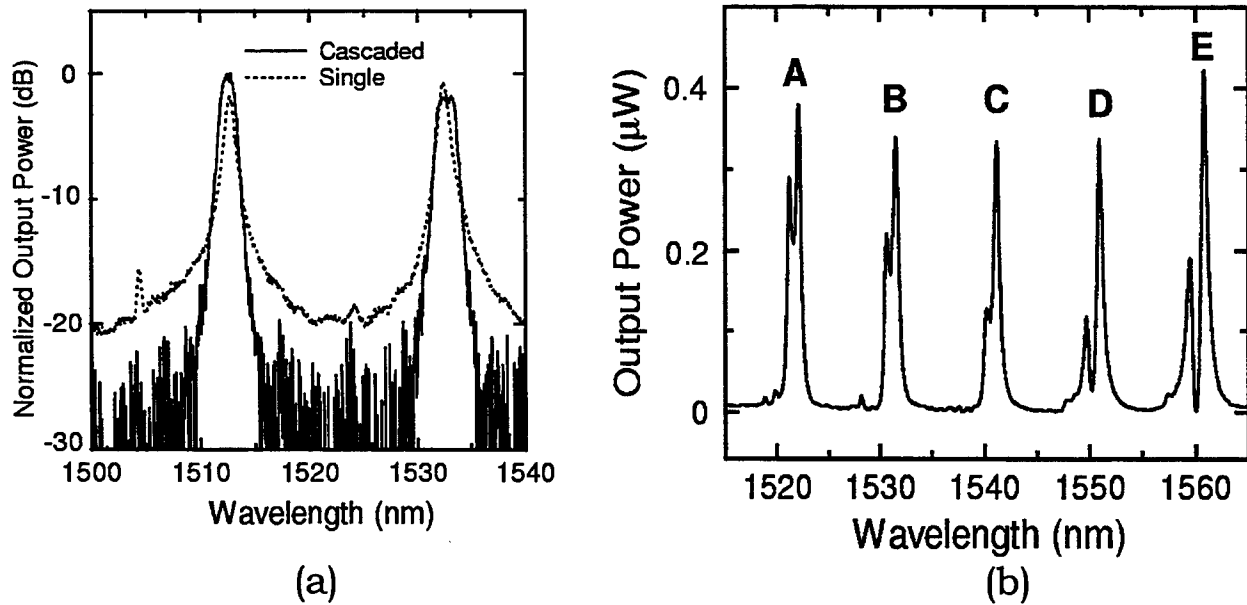


**Fig 3.** (a) Spectral response of the two cascaded rings  $R_1$  and  $R_2$  in Fig. 2. Here  $R_1 = 10.0 \mu\text{m}$ ,  $R_2 = 10.15 \mu\text{m}$  and  $n_c = 1.6532$ . (b) Spectral response of the two parallel coupled rings depicted in Fig. 1c. Here  $R = 25.0 \mu\text{m}$  and  $n_c = 1.539$ .

$N$  is some integer. If the phase delay is instead  $2\pi N$ , then the response of the two rings interfere destructively, leading to a broadened response with nodes within the peaks. Both the resonant wavelengths and the phase delay might be brought into alignment by means of post fabrication UV trimming, as has been recently demonstrated<sup>[7]</sup>

## References

- [1] B. E. Little, S. T. Chu, H. A. Haus, J. Foresi, and J.-P. Laine, *IEEE J. Lightwave Tech.*, **15**, 998 (1997).
- [2] B. E. Little, H. A. Haus, J. S. Foresi, L. C. Kimerling, E. P. Ippen, and R. J. Ripin, *IEEE Photonic Tech. Lett.*, **10** 816 (1998).
- [3] B. E. Little, J. Foresi, H. A. Haus, E. P. Ippen, and W. Greene, and S. T. Chu, "Ultra-compact Si/SiO<sub>2</sub> micro-ring resonator channel dropping filter," *IEEE Photonic. Tech. Lett.*, vol. 10, pp. 549-551, 1998.
- [4] D. Rafizadeh, J. P. Zhang, S. C. Hagness, A. Taflav, K. A. Stair, S. T. Ho, and R. C. Tiberio, "Waveguide-coupled AlGaAs/GaAs microcavity ring and disk resonators with high finesse and 21.6 nm free spectral range," *Opt. Lett.*, vol. 22, pp.1244-1246, 1997.
- [5] B. E. Little, S. T. Chu, W. Pan, D. Ripin, T. Kaneko, Y. Kokubun, E. Ippen, "Vertically coupled glass microring resonator channel dropping filters," *IEEE Photonic. Tech. Lett.*, vol. 11 pp. 215-217, 1999.
- [6] S. T. Chu, W. Pan, S. Sato, T. Kaneko, Y. Kokubun, B. E. Little, "An 8 channel wavelength add/drop filter using vertically coupled microring resonators over a cross grid," to be published, *IEEE Photonic Tech. Lett.*, June 1999.
- [7] S. T. Chu, W. Pan, S. Sato, T. Kaneko, Y. Kokubun, B. E. Little, "Wavelength trimming of a microring resonator filter by means of a UV sensitive polymer overlay," to be published, *IEEE Photonic Tech. Lett.*, June 1999.

**Integrated Photonics Research**

# **IR, Mid-IR and THz Modeling**

**Tuesday, July 20, 1999**

**Dennis Deppe, University of Texas at Austin, USA**  
Presider

**RTuC**  
**8:30am–10:15am**  
Anacapa

## Coherent pump-probe interactions and terahertz intersubband gain in semiconductor quantum wells

Ansheng Liu<sup>§</sup> and C. Z. Ning

*NASA Ames Research Center, M/S T27A-1, Moffett Field, CA 94035*

*<sup>§</sup>Department of Electrical Engineering, Arizona State University, Tempe, AZ 85287*

*Fax: (650)604 3957; Email: cning@nas.nasa.gov*

In recent years there has been considerable interest in intersubband-transition-based infrared semiconductor quantum well (QW) lasers because of their potential applications. In the mid-infrared range, both electrically-injected quantum cascade lasers [1] and optically-pumped multiple QW lasers [2] have been experimentally realized. In these studies, optical gain is due to population inversion between the lasing subbands. It was also proposed that stimulated Raman scattering in QW systems can produce net infrared optical gain [3]. In such a nonlinear optical scheme, the appearance of optical gain that may lead to intersubband Raman lasers does not rely on the population inversion. Since, in the resonant Raman process (Raman gain is the largest in this case), the pump field induces population redistribution among subbands in the QW system, it seems that a realistic estimate of the optical gain has to include this effect. Perturbative calculations used in the previous work [3] may overestimate the Raman gain.

In this paper we present a nonperturbative calculation of terahertz gain of optically-pumped semiconductor step quantum wells. Limiting optical transitions within the conduction band of the QW, we solve the pump-field-induced nonequilibrium distribution function for each subband of the QW system from a set of coupled rate equations. Both intrasubband and intersubband relaxation processes in the quantum well system are included. Taking into account the coherent interactions between pump and THz (signal) waves, we derive the susceptibility of the QW system for the THz field. For a GaAs/AlGaAs step QW, we calculate the THz gain spectrum for different pump frequencies and intensities. Under moderately strong pumping ( $\sim 0.3 \text{ MW/cm}^2$ ), a significant THz gain ( $\sim 300 \text{ cm}^{-1}$ ) is predicted. It is also shown that the coherent wave interactions (resonant stimulated Raman processes) contribute significantly to the THz gain. Our theory is outlined as follows.

We consider an asymmetric step quantum well structure with three subbands. The two upper subbands are the lasing states, and the subband energy separation ( $E_{32}$ ) at zero wave vector of electrons ( $k_{\parallel} = 0$ ) lies in the THz frequency range (1-10 THz or 4-40 meV). The conduction band nonparabolicity is taken into account by using a subband-energy-dependent effective mass scheme. A strong pump field of frequency  $\omega_p$  ( $\hbar\omega_p \approx E_{31}$ ) drives the QW system, as illustrated in the inset of Fig. 1. The pump field induces a redistribution of electrons among the three subbands. The rate equations that govern the electronic distribution functions [ $f_m(k_{\parallel}) \equiv f_m(m = 1, 2, 3)$ ] are given by [4]

$$\frac{\partial f_1}{\partial t} = -W_{12}(f_1 - f_2) - W_{13}(f_1 - f_3) - \frac{f_1 - f_1^F}{T_{cc}} + \frac{f_2}{\tau_{21}} + \frac{f_3}{\tau_{31}}, \quad (1)$$

$$\frac{\partial f_2}{\partial t} = W_{12}(f_1 - f_2) - \frac{f_2 - f_2^F}{T_{cc}} - \frac{f_2}{\tau_{21}} + \frac{f_3}{\tau_{32}}, \quad (2)$$

$$\frac{\partial f_3}{\partial t} = W_{13}(f_1 - f_3) - \frac{f_3 - f_3^F}{T_{cc}} - \frac{f_3}{\tau_{31}} - \frac{f_3}{\tau_{32}}, \quad (3)$$

where

$$W_{mn} = \frac{2\Gamma_{mn}}{\hbar} \frac{|H'_{mn}|^2}{[\hbar\omega_p - E_{nm}(k_{||})]^2 + \Gamma_{mn}^2}. \quad (4)$$

In the above equations  $T_{cc}$ ,  $\tau_{mn}$ , and  $\Gamma_{mn}$  are the intrasubband carrier-carrier scattering time, intersubband relaxation time, and line broadening, respectively. In the electrical dipole approximation, the matrix element of the light-quantum-well interaction Hamiltonian is  $H'_{mn} = -E_p \mu_{mn}$ , where  $E_p$  denotes the amplitude of the pump electric field that is polarized perpendicular to the wells and  $\mu_{mn}$  is the dipole matrix element between subband  $m$  and subband  $n$ . The quantities  $f_m^F (m = 1, 2, 3)$  are considered to be the quasi-equilibrium distribution functions since the intrasubband relaxation processes in QW systems are usually very fast (in fs ranges). For a given temperature and electron density, the steady-state nonequilibrium distribution function for each subband is uniquely determined from Eqs. (1)-(3). Here we would like to emphasize that the total particle number in our QW system is conserved in our treatment.

Taking into account the pump and THz wave interactions in the QW system, we find the off-diagonal element of the density matrix operator between subband 3 and subband 2 at the THz frequency  $\omega$  is given by [4]

$$\rho_{32}(\omega) = \frac{f_2 - f_3 - \mathcal{R}(\omega, \omega_p)}{\hbar\omega - E_{32}(k_{||}) + i\Gamma_{23} - \Delta(\omega, \omega_p)} (-\mu_{32}E_\omega) \equiv -A(\omega, \omega_p, k_{||})\mu_{32}E_\omega, \quad (5)$$

where  $E_\omega$  is the THz field in the QW, and

$$\Delta(\omega, \omega_p) = \frac{|H'_{31}|^2}{\hbar(\omega - \omega_p) + E_{21}(k_{||}) + i\Gamma_{12}} + \frac{|H'_{21}|^2}{\hbar(\omega_p + \omega) - E_{31}(k_{||}) + i\Gamma_{13}}, \quad (6)$$

$$\begin{aligned} \mathcal{R}(\omega, \omega_p) = & \frac{|H'_{31}|^2(f_1 - f_3)}{[\hbar(\omega - \omega_p) + E_{21}(k_{||}) + i\Gamma_{12}][\hbar\omega_p - E_{31}(k_{||}) - i\Gamma_{13}]} \\ & + \frac{|H'_{21}|^2(f_1 - f_2)}{[\hbar(\omega_p + \omega) - E_{31}(k_{||}) + i\Gamma_{13}][\hbar\omega_p - E_{21}(k_{||}) + i\Gamma_{12}]} . \end{aligned} \quad (7)$$

$\Delta(\omega, \omega_p)$  in Eq. (5) is responsible for the optical Stark effect while  $\mathcal{R}(\omega, \omega_p)$  gives rise to the Raman gain of the QW system. From Eq. (5) we define the susceptibility for the THz probe field as

$$\chi(\omega) = -\frac{2|\mu_{23}|^2}{\epsilon_0 L_w} \int \int \frac{d^2 k_{||}}{(2\pi)^2} A(\omega, \omega_p, k_{||}), \quad (8)$$

$L_w$  being the width of the active layer. Therefore, the optical gain is given by

$$G(\omega) = -\frac{\omega}{c_0 n_b} \text{Im}[\chi(\omega)]. \quad (9)$$

Using Eqs. (1)-(9) we calculated the THz gain spectrum of a GaAs/AlGaAs step QW at different pump frequencies and intensities. A typical result is shown in Fig. 1. In calculating

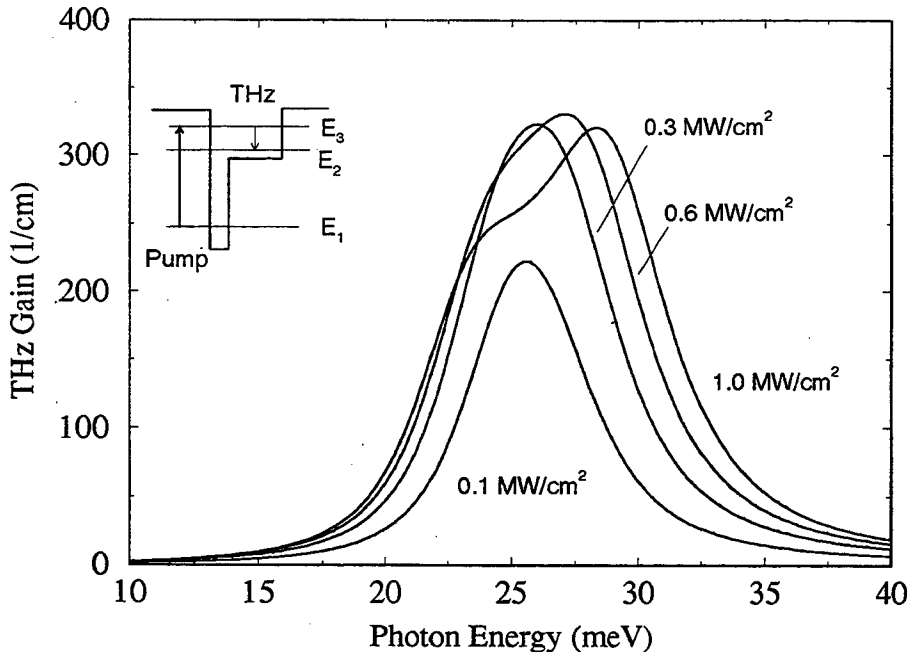


Figure 1: THz gain spectrum of a GaAs/AlGaAs step quantum well with a subband separation of  $E_{32} \approx 25$  meV for different pump intensities, i.e. 0.1, 0.3, 0.6, and 1.0 MW/cm<sup>2</sup>. The pump photon energy is  $\hbar\omega_p = E_{31} \approx 125$  meV. The other parameters used in the calculation are given as follows: the sheet electron density is  $5.16 \times 10^{10}$  cm<sup>-2</sup>,  $T_{cc}=0.6$  ps,  $\tau_{21}=1.0$  ps,  $\tau_{31}=1.2$  ps,  $\tau_{32}=1.5$  ps, and  $\Gamma_{12}=\Gamma_{13}=\Gamma_{23}=3.0$  meV.

Fig. 1, the following parameters were employed: the deep well width is 65 Å, the shallow well width is 130 Å,  $\Gamma_{12}=\Gamma_{13}=\Gamma_{23}=3.0$  meV,  $T_{cc}=0.6$  ps,  $\tau_{21}=1.0$  ps,  $\tau_{31}=1.2$  ps, and  $\tau_{32}=1.5$  ps. The sheet electron density is  $5.16 \times 10^{10}$  cm<sup>-2</sup>. The temperature is T=100 K. The pump photon energy is  $\hbar\omega_p = E_{31} \approx 125$  meV. The pump intensity is varied from 0.1 to 1.0 MW/cm<sup>2</sup>. Our calculations show that the optical gain is strongly dependent on the pump intensity and frequency, and the maximum gain is not linearly proportional to the pump intensity as given in the previous perturbative calculations [3] even when the pump field is moderately strong because of the optical Stark effect as well as the pump-induced population redistribution among the subbands.

1. J. Faist, F. Capasso, D. Sivco, C. Sirtori, A. L. Hutchinson, S. N. G. Chu, and A. Y. Cho, Science **264**, 553 (1994); Appl. Phys. Lett. **68**, 3680 (1996).
2. O. Gauthier-Lafaye et. al., Appl. Phys. Lett. **71**, 3619 (1997).
3. J. B. Khurgin, G. Sun, L. R. Friedman, and R. A. Soref, J. Appl. Phys. **78**, 7398 (1995); J. Opt. Soc. Am. B **15**, 648 (1998).
4. A. Liu, J. Opt. Soc. Am. B **15**, 1741 (1998).

## Optically-pumped type-II interband terahertz lasers

I. Vurgaftman and J. R. Meyer  
 Code 5613, Naval Research Laboratory, Washington, DC 20375  
 Phone: (202) 404-8604 FAX (202) 404-8613  
[vurgaftm@aphrodite.nrl.navy.mil](mailto:vurgaftm@aphrodite.nrl.navy.mil)

Dramatic successes of the quantum cascade laser in the 5-17  $\mu\text{m}$  spectral range have led to the perception that intersubband devices offer the only viable approach to THz lasing based on III-V quantum wells. This impression had been reinforced by the total absence of any analogous interband demonstrations at wavelengths beyond 5.3  $\mu\text{m}$ . However, quite recently optically-pumped type-II "W" structures not only extended the maximum wavelength for interband III-V lasers to 7.1  $\mu\text{m}$ , but achieved cw operation up to 130 K at that wavelength.<sup>1</sup> Furthermore, at  $\lambda = 5.9 \mu\text{m}$  the cw  $T_{\max}$  of 210 K was higher than any previous III-V result (interband or intersubband) for  $\lambda > 3 \mu\text{m}$ .<sup>2</sup>

In the long-wavelength limit, the intersubband Auger-like process, in which two electrons in the upper subband each scatter to the lower subband with opposite momentum transfers, is non-activated and has a shorter lifetime at low  $T$  than that for the thermally activated interband Auger process. Interband lasers can therefore achieve much higher optical gain and are expected to regain their advantage in the long-wavelength limit, especially when optical pumping is employed.

A critical issue for a successful THz laser is the high internal loss, *e.g.*, associated with free carriers populating the active region, doped optical cladding layers, and  $n^+$  contacting layers. Those losses tend to scale as  $\approx \lambda^2$ , which implies that for an intersubband device emitting at  $\lambda_o = 60 \mu\text{m}$ ,  $\alpha_{\text{int}}$  may exceed 1000  $\text{cm}^{-1}$ . At that point, it is difficult to see how lasing can be achieved at all. Gains of that magnitude would require much higher inversion carrier densities than for mid-IR QCLs, and may in fact be beyond the maximum attainable at far-IR wavelengths. Below we will consider the unfortunate but seemingly necessary solution of employing optical rather than electrical pumping. That removes the requirement for doped layers and should result in a substantial reduction of the loss.

A further challenge is confinement of the optical mode. A simple linear scaling with  $\lambda_o$  leads to net cladding-layer thicknesses that are altogether impractical for MBE fabrication even if a lower-index substrate functions as the bottom clad. Electrical pumping would then seem to require the use of a heavily doped plasma reflector above the active region, which will further increase the loss. However, with optical pumping we may employ the recently-demonstrated diamond-pressure-bonding (DPB) technique, in which the diamond not only provides an excellent heat sink, but also serves as the top optical cladding layer and provides a transparent window for topside optical pumping.

The type-II W approach<sup>3</sup> developed for mid-IR lasers is easily tailored to THz emission simply by increasing the thicknesses of the two InAs electron quantum wells in each period. These surround a single GaInSb hole well to enhance the gain and differential gain, which are especially critical at far-IR wavelengths as discussed above. We first consider a 58-Å InAs/30-Å GaIn<sub>0.25</sub>Sb<sub>0.75</sub>/50-Å InAs/100-Å GaAs<sub>0.25</sub>Sb<sub>0.75</sub> structure designed for emission at  $\lambda_o = 27 \mu\text{m}$ . Whereas most mid-IR W lasers have employed AlSb-based barriers between periods, here the use of GaAsSb serves to increase the active-region refractive index. More important, were AlSb-like longitudinal optical (LO) phonon modes with an energy of 43 meV present in the structure (as compared to the energy gap and lasing photon energy of 46 meV), they would be expected to increase the nonradiative recombination rate and internal loss. Instead, the gap significantly exceeds the largest LO phonon mode energy of 36 meV (GaAs-like). Thus the non-

radiative lifetime is dominated by Auger processes. Using the InAs substrate as the bottom clad and the diamond heat sink as the top clad, a 7- $\mu\text{m}$ -thick active region results in an optical confinement factor of 67%.

Calculations as a function of carrier density and temperature yield a maximum available gain of  $> 1000 \text{ cm}^{-1}$ . To compute the internal loss due to free carrier absorption of TE-polarized photons in the active region, we employ the classical Drude expression and also a density-independent contribution of due to scattering losses or unintentional doping. Auger, Shockley-Read, and acoustic-phonon-assisted recombination processes were included in a rate equation model for the electron, photon, and carrier/lattice temperature dynamics. Figure 1 shows calculated pulsed and cw light-light curves for the 27- $\mu\text{m}$  W emitter pumped by a 10.6  $\mu\text{m}$  CO<sub>2</sub> laser. Pulsed operation is predicted up to 60 K and cw to 35 K, and output powers exceeding 100 mW appear quite feasible.

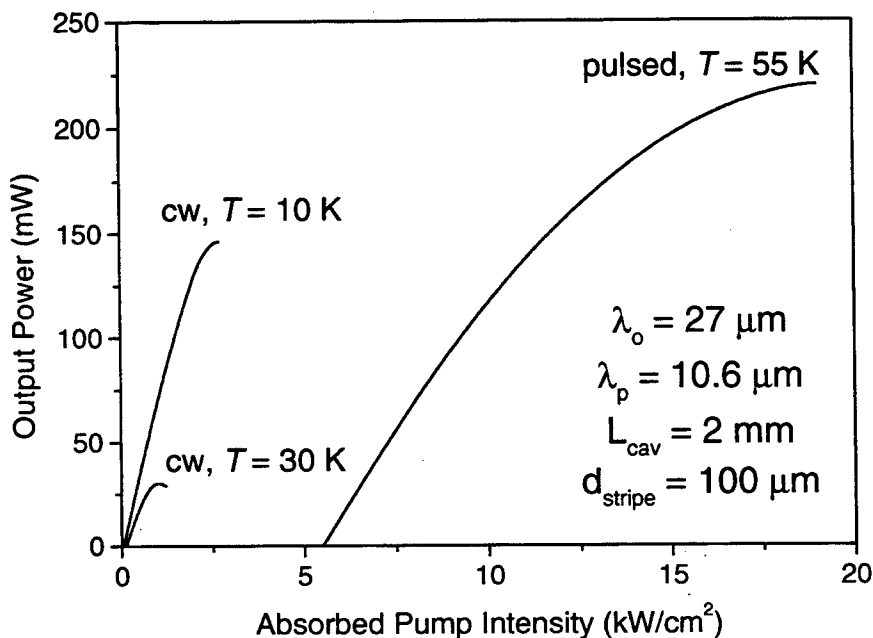


**Figure 1.** Calculated pulsed and cw output powers vs. absorbed pump intensity for a type-II W laser emitting at 27  $\mu\text{m}$ .

Operation within or near the optical phonon bands of the constituent bulk materials is problematic for both interband and intersubband lasers due to femtosecond nonradiative recombination and strong phonon absorption, ruling out emission in the  $\approx 30\text{-}50 \mu\text{m}$  spectral region. At longer wavelengths, activated phonon-assisted recombination processes involving thermally-excited electrons and holes must be taken into account.

To illustrate the longer-wavelength analysis, we consider a W laser designed for emission at  $\lambda_0 = 60 \mu\text{m}$ : 72.5 Å InAs/30 Å GaSb/62.5 Å InAs/65 Å AlSb. This all-binary structure avoids the presence of any InSb-like optical phonon modes ( $\hbar\omega_{ph} = 24 \text{ meV}$ ), which would have contributed substantially more activated recombination than the GaSb-like (29 meV), InAs-like (30 meV), and AlSb-like modes.

The solid curves of Fig. 2 show calculated polar-optical-phonon (POP) emission lifetimes for the 60- $\mu\text{m}$  W structure as a function of injected carrier density at carrier temperatures ( $T_e$ ) of 4 K, 12 K, and

16.5 K. For 12 K, we also plot the total lifetime ( $\tau_{tot}$ , dotted), the acoustic phonon emission lifetime ( $\tau_{ac}$ , dash-dot) and the Auger lifetime ( $\tau_A$ , dashed). At  $T_e = 4$  K,  $\tau_A$  is off the scale of the plot while  $\tau_{ac}$  is nearly the same so that acoustic phonons dominate at the lasing threshold. At  $T_e = 12$  K, which corresponds to a lattice temperature of  $\approx 10$  K ( $T_{max}$  in this structure), the POP scattering process dominates. The rapid activation of that process limits the lasing temperature for this structure to low  $T$ . However, if the energy gap is decreased further, the POP lifetime increases, while the Auger lifetime decreases exponentially. We predict that Auger recombination should again become dominant for wavelengths longer than 75  $\mu\text{m}$ . The carrier lifetime for the 60- $\mu\text{m}$  structure is 300 ps for the threshold density of  $3.6 \times 10^{10} \text{ cm}^{-2}$  at  $T_{max} = 10$  K. This lifetime is far longer than the value calculated for electron-electron scattering in an intersubband cascade laser. It is estimated that pulsed lasing at 4 K should be achievable to wavelengths as long as  $\approx 100$   $\mu\text{m}$ .

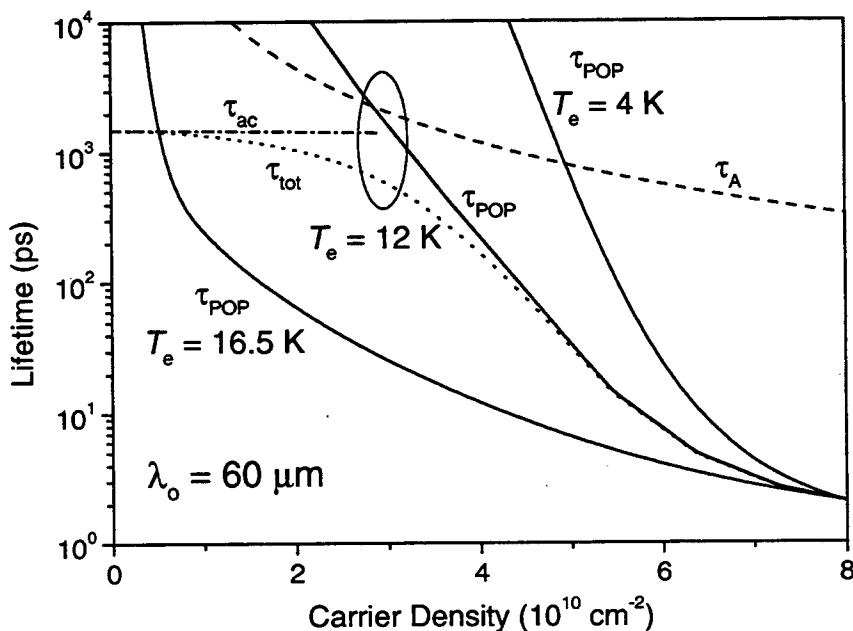


**Figure 2.** Polar-optical-phonon (POP, solid curves), Auger (dashed curve), acoustic (dash-dotted curve), and total (dotted curve) nonradiative lifetimes vs. carrier density for the structure designed to emit at 60  $\mu\text{m}$  at a carrier temperature of 12 K. The POP lifetimes at  $T_e = 4$  K and 16.5 K are also shown.

<sup>1</sup> C. L. Felix, W. W. Bewley, L. J. Olafsen, D. W. Stokes, E. H. Aifer, I. Vurgaftman, J. R. Meyer, M. J. Yang and B. V. Shanabrook, submitted for publication.

<sup>2</sup> W. W. Bewley, C. L. Felix, I. Vurgaftman, D. W. Stokes, E. H. Aifer, L. J. Olafsen, J. R. Meyer, M. J. Yang, B. V. Shanabrook, H. Lee, R. U. Martinelli, and A. R. Sugg, *Appl. Phys. Lett.* **74**, 1075 (1999).

<sup>3</sup> J. R. Meyer, C. A. Hoffman, F. J. Bartoli, and L. R. Ram-Mohan, *Appl. Phys. Lett.* **67**, 757 (1995).

# Electronic structure engineering of mid-infrared lasers

**Michael E. Flatté, J. T. Olesberg, T. F. Boggess, T. C. Hasenberg**

Department of Physics and Astronomy and Optical Science and Technology Center,  
University of Iowa, Iowa City, Iowa 52242  
flatte@uiowa.edu

**C. H. Grein**

Department of Physics, University of Illinois, Chicago, Illinois 60607

Mid-infrared semiconductor lasers have a variety of potential applications, including as spectroscopic probes for pollution monitoring and non-invasive medical sensing and high-power sources for military infrared countermeasures. Lasers have been successfully demonstrated based on interband and intersubband transitions in both type-I and type-II heterostructures.<sup>1,2,3,4,5</sup> Devices from each of these categories hold performance world records of various types. The role of electronic structure engineering in these materials is of particular importance first, because it is primarily the *intrinsic* material properties of the device constituents (particularly the active region) which determine the ultimate laser performance, and second, because these intrinsic properties can be dramatically altered by proper choices of layer thicknesses and compositions in superlattice and quantum well materials. Examples of these crucial material properties include Auger recombination, optical loss, differential gain, and the linewidth enhancement factor.

Many of the deleterious intrinsic material effects in semiconductor lasers are exacerbated in mid-infrared structures. The difference between the conduction and valence density of states in bulk mid-infrared semiconductors is greater than at shorter wavelengths because the electron effective mass is proportional roughly to the wavelength. Imbalances between the densities of states at the band edge increase the threshold carrier density, which leads to a dramatic increase in Auger recombination and intersubband absorption (and thus to optical loss). The differential gain and linewidth enhancement factor also suffer in an unbalanced system. Furthermore, in addition to the increase in the Auger rate due to increased threshold carrier densities, the Auger rate at a fixed density also increases dramatically with wavelength.

Fortunately the ability to adjust optoelectronic properties is also greater in the mid-infrared, due to the existence of three binary semiconductors, InAs, GaSb, and AlSb, which are roughly lattice matched and have relative band offsets greatly exceeding mid-infrared energy gaps. We will focus on a particular structure,<sup>6</sup> a four-layer broken-gap superlattice (BGSL) based on the InAs/GaInSb material system and designed to function as a laser active region at 4.0  $\mu\text{m}$ . The carrier recombination rate, optical loss via intersubband absorption, and linewidth enhancement factor for this structure will be presented. Finally we will compare the optimum net gain to volumetric current of this structure to that of type-I quantum wells also used as active regions in the mid-infrared.<sup>7</sup> Based on the calculated properties of the BGSL, and given reasonable assumptions about the modal loss, we find that active regions of the four-layer BGSL could be made extremely thin. This suggests the possibility of single quantum well lasers.

The electronic structure of the mid-infrared materials considered is calculated using a semi-empirical fourteen-band superlattice  $\mathbf{K}\bullet\mathbf{p}$  formalism. Unlike commonly used eight-band models, which treat the heavy hole separately from the light bands and within which cubic symmetry must be introduced somewhat *ad hoc*, the fourteen band model produces the appropriate zone-center electronic structure in a minimal restricted basis. The Auger recombination rates and optical properties are calculated from the resulting electronic structure. We note that there are no adjustable parameters in these calculations.

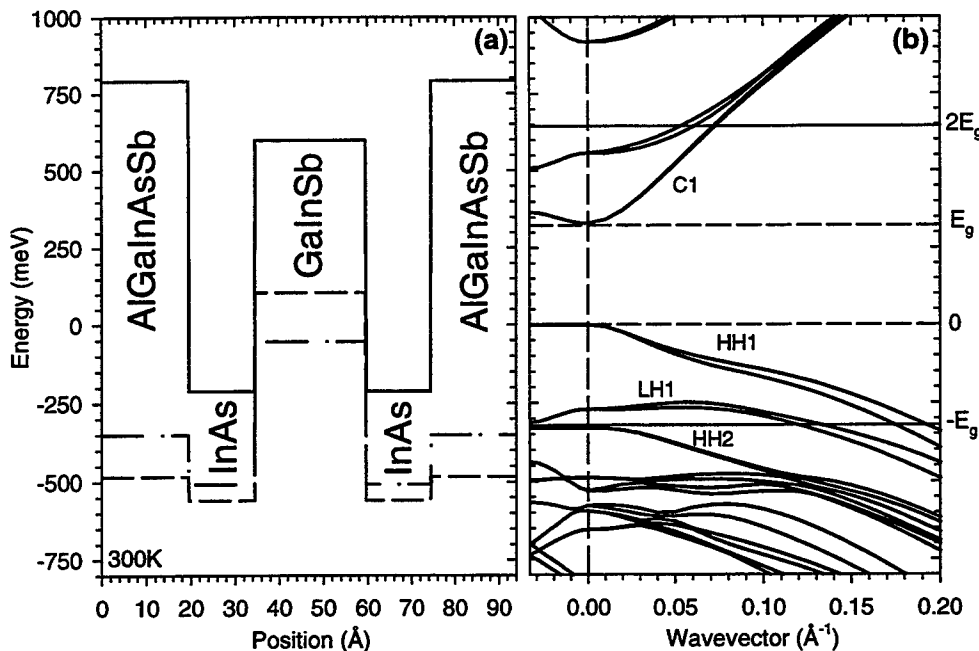


Fig.1: (a) Band edges of the constituents of a four-layer superlattice, and (b) the resulting band structure. The band offsets of the constituents greatly exceed the energy gap of the superlattice. The gaps near zone center that occur an energy gap away from the band edges lead to reduced Auger recombination and optical loss.

Optimized interband mid-infrared laser active regions. The dominant mechanism for carrier recombination near lasing threshold in interband mid-infrared lasers is direct Auger recombination, whereas the dominant mechanism for optical loss is intersubband absorption. This has led to detailed investigations of how the structure of the laser active region may be chosen to minimize these two processes. One strategy for reducing Auger recombination, familiar from near-infrared lasers, is to improve the balance between the conduction and valence densities of states near the band edge through strain and quantum confinement. In mid-infrared lasers, however, it is also possible to influence the available *final* states for Auger processes. Since these final states reside in the bands more than the energy gap away from the band edges, the active region must be constructed of materials with band offsets large compared to the energy gap of the material. Figure 1 shows the band edges and band structure of a four-layer BGSL based on the InAs/GaInSb material system, which has a 300K energy gap of 4.0 μm. The large band offsets in this material system allow for the creation of effective gaps near zone center in the band structure one energy gap below the valence maximum and above the conduction minimum. These gaps are properly positioned with appropriate choices of layer thicknesses and compositions. Calculations of the Auger rate for this structure agree with experiment within 20%.<sup>6</sup>

These gaps in the electronic structure also play an important role in reducing the intersubband absorption (ISBA), and thus the optical loss. The final states for intersubband absorption at the lasing energy lie in similar regions of the band structure to the final states for Auger. Thus, whereas the intersubband absorption at carrier densities appropriate for lasing in other mid-infrared structures can be many hundreds of cm⁻¹, strong absorption features for the four-layer BGSL lie outside the region of peak gain, as shown in Fig. 2. In type-I quantum well active regions, by contrast, the final states are essentially unstructured and thus the intersubband absorption is broad, featureless, and large. Improvements in the density of states balance between the conduction and valence band also reduce the intersubband absorption by reducing the optimal carrier density for lasing.

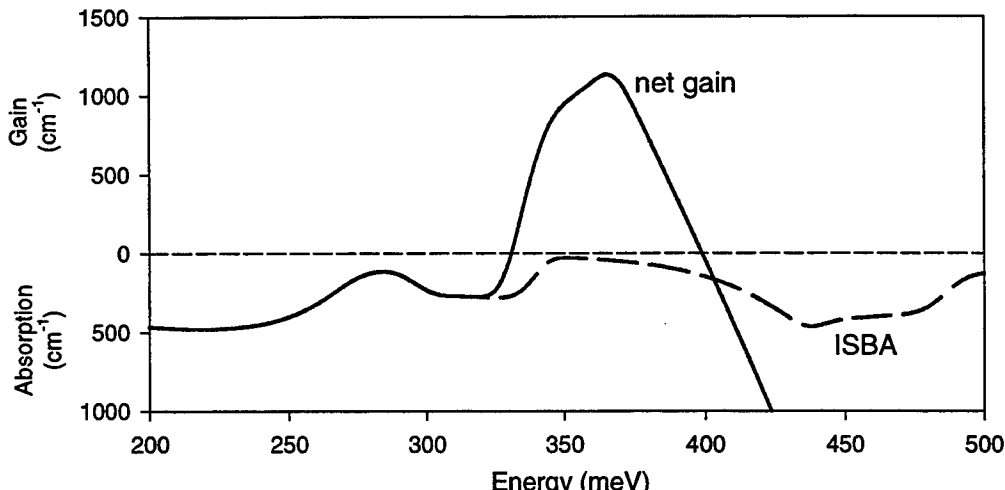


Fig. 2: The ISBA in the BGSL at the optimal carrier density ( $10^{18} \text{ cm}^{-3}$ ) does not overlap with the peak gain.

Comparisons among material systems. After calculating the optical and electronic properties that affect laser device performance it is important to weigh them appropriately in choosing an ideal system. The appropriate means of comparing mid-infrared laser diode active regions is through the optimum net gain per unit recombination current density of each structure.<sup>7</sup> In a properly designed laser structure the threshold current density is inversely proportional to this figure of merit. The theoretical figure of merit of type-I quantum wells<sup>1</sup> exceeds that of bulk materials by an order of magnitude, whereas that of type-II heterostructures<sup>2,6</sup> exceeds that of type-I quantum wells by an additional factor of five. For the BGSL the ideal 300K threshold current density for a mode width of  $2\mu\text{m}$  and a modal loss of  $10\text{cm}^{-1}$  is  $730 \text{ A/cm}^2$ .

Calculations of the material gain indicate that the optimum thickness of an active region based on the BGSL is merely  $200\text{-}300\text{\AA}$ . This suggests the possibility of single quantum well lasers based on BGSL's. Such a structure (further optimized) is calculated to have a 300K threshold current density of  $74\text{A/cm}^2$ .

This research was supported in part by the U.S. Air Force, Air Force Materiel Command, Air Force Research Laboratory, Kirtland AFB, New Mexico, 87117-5777 (Contract No. F29601-97-C-0041), and the National Science Foundation (Grant No. ECS-9707799).

<sup>1</sup> H. K. Choi, G. W. Turner, M. J. Manfra, and M. K. Connors, *Appl. Phys. Lett.* **68**, 2936 (1996); S. R. Kurtz, A. A. Allerman, and R. M. Biefeld, *Appl. Phys. Lett.* **70**, 3188 (1997).

<sup>2</sup> T. Ashley, C. T. Elliott, R. Jefferies, A. D. Johnson, G. J. Pryce, A. M. White, and M. Carroll, *Appl. Phys. Lett.* **70**, 931 (1997).

<sup>3</sup> T. C. Hasenberg, R. H. Miles, A. R. Kost, and L. West, *IEEE J. Quantum Electron.* **33**, 1403 (1997); J. I. Malin, J. R. Meyer, C. L. Felix, J. R. Lindle, L. Goldberg, C. A. Hoffman, and F. J. Bartoli, *Appl. Phys. Lett.* **68**, 2976 (1996); D. H. Chow, R. H. Miles, T. C. Hasenberg, A. R. Kost, Y. H. Zhang, H. L. Dunlap, and L. West, *Appl. Phys. Lett.* **67**, 3700 (1995).

<sup>4</sup> L. J. Olafsen, E. H. Aifer, I. Vurgaftman, W. W. Bewley, C. L. Felix, J. R. Meyer, D. Zhang, C.-H. Lin, and S. S. Pei, *Appl. Phys. Lett.* **72**, 2370 (1998).

<sup>5</sup> J. Faist, F. Capasso, D. L. Sivco, C. Sirtori, A. L. Hutchinson, and A. Y. Cho, *Science* **264**, 553 (1994).

<sup>6</sup> M. E. Flatté, J. T. Olesberg, S. A. Anson, T. F. Boggess, T. C. Hasenberg, R. H. Miles, and C. H. Grein, *Appl. Phys. Lett.* **70**, 3212 (1997); M. E. Flatté, C. H. Grein, T. C. Hasenberg, S. A. Anson, D.-J. Jang, J. T. Olesberg, and T. F. Boggess, *Phys. Rev. B* **59**, 5745 (1999).

<sup>7</sup> J. T. Olesberg, M. E. Flatté, B. J. Brown, C. H. Grein, T. C. Hasenberg, S. A. Anson, and T. F. Boggess, *Appl. Phys. Lett.* **74**, 188 (1999).

## Carrier transport in GaInP laser structures

Peter Blood<sup>1</sup>

Scott Wood and Catherine Molloy

Department of Physics and Astronomy  
Cardiff University, PO Box 913, Cardiff CF2 3YB, UK

The reliable, comprehensive simulation of laser diode operation demands a detailed knowledge of the physical process within the device and of the values of the parameters which govern these processes. Red-emitting AlGaInP lasers can suffer from a thermally-activated contribution to the threshold current at room temperature and above which also causes a decrease in differential efficiency with increasing temperature. The design of high quality devices in this material system is often concerned, in whole or in part, with minimising this excess current. From detailed studies of the thermal activation energy of this excess leakage current it has been established that it is due to loss of electrons from the active region via the indirect X conduction band minima [1]. Computer simulations, which include drift and diffusion of electrons through the p-cladding layer, agree very well with experimental data for threshold current as a function of temperature [2]. However there is very little experimental data for many of the parameters required for these simulations and agreement with experiment has been achieved using "reasonable" values. The most critical parameters are the ionisation energy of the acceptors and the mobilities of majority and minority carriers.

While these simulations provide a good *description* of the experimental data, the agreement achieved does not constitute a *proof* that carrier loss occurs by drift and diffusive leakage. In principle carrier loss could occur by non-radiative recombination across the indirect gap via deep states, though numerical estimates suggest that the capture cross sections and deep state concentrations must be quite large to account for the magnitude of the leakage current observed in some devices. If the drift/diffusion model is accepted as responsible for the electron loss, it remains important to be able to incorporate it correctly into computer models because of its on the temperature dependence of threshold current, the differential efficiency above threshold, and the modulation response. Thus it is desirable to confirm the reliability of the drift/diffusion model for carrier loss and to obtain more accurate values for the material parameters which control the process, particularly the minority carrier mobility.

We have obtained direct evidence for electron leakage through the p-cladding layer by the drift/diffusion process and have obtained a value for the electron mobility in p-AlGaInP. The band diagram in figure 1 illustrates the principle of the experiment. A direct-gap collector or monitor layer was inserted into the p-cladding layer of the laser close to the p-GaAs contact layer, with the intention that electrons which leak through the cladding layer are collected in this region where they recombine with majority carrier holes. By judicious choice of layer

---

<sup>1</sup> Phone: (+44) (0)1222 874785, fax: (+44) (0)1222 874056; email: bloodp@cf.ac.uk

compositions it is possible to arrange that radiation from the quantum well, waveguide core, and monitor layer can be spectrally resolved and that the monitor layer is not optically pumped by radiation from other parts of the device. The radiation was observed as spontaneous emission through a window in the top contact of the device.

The structures were grown by MOCVD (by C C Button at the University of Sheffield) as conventional single well GaInP lasers. The current-voltage and light-current characteristics measured over the range 200K to 380K are not affected by the presence of the monitor layer. We observe emission from the monitor layer over a wide range of drive currents, indicating that there is an electron flow through the p-cladding layer. The spontaneous emission from the quantum well saturates above threshold whereas the emission from the monitor layer continues to increase with current. We interpret this as evidence for a drift component to the leakage current which continues to increase with current, even when the Fermi levels in the well are pinned, due to the increasing electric field across the cladding layer. This interpretation has been confirmed by computer simulation.

With the laser maintained electrically in forward bias, we injected pulses of electron-hole pairs into the quantum well using 20ps pulse excitation at 630nm from a dye laser. The spontaneous emission from the monitor layer was detected at 585nm using standard single photon counting techniques. Figure 2 shows the measured time response of the monitor layer for two different electrical drive currents, with the scattered pump light from the sample surface providing a reference signal which also indicates the overall time resolution of the measuring system. Superimposed on the steady electro-luminescence we observe the transient response of the monitor layer to optical excitation of the well. The delay time between well and monitor layer luminescence is about 0.5ns. The response of the monitor layer is influenced by the rise-time of the carrier population in the well, the transit time through the cladding layer, and the rise-time of the carrier population in the monitor layer. Because the pulse length is short compared with the recombination time, the rise-time in the well is determined by the pulse length. The lifetime in the monitor layer was measured to be 0.6ns.

To determine the influence of the transit time on the time delay we carried out a finite-difference rate equation simulation of the experiment, including emission and capture of electrons at the well, carrier transport through the cladding layer, carrier recombination in the well, cladding layer and monitor region, and the temporal response of the measuring system. The monitor layer response was insensitive to the values used for the hole mobility for values above  $10\text{cm}^2\text{V}^{-1}\text{s}^{-1}$  whereas the simulated delay was dependent upon the value of the electron mobility, which was varied between  $60\text{cm}^2\text{V}^{-1}\text{s}^{-1}$  and  $180\text{cm}^2\text{V}^{-1}\text{s}^{-1}$ . With a hole mobility of  $10\text{cm}^2\text{V}^{-1}\text{s}^{-1}$ , an electron mobility of  $160\text{cm}^2\text{V}^{-1}\text{s}^{-1}$  reproduced the measured time delay using experimentally determined values for the monitor layer recombination time. We conclude that this is the value of the electron mobility in our material. Using the simulation we have examined the current dependence of the drift/diffusion process and the behaviour of the frequency response of the device.

[1] P M Smowton and P Blood, Journ Quantum Electronics, **31** (1995) 2159

[2] D L Foulger, P M Smowton, P Blood, and P A Mawby, IEE Journ Quantum Electronics

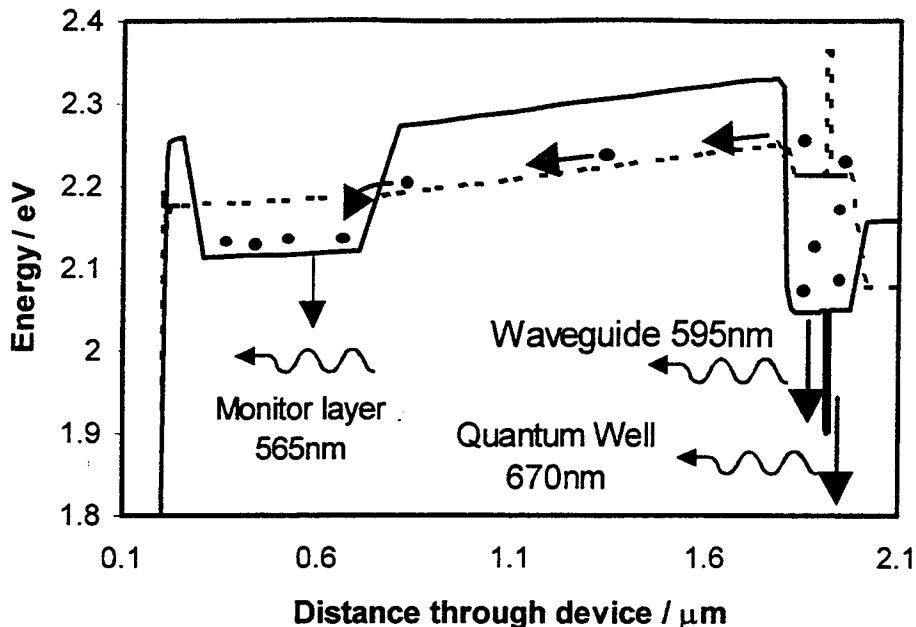


**Figure 1.** Energy band diagram as a function of distance through the active region, the p-cladding layer and the contact layer, illustrating the capture of electrons which leak through the cladding layer by the monitor layer. The dash line shows the indirect X-conduction band minimum.

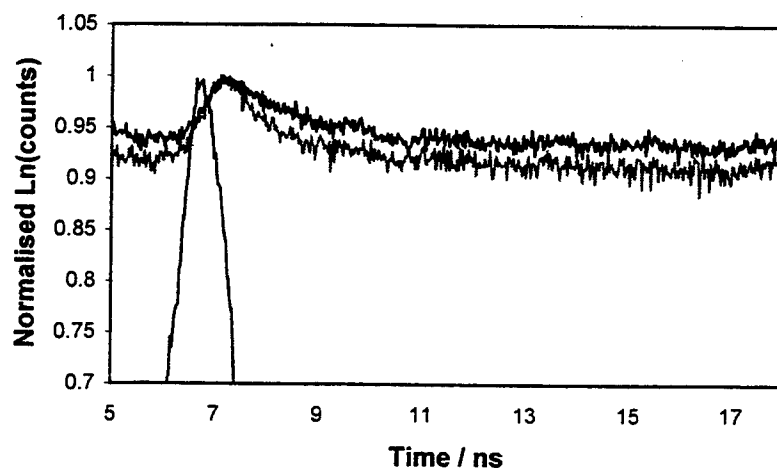


**Figure 2.** Temporal response of the emission from the monitor layer following pulse optical excitation of the quantum well with forward bias currents of 20mA and 50mA. Scattered pump light is also shown to provide an indication of the response of the measuring system. The light output is plotted on a logarithmic scale and the emission from the monitor layer at each current is normalised to the same peak value.

# Optical Properties of Active Semiconductor Waveguides For Integrated Photonics Device Modeling

Valery I. Tolstikhin

*Optiwave Corporation, 16-100 Concourse Gate, Nepean, Ontario K2E 7S8 Canada  
Tel: (613) 224-4700 ext. 230, Fax: (613) 224-4706, E-mail: valery\_t@optiwave.com*

## I. INTRODUCTION

Waveguide devices made up from multi-layer III-V semiconductor heterostructures are the very basic elements of integrated photonics. In their design, detail knowledge of optical properties of active semiconductor waveguides, subject to change under the operational conditions, is crucial. Although semiconductor waveguides have been extensively studied, an adequate approach to their description that would be suitable for device modeling is difficult to find in literature. It is rather common to use heavily empirical models fitted to experiment in a narrow range of parameters [1-5]. With a virtually infinite variety of the device structures and operational conditions, this does not seem to be a practical approach. In this paper, a physics-based model for the optical properties of active semiconductor waveguides is proposed, which is believed to partially fill the gap. As a modeling example, it is applied to the analysis of mode properties of a typical waveguide, which are found to be essentially effected by free carriers.

## II. MODEL DESCRIPTION

At the microscopic level, our approach is based on Kane and Kohn-Luttinger models for a band structure, using of dipole approximation for electron-photon interaction and considering direct and indirect (impurity or phonon assisted) radiative transitions as the first and second order processes, respectively. Many-body effects, such as the screened Coulomb interaction and the exchange-correlation interaction, are incorporated phenomenologically. Collective phenomena are taken into account through an accurately calculated dynamic polarization of the free carrier plasma. At the macroscopic level, the complex dielectric function and spontaneous emission in both the bulk and quantum well (QW) semiconductor layers are computed at any actual photon energy as the functions of technological parameters, carrier concentrations and effective temperatures of these layers. Then, guided modes, absorption, transmission and (amplified) spontaneous emission spectra of the multi-layer semiconductor waveguide as a whole are modeled under the operational conditions, e.g. when free carriers are injected into the device active layer.

Special consideration is given to free carrier effects since most of the semiconductor waveguide devices have doped layers or employ carrier injection or both. The free carrier related features included into the model are: a) screening of the Coulomb interaction between electron and hole; b) band filling; c) band gap shrinkage; d) intervalence band absorption; e) intraband (intravalence band) absorption; f) anomalous dispersion and g) dynamic polarization of the free carrier plasma. In the QW layers, unbound (3D) and bound (2D) state carriers are considered as different yet coupled (through various mechanisms of interaction) sort carriers, each of which effects the optical properties of the semiconductor layers and the device as a

whole. In so doing, the charge imbalance in QWs and related band bending in the vicinity of charged QWs are taken into account in a self-consistent manner.

### III. MODELING EXAMPLE

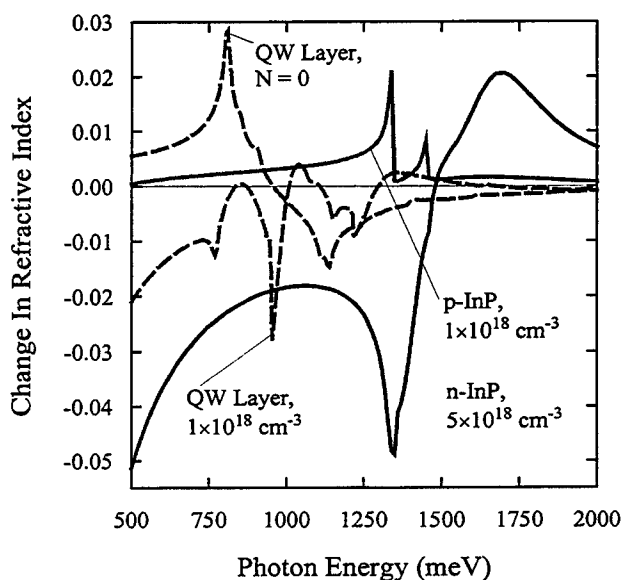
As a modeling example, a typical structure (specified in Table 1) of the *InGaAsP/InP* QW laser operating in  $\lambda=1.55 \mu\text{m}$  wavelength is considered throughout. This is also a standard as-grown *InP*-based structure for a monolithic integration of the optically interconnected photonic devices [6]. Fig. 1 shows spectra of the free carrier induced change in refractive index of *n*- and *p*-type *InP* layers as the substrate and *p*-contact II, respectively. Difference between them, not only in the absolute value but also in sign of the change in index, is evident from the plots and it can be explained as follows. In a spectral range well below the fundamental absorption edge, regardless of the type of doping, band gap shrinkage increases the refractive index while screening of the Coulomb interaction, band filling, and dynamic plasma polarization all result in a reduction of the index. Then, carrier concentration rather than effective mass determines the band gap shrinkage and screening and hence either of these two effects changes equally the refractive index in equally doped *n*- and *p*-type materials. On the other hand, band filling and plasma polarization are more pronounced in *n*-type material because of the lighter effective mass and lower density of states in conduction band as compared to valence band. Over the actual range of the doping concentrations, below absorption

Metal Clad		
Semiconductor Layer	Width	Doping
<i>p</i> <sup>+</sup> - <i>InGaAs</i> Cap	0.2 $\mu\text{m}$	$1\times 10^{19} \text{ cm}^{-3}$ (Be)
<i>p</i> - <i>InP</i> Contact II	1.3 $\mu\text{m}$	$1\times 10^{18} \text{ cm}^{-3}$ (Be)
<i>p</i> - <i>InGaAsP</i> ( $\lambda = 1.3 \mu\text{m}$ ) Etch Stop	0.01 $\mu\text{m}$	$5\times 10^{17} \text{ cm}^{-3}$ (Be)
<i>p</i> - <i>InP</i> Contact I	0.2 $\mu\text{m}$	$5\times 10^{17} \text{ cm}^{-3}$ (Be)
<i>i</i> - <i>InGaAsP</i> ( $\lambda = 1.3 \mu\text{m}$ ) Confinement	0.05 $\mu\text{m}$	Undoped
$5 \times i$ - <i>InGaAs</i> + $6 \times i$ - <i>InGaAsP</i> ( $\lambda = 1.3 \mu\text{m}$ ) Active	$5 \times 0.006 \mu\text{m}$ + $6 \times 0.02 \mu\text{m}$	Undoped
<i>i</i> - <i>InGaAsP</i> ( $\lambda = 1.3 \mu\text{m}$ ) Confinement	0.05 $\mu\text{m}$	Undoped
<i>n</i> - <i>InP</i> Contact <i>n</i> - <i>InP</i> Contact	1.5 $\mu\text{m}$	$1\times 10^{18} \text{ cm}^{-3}$ (Si)
<i>n</i> <sup>+</sup> - <i>InP</i> Substrate, $5\times 10^{18} \text{ cm}^{-3}$ (Si)		

Table 1. Layer structure of the modeled active semiconductor waveguide from *InGaAsP/InP* material system.

reduction of the index. Then, carrier concentration rather than effective mass determines the band gap shrinkage and screening and hence either of these two effects changes equally the refractive index in equally doped *n*- and *p*-type materials. On the other hand, band filling and plasma polarization are more pronounced in *n*-type material because of the lighter effective mass and lower density of states in conduction band as compared to valence band. Over the actual range of the doping concentrations, below absorption

Fig. 1. Spectra of change in refractive index of the doped *InP* layers (solid lines) and undoped QW active layer (dashed lines) from the waveguide structure described in Table 1. In the bulk doped layers, the change in index is referred to that of the intrinsic material. In the QW layer, the change in the effective index is calculated with respect to that of intrinsic bulk *InGaAsP* as the material for barrier and confinement layers.



edge bandgap shrinkage is the main contribution to the change in index of  $p$ -InP, while band filling and dynamic plasma polarization are the main effects contributing to the change in index of  $n$ -InP. Correspondingly, this change is positive in the first case and it is negative in the second case. Since growth (drop) of the index in some particular layer increases (decreases) confinement factor of the ground mode with that layer, doping effectively shifts this mode toward the upper  $p$ -doped layers. In a combination with high intervalence band absorption (not available in  $n$ -type material) this results in a higher optical loss as compared to that predicted without careful analysis of the free carrier effect on the index of the doped layers. Then, free carriers injected into the QW active layer reduce the effective index (compare

the two dashed curves in Fig. 1) and optical confinement factor of this layer resulting in a lower gain as compare to that predicted without taking into account the free carrier effect on the refractive index. Further details of the carrier injection effect on the ground ( $TE_0$ ) mode properties are illustrated with Fig. 2, where PL and gain peak energies and generation frequency shift (for a DFB laser with identical waveguide) all are plotted as the functions of the free carrier concentration in the active layer. Note that the modal gain peak energy decreases with an increase of the free carrier concentration despite enhancement of the band filling and shift of the electron quasi-Fermi level further in the conduction band. This is due to band gap shrinkage, easily seen from the modal PL peak energy plot in Fig. 2.

#### IV. CONCLUSION

In conclusion, a physics-based model for optical properties of active semiconductor waveguides has been developed, which is microscopically justified yet reasonable for simulating of the real photonic devices. Application of this model to typical integrated photonics structures reveals an important role that the free carrier effects play on their optical properties.

#### REFERENCES

- [1] F. Feidler and A. Schlachetzki, *Solid State Electron.*, Vol. 30, pp. 78-83, 1987.
- [2] B.R. Bennet, R.A. Soref, and J.A. Del Alamo, *IEEE J. Quantum Electron.*, Vol. QE-26, pp. 113-122, 1990.
- [3] B. Rheid, R. Maciejko, and A. Champagne, *Canadian J. of Physics*, Vol. 71, pp. 410-416, 1993.
- [4] J.-P. Weber, *IEEE J. Quantum Electron.*, Vol. QE-26, pp. 1801-1816, 1994.
- [5] C. Glingener, D. Schulz, and E. Voges, *IEEE J. Quantum Electron.*, Vol. QE-26, pp. 101-112, 1995.
- [6] S. Charbonneau, E.S. Koteles, P.J. Poole et al, *IEEE J. Selected Topics Quantum Electron.*, Vol. STQE-4, pp. 772-793, 1998.

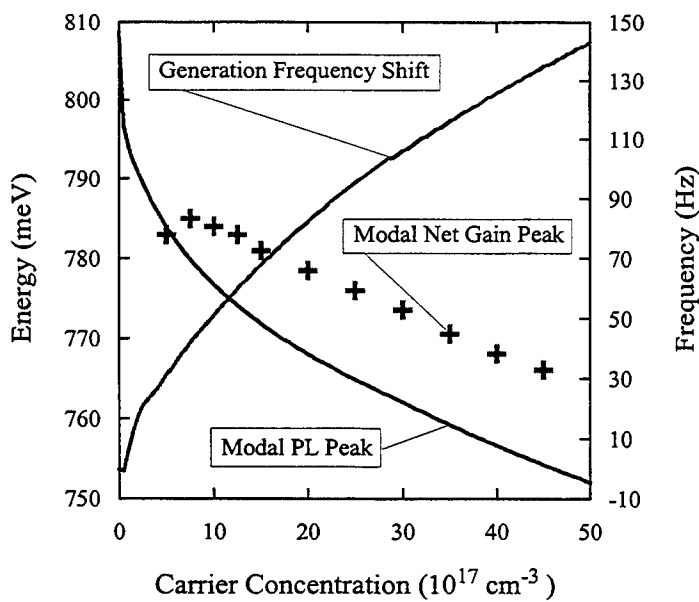


Fig. 2. Modal PL and net gain (crosses) peak energies as functions of the carrier concentration into the active layer defined as the total sheet concentration (combining contributions from both the 2D and 3D carriers) in the layer divided by layer width. Also plotted is the value of a negative shift in generation frequency of a DFB laser with identical vertical structure.

**Integrated Photonics Research**

# Integrated Optical Switches

**Tuesday, July 20, 1999**

**Jaymin Amin, Corning Inc., USA**  
Presider

**RTuD**  
**10:30am–Noon**  
Sierra Madre North

# Polarization independent InP-based space switch with double-etched waveguide structure

D.H.P. Maat, F.H. Groen, H. van Brug, H.J. Frankena, C.G.P. Herben<sup>1</sup>, B.H.P. Dorren<sup>2</sup>

Research Group for Optics, Department of Applied Physics, Delft University of Technology  
P.O. Box 5046, NL-2600 GA Delft, The Netherlands, email: maat@optica.tn.tudelft.nl

<sup>1</sup>Department of Information Technology and Systems, Delft University of Technology, Delft, The Netherlands.

<sup>2</sup>Department of Physics, Eindhoven University of Technology, Eindhoven, The Netherlands.

## I. INTRODUCTION

Optical space switches play a key role in advanced optical networks, both for WDM and single wavelength applications. Besides low crosstalk, low loss and polarization independence an important requirement for these switches is small size. Especially in larger structures like crossconnects and add-drop nodes the (small) size of the different components is an important property.

In this paper we analyze the performance of MZI-switches realized with a double etch technique, applied earlier to PHASAR's [1], for integration in a compact optical crossconnect

## II. DESIGN AND FABRICATION

In the switch MMI's are used as 3 dB splitting and combining elements. In between are two sets of phase shifting sections. In the first set, the phase shifting sections (2 mm) are oriented at an angle of 28 degrees with respect to the  $[1\bar{1}0]$  direction to achieve polarization independent switching [2]. The second set has phase shifting sections in the  $[110]$  direction. By applying a proper voltage to one of both sections of this last set, a small polarization dependence due to variations in layer thickness and doping profile can be removed.

To reduce the size of the switch, the etch depth of all bends and the MMI's is changed from 1.30  $\mu\text{m}$  as in our previous design [3] (100 nm into the quaternary layer; 'shallow-etch') to an etch depth of 1.75  $\mu\text{m}$  (etched through the quaternary layer; 'deep-etch'). In this way the index contrast and thus the optical confinement increases allowing reduced dimensions of all bends and the MMI's (Table 1) with respect to the previous design. The schematic layout of the resulting switch is shown in Fig. 1.

**Table 1** Waveguide dimensions in both the shallow-etch regions and the deep-etch regions.

	waveguide width	bend radius	MMI size
shallow-etch	3 $\mu\text{m}$	500 $\mu\text{m}$	16 $\times$ 400 $\mu\text{m}$
deep-etch	2 $\mu\text{m}$	100 $\mu\text{m}$	10 $\times$ 140 $\mu\text{m}$

To avoid problems with the higher order modes, the width of the waveguides in the deep-etch regions has been set to 2  $\mu\text{m}$ . To achieve low losses, special attention has been paid to the transition from the deep-etch region to the shallow-etch region and vice versa. A straight waveguide at the end of the taper which connects the waveguides of both regions is used for crossing the transition (see inset of Fig. 1). The length of this waveguide is set to 5  $\mu\text{m}$  to enable the alignment of the mask which defines the deep-etch region. Its width is optimized for the low loss.

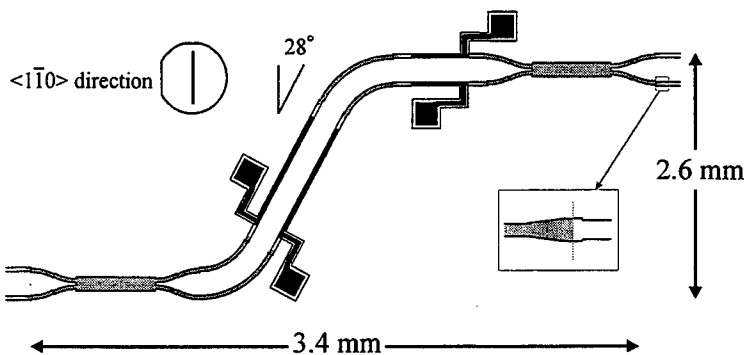


**Figure 1** Schematic layout of the deep-etch MZI-switch. The metal contacts are drawn in black, the deep-etch waveguide structures are in gray.

The InGaAsP/InP/InGaAs layer stack was grown on a (001) oriented  $n^+$  substrate. The thicknesses and doping levels of the various layers are shown in Fig. 2. The thickness of the p-InP is chosen to be 970 nm to provide sufficient distance between the optical field and the metal contacts (for low loss). The InGaAsP guiding layer is n-doped such that the switch is already close to polarization independence and at the same time has low loss [4].

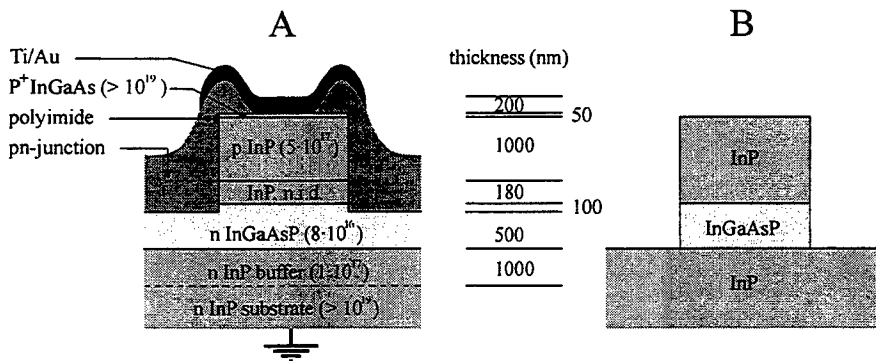


**Figure 2** (A) Cross section of the switch at the phase shifting sections (doping levels in  $\text{cm}^{-3}$ ) showing a shallow-etch waveguide structure. (B) Waveguide structure in deep-etch region.

The fabrication of the switch starts with removing the p+ InGaAs from the wafer, by using wet chemical etching, except in those regions where the metal contacts will be placed in a later stage of the fabrication process. In the next step the waveguides are realized with a  $\text{CH}_4\text{-H}_2\text{/O}_2$  RIE/descum process, using (PECVD) silicon-nitride masking. In order to have electrical insulation between the four phase shifting sections of the switch, a section of the waveguides is etched down to the pn-junction at either side of each contact. When the shallow-etch waveguides are completed, this region is covered with photo resist after which the deep-etch waveguides are finished using a second etch step with the same  $\text{Si}_x\text{N}_y$ -mask and RIE process. Due to the dry etching of the waveguides in an  $\text{H}_2$  atmosphere the acceptors are passivated, which gives rise to high leakage currents. The acceptors have been reactivated using an RTP anneal step. Next, the pn-junction is passivated with cured polyimide. The switch is completed by depositing Ti/Au contacts on the phase shifting sections using a lift-off technique.

### III. MEASUREMENT RESULTS AND DISCUSSION

The switches have been measured at 1.5  $\mu\text{m}$  using a microscope objective at the input side and a single mode fiber at the output side. Fig. 3 shows the resulting switching curves.

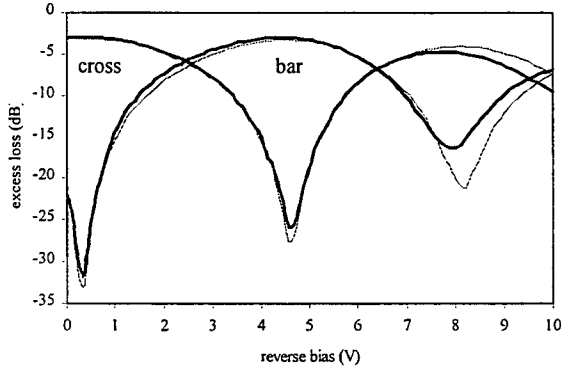


**Figure 3** Measured response of the switch. The thin line represents TE, the bold line TM polarization.

In Table 2 the values retrieved from the measurements are given and compared with the values of our previous design [3]. The losses of the deep-etch switch are a little higher due to (a) the large amount of transitions from deep- to shallow-etch regions (and v.v.), and (b) the higher waveguide loss of deeply etched waveguides. A single junction transition has a loss of 0.09 dB for TE and 0.05 dB for TM polarization. The additional losses of the deeply etched 2  $\mu\text{m}$  waveguides are about 2.5 dB/cm for both polarizations.

The crosstalk value of the deep-etch switch is slightly better than the crosstalk of our previous design, especially for the cross state. The crosstalk of the bar state is limited by a small power imbalance at the beginning of the second MMI due to electro-optical absorption. If the switch is corrected for this, the bar state crosstalk (and thus switch crosstalk) is reduced to -24 dB. In this case however, polarization independence is not preserved.

**Table 2** Measured values of both the previous design and the switch with deep-etch regions.

	crosstalk	loss	dimensions
previous design	< -20 dB	2dB	4.3 $\times$ 2.7 mm
deep-etch switch	< -22 dB	3dB	3.4 $\times$ 2.6 mm

#### IV. CONCLUSIONS

We analyzed the performance of MZI-switches realized with a double etch technique. Switch dimensions are reduced by 25%. The polarization independent crosstalk was found to be -22 dB, which is slightly better than the performance of devices realized in a single etch step. Insertion loss is 1 dB higher due to increased scatter and junction transition losses. Our conclusion is that, although the increase in switch performance does not justify the double etch step in itself, the use of double-etched switches is advantageous if the double etch step introduces no additional complexity e.g. when integrating the switch with compact PHASAR's in optical crossconnects.

#### V. REFERENCES

- [1] C.G.P. Herben et al., "Low-loss and compact phased array demultiplexer using a double etch process", *Proc. 9<sup>th</sup> Eur. Conf. Integrated Optics (ECIO '99)*, Turin, Italy, 1999.
- [2] R. Krähenbühl et al., 'Low-Loss Polarisation-Insensitive InP-InGaAsP Optical Space Switches for Fiber Optical Communication', *IEEE Phot. Techn. Lett.*, vol 8(5), pp 632-34, 1996.
- [3] T. Uitterdijk et al., 'Integrable Polarisation Insensitive InGaAsP Mach-Zehnder Switch', *Integrated Photonic Research*, vol. 6, 1996 OSA Technical Digest series, pp 486-489.
- [4] J.F. Vinchant et al., 'InP/InGaAsP guided-wave phase modulators based on carrier-induced effects: theory and experiment', *Journ. Lightw. Techn.*, vol. 10, no. 1, pp 63-69, January 1992.

# Polymeric 1x3 Thermo-Optic Switch

Tae-Won Oh and Sang-Yung Shin

Department of Electrical Engineering, Korea Advanced Institute of Science and Technology,  
373-1 Kusung-dong, Yusung-gu, Taejon, 305-701, Korea  
twoh@eeinfo.kaist.ac.kr, syshin@ee.kaist.ac.kr

## I. Introduction

The optical space switch is a key component in optical cross-connects. Large-scale matrix switches are required to meet the increasing switching capacity. The conventional matrix switches using planar lightwave circuits are based on a 1x2 switching unit [1]. Their dimension can be very large as the number of port increases. Therefore, a basic switching unit with a large port-count is preferable to reduce their dimensions and optical losses. The optical switch with a multibranch waveguide may be a solution. Various types of three-branch optical waveguide switches have been demonstrated in LiNbO<sub>3</sub> and polymer [2,3]. Especially, polymeric optical waveguide switches have attracted much attention because the polymer has a large thermo-optic coefficient. Propstra et al.[3] has realized a 1x3 thermo-optic switch in polymer. However it has a major drawback. For three switching states, it employs four heaters. If we use it as a building block, the number of heaters will exponentially increase and their control will become very complex. In this paper, we report a new 1x3 polymeric thermo-optic switch based on a three-branch waveguide. It has a simple heater structure and an initial routing path. Therefore, it is advantageous to use our switch as a basic switching unit or a protection switch.

## II. Switch and Its Design

The operation of our switch is based on the modal evolution effect in an adiabatic three-branch waveguide [4]. In adiabatic single-mode waveguide branches, the light eventually propagates along the output waveguide whose effective refractive index is the highest. The three branches of the proposed device consist of a wide central arm and two narrow side arms. The width of the central arm is equal to that of the input waveguide. Two heaters are used, instead of four in Propstra et al. They are located along the central arm with a transverse offset. In the initial state, the input light is routed to the central arm ([010] state). When one of the heaters is activated, the effective index of the underlying waveguide is decreased and the light is routed to the opposite side arm ([100] or [001] state).

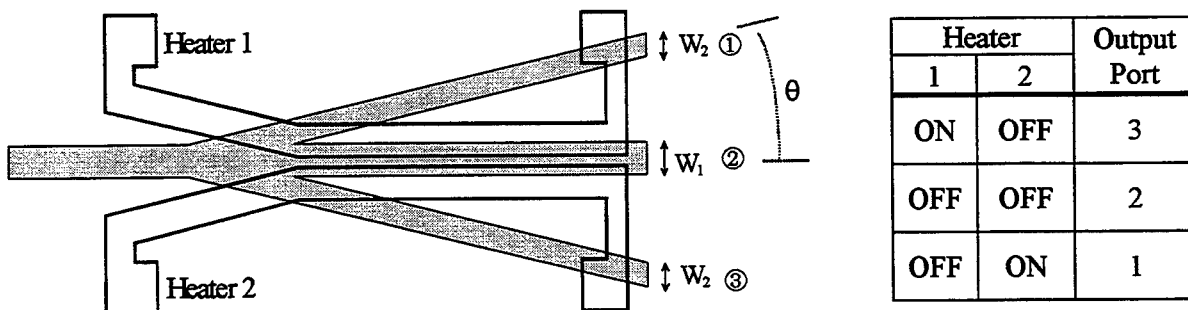


Fig. 1 The configuration of a 1x3 thermo-optic switch

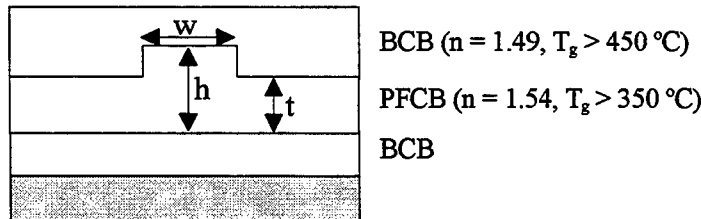


Fig. 2 Cross-section of oversized rib waveguides

Our waveguide design is based on the concept of the oversized rib waveguide [5]. It offers a single-mode waveguide with a large cross-section in spite of the high-index contrast between the core layer and the cladding layers. Moreover, it allows large fabrication tolerance since it is not so sensitive to the index deviations of polymer layers that may result from the curing process. This design concept is also important for thermo-optic switches because the thin over-cladding layer allows the high temperature difference between the adjacent waveguides. A simple approximation for the single mode waveguide condition [5] is as follows:  $w \leq 0.3 h + t / \sqrt{1 - (t/h)^2}$  with w, h and t defined in Fig. 2.

The difference between the widths of the output arms has to be determined by the initial crosstalk and the switching power. As the difference increases, the initial crosstalk decreases. However the switching power increases. The branching angle should be small enough to satisfy the adiabatic condition for modal evolution. The locations of two heaters are optimized to maximize the temperature difference between the waveguides. The finite difference beam propagation method and the finite element method are utilized to investigate the propagation characteristics and the thermal distribution, respectively. The device parameters are as follows:  $w_1 = 6.5 \mu\text{m}$ ,  $w_2 = 5 \mu\text{m}$ ,  $h = 5.5 \mu\text{m}$ ,  $t = 3.8 \mu\text{m}$  and  $\theta = 0.12^\circ$ . For matching the output modes, the narrow arms are connected to the output waveguides using lateral tapers.

### III. Experimental Results

The polymers from Dow Chemical used in this work are benzocyclobutene(BCB) for core layer and perfluorocyclobutane(PFCB) for cladding layer. They have good thermal and environmental properties (BCB:  $T_g > 350^\circ\text{C}$ , PFCB:  $T_g > 450^\circ\text{C}$ ) [6,7]. The core and the cladding layers are spin coated and thermally cured under nitrogen atmosphere. After curing the core layer, the rib channel is formed by the reactive ion etching with a mixture of  $\text{CF}_4$  and  $\text{O}_2$ . For the heater, Cr-Au is deposited successively by the thermal evaporation and patterned by the conventional photolithography and the wet etching.

In order to characterize the switch, light from a  $1.55 \mu\text{m}$  laser diode is coupled into the input port. The intensity profile of the guided mode is measured by a CCD camera. The waveguide supports a well-confined mode for both TE and TM polarizations. Fig. 3 shows the measured output power with respect to the applied electric power for TE mode. The initial crosstalks between the central arm and the side arms are better than  $-21 \text{ dB}$ . In the switching states, the crosstalks between the routed arm and the others are better than  $-20 \text{ dB}$  at about  $200 \text{ mW}$ . The switching time is less than  $1 \text{ msec}$  as shown in Fig. 4. The

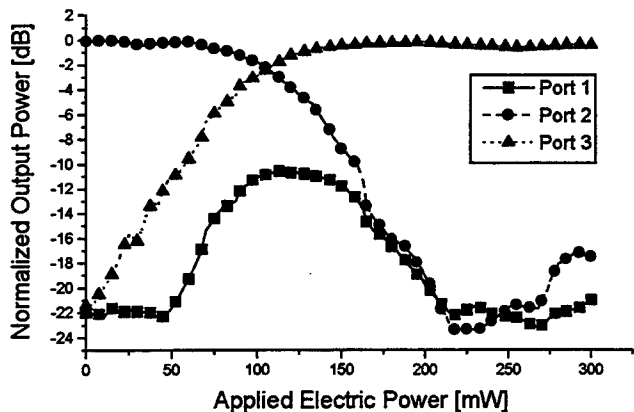


Fig. 3 Transfer Characteristics

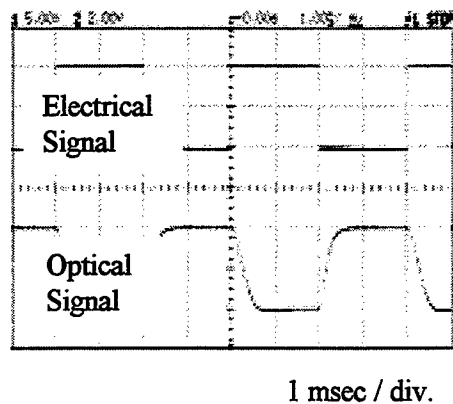


Fig. 4 Switching Characteristics

measurement results for TM mode are similar. The length of the device is about 1.5 cm. The excess loss with reference to the straight waveguide is about 0.4 dB.

#### IV. Conclusion

We demonstrated a new 1x3 thermo-optic switch based on a polymeric three-branch waveguide. The switch has a simple structure and is suitable as a basic switching unit for large-scale matrix switches. The device was fabricated by using highly stable polymers, BCB and PFCB. The measured crosstalk is better than –20 dB.

#### [References]

1. A. Borreman, T. Hoekstra, and M. Diemeer, "Polymeric 8x8 digital optical switch matrix," Proc. ECOC'96, Oslo, vol. 5, pp. 59-62.
2. M. Belanger and G. L. Yip, "Theoretical and experimental investigation of an active three-branch Ti:LiNbO<sub>3</sub> optical waveguide switch," Appl. Opt. vol. 28, no. 1, pp. 53-59, 1989
3. K. Propstra, T. Hoekstra, A. Borreman, M. Diemeer, H. Hoekstra, and P. Lambeck, "First thermo-optic 1x3 digital optical switch," ECIO '97, Stockholm, post deadline papers, PD3-4
4. E. Kapon and R. N. Thurston, "Multichannel waveguide junctions for guided-wave optics," Appl. Phys. Lett., vol. 50, pp. 1710-1712, 1987
5. R. A. Soref, J. Schmidchen, and K. Petermann, "Large single-mode rib waveguide in GeSi-Si, and Si-on-SiO<sub>2</sub>," IEEE J. Quantum Electron., vol. 27, no. 8, pp. 1971-1974, 1991
6. C. Langhoff, T. Stokich, and B. Heistand, "Benzocyclobutene(BCB): A polymer system for passive optical interconnects," Proc. SPIE, vol. 1849, pp. 336-341, 1993
7. G. Fischbeck, R. Moosburger, C. Kostrzewa, A. Achen, and K. Petermann, "Singlemode optical waveguides using a high temperature stable polymer with low losses in the 1.55 mm range," Electron. Lett., vol. 33, no. 6, pp. 518-519, 1997

# MEMS 2D Scanning Mirror for Dynamic Alignment in Optical Interconnect

Guo-Dung J. Su, Wibool Piyawattanametha, Raphael Rollier, Li Fan\* and Ming C. Wu

University of California, Los Angeles, Electrical Engineering Department  
 Room 63-128, Engineering IV, 405 Hilgard Avenue, Los Angeles, CA 90095-1594  
 TEL: 310-825-7338, FAX: 310-794-5513, EMAIL: [johnsu@icsl.ucla.edu](mailto:johnsu@icsl.ucla.edu)  
 \* Optical Micro-Machines, San Diego, CA 92121

There has been a great deal of interests in optical interconnect to solve the I/O bottleneck in electronic systems [1,2]. Currently, most of the optical interconnect schemes employ passive optical alignment [3,4]. The alignment tolerance is very tight because it has to accommodate a wide range temperature and environmental changes. Therefore, active optical alignment with dynamic tracking is desirable for practical systems. By incorporating a compact 2D scanning mirror in the Fourier plane of the optical system [5], tilting of the scanning mirror results in parallel a translation in the image plane, as shown in Fig. 1. Compact, batch-fabricated micro-electro-mechanical (MEMS) 2D scanners are ideal for this application. They can also perform dynamic tracking to increase of the robustness of optical interconnect against vibrations and temperature variations. Electrostatically actuated MEMS scanning mirrors have very low power consumption ( $\sim \mu\text{W}$ ) and can be integrated with other optoelectronic components on the microbench. In this paper, we report a novel surface-micromachined 2D scanning mirror with large mirror area, large scanning angles, and reasonable actuation voltage. The scanner is completely self-assembled by the integrated stress-bimorph structures without using any external power supply.

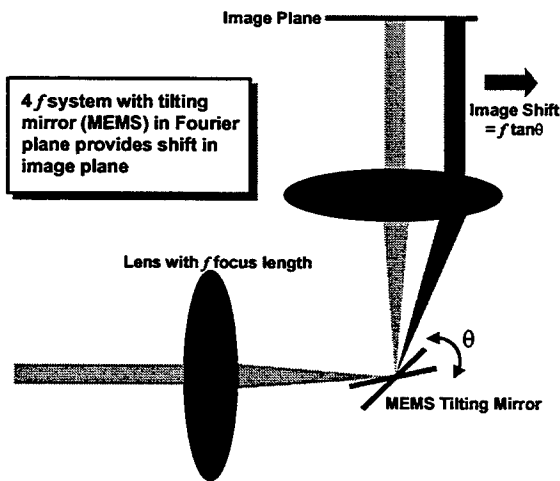
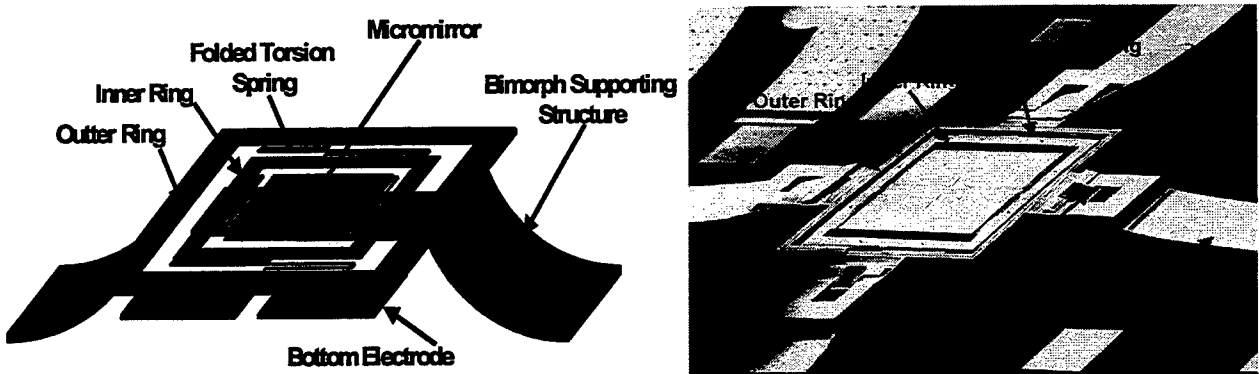


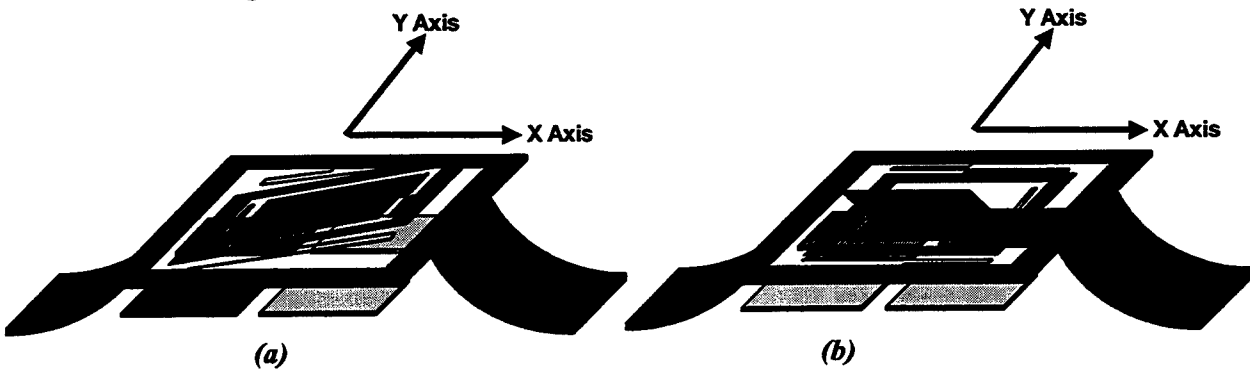
Figure 1. Schematic drawing of 2D scanning mirror for 4f optical system

The schematic drawing and scanning electron micrograph (SEM) of the 2D optical scanning micro-mirror are shown in Fig. 2. It is based on a novel Micro-Elevator by Self-Assembly (MESA) structure [6], which allows large micromirrors to be suspended at several hundreds micrometers above the substrate for large scan angles. The scanning micromirror is connected to two nested rings by orthogonal flexure beams. The size of micromirror is  $400\mu\text{m} \times 400\mu\text{m}$ . The outer ring is attached to the MESA platform that is raised  $150\mu\text{m}$  above the substrate by four stress-induced bimorph structures. The structure is totally self-assembled without using any external power supply or bias. The scan mirror can be rotated around two axes by applying electrostatic force between the mirror and the quadrant electrodes underneath the mirror. When a voltage is applied to the two left (or right) electrodes, the

electrostatic force causes the mirror to rotate around the X axis. Similarly, voltage applied to the two upper (or lower) electrodes causes the mirror to rotate around Y axis. These are illustrated in Fig. 3 (a) and (b), respectively. This scanner is fabricated through the MUMPs service offered by MCNC [7].

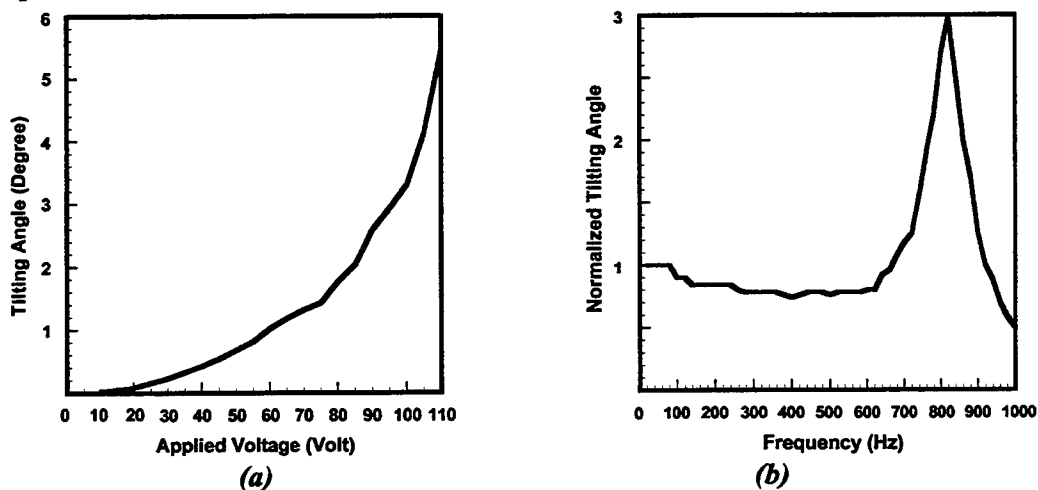


**Figure 2.** Schematic drawing and SEM of micro 2D scanning mirror



**Figure 3.** Biasing scheme along (a) X-axis (b) Y-axis for the 2D scanning mirror

The measured optical deflection angle of the micromirror versus the applied voltage and the actuation frequency are shown in Fig. 4 (a) and (b), respectively. The resonant frequency and maximum optical tilting angle of the micromirror are measured to be 820 Hz and 5.7° (limited by the voltage amplifier), respectively. We characterize the displacement of the micromirror using computer controlled position sensing detector (PSD). The pointing accuracy of the micromirror is shown to be better than 3 urad. The performance of MEMS 2D scanning mirror is summarized in Table 1.

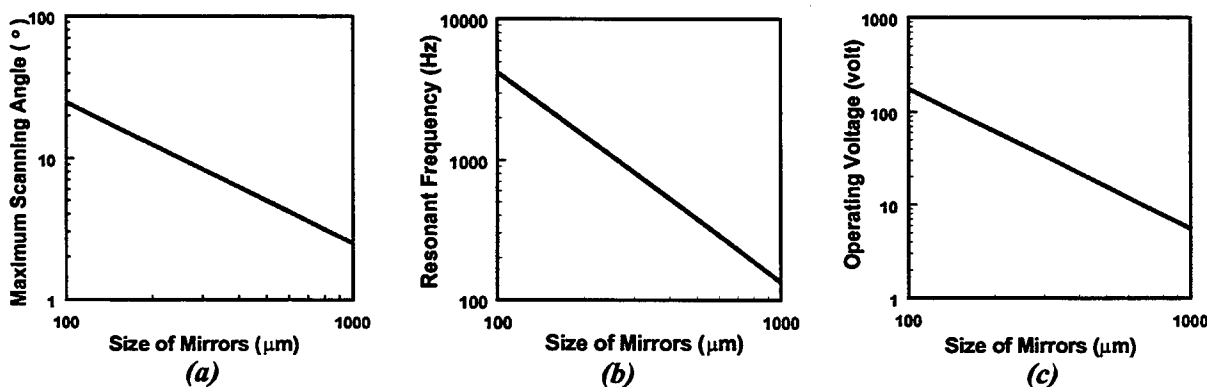


**Figure 4.** (a) Optical deflection angle, and (b) frequency response of inner ring of 2D scanner

Mirror Area	400um × 400um
Scan Angle	±5.7 degree
Resonant Frequency	~ 800 Hz
Operating Voltage	< 150 Volt
Repeatability	52 urad
Pointing Accuracy	3 urad

**Table 1.** Experimental results of MEMS 2D scanning mirror

We have performed systematic simulation on the performance of the 2D scanning mirror for various mirror sizes. Figure 5 shows the variation of (a) scan angle, (b) resonant frequency, and (c) operating voltage with the mirror size. For mirror size of 1 mm, the operating voltage reduces to less than 10V at the expense of scan angle (~3°) and resonant frequency (~100Hz). It is possible to trade the large reduction in operating voltage for higher resonant frequencies. For example, stiffer springs will increase the resonant frequency and the operating voltage. Overall system optimization of the 2D scanner depends on the requirement of the optical system.

**Figure 5.** Simulation results of mirror size effects on scanning angle, resonant frequency and voltage.

In summary, we have experimentally demonstrated a novel self-assembled MEMS 2D scanning mirror with large area (400um × 400um) and large scan angle (5.7°). The scanning mirror is fabricated by the standard surface-micromachining technology. The use of compact MEMS scanning mirrors will greatly improve the optical alignment tolerance of free space optical interconnect.

### Reference:

- [1]. S. Esener and P. Marchand, "3D optoelectronic Stacked Processors: Design and Analysis," *OC computing '98*, Bruges, Belgium, June 1998.
- [2]. Philippe Marchand, "Parallel Systems Based on Free Space Optoelectronic and Stacked Silicon Chips," *ASME Int. Mechanical Engineering Congress and Exposition*, Session EEP-12, multidisciplinary design of photonic devices and systems, Anaheim, CA, November 1998.
- [3]. M. F. Dautartas, A. Benzoni, S. Broutin, A. Coucoulas, D. Moser, Y. Wong and Y. Wong, "Optical Performance of Low Cost Self-Aligned MCM-D Based Optical Data Links," *IEEE Transactions on Components, Packaging and Manufacturing Technology*, pp. 554-561, August 1996.
- [4]. A. Muller, J. Gottert, M. Roniger, "Fabrication of Stepped Microoptical Benches for Fiber and Free Space Applications," *Microsystem Technologies 2*, pp. 40-45, 1996.
- [5]. Philippe Marchand, private communication.
- [6]. Li Fan, Ming C. Wu, Kent D. Choquette, and Mary H. Crawford, "Self-assembled Microactuated XYZ Stages for Optical Scanning and Alignment," *Proc. of International Solid State Sensor and Actuators Conference (Transducers '97)*, Chicago, IL, USA, pp. 319-322, June 16-19, 1997.
- [7]. K. W. Markus, D. A. Koester, A. Cowen, R. Mahadevan, V. R. Dhuler, D. Roberson, L. Smith, "MEMS Infrastructure: The multi-user MEMS process (MUMPs)," *Proc. SPIE*, vol. 2639, pp. 225-235, 1996.

## Polymeric Tunable Optical Attenuator for Dynamic Channel Power Regulation in WDM Systems

Sang-Shin Lee, Yong-Sung Jin, and Yung-Sung Son

Devices and Materials Laboratory, LG Corporate Institute of Technology

16 Woomyeon-Dong, Seocho-Gu, Seoul 137-724, Korea.

Tel: +82-2-526-4489, Fax: +82-2-578-5513, E-mail: sslee@lgcit.com

Jae-Hoon Jung and Ki-Woon Na

Transmission Division R&D Center, LG Information & Communications, Ltd.

533, Hogye-Dong, Dongan-Gu, Anyang-Shi, Kyongki-Do, 431-080, Korea

A tunable optical attenuator (TOA) is one of the essential components for the implementation of wavelength division multiplexed (WDM) systems [1, 2]. It is useful for gain control of optical amplifiers in WDM networks and for dynamic channel power equalization and regulation in cross-connected nodes. Integrated optic attenuators using polymers have advantages like compact size desirable for arrays, low electrical power consumption, and enhanced environmental stability due to no moving parts. In this paper, we have presented a TOA using polymeric thermooptic (TO) devices with asymmetric branching waveguides, and then it was used to demonstrate an efficient dynamic channel power regulation in a simple WDM transmission system.

The proposed polymeric TOA is based on an asymmetric Y-branch waveguide, and its structure is shown in Fig. 1 [3]. For the asymmetric branch, the upper arm has larger width than the lower arm. The straight waveguide combined with the wide arm is used for the main output port. The narrow arm is connected to a tapered S-bend waveguide to enlarge the distance between the two waveguides of the branch. The device is operated based on the modal evolution effect, and thus features improved wavelength sensitivity and enhanced fabrication tolerance. With no electrical power the optical power launched from the input waveguide is predominantly coupled to the wide arm of the branch. Therefore, the device provides maximum transmission without initial electrical bias. When electrical power is supplied to the electrode for inducing the TO effect, the effective refractive index of the wide arm is decreased, and so the input optical power is transferred gradually to the narrow arm. As a result, the optical output decreases with applied electrical power enabling an efficient attenuation of the input optical power. The residual power resulting from attenuation is bypassed through the narrow arm and then the S-bend waveguide without disturbing other parts of the device including the main port. The proposed device was designed by using the beam propagation method and then fabricated by employing a standard procedure including spin-coating, thermal curing, and dry etching.

The performance of the TOA was measured by using light at the wavelength of 1550 nm. The optical output of the device was detected by both a power meter and a photodetector. First, the transfer characteristics of the device were observed by varying the electrical power for TE and TM polarizations. Fig. 2 shows the attenuation versus electrical power consumption for the two polarizations. The measured dynamic attenuation range was more than 20 dB with the electrical power of 200 mW. The polarization dependent loss was negligibly small with no electrical power, and it increased with attenuation reaching ~2 dB for the attenuation of 10 dB. However, the effect of the polarization on the

attenuator performance was greatly reduced by adopting a continuous electronic feedback control. By employing a fiber coupler a fraction (~10%) of the attenuator output power was tapped and fed back to the electrical driver to maintain it regardless of the variation in the input light polarizations. It was experimentally confirmed that the attenuator output was maintained within 0.2 dB in spite of random variation in light polarizations. And we have investigated the operation speed by applying an electrical square wave to our attenuator. An optical response speed of 1 ms was obtained.

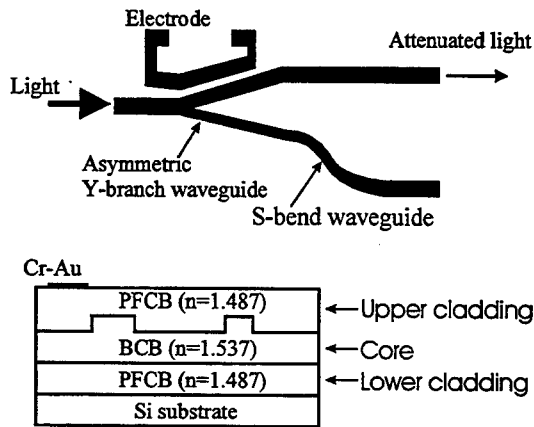


**Fig. 1.** Structure of the proposed polymeric tunable optical attenuator.

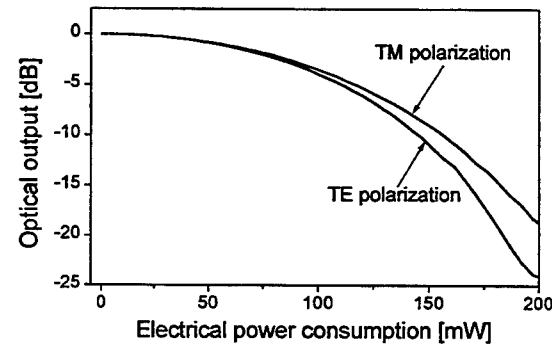


**Fig. 2.** Attenuation vs. electrical power consumption.

Finally, we have tested our polymeric TOA as an optical power regulator. The light source power was deliberately modulated to simulate practical fluctuation. This fluctuating signal was appropriately attenuated, when 10% of the attenuator output was tapped and fed back to the electronic feedback control circuit through a fiber coupler. In Fig. 3, the top triangular signal is the source power which is fluctuating by 3 dB. And other signals represent for the regulated optical output for attenuation levels ranging from 4 to 12 dB. They are shown to be well regulated within 0.2 dB.

And then we have performed similar experiment in a simple WDM transmission system shown in Fig. 4. Four diode lasers with different wavelengths (1.6 nm spaced) were used for the light source. The optical power of one of the four sources was externally modulated, and a TOA was placed next to the modulator. The four optical signals are multiplexed, go through three EDFA's with a fixed gain, and are demultiplexed. In order to regulate the optical signal at the output of the demultiplexer, a fraction of it is fed back to the TOA. In Fig. 5, all the signals corresponding to the modulated laser source ( $\lambda=1547.7$  nm) were taken continuously at the output of the demultiplexer. With no modulation and no feedback control the optical output is flat containing a little noise. When the modulation is performed, it begins to fluctuate by 3 dB. And by starting the feedback control, the optical output is attenuated by 3.5 dB and regulated within 0.4 dB. These experimental results confirmed that the TOA is very useful for regulating channel powers in practical WDM systems. Also a power equalization between multiple channels will be possible if multiple TOA's are employed.

## References

- [1] J. E. Ford, J. A. Walker, D. S. Greywall, and K. W. Goossen, "Micromechanical fiber-optic attenuator with 3  $\mu$ s response," *J. Lightwave Technol.*, vol. 16, no. 9, pp. 1663-1670, 1998.
- [2] T. Kawai, M. Koga, M. Okuno, and T. Kitoh, "PLC type compact variable optical attenuator for photonic transport network," *Electron. Lett.*, vol. 34, no. 3, pp. 264-265, 1998.
- [3] Sang-Shin Lee, Yong-Sung Jin, Yung-Sung Son, and Tae-Kyung Yoo, "Polymeric tunable optical attenuator with an optical monitoring tap for WDM transmission network," *to be published in May issue, IEEE Photon. Technol. Lett.*, 1999.

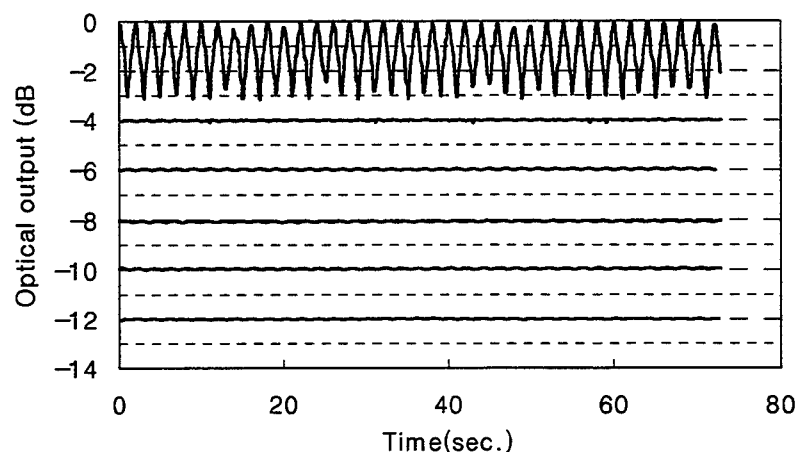


**Fig. 3. Dynamic channel power regulation.**

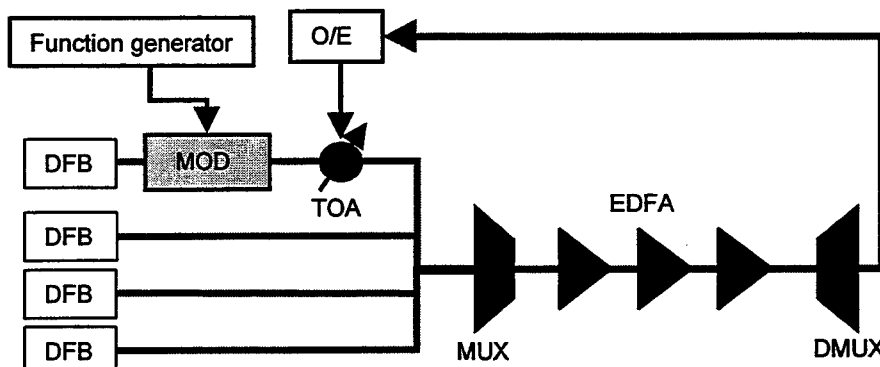


**Fig. 4. System configuration for the channel power regulation.**

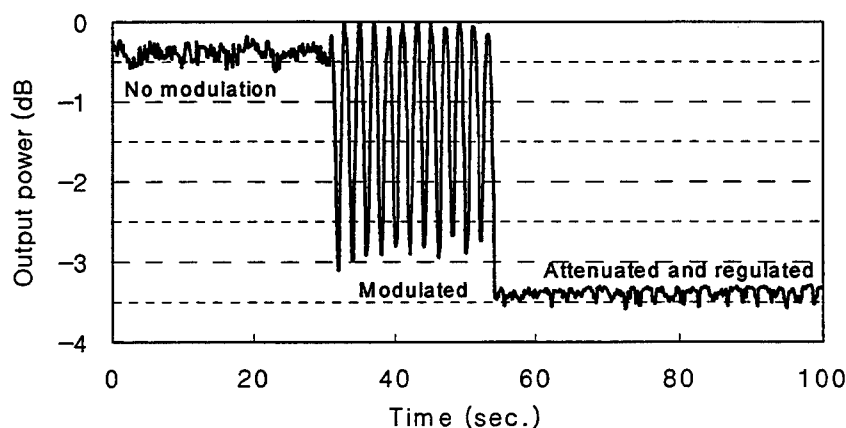


**Fig. 5. Dynamic channel power regulation in a system.**

# Silica-based thermooptic switch with layered wiring patterns

Mikitaka Itoh, Masayuki Okuno, Takashi Goh,  
Kazuyuki Moriwaki, Yasuji Ohmori and Akira Himeno

NTT Photonics Laboratories  
162, Tokai, Ibaraki 319-1193, Japan  
Tel: +81-29-287-7766; Fax: +81-29-287-7871  
e-mail: itoh@iba.iecl.ntt.co.jp

## 1. Introduction

Space-division optical switches such as non-blocking NxN matrix switches and add/drop switches are indispensable for advanced fiber-optic communication systems. Recently, the network service capacity has increased with developments in optical wavelength-division-multiplexing (WDM) transport networks [1]. This increase in capacity has led to a demand for densely integrated large-scale switches. To meet this demand, we have developed thermooptic (TO) switches which employ silica-based planar lightwave circuit (PLC) technology, because of their suitability for large-scale integration [2,3].

Silica-based TO switches consist of waveguides and wiring patterns and so both must be densely integrated. However, with our previously reported 16x16 matrix switch with 1024 heaters, lack of space made it very difficult to lay out the wiring pattern, even though we fabricated the switch on a 6 inch wafer[3].

To overcome this problem, we propose PLC TO switches with multi-layered wiring patterns. To confirm the effectiveness of this configuration, we demonstrated 8 ch 2x2 add/drop TO switches with single and double layered wiring patterns. These two switches exhibited good optical performance with an average insertion loss less than 2 dB and an average extinction ratio greater than 50 dB. The wiring area of the double layered wiring switch was 40 % smaller than that with single layered wiring. This enables us to realize a large-scale TO switch with densely integrated wiring patterns.

## 2. Switch configuration and layered wiring fabrication

Figure 1 shows the 8 ch 2x2 add/drop TO switch configuration we fabricated. The switching unit shown in Fig.1(a) is composed of a waveguide Mach-Zehnder interferometer and thin film heaters for phase trimming and optical switching [4]. Figure 1(b) shows the logical arrangement of the add/drop switch. The units in the first and third stages function as the add/drop 2x2 TO switch. The second stage units act as a gate switch to eliminate the crosstalk to the through port.

We operated the heaters distributed over the wafers by using patterned wiring to connect them to electrode pads aligned along the PLC chip edges. Figure 2 shows the layouts of the single and double layered wiring. The area occupied by the wiring is reduced by about 40% by stacking the trimming heater wiring on the switching heater wiring.

We fabricated the waveguides by the flame hydrolysis deposition [5], and then made the wiring as follows. First, we formed a lower Au wiring pattern on a Ta<sub>2</sub>N heater pattern. Next, we deposited a SiO<sub>2</sub> insulating layer which enabled us to stack and cross the wiring, as shown in Fig.3(a). We then formed the contact holes by the reactive ion etching method as shown in Fig.3(b). Finally, we fabricated the upper Au wiring pattern on the SiO<sub>2</sub> layer.

### 3. Results and discussion

Figure 4 compares the heater resistance of the double layered wiring with that of the single layered wiring. Since the standard deviation is not increased by doubling the wiring patterns, the contact holes and the cross wiring were successfully fabricated. The switch characteristics are summarized in Table 1. These two switches exhibited good optical properties including an extinction ratio of greater than 50 dB and an insertion loss of less than 2 dB, therefore the interference condition of the MZI's did not degenerate when the wiring patterns were fabricated.

We gain two advantages by employing double layered wiring. The first is a reduction in the area occupied by the wiring. We have already demonstrated a 6 inch 16x16 TO matrix switch with a double gate switch configuration (1024 heaters in total) and a single layered wiring pattern. However, the switch only has a wiring pattern which is connected to the heaters for optical switching and so the heaters must also be used for phase trimming. This is because, as shown in Fig.5, the area necessary for the wiring exceeds the 6 inch wafer size. However, by doubling the wiring patterns, we can realize a 16x16 TO matrix switch with full wiring for 1024 heaters, which is very suitable for practical use.

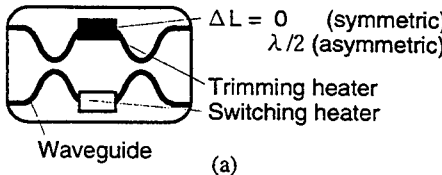
The other advantage is an increase in wiring pattern flexibility through the realization of cross wiring patterns. An example of such cross wiring is the separate alignment of the electrode pads for the switching heaters from those for the trimming heaters. This separate pad configuration is very convenient for the trimming process when assembling the TO switch as a module. For a module employing a single layered wiring TO switch, we install the PLC chip on a ceramic substrate containing several layers of wiring. However, if the separate alignment can be realized on a PLC chip, the ceramic substrate becomes unnecessary. This enables us to realize compact TO switch modules at a reduced cost.

### 4. Conclusion

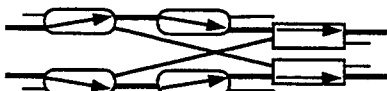
We have demonstrated 8 ch 2x2 thermooptic add/drop switches with single and double layered wiring patterns. The two switches exhibited good optical properties with an average insertion loss of less than 2 dB and an average extinction ratio greater than 50 dB. The wiring area of the double layered wiring switch was 40% smaller than that with the single layered wiring. This enables us to realize densely integrated large-scale TO switches, in which a large amount of complicated wiring is needed.

### References

- [1] A.Himeno et al., IEEE J. Selected Topics in Quantum Electronics 4(1998)924.
- [2] T. Goh et al., IEEE Photon. Technol. Lett. 10(1998)358.
- [3] T. Goh et al., IEEE Photon. Technol. Lett. 10(1998)810.
- [4] K. Moriwaki et al., Tech. Dig. OFC'95, p.211.
- [5] M. Kawachi, Opt. Quantum Electron., 22(1990)391.



1) Bar state (all heaters off).



2) Cross state (all heaters on).

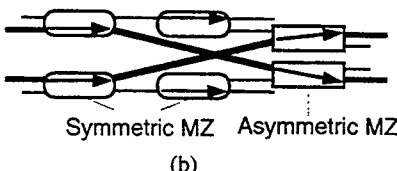
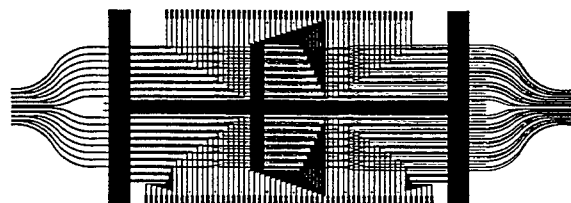
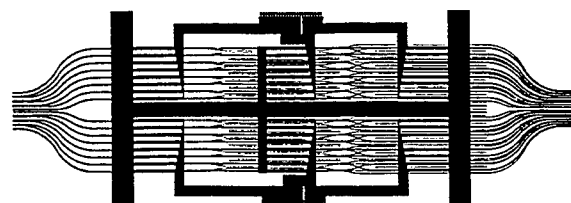


Fig.1. 2x2 switch configuration: (a) switching unit and (b) logical arrangement of 2x2 switch.



(a)



(b)

Fig.2: Layouts of single layered wiring pattern (a) and double layered wiring pattern (b).

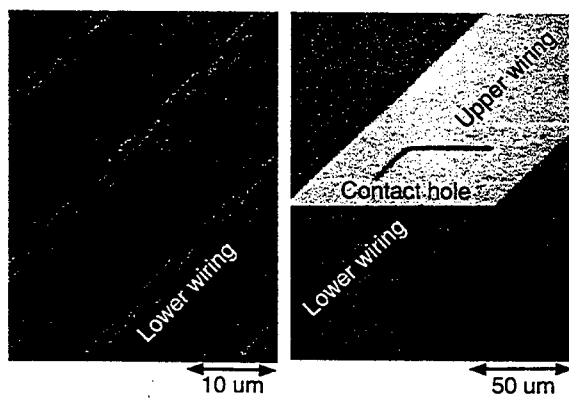


Fig.3: SEM micrographs of double layered wiring: (a) cross wiring and (b) contact hole.

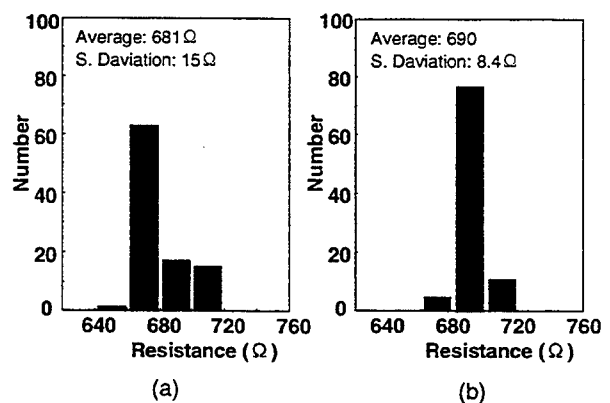


Fig.4: Resistance of single layered wiring (a) and double layered wiring(b).

	Single layered wiring	Double layered wiring
Chip size (mm <sup>2</sup> )	22x66	
Wiring area (mm <sup>2</sup> )	149.2	89.8
Ave. resistance (ohm)	Upper 681(15) Lower 694(8)	687(7)
Ave. switching power (W)	0.340(0.0002)	0.351(0.0004)
Ave. insertion loss (dB)	1.84(0.11)	1.90(0.20)
Ave. extinction ratio (dB)	59.4(4.3)	52.9(7.6)

( ): Standard Deviation

Table 1: Characteristics of 8ch 2x2 switches.

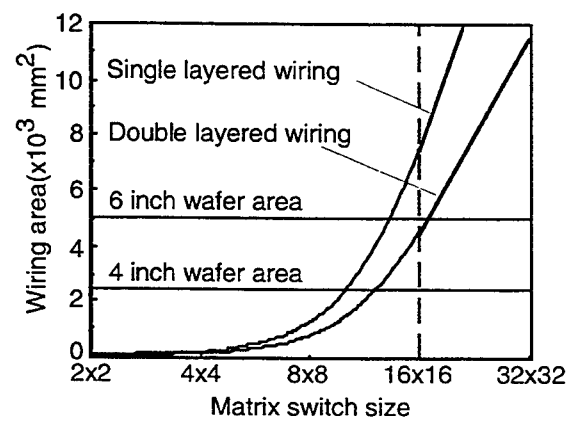


Fig.5: Switch size and wiring area

**Integrated Photonics Research**

# **PBG Structures and Devices**

**Tuesday, July 20, 1999**

**Richard W. Ziolkowski, University of Arizona, USA;  
Brent E. Little, Massachusetts Institute of Technology, USA  
Presiders**

**RTuE  
10:30am-12:15pm  
Sierra Madre South**

## Photonic microstructures: a key approach for high density integrated optoelectronics

R.M. De La Rue, C.J.M. Smith, C.D.W. Wilkinson and T.F. Krauss  
Optoelectronics Research Group, Department of Electronics and Electrical Engineering,  
University of Glasgow, Glasgow G12 8QQ, Scotland, U.K.

H. Benisty, C. Weisbuch and D. Labilloy,  
Laboratoire de Physique de la Matière Condensée, Ecole Polytechnique, 91128 Palaiseau  
cedex, France

R. Houdré, M. Illegems and U. Oesterle,  
Institut de Micro et Opto-électronique, Ecole Polytechnique Fédérale Lausanne, CH-  
1015, Lausanne, Switzerland

One-dimensional and two-dimensional grating structures which, in their in-plane operation, approximate closely to true photonic bandgap behaviour have been fabricated using a combination of high-resolution, direct-write, electron-beam lithography (EBL) and reactive ion etching (RIE)[1,2]. Direct-write electron beam lithography is preferred for pattern generation because of its unrivalled combination of precision and programmability. The approach used is to etch deep, high aspect-ratio, grooves (one-dimensional structures) or holes (two-dimensional structures) through the waveguide core and, in many cases, some distance into the lower cladding of the epitaxial structure. This format makes it possible to maintain the mechanical integrity of the planar waveguide and simultaneously to deliver a large fraction of the light which interacts with the microstructure in the desired in- or out-of-plane form. Fig. 1 shows a cross-sectional view of such a 2D photonic microstructure.

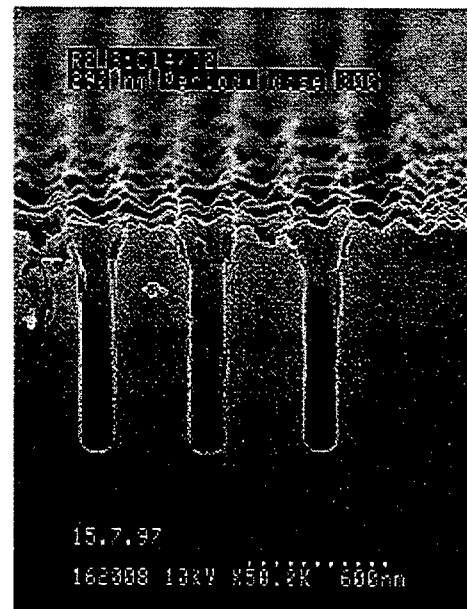


Fig. 1: Cross-sectional scanning electron-micrograph of 2D photonic microstructure in AlGaAs/GaAs waveguide.

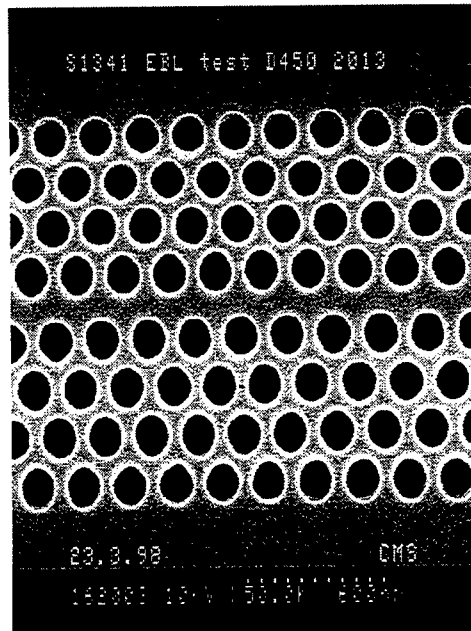


Fig. 2: Plan view of 1D cavity using 2D photonic microstructure mirrors.

The device possibilities of such structures have been clearly demonstrated, but these initial demonstrations are likely to be only the start of the evolution of integrated optics towards much greater device packing densities. In the last three years, the basic properties of two dimensional and one-dimensional microstructures with this deeply etched format have been evaluated [3-6] and moderate to high Q-factor (as much as several thousand) waveguide resonators have been fabricated. These resonators have been investigated using light generated by photoluminescence in embedded quantum-wells and Stranski-Krastanow grown quantum-dots [7,8]. Alternative waveguide photonic microstructure configurations include membranes [9,10] and all-solid configurations [11] having large index contrast between the waveguide core and substrate. These configurations are intrinsically superior in important respects, but engineering judgement and experimental results show clearly that our approach is viable in many practical circumstances.

Photoexcitation both outside and inside the cavity has shown how such resonators could form an essential part of efficient and compact light sources, with either incoherent or coherent characteristics, as well as providing wavelength selection for coarse WDM applications. In the latter case, a large potential reduction in the substrate area required to realise important device functions seems possible, in comparison with existing integrated optics approaches. Fig. 2 shows a section of a short one-dimensional cavity formed between two-dimensional microstructure mirrors. (Propagation is normal to the axis of the gap.) The level of precision required in the fabrication of such structures is high - and could lead to the need for a secondary tuning approach to hit target wavelengths

accurately. Much the same structure could also be used as a waveguide channel for light propagating along the gap axis.

Compact, current injection-pumped, edge-emitting DBR lasers have also been produced [12-14]. With demonstrated cavity lengths as short as 40 µm and threshold current densities for sub-100 µm cavity lengths close to infinite-cavity values, these lasers open up the possibility of high packing density arrays of 'horizontal VCSELs' with the correct orientation to feed into low-loss stripe geometry interconnecting waveguides for integrated optical circuits. More generally, the waveguide photonic microstructure approach can be used to provide either LEDs or lasers in compact form. Finding efficient ways of launching the light from such lasers or LEDs into single transverse mode waveguide channels is a significant further challenge. Narrow-gap, semiconductor-air mirror-stacks etched vertically into a planar waveguide can deliver reflectivity values around 95% - and technology already in existence should make it possible to approach even closer to the ideal value of 100%. But this type of mirror should also be adaptable, with a limited number of sections, to the provision of controlled amplitude and phase transformation capabilities for multiple-cavity semiconductor lasers. At the same time, suitable forms of photonic microstructure will also permit light to be emitted out of the substrate plane with controlled beam shape and localization. Obtaining efficient and sustainable current injection luminescence from epitaxial III-V semiconductor photonic microstructures where the gain is produced within the microstructured material (as opposed to a separate region close by) remains an important challenge.

The emphasis in this presentation is on planar photonic microstructures in waveguides - and on the use of etched 'air-holes' to provide large refractive index contrast. Additional technological processes such as compositionally selective oxidation (the 'Alox' process) [15-17] and quantum-well intermixing [17,18] could play a role in a photonic microstructure-based integrated optics. The refractive index contrast for the 'Alox'-semiconductor system is large enough for photonic bandgap behaviour to be obtainable - and the electrically insulating nature of selectively oxidised III-V semiconductors is now of adequate quality for such material to be a 'routine' component of devices such as VCSELs [19], which necessarily involve a large current concentration. Quantum well intermixing could, in addition to its already recognized capabilities of band-gap shifting and refractive index modification, be used to change the oxidation rate locally by large amounts. Achieving all the process resolution and control necessary to produce photonic microstructures via selective oxidation at the scale required remains a substantial challenge.

We have emphasized photonic microstructures based on III-V semiconductors in this presentation, but other materials are of interest. Even with only a fraction of the refractive index contrast available in the air-semiconductor combination, it should be possible to realise practical devices via the same general approach. Within the III-V semiconductor materials, fabrication technology still needs to be developed to enable similar structures to be produced routinely across the range of arsenides, phosphides, nitrides and antimonides now available - and used at operating wavelengths ranging from the near uv to the mid IR. Mass-production for visible and near infra-red wavelength photonic

microstructures may require 'conventional' VLSI lithographic techniques to go at least one stage further than the present leading-edge provided by excimer lasers.

## References

1. T.F. Krauss, C.J.M. Smith, B. Vögele, S.K. Murad, C.D.W. Wilkinson, R.S. Grant, M.G. Burt and R.M. De La Rue, Microelectronic Eng., **35**, pp.29-32, (1997).
2. C.J.M. Smith, S.K. Murad, T.F. Krauss, R.M. De La Rue and C.D.W. Wilkinson, J. Vac. Sci. Tech., **B17**, pp.113-117, (1999).
3. T.F. Krauss and R.M. De La Rue, Appl. Phys. Lett., **68**, pp.1613-1615, (1996).
4. T.F. Krauss, R.M. De La Rue and S. Brand, Nature, **383**, pp. 699-702, (1996).
5. T.F. Krauss, B. Vögele, C.R. Stanley and R.M. De La Rue, IEEE Photonics Technol. Lett., **9**, pp.176-178, (1997).
6. D. Labilloy, H. Benisty, C. Weisbuch, T.F. Krauss, R.M. De La Rue, V. Cardinal, R. Houdré, U. Oesterle, D. Cassagne and C. Jouanin, Phys. Rev. Lett., **79**, , pp. 4147-4150, (1997).
7. C. J. M. Smith, T. F. Krauss, R. M. De La Rue, D. Labilloy, H. Benisty, C. Weisbuch, U. Oesterle and R. Houdré, IEE Proc.-Optoelectron., **145**, pp. 373-378, (1998).
8. C. J. M. Smith, H. Benisty, D. Labilloy, U. Oesterle, R. Houdré, T. F. Krauss, R. M. De La Rue and C. Weisbuch, Electron. Lett., **35**, pp. 228-230, (1999).
9. J.S. Foresi et al, Nature, **390**, pp.143-145, (1997).
10. O. Painter et al, Integrated Photonics Research, Victoria B.C., paper ITuD2, (30th March - 1st April 1998).
11. D.N. Atkin et al, J. Modern Optics, **43**, pp.1035-1053, (1996).
12. T.F. Krauss, O. Painter, A. Scherer, J.S. Roberts and R.M. De La Rue, Optical Engineering, **37**, pp.1143-1148, (1998).
13. T.F. Krauss, A. Scherer, J.S. Roberts and R.M. De La Rue, Integrated Photonics Research, IPR '98, Victoria B.C., paper IWB3, (30th March -1st April 1998).
14. T. Baba et al, Jap. Jour. Appl. Phys., **35** (Pt. 1), pp. 1390-1394, (1996)
15. J.M. Dallesasse et al, Appl. Phys. Lett., **57**, pp.2844-2846, (1990).
16. C.J.M. Smith, L.Hobbs, T.F. Krauss, R.M. De La Rue and M. Dawson, 11th LEOS Annual Meeting, Orlando, USA, (December 1998).
17. R.M. De La Rue and T.F. Krauss, in 'Microcavities and Photonic Bandgaps: Physics and Applications', pp.175-192, Kluwer, Dordrecht, (1996).
18. O.P. Kowalski, C.J. Hamilton, S.D. McDougall, J.H. Marsh, A.C. Bryce, R.M. De La Rue, B. Vögele, C.R. Stanley, C.C. Button and J.S. Roberts, Appl. Phys. Lett., **72**, pp.581-583, (1998).
19. K.D. Choquette and H.Q. Hou, Proc. IEEE, **85**, pp. 1730-1739, (1997).

# FDTD Analysis of PBG Waveguide Power Splitters and Switches for Integrated Optics Applications

Richard W. Ziolkowski<sup>1</sup> and Masahiro Tanaka<sup>2</sup>

<sup>1</sup> Department of Electrical & Computer Engineering, The University of Arizona, 1230 E. Speedway, Tucson, AZ 85721-0104, E-mail: ziolkowski@ece.arizona.edu

<sup>2</sup> Department of Information Science, Gifu University, 1-1 Yanagido, Gifu city, Gifu 501-11, Japan, E-mail: masahiro@info.gifu-u.ac.jp

Nanometer and micron sized optical devices are currently being explored for their applications in a variety of systems associated with communications, data storage, optical computing, etc. However, as the size of optical devices is pushed to the size of an optical wavelength and less, the need for more exact materials and response models is tantamount to the successful design and fabrication of those devices. The finite-difference time-domain (FDTD) (see [1, 2] for extensive reviews on this approach and its applications) method is receiving intensive study for modeling a variety of optical structures.

This paper further illustrates the ability of the FDTD approach to model finite-sized PBG waveguiding structures. The photonic band gap (PBG) structure has become a very important subject in the optics regime for microcavity laser mirrors and filters [3]. In particular, it has been demonstrated computationally and experimentally that photonic bandgap (PBG) structures can be used to form nanometer sized waveguiding structures for a variety of optical applications. The ability of the FDTD approach to model finite-sized PBG structures and to recover known behaviors has been demonstrated. The simulator used in the present PBG waveguide analysis has been validated previously [4] and has been extended recently to study dispersive effects in PBG structures[5]. Results for basic sub-wavelength waveguiding structures in triangular PBGs formed in a dielectric substrate with air holes and fed by dielectric waveguides are presented. These structures have potential applications in integrated optics. Waveguide channels in these PBGs are formed by the removal of particular sets of rods; Y-power splitters have been designed. By introducing further defects into the PBG structure, we have demonstrated that control of the electromagnetic power flow in the waveguides can be achieved. A power splitter with additional defects leads to a switch configuration. This defect-based switch has been characterized with the FDTD approach.

For the triangular PBG formed by air holes (oriented in the  $y$ -direction) in a dielectric substrate, bandgaps for both TM ( $E_y$ ,  $H_x$ , and  $H_z$  field components) and TE ( $H_y$ ,  $E_x$ , and  $E_z$  field components) polarizations have been demonstrated. Two dimensional standard staggered grid, leap-frog time integration scheme FDTD codes for both polarizations have been developed and validated. The FDTD mesh is terminated with the Berenger PML absorbing boundary condition. The PBG waveguide structure used in our investigation is shown in Figure 1. It is a triangular lattice consisting of 13 columns  $\times$  30 rows of circular air holes in a GaAs dielectric material ( $\epsilon = 11.43\epsilon_0$ ). The electric field is polarized along the rods in the TM polarization; the magnetic field in the TE polarization. The input waveguide is excited with the lowest order mode with a broadband width ( 3 cycle ) pulse centered about  $f_0 = 2.0 \times 10^{14}$  Hz corresponding to a free space wavelength of  $\lambda_0 = 1.5 \mu m$ . The space was discretized to  $\Delta = \lambda_0/88$ . The radius of the rods was  $r = 20$  cells; the horizontal distance between the hole centers was  $d_{hori} = 38$  cells; and the vertical distance between the hole centers was  $d_{vert} = 44$  cells. The waveguides are formed by removing particular sets of rods. The waveguide width is  $2(a - r) = 48$  cells; slightly larger than  $\lambda_0/2$ . A Y-junction was formed in the PBG structure in a straightforward manner.

We characterized the electromagnetic behavior of the PBG and the resulting waveguide structures by various power transmission and reflections coefficients. They were obtained by measuring

the electric and magnetic fields on specified surfaces in the FDTD mesh, fast Fourier transforming these time histories, and then forming the total time-averaged Poynting's vector through those surfaces. Thus, with one broad bandwidth pulse simulation the frequency domain transfer function of the finite PBG structure was generated.

The normalized power transmission spectrum for one arm of the power splitter is shown in Figure 2 for the *TE* polarization. It was found that about 36% of the total input power can be channeled through the PBG structure into the output waveguides at  $f = 0.767 f_0$ , the location of the largest peak in the transmission spectrum. Note that considerable power is lost to the waves which must scatter to fill the PBG structure and to the insertion loss from the waveguide into the arms of the splitter. The corresponding *TM* polarization results exhibited similar multiple transmission peaks but with much less total throughput, about 20% at  $f = 0.881 f_0$ .

These results demonstrate that an integrated optics power splitter can be achieved in a micron sized environment using PBG waveguiding structures. It has been found that by introducing additional defects into this splitter that a switch can be obtained that regulates the amount of power flow between each of the arms of the splitter. The additional defect(s) control the flow of light in the waveguide system.

One way to introduce additional defects to affect control over the electromagnetic power flow is to change the permittivity in some manner in the rods associated with one of the arms of the splitter. A potential method would be to integrate a MEMS device with the PBG structure that could selectively insert or remove some of the defect rods much like the control rods in a nuclear pile. For instance, one could insert a rod with either the same or a different dielectric strength into a specified set of the holes. The introduction of the additional defects breaks the symmetry of the original structure; the power of each arm will no longer be equal to that of other. Although this would most probably result in a slow switch, the resulting device would have interesting isolation capabilities between the two arms of the splitter. One could envision the blockage structure shown in Figure 3. The MEMS device would remove three posts from one the left waveguide channel. The spectrum of the power output in the left and right arms of this structure for *TE* polarization is shown in Figure 4. At the target (best throughput for the unperturbed Y-splitter) frequency of  $f = 0.767 f_0$ , a 808 : 1 isolation is achieved between the left and right arms. Moreover, the total output power of the device is increased to 53.6%; the power channeled to the left half of the PBG structure is effectively channeled into its right arm. The corresponding *TM* case at  $f = 0.881 f_0$  had an isolation of 101 : 1 between the right and left arms but in fact had a lowering of the total output power to 13.4%. The defects caused a much larger perturbation in the overall *TM* field structure. Thus, an effective switch state was realized for both polarizations.

The contributions to this work by Ziolkowski were supported in part by the Air Force Office of Scientific Research, Air Force Materiel Command, USAF, under grant number F49620-96-1-0039. The work performed by Tanaka occurred as a Visiting Scholar with the Department of Electrical and Computer Engineering at the University of Arizona.

## References

1. A. Taflove, *Computational Electrodynamics*, Artech House, Norwood, MA, 1995.
2. A. Taflove, *Advances in Computational Electrodynamics*, Artech House, Norwood, MA, 1998.
3. J. D. Joannopoulos, R. D. Meade, and J. N. Winn, *Photonics Crystals: Molding the Flow of Light*, Princeton University Press, Princeton, NJ, 1995.
4. R. W. Ziolkowski and M. Tanaka, "FDTD Analysis of PBG Waveguides, Power Splitters, and Switches," to appear in *Opt. and Quan. Electr.*, 1999.
5. R. W. Ziolkowski and M. Tanaka, "Finite-difference time-domain modeling of dispersive material photonic band-gap structures," to appear in *J. Opt. Soc. Am. A*, 1999.

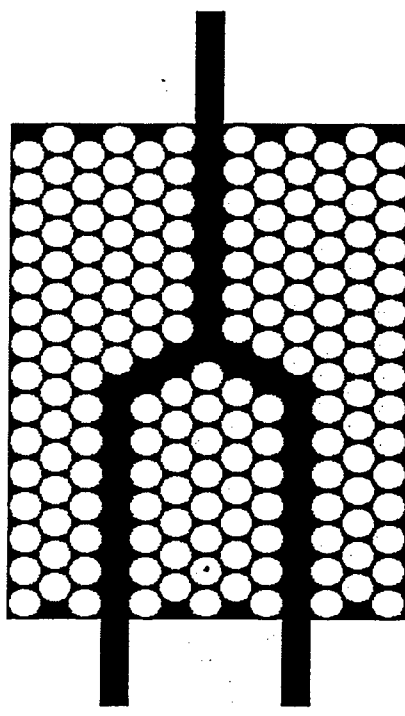


Figure 1: Triangular lattice Y splitter

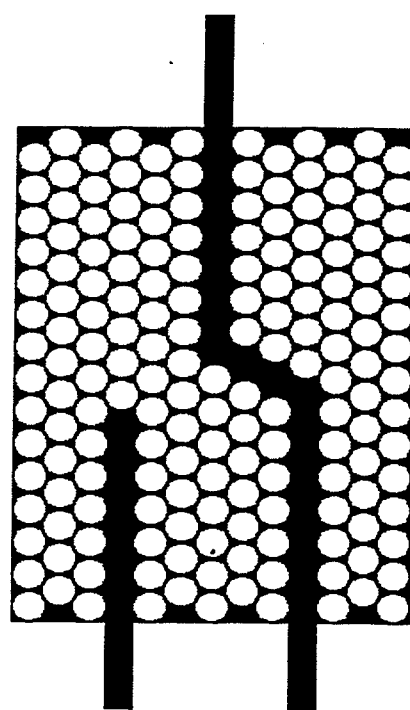


Figure 3: Triangular lattice Y splitter with additional defects

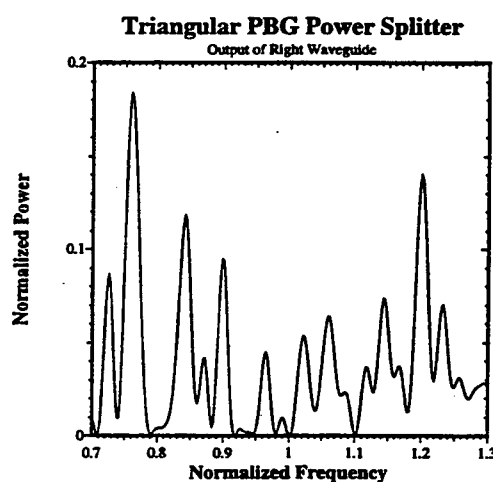


Figure 2: Transmission spectrum of the right arm of the triangular lattice Y splitter

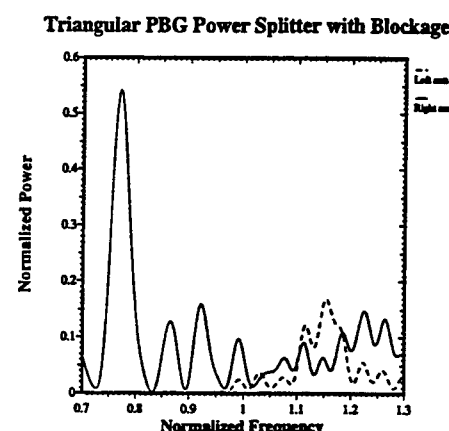


Figure 4: Transmission spectrum in the left and right arms of the Y power splitter

# Observation of Light Propagation in Photonic Crystal Optical Waveguides with Bends

Toshihiko Baba, Naoyuki Fukaya and Jun Yonekura

Yokohama National University, Division of Electrical and Computer Engineering

79-5 Tokiwadai, Hodogayaku, Yokohama 240-8501, Japan

Phone +81-45-339-4258, Fax +81-45-338-1157, E-Mail baba@dnj.ynu.ac.jp

**Abstract** — We observed the light propagation in 2-D photonic crystal waveguides with bends, which were composed of densely-packed holes formed in a GaInAsP thin film. Wavelength and polarization dependence of propagation characteristics was observed at  $\lambda = 1.47 - 1.60 \mu\text{m}$ .

## 1. Introduction

Photonic crystals are expected to be omni-directional mirrors with a high reflectivity by the photonic bandgap (PBG). One of potential applications so far suggested is a waveguide with the strong optical confinement, in which photonic crystals are used as claddings. The low loss propagation through waveguides with sharp bends, branch, etc., have been theoretically estimated[1,2], and a part of them have been experimentally demonstrated by using a large crystal designed for millimeter waves[3]. However, experiments are much more difficult for lightwaves. The light propagation in straight waveguides has been reported recently[4]. Still, the effect of photonic crystal claddings was not clear, since the waveguide was as short as several microns. In this paper, we report the first observation of light propagation in such waveguides with bends.

## 2. Fabrication

The schematic of a fabricated waveguide is shown in Fig. 1. A GaInAsP film epitaxially grown on InP substrate was used as a waveguide material. The thickness and bandgap wavelength were  $0.35 \mu\text{m}$  and  $1.27 \mu\text{m}$ , respectively. Using a thin epoxy, it was bonded on a host substrate whose surface was covered with a  $\text{SiO}_2$  film of  $3 \mu\text{m}$  in thickness. Then, the first InP substrate was removed by a selective wet etching. Thus, the GaInAsP film acts as a slab waveguide with the upper air and the lower  $\text{SiO}_2$  claddings. Before the bonding process, a 2-D photonic crystal was formed in the GaInAsP film by the EB lithography and the dry etching. It was composed of densely-packed holes. The designed diameter and pitch of holes were  $0.5 \mu\text{m}$  and  $0.6 \mu\text{m}$ , respectively. According to the 2-D photonic band calculation, they allow a full PBG in a wavelength range of  $\lambda = 1.5 - 1.6 \mu\text{m}$  when the refractive index of semiconductor is 3.38[5]. A channel waveguide was composed of a single line of defects of the crystal, i.e., GaInAsP corrugated stripe of  $0.7 \mu\text{m}$  in narrowest width. The photonic crystal pattern includes straight waveguides of  $25 \mu\text{m}$  in length and those with a 60-degree or a 120-degree bend. Fig. 2 shows the crystal before the bonding process. Holes just beside waveguides became

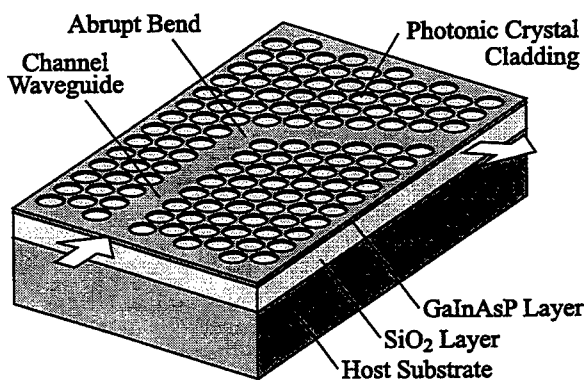


Fig. 1 Schematic of photonic crystal waveguide.

20 – 30 % smaller than the designed one due to the nonuniform exposure in the lithography process, while other holes were almost the same as the designed one. After the bonding process, however, the waveguide width was expanded to 2.4  $\mu\text{m}$ , since the dry etching did not pierce the smaller holes.

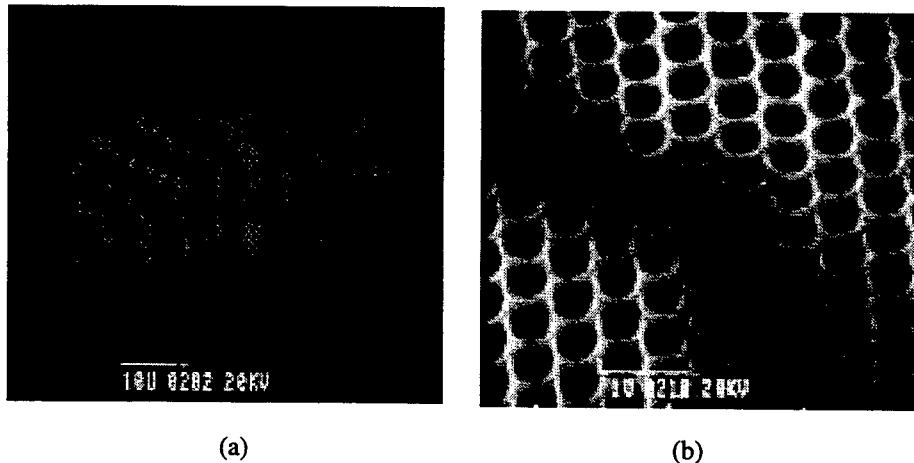


Fig. 2 SEM views of photonic crystal before bonding and substrate removing process. (a) shows total view and (b) magnified view around channel waveguide. After bonding process, patterns were reversed.

### 3. Measurement

A tunable laser of  $\lambda = 1.47 - 1.60 \mu\text{m}$  was used as a light source. The light was focused on a cleaved facet of the sample. The light path was observed from the top of the surface using an infrared TV camera. For the film without the photonic crystal and unexpected defects, the light path was not observed due to the small surface scattering of light. The light propagation in the slab waveguide was confirmed over the above wavelength range from the scattered light at some cracks of the film, which might be caused by the residual tension in the epoxy. We considered that it was a guided mode in the GaInAsP, not a cladding mode in the  $\text{SiO}_2$ , since the calculated propagation loss of the cladding mode was as large as 43 – 45 dB/mm for arbitrary polarization. For a channel waveguide, we confirmed the light propagation, as shown in Fig. 3. The straight light path was seen for the straight waveguide. We consider that the scattering of guided mode at core/cladding boundaries caused the light path. The strong light output was seen at a deep crack near the right end of Fig. 3. The distance of the crack from the waveguide end was 93  $\mu\text{m}$ . The width of the major light intensity at the crack was 25  $\mu\text{m}$ . Let us consider the light propagation from the waveguide end to the crack as that of a Gaussian beam and the width of the major intensity as the full width at  $1/e^2$  of its maximum. Assuming an equivalent refractive index of 3.0 for the slab waveguide, the spot diameter at the waveguide end was calculated to be 2.4

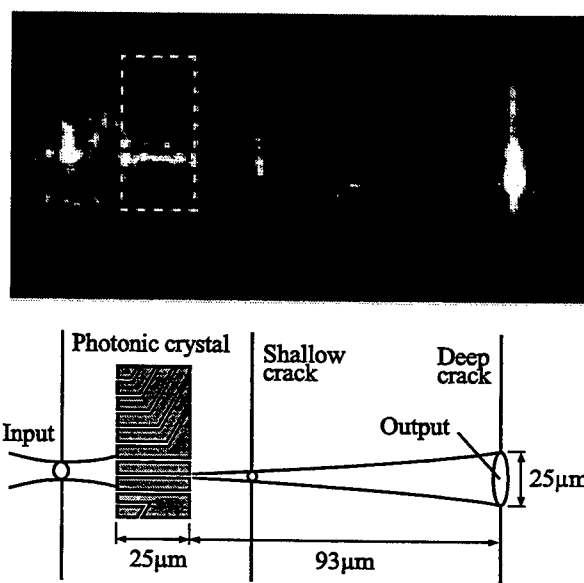


Fig. 3 Light path observed at  $\lambda = 1.51 \mu\text{m}$ .

$\mu\text{m}$ . This value is absolutely the same as the waveguide width, as mentioned above.

Fig. 4 shows light paths when the light was widely inserted to the end of the photonic crystal. For the TE polarization, the light path was drastically changed with wavelength. For  $\lambda = 1.51 - 1.56 \mu\text{m}$ , the path was clearly seen for waveguides. The light propagates even in waveguides with bends. Outside this range, the light almost passed through the crystal; over the photonic crystal area, the scattering was enhanced at  $\lambda < 1.51 \mu\text{m}$ , while suppressed at  $\lambda > 1.56 \mu\text{m}$ . This indicates that a PBG exists at  $\lambda = 1.51 - 1.56 \mu\text{m}$ . For the TM polarization, the light path for waveguides was barely observed at  $\lambda = 1.51 - 1.53 \mu\text{m}$ . However, it was more indistinct than for the TE. It might be caused by a narrow PBG for the TM, which were expected from the photonic band calculation[5].

#### 4. Conclusion

We fabricated thin film channel waveguides with 2-D photonic crystal claddings of closely packed holes, and successfully observed the light propagation at  $\lambda = 1.51 - 1.56 \mu\text{m}$ . In this study, we did not use a 3-D calculation for the design, but only a 2-D one. Nevertheless, the evaluated PBG roughly agreed with the expected one. In the near future, we will discuss the reason as well as the further detail of propagation characteristics and the correspondence to a 3-D theory.

**Acknowledgments** — We would like to thank Prof. Y. Kokubun, Yokohama National University, and Prof. K. Iga and Associate Prof. F. Koyama, Tokyo Institute of Technology, for discussion. We also thank Dr. T. Miyamoto, Tokyo Institute of Technology, for the supply of epitaxial wafer. This work was partly supported by The Grant-in-Aid #10210203, The Priority Area “The control of electromagnetic radiation in photonic crystals”, by the Ministry of Education, Science, Sports and Culture.

#### References

- [1] A. Mekis, J. C. Chen, I. Kurland, et.al., *Phys. Rev. Lett.*, 1996, **77**, (18), pp. 3787-3790.
- [2] J. Yonekura, M. Ikeda and T. Baba, *IEEE/OSA J. Lightwave Technol.*, submitted in 1998.
- [3] B. Temelkuran and E. Ozbay, *Appl. Phys. Lett.*, 1999, **74**, (4), pp. 486-488.
- [4] O. Hanaizumi, Y. Ohtera, T. Sato and S. Kawakami, *Appl. Phys. Lett.*, 1999, **74**, (6), pp. 777-779.
- [5] J. D. Joannopoulos, et.al., *Photonic Crystals, Molding the Flow of Light*, Princeton Univ. Press, 1995.

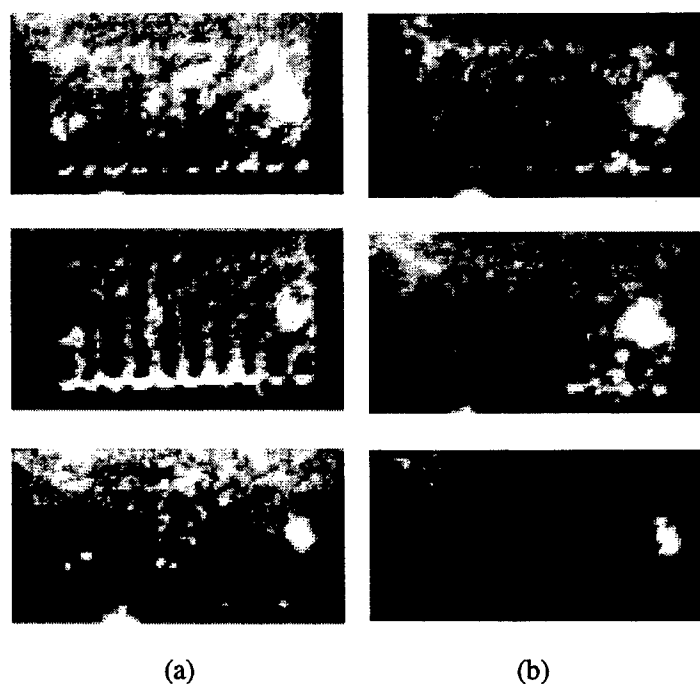


Fig. 4 Observed light paths against uniform incident wave. (a) and (b) indicate TE and TM polarizations. Upper, middle and lower figures indicate  $\lambda = 1.49$ ,  $1.53$  and  $1.58 \mu\text{m}$ , respectively.

## **Electromagnetic Band Gap Structures:** *Advances in Computational Techniques*

Yahya Rahmat-Samii  
Department of Electrical Engineering  
University of California, Los Angeles  
Los Angles, CA 90095-1594  
rahmat@ee.ucla.edu

**Abstract:** Electromagnetic band gap structures (the counterpart of the optical photonic band gaps, PBG) are synthesized 2-D or 3-D multi-layered periodic structures that effectively prevent the propagation of electromagnetic waves in a specified band of frequency. Generally speaking, it is desired that this property be held for any incidence angles and polarizations of electromagnetic waves in the prevention band. These band gap structures may be constructed in a variety of ways either through periodic perforations of multi-layered substrates or through the development of properly stacked 2-D or 3-D periodic metallic or dielectric structures. Because of the wide-bandwidth of the propagation prevention band gap, these structures may be used in various microwave/millimeter wave devices and antennas. Potential applications may be found in antenna gain enhancement, miniaturization of antenna dimensions, ground planes, cavities, waveguide structures, etc.

In the recent past, most of the activities were directed towards the design and experimental performance evaluation of these structures. More recently attention has been focused on the EM theoretical/numerical modeling and performance characterization of these complex structures. In this presentation, application of modern numerical techniques will be presented. Among these techniques special emphasis will be given to the application of FDTD and periodic method of moments. The performance of several candidate structures will be evaluated to critically examine the EM properties of these structures and their potential utilization in various applications with considerable emphasis given to provide physical and engineering insights.

**Antennas on Perforated High Dielectric Constant Substrates:** Smaller physical size and wider bandwidth are two engineering goals of great interest in the wireless world. To this end the concept of substrate perforation is applied to patch antennas mounted on high dielectric material. The goal has been to overcome the undesirable features of thick and high dielectric constant substrates for patch antennas without sacrificing any of the desired features, namely, small element size and bandwidth. The idea is to use substrate perforation exterior to the patch to lower the effective dielectric constant of the substrate surrounding the patch. The data presented is based on the application of FDTD technique. Various aspects of the exact layout of the perforation relative to the patch and ground have been explored and implementation guidelines have been generated. It has been found that the perforation must not be located too close to the patch due to the fringing fields.

**Band-Gaps Composed of Multi-layered Periodic Structures:** Characteristics of purely metallic band gap structures are determined using a novel periodic method of moment implementation for the solution of the integral equation. The structure is infinitely periodic in two dimensions with a finite periodicity in the third dimension. It is shown that an effective band-gap exists when within a certain frequency range, the reflection is 100% for all angles of incidence and all polarizations. The performance of the structure is explained from a physical point of view by isolating the effects of each parameter of the structure. Cascading two periodic arrays with a very small separation distance has shown to give a capacitance effect for the overlap region. The capacitance has shown to control the lower edge of the band gap. The coupled periodic arrays give a rejection band, with the separation controlling the upper edge of the band. An effective band-gap is shown to exist when different layers are connected with vias that allows the incidence angle to reach an almost grazing angle.

**Mode Volume in a Dielectric Nano-Cavity:** In a photonic crystals, electromagnetic waves can be confined in all three dimensions, leading to very small mode volumes. A detailed computational search for the characterization of the mode volumes have been performed. The small mode volume could lead to a significant enhancement of the spontaneous emission rates in semiconductor nano-cavities. The computational power of FDTD is used to characterize the mode volume. The method has been proven to be very effective in providing a wealth of data form which it has been possible to derive all the quantities of interest for the design of nano-cavities. Numerous possible configurations of the dielectric cavity created by introduction of defect into a 2-D photonic crystal have been investigated. The baseline 2-D photonic crystal consists of a thin slab with a triangular array of holes. It has been shown that the defect modes in a dielectric slab photonic crystals can be numerically optimized using FDTD.

## Finite-Difference Time-Domain Modeling of Complex Integrated Optics Structures

*Stoyan Tanev, Dazeng Feng, Velko P. Tzolov and Z. Jan Jakubczyk*

Optiwave Corporation, 16 Concourse Gate, Suite 100, Nepean, Ontario, Canada K2E 7S8  
Tel. (613) 224 4700, Fax (613) 224 4706, e-mail: [info@optiwave.com](mailto:info@optiwave.com), [www.optiwave.com](http://www.optiwave.com)

The Finite-Difference Time-Domain (FDTD) method<sup>1</sup> is becoming popular engineering tool for integrated and diffractive micro optics device simulations. This is due to its unique combination of features, such as the ability to model light propagation, scattering, diffraction and reflection. Waveguide grating and Photonic Band Gap (PBG) optical structures<sup>2</sup> are among the most challenging areas of application of the FDTD approach. In a recent publication<sup>3</sup> we have reported results on the FDTD modeling of a grating-assisted waveguide coupler combined with a 2D PBG mirror. A similar Waveguide Division (De)Multiplexing (WDM) configuration has been previously proposed and modeled by Ziolkowski and Liang<sup>4</sup> but a linear (1D) multi-layer PBG structure was used as a mirror. In our configuration, the 2D PBG mirror consisted of a square lattice of GaAs rods situated in air. One of the advantages of 2D PBG structures over the 1D ones is the ability to reflect light incoming from any angle in a plane perpendicular to the dielectric rods<sup>2</sup>. Another advantage is the possibility to introduce different defects in the 2D PBG structure aiming to implement specific output beam shaping functions such as deflecting, splitting or focusing.

Specific beam shaping functions of the waveguide grating coupler output channels could also be implemented in other ways. In the present contribution we report our preliminary FDTD modeling results of a Focusing Waveguide Grating Coupler (FWGC) using the waveguide grating structure described above<sup>3</sup> with an integrated micro Fresnel lens (Fig. 1).

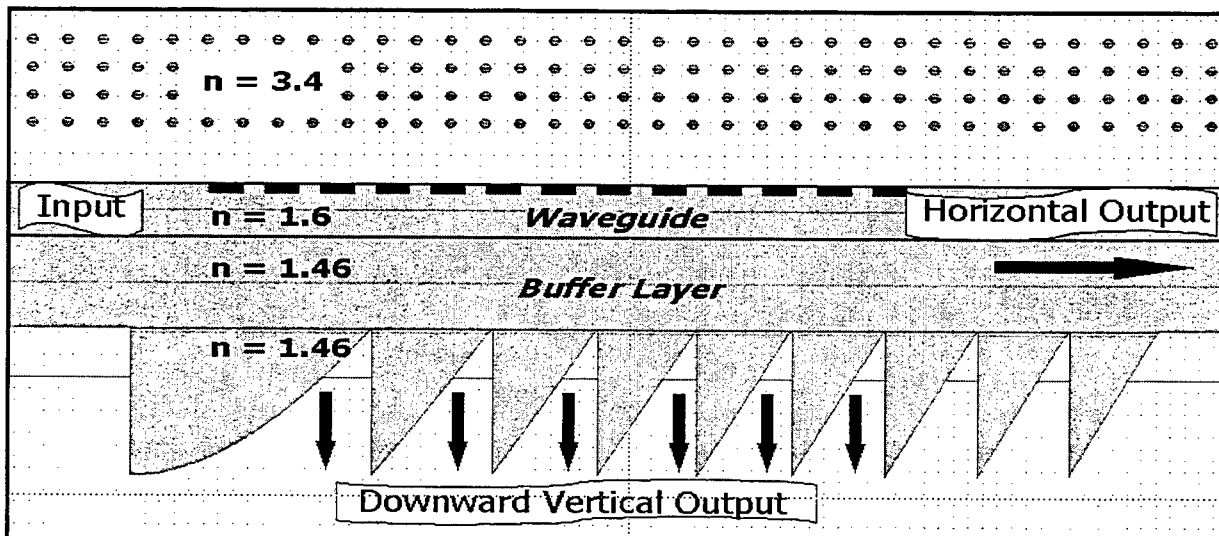


*Fig. 1 Focusing waveguide grating coupler using a 2D PBG mirror and a micro Fresnel lens.*

The FWGC simultaneously features two functions: to couple out the guided wave propagating in the waveguide structure and to focus the downward output beam into a small spot. A similar configuration, without the mirror and using a chirped binary-phase-only diffractive lens, was

investigated both theoretically and experimentally by Sheard *et al.*<sup>5</sup> The integration of the micro Fresnel lens in our configuration (with a 2D PBG mirror) makes the device really challenging from modeling point of view. Nevertheless, if the waveguide grating coupler and the Fresnel lens are well physically separated, their functionality can be analyzed in an independent way.

The 2D PBG mirror enhanced waveguide grating coupler<sup>3</sup> operates resonantly at  $\lambda = 1.5 \mu\text{m}$ . The parameters of the 2D photonic crystal are as follows: refractive index  $n = 3.4$ , inter-column distance  $a = 0.6 \mu\text{m}$ , column radius  $r = 0.1 \mu\text{m}$ . In devices incorporating PBG structures the effect of the finite dimensions of the photonic crystals is an important issue. The reflectivity of the photonic crystal was optimized as a function of the number of column layers. A four column layers photonic crystal wall was found to have an excellent reflectivity. The integration of the Fresnel lens requires a buffer layer to be designed. This obviously changes the refractive index distribution of the whole structure<sup>3</sup> and some of the material parameters have to be reconsidered. The refractive index of the main waveguide layer (thickness  $1.2 \mu\text{m}$ ) is  $n = 1.6$ . The finite-length perfectly electric conductor (PEC) grating on top of the waveguide layer is designed to diffract normally. It has a period  $\Lambda = 0.97 \mu\text{m}$  and consists of 13 periods, each with duty factor 0.5 and a depth of  $0.2 \mu\text{m}$ . The value of the distance between the PEC grating and 2D PBG mirror ( $1.35 \mu\text{m}$ ) ensures maximum intensity of the downward output channel of the coupler<sup>3,4</sup>. The thickness of the buffer layer ( $n = 1.46$ ) was continuously increased to about  $2 \mu\text{m}$  by monitoring the deformation of the waveguide mode field profile.

The micro Fresnel lens was designed to have a maximum focusing efficiency. It consists of a series of concentric zones. The phase (optical path) difference between two successive zones is  $2\pi$ . For a normally incident plane wave the radius and the profile of the  $m$ -th ring are given by:  $r_m = \sqrt{2m\lambda F + (m\lambda)^2}$ , ( $m = 0, 1, 2, \dots$ ) and  $T_m(r)/T_0 = 1 + m + (F - \sqrt{F^2 + r^2})/\lambda$ ,  $r_m < r < r_{m+1}$ , where  $T_0 = \lambda/(n-1)$  is the optimum lens thickness and  $F = 5 \mu\text{m}$  is the focus length. A more realistic lens profile design (resulting from a real fabrication process) would decrease the focusing efficiency of the Fresnel lens but our main aim here is to validate the application of the FDTD approach for the analysis of such a high complexity integrated optics device.

Fig. 2 shows the electric field intensity distribution of a TE ( $H_x, E_y, H_z$ ) CW FDTD simulation of the FWGC. The transverse and the longitudinal discretization steps are  $0.05$  and  $0.02 \mu\text{m}$ , respectively. The computational window is  $(18 \times 25) \mu\text{m}$ . The FDTD solver uses an un-split version of PML boundary conditions<sup>1</sup>. The fundamental TE mode ( $n_{\text{eff}} = 1.54421$ ) of the waveguide structure is introduced at a total field/scattered field interface located at a certain distance from the back PML layer. All the PML layers have 16 cells length. The simulation ran for 40000 time steps.

The numerical results show that the FWGC combines two functions – focusing and deflection of the downward output light beam. The high focusing efficiency is a result of the fact that the micro Fresnel lens has the optimum profile predicted by the scalar diffraction theory<sup>6</sup>. A drawback is that the integration of the lens increases the intensity of the horizontal output channel of the coupler (Fig. 2) and the downward output beam extraction becomes less effective. A way to overcome this problem is to use a resonant filter operating at the same wavelength as the FWGC. This filter, located at the end of the waveguide structure, will reflect back the desired

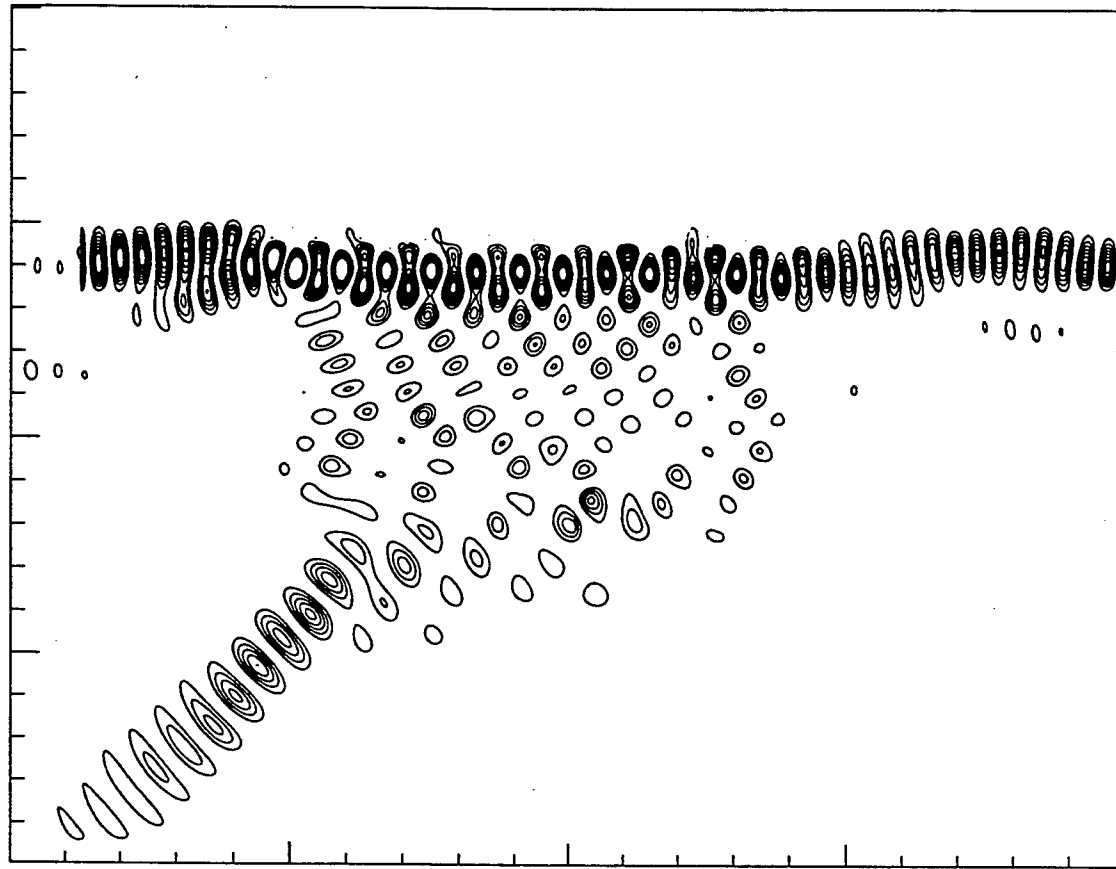


*Fig. 2 Micro Fresnel lens focusing of the downward output coupler beam. Focus length 5  $\mu\text{m}$ .*

signal and force it to diffract once again focusing into the same spot. Such a double pass FWGC will be very efficient for WDM applications. A study of the functional optimization of the device is in progress.

In conclusion, the FWGC modeling results presented here demonstrate the ability of the FDTD approach to model highly complex integrated optics structures.

This work is supported by the Industrial Research Assistance Program from NRC of Canada. D. Feng acknowledges the Industrial Research Fellowship support from NSERC of Canada.

#### REFERENCES

1. Taflove, A., Editor, *Advances in Computational Electrodynamics – The Finite-Difference Time Domain Method*, Artech House, Boston, 1998.
2. Joannopoulos, J. D., Meade, R. D. and Winn, J. N., *Photonic Crystals*, Princeton University Press, 1995.
3. Velko P. Tzolov, Dazeng Feng, Stoyan Taney, and Z. Jan Jakubczyk, "Modeling tools for integrated and fiber optical devices", Invited Paper on SPIE Photonics West'99, Integrated Optics Devices III Conference, 23-29 January 1999, San Jose, California.
4. Ziolkowski, R. W. and Liang, T., *Optics Letters* 22, pp. 1033-1035, 1997.
5. Sheard, S., Liao, T., Yang, G., Prewett, P., and Zhu, J., *Applied Optics* 36, pp. 4349-53, 1997.
6. Nishihara, H., Suhara, T., "Micro Fresnel Lenses", *Progress in Optics* XXIV, Elsevier, 1987.

**Integrated Photonics Research**

# GaN Device Modeling

**Tuesday, July 20, 1999**

**Shuji Seki, NTT, Japan**

Presider

**RTuF**

**10:30am–11:45am**

Anacapa

## Many-body theory of gain in InGaN and GaN quantum well lasers

W. W. Chow  
Sandia National Laboratories  
Albuquerque, NM 87185-0601  
Tel. no. 505-844-9088  
Fax: 505-844-3211  
email:wwchow@somnet.sandia.gov

Group-III nitride lasers are currently intensely studied because of their application potential as light sources in the ultraviolet and visible wavelength regions. [1] To understand the behavior of these lasers, it is useful to know their gain and spontaneous emission properties. This paper describes an approach for calculating these properties for different experimental conditions.

The theoretical approach is based on the semiconductor Bloch equations, where collision effects are treated at the level of quantum kinetic theory. [2,3] The bandstructure effects are described with  $\vec{k} \cdot \vec{p}$  theory, [4] with effects of the screened piezoelectric field systematically included by the simultaneous solution of the coupled Poisson equation and the Luttinger Hamiltonian in the envelope approximation. Solving the semiconductor Bloch equations under small signal conditions and with the results of the bandstructure calculation as input gives the gain spectrum. Using the calculated gain spectrum and applying a phenomenological relationship between stimulated and spontaneous emission, [5] we obtain the corresponding spontaneous emission spectrum.

An application of the above analytical approach is illustrated in Fig. 1, where we use the gain and spontaneous emission spectra computed for a range of carrier densities to estimate the theoretical limit to the threshold current density in two quantum well configurations. From the gain spectra, we obtain the peak gain versus carrier density for 2nm and 4nm  $In_{0.2}Ga_{0.8}N$ -GaN quantum well structures, which are representative of the laser gain regions presently used in experiments. The corresponding spontaneous emission currents are obtained by integrating over frequency the spontaneous emission spectra. An interesting result is the prediction of lower threshold current density for the wider 4nm quantum well. The reason is the stronger quantum confined Stark effect in the 4nm quantum well which causes a greater reduction in the optical dipole matrix element. This in turn reduces both the gain and the spontaneous emission. Our calculation shows that the reduction in spontaneous emission loss more than compensates the reduction in gain.

Comparison of the two curves close to transparency illustrates the very different physical mechanisms leading to the onset of gain. In the narrow 2nm quantum well, the onset of gain is due to band filling. In contrast, a significant population inversion already exists in the wide 4nm quantum well at the onset of gain. Here, the appearance of gain is due to the switch on of the interband dipole matrix element by the screening of quantum

confined Stark effect. We wish to emphasize that in an experiment, gain in the 4nm quantum well will not occur as close to the origin as shown in Fig. 1, because of the presence of nonradiative losses.

In summary, this paper describes an analytical approach to investigating III-V nitride lasers. The approach, which is based on a microscopic theory where carrier-carrier collisions are treated at the level of quantum kinetic theory, requires as input only the bulk material parameters. This leads to an improvement in predictive capability over the conventional relaxation rate gain models, because the dephasing rate is not a free parameter. When applied to investigate the laser threshold properties, our analysis shows a strong dependence of the laser threshold current density on the quantum well width, due partly to the spatial displacement of the carriers by the piezoelectric effect.

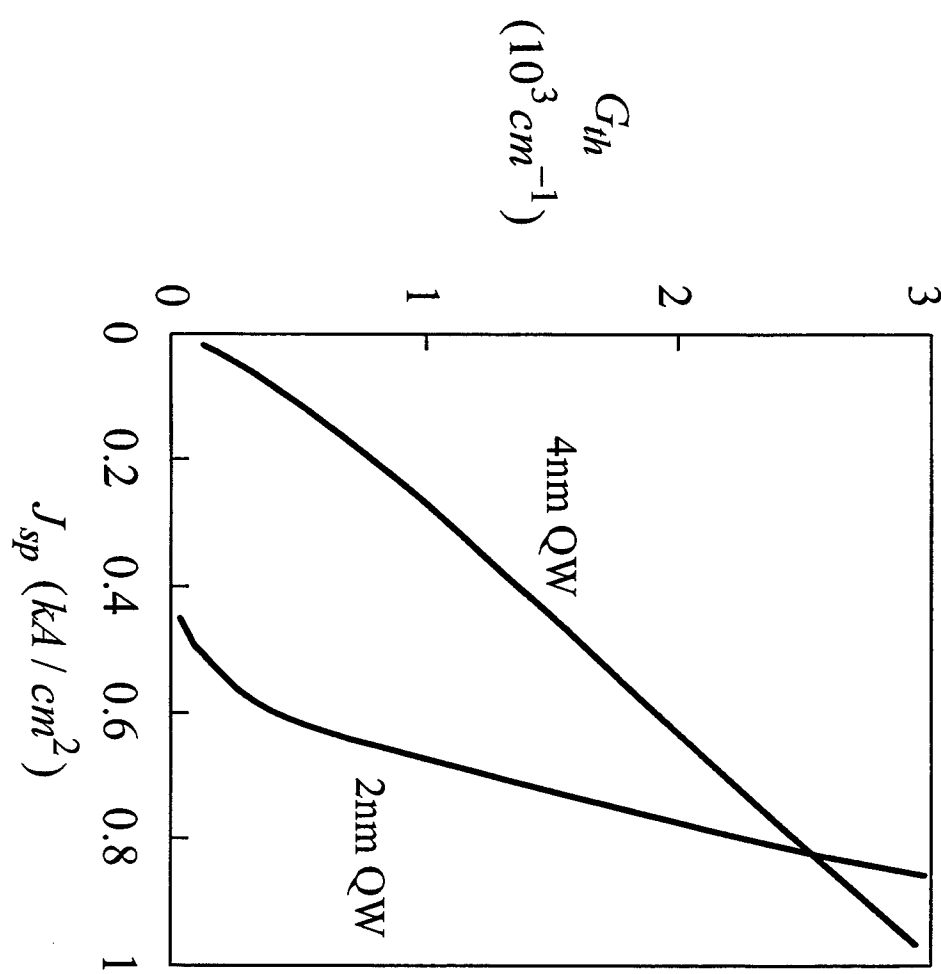
This work was supported in part by the U. S. Department of Energy under contract No. DE-AC04-94AL85000.

### References

1. S. Nakamura and G. Fasol, *The Blue Laser Diode* (Springer, Berlin, 1997).
2. W. W. Chow, A.F. Wright, A. Girndt, F. Jahnke and S. W. Koch, *Appl. Phys. Lett.* **71**, 2608 (1997).
3. W. W. Chow and S. W. Koch, *Semiconductor-Laser Fundamentals: Physics of the Gain Materials* (Springer, Berlin, 1999).
4. S. L. Chuang and C. S. Chang, *Phys. Rev. B* **54**, 2491 (1996).
5. C. H. Henry, R. A. Logan and F. R. Merritt, *J. Appl. Phys.* **51**, 3042 (1980).

### Figure Caption

Fig. 1. Calculated TE threshold gain vs. spontaneous emission current for 2nm and 4nm  $\text{In}_{0.2}\text{Ga}_{0.8}\text{N-GaN}$  quantum wells at T=300K.



## Piezoelectric and Spontaneous Polarization Effects in Nitride Heterostructure Optoelectronics

Hongtao Jiang, Yifei Zhang and Jasprit Singh  
 Department of Electrical Engineering and Computer Science  
 University of Michigan, Ann Arbor, MI 48109-2122

### 1. INTRODUCTION

Materials in the III-V nitride family (InN, GaN and AlN) have physical properties that are very attractive for short wavelength light emission and for high power/high temperature electronics. Alloys and heterostructures based on these materials are therefore being studied with great interest. In addition to providing semiconductors with large bandgaps the nitrides have two very interesting features: (i) there is a spontaneous polarization present in the structures as a result of the cation and anion positions in the lattice [1]; (ii) in heterostructures with strain (resulting from epitaxy) the piezoelectric effects are so large that effective built-in fields of  $\sim 10^6$  V/cm can be produced near the interfaces [2]. These two features are critical to understanding the physical properties of nitride heterostructures. Such an understanding can be exploited to design superior devices for electronic and optoelectronic applications.

### 2. SPONTANEOUS POLARIZATION AND PIEZOELECTRIC EFFECTS

A number of material systems have spontaneous polarization effects arising from an imbalance of the cation and anion charges. One of the most important material systems which have a large spontaneous polarization are the perovskites like barium titanate (spontaneous polarization  $26 \times 10^{-6}$  C/cm<sup>2</sup>) and lithium niobate (spontaneous polarization  $300 \times 10^{-6}$  C/cm<sup>2</sup>). In the nitride system the spontaneous polarization values are not as high but are significant enough to cause important effects in the band profiles of nitride heterostructures. The values of the spontaneous polarization are

$$\text{InN} : P_{sp} = -3.2 \times 10^{-6} \text{ C/cm}^2$$

$$\text{GaN} : P_{sp} = -2.9 \times 10^{-6} \text{ C/cm}^2$$

$$\text{AlN} : P_{sp} = -8.1 \times 10^{-6} \text{ C/cm}^2$$

In addition to the spontaneous polarization, when a system is under strain, the relative positions of the cation and anion atoms in the unit cell can change. This can result in addition polarization effects in the system. In heterostructure growth strain can be incorporated as a result of pseudomorphic growth of a thin overlayer on a substrate. In the nitride system there are considerable differences in the lattice constants of individual materials which can be exploited to tailor

the strain values in a heterostructure. The lattice constant values  $a$  and  $c$  for InN, GaN and AlN are

$$\begin{aligned} \text{InN : } & a = 3.54 \text{ \AA}; c = 5.70 \text{ \AA} \\ \text{GaN : } & a = 3.189 \text{ \AA}; c = 5.185 \text{ \AA} \\ \text{AlN : } & a = 3.11 \text{ \AA}; c = 4.98 \text{ \AA} \end{aligned}$$

The two effects described above become important when heterostructures are grown. In the case of spontaneous polarization the presence of a heterostructure between materials with different spontaneous polarization values causes a net charge at the interface which causes built-in electric fields in the structure. Similarly in case the lattice constants of the components of the heterostructure are different, the resulting strain present (assuming minimal dislocation generation) causes charges at the interfaces due to the piezoelectric effect.

The magnitude and direction of the electric fields associated with spontaneous polarization and piezoelectric effect depend on the substrate, the growth orientation and the nature of the surface (cation terminated or anion terminated). For the results given here we will discuss the most common growth conditions employed for the nitride systems where growth is on sapphire and is along the (0001) direction with Ga terminated surface. The effective substrate is defined by the a thick overlayer that is grown on the starting substrate (sapphire). Once dislocations are generated the thick overlayer forms its own lattice and acts as a substrate for the next layers as long as the growth is coherent i.e overlayer thickness is small enough to generate no dislocations. The overlayer now grows with a lattice structure which fits the in-plane lattice of the substrate and has an out of plane lattice constant defined by total energy minimization. Thus a compressive strain in the plane of growth causes a tensile strain out of plane.

Consider for example a case where the effective substrate is GaN and an  $\text{Al}_x\text{Ga}_{1-x}\text{N}$  overlayer is grown coherently. The polarization is found to have the value

$$\begin{aligned} P(x) &= P_{pz} + P_{sp} \\ &= -5.2 \times 10^{-6}x \text{ C/cm}^2 - 5.2 \times 10^{-6}x \text{ C/cm}^2 \end{aligned} \quad (1)$$

We see that in this system the effects arising from piezoelectric effect and spontaneous polarization mismatch are equal. Note that the two effects can have opposite directions as well depending on the surface termination conditions and the lattice mismatch between the overlayer and the effective substrate. The electric field associated with the polarization given above is

$$F(x) = -13.8x \text{ MV/cm} \quad (2)$$

We see that the built-in field and sheet charge values are very large. It is easy to produce fields around  $10^6 \text{ V/cm}$  and charge density around  $10^{13} \text{ cm}^{-2}$ .

For the heterostructure  $\text{In}_x\text{Ga}_{1-x}\text{N}$  grown on a GaN effective substrate the polarization charge density and field values are

$$\begin{aligned} P(x) &= 17 \times 10^{-6}x \text{ C/cm}^2 - 0.3 \times 10^{-6}x \text{ C/cm}^2 \\ F(x) &= 12.5x \text{ MV/cm} \end{aligned} \quad (3)$$

In this system the spontaneous polarization effect is negligible. However, the piezoelectric effect is very strong.

### 3. APPLICATIONS

The ability to introduce strong electric fields at interfaces and to create mobile charge at interfaces *without doping* can be exploited in essentially every kind of electronic and optoelectronic device. In heterostructure field effect transistors (HFETs) very high sheet charge densities of 2-dimensional mobile carriers can be created by exploiting spontaneous polarization and piezoelectric effects. From Eqn. 1 we can see that sheet charge densities can exceed  $10^{13} \text{ cm}^{-2}$  for AlGaN/GaN HFETs when the barrier Al composition exceeds 0.2. Such high sheet charge densities are useful not only for high currents and high transconductance but in any part of the device where traditionally one needs dopants. These regions include contacts. Also since the position and magnitude of the polarization charge is determined by the interface strain and basic material properties, the usual statistical fluctuations associated with dopants will be absent.

Another implication of the strong built-in fields one can get in heterostructures is enhancement in Quantum Confined Stark Effect (QCSE). This effect can be exploited for designing both electro-absorption and electro-optic modulators. At low electric fields this effect is quadratic in applied field but at high field it becomes linear. The presence of a high built-in field in structures like InGaN/GaN can therefore enhance modulator performance without the need to apply large external bias values. The built-in fields can be easily tailored by altering the strain values through compositional control. This can be exploited to selectively inject or extract charges in devices such as lasers and detectors.

### ACKNOWLEDGEMENTS

Discussions with Umesh Mishra are gratefully acknowledged. This work has been supported by a grant from the US Office of Naval Research.

### REFERENCES

1. F. Bernardini, V. Fiorentini and D. Vanderbilt, *Phy. Rev. B* **56**, R10024 (1997).
2. W. Q. Chen and S. K. Hark, *J. Appl. Phys.* **77**, 5747, (1995).

## Analysis of excitons in gallium nitride-based quantum wells under valence band mixing, strain and piezoelectric field

C. Bulutay, N. Dagli\*, and A. Imamoğlu

Department of Electrical and Computer Engineering, University of California, Santa Barbara, CA 93106.

\*phone: (805) 893 4847, fax: (805) 893 3262, e-mail: dagli@ece.ucsb.edu

The binding energy of excitons in bulk GaN is about 26 meV [1], which is larger than in GaAs by more than six times. In principle the binding energy of excitons in quantum wells (QW's) can be enhanced further up to four times. Note that even the bulk excitons in GaN can survive at room temperature. Hence, excitons in GaN-based QW's are very attractive for linear and nonlinear optics applications. As a step in this direction, here we present a theoretical analysis of excitons in GaN-Al<sub>x</sub>Ga<sub>1-x</sub>N-based QW's.

For the optically generated excitons, in a QW with the growth direction chosen along the z-axis, the exciton envelope function is a vector  $\bar{g}(\rho; z_e, z_h)$  having *A*, *B* and *C*-like hole components due to significant coupling in the valence bands [2];  $\rho = \rho_e - \rho_h$  is the relative coordinate in the QW plane, and the subscripts *e* and *h* discriminate the electron and hole coordinates, respectively. The Hamiltonian governing the exciton eigenstates, under strain and the associated piezoelectric field, is of the form

$$\begin{aligned} & [E_c(-i\nabla_e) + U_{pz}(z_e)] \bar{g}(\rho; z_e, z_h) - [\bar{\bar{H}}_v(-i\nabla_h) - U_{pz}(z_h) \bar{\bar{I}}] \bar{g}(\rho; z_e, z_h) \\ & + U_C(|\mathbf{r}_e - \mathbf{r}_h|) \bar{g}(\rho; z_e, z_h) = E_x \bar{g}(\rho; z_e, z_h), \end{aligned} \quad (1)$$

where  $E_c(-i\nabla_e)$  is the kinetic energy term for the electrons which also contains the conduction band edge discontinuity forming the QW,  $\bar{\bar{H}}_v(-i\nabla_h)$  is the Rashba-Sheka-Pikus matrix for the valence band holes [2,3] that also contains the valence band edge discontinuity,  $U_C(\mathbf{r}) = -e^2/4\pi\varepsilon_0\varepsilon_{avg}|\mathbf{r}|$  is the attractive Coulomb interaction between the electron and the hole, responsible for the formation of an exciton, with  $\varepsilon_{avg}$  and  $\varepsilon_0$  being the average background dielectric constant of the active region and the free space permittivity, respectively. For a wurtzite material grown along the (0001) direction, the strain-induced piezoelectric field is entirely longitudinal (i.e., along the z-direction) [4]. If the base barrier layer is thick enough, then it attains its equilibrium lattice constant. Therefore, under pseudomorphic growth conditions, strain and the corresponding piezoelectric field can be assumed to be present only in the well region; the corresponding potential energy is represented by  $U_{pz}$  in the Hamiltonian. Furthermore, the well region is considered to be free of carriers, without causing any screening effects.

We apply the following decoupling approximation for the transverse and perpendicular functional dependences

$$\bar{g}(\rho; z_e, z_h) = \bar{\Phi}(\rho) \bar{s}(z_e, z_h), \quad (2)$$

however, we do not extend this separable form to the vector-valued-function  $\bar{s}(\cdot)$  for the  $z_e$  and  $z_h$  dependences. For the in-plane behavior, a simple variational form is employed

$$\Phi_{ij}(\rho) = \frac{1}{\lambda_i} \sqrt{\frac{2}{\pi}} e^{-\rho/\lambda_i} \delta_{ij}, \quad (3)$$

with  $\lambda_i$ 's being the variational parameters determined eventually by minimizing the exciton energy. For the differential operators in the Hamiltonian due to kinetic energy terms, we resort to the Finite Element method [5]. The technical details of our approach and the material parameters used are given in Ref. [6].

The excitonic absorption spectra under the assumption of a Lorentzian broadening with a linewidth  $\Gamma_x$  is given by [7]

$$\alpha(E) = \frac{\pi e^2 \hbar}{c n_r \epsilon_0 m_0 L_z} \sum_x f_x \frac{\Gamma_x}{\pi [(E - E_x)^2 + \Gamma_x^2]}, \quad (4)$$

where  $E$  is the energy of the photons,  $c$  is the speed of light,  $n_r$  is the average index of refraction of the QW,  $f_x$  is the oscillator strength per unit area [6]. In the absorption expression, for  $L_z$ , the physical width ( $W$ ) of the QW is commonly used [7,8]. However, in general,  $W$  does not correlate with the actual spread of the excitonic envelope function, especially for the narrow QW's and also under high electric fields. In this work, for  $L_z$ , we use the spread of the exciton wavefunction centered around the mean values along the  $z_e$  and  $z_h$  axes as:

$$L_{z,x} = 2 \sum_\nu \int_{-\infty}^{+\infty} dz_e \int_{-\infty}^{+\infty} dz_h \sqrt{(z_e - \eta_{ex})^2 + (z_h - \eta_{hx})^2} |s_{\nu x}(z_e, z_h)|^2, \quad (5)$$

where  $s_{\nu x}(z_e, z_h)$  is defined in (2) and  $\eta_{ex}$  and  $\eta_{hx}$  are the mean values of the excitonic wavefunction along the  $z_e$  and  $z_h$  axes, which are in general nonzero in the presence of electric field.

In Fig. 1(a), the effect of the piezoelectric field on the binding energy is shown for the lowest four exciton levels  $A1$ ,  $B1$ ,  $A2$  and  $B2$ . For larger well widths, the effect of the piezoelectric field is more pronounced, reducing the overlap between the electron and hole wavefunctions. Accordingly, after certain well widths, the second subband hole wavefunctions,  $A2$  and  $B2$ , have larger overlap with the electron wavefunctions, hence have larger binding energies than the  $A1$  and  $B1$  excitons. Another implication of Fig. 1(a) is that, ideally excitons will not be ionized at room temperature for well widths less than about 60 Å. The corresponding oscillator strengths of these four exciton levels for an *in-plane averaged* TE (to growth axis) light are shown in Fig. 1(b). Observe that the oscillator strength of  $A2$  and  $B2$  excitons peak around  $W = 45$  Å. This is the quantum-confined Franz-Keldysh effect [9], responsible for converting forbidden transitions (here excitons levels) to allowed ones. As, well width is further increased, both lobes of the hole wavefunction are separated from the electron wavefunction, thereby decreasing the oscillator strength.

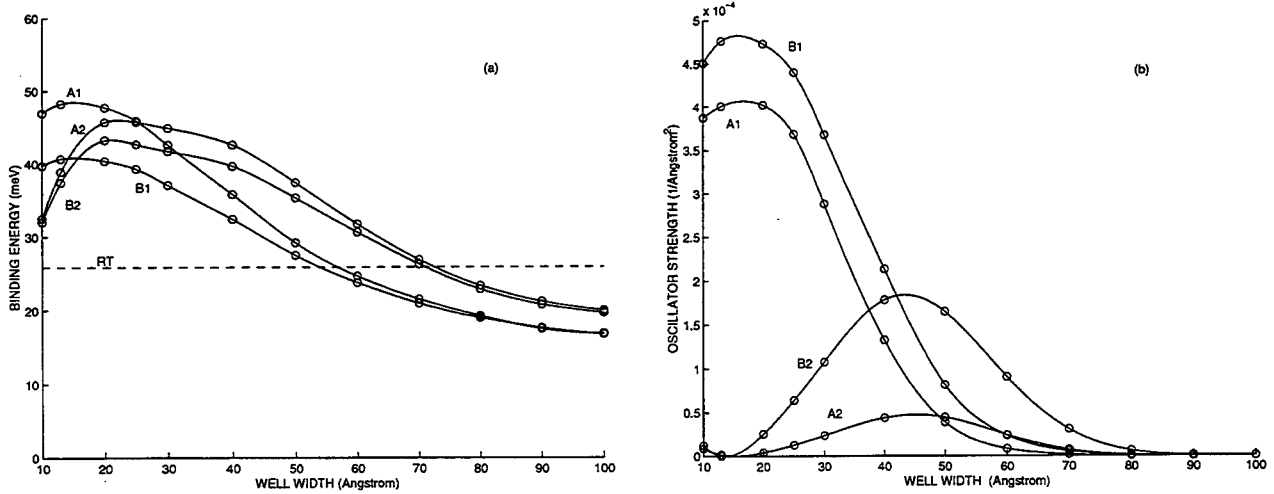


Figure 1: The binding energy (a) and the oscillator strength (b) results for a GaN-Al<sub>0.15</sub>Ga<sub>0.85</sub>N QW under piezoelectric field. The dashed line in part (a) indicates the thermal energy at room temperature.

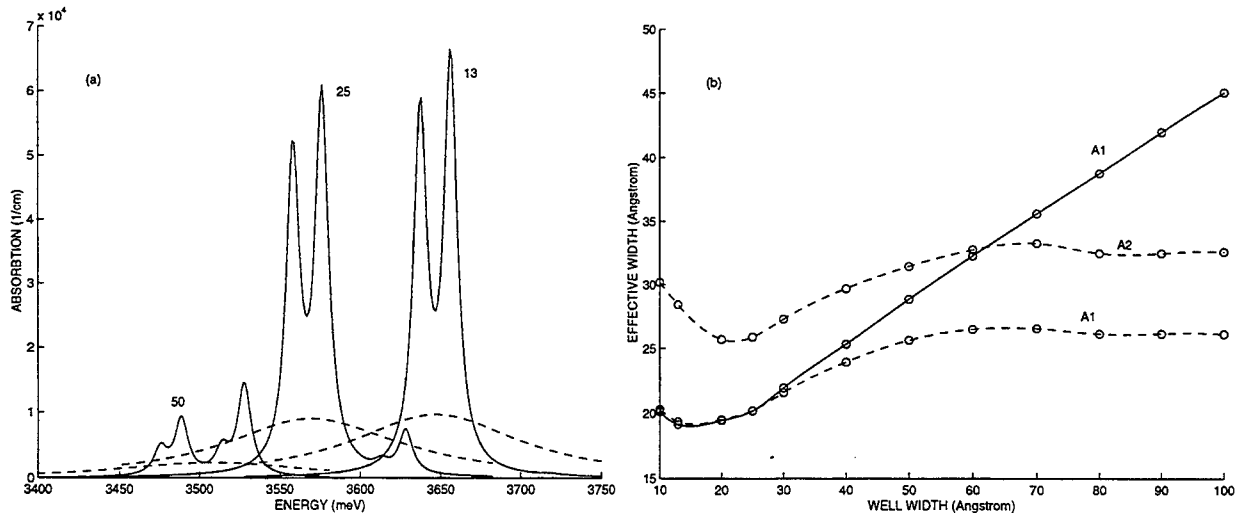


Figure 2: (a) Absorption spectra associated with the excitons considered in Fig. 1; three well width values are given as indicated. Two values are used for the broadening parameter; 5 meV (solid) and 60 meV (dashed). (b) Effective width of the exciton envelope wavefunction with (dashed) and without (solid) the piezoelectric field.

Fig. 2(a) displays the absorption profile of a few low-lying excitons for (in-plane averaged) TE light; two different linewidths are used,  $\Gamma_x = 5$  and 60 meV, representing small and large broadenings, respectively. In Fig. 2(b) we plot the effective width of the QW (using Eq. (5)), corresponding to  $A$  excitons both with and without the piezoelectric field, with respect to the physical width ( $W$ ) of the QW. For a QW of 10 Å width, the effective mass approximation should be presumably very crude, however, the actual exciton wavefunction is barely confined for such narrow QW's as seen by the effective width reaching twice the value of the physical width. For QW's wider than 30 Å, the effective width attains a single slope in the absence of the piezoelectric field, and its value is lower than the physical width ( $W$ ), as the wavefunction is concentrated in the center of the well. In the presence of the piezoelectric field, for well widths larger than 60 Å, the effective width saturates; this indicates that electron and hole are trapped in the triangular potentials on either side of the QW, and further increase of the well width does not enlarge the confinement width. We anticipate that our results will be useful for the up-coming room temperature "absorption" spectra dominated by  $1s$  excitons. For low temperature and high quality samples, where fine structure of excitons can be resolved, the theoretical analysis should also be refined by relaxing equation (3).

## References

- [1] S. Chichibu, T. Azuhata, T. Sota, and S. Nakamura, J. Appl. Phys. vol. 79, p. 2784, 1996.
- [2] Yu. M. Sirenko, J. B. Jeon, B. C. Lee, K. W. Kim, M. A. Littlejohn, M. A. Stroscio, and G. J. Iafrate, Phys. Rev. B, vol. 55, pp. 4360, 1997.
- [3] S. L. Chuang and C. S. Chang, Phys. Rev. B, vol. 54, pp. 2491, 1996.
- [4] A. Bykhovski, B. Gelmont, and M. Shur, J. Appl. Phys., vol. 6734, 1993.
- [5] J. C. Yi and N. Dagli, IEEE J. Quantum Electron., vol. 31, pp. 208, 1995.
- [6] C. Bulutay, N. Dagli, and A. Imamoğlu, to be published in IEEE J. Quantum Electron., 1999.
- [7] C. Y.-P. Chao and S. L. Chuang, Phys. Rev. B, vol. 48, pp. 8210, 1993.
- [8] Y. Kan, H. Nagai, M. Yamanishi, and I. Suemune, IEEE J. Quantum Electron., vol. 23, pp. 2167, 1987.
- [9] D. A. B. Miller, D. S. Chemla, and S. Schmitt-Rink, Phys. Rev. B, vol. 33, pp. 6976, 1986.

**Integrated Photonics Research**

# **Active Devices**

**Tuesday, July 20, 1999**

**Ramu V. Ramaswamy, University of Florida, USA**

Presider

**RTuG**

**1:30pm–3:00pm**

Sierra Madre North

# Bi-directional optical module based on a GoS hybrid integration for access network applications

Maurizio Lenzi, Massimo Magliocco, Lucio Cibinetto

Italtel, Photonic Unit – 20019 Castelletto di Settimo Milanese, ITALY

[maurizio.lenzi@italtel.it](mailto:maurizio.lenzi@italtel.it), [massimo.magliocco@italtel.it](mailto:massimo.magliocco@italtel.it), [lucio.cibinetto@italtel.it](mailto:lucio.cibinetto@italtel.it)

## Introduction

Optical transceiver modules, able to transmit and receive data via a single fiber [i], are key components for asynchronous-transfer-mode passive optical network systems (ATM-PON). High volume, low cost devices are required, thus the development must be based on an inexpensive and well known technology; one of the most promising is the «Glass on Silicon» [ii] that allows hybrid integration of active and passive devices.

We developed a new device, including both active (transmitter and receiver) and passive (WDM) optical functionality, representing Italtel's state of the art Glass on Silicon technology (GOS).

## Module description

The module is composed of 3 blocks (fig. 1):

- B1) a transmitter unit (Laser Pill) including a MQW FP laser
- B2) a planar lightwave circuit (PLC) including: an InGaAs PIN detector (RX), a monitor PIN diode (M) and a WDM realised in GOS technology.
- B3) a V-block to allow SM fiber to device interface

The three parts are coupled by mean of a new active alignment process developed in Italtel, able to achieve low insertion loss. The device is a compact, 24 pin, Dual in Line (DIL) hermetic package. The outer dimensions of the ceramic package are: 40x10x12 mm.

### Laser Pill description

The Laser Pill is the transmitter side of the device.

A MQW 1.3  $\mu\text{m}$  FP laser chip is die attached on a silicon submount, where a Chromium resistor is integrated. The metallized fibre is aligned and soldered by mean of Tin-Gold preform, melted by driving current through the resistor. The efficiency of the active laser-fibre coupling is about 75%. The high coupling between the laser and the fiber is achieved by chemically etching a microlens on the tip of the fiber [iii].

A silicon micromachined lid, including a groove for the chip and a V-groove to guide the fibre, is placed on the top of the laser submount and attached by mean of heat curing epoxy adhesive. The submount is larger than the lid in order to leave the contact pad available for wire bonding. As a final step, the fiber is cleaved and the whole device is angle polished.

### PLC description

As already mentioned, the PLC is a Glass on Silicon bench including the WDM structure and two bottom illuminated PINs for receiving (RX) and monitor (M) functions. The PLC dimensions are 25x4x0.5 mm. In order to reduce reflections, both sides of the PLC are angle polished.

The WDM structure is based on a direction coupler; the tailored design allows the device to work both as single wavelength, TX 1.3- RX 1.3, and dual wavelength, TX 1.3- RX 1.5 (1.3 and 1.5 are wavelengths in  $\mu\text{m}$ ). This functionality has been achieved by the design of a coupler that works:

for  $\Lambda_a=1.3 \mu\text{m}$  as a 50/50 splitter

for  $\Lambda_b=1.5 \mu\text{m}$  as a WDM (that is the 1.5  $\mu\text{m}$  light, coming from the optical fibre, is almost completely coupled to the RX PIN).

Fig.2 is a drawing of the spectral response of the coupler (ports assignments are defined in fig. 1). The simulation is based on measurements made on test structures. Measured splitting ratio of the WDM @1.3

$\mu\text{m}$  is 45/55, that is 45% of the light coupled inside the waveguide goes to the receiver (RX or Monitor), and 55% goes towards the output fiber; this data being in good agreement with the design.

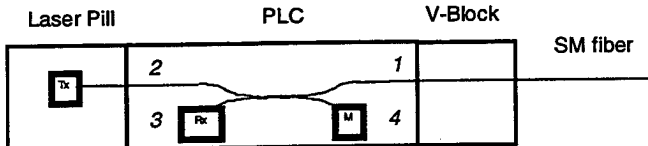


Fig.1 - Schematic drawing of the device

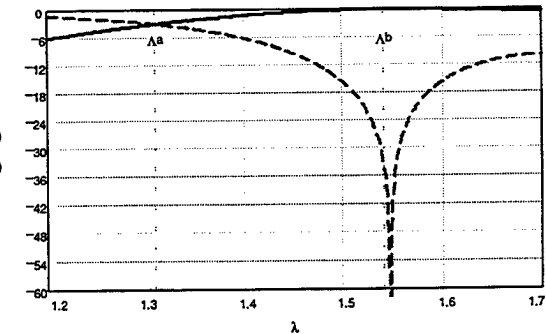


Fig.2 - coupler spectral response (simulation)  $P_{nm}$ = transfer function of ports  $nm$

#### Integrated Mirror

The coupling between the optical waveguide and the bottom illuminated PINs is obtained by mean of a mirror integrated on the PLC and a self alignment technique for precise PIN attach over the mirror.

The mirror is realised by means of a special wet etching process able to make a 52° surface in silica layers. The surface is then gold plated to achieve good reflectivity.

The measured coupling efficiency of the mirror is better than 75%.

#### Module assembling

The three blocks, formerly described, are simultaneously aligned and fixed by mean of optical epoxy adhesive. Since the epoxy must be cured at about 110°C, the optical alignment is done while working at this temperature. The assembling bench is composed of three parts: a heated central fixed fixture to hold down the PLC, a passive fixture to hold down the V-block and an active fixture to hold down and bias the Laser Pill, both mounted on two 6 axis piezo-controlled stages.

The three parts are actively aligned using the output optical power from the Laser Pill at a given bias current as reference. When coupling efficiency is maximised, both optical interfaces are glued together with optical epoxy. The complete pigtailed device is then removed from the optical bench and epoxied to the package; and finally the optical fiber is epoxied inside the ferrule (fig. 3). The package's lid is hermetically sealed by mean of a roll welding process.

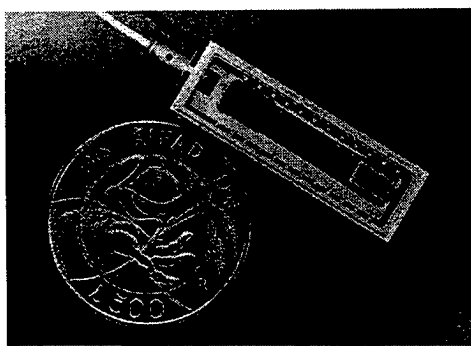


Fig. 3 – Packaged device

#### Performance of Transceiver Module

Measured parameters at room temperature are listed below.

The high output power (fig. 4) and good receiver responsivity are main characteristics of the device.

The Optical Crosstalk value (CRT) is about -30 dB for the 1.3-1.3 device and about -35 dB for the 1.3 - 1.5 device; these CRT values are merely due to internal reflections, related both to PLC to fiber coupling and to the small PLC dimensions. CRT could be reduced using a silicon lid for the PIN and introducing a leaky ray stops in the design of the PLC. Moreover the CRT value of the 1.3-1.5 device can be lowered to less than -50 dB using, as receiving PIN (RX), a commercially available «pass band photodiode».

Parameters	measurement conditions	min/max value		Units
<i>Threshold Current</i>		8.5	9.5	mA
<i>Output Optical power</i>	@ I=50 mA	3.0	4.0	MW
<i>Monitor Responsivity</i>	@ I=50 mA	0.5	0.6	A/W
<i>Device Responsivity</i>	@ $\lambda=1.3 \mu\text{m}$	0.2	0.3	A/W
	@ $\lambda=1.5 \mu\text{m}$	0.5	0.6	A/W
<i>Optical Crosstalk</i>	@ P=0.2 mW, $\lambda=1.3 \mu\text{m}$	-30	-35	DB
	@ P=0.2 mW, $\lambda=1.5 \mu\text{m}$	-35	-40	DB

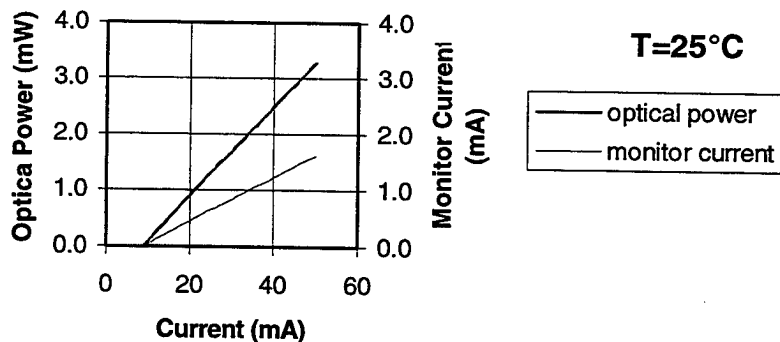


Fig. 4 -  $P(I)$  characteristic of device #22 @ $T=25^\circ\text{C}$

## Conclusions

We have developed an optical transceiver module able to work as single wavelength and dual wavelength. The reported results demonstrate the quality of the design and the mature state of Italtel's Glass on Silicon technology.

## Acknowledgement

The authors would like to thank the technicians working in Italtel's wafer fab and assembling groups.

## References

- [i] T. Miki, "Fiber-optic subscriber networks and system development", IEICE Trans, vol. E74, p 93-100, 1991
- [ii] Y.P. Lee, C.H. Henry, «Silica-based optical integrated circuit», IEE proceeding optoelectronic vol. 143, n°5, October 1996
- [iii] G. Eisenstein, D. Vitello, «Chemically etched conical microlens for coupling single-mode lasers into single-mode fibers», Appl. Optics, vol. 21, No 19, p. 3470, 1 October 1982

## Second harmonic generation in 10 $\mu\text{m}$ -thick single-crystal z-cut LiNbO<sub>3</sub> films obtained by epitaxial lift-off

A.M. Radojevic, M. Levy and R.M. Osgood, Jr.

*Microelectronics Sciences Laboratories, Columbia University  
530W 120<sup>th</sup> Street, Rm. 1001, MC 8903, New York, NY 10027*

*Tel: (212) 854-8449, Fax: (212) 860-6182, Email: tony@cumsl.ctr.columbia.edu*

**A. Kumar and H. Bakhru**

*Department of Physics, State University of New York at Albany  
1400 Washington Avenue, Albany, NY 12222*

The development of the technique of crystal ion slicing (CIS)<sup>1</sup> has made it possible to obtain high-quality single-crystal films of LiNbO<sub>3</sub> for heterogeneous integration of planar optical systems on non-LiNbO<sub>3</sub> platforms (e.g. GaAs, YIG). The technique has been applied to different LiNbO<sub>3</sub> crystal orientations<sup>2</sup> as well as other ferroelectric materials such as PZN<sup>3</sup>. The technique employs the formation and subsequent preferential etching of a buried-damage sacrificial layer obtained by energetic He<sup>+</sup> implantation. The linear optical properties of these films have been tested and found comparable to bulk systems. Here we report on second harmonic (SH) generation in CIS films bonded onto a glass substrate. The experiment demonstrates that CIS films are suitable for heterogeneous integration of nonlinear optical elements.

Several features contribute to phase matching of nonlinear optical responses in CIS films. Ion implantation with light ions has been used to fabricate optical waveguides in various nonlinear optical materials in the bulk form.<sup>4</sup> The implantation is known to induce small reproducible alterations in the refractive index profile in the implanted layer.<sup>5</sup> The change is positive for the extraordinary index of refraction (~1%) and negative for the ordinary (<-0.5%).<sup>5</sup> Although the profile is depth-dependent, it can be approximated by a plateau over most of the implanted region and a sharp minimum at the end of the ion range. Recently, the  $d_{33}$  nonlinear optical coefficient of such waveguides has been probed in implanted Y-cut LiNbO<sub>3</sub> via surface harmonic generation and found commensurate with that of the virgin bulk.<sup>6</sup> However, the birefringence of bulk LiNbO<sub>3</sub> does not allow for SHG phase matching for propagation normal to the optic axis at 1.55 $\mu\text{m}$  ( $n_o(\omega) \sim 2.21$ ,  $n_e(2\omega) \sim 2.18$ , 25°C). Upon ion implantation, the offset between  $n_o(\omega)$  and  $n_e(2\omega)$  is effectively reduced and combined with waveguide dispersion in CIS z-cut LiNbO<sub>3</sub> films allows for the temperature-controlled effective-index matching of the fundamental (TE) and SH frequency (TM). The corresponding effective indices attain the following form:

$$\begin{aligned} n_{o,m}^{\text{eff}}(\omega, T) &= n_o^B(\omega, T) + \Delta n'_o(\omega, T) + \Delta n_{o,m}^W(\omega) \\ n_{e,l}^{\text{eff}}(2\omega, T) &= n_e^B(2\omega, T) + \Delta n'_e(2\omega, T) + \Delta n_{e,l}^W(2\omega) \end{aligned}$$

where  $m$  and  $l$  are the mode numbers,  $n_o^B$  and  $n_e^B$  are the bulk index values, while  $(\Delta n'_o, \Delta n'_e)$  and  $(\Delta n_{o,m}^W, \Delta n_{e,l}^W)$  stand for the ion- and waveguide dispersion-induced refractive index changes, respectively. By tuning the temperature, the propagation constants of various guided TE <sub>$m$</sub> ( $o, \omega$ ) and TM <sub>$l$</sub> ( $e, 2\omega$ ) modes can be matched so that at phase-matching  $n_{o,m}^{\text{eff}}(\omega, T_m) = n_{e,l}^{\text{eff}}(2\omega, T_m)$ , where  $T_m$  is the phase-matching temperature. Our calculations show that for 8-10 $\mu\text{m}$  CIS films obtained from a stoichiometric melt, phase-matching is satisfied for the TE <sub>$o$</sub> ( $\omega$ ) to TM <sub>$o$</sub> ( $2\omega$ ) mode conversion at temperatures ~210°C. In the analysis we assumed that ion-induced index alterations exhibit a bulk temperature dependence scaled down by the relative ion-created change as indicated above. In addition, no walk-off effect is expected in

the non-confined direction since the waves propagate perpendicular to the optic axis. Therefore, a significant power transfer from the fundamental to the second harmonic is expected.

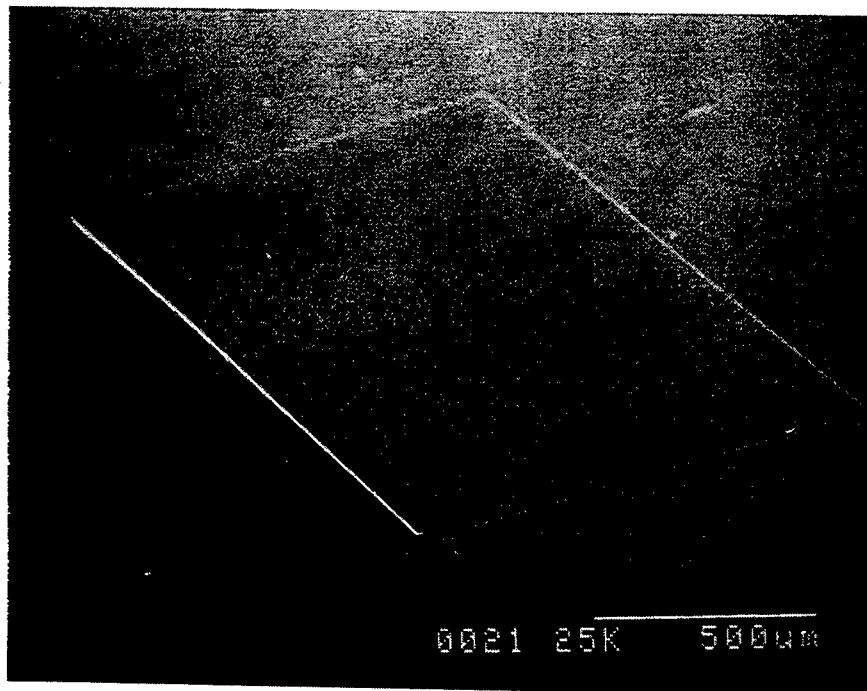


Fig. 1 Scanning electron micrograph of a Crystal Ion Sliced (CIS)  $z$ -cut  $\text{LiNbO}_3$  on a glass substrate

Our experiments use a  $z$ -cut bulk  $\text{LiNbO}_3$  crystal (stoichiometric melt) obtained from a  $z$ -poled single-crystal Czochralski boule. The samples are cut and polished normal to the  $z$ -axis and implanted with  $3.8\text{MeV He}^+$  ( $5 \times 10^{16} \text{ cm}^{-2}$  dosage). For this ion energy, a TRIM96-based calculation predicts an ion range of  $\sim 10\mu\text{m}$ . After facet-polishing, the samples are rapid thermally annealed at  $400^\circ\text{C}$  and etched in hydrofluoric acid.<sup>1,2</sup> Rapid thermal annealing restores the bulk nonlinear properties,<sup>4</sup> but does not (completely) remove the ion implantation-induced refractive index change. High-quality single-crystal CIS  $\text{LiNbO}_3$  films are obtained and bonded onto a glass substrate. The samples had  $\lesssim 10\mu\text{m}$  thickness and lengths ranging from 500 to  $1500\mu\text{m}$ . Figure 1 shows a scanning electron micrograph of one such film ( $0.8\text{mm} \times 1.3\text{mm} \times 10\mu\text{m}$ ) bonded onto a glass substrate.

To probe the nonlinear response of these waveguides, a mode-locked laser source at  $1.55\mu\text{m}$  is used (50mW, 120fs, 40MHz). The input polarization is controlled with a fiber polarizer and the infrared light is end-fire coupled into the film from a single-mode fiber so that confinement is achieved along the optic axis while the beam remains laterally diffracted. The average laser power delivered to the slab front facet is  $\sim 25\text{mW}$ . The second harmonic response is tuned and optimized via resistive-heat temperature control (CIS waveguides are mounted onto a 10W resistor). The near-field output pattern is monitored with an IR digital camera, and the frequency doubled signal is measured with a photodetector. The optical setup is depicted in Figure 2.

The input IR signal propagates as an  $o$ -wave in the fundamental TE mode. The second harmonic is always TM-polarized while its modal structure is a strong function of temperature. At room temperature, the 775nm output is multimode and the average detected power level of  $< 3\mu\text{W}$  is obtained. As the temperature is raised, the mode pattern changes continuously so that at higher temperatures

( $>170^{\circ}\text{C}$ ) most light is generated in the fundamental and the first higher even mode, as predicted by the analysis. At the same time, the SH intensity passes through a sequence of minima and maxima indicating the changes in the coherence length ( $\sim \lambda/[n_{o,m}^{\text{eff}}(T,\omega) - n_{e,l}^{\text{eff}}(T,2\omega)]$ ). The highest signal level thus far measured is  $\sim 30\mu\text{W}$  for a  $\sim 1\text{mm}$ -long sample at  $T \sim 190^{\circ}\text{C}$ . The total measured loss in the  $z$ -cut CIS films at  $1.55\mu\text{m}$  and  $775\text{nm}$  is  $3\text{dB}$  and  $3.5\text{dB}$ , respectively. The estimated average frequency doubled power generated in the slab is on the order of  $\sim 40\mu\text{W}$ .

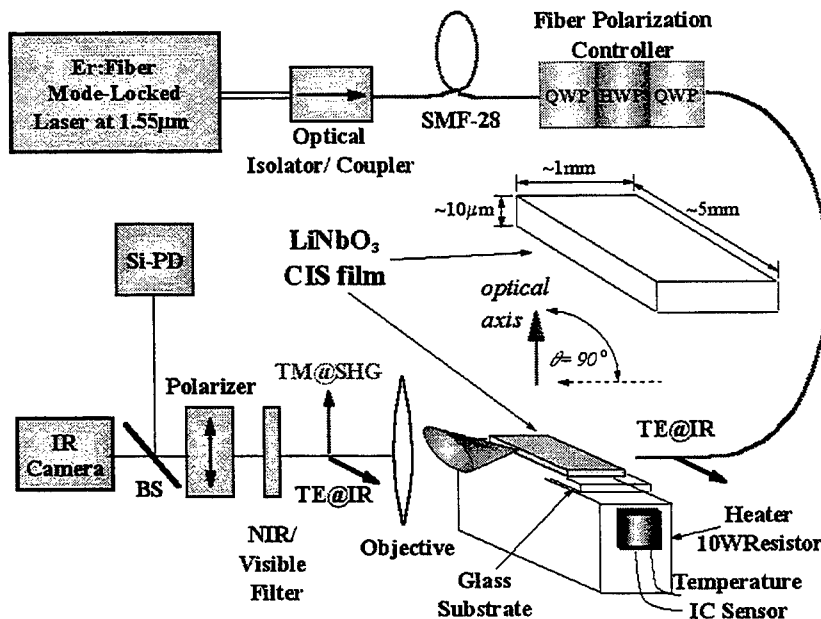


Fig. 2 Experimental setup

As a comparison, bulk samples of comparable lengths were cut from a  $\text{LiNbO}_3$  crystal *phase-matched* for room-temperature frequency doubling at  $1.55\mu\text{m}$  ( $\theta = 46.9^{\circ}$ ,  $\varphi = 30^{\circ}$ ) and tested in the same setup configuration. The measured SH power for these crystals was  $< 100\mu\text{W}$ . This result indicates that heterogeneous-substrate-compatible single-crystal  $\text{LiNbO}_3$  films obtained by crystal ion slicing preserve a strong optical nonlinearity of the bulk single crystal. The difference between the calculated and experimentally obtained results stems from the approximate nature of the profile used for phase matching temperature computation. Further experiments on second harmonic generation in the freestanding  $z$ -cut CIS  $\text{LiNbO}_3$  films are underway.

## References

- [1] M. Levy, R.M. Osgood, Jr., R. Liu, L.E. Cross, G.S. Cargill III, A. Kumar and H. Bakhru, *Appl. Phys. Lett.* **73**, 2293 (1998)
- [2] A.M. Radojevic, M. Levy, R.M. Osgood, Jr., A. Kumar and H. Bakhru, accepted for publication in *Appl. Phys. Lett.*
- [3] M. Levy and R.M.Osgood, Jr., to be published in *Appl. Phys. Lett.*
- [4] P.D. Townsend, P.J. Chandler, and L. Zhang, *Optical Effects of Ion Implantation* (Cambridge University Press, Cambridge, 1994)
- [5] F. Lu, M.Q. Meng, K.M. Wang, X.D. Liu and H.C. Chen, *Jpn. J. of Appl. Phys.* **36**, 4323 (1997)
- [6] J. Rams, J. Olivares, P.J. Chandler, and P.D. Townsend, *J. of Appl. Phys.* **84**, 5180 (1998)

# High-speed Er-doped LiNbO<sub>3</sub> waveguide lasers

H. SUCHE

Universität-GH Paderborn, Angewandte Physik, D-33098 Paderborn, Germany  
phone: +49-5251-602713, fax: +49-5251-603422, e-mail: h.suche@physik.uni-paderborn.de

## 1 Introduction

In the last few years Er-doped lasers in LiNbO<sub>3</sub> operating around 1.56 μm wavelength have attracted considerable attention. The combination of the amplifying properties of erbium with the excellent electrooptic, acoustooptic and nonlinear optical properties of LiNbO<sub>3</sub> has led to the development of a whole new family of laser devices of higher functionality [1].

Modelocked Ti:Er:LiNbO<sub>3</sub> waveguide lasers of high pulse repetition rate are attractive devices for high speed digital optical (RZ-type) data transmission in the 3rd telecommunication window. They can be actively modelocked using a monolithically integrated electrooptic phase- (or amplitude-) modulator as the modelocker inside the laser cavity [2]. By modulation synchronous with the fundamental [2] or with harmonics [3] of the axial mode frequency spacing of the laser cavity a comb of axial modes is phase locked leading to a train of short optical pulses in the time domain.

Harmonic modelocking in a long cavity allows to combine efficient pump absorption in the Er-doped waveguide with the generation of pulses of high repetition frequency. Moreover, pulses can be shortened in comparison with fundamental modelocking [4].

However, harmonically modelocked lasers usually emit more than one comb of axial modes (called supermode) causing high frequency noise [5]. In section 2, Ti:Er:LiNbO<sub>3</sub> waveguide lasers will be discussed which have been stabilized on a single supermode.

Er:LiNbO<sub>3</sub> is also a very attractive material for Q-switched waveguide lasers. Its long fluorescence lifetime is a prerequisite for a high energy storage capability and the incorporation of Er up to the solid solubility limit without fluorescence quenching [6] leads to an efficient power conversion from a diode pump to the Q-switched output. Such a laser emitting pulses of high peak power at wavelengths beyond 1.4 μm is a promising source, e. g. for laser RADAR applications in the eye-safe spectral range and as the pump for nonlinear optical frequency conversion into the mid infrared region.

In section 3 Q-switched waveguide lasers with an interferometric switch of high extinction ratio will be discussed.

Finally, section 4 will conclude the paper with an outlook for future activities.

## 2 Modelocked waveguide lasers

The basic structure of our FM-modelocked waveguide laser consists of an Er-diffusion doped, Ti-diffused waveguide Fabry Perot with a coplanar stripe (CPW) travelling wave electrode on top of the waveguide as the phase modulator [3] (FM-modelocker). Besides this basic structure additional components are required to achieve harmonic modelocking of high amplitude stability. They are discussed in the next subsection.

**Laser design:** Several methods for the stabilization of a single supermode have been reported for fibre lasers. E. g. intracavity filtering with a Fabry Perot has been successful [7]. Contrary to this high finesse transmission type filter we coupled the active laser cavity to a passive Fabry-Perot of low finesse operated as a reflection type filter. This concept has the potential for a monolithic integration. Depending on the free spectral range of the filter Fabry-Perot modelocking at different harmonic orders can be selected. Up to now 5th [9] and 10th harmonic [10] modelocking at about 5 and 10GHz pulse repetition frequency, respectively, have already been demonstrated using waveguide lasers on Z-cut LiNbO<sub>3</sub>. As an example, for 10th harmonic modelocking the reference cavity of about 10GHz free spectral range has been glued to the rear end of the laser cavity of about 1GHz free spectral range. The reflectances of the filter cavity of 75 and 30%, respectively, result in a finesse of about 4.3 which is sufficient for the stable selection of one supermode and the suppression of the others. Details of the fabrication of the laser, its Er-diffusion doping, Ti-diffused waveguide structure, SiO<sub>2</sub>-buffer layer, electro-plated Au-electrodes and dielectric cavity

mirrors are given in [10]. In addition to the CPW-modelocker electrodes 2 lumped electrodes at both ends of the active cavity have been provided for low frequency push-pull phase modulation. This step together with feedback controlled pumping [8] reduces the relative intensity noise (RIN) at the relaxation oscillation frequency during modelocking by about 40dB[9].

The laser has been pigtailed directly to the common branch of a fiberoptic wavelength division multiplexer (WDM) and finally packaged including temperature stabilization, optical isolation and two fibre optic power splitters to extract besides the main output two tap outputs (1% and 9%), one for spectral monitoring and another one for feedback controlled pumping.

**Single supermode operation and pulse properties:** For 10th harmonic modelocking 29 dBm of rf-power at 9.93 GHz has been fed to the modelocker. To monitor the supermode stabilization the output pulses have been detected using a fast photodiode and fed to an rf-spectrum analyzer. Simultaneous oscillation on more than one supermode results in strong electronic beat components (side modes) at frequencies which are integers of the axial mode spacing apart from the modelocking frequency.

The output of the coupled cavity laser has been compared to the output of the modelocked laser without reference cavity. The side mode suppression ratio (SMSR) has been drastically improved from -8 dB to about -55dB for the coupled cavities. The output of the laser has been investigated furthermore by measuring the autocorrelation and the optical spectrum with a resolution of 0.08 nm. At a drive frequency of 9.930 GHz the smallest pulse width of 4.4 ps has been measured. Together with the spectral width of 0.82 nm a time bandwidth product of 0.44 results - indicating that the Gaussian-shaped pulse is chirp-free.

Such a modelocked laser has been successfully used in 10Gbit/s soliton-type data transmission over highly dispersive standard single mode fibre at  $1.562\mu\text{m}$  wavelength [13]. In a back-to-back configuration the critical  $10^{-9}$  bit-error-ratio (BER) has been achieved with only -36.5dBm received optical power. Without any inline filtering and dispersion control this critical BER-figure could be maintained after up to 5 amplified fibre spans of 40km each.

Besides supermode stabilization the filter Fabry-Perot can serve as a repetition rate multiplicator [10]. If the modelocked laser is driven at 5GHz the Fabry-Perot filter of 10GHz free spectral range selects each 2nd harmonic of the generated Fourier spectrum leading to a spectrum with a mode spacing of 10 GHz. The filter suppresses the rf-component at about 5GHz by 28dB compared to the 10GHz-component.

### 3 Q-switched waveguide lasers

Efficient Q-switched lasers require an intracavity switch of high extinction ratio to prevent CW-prelasing. Waveguide lasers using a directional coupler [11] or coupler-fed interferometer [1] suffered from an insufficient extinction ratio of the Q-switch.

A considerable improvement has been achieved by using a Mach-Zehnder type switch [12] with polarization-insensitive Y-junction as discussed in the next subsection.

**Laser design:** The Ti:Er:LiNbO<sub>3</sub> waveguide laser utilizes a folded intracavity Mach-Zehnder (one Y-junction together with the rear broadband cavity mirror) as the Q-switch. Similar to the modelocked laser, the pump radiation is launched into the waveguide cavity via a fibre-optic WDM and the Q-switched laser emission is extracted in backward direction. The folded interferometer design minimizes the excess loss in the high Q-phase of the laser and allows double pass pumping even during the low Q-phase. The excess loss of the optimized Y-junction of about 0.15dB and the deviation from a symmetric power splitting of < 0.2dB lead to an estimated modulator extinction ratio better than -25dB. In this way a high inversion level of the Er<sup>3+</sup>-ions can be achieved during the low Q-phase without CW-prelasing.

Details of the Er-diffusion doping, the Ti-diffused waveguide structure, the electrode structure and the cavity design are given in ref. [12]. The most significant difference of the cavity compared to the modelocked lasers is the epoxy-free design of the pump/output coupler which can withstand peak power densities of the Q-switched pulses of several GW/cm<sup>2</sup>. A piezoelectrically driven air gap etalon formed by the endfaces of the pump input/signal output fiber (common branch of the WDM) and the polished Ti:Er:LiNbO<sub>3</sub>-waveguide endface allows to adjust the effective reflectance of this mirror in the range 0.03 < R < 0.3. Using this design a fully packaged and diode-pumped Q-switched laser has been realized and operated for several months

without problems.

**Laser performance:** With diode pumping threshold figures of about 90mW and slope efficiencies up to 22% have been achieved for  $\sigma$ -polarized emission at 1562nm wavelength. The modulator has been operated with a DC-bias voltage to give maximum optical extinction and an AC-square wave switching voltage of amplitude  $V_\pi$  and about 5% duty cycle in the frequency range  $1\text{kHz} < \nu < 5\text{kHz}$ . No evidence of CW-prelasing could be identified. Recently, peak power levels up to 2.5kW have been achieved at 1kHz pulse repetition rate. Build-up of the Q-switched pulses took about 80ns from the leading edge of the electrical switching pulses. With a detector of 1.5GHz bandwidth a periodic fine structure of the Q-switched pulses could be observed. The distance between adjacent peaks under the pulse envelope agrees with the round trip time in the laser cavity indicating the appearance of self-modelocking. The width of the pulse envelope was about 2ns (FWHM).

Such a laser emitting short pulses of high peak power in the eye-safe spectral range is an interesting source for laser RADAR applications and for nonlinear optical frequency conversion.

## 4 Conclusions

Coupled cavity harmonically modelocked waveguide lasers have been demonstrated to generate single super-mode pulse trains of excellent amplitude stability. Repetition rate doubling could be an interesting technique to increase of the modelocking frequency considerably beyond 10GHz which is one of the goals for the future. A further goal will be the monolithic integration of a modelocked laser with an external encoding modulator.

For the Q-switched waveguide lasers a wavelength selective DBR-cavity would be desirable. Such a laser would have a more stable and narrow linewidth emission and render possible the monolithic integration with quasi-phasematched parametric frequency converters of high efficiency.

## References

- [1] I. Baumann, S. Bosso, R. Brinkmann, R. Corsini, M. Dinand, A. Greiner, K. Schäfer, J. Söchtig, W. Sohler, H. Suche, and R. Wessel, IEEE J. Selected Topics Quantum Electron., **2**, 355 (1996)
- [2] H. Suche, I. Baumann, D. Hiller, and W. Sohler, Electron. Lett., **29**, 1111 (1993)
- [3] H. Suche, R. Wessel, S. Westenhöfer, W. Sohler, S. Bosso, C. Carmannini, and R. Corsini, Opt. Lett. **20**, 596 (1995)
- [4] D. J. Kuizenga and A. E. Siegman, IEEE J. Quantum Electron., **6**, 694 (1970)
- [5] M. Becker, D. J. Kuizenga, A. E. Siegman, IEEE J. Quantum Electron., **8**, 687 (1972)
- [6] M. Fleuster, Ch. Buchal, E. Snoeks, and A. Polman, J. Appl. Phys. **75**, 173 (1994)
- [7] J. S. Wey, J. Goldhar, and G. L. Burdge, IEEE J. Lightwave Technol., **15**, 1171 (1997)
- [8] H. Suche, A. Greiner, W. Qiu, R. Wessel, and W. Sohler, IEEE J. Quantum Electron., **33**, 1642 (1997)
- [9] R. Wessel, K. Rochhausen, H. Suche, and W. Sohler, Proc. CLEO-Europe 1998, post deadline paper CPD 1.5
- [10] R. Wessel, R. Ricken, K. Rochhausen, H. Suche, and W. Sohler, to appear in Proc. ECIO99, Torino
- [11] E. Lallier, D. Papillon, J. P. Pocholle, M. Papuchon, M. De Micheli, D. B. Ostrowsky, Electron. Lett., **29**, 175 (1993)
- [12] H. Suche, T. Oesselke, J. Pandavanes, R. Ricken, K. Rochhausen, W. Sohler, S. Balsamo, I. Montrosset, and K. K. Wong, Electron. Lett. **34**, 1228 (1998)
- [13] H. Suche, Photonics West99, Symposium on "Rare-Earth-Doped Materials and Devices III", to appear in SPIE, Vol.3622, paper 3622-14

## Optimized Si-on-LiNbO<sub>3</sub> Waveguide Reflectors with Low Loss and Record-High Reflectance

Hao Feng, Robert F. Tavlykaev, and Ramu V. Ramaswamy

Photonics Research Laboratory, 339 Larsen Hall, University of Florida, Gainesville, FL 32611

Tel: (352) 392-9265, Fax: (352) 392-4963, http: nervm.nerdc.ufl.edu/~photon

**INTRODUCTION:** While high-reflectance gratings in ferroelectrics, such as LiNbO<sub>3</sub> and the like, are desired, for example, for waveguide laser applications [1], the inherent difficulties of making efficient gratings in these high-index, etching resistant, materials has long hindered progress. Recently, LiNbO<sub>3</sub> waveguides with Si overlays have been proposed for use in high-reflectance gratings, even though their intriguing modal behavior was not fully understood at the time [2]. Subsequently, the modal behavior has been analyzed theoretically [3]. The analytical model underscored the unusual properties of the composite Si-on-LiNbO<sub>3</sub> waveguide structure and confirmed the unique possibility of achieving large perturbation of the effective mode index and low loss at the same time. Thus, the conditions necessary for realizing low-loss high-reflectance gratings can be met. Furthermore, the theory predicted a periodic dependence of loss and index perturbation versus the thickness of the Si overlay. In this paper, we report the results of an experimental study performed to verify theory and maximize the reflectance of waveguide DBRs based on Si overlay gratings over channel waveguides in LiNbO<sub>3</sub>. By optimizing the parameters of the composite structure, we have achieved reflectance of 88% from a 6.5 mm long grating at a center wavelength of 1513 nm with a FWHM bandwidth of 4.3 Å. The achieved value of reflectance is, to the best of our knowledge, the highest value for waveguide gratings in LiNbO<sub>3</sub> waveguides reported thus far.

**OUTLINE OF THEORETICAL ANALYSIS:** The key to achieving high-reflectance gratings has been the use of a Si overlay to substantially perturb the mode index of an optical waveguide in LiNbO<sub>3</sub> underneath it (Fig.1). Si has been selected on account of its processibility, low cost, and most importantly, its large refractive index (~3.4 at 1.5 μm) which enables large index perturbation. The presence of a Si overlay with a refractive index higher than that of the optical waveguide causes the effective mode index to modify. Hence, a modulation of the mode index can be produced by forming a corrugated Si overlay (Fig.2). It has been found experimentally and explained theoretically that a Si layer over a waveguide in LiNbO<sub>3</sub> can create a considerable perturbation of the effective mode index, yet without producing excessive loss. A surprising behavior was observed in that even thick Si films, capable of supporting multiple, planar modes by themselves, did not necessarily have a measurable effect on both the loss and the field distribution of the underlying LiNbO<sub>3</sub> single-mode channel waveguide, while the effective mode index was impacted significantly.

The above phenomena have been shown to result from rapid mode evolution with increasing Si thickness when the power carried by a guided mode is redistributed between Si and LiNbO<sub>3</sub>. In a nutshell, the field of a guided mode of the composite Si-on-LiNbO<sub>3</sub> structure near cut-off resides in LiNbO<sub>3</sub>, rather than in Si. As a result, all guided modes, except for the highest-order mode if near cut-off, are tightly confined in the Si overlay and absorbed as they propagate along the structure. In contrast, the highest-order mode near cut-off propagates with low loss and with most of its field localized in LiNbO<sub>3</sub>. In this case, since very little power is carried in the Si overlay for this mode, the effect of intrinsic loss of Si on the propagation loss is dramatically diminished. At the output, this mode may resemble the fundamental mode of the LiNbO<sub>3</sub> waveguide, however, with a significantly modified (increased) mode index.

The result of numerical analysis, performed by the Finite Element Method, of a graded-index annealed proton-exchanged waveguide fabricated in Z-cut LiNbO<sub>3</sub> with a Si overlay is shown in Fig.3, while the details of the simulation as well as the parameters of the modeled structure can be found in Ref. [3]. In Fig.3, the dispersion curves of the guided modes of the entire structure are plotted versus Si thickness. As seen from the Figure, the curve for each mode starts at cut-off with the effective mode index  $N_{\text{eff}}$  equal to the LiNbO<sub>3</sub> substrate index  $n_s$  (for the lowest order mode, it is equal to the effective mode index of the

isolated LiNbO<sub>3</sub> waveguide) with the mode energy almost completely confined in LiNbO<sub>3</sub>.  $N_{\text{eff}}$  slowly increases with Si thickness, until a ‘knee’ is reached, after which the dispersion curve is steep and  $N_{\text{eff}}$  rises rapidly above the LiNbO<sub>3</sub> waveguide index (~2.2), indicating that the mode becomes localized more in Si rather than in LiNbO<sub>3</sub>. As soon as the Si overlay is able to support any new mode, its effect is dominant, since the overlay pulls in virtually all of the energy from the lower LiNbO<sub>3</sub> waveguide. Conversely, beneath the knee of the dispersion curve of any order mode, the associated field profile resembles that of the isolated LiNbO<sub>3</sub> waveguide fundamental mode.

The calculated modal evolution with Si thickness is illustrated in Fig.4 showing the intensity plots of the highest-order mode for varying Si thickness. As seen, there is *periodic* switching of optical power between the two waveguides as Si thickness increases. The theory [3] also showed that the highest-order mode resides in the LiNbO<sub>3</sub> waveguide except when Si thickness falls into one of comparatively narrow intervals (‘forbidden zones’) of values just after the knees. Within these zones, the highest-order mode is tightly confined in the Si overlay and, hence, suffers higher propagation loss.

**EXPERIMENT:** Experimental waveguide structures were fabricated by proton exchanging Z-cut LiNbO<sub>3</sub> samples at 200°C for 50min in pyrophosphoric acid and annealing them at 350°C for 420min. Gratings with a period of 0.359nm were patterned from an e-beam deposited Si film with the conventional optical interference method (using a 442nm laser) and subsequent dry etching to a depth of 850Å. A set of samples with varying thickness of the deposited Si layer was fabricated.

The fabricated samples were tested with a tunable laser. Figure 5 shows the reflectance at the center wavelength and transmission (away from the reflection peak) measured in the fabricated samples. As seen, a *periodic* dependence of the grating reflectance and transmission (loss) versus Si thickness is observed. Note the significant and synchronous variation of these two parameters with increasing Si thickness. The ‘period’ of the dependences is about 3400Å, in good agreement with the theoretical value of 3300Å (see Fig.3). The region around 3500Å results in low reflectance and transmission, that is the guided-mode suffers high loss. Once again this results is quite consistent with the theory predicting the existence of a ‘forbidden’ area for a Si thickness of about 3000Å within which the highest-order mode ( $H_y^{21}$  in Fig.3) is localized in the Si overlay and, as a result, suffers loss. On the other hand, for Si thicknesses around 2000Å and 5400Å (note they are close to the cut-off regions in Fig.3) both high reflectance and low loss were reached. Figure 6 shows the spectral transmission through a sample with a 6.5 mm long and 5300Å thick Si grating over a 5μm wide waveguide. A reflectance of 88% was achieved which is, to the best of our knowledge, the highest value reported thus far for waveguide DBRs in LiNbO<sub>3</sub>. Even higher reflectance (up to 92%), however, with a broader bandwidth, was achieved in a sample with a 1900 Å thick Si grating.

**CONCLUSION:** DBR gratings in LiNbO<sub>3</sub> with drastically improved efficiencies can be achieved by integrating Si and LiNbO<sub>3</sub>, a technology that has tremendous potential, as demonstrated by recent advances in device performance. By refining this technology and applying the results of theoretical analysis, we have realized narrowband waveguide DBRs with reflectance about 90% at a center wavelength around 1.55μm. The achieved value of reflectance is, to the best of our knowledge, the highest value for waveguide gratings in LiNbO<sub>3</sub> waveguides reported thus far. The realized structures are ideally suited for waveguide narrow-band tunable filters and lasers in LiNbO<sub>3</sub> as well as for other applications where high-reflectance waveguide reflectors are crucial.

- REFERENCES:**
1. I. Baumann et al, *J. Selected Topics in Quant. Electron.*, vol.2, no.2, pp.355-365, 1996.
  2. C. P. Hussell and R. V. Ramaswamy, *Photon. Technol. Lett.*, vol. 9, no. 5, pp. 636-638, 1997.
  3. T. Conese, R. F. Tavlykaev, C. P. Hussell, and R. V. Ramaswamy, *J. Lightwave Technol.*, vol. LT-16, no.6, pp.1113-1122, 1998.

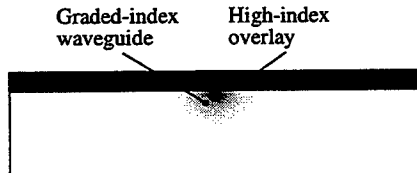


Fig.1 Transverse cross-section of a graded-index channel waveguide with a high-index overlaying Si film

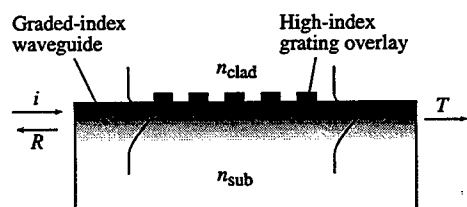


Fig.2 Longitudinal cross section of a DBR corrugated waveguide made from a high-index Si overlay.

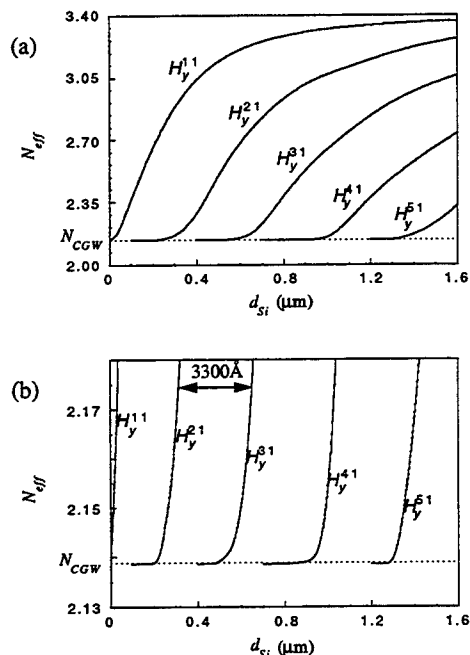


Fig.3 Effective mode index of Si-on-LiNbO<sub>3</sub> waveguide versus Si thickness (a); same plot with magnified cut-off regions (b).

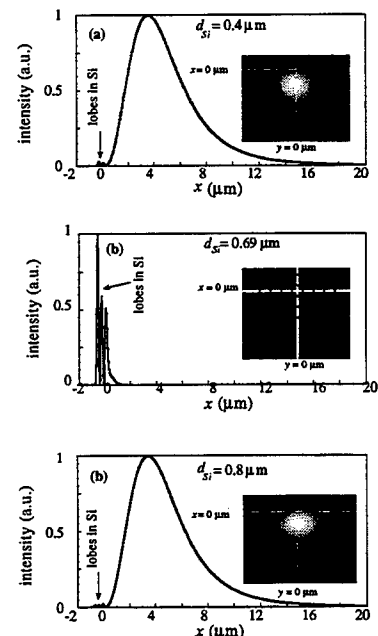


Fig.4 Evolution of the field of the highest-order mode upon increasing Si thickness.

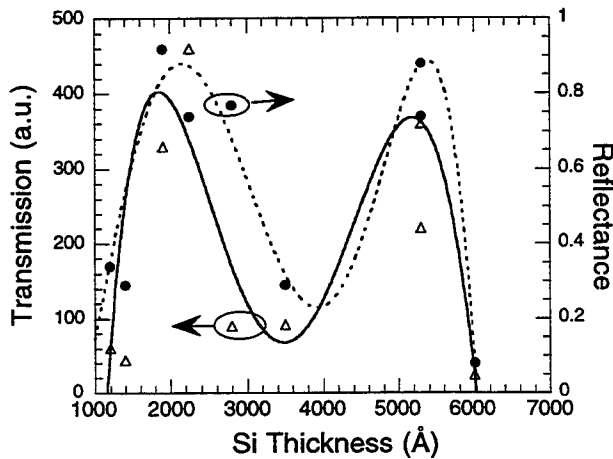


Fig.5 Transmission (solid, triangles) and reflectance (dotted, filled circles) vs Si thickness.

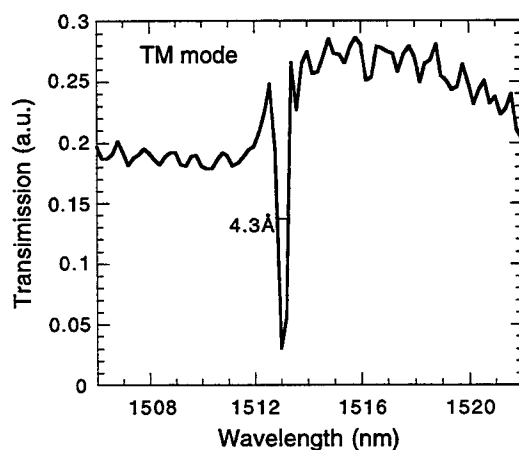


Fig.6 Spectral transmission in a sample with the maximum reflectively of 88%.

# Proposal of DFB lasers with refractive index modulated upper cladding layer of the grating for reducing spatial hole burning effect

Hong-Seok Lee and Byoungho Lee

School of Electrical Engineering, Seoul National University

Shinlim-dong, Kwanak-ku, Seoul 151-742, Korea

Tel: +82-2-880-7252, Fax: +82-2-873-9953

[hongseok@snu.ac.kr](mailto:hongseok@snu.ac.kr), [byoungho@plaza.snu.ac.kr](mailto:byoungho@plaza.snu.ac.kr)

Hong-Kuk Kim and Boo-Gyoun Kim

Department of Electronic Engineering, Soongsil University

Sangdo-dong, Dongjak-ku, Seoul 156-743, Korea

Tel: +82-2-820-0635, Fax: +82-2-813-1596

[smile@sunbee.soongsil.ac.kr](mailto:smile@sunbee.soongsil.ac.kr), [bgkim@sunbee.soongsil.ac.kr](mailto:bgkim@sunbee.soongsil.ac.kr)

Quarter wavelength shifted (QWS) DFB lasers have been studied extensively due to their large potential for stable single mode operation. However, the single mode gain difference decreases and the emission wavelength varies as the injection current increases in a QWS DFB laser due to the spatial hole burning (SHB) effect which comes from the non-uniform optical field intensity distribution along the laser cavity [1]. To reduce the SHB effect, various methods have been proposed either by flattening the optical field intensity distribution [2-4] or by enlarging the single mode gain difference [5].

In this paper, we propose a new structure - refractive index modulated DFB (RIM-DFB) laser of which center section has different refractive index. This structure might have a merit of easy fabrication because only uniform grating is needed. The effects of distributed effective phase shift and distributed coupling coefficients (coming from different sections with different refractive indices of the upper cladding layer of the grating) make this structure to maintain large single mode gain difference and small variation of emission wavelength as injection current increases.

The structure of the RIM-DFB laser proposed is illustrated in Fig. 1.

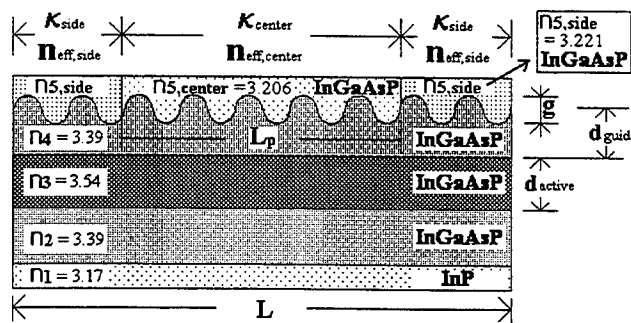


Fig.1. Schematic diagram of a refractive index modulated (RIM) phase shifted DFB Laser.

To obtain an effective  $\lambda/4$  phase shift in the center section, the refractive indices of the center section and the side sections of the upper cladding layer are set at 3.206 and 3.221, respectively for the case of  $L_p/L = 0.3$ . The cavity length  $L$  is 400  $\mu\text{m}$  and  $L_p$  is the length of the center region as shown in Fig.1. In this structure, only uniform grating is needed, while a QWS-DFB laser and a CPM-DFB laser need abrupt change of grating phase or the precise control of the grating pitch.

To confirm the reduction of the SHB effect in a RIM-DFB laser, the normalized single mode gain difference  $\Delta\alpha L$  ( defined by  $(\alpha_{th1} - \alpha_{th0})L$  ) and the normalized frequency detuning  $\delta\bar{\omega}$  ( defined by  $2\pi m_{eff}(1/\lambda_1 - 1/\lambda_B)$  ) are calculated as a function of injection current using the transfer matrix method (TMM).

For simulation, we take grating depth  $g = 0.035 \mu\text{m}$ , guide layer thickness  $d_{\text{guide}} = 0.14 \mu\text{m}$ , active layer thickness  $d_{\text{active}} = 0.07 \mu\text{m}$  and other parameters in Ref. 6. We assume both facets are anti-reflection coated. We calculate the coupling coefficient as  $\kappa_{\text{center}} = 79.82 \text{ cm}^{-1}$ ,  $\kappa_{\text{side}} = 75.01 \text{ cm}^{-1}$  and effective refractive index as  $n_{\text{eff-center}} = 3.290$ ,  $n_{\text{eff-side}} = 3.294$  from the structure parameters using the extended additional layer method [7]. The normalized coupling coefficient calculated is  $(\kappa L)_{\text{total}} = 3.06$ .

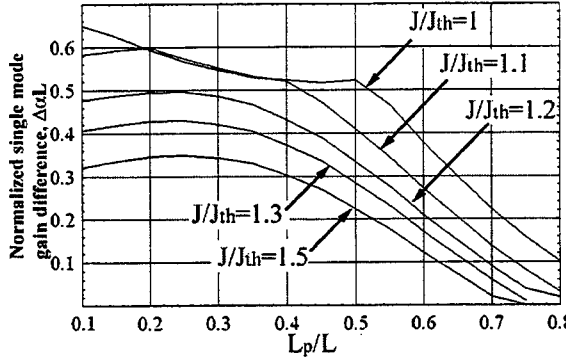


Fig.2. Normalized single mode gain difference as a function of  $L_p/L$  for various injection current densities ( $L=400 \mu\text{m}$ )

To optimize the center section length  $L_p$ ,  $\Delta\alpha L$  is calculated as a function of  $L_p/L$  for various values of  $J/J_{\text{th}}$  as shown in Fig. 2. For this calculation, the refractive index of the side sections of the upper cladding layer,  $n_{\text{5,side}}$ , is fixed to 3.221. The effective refractive index and the coupling coefficient of side sections calculated are  $n_{\text{eff-side}} = 3.294$  and  $\kappa_{\text{side}} = 75.01 \text{ cm}^{-1}$ , respectively. And  $n_{\text{5,center}}$  is chosen to make effective  $\lambda/4$  phase shift in the center section for each  $L_p/L$ . The total normalized coupling coefficient  $(\kappa L)_{\text{total}}$  is maintained almost the same value, 3.06 for each  $L_p/L$ . As  $L_p/L$  goes to 0, the structure becomes a QWS-DFB, and when  $L_p/L$  goes to 1, the structure becomes a uniform grating DFB laser. As shown in Fig 2,  $\Delta\alpha L$  in the case of  $L_p/L = 0.3$  maintains large value as injection current increases compared to that of other values of  $L_p/L$ .

To calculate the characteristics of a CPM-DFB laser, the same structure shown in Fig. 1 is used except that the refractive index of the upper cladding layer is fixed to 3.206. The corrugation pitch of a CPM-DFB laser is adjusted to obtain an effective  $\lambda/4$  phase shift in the center section. A CPM-DFB laser also shows that  $\Delta\alpha L$  in the case of  $L_p/L = 0.3$  maintains large value compared to that of other values of  $L_p/L$ . The normalized coupling coefficient calculated is 3.19 for both CPM and QWS-DFB lasers.

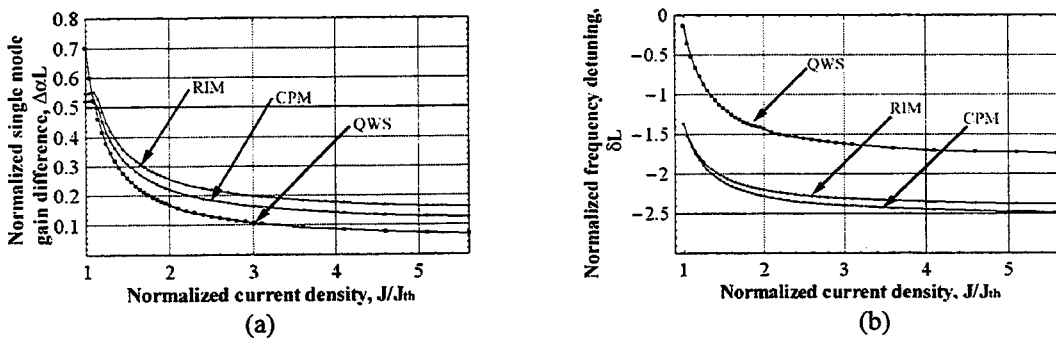


Fig.3. (a) Normalized single mode gain difference  $\Delta\alpha L$  and (b) normalized frequency detuning  $\delta L$  as a function of  $J/J_{\text{th}}$  for various DFB lasers with  $L_p/L = 0.3$ .

Figure 3(a) shows the variation of  $\Delta\alpha L$  as a function of injection current for a QWS-DFB laser, a CPM-DFB laser, and a RIM-DFB laser with  $L_p/L = 0.3$ . At threshold current,  $\Delta\alpha L$  of the QWS-DFB laser is larger than that of other structures as expected. However,  $\Delta\alpha L$  of the QWS-DFB laser decreases rapidly compared to that of other structures as injection current increases due to the SHB effect. Thus,  $\Delta\alpha L$  of other structures are larger than that of the QWS-DFB laser when  $J/J_{\text{th}} \geq 1.1$ .  $\Delta\alpha L$  of the RIM-DFB laser is larger than that of the CPM-DFB laser over the whole range of injection

current due to the effect of distributed coupling coefficients. Figure 3(b) shows the variation of the normalized frequency detuning as a function of injection current for a QWS-DFB laser, a CPM-DFB laser, and a RIM-DFB laser with  $L_p/L = 0.3$ . The variation of  $\delta L$  in the RIM-DFB is small ( $\Delta(\delta L) \sim 1$ ), while that in the QWS-DFB is large ( $\Delta(\delta L) \sim 1.7$ ). This means that the variation of emission wavelength in the RIM-DFB laser is small compared to that in the QWS-DFB laser. The variation of  $\delta L$  in the RIM-DFB is slightly smaller than that in the CPM-DFB.

The photon density profiles  $P(z)$  along the laser axis of the QWS-DFB laser, the CPM-DFB laser and the RIM-DFB laser are shown in Fig. 4.  $P(z)$  of the RIM-DFB laser is almost the same as that of the CPM-DFB laser. And  $P(z)$  of the two lasers are flatter than that of the QWS-DFB laser. This means that the SHB effect of the RIM-DFB laser is smaller than that of the QWS-DFB.

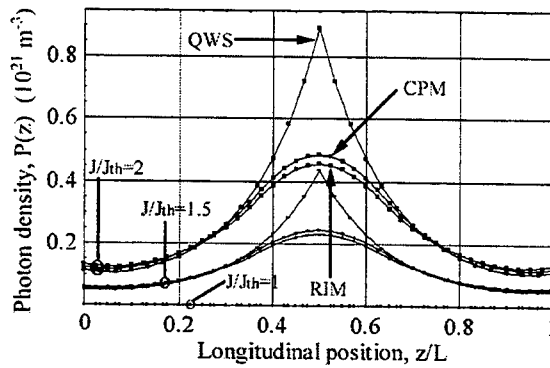


Fig.4. Photon density profile  $P(z)$  for various DFB lasers with  $L_p/L = 0.3$ .

In conclusion, we have proposed a new structure of which the refractive index of center section of the upper cladding layer of the grating is different from that of side sections. This structure has two effects. One is a distributed effective phase shift effect that reduces the SHB effect, and the other is a distributed coupling coefficient effect that enhances the single mode gain difference. To confirm the possibility of the proposed structure, we have calculated above-threshold characteristics and compared them with those of other structures. The variations of the single mode gain difference and the emission wavelength of RIM-DFB lasers as a function of injection current are small compared to those of QWS-DFB lasers and CPM-DFB lasers. The effect of the length of the center section on the above threshold characteristics of RIM-DFB lasers is investigated.

- [1] H. Soda, Y. Kotaki, H. Sudo, H. Ishikawa, S. Yamakoshi, and H. Imai, *IEEE J. Quantum Electron.*, vol. QE-23, p.804, 1987.
- [2] G. P. Agrawal, J. E. Geusic, and P. J. Anthony, *Appl. Phys. Lett.*, vol. 53, p.178, 1988.
- [3] M. Okai, N. Chinone, H. Taira, and T. Harada, *IEEE Photon. Technol. Lett.*, vol. 1, no. 8, p.200, 1989.
- [4] K. Tada, Y. Nakano, and A. Ushirokawa, *Electron. Lett.*, vol. 20, p.82, 1984.
- [5] T. Fessant and X. Doyelle, *IEEE Photon. Technol. Lett.*, vol. 10, p.33, 1998.
- [6] P. Correc, *IEEE J. Quantum Electron.*, vol. 30, p2467, 1994.
- [7] S.-C. Cho, B.-G. Kim, and N. Dagili, *Microwave Optic. Technol. Lett.*, vol. 16, p143, 1997.

**Integrated Photonics Research**

# **High-Q Resonators**

**Tuesday, July 20, 1999**

**Richard W. Ziolkowski, University of Arizona, USA**  
Presider

**RTuH**  
**1:30pm–3:15pm**  
Sierra Madre South

## In-plane photonic crystal microcavities for high-Q optical resonators

Axel Scherer  
California Institute of Technology, USA  
[Etcher@cco.caltech.edu](mailto:Etcher@cco.caltech.edu)

Summary not available at press time.

## Coupling, Q-factor, and Integration Aspects of Microsphere Applications

V.S.Ilchenko, X.S.Yao, L.Maleki

298-100 Jet Propulsion Laboratory, California Institute of Technology  
4800 Oak Grove Dr. Pasadena CA 91109

With suggested applications varying from microlaser and cavity QED through optical locking of diode lasers to modulators and sensors [1-3], high-Q silica microspheres with whispering-gallery (WG) modes so far remain the subject of tabletop feasibility demonstrations. Despite the uniquely high quality-factor and submillimeter dimensions suitable for tight packaging, this novel type of high-finesse cavity still has to be adapted to fiber- and integrated-optic hardware.

In the visible and near infrared-band experiments (633-850nm) measuring the ringdown time  $\tau$  of free oscillations,  $Q = (0.6 \text{ to } 0.8) \times 10^{10}$  has been obtained in silica spheres of diameter  $\sim 800\mu\text{m}$  [4] (corresponding  $\tau = 3 \text{ to } 4 \mu\text{s}$ ). It was proved that under normal laboratory conditions, quality-factor is subject to deterioration within several-minute scale down to  $(2 \dots 3) \times 10^9$ . The responsible mechanism was identified as adsorption of a monolayer of atmospheric water, so that preservation of the ultimate  $Q$  requires manipulation in dry environment, or fast packaging into sealed devices. Larger  $Q$  can be expected closer to minimum of attenuation in fused silica  $\alpha = 0.2 \text{ dB/km}$ ;  $Q_{\text{mat}}^{-1} \geq 1 \times 10^{11}$  at  $\lambda=1.55\mu\text{m}$ , with corresponding energy storage time  $\tau \sim 0.1\text{ms}$ . Experiments are currently underway to determine whether this high  $Q$  can be realized experimentally. The evident difficulty is that OH-related optical absorption has its peaks located near the reported minimum of attenuation in silica. We can also mention here that some of proposed fiber materials, yet not ready for fiber drawing, have been predicted to have smaller attenuation than fused silica and may be suitable for microsphere fabrication (sodium-magnesium silicate glass,  $\alpha = 0.06 \text{ dB/km}$  [5]).

WG modes possess very small radiative loss (it does not prevent  $Q \sim 10^{20}$  and more) and therefore are electromagnetically isolated and cannot be excited by free-space beams. If no modification (such as grating) is made on the sphere surface, the coupling has to be provided by an appropriate near-field device. A systematic theoretical approach has been recently developed to quantify the performance of near-field couplers for WG modes [6]. Efficient coupling can be obtained upon fulfillment of two main conditions: 1) mode matching and 2)sufficient coupling strength to provide the buildup of a WG mode with a given intrinsic loss. In other words, the wave in the coupler has to be phase-matched and sufficiently overlapped with the WG mode to provide enough buildup in the cavity. If the coupling efficiency is characterized by the fractional depth  $K^2$  of the resonance dip in intensity transmittance observed upon varying the frequency of the exciting wave in the coupler,

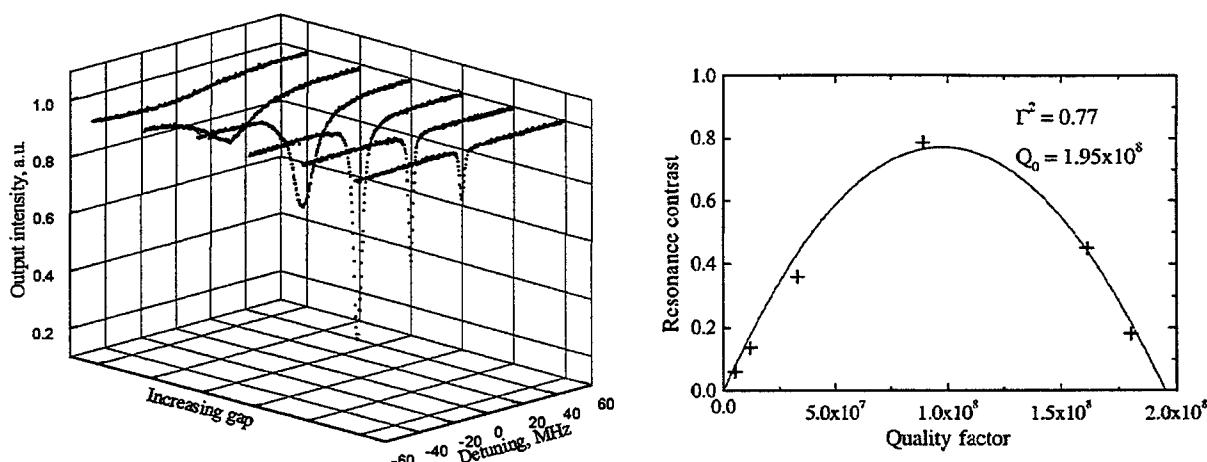


Fig.1. Effect of variable coupling (increasing microsphere-coupler gap) on the loaded quality-factor and contrast of WG mode resonance observed as depletion peak in transmitted power. Single prism coupler; wavelength 633nm; fused-silica microsphere with diameter  $270\mu\text{m}$ ; unloaded  $Q_o \approx 2 \times 10^8$

then it can be expressed in the following way through  $Q_c$  and the intrinsic quality-factor of the mode  $Q_o$ :

$$K^2 = 4 Q_o Q_c \Gamma^2 / (Q_o + Q_c)^2,$$

With complete mode matching  $\Gamma=1$ , the critical coupling  $K^2 = 1$ , or 100% absorption of the input wave in resonance, is possible when  $Q_c$  can be made equal or smaller than  $Q_o$ . Both contrast of the visible resonance  $K$  and the loaded quality-factor  $Q_L = (Q_o^{-1} + Q_c^{-1})^{-1}$  can be adjusted by varying the gap between the coupler device and the sphere, giving a unique (in optics) opportunity to easily control the bandwidth of the cavity. Typical evolution of the observed absorption resonance with increasing of the gap is illustrated in Fig.1. Results are obtained with prism coupler at the wavelength 633nm. The “disappearance” of the resonance dip in overloaded regime with well-matched coupler does not mean reduced energy exchange; it reflects only the well known fact in RF engineering that maximum absorption at resonance requires that coupling loss be equal to intrinsic cavity loss critical  $Q_c = Q_o$ , or  $Q_L = 1/2Q_o$ . If  $Q_c \perp Q_o$ , the power is recycled in the mode and is fed back to the coupler with shifted overall phase.

At present moment, in addition to the well-known prism coupler with frustrated total internal reflection [1-3,6], few attempts have been reported to directly couple a sphere to an optical fiber. However these fiber couplers had either limited efficiency due to residual phase mismatch (side-polished bent fiber coupler [7]), or still appreciable size including fragile core-to-cladding transformers (tapered fiber coupler [8]). Recently, we have demonstrated a new and simple method of direct fiber coupling to high-Q WG modes, which in essence is a hybrid of waveguide and prism coupler. A close-up of the experimental setup with microsphere and two couplers is shown in Fig.2a. The tip of a single-mode fiber is angle-polished under steep angle. Upon incidence on the angled surface, the light propagating inside the fiber core undergoes total internal reflection and escapes the fiber. With the sphere positioned in the range of the evanescent field from the core area, the configuration provides efficient energy exchange in resonance between the waveguide mode of single-mode fiber and the whispering-gallery mode in the sphere. The angle of the polish is chosen to secure the phase matching requirement:  $\Phi = \arcsin(n_{sphere}/n_{fiber})$ . Here  $n_{fiber}$  stands for the effective refraction index to describe the guided wave in the fiber core truncation area, and  $n_{sphere}$  stands for the effective refraction index to describe azimuthal propagation of WG modes (considered as closed waves undergoing total internal reflection in the sphere), see plot in Fig. 3. Since the linear dimensions of the angle-

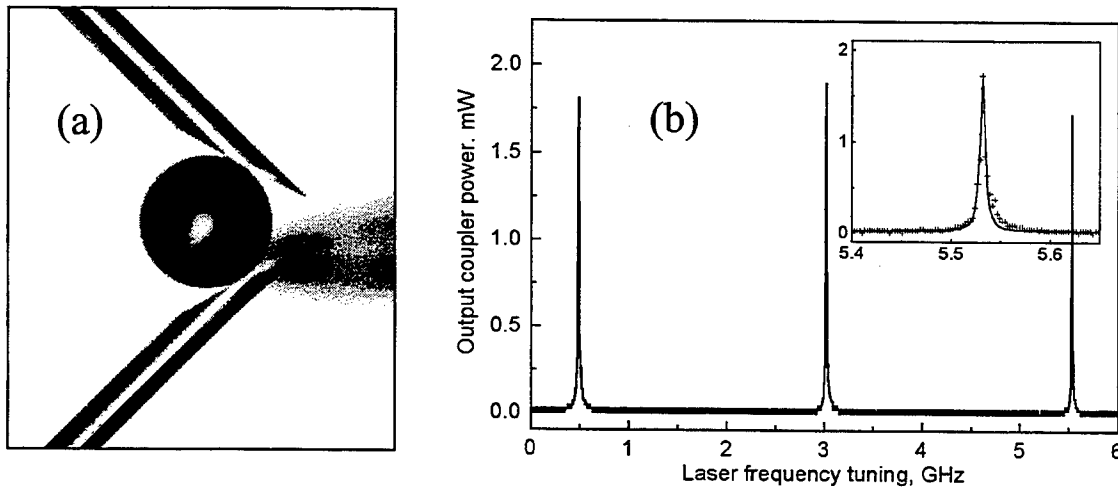


Fig.2. Close-up view (a) and optical transmission characteristic (b) of a microsphere with two side-polished fiber couplers. Input power 7.5...8.3mW; maximum transmission at resonance ~23.5% (fiber-to-fiber loss 6.3dB);  $Q_L > 3 \times 10^7$  at 1550nm; sphere diameter 405μm. Unloaded  $Q_o \approx 1.2 \times 10^8$ . Fiber: SMF-28, polished at ~76°.

cut core area match well the area of evanescent field overlap, the new system is equivalent to a prism coupler with eliminated collimation/focusing optics. The effective refraction index to describe the azimuthal propagation of WG modes near the surface of the sphere can be calculated, for example, on the basis of asymptotic expressions [9] for WG mode frequencies  $\omega_{q_\ell}$ , where  $n_{sphere} = 2cl / D\omega_{q_\ell}$ . Single coupler efficiency in our experiment was more than 60%, comparable with the best reported results for prism coupler (78%) and fiber taper (90%); total fiber-to-fiber transmission at resonance ~23% (insertion loss 6.3dB). The demonstrated simple “pigtailing” of the microspheres

will lead to their wider use in fiber optics, enabling the realization of a whole class of new devices ranging from ultra-compact narrow band filters and spectrum analyzers and high-sensitivity modulators and sensors, to compact laser frequency stabilization schemes and opto-electronic microwave oscillators.

Apart from "discrete element" fiber optics applications, microspheres present further challenge for true integration with planar optics devices. Very high  $Q \geq 10^8 \dots 10^9$ , uncommon for existing planar microcavities, would open way for sub-kHz-linewidth integrated laser sources [3] and single-chip microwave optoelectronic oscillators [10]. The ultimate goal is the replacement of laboratory hand preparation of spheres (fusion of silica preforms in oxy-hydric flame or  $\text{CO}_2$  laser beam) by appropriate microfabrication technology. It is worth to note here that such a task may not be extraordinary difficult, given the progress in planar silica waveguides and successful demonstrations of thermal treatment techniques for formation of smooth curvilinear integrated optics elements. The other part of the integration is the development of appropriate waveguide coupler elements. This task can possibly be solved along three routes: a) precise tailoring of propagation constant in the waveguide to match that of the sphere; b) truncation, or "reflection" of the waveguide from vertical cleave, by analogy with the above-described fiber coupler; c) deposition of appropriate modulation grating on the waveguide (see recent report on free-space coupling to microspheres using UV-assisted surface grating [11]).

The research described in this paper was carried out, in part, by the Jet Propulsion Laboratory, California Institute of Technology, under a contract with the National Aeronautics and Space Administration.

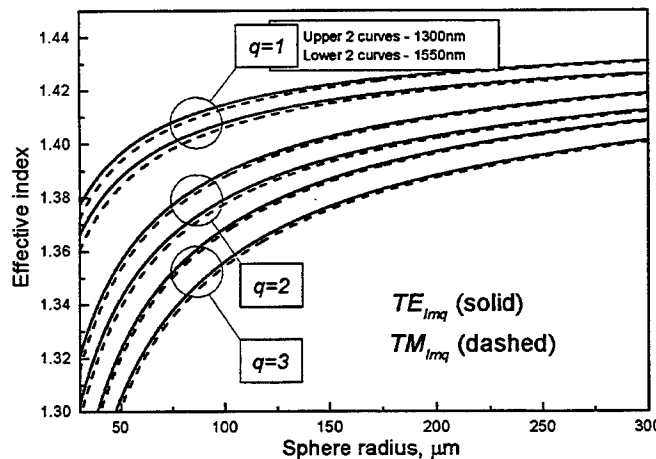


Fig.3. Effective index for WG mode azimuthal propagation  
(based on mode frequency approximation  
by C.C.Lam *et al* [9])

- [1] V.B.Braginsky, M.L.Gorodetsky, V.S.Ilchenko, *Phys.Lett.* **A37**, 393 (1989); H.Mabuchi, H.J.Kimble, *Opt.Lett.* **19**, 749 (1994); V.Sandoghdar, F.Treussart, J.Hare, V.Lefevre-Seguin, J.-M.Raimond, S.Haroche, *Phys.Rev.* **A54**, R1777 (1996);
- [2] D.W.Vernooy, A.Furusawa, N.P.Georgiades, V.S.Ilchenko, H.J.Kimble, *Phys.Rev.*, **A57**, pp.R2293-6, 1998; M.Nagai, F.Hoshino, S.Yamamoto, R.Shimano, M.Kuwata-Gonokami, *Opt.Lett.*, **22**, pp.1630-32, 1997
- [3] V.V.Vasilev, V.L.Velichansky, M.L.Gorodetsky, V.S.Ilchenko, L.Hollberg, A.V.Yarovitsky, *Opt.Commun.* **158**, 305 (1998); B.E.Little, S.T.Chu, H.A.Haus, *Opt.Lett.* **23**, 894 (1998)
- [4] M.L.Gorodetsky, A.A.Savchenkov, V.S.Ilchenko, *Opt.Lett.* **21**, 453 (1996); D.W.Vernooy, V.S.Ilchenko, H.Mabuchi, E.W.Streed, H.J.Kimble, *Opt.Lett.* **23**, 247 (1998)
- [5] S. Todoroki, S. Sakaguchi, M. Peeters, *J. Amer. Ceramic Soc.*, **80**, pp.313-6, 1997.
- [6] M.L.Gorodetsky, V.S.Ilchenko, *J.Opt.Soc.Am.* **B16**, 147 (1999)
- [7] A.Serpenguezel, S.Arnold, G.Griffel, *Opt.Lett.* **20**, 654 (1995); N.Dubreuil, J.C.Knight, D.Leventhal, V.Sandoghdar, J.Hare, V.Lefevre, *Opt.Lett.* **20**, 813 (1995)
- [8] J.C.Knight, G.Cheung, F.Jacques, T.A.Birks, *Opt.Lett.* **15**, 1129 (1997)
- [9] C.C.Lam, P.T.Leung, K.Young, *J.Opt.Soc.Am.* **B9**, 1585 (1992)
- [10] X.S.Yao, L.Maleki, *Opt.Lett.*, **22**, pp.1867-9, 1997
- [11] V.S.Ilchenko, D.S.Starodubov, M.L.Gorodetsky, L.Maleki, J.Feinberg, CTuC4 presented at CLEO/QELS, Baltimore, May 23-28, 1999

**Coupling of excited molecules and nanocrystals with photonic atoms**

**(microspheres) and photonic molecules,** S.Arnold and N.L.Goddard, *MP3L*,

*Polytechnic University, Brooklyn, NY 11201*

Tel: 718 260 3296

Fax: 718 260 3136

Spherical dielectric microparticles have been called "photonic atoms"<sup>1</sup> because of their ability to confine photons in a similar form to the confinement of an electron in an atom, and because of their newly demonstrated ability, when joined, to mimic molecular states ("photonic molecules"<sup>2</sup>). Just as in other photonic containers, the modes of a photonic atom are virtual. However, the Qs of these modes are unprecedentedly large for a microstructure,  $\sim 10^9$ .<sup>3</sup> Such a long lived mode in a structure several wavelengths in size has a density of photon states well in excess of the vacuum density, and consequently enhanced coupling to atoms,<sup>4</sup> molecules,<sup>5</sup> and quantum-dots is possible.

Aside from their obvious quantum mechanical behaviour excited molecules represent extended systems with body-fixed emission moments, nanoscopic antennae. These antennae can be aligned in relation to a photonic atom or photonic molecule by understanding local interactions and utilizing self-assembly. The emission spectrum from the aligned molecules as well as its polarization dependence, gives proof of their orientation.<sup>6</sup> By manipulating the alignment of the molecular structure on a sphere, one can control the gain spectrum. By the additional control of the density of states through size change one can envision the molecular design of microcavity devices (e.g. lasers, LED's, etc.)

---

<sup>1</sup>. S. Arnold et al. *J. Opt. Soc. Am.B* **9**, 819(1992).

<sup>2</sup>, T. Mukaiyama, K. Takeda, H. Miyazaki, Y. Jimba, and M. Kuwata-Gonokami, "Tight-Binding Photonic Molecule Modes of Resonant Bispheres" (*Phys. Rev. Lett.*, in press)

- <sup>3</sup>. M.D. Gorodetsky, A.A. Savchenko, and V.S. Ilchenko, Opt. Lett. **21**, 453(1996).
- <sup>4</sup>. H.-B. Lin, J.D. Eversole, C.D. Merrit and A.J. Campillo, Phys. Rev. A **45**, 1656(1992)
- <sup>5</sup>. S. Arnold, J. Chem. Phys. **106**, 8280(1997).
- <sup>6</sup>. S. Arnold, S. Holler, N.L. Goddard, and G. Griffel, Opt. Lett., **22**, 1452 (1997); S. Holler, N.L. Goddard, and S. Arnold, J. Chem. Phys. **108**, 6545 (1998).

## Novel techniques for whispering-gallery-mode excitation in silica microspheres

J.P. Laine, B.E. Little, D. Lim, and H.A. Haus

Massachusetts Institute of Technology, Research Laboratory of Electronics, Cambridge MA  
02139

Tel: (617) 253 8524 Fax: (617) 253 9611

In recent years, dielectric microsphere resonators have received increasing attention due to their very high Q factors [1,2]. Envisioned uses for these resonators include, for example, high-resolution spectroscopy, sensor applications, laser frequency stabilization, and cavity QED experiments [3,4,5]. Analytic expressions for coupling from tapered fibers and polished half-blocks into microsphere resonators have also been developed [6].

The high-Q resonances encountered in microspheres are exclusively due to whispering-gallery-modes (WGM) supported within the spherical cavity. Several techniques have been proposed for coupling light selectively and efficiently into the sphere WGMs. Generally, the most efficient methods incorporate phase-matched evanescent wave coupling [7]. In this vein, the best overall performance and easiest coupling is gained by accessing the field in a waveguide. A common approach is to polish down the cladding of an optical fiber to the point where the evanescent field is locally exposed [8]. In another method, a narrow waist is formed on a fiber by heating and gradual stretching [9]. Although these techniques have been used successfully, certain challenges remain. For example, residual phase mismatching between the fiber coupler and the sphere, as well as leakage from sphere modes into fiber cladding modes both result in a lower coupling efficiency. Also, the fabrication of either type of device is not entirely trivial, and the resulting couplers are quite fragile.

In order to address some of the problems we propose two new coupling arrangements: a chemically etched fiber taper and the ARROW (antiresonant reflective optical waveguide) [10] coupler structure.

The ARROW structure provides a robust waveguide-based coupling platform and opens the possibility of integrating microspheres onto waveguide chips. The principal feature of the ARROW for use in sphere coupling is that the silica waveguide mode is well matched to the effective index of the silica sphere, while the high reflectivity layers of the ARROW simultaneously isolate the sphere from the substrate. Therefore, the modes in the sphere couple only to the guided mode of the ARROW, and not to the substrate radiation modes. The structure of the fabricated ARROW waveguide, and a simulation of the guided mode field pattern, is depicted in Fig. 1. Using proper combinations of layer materials and thicknesses, it is possible to reach almost 100% reflectivity at the first interface, between the core and the first cladding layer.

The principal motivation for etch-eroded tapers lies in the low cost and simplicity of fabrication compared to other fiber-based coupling techniques. Properties include precise erosion depth control, a radially symmetric mode profile, and consistent modal characteristics over the entire etched region. The fiber core can be exposed fully, eliminating the issue of sphere modes coupling back into the cladding modes of a partially polished fiber.

In order to perform the etching, we mounted a bare fiber on a translatable stage above a convex meniscus of hydrofluoric acid (HF). Etch parameters such as etch-region length and taper slope could be controlled by changing the position of the fiber in the HF meniscus. In order to terminate etching, the fiber was lifted clear of the acid, then cleaned and dried with a pressurized aerosol. During erosion, etch quality and progress was monitored with fiber throughput loss measurements and microscopy. A 48%, room temperature HF solution was used in all etching experiments. The etched fibers were of a standard single-mode telecommunications type.

The etching process can be roughly divided into two stages: erosion of the fiber cladding, and core tapering. Good coupling performance is attained at the interface, where the cladding has been all but removed or less than 2-3  $\mu\text{m}$  of the core diameter is etched. The removal of the cladding enhances coupling efficiency by eliminating sphere-mode coupling back into fiber cladding modes, yet maintains a relatively robust fiber core diameter. Etching deeper into the core would allow better matching of the fiber and sphere propagation constants. However, this seems to significantly increase propagation losses in the fiber. This is apparently due to the increasing influence of scattering from etch-surface roughness as a function of reduced core diameter. Fig. 2 shows a microsphere coupled to an etched fiber.

Silica microspheres of diameter 60-400  $\mu\text{m}$  were used to perform the coupling experiments. All spheres were fabricated by arc-melting a cleaved fiber end. In the coupling tests, a microsphere was brought into contact with the fiber at the etched region. Frequency scans were then carried out with a tunable diode source operating in the 1.5  $\mu\text{m}$  range at 1 MHz line width, while a photodiode coupled to a lock-in amplifier acted as the detection stage. At the WGM resonances light was coupled out of the fiber into the sphere, which results in a dip in the output signal. To date, we have demonstrated coupling efficiencies higher than 30% with the etched-fiber coupler.

In conclusion, we present two new methods for coupling light into the whispering-gallery-modes of dielectric micropsheres: the etch-eroded fiber coupler, and the ARROW waveguide structure. ARROW structures provide a stable and durable microsphere coupling platform, with potentially great utility in measurement and sensing applications. Etch-erosion allows precise control in exposing a fiber's evanescent field, with a minimum of equipment and preparation time compared to other fiber-based coupling methods.

1. L. Collot, V. Lefevre-Seguin, M. Brune, J.M. Raimond, and S. Haroche, *Europhys. Lett.* **23**, 327 (1993).
2. M.L. Gorodetsky, A.A. Savchenkov, and V.S. Ilchenko, *Opt. Lett.* **21**, 453 (1996).
3. B.E. Little, S.T. Chu, and H.A. Haus, *Opt. Lett.* **23**, 894 (1998).
4. A.B. Matsko, S.P. Vyatchanin, H. Mabuchi, and H.J. Kimble, *Phys. Lett. A.* **192**, 175 (1994).
5. S.Schiller, R.Byer, *Opt. Lett.* **16**, 1138 (1991).
6. V.B. Braginsky, M.L. Gorodetsky, and V.S. Ilchenko, *Phys. Lett. A* **137**, 393 (1989).
7. B. E. Little, J.-P. Laine, and H. A. Haus, *IEEE J. Lightwave Tech.* **17**, April (1999).
8. N. Dubreuil, J.C. Knight, D.K. Leventhal, V. Sandoghdar, J. Hare, and V. Lefevre, *Opt. Lett.* **20**, 813 (1995).
9. J.C. Knight, G. Cheung, F. Jacques, and T.A. Birks, *Opt. Lett.* **22**, 1129 (1997).
10. M.A. Duguay, Y. Kokubun, T.L. Koch, and L. Pfeiffer, *Appl. Phys. Lett.* **49**, 13 (1986).

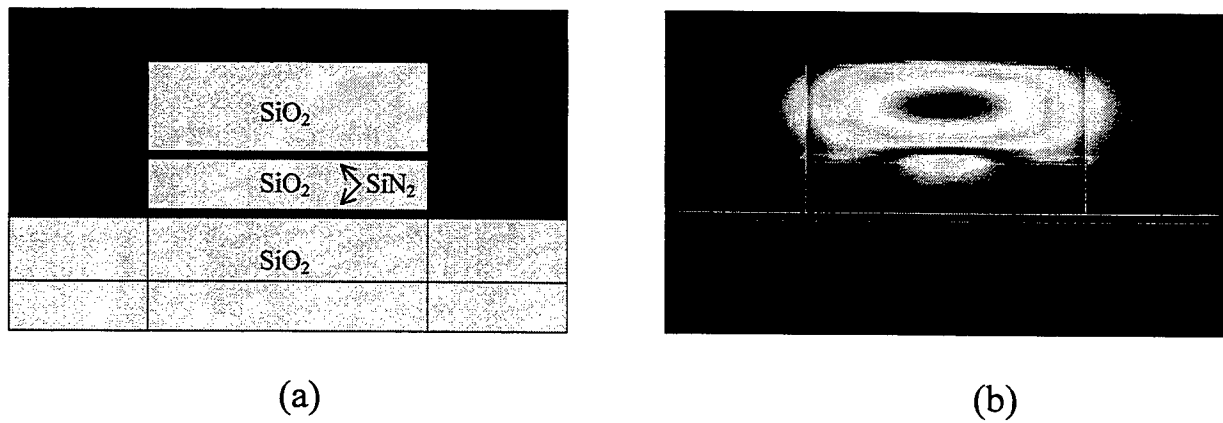


Fig 1. (a) Structure and (b) mode field profile of the proposed ARROW waveguide coupler.

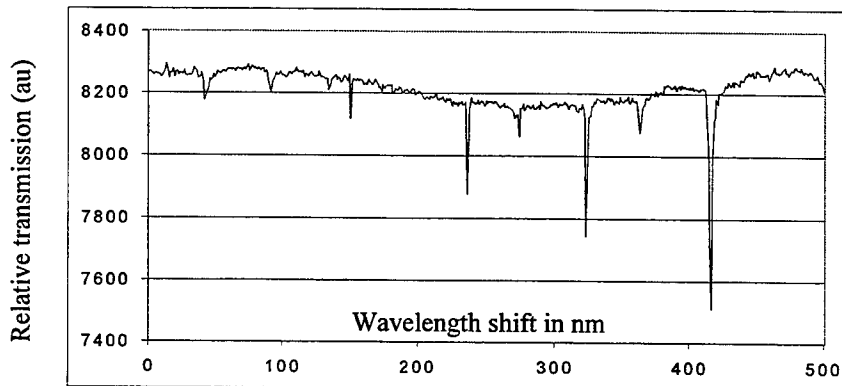
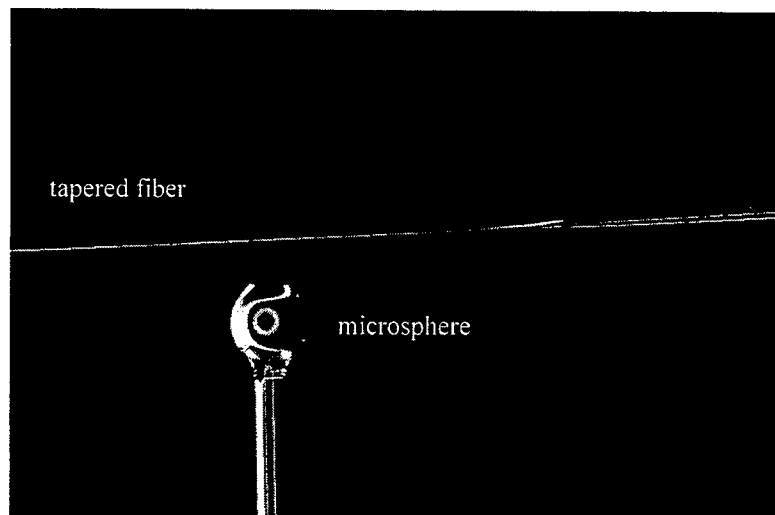


Fig 2. A microsphere coupled to an etched fiber and transmission data

**Integrated Photonics Research**

# **Finite-Difference Modeling**

**Tuesday, July 20, 1999**

**Yongchul Chung, Kwangwoon University, South Korea**  
Presider

**RTul**  
**1:30pm–3:00pm**  
Anacapa

## High-Accuracy Finite Difference Equations for Simulation of Photonic Structures

G. Ronald Hadley  
Sandia National Laboratories  
Albuquerque, New Mexico 87185-5800  
(505)844/4015  
(505)844/8985 (FAX)  
[grhadle@sandia.gov](mailto:grhadle@sandia.gov)

The success of the next generation of photonic structures will depend strongly on our ability to simulate those structures numerically prior to fabrication. Even with the recent increases in computer speeds and memory, the demands imposed by circuitry size are growing faster than our simulation capability. One partial solution to this dilemma is the introduction of new simulation algorithms that allow (to a great degree) *grid-independent computing*. By this is meant algorithms that are capable of providing predictions of device performance to acceptable accuracy *on any reasonable grid*. Codes based on such algorithms are of obvious use to experimenters who may wish to do design simulations, but who may not be experienced in the art of numerical computation. More importantly, the high accuracy of these algorithms will allow the use of coarse grids (that would otherwise result in unacceptable errors) and consequently will provide the capability to model large structures without the need for mainframe computer resources.

Progress towards the development of such algorithms as been reported for waveguide analysis<sup>1-3</sup> and vertical-cavity laser simulation<sup>4</sup>. In all these cases, the higher accuracy order was obtained for a single spatial dimension. More recently, this concept was extended to differencing of the Helmholtz Equation on a 2-D grid, with uniform regions treated to 4<sup>th</sup> order and dielectric interfaces to 3<sup>rd</sup> order<sup>5</sup>. No attempt was made to treat corners properly. In this talk I will describe the extension of this concept to allow differencing of the Helmholtz Equation on a 2-D grid to 6<sup>th</sup> order in uniform regions and 5<sup>th</sup> order at dielectric interfaces. In addition, the first known derivation of a finite difference equation for a dielectric corner that allows correct satisfaction of all boundary conditions will be presented. This equation is only accurate to first order, but as will be shown, results in simulations that are third-order-accurate.

In contrast to a previous approach<sup>3</sup> that utilized a generalized Douglas scheme to increase the accuracy order of the differenced second derivative, the present method invokes the Helmholtz Equation itself to convert derivatives of high order in a single direction into mixed

derivatives of lower order that can be differenced using a nine-point stencil. Such a stencil results in no substantial increase in matrix bandwidth and thus computer memory or runtime. At present, such high accuracies require a uniform grid with  $\Delta x = \Delta y$ , but it is expected that this restriction will be relaxed through future derivations with at most a two-order loss in truncation error.

The utility of these difference equations is aptly illustrated by incorporating them into an eigenmode solver and testing them on problems of varying complexity using a series of refined grids. For simple box modes involving a single dielectric interface, uncertainties in the modal index for low-order modes were typically  $5 \times 10^{-6}$  for coarse grids ( $6 \times 8$ ) and  $3 \times 10^{-12}$  for fine grids ( $96 \times 128$ ). For problems with a single corner the coarse results were similar and the fine results were slightly less accurate with uncertainties of  $6 \times 10^{-10}$ . These results demonstrate the power of grid-independent computing since the uncertainties obtained with the coarsest grid would likely be satisfactory to a designer in most situations. Of course, the derivations to be presented also are applicable to other types of problems, such as the simulation of reflecting structures by direct solution of the Helmholtz Equation<sup>5</sup>.

1. J. Yamauchi, J. Shibayama and H. Nakano, "Wide-angle propagating beam analysis based on the generalized Douglas scheme for variable coefficients", Opt. Lett. 20,7(1995).
2. R. Pregla, "High Order Approximation for the Difference Operators in the Method of Lines", IEEE Micro. and Guided Wave Lett. 5,53(1995).
3. G. Ronald Hadley, "Low-Truncation-Error Finite Difference Equations for Photonics Simulation I: Beam Propagation", J. Lightwave Tech. 16,134(1998).
4. G. Ronald Hadley, "Low-Truncation-Error Finite Difference Equations for Photonics Simulation II. Vertical-Cavity Surface-Emitting Lasers", J. Lightwave Tech. 16,142(1998).
5. G. Ronald Hadley, "Low-Truncation-Error Finite Difference Representations of the 2-D Helmholtz Equation", Int. J. Electron. Commun. (AEU) 52,310(1998).

## Stability Condition of the Nonlinear FDTD Method for Optical Device Simulation

Vien Van and Sujeeet K. Chaudhuri

*Department of Electrical and Computer Engineering  
University of Waterloo, Waterloo, Ontario, Canada, N2L 3G1  
Tel. (519) 885-1211, Fax. (519) 746-3077  
Email: vvan@maxwell.uwaterloo.ca*

### 1. Introduction

Over the past decade the Finite-Difference Time-Domain (FDTD) method has emerged as one of the most versatile numerical techniques for simulating propagation in optical waveguiding structures [1]. The success of the technique results from its ability to handle almost any type of materials and its ease of implementation. Recently the method has also been extended to simulate propagation in nonlinear media [2,3]. While numerical issues such as stability and dispersion are well understood for linear FDTD schemes, they have not been adequately addressed for nonlinear media. In most cases stability is verified by actually running the simulation and observing that the numerical solution remains bounded. In this paper, we present a rigorous stability analysis for the nonlinear FDTD method in two-dimensional structures, with emphasis on the two most common types of optical nonlinearity: second-order and third-order nonlinearities.

### 2. Stability of the nonlinear FDTD scheme

In 2D nonlinear optical waveguides with  $\partial/\partial y = 0$ , Maxwell's equations for the propagation of TE-polarized light with field components  $E_y$ ,  $H_x$  and  $H_z$  can be reduced to the nonlinear wave equation

$$\frac{1}{c^2} \frac{\partial^2}{\partial t^2} (\varepsilon_r E_y) = \left( \frac{\partial^2}{\partial z^2} + \frac{\partial^2}{\partial x^2} \right) E_y, \quad (1)$$

where  $\varepsilon_r$  is the relative permittivity. For nonlinear media,  $\varepsilon_r$  is a function of the electric field. Using the notation  $E_{i,j}^N = E_y(N\Delta t, i\Delta z, j\Delta x)$ , we discretize (1) using the conventional explicit time-stepping scheme as

$$\frac{(\varepsilon_r E)_{i,j}^{N+1} - 2(\varepsilon_r E)_{i,j}^N + (\varepsilon_r E)_{i,j}^{N-1}}{(c\Delta t)^2} = \frac{E_{i+1,j}^N - 2E_{i,j}^N + E_{i-1,j}^N}{(\Delta z)^2} + \frac{E_{i,j+1}^N - 2E_{i,j}^N + E_{i,j-1}^N}{(\Delta x)^2} \quad (2)$$

Note that the above discrete equation is numerically identical to the explicit leap-frog scheme with field components  $E_y(N\Delta t, i\Delta z, j\Delta x)$ ,  $H_x((N-1/2)\Delta t, (i-1/2)\Delta z, j\Delta x)$  and

$H_z((N-1/2)\Delta t, i\Delta z, (j-1/2)\Delta x)$ . Letting  $\theta_z = c\Delta t/\Delta z$ ,  $\theta_x = c\Delta t/\Delta x$ ,  $g_{i,j}^N = (\varepsilon_r E)_{i,j}^N$ ,

we rewrite (2) as

$$\begin{aligned} g_{i,j}^{N+1} + g_{i,j}^{N-1} &= 2g_{i,j}^N + \theta_z^2(E_{i-1,j}^N - 2E_{i,j}^N + E_{i+1,j}^N) + \theta_x^2(E_{i,j-1}^N - 2E_{i,j}^N + E_{i,j+1}^N) \\ &= F(E_{i,j}^N, E_{i-1,j}^N, E_{i+1,j}^N, E_{i,j-1}^N, E_{i,j+1}^N) \end{aligned} \quad (3)$$

We now show that a sufficient condition for (2) to be stable is that the function  $F$  is monotonically increasing. Defining  $E_{\min}^N = \min\{E_{i,j}^N\}$  and  $E_{\max}^N = \max\{E_{i,j}^N\}$  for all  $i$  and  $j$ , and observing that  $g = \varepsilon_r E$  is also maximum at  $E_{\max}$  and minimum at  $E_{\min}$ , we have from (3) that if  $F$  is monotonically increasing,

$$F_{\min} = F(E_{\min}^N, E_{\min}^N, E_{\min}^N, E_{\min}^N, E_{\min}^N) = 2g_{\min}^N, \quad (4)$$

$$\text{and } F_{\max} = F(E_{\max}^N, E_{\max}^N, E_{\max}^N, E_{\max}^N, E_{\max}^N) = 2g_{\max}^N. \quad (5)$$

It then follows from (3), (4) and (5) that

$$2g_{\min}^N - g_{\min}^{N-1} \leq g_{i,j}^{N+1} \leq 2g_{\max}^N - g_{\max}^{N-1} \quad \text{for all } i, j. \quad (6)$$

The above condition shows that  $g$  at any time step is always bounded by the extreme values at the previous time steps, implying that the numerical scheme (2) is stable.

The condition for  $F$  to be monotonically increasing is that all its first-order partial derivatives must be positive, which leads to the following stability condition for the nonlinear explicit scheme:

$$(c\Delta t)^2 \left( \frac{\partial g_{i,j}^N}{\partial E_{i,j}^N} \right)^{-1} \left[ \frac{1}{(\Delta z)^2} + \frac{1}{(\Delta x)^2} \right] \leq 1. \quad (7)$$

The above condition is similar to the CFL stability condition in linear schemes [1], except that in place of the linear relative permittivity  $\varepsilon_r$ , we have the term

$$\frac{\partial g_{i,j}^N}{\partial E_{i,j}^N} = \frac{\partial}{\partial E_{i,j}^N} (\varepsilon_r E)_{i,j}^N = \varepsilon_r (E_{i,j}^N) + \left( \frac{\partial \varepsilon_r}{\partial E} \right)_{i,j}^N E_{i,j}^N. \quad (8)$$

For third-order optical nonlinearity the permittivity depends on the intensity and can be expressed in the general form

$$\varepsilon_r = n_0^2 + f(|E|^2), \quad (9)$$

where  $n_0$  is the linear refractive index and  $f$  is a positive, monotonically increasing function describing the nonlinear model (e.g., exponential saturation, two-level saturation). We thus have

$$\frac{\partial g_{i,j}^N}{\partial E_{i,j}^N} = n_0^2 + f(|E_{i,j}^N|^2) + 2 \left( \frac{df}{dE} \right)_{i,j}^N |E_{i,j}^N|^2 \geq n_0^2. \quad (10)$$

Substituting (10) into (7) shows that the stability condition for the nonlinear scheme is equivalent to the CFL condition imposed in a linear medium with refractive index  $n_0$ .

For second-order optical nonlinearity, the relative permittivity is given by

$$\epsilon_r = n_0^2 + \chi^{(2)} E, \quad (11)$$

where  $\chi^{(2)}$  is the second-order susceptibility. In this case we have

$$\frac{\partial g_{i,j}^N}{\partial E_{i,j}^N} = n_0^2 + 2\chi^{(2)} E_{i,j}^N \geq n_0^2 - 2\chi^{(2)} E_{\max}, \quad (12)$$

where  $E_{\max}$  is the maximum field in the simulation. The stability condition of the FDTD scheme for second-order nonlinearity is thus equivalent to the CFL condition for a linear medium with relative permittivity equal to  $n_0^2 - 2\chi^{(2)} E_{\max}$ .

The above nonlinear stability conditions have been verified by performing FDTD simulations of waves propagating in nonlinear media. For third-order nonlinearity, simulations running at the linear CFL limit were observed to remain stable under continuous wave excitation; while for second-order nonlinearity, stability was achieved at a slightly smaller time step which corresponds to the CFL limit imposed on a linear medium with  $\epsilon_r = n_0^2 - 2\chi^{(2)} E_{\max}$ . In the simulations  $E_{\max}$  was estimated to be equal to the maximum input field.

### 3. Conclusions

We have presented a stability analysis for the explicit nonlinear FDTD method. The result and numerical verification indicate that for third-order optical nonlinearity the condition for the nonlinear scheme to be stable is identical to the linear CFL condition. The stability condition for the second-order nonlinearity is slightly more stringent than the CFL limit and depends on the estimated maximum field which occurs during the simulation. These stability conditions give the maximum time step that can be used in the FDTD simulation without causing unbounded growth in the numerical solution.

### References

- [1] Chu, S.T., and Chaudhuri, S.K., "Finite-difference time-domain method for optical waveguide analysis", *Progress in Electromagnetics Research 11* (editor: W.P. Huang), EMW Publishing, Cambridge, MA, pp. 255-300, 1995.
- [2] Ziolkowski, R.W. and Judkins, J.B., "Nonlinear finite-difference time-domain modeling of linear and nonlinear corrugated waveguides", *J. Opt. Soc. Am. B*, vol. 11, no. 9, pp. 1565-1575, Sep. 1994.
- [3] Joseph, R.M. and Taflove, A., "FDTD Maxwell's equations models for nonlinear electrodynamics and optics", *IEEE Trans. Antennas Propagat.*, vol. 45, no. 3, pp. 364-374, Mar. 1997.

# EXTENDED TIME-DOMAIN FINITE-DIFFERENCE BEAM PROPAGATION METHODS

Jun Shibayama, Tomokazu Takahashi, Junji Yamauchi, and Hisamatsu Nakano

College of Engineering, Hosei University

3-7-2, Kajino-cho, Koganei, Tokyo 184, Japan

Tel: 423-87-6190, Fax: 423-87-6381, e-mail: j.yma@k.hosei.ac.jp

## 1 Introduction

A finite-difference time-domain method (FD-TDM) has successfully been applied to electromagnetic problems including optical waveguides [1]. Although the FD-TDM can analyze the transient behavior of a propagating field, it consumes much computational time for the simulation of optically large structures. Therefore, a time-domain beam-propagation method (TD-BPM) based on the slowly-varying envelope approximation (SVEA) has received research attention in recent years [2]-[8]. We can employ larger time steps in the TD-BPM than those in the FD-TDM.

The conventional finite-difference TD-BPM [3]-[5] is based on the Crank-Nicholson scheme. Consequently, the truncation error in space is  $O(\Delta)^2$ , where  $\Delta$  is the transverse sampling width. On the other hand, the generalized Douglas (GD) [9] scheme attains a truncation error of  $O(\Delta)^4$ , provided that uniform or graded-index materials are treated [10]. This fact motivates us to apply the GD scheme to the TD-BPM for efficient analysis. After formulating the TD-BPM based on the GD scheme, we analyze the propagation of an optical pulse in a slab waveguide and demonstrate high efficiency of the method.

In the TD-BPM, analysis has been limited only to a two-dimensional problem and no literature has been found to treat a three-dimensional problem. Therefore, consideration is also given to the extension of the TD-BPM to circularly symmetric fields. To validate the method, we analyze a fiber Bragg grating and compare the result with that obtained from the FD-TDM [11].

## 2 TD-BPM based on the GD scheme

We present the brief derivation of the TD-BPM based on the GD scheme. After applying the SVEA to the wave equation and eliminating the second derivative in time, we obtain the following first-order equation:

$$-2j\frac{\omega n^2}{c^2}\frac{\partial E}{\partial t} = \frac{\partial^2 E}{\partial x^2} + \frac{\partial^2 E}{\partial z^2} + \frac{\omega^2 n^2}{c^2}E, \quad (1)$$

where  $\omega$  is the angular frequency,  $n$  is the refractive index and  $c$  is the speed of light in vacuum. Eq.(1) is discretized by the alternating-direction implicit (ADI) method based on the GD scheme [9]. After a bit of algebra, we obtain the following difference equation split into two steps [7]:

$$\eta_{x,i-1,j}^- E_{i-1,j}^{n+1/2} + \xi_{x,i,j}^- E_{i,j}^{n+1/2} + \eta_{x,i+1,j}^- E_{i+1,j}^{n+1/2} = \eta_{z,i,j-1}^+ E_{i,j-1}^n + \xi_{z,i,j}^+ E_{i,j}^n + \eta_{z,i,j+1}^+ E_{i,j+1}^n \quad (2)$$

$$\eta_{z,i,j-1}^- E_{i,j-1}^{n+1} + \xi_{z,i,j}^- E_{i,j}^{n+1} + \eta_{z,i,j+1}^- E_{i,j+1}^{n+1} = \eta_{x,i-1,j}^+ E_{i-1,j}^{n+1/2} + \xi_{x,i,j}^+ E_{i,j}^{n+1/2} + \eta_{x,i+1,j}^+ E_{i+1,j}^{n+1/2} \quad (3)$$

where

$$\eta_{\alpha,i,j}^\pm = -\frac{j\omega n_{i,j}^2}{6c^2\Delta t} \pm \frac{\omega^2 n_{i,j}^2}{48c^2} \pm \frac{1}{2\Delta\alpha^2}, \quad \xi_{\alpha,i,j}^\pm = -\frac{5j\omega n_{i,j}^2}{3c^2\Delta t} \pm \frac{5\omega^2 n_{i,j}^2}{24c^2} \mp \frac{1}{\Delta\alpha^2}$$

in which  $\alpha = x$  or  $z$ . Since (2) and (3) are the six-point schemes, they can readily be implemented with only slight modification to the conventional ADI-BPM algorithm.

To demonstrate high efficiency of the present method, we investigate the propagation of an optical pulse in a step-index slab waveguide whose core width is  $2d = 1.458\mu m$  (see Fig.1). The indices of the core and cladding are 3.6 and 3.564, respectively, and a wavelength of  $1.55\mu m$  is used. The optical pulse to be used consists of the fundamental mode profile in the transverse direction and the Gaussian profile with a  $1/e$  full-width of  $4\mu m$  in the longitudinal direction. The calculation region is  $14.58\mu m \times 40\mu m$ . The absorbing boundary regions are placed at the edges of the computational window.

Fig.2 shows the propagation distance of the peak of the optical pulse and the CPU time per propagation step. Each data is expressed as a function of  $\Delta z$ , and the propagation distance is observed at  $t = 200fs$ . For comparison, the results obtained with the conventional method are also shown. Here the time step and the transverse sampling width are fixed to be  $\Delta t = 1fs$  and  $\Delta x = d/5$ , respectively. It is found that the propagation distance of the present method almost converges to  $16.2\mu m$  with  $\Delta z = 0.05\mu m$  (Note that the exact propagation distance is calculated to be  $16.7\mu m$ ). For the conventional method, however, it is required that  $\Delta z$  be reduced to less than  $0.015\mu m$  so as to obtain the same accuracy. In this case, the present method can reduce the CPU time to one third of that in the conventional method, while maintaining the comparable accuracy.

### 3 TD-BPM for circularly symmetric fields

Next, we extend the TD-BPM to circularly symmetric fields in three-dimensional waveguides. The first-order equation in cylindrical coordinates is expressed as

$$-2j\frac{\omega n^2}{c^2}\frac{\partial E}{\partial t} = \frac{\partial^2 E}{\partial r^2} + \frac{1}{r}\frac{\partial E}{\partial r} + \frac{\partial^2 E}{\partial z^2} + \frac{\omega^2 n^2}{c^2}E. \quad (4)$$

Eq.(4) can be discretized by the ADI method. When  $r = 0$ , L'Hospital's rule is utilized. The resultant finite-difference equations for  $r \neq 0$  are

$$-A_{r,i-1,j}^-E_{i-1,j}^{n+1/2} + B_{r,i,j}^+E_{i,j}^{n+1/2} - A_{r,i+1,j}^+E_{i+1,j}^{n+1/2} = C_{z,i,j-1}E_{i,j-1}^n + B_{z,i,j}^-E_{i,j}^n + C_{z,i,j+1}E_{i,j+1}^n \quad (5)$$

$$-C_{z,i,j-1}E_{i,j-1}^{n+1} + B_{z,i,j}^+E_{i,j}^{n+1} - C_{z,i,j+1}E_{i,j+1}^{n+1} = A_{r,i-1,j}^-E_{i-1,j}^{n+1/2} + B_{r,i,j}^-E_{i,j}^{n+1/2} + A_{r,i+1,j}^+E_{i+1,j}^{n+1/2} \quad (6)$$

where

$$A_{r,i,j}^\pm = \frac{1}{2\Delta r^2} \pm \frac{1}{4(i-1)\Delta r^2}, \quad B_{\alpha,i,j}^\pm = -\frac{2j\omega n_{i,j}^2}{c^2\Delta t} \mp \frac{\omega^2 n_{i,j}^2}{4c^2} \pm \frac{1}{\Delta \alpha^2}, \quad C_{z,i,j} = \frac{1}{2\Delta z^2}$$

in which  $\alpha = r$  or  $z$ . It is again found that the equations to be solved are tridiagonal matrices to which the standard solution scheme can be applied.

To validate the present method, we analyze a fiber Bragg grating shown in Fig.3. The refractive indices of the core are  $n_+ = 1.55$  and  $n_- = 1.50$ , respectively. The index of the cladding is  $n_{cl} = 1.45$ . The radius of the core is  $\rho = 1.0\mu m$ . The grating period is  $\Lambda_+ = \Lambda_- = 0.25\mu m$  and there are 60 periods in the core. The numerical parameters are  $\Delta r = \rho/19.5$ ,  $\Delta z = 0.025\mu m$ , and  $\Delta t = 1fs$ . An incident field is a pulse wave generated by a one-way excitation [12]. Due to its symmetry, we analyze only the lower half of Fig.3.

Fig.4 shows the power reflectivity as a function of wavelength, in which the data is calculated by the discrete Fourier transform. For comparison, the result obtained from the FD-TDM [11] is also included. Note that  $\Delta t$  in the FD-TDM should be less than  $0.11fs$  from the stability criterion, when the same sampling widths mentioned above are used. It is found that the TD-BPM result agrees well with that obtained from the FD-TDM [11], although  $\Delta t$  is ten times larger than that in the FD-TDM. This fact contributes to reduction in computational time.

### 4 Conclusion

We have presented two extended TD-BPMs: one is based on the GD scheme for efficient analysis and the other is extended to circularly symmetric fields in three-dimensional waveguides. In the former, the effectiveness is demonstrated through the analysis of optical pulse propagation. In the latter, the validity is confirmed by the power-reflectivity analysis of a fiber Bragg grating.

## References

- [1] W. P. Huang et al., IEEE Photon. Technol. Lett., vol.5, pp.1071-1073, 1993.
- [2] M. Scalora and M. E. Crenshaw, Optics Commun., vol.108, pp.191-196, 1994.
- [3] R. Y. Chan and J. M. Liu, IEEE Photon. Technol. Lett., vol.6, pp.1001-1003, 1994.
- [4] P. L. Liu et al., IEEE Photon. Technol. Lett., vol.7, pp.890-892, 1995.
- [5] G. H. Jin et al., IEEE Photon. Technol. Lett., vol.9, pp.348-350, 1997.
- [6] F. Ma, J. Lightwave Technol., vol.15, pp.1974-1985, 1997.
- [7] J. Shibayama et al., IEICE Trans. C-1, vol.81, pp.38-39, 1998.
- [8] M. Hikari et al., IEICE Trans. C-1, vol.81, pp.667-672, 1998.
- [9] J. Yamauchi et al., J. Lightwave Technol., vol.14, pp.2401-2406, 1996.
- [10] J. Shibayama et al., J. Lightwave Technol., vol.17, no.4, 1999.
- [11] J. Yamauchi et al., Opt. Quantum Electron., vol.29, 451-460, 1997.
- [12] J. Yamauchi et al., Opt. Lett., vol.22, pp.259-261, 1997.

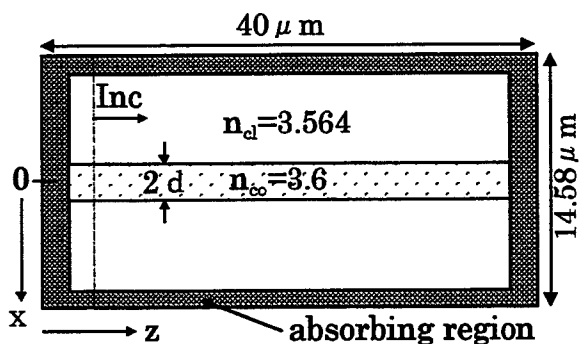


Fig.1 Slab waveguide geometry.

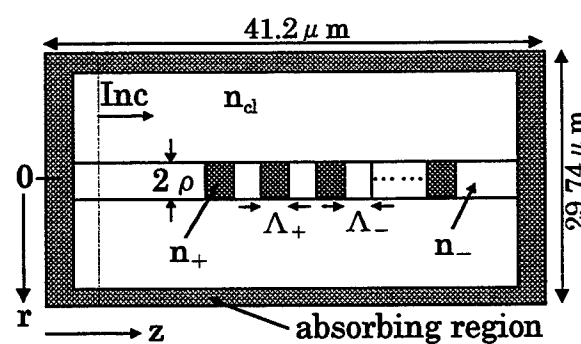


Fig.3 Fiber grating geometry.

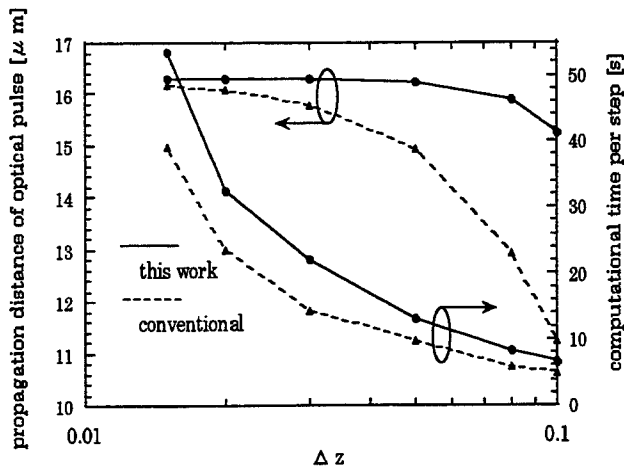


Fig.2 Propagation distance  
of optical pulse and CPU time.

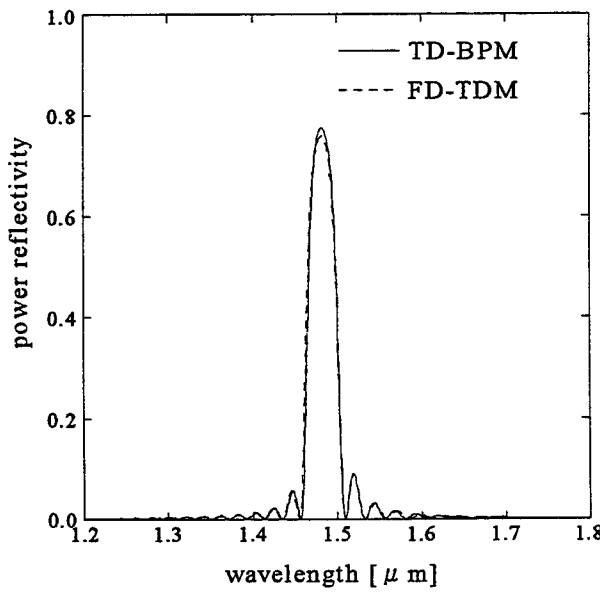


Fig.4 Power reflectivity as a function of wavelength.

N-space staircase-free Finite-Difference Time-Domain formulation for  
arbitrary material distributions: numerical investigations of a focusing  
grating coupler in dielectric waveguides

Kim Dridi, Center for Communications, Optics and Materials, COM, bldg 349, Technical University of Denmark, 2800 Lyngby, Denmark,

Email: kd@com.dtu.dk, Telephone: +45 45 88 14 44, Fax: +45 45 93 65 81

Jan S. Hesthaven, Div. of Applied Mathematics, Brown University, Box F, Providence, RI 02912, USA  
Email: jansh@cfm.brown.edu, Telephone: (401) 863-2671, Fax: (401) 863-1355

**Introduction:** The never-ending quest for higher capacity in higher speed communication and computing systems justifies the ongoing miniaturization and integration of optical waveguide technology and components of diverse optical electromagnetic properties. This puts high requirements on modeling and design tools. These should offer modest simulation times and good accuracy in space and time. Furthermore, the complex sub-wavelength geometry and multi-dimensional material composition of optical devices often prohibits an exact analytical solution and deceives the intuitive understanding of their physics. A number of two-dimensional vectorial numerical methods such as the Finite-Difference Time-Domain (FDTD) method [1] and the spectral method [2,3] have successfully been applied to Maxwell's equations for a wide range of optical simulations. The FDTD method has the advantage of being relatively simple in its formulation, in its definition of the geometry (grid-layout), and is the most popular method. However, the FDTD approach based on the classical Yee scheme [4] with quadratic cell mapping in space gives the modeled structures a "staircase nature" and requires many points per wavelength to efficiently resolve the geometry. Furthermore, the classical FDTD approach is not suited for arbitrary geometries with multiple materials as the electromagnetic boundary conditions are not automatically nor exactly imposed and satisfied at these boundaries [5]. This presents a source of local spatial errors to add to the numerical dispersion. The larger the computational domain and the more complex material distributions are, the more the noise accumulates in the numerical solution. These errors grow at least linearly in time. In order to enforce the boundary conditions, eliminate the effects of staircasing and reduce the required number of points per wavelength, a stable second and fourth order accurate FDTD formulation is presented. The numerical scheme can be adapted and applied on dielectrics as well as perfect electric conductors (PEC) in any coordinate system. Numerical investigations will demonstrate its greater efficiency and its direct applicability to arbitrary geometries. The design of an efficient two-dimensional focusing grating coupler integrated in dielectric waveguides will be presented and its performance analyzed numerically.

**The numerical method:** To introduce the numerical scheme, we consider Maxwell's equations in a Cartesian coordinate system in one-dimensional space (see Fig. 1)

$$\left[ \frac{\partial E_y}{\partial t}, \frac{\partial H_z}{\partial t} \right] = \left[ \frac{1}{n^2(x)} \frac{\partial H_z}{\partial x}, \frac{\partial E_y}{\partial x} \right], \quad (1)$$

where  $E_y$  is the electric field normalized with the free-space intrinsic impedance,  $H_z$  is the magnetic field,  $n(x)$  the refractive index, while  $t$  and  $x$  are the dimensionless time and space variable, respectively. The mapping in space is done in such a way that each sub-domain is homogeneous with respect to optical-electromagnetic material parameters. We define our computational window to include physical space defined in  $[x_1; x_N]$ . The grid line contains  $N$  segments where  $h_x = (x_N - x_1)/(N - 1)$ . We have investigated the stability and accuracy of staggered and non-staggered schemes for Maxwell's equations numerically and found that, in accordance with [6], the staggered schemes are more attractive in terms of accuracy and stability. We therefore apply the staggered scheme such that the electric and magnetic field points alternate, separated by  $0.5h_x$ . Each sub-domain has 2 outer points within its area, before or on the material boundaries on its left and right side. These outer points can either be "electric or magnetic field points". Each area is then assigned two values,  $\gamma_l$  and  $\gamma_r$ , where  $\gamma_l h_x$  is the distance from the left boundary to the first point in the area and  $\gamma_r h_x$  the distance from the right boundary to the last point in the area. Obviously,  $\gamma$  values are to be found within  $[0; 0.5]$ . We can then find finite difference weights to evaluate derivatives of any order  $m$ , approximated to any level of accuracy, say, of order  $\nu$ , at any point  $x'$  with the help of an algorithm based on Lagrange interpolation polynomials [7]. The point  $x'$  need not be a grid point. We denote by

$$W_{[\frac{\partial}{\partial x}]^{(m)} \zeta(x')}^{\nu} \quad (2)$$

the mentioned evaluation of field component  $\zeta$ 's  $m$ 'th derivative with respect to  $x$ , at  $x'$ , to the accuracy order  $\nu$ . We use fourth order accurate Runge-Kutta methods for the time derivatives [8]. In the next sections, we will discuss a few specific materials and the adaptation of the method with respect to these, as the formulation depends on the material boundary conditions of the fields.

**Non-magnetic, charge free, dielectrics:** As a testcase, we consider non-magnetic, charge free materials with multiple dielectrics and zero surface charge densities. At  $x_\gamma$  (see Fig. 1), the boundary conditions express that the tangential electric and magnetic fields are continuous at the material boundaries [9]. For the moment we disregard situations where  $\gamma$  has the exact value of zero. They can be avoided by "off-setting" the grid by a small amount of space. We will later comment on this special case. We consider the second order accurate case ( $\nu = 2$ ) for simplicity. In this case all spatial derivatives at inner points in each area are computed as in the Yee scheme with two symmetrically surrounding points. The spatial derivatives at outer points are evaluated using the following approximations of order  $(\nu - 1)$  and by applying the field boundary conditions. We describe the case where area  $I$  "ends with a magnetic field point  $H_M$ " and area  $I + 1$  "starts with an electric field point  $E_1$ ". The other case is treated similarly.

$$\left[ \frac{\partial E_1}{\partial t}, \frac{\partial H_M}{\partial t} \right] \left[ \frac{1}{n_{I+1}^2} W_{[\frac{\partial}{\partial x}]^{(1)} H(x_1^{I+1})}^1(H_{\gamma_I^I}, H_1), W_{[\frac{\partial}{\partial x}]^{(1)} E(x_M^I)}^1(E_M, E_{\gamma_I^{I+1}}) \right] \quad (3)$$

In the evaluations above we indicate in parentheses the field points needed to make the weighted interpolation. In evaluating the field derivatives at outer points we incorporate and apply the electromagnetic boundary conditions in a way to secure that field information is communicated in between areas, as area  $I$  gets tangential electric field data  $E_{\gamma_I^{I+1}}$ , while area  $I + 1$  gets tangential magnetic field data  $H_{\gamma_I^I}$ , extrapolated in the following manner.

$$[H_{\gamma_I^I}, E_{\gamma_I^{I+1}}] [W_{[\frac{\partial}{\partial x}]^{(0)} H(x_\gamma)}^1(H_{M-1}, H_M), W_{[\frac{\partial}{\partial x}]^{(0)} E(x_\gamma)}^1(E_1, E_2)] \quad (4)$$

**Results:** Actual simulations show that the new method has  $L_2$  errors that are orders of magnitude lower than the Yee scheme for the same resolution. Numerical investigations have been performed in the design phase of a focusing grating coupler (FGC) in dielectric waveguiding materials described in [1]. The two-dimensional FGC is a miniaturized diffractive optical element (DOE) where the surface-relief profile is etched on top of the filmlayer. We define the profile  $p(x')$  in the cartesian coordinate system shown in Figure 2, where the planar waveguide consists of a filmlayer of thickness  $0.65\lambda$  ( $\lambda$  being the free-space wavelength) outside the grating region, and a substrate, of refractive indices 1.58 and 1.47, respectively. The optical electromagnetic field propagates in the positive  $x'$  direction and is diffracted into free-space above the DOE in the corrugated region of length  $L$ . The incident field is chosen as the solution to the planar waveguide geometry and sees the effective refractive index  $n_{eff} = 1.51312$  as discussed in [1]. In order to optimize the structure with respect to the diffraction efficiency in a reduced focal area (spotsize) and minimize power losses in unwanted directions, we first combine the geometric requirement for obtaining a focus in  $0 < z < 2L$  and  $-L/2 < x < L/2$  with the grating equation [1] to form an "educated guess" at

$$\frac{1}{\Lambda(x')} = \left[ \frac{x' - L_f}{\sqrt{a^2 f^2 + (x' - L_f)^2}} + n_{eff} \right], \quad (5)$$

the grating's spatial frequency profile, where  $L_f$ ,  $f$  and  $a$  are focus-positioning parameters. Figure 2 shows the near-field intensity pattern for this device with  $L/\lambda = 100.0$ ,  $A(x')/\lambda = 0.10075$ ,  $L_f/\lambda = 96.49$ ,  $f/\lambda = 100.0$ , and  $a = 2.3$ , around the focal region as a function of space variables. The asymmetry in the patterns is clearly due to the asymmetric grating profile. The focus is found at  $z/\lambda = 113$  for a DOE length of  $L/\lambda = 100.0$ . The main lobe at the focus has a width of  $1.79\lambda$  (with a main lobe truncation at the gaussian beam width  $1/e^2$ ) whereas the classical diffraction limit of a lens of diameter  $L$  and focal length  $f$  is  $2.44\lambda f/L = 2.44\lambda$  as predicted by geometrical optics. The new

models can be used for the further optimization of this design at vastly reduced computational expense. Further details will be found in [10].

**Conclusions:** We have developed an efficient FDTD method that eliminates the effects of staircasing and reduces the required number of points per wavelength needed to accurately resolve the modeled geometry. The  $L_2$  errors of the new methods prove to be orders of magnitude lower than the ones for the Yee scheme. For a given accuracy, the new methods are more efficient as they require fewer points per wavelength. Furthermore, the new method makes it possible to perform optical-electromagnetic simulations on arbitrary geometries with complex material distributions efficiently in cartesian coordinate systems. The method has been applied to perfect electric conductors as well as dielectrics with numerical schemes of spatial accuracy of order 2 and 4. The design of a promising miniaturized focusing grating coupler has been performed. Its focusing efficiency is higher than what would be expected of a classical geometrical optical lense. Further results for the multi-domain formulation with second and fourth order accuracy will be presented with comparisons to the Yee scheme for several dielectric and PEC materials.

#### References:

- [1] K. Dridi, A. Bjarklev, "Optical electromagnetic vector-field modeling for the accurate analysis of finite diffractive structures of high complexity", J. of Applied Optics, to be published in 1999.
- [2] B. Yang, D. Gottlieb and J.S. Hesthaven, "Spectral Simulations of Electromagnetic Wave Scattering", J. Comput. Phys. 134(2), pp.216-230.
- [3] P.G. Dinesen, J.S. Hesthaven, J.P. Lynov, "Pseudo-spectral method for the analysis of diffractive optical elements", J. of Opt. Soc. America A, submitted.
- [4] K.S. Yee, "Numerical solution of initial boundary value problems involving Maxwell's equations in isotropic media", IEEE Transactions on Antennas and Propagation, 1966, pp. 302-307.
- [5] S. Abarbanel, A. Ditkowsky, A. Yefet, "Bounded Error Schemes for the Wave Equation on Complex Domains", ICASE Report No. 98-50, NASA Langley Research Center Hampton, November 1998, p. 17.
- [6] D. Gottlieb, B. Yang, "Comparisons of staggered and non-staggered schemes for Maxwell's equations". Conference Proceedings, 12th Annual Review of Progress in Applied Computational Electromagnetics at the Naval Postgraduate School, Monterey, CA, March 18-22, 1996, pp. 1122-1130.
- [7] B. Fornberg, "Calculation of weights in finite difference formulas", SIAM Review, vol. 40, p. 685-691
- [8] Canuto, Hussaini, Quarteroni, Zang, "Spectral Methods in Fluid Dynamics". Springer-Verlag, 1988, p. 108
- [9] Ramo, Whinnery, Van Duzer, "Fields and Waves in Communications Electronics.", 3d edition, Wiley, 1994, pp. 145-149.
- [10] K. Dridi, A. Ditkowsky, J.S. Hesthaven "Stable high-order Cartesian grid methods for hyperbolic problems in general geometries.", J. of Computational Physics, submitted.

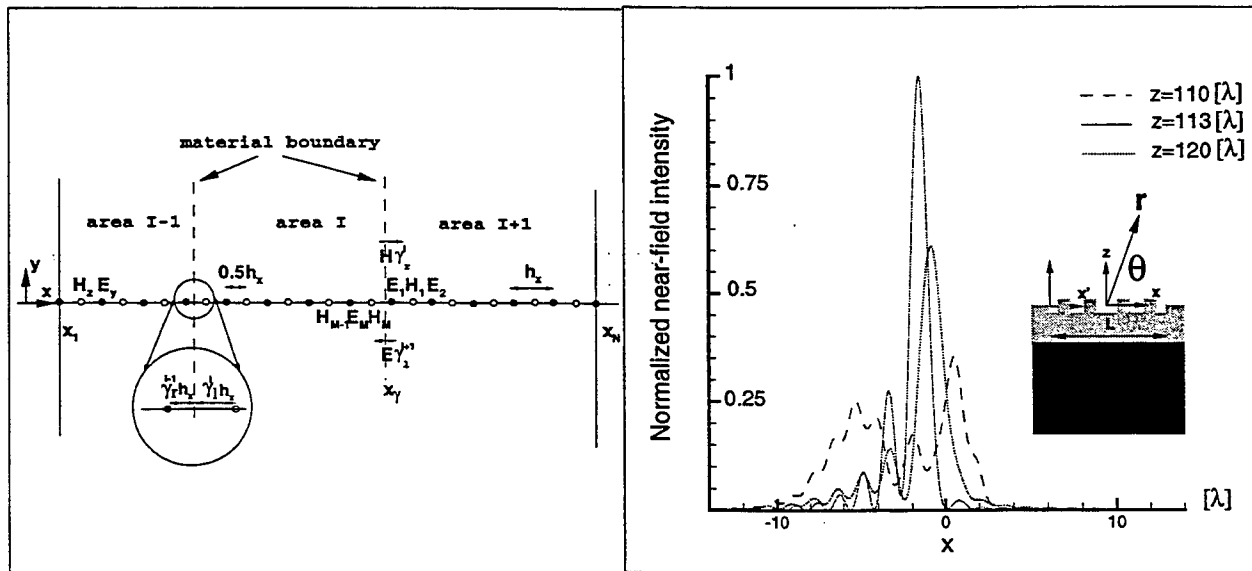


Figure 1: Mapping in one-dimensional space composed of several areas with different refractive indices. A staggered grid is defined in a cartesian coordinate system.

Figure 2: Focusing grating coupler-near-field intensity distribution as a function of space. The fields right above the FGC surface are computed with the FDTD method. Exact radiation integrals are then used to evaluate the intensity through space.

## Modeling of thin dielectric layers in finite difference schemes

Stefan F. Helfert and Reinhold Pregla

FernUniversität, D-58084 Hagen, Germany

e-mail: Stefan.Helfert@FernUni-Hagen.de R.Pregla@FernUni-Hagen.de

**Introduction:** Numerical methods are widely used for the modeling of optical waveguides because it is difficult or even impossible to obtain analytical solutions. Among these numerical methods a lot of algorithms base on finite differences (FD). To analyze complicated structures like those with thin layers the obvious solution is the use of a very fine grid. However, the numerical effort can be enormous in this case. Hence, the current research deals with reducing this numerical effort, e.g. by introducing higher order finite difference schemes (e.g. [1],[2]) or by studying the treatment of dielectric boundaries in the FD-scheme (e.g. [3]). In this paper we will describe a modification of the finite differences by using an analytic approach due to very thin dielectric layers if we want to use a relative coarse mesh. Similar examinations have been done for thin metal layers [4], and for dielectric boundaries [5]. In the latter paper also formulas for thin layers have been given. However, those expressions could be improved significantly, as will be shown by the numerical results.

**Theory:** In this section we will describe the modification of the finite difference scheme due to thin dielectric layers. The formulas will be given in a form allowing the direct implementation into the method of lines (MoL) [6][7] though they may also be used for other finite difference algorithms. The MoL is a special finite difference algorithm in which the discretization is done only as far as necessary while analytic solutions are used otherwise. Applying the MoL the structure is divided into homogeneous sections in the direction of propagation ( $z$ ). We will examine only such homogeneous sections here. Now, consider the structure shown in Fig. 1 including a thin layer (width  $w$ ). In each of the three regions ( $i = 1, 2, t$ ) the wave equation for TE- as well as for TM-polarization is:

$$\left( \frac{\partial^2}{\partial z^2} + \frac{\partial^2}{\partial x_i^2} + \varepsilon_{ri} \right) \psi_i = 0 \quad (1)$$

All overlined quantities have been normalized to the free wave-space number  $k_0$ , e.g.  $\bar{z} = k_0 z$ ,  $\psi$  stands for the tangential field components ( $E_y$ -TE,  $H_y$ -TM) or for the component of a vector potential. (For the sake of simplicity we will use the name potential in the rest of the paper, though it may also be a field component.) Following the MoL the wave equation is discretized in  $x$ -direction by finite differences while analytic expressions are used for the description of the  $z$ -dependence. Due to the discretization the continuous potentials are only determined on discrete lines labeled  $k$  and  $k+1$  in Fig. 1. (Note: No line is placed inside the thin layer.) The transition from continuous potentials to discrete ones is indicated by different notations ( $\psi \rightarrow \Pi$ ). The wave equation on line  $k$  ( $\varepsilon_k$ : discretized permittivity) in discrete form is:

$$\frac{d^2 \Pi_k}{d \bar{z}^2} + \frac{\Pi_{k-1} - 2\Pi_k + \tilde{\Pi}_{k+1}}{\bar{h}_x^2} + \varepsilon_k \Pi_k = 0 \quad (2)$$

If not all  $\Pi_\nu$  ( $\nu = k-1, k, k+1$ ) in (2) are within the same homogeneous region, we have to use extrapolated values (i.e. for  $\Pi_{k+1}$  in Fig. 1 indicated by ' $\sim$ ').

The goal is to determine the extrapolated value  $\tilde{\Pi}_{k+1}$  as function of the original ones ( $\Pi_k$  and  $\Pi_{k+1}$ ). To find useful expressions we rewrite the wave equation (1):

$$\left( \frac{\partial^2}{\partial x_i^2} - Q_i^2 \right) \psi_i = 0 \quad \text{with} \quad Q_i = \sqrt{-\frac{\partial^2}{\partial z^2} - \varepsilon_{ri}} \quad (3)$$

Formally, the solution of (3) for each of the three regions (1,2,t) in Fig. 1 is:

$$\psi_i = \cosh(Q_i \bar{x}_i) \cdot A_i + \sinh(Q_i \bar{x}_i) \cdot B_i \quad (4)$$

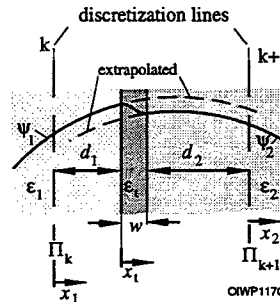


Fig. 1 Structure with a very thin layer

At the interfaces between the different sections the tangential field components have to be matched, resulting in expressions for  $\psi$  and for the first derivative of  $\psi$  with respect to  $\bar{x}$ . The matching expressions read (coordinate system see Fig. 1):

$$\begin{aligned}\psi(\bar{x}_1 = \bar{d}_1) &= \psi(\bar{x}_t = 0) & \psi(\bar{x}_t = \bar{w}) &= \psi(\bar{x}_2 = -\bar{d}_2) \\ \frac{1}{\varepsilon_1^\mu} \frac{\partial \psi}{\partial \bar{x}_1} \Big|_{\bar{x}_1=\bar{d}_1} &= \frac{1}{\varepsilon_t^\mu} \frac{\partial \psi}{\partial \bar{x}_t} \Big|_{\bar{x}_m=0} & \frac{1}{\varepsilon_1^\mu} \frac{\partial \psi}{\partial \bar{x}_t} \Big|_{\bar{x}_t=\bar{w}} &= \frac{1}{\varepsilon_t^\mu} \frac{\partial \psi}{\partial \bar{x}_2} \Big|_{\bar{x}_2=-\bar{d}_2} \end{aligned} \quad \text{with } \mu = \begin{cases} 0 & \text{TE} \\ 1 & \text{TM} \end{cases} \quad (5)$$

Due to the analytical solution (4) we obtain from this matching process:

$$\begin{aligned}\cosh(X_1)A_1 + \sinh(X_1)B_1 &= A_t \\ P_1[\sinh(X_1)A_1 + \cosh(X_1)]B_1 &= P_t B_t \\ \cosh(X_t)A_t + \sinh(X_t)B_t &= \cosh(X_2)A_2 + \sinh(-X_2)B_2 \\ P_t[\sinh(X_t)A_t + \cosh(X_t)]B_t &= P_2[\sinh(-X_2)A_2 + \cosh(X_2)]B_2\end{aligned} \quad (6)$$

where we introduced the abbreviations

$$X_i = Q_i \cdot \bar{d}_i \quad P_i = Q_i / \varepsilon_i^\mu \quad i = 1, 2, t \quad (d_t = w)$$

The chosen coordinate system yields that  $A_1$  and  $A_2$  are identical to the potentials on the discretization lines [ $A_1 = \psi_1(x_1 = 0)$ ,  $A_2 = \psi_2(x_2 = 0)$ ]. Hence, we must replace the other terms ( $B_1$ ,  $B_2$ ,  $B_t$  and  $A_t$ ) by  $A_1$  and  $A_2$ . We obtain from (6):

$$B_1 = a_{11}A_1 + a_{12}A_2$$

with

$$\begin{aligned}\det &= -[\cosh(X_t)\sinh(X_1) + \sinh(X_t)b_{t1}\cosh(X_1)] \cdot \cosh(X_2) \\ &\quad + b_{2t}[\sinh(X_t)\sinh(X_1) + \cosh(X_t)b_{t1}\cosh(X_1)] \cdot \sinh(X_2) \\ \det \cdot a_{11} &= \cosh(X_2)[\cosh(X_t) \cdot \cosh(X_1) + \sinh(X_t) \cdot b_{t1} \cdot \sinh(X_1)] \\ &\quad - \sinh(X_2)b_{2t}[\sinh(X_t)\cosh(X_1) + \cosh(X_t) \cdot b_{t1} \cdot \sinh(X_1)] \\ \det \cdot a_{12} &= -1 \quad b_{2t} = P_2^{-1}P_t \quad b_{t1} = P_t^{-1}P_1\end{aligned} \quad (7)$$

All derivations up to this point have been done analytical. However, (7) contains hyperbolic sine and cosine functions of formal operators. Thus, we must find suitable formulas for numerical evaluation. For this purpose we introduce Taylor series:

$$\cosh(X) = 1 + X^2/2 + X^4/4! + \dots \quad \sinh(X) = X + X^3/3! + \dots \quad (8)$$

Now, extrapolating the continuous potential by using (4) (see Fig. 1)

$$\psi_1(x_1 = h_x) = \cosh(Q_1 \bar{h}_x)A_1 + \sinh(Q_1 \bar{h}_x)(a_{11}A_1 + a_{12}A_2) \quad (9)$$

we obtain by introducing the Taylor series (8) into (7) the following expression for the extrapolated potential in discrete form:

$$\tilde{\Pi}_{k+1} = \left( g_1 + g_2 \frac{\partial^2}{\partial \bar{z}^2} \right) \Pi_k + \left( g_3 + g_4 \frac{\partial^2}{\partial \bar{z}^2} \right) \Pi_{k+1} \quad (10)$$

Hence, the discretized wave equation on the line  $k$  takes the following form (the formulas for the line labeled  $k+1$  are analogous):

$$\frac{\partial^2}{\partial \bar{z}^2} \left[ \left( 1 + \frac{g_2}{\bar{h}_x^2} \right) \Pi_k + \frac{g_4}{\bar{h}_x^2} \Pi_{k+1} \right] + \frac{\Pi_{k-1} + (g_1 - 2)\Pi_k + (g_3 + 1)\Pi_{k+1}}{\bar{h}_x^2} + \varepsilon_k \psi_k = 0 \quad (11)$$

Keeping in mind what  $Q_i^2$  stands for in (3) we find that due to the Taylor series in (8) and because of the products in (9) terms of the form

$$\left( -\frac{\partial^2}{\partial \bar{z}^2} - \varepsilon_{r\alpha} \right) \left( -\frac{\partial^2}{\partial \bar{z}^2} - \varepsilon_{r\beta} \right) \quad (\varepsilon_{r\alpha}, \varepsilon_{r\beta} - \text{any of the permittivities } \varepsilon_{r1}, \varepsilon_{r2}, \varepsilon_{rm})$$

occur. Since the second derivative with respect to  $\bar{z}$  appears only linearly in (10)–(11), we must find (partial) a reasonable estimation for  $\partial^2/\partial \bar{z}^2 = -\varepsilon_{eff}$ . Omitting all terms of the form  $Q_\alpha^2 Q_\beta^2$  ( $\alpha, \beta = 1, 2, t$ ) as has been done in [5] we find formulas where such an estimation is not required.

**Numerical results:** The derived FD-scheme has been introduced into the Method of lines [6] [7]. We examined a slab waveguide with a film-layer smaller than the discretization distance (see Fig. 2). A parameter  $u$  was introduced measuring the distance between one boundary and a fixed discretization line. The fundamental modes (TE and TM) were determined as function of  $u$ . Fig. 2 shows the normalized effective index  $B$  [ $B = (n_{eff}^2 - n_s^2)/(n_f^2 - n_s^2)$ ] computed with the presented FD-scheme and compared with analytical values. The Taylor series for the hyperbolic cosine function in (8) were developed to the order  $m$ . This  $m$  was used as parameter in Fig. 2. We observe in the TE- as well as in the TM-case only a small variation of  $B$  ( $5^{th}$  digit). Using higher order terms ( $m = 4$ ) gives better results than choosing  $m = 2$ . However, a further increase of this order does not improve the results significantly so that  $m = 4$  is a good choice. Also shown are results obtained by omitting products of the form  $Q_\alpha^2 Q_\beta^2$  ("no higher term") as has been done earlier [5]. In this case the  $4^{th}$  digit of  $B$  becomes different showing the improvement because of the formulas given in this paper.

When the width of the thin layer is zero, the derived expressions can also be used for modifying the FD-Scheme at interfaces. Thus, the formulas were used to examine a Bragg-grating. The TE-case has been examined exhaustively within the COST-240 project where also the authors of this paper participated [8] [9] [10](chap.3.4). It has been reported earlier [5] that in the TE-case the results were independent of the mesh position whereas the TM-polarization was not treated that satisfactorily, yet. Now, by considering higher terms in the Taylor series (8) the results could be improved. Fig. 3 shows the reflection coefficient as function of the number of periods, determined for different positions of the mesh relative to the boundaries (see inlay). Comparing the values for 2000 periods of the curves for  $u = 0$  and  $u = 0.3$  we find a difference  $\Delta|r| \approx 0.2$  which corresponds to a relative difference of approx. 10%. However, it should be mentioned that this variation is still higher than in the TE-case [5], though the (analytic) effort is higher for the TM-polarization.

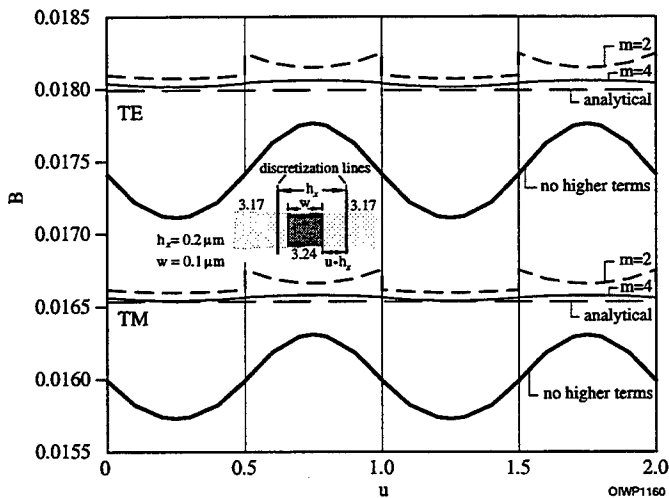


Fig. 2 Normalized effective index vs.  $u$

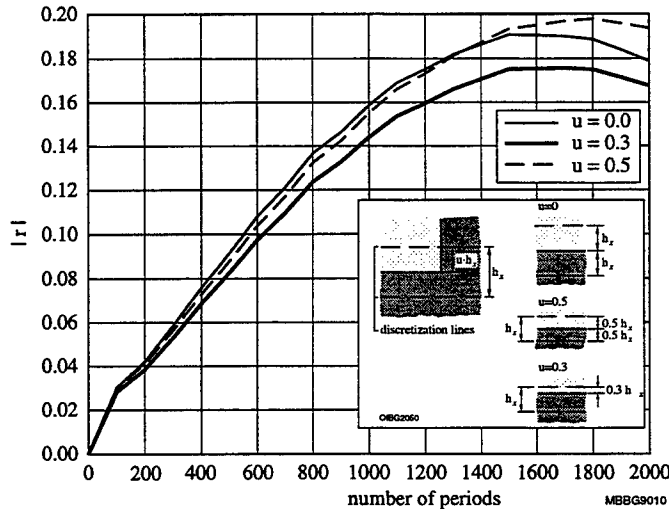


Fig. 3 Reflection coefficient vs. number of periods

## References

- [1] G. R. Hadley, *J. Lightwave Technol.*, vol. 16, no. 1, pp. 134–141.
- [2] R. Stoffer and H. J. W. M. Hoekstra, *Opt. Quantum Electron.*, vol. 30, pp. 375–383, 1998.
- [3] Charles Vassallo, *IEE Proc.-J*, vol. 139, no. 2, pp. 137–142, 1992.
- [4] O. Conradi, S. Helfert, and R. Pregla, *Opt. Quantum Electron.*, no. 5/6, vol. 30, pp. 369–373, 1998 corrected version no. 1, vol. 31, 1999.
- [5] S. F. Helfert and R. Pregla, accepted for publication in *Opt. Quantum Electron.* special issue on Optical Waveguide Theory and Numerical Modelling, 1999
- [6] R. Pregla and W. Pascher, in *Numerical Techniques for Microwave and Millimeter Wave Passive Structures*, T. Itoh, (Ed.), pp. 381–446. J. Wiley Publ., New York, USA, 1989.
- [7] R. Pregla, in *Methods for Modeling and Simulation of Guided-Wave Optoelectronic Devices*, W.P. Huang, (Ed.), number PIER 11 (EMW Publishing, Cambridge, Massachusetts, USA, 1995) pp. 51–102.
- [8] S. F. Helfert and R. Pregla, *J. Lightwave Technol.*, vol. 16, no. 9, pp. 1694–1702, 1998.
- [9] J. Čtyroký, S. Helfert, and R. Pregla, *Opt. Quantum Electron.*, vol. 30, pp. 343–358, 1998.
- [10] Georg Guekos, (Ed.), *Photonic devices for telecommunications*, Springer Verlag, Heidelberg, Germany, 1998.



**Integrated Photonics Research**

# **Optical Transmission and WDM Modeling**

**Tuesday, July 20, 1999**

**Carl M. Weinert, Heinrich-Hertz Institute, Germany**  
Presider

**RTuJ**  
**3:30pm–5:00pm**  
Sierra Madre North

## New Approaches to Modeling High Data Rate Optical Fiber Transmission

C. R. Menyuk

Department of Computer Science and Electrical Engineering  
University of Maryland Baltimore County  
Baltimore, MD 21250  
tel. no. (410)-455-3501

The invention of erbium-doped fiber amplifiers has powered a tremendous growth in the capacity of optical fiber transmission systems. In just a decade, systems have gone from capacities of 200 Mbits/sec to 240 Gbits/sec, and the capacities keep climbing. I have no doubt that the figure of 240 Gbits/sec that I just mentioned will be too low by roughly a factor of two by the time this summary sees the light of day!

This tremendous growth in capacity has not come without cost. Prior to the invention of the Er-doped optical fiber amplifier, the optical fiber was essentially a hollow tube. Fiber impairments did not matter because they were removed every 20 km by the repeaters. By contrast, amplifiers only compensate for attenuation, allowing the impairments due to chromatic dispersion, nonlinearity, and polarization effects to accumulate unchecked. Additionally, the amplifiers add amplified spontaneous emission (ASE) noise to the system, setting a minimum level on the power required to achieve an acceptable signal-to-noise ratio and thus assuring that nonlinearity plays a role in the system behavior. The four effects just mentioned—the four horsemen of optical fiber transmission—interact in a complex way, necessitating the use of sophisticated numerical approaches to design systems that can ameliorate these effects using a reasonable amount of computer time.

There is still some controversy about what formats are of most practical use in communication systems. The debates on TDM (time division multiplexing) vs. WDM (wavelength division multiplexing) and solitons vs. NRZ still go on to some degree. However, these old debates are slowly winding down. The optical fiber communication community appears as a practical matter to have converged on a uniform approach to these issues. Individual channels are multiplexed up in the time domain to the highest levels for which

electronic transmitters and receivers exist. At that point, further multiplexing is carried out in the wavelength domain. Dispersion management and return-to-zero formats are increasingly used and whether the transmitted pulses are referred to as solitons, chirped RZ, or something else is almost a matter of taste.

My colleagues and I have been responding to these changes by developing new approaches to study communication systems. These approaches include applications of multiple length scale methods to determine the equations, split-step integration methods for solving the equations, and reduced methods that are used under circumstances in which the full numerical models are too time-consuming.

The length scales in the optical fiber divide naturally into three groups: (1) A short scale from  $10^{-6} - 10^{-4}$  m in which Maxwell's equations apply. (2) An intermediate length scale from  $10^{-4} - 10^3$  m in which the coupled nonlinear Schrödinger equation applies and in which birefringence effects in the fiber predominate. (3) A long length scale from  $10^3 - 10^8$  m in which nonlinear and dispersive effects are important. In the first regime, one must use Maxwell's equations. In the second regime, the coupled nonlinear Schrödinger equation applies. In the third regime, in which one averages over the rapidly varying birefringence, the coupled Manakov-PMD equation applies. When, in addition, polarization mode dispersion is negligible and light is launched in a single polarization state, the usual nonlinear Schrödinger equation applies. All the textbook derivations of the nonlinear Schrödinger equation to date assume a perfectly circular fiber and therefore do not include all the correct physics.

In addition to applying the multiple length scale approach to derive the Manakov-PMD equation and from there the nonlinear Schrödinger equation, we have pursued other applications. First, we may take advantage of the short length scale in which bits in highly dispersive channels pass through each other to average over the rapid variations. This approach allows us to avoid problems with the scaling of WDM system simulations in which the time required scales as the square of the number of channels. Second, we have studied long-term polarization effects using a model in which we only follow the Stokes parameters for each channel. Doing so allows us to examine the statistics of hundreds of thousands of fibers and predict the probability of failure over the system lifetime.

Another area of inquiry is improving the methods we use to explore random effects. There are two main sources of random variations. The first is randomly varying birefringence in the fibers; the second is the ASE noise from the amplifiers. Traditionally, both these effects have been modeled using Monte Carlo methods. We have been exploring the use of linearization to replace Monte Carlo methods. These have previously been used around an *assumed* undisturbed signal evolution, but our work is the first to linearize around an arbitrary, numerically-determined signal. To date, we have successfully applied this approach to calculate the timing jitter and energy fluctuations of soliton, RZ, and NRZ pulses. These results have also been successfully compared to our group's experiments and result in vast computational savings. We are now extending this approach to the calculation of eye diagrams.

Our modeling effort has worked hand-in-glove with an experimental effort to study dispersion-managed solitons in a 100 km recirculating loop. By carefully including all the key physical effects, in particular gain saturation in the optical amplifiers, we have been able to obtain superb agreement between the models and the experiments for not only the dynamical evolution but also the noise margins. When we extended these results from 10 Gbits/sec to 20 Gbits/sec, we predicted in advance of the experiments the distances that should be obtainable. When we failed to obtain those distances at first, we pinpointed a poor extinction ratio in the source as the culprit. This study led us to search for a better source and, ultimately, to our world record distance  $\times$  length product, thus indicating the value of a strong modeling effort.

In conclusion, optical fiber transmission systems are rapidly changing, and, within the last five years, it has become generally recognized that optical fiber modeling has a critical role to play in designing transmission systems. New algorithms that can respond to the current situation have been created by ourselves and by others and continue to be an intellectually exciting area in which to work as new ideas continue to percolate.

This work was supported by AFOSR, DOE, and NSF.

# Wavelength-Domain Simulation: an efficient technique for the design of Multiwavelength Optical Networks

I. Roudas<sup>†</sup>, N. Antoniades<sup>†</sup>, D. H. Richards<sup>†</sup>, J. L. Jackel<sup>†</sup> and R. E. Wagner<sup>§</sup>

<sup>†</sup>Telcordia Technologies (formerly Bellcore), 331 Newman Springs Rd., Red Bank, NJ 07701-5699, USA

<sup>‡</sup>Previously with Bellcore. Currently with Corning Inc., 2200 Cottontail Ln., Somerset, NJ 08873, USA.

<sup>§</sup>Previously with Bellcore. Currently with Corning Inc., Corning, NY 14831, USA

Corresponding author: I. Roudas, Tel: (732)748-3716, Email: roudasj@corning.com

**Introduction –** Efficient computer-aided design of the optical transport layer of large-scale multiwavelength optical networks requires an abstract and simplified computer representation for the optical signals and network components.

This paper reviews the wavelength-domain representation of optical signals and network components. In this representation, optical signals are characterized by their carrier wavelength and average power exclusively and not by their temporal waveform, as is customary in simulation of analog and digital communication systems [1]. In addition, the constituent parts of the network are fully characterized by their loss or gain as a function of wavelength.

In the following, the key assumptions and concepts of wavelength-domain representation are summarized and an example of implementation is presented.

**Principles –** It is assumed that the constituent parts of the optical transport layer do not alter the shape of the signal waveforms (quasi-transparent components). Signal distortion due to linear or non-linear effects is ignored. The action of the network components consists in a simple scaling of the signal power by a multiplicative factor (gain or loss).

The constituent parts of the network are described by step-like transmittance transfer functions (Fig. 1). The wavelength axis is discretized into  $N$  wavelength bins. The choice of the wavelength bin size is arbitrary and depends on the desired accuracy. Typically, the wavelength bin bandwidth is several times the bit-rate. The central wavelengths of these wavelength bins define a grid. In Fig. 1, only five nodes of the wavelength grid are shown. The gain or loss is assumed to be approximately constant within a single wavelength bin but may be different for signals at adjacent wavelength bins. The gain or loss may also vary as a function of time but this variation is slow compared to the bit period (quasi-static components). The phase transfer functions of the network components are discarded.

The representation of the optical signals differs depending on if they occupy one or several wavelength bins (narrowband or wideband optical signals respectively). For simulation purposes, we define three different types of optical signals, namely optical signals produced by laser sources (narrowband), ASE noise (wideband), and interference (narrowband). Each type is represented separately. 1) Optical signals produced by laser sources are fully characterized by a pair of numbers (carrier wavelength, average power) and are represented by a single point in the (wavelength, power) space. 2) ASE noise is represented by a set of  $N$  pairs of numbers (i.e. values of the average power at the nodes of the grid). 3) Interfering terms originating from the same laser source as an optical signal and recombining with it after propagation through different optical paths (i.e. multipath optical crosstalk) are represented as distinct narrowband optical signals in the same wavelength bin as the optical signal. The modulation, phase and polarization of all types of optical signals is ignored.

For illustration purposes, Fig. 2 shows the wavelength-domain representation of an optical signal produced by a laser source contaminated by ASE noise and six multipath interferers. Similar to Fig. 1, only five nodes of the wavelength grid are shown. All signal power is concentrated into the third wavelength bin (black column). ASE noise power is distributed into all five wavelength bins (white columns). The six multipath interferers, denoted by  $x_1-x_6$ , are represented by distinct gray columns in the same wavelength bin as the optical signal.

A WDM signal composed of  $M$  individual optical signals is represented in the wavelength-domain by a set of  $M$  3-D graphs similar to Fig. 2, one for each different laser source.

As optical signals, ASE noise, and optical crosstalk pass from one module to the other, their average powers at the  $N$  grid nodes are multiplied by the corresponding values the gain/loss of the modules. It is thus possible to evaluate the average powers of optical signal, ASE noise, and optical crosstalk at every point of the network.

The above simplified representation is advantageous in terms of execution speed compared to other, more accurate representations [1]. The price to pay is that all distortion impairments can not be studied in the wavelength-domain.

**MONET wavelength-domain simulation tool** – A general purpose simulation tool based on the above representation was implemented in the context of the Multiwavelength Optical Networking (MONET) project [2]. This tool can compute the optical signal, ASE noise and linear optical crosstalk power spectra at all points in the network in both steady-state and transient regime.

Fig. 3 shows the organization of the optical library of the MONET wavelength-domain simulation tool. An indicative list of modules is given on the right side in Fig. 3. The modules of the optical library are divided into three hierarchical categories, namely Network Elements, Network Element Components, and Elementary Units. Each module is implemented using different designs, technologies, and simulation models, and can have uni- or bi-directional fiber interfaces, steady-state or dynamic properties, and so forth. Modules can be combined in any order to simulate various WDM network topologies.

A modeling example of a uni-directional four Wavelength Add-Drop Multiplexer (WADM) ring topology is shown on the left side of Fig. 3. The WADMs are represented by circles. At the next hierarchical level, the architecture of a simplified Wavelength Add-Drop Multiplexer (WADM) [2] is shown. The depicted WADM consists of two EDFA (1), a multiplexer/demultiplexer (MUX/DMUX) pair (2), 2x2 optical switches for signal adding/dropping (3), and variable attenuators for power equalization (4). At the lowest hierarchical level, the structure of the EDFA is shown. In this particular example, the EDFA are identical single-stage forward-pumped amplifiers, composed of two isolators (5), a laser diode (6), a wavelength selective coupler (WSC) (7), and a strand of Erbium-Doped Fiber (EDF) (8).

The MONET wavelength-domain simulation tool was used in the past to study automatic gain control in Erbium-doped fiber amplifiers (EDFA) and EDFA chains [3], network topologies [4], [5], and network functionalities [6], [7]. To illustrate the computing capabilities of the MONET wavelength-domain simulation tool, sample results will be presented at the conference.

This work was performed as a part of the MONET consortium under DARPA funding agreement MDA 972-95-3-0027.

## References

- [1] K. S. Shanmugam, "Simulations and implementation tools for signal processing and communication systems", *IEEE Comm. Mag.*, pp. 36-40, Jul. 1994.
- [2] R. E. Wagner, R. C. Alferness, A. A. M. Saleh, and M. S. Goodman, "MONET: Multiwavelength optical networking," *J. Lightwave Technol.*, vol. 14, pp. 1349-1355, Jun. 1996.
- [3] D. H. Richards, J. L. Jackel, and M. A. Ali, "A theoretical investigation of dynamic all-optical automatic gain control in multichannel EDFA's and EDFA cascades," *IEEE J. Select. Topics Quantum Electron.*, vol. 3, pp. 1027-1036, Aug. 1997.
- [4] N. Antoniades, I. Roudas, R. E. Wagner, and S. F. Habiby, "Simulation of ASE noise accumulation in a wavelength add-drop multiplexer cascade," *IEEE Phot. Tech. Lett.*, vol. 9, pp. 1274-1276, Sep. 1997.
- [5] N. Antoniades, I. Roudas, R. E. Wagner, T. E. Stern, J. L. Jackel, and D. H. Richards, "Use of wavelength- and time-domain simulation to study performance degradations due to linear optical crosstalk in WDM networks," *OSA TOPS, Opt. Net. Appl.*, vol. 20, pp. 288-293, 1998.
- [6] I. Roudas, J. L. Jackel, D. H. Richards, N. Antoniades, and J. E. Baran, "Transient effects in wavelength add-drop multiplexer chains," in *Optical Fiber Communication Conference (OFC)*, no. TuR2, (San Diego, CA), OSA, Feb. 1999.
- [7] D. H. Richards, J. L. Jackel, I. Roudas, W. Xin, N. Antoniades, and M. Ali, "Method for detecting fiber cuts in a WDM ring with saturated EDFA's," in *Optical Fiber Communication Conference (OFC)*, no. FJ4, (San Diego, CA), OSA, Feb. 1999.

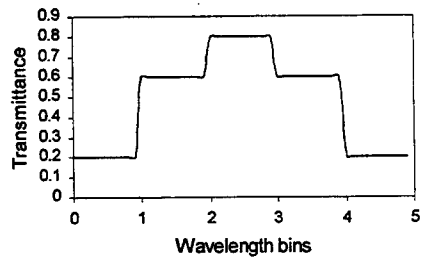


**Fig. 1** Wavelength-domain representation of an optical component.

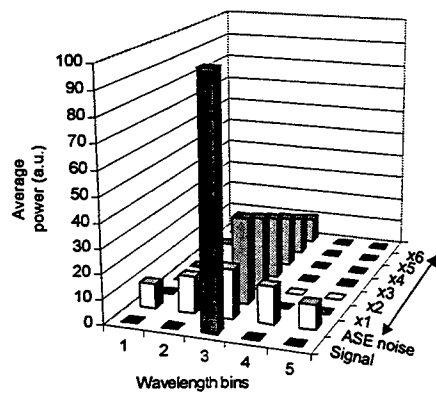


**Fig. 2** Wavelength-domain representation of an optical signal contaminated with ASE noise and interference.

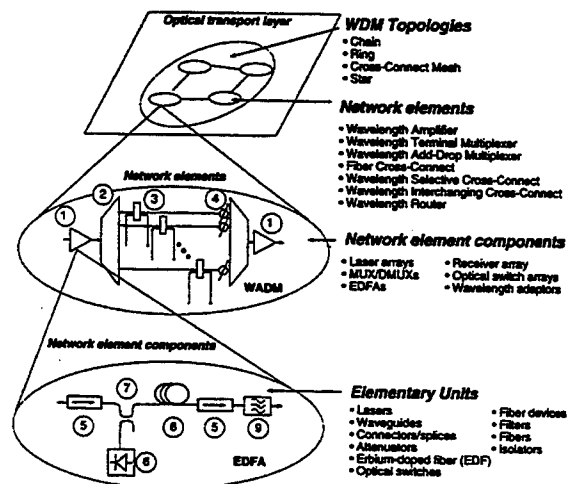


**Fig. 3** Hierarchical organization of the MONET wavelength-domain simulation tool.

# Dynamic dispersion compensation using a parabolic phase apertured active arrayed-waveguide grating

Michael C. Parker\*, and Stuart D. Walker<sup>†</sup>

\* Fujitsu Telecommunications Europe Ltd. Research,  
Northgate House, St Peter's St, Colchester, Essex, CO1 1HH, UK.  
Tel: +44 1206 363000, Fax: +44 1206 363009  
Email: M.Parker@ftel.co.uk

<sup>†</sup>University of Essex, Department of Electronic Systems Engineering,  
Wivenhoe Park, Colchester, Essex, CO4 3SQ, UK.  
Tel: +44 1206 872413, Fax: +44 1206 872900  
Email: stuwal@essex.ac.uk

Dispersion compensation (DC) techniques are now seen as a critical element in the design of future high-capacity lightwave communication systems. DC can be achieved by both fibre Bragg gratings (FBGs) [1] [2] and arrayed-waveguide gratings (AWGs) [3] [4]. Whilst dynamically tunable FBGs have been recently reported [5], there is apparently no AWG with equivalent characteristics. In this paper, we present an AWG design which is tunable and has dynamic dispersion compensation capability. We also provide a novel theory, based on Fourier-Fresnel diffraction integrals, which describes the DC behaviour of the device. Simulation results show good agreement and indicate that an optimum AWG phase profile exists which can easily produce both positive and negative DC of the order of 3.1ns/nm. Features of such AWG compensators are expected to include: multiwavelength control, non-mechanical operation and compact realisation.

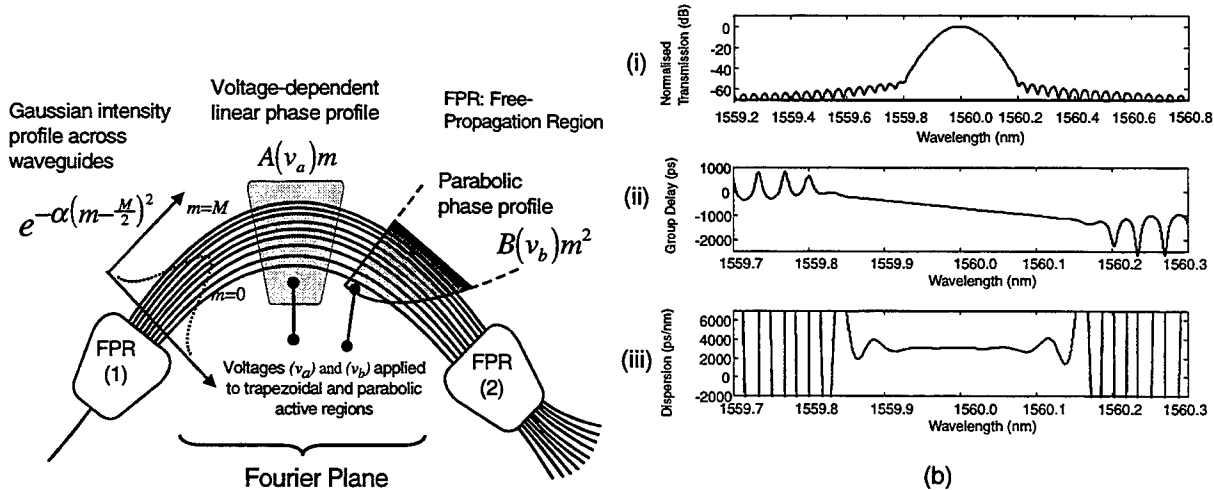


Figure 1: a) Schematic of dynamic dispersion compensating AWG with trapezoidal and parabolic active regions b) Typical spectral plot  $|t(\lambda)|^2$ , group delay  $\tau_d(\lambda)$  and dispersion characteristic  $D(\lambda)$ .

Figure 1a shows a schematic of a two contact active AWG which we have used for our simulations. The parabolic shaped active region (B) causes increasing phase differences between adjacent guides resulting in passband widening due to superposition of the detuned spectra (analogous to a defocusing lens.) A side-effect of the parabolic phase profile is an associated centre-wavelength shift, which is removed by a

compensating trapezoidal active region (A) as shown. Such tuning compensation is difficult to achieve with a variable-chirped FBG, which suffers a similar problem [5]. The basic equation describing the spectral amplitude transmission  $t(\lambda)$  after a parabolic and linear phase aperture function in the Fourier plane of an AWG is given by:

$$t(\lambda) = \sum_{m=0}^M e^{-\alpha(m-\frac{M}{2})^2 + j\frac{2\pi n \Delta l}{\lambda} (A(v_a)m + B(v_b)m^2)} \quad (1)$$

where  $\lambda$  is the wavelength,  $\alpha$  determines the  $1/e$ -width of the Gaussian amplitude profile,  $n$  is the material passive refractive index, and  $\Delta l$  is the incremental pathlength difference between neighbouring waveguides, there being  $M+1$  waveguides in the array. The voltage-dependent coefficient  $A(v_a)$  determines the central wavelength  $\lambda_0$  of the AWG passband, while the voltage-dependent coefficient  $B(v_b)$  controls the strength of the parabolic phase-profile and hence the degree of dispersion compensation. For retuning the AWG passband centre back to  $\lambda_0$ , the relationship between the coefficients  $A(v_a)$  and  $B(v_b)$  is given by  $A(v_a) \approx 1 - MB(v_b)$ . Equation (1) can be understood as a discrete version of the Fresnel-Kirchoff diffraction integral, with both linear and quadratic terms, leading to hybrid Fourier-Fresnel diffraction. The transmission transfer function can thus be written in an analytic, closed form by the use of Fresnel Cosine and Sine integrals [6], thus:

$$t(\lambda) \approx \sqrt{\frac{\pi}{2}} \frac{M}{2b} \{C_1(a+b) - C_1(a-b) + jS_1(a+b) - jS_1(a-b)\} e^{j\phi} \quad (2)$$

where the normalised parameters  $a, b$  and  $\phi$  are given as follows:

$$a = \frac{\pi(\lambda_0 - \lambda)}{2FSR \sqrt{\frac{B\pi(\lambda_0 - \lambda)}{2FSR} + j\frac{\alpha}{4}}} \quad (3a) \quad b = M \sqrt{\frac{B\pi(\lambda_0 - \lambda)}{2FSR} + j\frac{\alpha}{4}} \quad (3b)$$

$$\phi = \frac{\pi M(\lambda_0 - \lambda)}{FSR} - \frac{\pi^2(\lambda_0 - \lambda)^2}{4FSR^2 \left( \frac{B\pi(\lambda_0 - \lambda)}{2FSR} + j\frac{\alpha}{4} \right)} \quad (3c)$$

and  $FSR = \frac{\lambda_0^2}{n\Delta l}$  is the AWG free-spectral range. The approximation sign of equation (2) is introduced by treating the series summation of equation (1) as an integral summation centered on a wavelength  $\lambda_0$ . We have modelled an active AWG with  $FSR = 4.8\text{nm}$ ,  $\lambda_0 = 1560\text{nm}$ ,  $n = 1.5$ , and 128 arrayed-waveguides. The normalised filter power response  $|t(\lambda)|^2$  is depicted in figure 1b(i), while the group delay  $\tau_d(\lambda)$  across the passband width is shown in figure 1b(ii). The associated dispersion characteristic  $D(\lambda)$  is plotted in figure 1b(iii), and is equal to 3100ps/nm across the 3dB width of the filter passband. For passband-flattened operation of the parabolic-phase profiled AWG, the optimum value of the Gaussian parameter  $\alpha$  is taken to be  $\alpha \approx 1.24 \left(\frac{2}{M}\right)^2$ , in accordance with standard synthetic aperture theory [7]. However, for dispersion compensation, the uniformity of the dispersion spectral characteristic  $D(\lambda)$  is optimised for  $\alpha \approx 4.5 \left(\frac{2}{M}\right)^2$ , which minimises the dispersion variance ( $\sigma^2$ ) as shown in figure 2a. Slight ripple is still present at the centre of the dispersion characteristic  $D(\lambda)$ , as is evident in figure 1b(iii).

Active AWG phase response  $\theta(\lambda)$  is a combination of three factors: linear and broadly parabolic terms about  $\lambda_0$ , corresponding to the phase profile  $\phi(\lambda)$  of equation (3c); and an additional phase response due to the Fresnel integrals, which follows the form of the Cornu spiral [8]. The group delay response  $\tau_d(\lambda)$  for a filter is given by the differentiation of the filter phase-response  $\theta(f)$  with respect to the frequency  $f$ , such that  $\tau_d = -\frac{d\theta(f)}{df} \approx \frac{\lambda_0^2}{c} \frac{\partial \theta(\lambda)}{\partial \lambda}$ .  $D(\lambda)$ , the dispersion characteristic, is given by the additional differentiation of  $\tau_d$  with respect to  $\lambda$ , yielding approximately:

$$D = \frac{\partial \tau_d}{\partial \lambda} \approx \frac{27\lambda_0^3 \pi^3}{112FSR^3 c \left[ \left( \frac{\pi \lambda_0 B}{2FSR} \right)^2 + \frac{\alpha^2}{16} \right]} B \quad (4)$$

Thus the dispersion  $D$  of the device tends to be proportional to the strength of the parabolic phase profile  $B$ , and hence proportional to the voltage  $v_b$  applied to the parabolic active region. However, as the

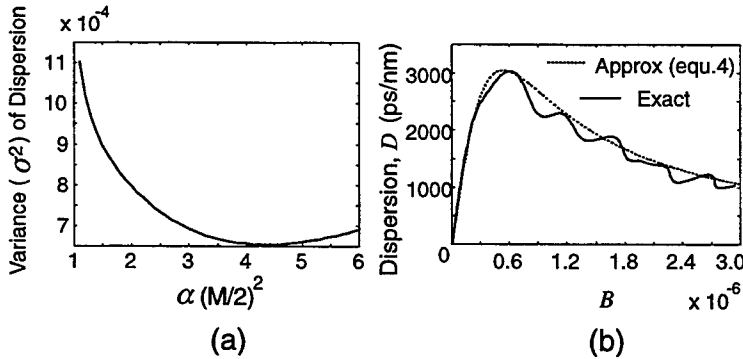


Figure 2: a) Optimisation of dispersion variation  $\sigma^2$  with Gaussian parameter  $\alpha$  b) Variation of dispersion characteristic  $D(\lambda_0)$  with voltage-dependent coefficient  $B$ .

parameter  $B$  increases further, the dispersion  $D$  starts reducing as the quadratic term in the denominator starts to dominate. Figure 2b plots the approximation of equation (4), and the simulated response  $D(\lambda_0)$  as  $B$  is varied, showing a close functional agreement. Equation (4) indicates an inverse cubic dependence of the dispersion with the AWG FSR, which allows substantial increases in DC capability accompanied by only marginal reductions in the FSR.

In conclusion, we have described a novel technique for dynamic dispersion control using an AWG consisting of trapezoidal and parabolic shaped active regions. Simulations have shown that dispersion compensation of up to  $\pm 3100$ ps/nm is possible. In principle, further higher-order polynomial-profiled active regions could be added to the AWG Fourier plane, to achieve dynamic compensation for the higher-order dispersion effects which are becoming evident in high-capacity lightwave communication systems.

## References

- [1] F. Ouellette, J.-F. Cliche, and S. Gagnon. All-fiber devices for chromatic dispersion compensation based on chirped distributed resonant coupling. *IEEE Journal of Lightwave Technology*, 12:1728–1738, 1994.
- [2] G. Lenz, B.J. Eggleton, C.K. Madesen, C.R. Giles, and G. Nykolak. Optimal dispersion of optical filters for WDM systems. *IEEE Photonics Technology Letters*, 10(4):567–569, 1998.
- [3] C. Dragone, C.A. Edwards, and R.C. Kistler. Integrated optics  $N \times N$  multiplexer on silicon. *IEEE Photonics Technology Letters*, 3(10):896–899, 1991.
- [4] A.J. Lowery and P.C.R. Gurney. 270-km 10Gbit/s WDM dispersion compensation using a chirped AWGM. *Proc. OFC'99*, San Diego, California:Paper FD5, February 1999.
- [5] B.J. Eggleton, J.A. Rogers, P.S. Westbrook, and T.A. Strasser. Electrically tunable power efficient dispersion compensating fiber Bragg gratings for dynamic operation in a nonlinear lightwave system. *Proc. OFC'99*, San Diego, California:Paper PD27, February 1999.
- [6] M.C. Parker and S.D. Walker. Bandpass filter transfer characteristic of a complex-apodised arrayed-waveguide grating. *Proc. OFC'99*, San Diego, California:Paper WM21, February 1999.
- [7] M.C. Parker and S.D. Walker. Design of arrayed-waveguide gratings using hybrid Fourier-Fresnel transform techniques. *submitted to IEEE Journal of Special Topics in Quantum Electronics on Fiber-Optic Passive Components*.
- [8] M.Born and E.Wolf. Principles of Optics. *Pergamon Press*, 6<sup>th</sup> Edition:430–433, 1959.

# Active Arrayed-Waveguide Gratings for Equalisation and WDM channel management

A. Yiptong, M.C. Parker\* and R.J. Mears

Cambridge University Engineering Department, Trumpington St., Cambridge CB2 1PZ  
Tel. (44) 1223 332784; Fax (44) 1223 332662 e-mail: rjm@eng.cam.ac.uk

\*Fujitsu Telecom Europe Ltd. Research, Northgate House, St. Peter's St., Colchester, CO1 1HH, UK,  
Tel. +44(0)1206 363007; Fax +44(0)1206 363009; e-mail: M.Parker@ftel.co.uk

## I. INTRODUCTION

Arrayed-waveguide gratings (AWGs) [1] are emerging as an important technology in optical telecommunications, generally functioning as passive multiplexers and demultiplexers for WDM. In this paper, we describe how an active AWG could potentially be configured as: an equalising filter; a channel dropping (suppressing) filter to yield optical add/drop multiplexing functionality; and a space/wavelength switch. This is achieved by actively tailoring the optical pathlength of each waveguide within the array to achieve a pre-determined passband response. Flattening of the passband response is also possible, as demonstrated in simulation results. Recent work [2] has demonstrated the possibility of dynamic phase modulation on individual waveguides in an array, so that the powerful holographic [3] techniques presented in this paper allow the AWG to become a dynamic device with full control of the light in the output waveguides. The phase-only conditioning of the Fourier-plane of the AWG is also attractive since it implies optimum use of the available light.

## II. FILTER DESIGN

The design of the AWG can be considered as a beam-propagation problem on the input and output waveguide couplers and a Fourier-plane design problem over the arrayed waveguides [4], as indicated in figure 1. In conventional AWG design the lengths of successive waveguides have a regular (monotonic) relationship. The designs presented here are realised by allowing the deviation in the optical pathlength of successive waveguides to differ from their usual relationship by up to  $\pm \pi$ , with a quantisation of four bits. By dividing the design problem in this way, digital optimisation techniques based on the FFT can be used to find the appropriate waveguide optical pathlengths according to the desired functionality. In this work we have used the simulated annealing algorithm [5] to find the best match to a given target passband response. The cyclical frequency response of the AWG gives rise to a correspondence between target filter responses with multiple spatial outputs at a single frequency, and targets with multiple frequency outputs at a single spatial output. This feature enables the design of filters with complex passband characteristics, as required for example by equalising filters and optical add/drop multiplexers.

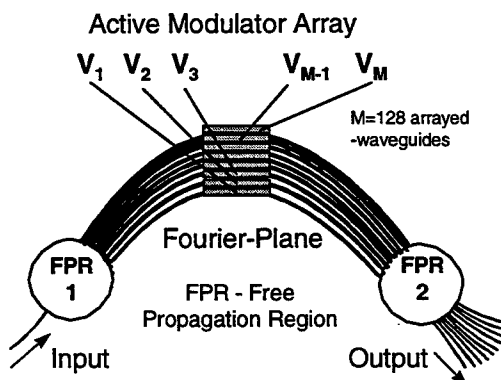


Figure 1: Schematic of active AWG, with phase-modulation in the Fourier-plane

### III. EQUALISING FILTER

As the number of WDM channels is increased, the demand for well-specified spectral equalisation of optical amplifiers becomes more urgent. If, as seems likely, there is a move towards greater optical transparency in switching, the need for dynamic control of WDM channels will become paramount. The “digital filter design” presented above will allow AWGs to fulfil this role. AWG devices using a similar phase-modulation technology have already been demonstrated [6], but the active waveguide array has been positioned within a Mach-Zehnder configuration rather than in the Fourier-plane of the AWG. In the case of individual phase-modulator failure, the Fourier-plane configuration will integrate the loss in performance across the spectral range of operation, whereas the Mach-Zehnder embodiment will tend to suffer the complete loss of a channel.

In our simulation, we have taken the design of a spectral equaliser required to compensate for a (hypothetical) 12dB dynamic range over the amplifier passband. In this case the target filter response is specified in narrow frequency bands about each of the 8 controlled channels and the optimisation is made for a four-bit quantisation of the relative pathlength difference. By using the full four bits, the errors between the target and AWG response can be reduced to less than 1dB. Figure 2 depicts the simulation results for an AWG consisting of 128 active waveguides, with a free-spectral range (FSR) equal to 6.4nm, equalising  $8 \times 100\text{GHz}$  channels over a 12dB dynamic range. In addition to the equalising functionality, good inter-channel amplified spontaneous emission (ASE) suppression >20dB is also achieved. Note that the cyclical frequency response of the AWG would allow this technique to be simply extended, for example to the control of 80 channels, by preceding 10 of these active AWGs by a passive passband-flattened (3dB-width = 6.4nm) conventional AWG of FSR=64nm.

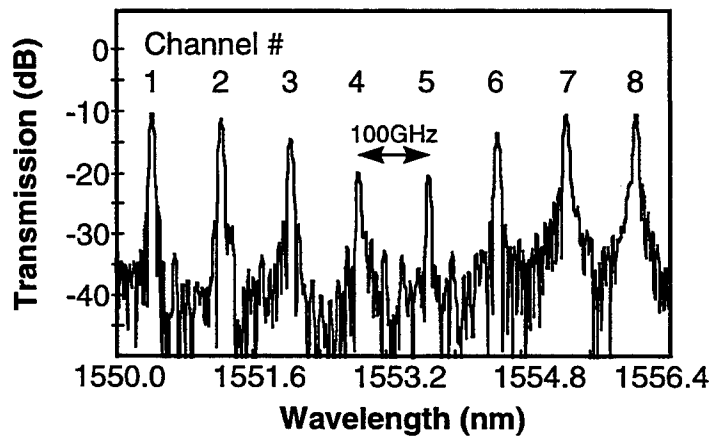


Fig.2 Simulation results for active AWG functioning as an equalising filter

Of great importance is the robustness of this design to fabrication tolerances. In order to test this, varying levels of random pathlength “jitter”, corresponding to  $\lambda/16$ ;  $\lambda/8$ ;  $\lambda/4$  and  $\lambda/2$  of the total optical pathlength deviation in the design have been simulated. The results are encouraging - the effect is barely noticeable at the  $\lambda/16$  level and at  $\lambda/8$  there is a small additional excess loss (~1dB) with little distortion of the passband shape. The design begins to break down for a pathlength jitter of  $\lambda/4$ . Hence 3-bit quantisation would tend to be sufficient, but we have adopted 4-bit quantisation.

### IV.CHANNEL DROPPING FILTER

The very good inter-channel suppression suggests that the filter design algorithm can also be used to realise arbitrary channel dropping (/combining) filters. As an example we present the same active AWG filter, but with a filter response designed to pass channels 1,2,4,6,7,8 and drop (suppress) channels 3 and 5. The simulated filter response is shown in Fig.3. The filter design algorithm has also been adapted to enable passband flattening, as is evident in the figure. This makes the device more robust to laser wavelength fluctuations, as well as temperature effects. However, this is at the expense of channel suppression of only

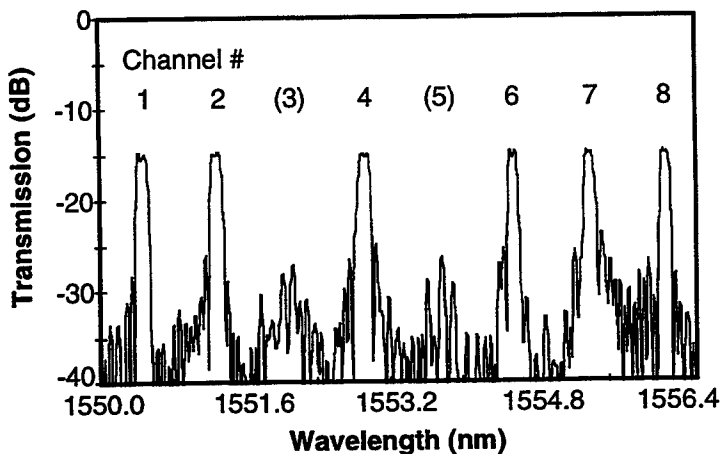


Fig. 3 Results for AWG design to implement channel dropping filter

15dB, and a greater device insertion loss. A higher number of arrayed-waveguides, and/or a reduced degree of passband broadening would improve both these figures.

## VI. CONCLUSIONS

In conclusion, we have described a novel holographic technique to achieve a variety of WDM functions by using a phase-modulation active AWG. Simulations have demonstrated EDFA equalisation of 12dB for 8×100GHz spaced WDM channels, with inter-channel ASE suppressed by greater than 20dB. Optical add/drop multiplexing of arbitrary channels has also been simulated with channel suppression of 15dB. The filter channel response has also been broadened to provide greater tolerance to temperature effects and wavelength fluctuations. The holographic designs are robust to individual phase-modulator failures and fabrication phase errors.

## REFERENCES

- [1] C. Dragone, C.A. Edwards, and R.C. Kistler, "An  $N \times N$  Optical Multiplexer Using a Planar Arrangement of Two Star Couplers", *IEEE Photonics Tech. Lett.*, vol. 3, no. 9, pp. 812-815, Sep. 1991.
- [2] S.M. Jackson et al., "A novel optical phase modulator design suitable for phased arrays", *IEEE Journal of Lightwave Technology*, vol.16(11), pp.2016-2019, 1998
- [3] M.C. Parker, A.D. Cohen, R.J. Mears, "Dynamic digital holographic wavelength filtering", *IEEE Journal of Lightwave Technology*, vol.16(7), pp.1259-1270, 1998
- [4] G. Lenz, B.J. Eggleton, C.K. Madeson, C.R. Giles and G. Nykolak, "Optimal dispersion of optical filters for WDM systems" *IEEE Photonics Tech. Lett.*, vol. 10, no. 4, pp. 567-569, 1998
- [5] M.A. Seldowitz, J.P. Allebach, D.W. Sweeney, "Synthesis of holograms by direct binary search", *Applied Optics*, 26(14), pp.2788-2798, 1987
- [6] C.R. Doerr, P. Schiffer, L.W. Stulz, M. Cappuzzo, E. Laskowski, A. Paunescu, L. Gomez, and J. Gates, "Compact integrated dynamic wavelength equalizer", *Proc. OFC'99*, San Diego, California, Paper PD30, February 1999



**Integrated Photonics Research**

# **Waveguide Modulators**

**Tuesday, July 20, 1999**

**Wolfgang Sohler, University GH Paderborn, Germany**  
Presider

**RTuK**  
**3:30pm–5:00pm**  
Sierra Madre South

## Linearized Optical Directional Coupler Modulators

**Chanin Laliew, Xiaobo Zhang, Anand Gopinath**

**Department of Electrical and Computer Engineering**

**University of Minnesota**

**Minneapolis, MN 55455, USA**

**Tel : (612) 625-1002**

**Fax : (612) 625-4583**

**e-mail : claliew@ece.umn.edu**

During the past decade there has been a rapidly-growing interest in analog transmission over the fiber-optic medium. The main interest for these investigations and experiments has been shown for microwave applications and cable-TV distribution<sup>1</sup>. For these applications, an external electrooptic modulator, which serves as an electrical-to-optical transducer, is a necessary device as directly modulating the optical source leads to spectral broadening, and hence limiting the bandwidth of the optical communication system. Two types of electrooptic modulators are commonly used : the Mach-Zehnder interferometric type and the directional coupler type. The basic Mach-Zehnder interferometric modulator has a squared-cosine response function (the dependence of the amplitude modulated optical power on the applied voltage) and the basic uniform directional coupler modulator has a quasi-squared-sinc response function, both of which are highly nonlinear, and to avoid crosstalk this leads to a relatively small modulation depth of about 2-5%, a rather poor figure in optical communication. Therefore there have been attempts to find external optical modulators which would provide much better linearity in their response functions so that the system capacity can be maximally exploited. A variety of linearization concepts have been proposed, and the goal of which is either to adjust the response function to fit a linear function or to eliminate or to suppress the cubic and/or higher-order terms in Taylor expansion of the response function. This gives rise to a variety of device configurations used, ranging from simple Mach-Zehnder interferometer, dual-parallel Mach-Zehnder interferometer, modified directional coupler, and a combination of Mach-Zehnder interferometer(s) and directional coupler(s).

In our project, we build the modulators from directional couplers, but instead of the coupler having a pair of waveguides running in parallel, i.e., having a constant or uniform coupling, we design them so that with the spacing between the two waveguides varying along the length of the device structure, the response function is of the desired form, specifically a linear (triangular) function. We use an inverse Fourier transform technique<sup>2</sup> to synthesize the coupling function from the ideal linear function. Figure 1 shows the result. We design our modulators, to be operating at 1.3  $\mu\text{m}$  wavelength, by truncating the full coupling function at its third null, and the response is expected to deviate slightly from the ideal linear function.

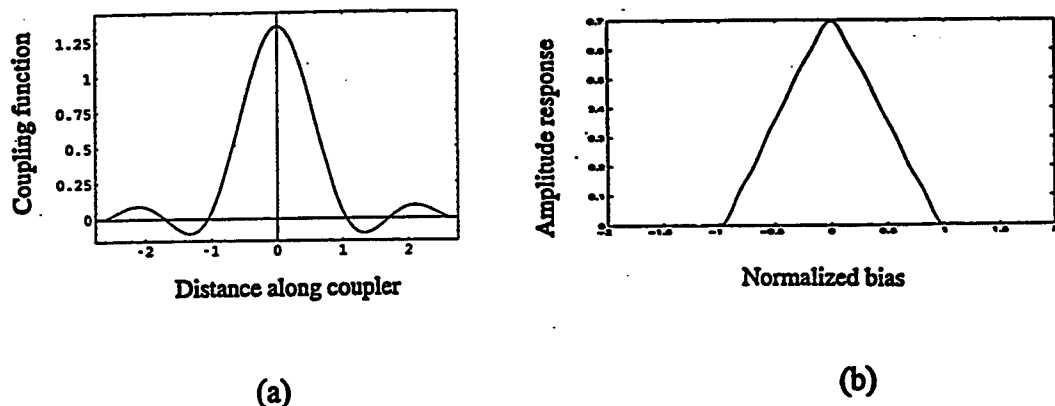


**Figure 1 : (a) Synthesized spatially-varying coupling function  
(b) The resulting response function**

We fabricated our devices on AlGaAs/GaAs material system because of its electrooptic effect and ease of integration with other photonic components offered by this material system. A schematic diagram of such a modulator is shown in figure 2 below.

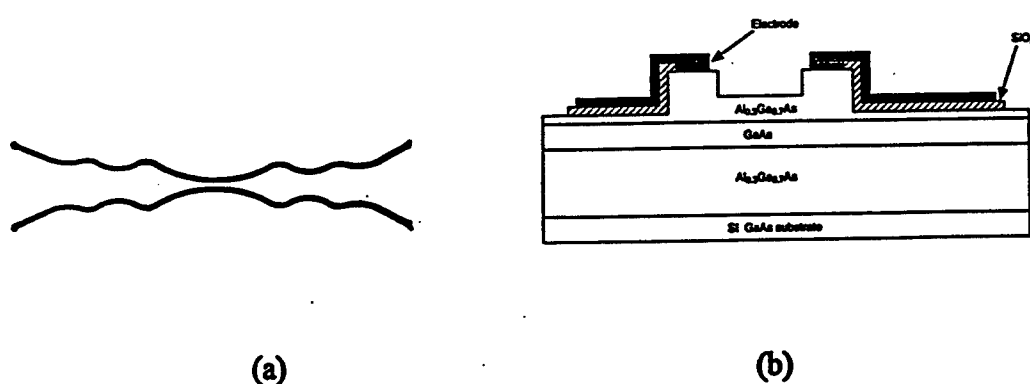


**Figure 2 : (a) Shape of a spatially-varying directional coupler modulator (top view)  
(b) Cross-sectional view of the modulator**

The length of the modulators is 5.1 mm. Measurements of the optical output power versus applied bias voltage reveals a fairly linear behavior as shown in figure 3.

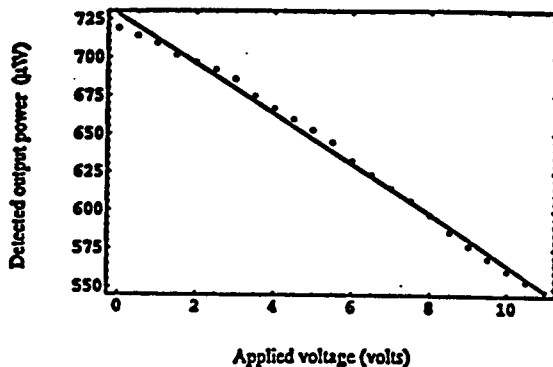


Figure 3 : Measured amplitude response of a linear modulator

A common way to evaluate the linearity of this device is to measure the third-harmonic distortion, defined as *10 log [power content of the third harmonic / power content of the fundamental]*, that the device produces under modulation. Plotted in figure 4 is the third-harmonic distortion level versus the optical modulation index of a device that we fabricated, biased at 5 V and measured at 500 MHz. When the modulating signal consists of two or more tones, there are intermodulation distortions in addition to harmonic distortions. We are now in the process of making a two-tone test. The result of this test will be presented at the meeting.

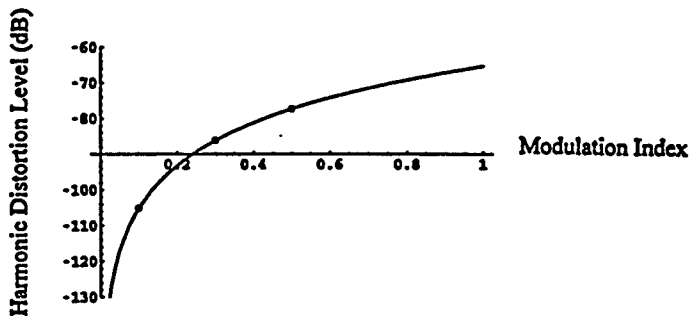


Figure 4 : Third-harmonic distortion level versus optical modulation index of a modulator

## References

1. Anders Djupsjobacka, A Linearization Concept for Integrated-Optic Modulators, IEEE Photon. Tech. Lett., vol.4, no.8, pp.869-872, August 1992.
2. Sigurd Weideman Lovseth, Chanin Laliew, Anand Gopinath, Amplitude Response of Optical Directional Coupler Modulators by Fourier Transform Technique, 8<sup>th</sup> European Conference on Integrated Optics Proceedings, pp.230-233, April 1997

# Integrated optical AC voltage sensor fabricated on LiNbO<sub>3</sub> platform

Tadashi Ichikawa, Manabu Kagami, and Hiroshi Ito

Toyota Central Research and Development Laboratories Inc.  
41-1 Yokomichi, Nagakute, Aichi-gun, Aichi, 480-1192, Japan.

Tel: +81-561-63-4625 Fax: +81-561-63-5426

Email: ichikawa@optics.tylabs.co.jp

## Introduction

We report developments in the formation and experimental evaluation of a novel integrated optical (IO) AC voltage sensor fabricated on the LiNbO<sub>3</sub> platform. This device is used in EMC measurement because it has intrinsic advantages such as large bandwidth, compact size, minimal field disturbance, noise immunity, and electromagnetic isolation of electronic instrumentation associated with the use of optical carrier signal.<sup>1,2</sup> In order for the above device to be useful for practical application, it must be low-cost and high performance. To overcome this cost issue, LiNbO<sub>3</sub> platform having a V-groove is prepared by a laser ablation technique for passive fiber alignment. The LiNbO<sub>3</sub> passive sensor device has measurement capabilities in the radio frequency, microwave, and millimeter waveband. In this paper, we presented a retroreflective type Mach-Zehnder interferometric waveguide sensing structure on the LiNbO<sub>3</sub> platform for realizing a compact and low-cost AC voltage sensor.

## Device description

Fig. 1 illustrates the Ti:LiNbO<sub>3</sub> IO AC voltage sensor. It consists of a Y-junction optical waveguide formed by Ti diffusion, and one pair of electrodes with metal probes for phase modulation. Mach-Zehnder interferometer type optical modulator can be half its size by employing a retroreflective structure<sup>1</sup>, as illustrated in Fig. 1. This structure allows the sensitivity of the device to be doubled at unit waveguide length, and its bandwidth is increased by the reduction in device capacitance. In addition, it is easier to pigtail on optical fiber to such a device. Improvements to the alignment and polishing processes were implemented using the laser ablation and saw-cut techniques. These techniques can be applied to various types of platform with hybrid integrated optical components by use of simple mechanical positioning. A V-groove for optical fiber alignment was fabricated in the LiNbO<sub>3</sub> device, as shown in Fig. 2. The groove was formed along the waveguide, from the substrate edge to the waveguide edge, by ablation with a KrF ( $\lambda=248$  nm) excimer laser with a rhombus-shaped output beam<sup>3</sup>,

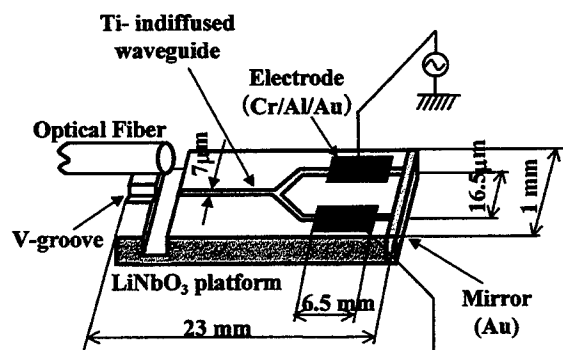


Fig.1 Schematic diagram of retro-reflective type AC voltage sensor.

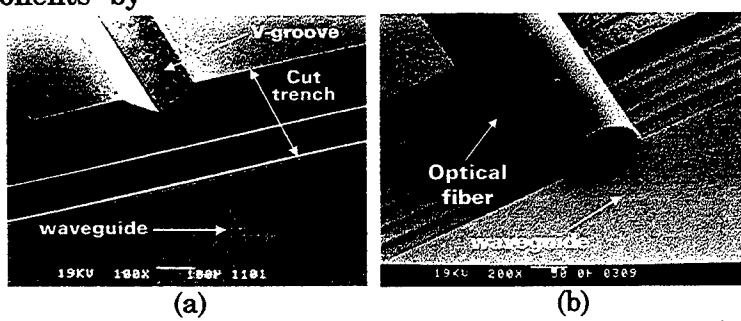


Fig.2 SEM photograph of the fiber coupling section of LiNbO<sub>3</sub> platform, (a) before, and (b) after fiber insertion to the V-groove.

as shown in Fig. 3. The incident laser fluence was estimated to be  $5 \text{ J/cm}^2$  at the substrate level.  $\text{O}_2$  was used as an ambient gas to reduce redeposition of ablated materials. Some roughness was observed on the surface of the high quality V-groove; it was observed otherwise no cracking or meltdown was seen. The substrate was placed on a computer-controlled x-y stage and was translated with this stage at a prescribed speed. The window shape of the mask and the translation speed were used to control the cross-sectional shape of the ablated V-groove.

In the saw-cut process, a high-speed-rotating cutting technique was used instead of a conventional polishing process realized using a diamond saw cutting along the normal direction of the wave-guide. This method realized a near optical-quality cut surface. A 200- $\mu\text{m}$ -thick, 52-mm-diameter resin-type blade was used with a 0.3 mm/s cutting speed and a blade rotation of 30,000 rpm. The measured coupling loss using a single-mode optical fiber was 0.5 dB/facet. This value was the same as the coupling loss for a waveguide with a polished end face. Finally, The sensor chip was pigtailed with an optical fiber using the V-groove, and it was fixed with a UV curing adhesive. The pigtalled device was assembled in a polymeric housing, as shown in Fig. 4. The above pigtalled and pack-aged device was tested in the range from 10 to 40 °C. An observed insertion loss variation of  $\pm 0.1$  dB is acceptable for most practical uses.

The above two proposed processes would be useful techniques for optical platform fabrication not only for  $\text{LiNbO}_3$  type devices but also for devices on glasses, polymers, and compound semiconductors.

#### Device Evaluation

The minimum detectable voltage and frequency response of fiber coupled devices were tested using a laser diode operating at a wavelength of  $\lambda=1.3 \mu\text{m}$ , as shown in the test setup in Fig. 5. A beam splitter was employed to separate the input light and the

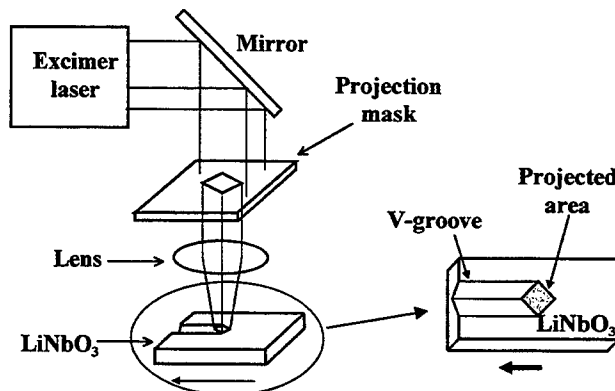


Fig.3 Schematic of the laser ablation apparatus for V-groove formation.

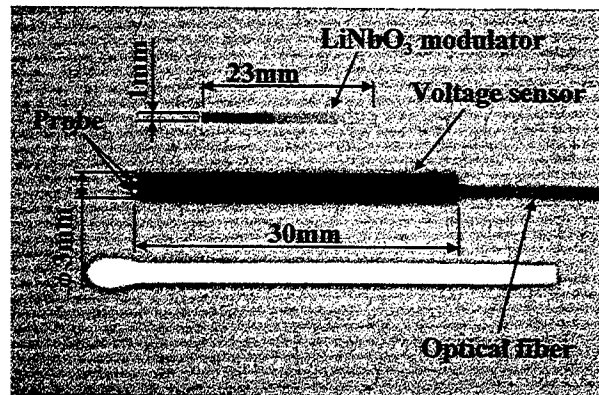


Fig.4 Fabricated sensor chip and packaged sensor head.

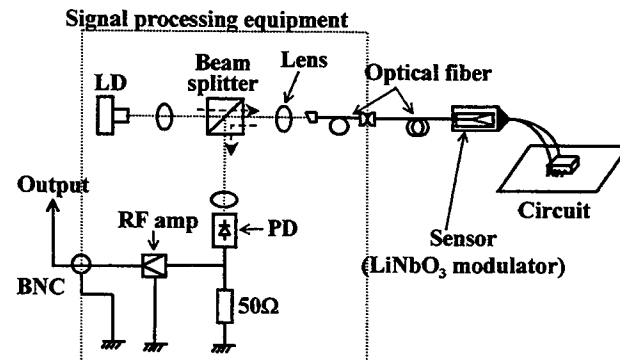


Fig.5 Block diagram of the test setup for sensing properties evaluation.

Table 1 Properties of retroreflective modulator

Half-wave voltage	4.5 V
Extinction ratio	15 dB
Insertion loss	8.9 dB

modulated light. A spectrum analyzer with 1 kHz resolution bandwidth, was used in this evaluation setup. The properties of a fabricated retroreflective modulator are shown in Table 1.

The sensing linearity was measured, as shown in Fig. 6. The graph shows that this sensor has more than 70 dB dynamic range. This power range is equivalent to a voltage range from 0.2 mV to 1.0 V at  $50\ \Omega$  load (Fig. 5). The reasons the lower and upper limitations are due to the AM noise of the laser diode and the presence of high frequency distortion (mainly second harmonics), respectively. Figure 7 shows a typical frequency response sweep from 1 Hz to 1.2 GHz. As can be seen, the response is flat from 6 Hz to 1 GHz. The lower limitation is due to the impedance of the modulator ( $C=2.5\ pF$ ,  $R=10^{10}\Omega$ ). At lower frequency, the modulator acts as a high pass filter. The high frequency limitation is due to the walking between the electrical signal and the optical wave. This delay depends on the distance between the electrodes and the retroreflective mirror. The variation for voltage measurement was estimated to be less than 2 % few a temperature range from 10 to 40 °C.

### Conclusion

We have demonstrated an excellent performing and totally passive pigtailed and packaged electrooptic AC voltage sensor. By employing a LiNbO<sub>3</sub> platform and retroreflective structure, we realized low-cost sensor chips because of small chip size and one point passive optical fiber connection. The device can perform remote sensing using only one optical fiber connection. Detection sensitivities of 0.2 mV have been measured with a frequency response from 6 Hz to 1 GHz. This unique sensor enables the precise voltage measurement in an EMC environment, even inside a computer.

### References

- [1] D.H.Naghski, J.T. Boyd, H.E. Jackson, S. Sriram, S.A. Kingsley, and J. Latess, "An integrated photonic Mach-Zehnder interferometer with no electrodes for sensing electric fields." IEEE J. Lightwave Technol., 12, pp.1092-1098 (1994).
- [2] H. Ito, T. Ichikawa, S. Kato, M. Matsuda, and N. Takahashi, "An electric field sensor using retroreflective type of Ti:LiNbO<sub>3</sub> waveguide modulator," in *Meeting Digest of Frontiers in Information Optics, Topical Meeting of the International Commission for Optics*, 4P-14, pp.252, Kyoto, Japan, April 1994.
- [3] T. Ichikawa, M. Kagami, and H. Ito, "LiNbO<sub>3</sub> platforms for optical fiber alignment," Opt. Lett., 23, pp.1138-1140 (1998).

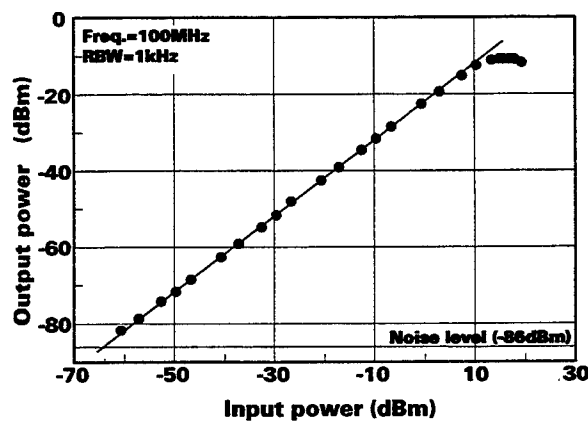


Fig.6 Output vs. input power for a proposed voltage sensor.

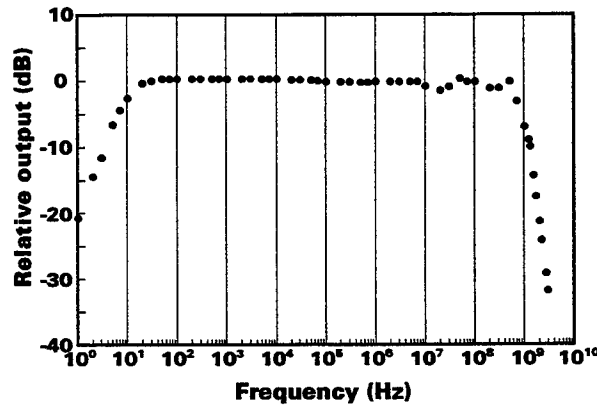


Fig.7 sensor frequency response.

## Enhancement of electro-optic effect in stoichiometric LiNbO<sub>3</sub>

Takumi FUJIWARA and Akira J. IKUSHIMA

*Research Center for Advanced Photonic Technology (RCAPT)*

*Toyota Technological Institute*

*2-12-1 Hisakata, Tempaku, Nagoya 468-8511, Japan*

*phone: +81 52 809 1881, fax: +81 52 809 1882*

*e-mail: fujiwara@toyota-ti.ac.jp*

Yasunori FURUKAWA and Kenji KITAMURA

*National Institute for Research in Inorganic Materials, 1-1 Namiki, Tsukuba 305-0044, Japan*

Lithium niobate (LiNbO<sub>3</sub>) single crystals have caught much attention to be applied to electro-optic (EO) devices such as optical switches and modulators, and to volume holographic memories. This is because LiNbO<sub>3</sub> has good mass producibility and a relatively high EO effect and photorefractive sensitivity. For possible enhancements, EO effect and photorefractivity have previously been studied in LiNbO<sub>3</sub> with various dopants. However, LiNbO<sub>3</sub> crystals so far studied was nonstoichiometric, where usually congruent composition was obtained from a melt with 48.6 mol. % Li<sub>2</sub>O. This is because the crystals with stoichiometric composition have hardly been grown by the conventional Czochralski method.

Kitamura et al. [1] have reported a novel crystal growing technique to yield stoichiometric LiNbO<sub>3</sub> crystals of high quality, where the stoichiometry is achieved by the continuous-charge double-crucible Czochralski method with 58.0 mol. % Li<sub>2</sub>O melt. Stoichiometric LiNbO<sub>3</sub> has advantages: photorefractivity has been thought to be enhanced, and much of previous work has focused on this important issue. Recently, the stoichiometric crystal shows a larger photorefractive gain and a faster response time than those in the commercially available Fe-doped congruent one [2]. The photo-induced index change should be closely related to the EO effect, and therefore quantitative measurement of the EO coefficients is strongly demanded to clarify the origin of large photorefractivity. In addition, possible increase of the EO coefficients in LiNbO<sub>3</sub> crystals has to be confirmed for photonic devices with much higher efficient EO effect than those to date. In a present work we have examined the EO coefficients in both the stoichiometric and congruent cases, using the Mach-Zehnder (MZ) interferometry at the wavelength of 0.633 μm.

LiNbO<sub>3</sub> crystals with stoichiometric composition were grown by the same technique as Ref. [1]. A congruent LiNbO<sub>3</sub> crystal was grown by a conventional Czochralski method.

Experimental setup of MZ interferometer is presented in Fig. 1. Either LiNbO<sub>3</sub> sample was placed in one arm of MZ interferometer, and He-Ne laser light was launched into the sample along

the its y-axis. He-Ne laser power density was kept below  $12.5 \text{ mW/cm}^2$  to ensure that no photorefractive effect was caused by the light source [3].

Aluminum electrodes were deposited to apply a DC voltage along the z-axis of crystals. Electrically induced refractive index change in the sample produces a phase retardation, which results in a sinusoidally modulated output intensity of the interferometer. Measuring the change as a function of the applied voltage, we obtained the EO coefficient.

EO coefficients, both  $r_{33}$  and  $r_{13}$ , were respectively determined with the light of linear polarizations parallel and perpendicular to applied electric field.

Figure 2 shows an example of the measured interference patterns of MZ interferometer. The results correspond to  $r_{33}$  and  $r_{13}$  in a stoichiometric  $\text{LiNbO}_3$  crystal, where dotted curves in the figure represent variations fitted to sinusoidal relations between the output intensity and phase retardation [4]. Using the half-wave voltage values obtained from the fitting,  $n_e^3 r_{33}$  and  $n_o^3 r_{13}$  were obtained to be  $402 \pm 15$  and  $124 \pm 10$  V for stoichiometric, and  $337 \pm 15$  and  $120 \pm 10$  V for congruent ones, respectively, where  $n_e$  and  $n_o$  are the extraordinary and ordinary refractive indices. Refractive indices for both types of crystals were then measured by prism coupling method, which yielded values of  $n_e$  and  $n_o$  at  $0.633 \mu\text{m}$  to be 2.1890 and 2.2860 for stoichiometric, and 2.2028 and 2.2866 for congruent  $\text{LiNbO}_3$  crystals, respectively.

The values of EO coefficients thus deduced are summarized in Table I. The stoichiometric  $\text{LiNbO}_3$  has  $r_{33}$  at least 20% larger than the congruent crystal, whereas  $r_{13}$  of stoichiometric  $\text{LiNbO}_3$  is unchanged from that of congruent case. The values of EO coefficients in congruent case are in a good agreement with previously reported values [5].

In this experiments, EO coefficients were measured under unclamped conditions almost always at a low-frequency or DC electric field, and furthermore increase of  $r_{33}$  in stoichiometric  $\text{LiNbO}_3$  crystal was also observed at higher frequencies. And, this results lead to materialize novel EO devices such as optical switches and modulators with lower driving voltages. From the standpoint of photonic applications, this increase of the EO coefficient by 20% should really bring a big breakthrough in EO devices based on  $\text{LiNbO}_3$  crystals.

As an alternative way to characterize the second-order optical nonlinearity in stoichiometric  $\text{LiNbO}_3$ , possible enhancement of SHG or d coefficient is the most interesting because SHG intensity is proportional to  $d^2$ . Measurement of d coefficient in stoichiometric  $\text{LiNbO}_3$  crystal used in this experiments is in progress and will be discussed at the meeting.

In summary, we report on the electro-optic coefficients,  $r_{33}$  and  $r_{13}$ , in both stoichiometric and congruent  $\text{LiNbO}_3$  crystals. Stoichiometric crystal has approximately 20% larger  $r_{33}$  than congruent one, whereas the  $r_{13}$  coefficient is insensitive to the composition. The increase of  $r_{33}$  could then be the origin of enhancement of photorefractive effect in stoichiometric  $\text{LiNbO}_3$  crystal.

The authors are grateful to Dr. Kiyofumi Chikuma of Corporate Research and Development Laboratory, Pioneer Electronic Corporation for his support to measure the refractive indices in LiNbO<sub>3</sub> crystals.

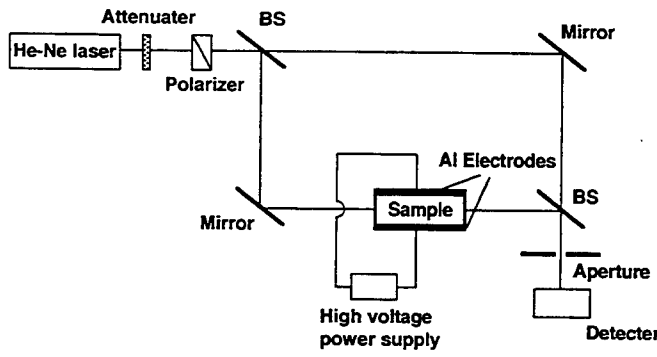


Fig. 1 Experimental setup for MZ interferometer.

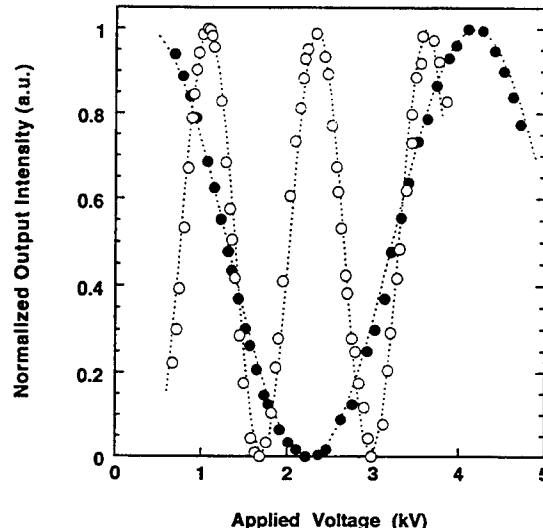


Fig. 2 Interference patterns of normalized output intensity from MZ interferometry in stoichiometric LiNbO<sub>3</sub>.

○  $r_{33}$ , ●  $r_{13}$

Table I Electro-optic coefficients of the LiNbO<sub>3</sub> crystals

Composition	$r_{33}$ (pm/V)	$r_{13}$ (pm/V)
Stoichiometric	$38.3 \pm 1.4$	$10.4 \pm 0.8$
Congruent	$31.5 \pm 1.4$	$10.0 \pm 0.8$

## References

- [1] K. Kitamura, J. K. Yamamoto, N. Iyi, S. Kimura, and T. Hayashi, *J. Crystal Growth*, **116**, 327 (1992).
- [2] Y. Furukawa, K. Kitamura, Y. Ji, G. Montemezzani, M. Zgonik, C. Medorano, and P. Günter, *Opt. Lett.*, **22**, 501 (1997).
- [3] T. Fujiwara, X.-F. Cao, R. Srivastava, and R. V. Ramaswamy, *Appl. Phys. Lett.*, **54**, 975 (1989).
- [4] T. Fujiwara, M. Takahashi, M. Ohama, A. J. Ikushima, Y. Furukawa, and K. Kitamura, to be published in *Electron. Lett.*
- [5] A. Yariv and P. Yeh,  
"Optical waves in crystals", John Wiley & Sons, 1984, pp. 232-233.

## High-Power Single-Mode LiTaO<sub>3</sub> Waveguides with Improved Temporal Stability

D. B. Maring, S.M. Kostritskii<sup>†</sup>, R.F. Tavlykaev, and R.V. Ramaswamy

Photonics Research Lab, 339 Larsen Hall, University of Florida, Gainesville, FL 32611

Tel: (352) 392-9265, Fax: (352) 392-4963, tav1@eel.ufl.edu

<sup>†</sup>Department of Physics, Kemerovo State University, Kemerovo, 650043 Russia.

**Introduction** Lithium Tantalate (LiTaO<sub>3</sub>) is an attractive host material for use in integrated optics due to its large electro-optic and nonlinear coefficients, comparable to those of Lithium Niobate (LiNbO<sub>3</sub>), and its high threshold for photorefractive damage, known to be more than an order of magnitude larger than that of LiNbO<sub>3</sub> at visible wavelengths [1]. In the infrared, although photorefractive damage is often considered negligible, damage has been observed at 1.3μm in Ti:LiNbO<sub>3</sub> for power levels around 5mW [2]. Photorefractive resistance of these waveguides, as well as those fabricated by annealed proton exchange (APE) in both LiNbO<sub>3</sub> and LiTaO<sub>3</sub>, at 1.55μm have not been investigated to date. In the case of long-haul fiber-optic networks operating at 1.55 μm, guided-wave devices fabricated in LiTaO<sub>3</sub>, such as rare-earth doped waveguide amplifiers and electro-optic modulators, are expected to withstand much higher pumping and throughput powers than is currently attainable in LiNbO<sub>3</sub>.

The APE technique, commonly used for the fabrication of waveguides in LiTaO<sub>3</sub>, facilitates fabrication at temperatures below the Curie point of the crystal. Low-loss waveguides with high index increments can be achieved with this process. However, a number of anomalies are known to exist for APE waveguides in LiTaO<sub>3</sub>; temporal instability, a decrease in index increment as proton concentration is increased beyond a certain concentration level, an increase in index increment with short annealing, and the likelihood of forming buried index profiles [3,4]. While compilation of the structural phase diagram for APE:LiTaO<sub>3</sub> [4] (relating proton-induced strain to index increment) has provided explanations for all of the aforementioned anomalies, waveguides with improved temporal stability, where the refractive index increment does not change over time, have yet to be realized.

In this paper, we present results on the temporal stability and power handling capability of APE waveguides and devices in LiTaO<sub>3</sub> operating near 1.5 μm. We demonstrate a higher degree of stability than previously reported [5] with a significantly larger degree of photorefractive resistance at high input powers than those in LiNbO<sub>3</sub>.

**Fabrication and Measurement Technique** In order to determine fabrication conditions yielding temporally stable APE waveguides at 1.55μm, a method of quantifying the amount of waveguide index change over time is needed. To do this, directional couplers of various channel widths, gaps, and interaction lengths were fabricated in X- and Z-cut LiTaO<sub>3</sub>. Pyrophosphoric acid and glycerin were used at different exchange and annealing times and temperatures so as to provide single-mode waveguides at 1.55μm in different regions of the structural phase diagram. The diagrams are reprinted in Fig. 1 for ease of reference. By using an array of couplers with the same channel width and gap and different interaction lengths, the coupling length was determined by plotting the ratio of output intensities in each arm as a function of interaction length. This coupling length was monitored for a period of months in order to track any change due to index instability. Changes in measured coupling length were then related to corresponding index increment changes through a Finite Difference Method (FDM) computer simulation of a directional coupler. For each fabrication condition, the index profile of the waveguides comprising the directional couplers were measured by reflectivity profiling and rocking curve analysis [4]. By way of the established procedure, the rate of index change instability of waveguides in different regions of the structural phase diagram could be monitored over time and correlated with phases, and associated fabrication conditions, to determine which phases, if any, yield temporally stable waveguides.

The other goal of this study was to examine the photorefractive resistance of waveguides near 1.55μm. To do this, straight channel waveguides were fabricated in X-cut LiTaO<sub>3</sub> using glycerin at 260°C for 24 hours and in X-cut LiNbO<sub>3</sub> using pyrophosphoric acid at 200°C for 50 minutes followed by annealing at 350°C for 7

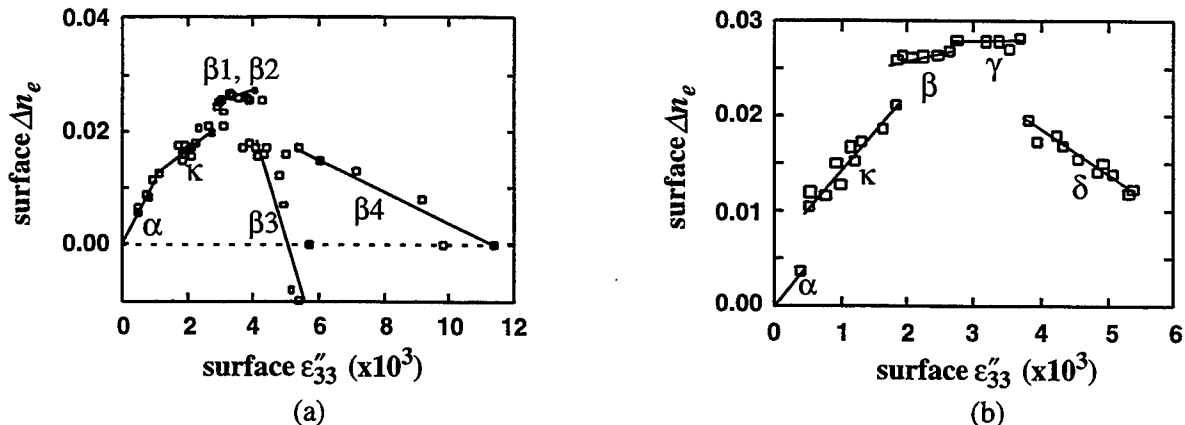


Fig.1. Structural phase diagrams for X-cut [4] (a) and Z-cut APE:LiTaO<sub>3</sub> [6] (b), relating surface index increment  $\Delta n_e$  to proton-induced lattice strain  $\epsilon''_{33}$  at the surface.

hours with a 2 hour ramp period at each end. To provide high input intensities needed for measurements, a Fiber-Raman Laser at  $1.48\mu\text{m}$  was used. Light from the laser was coupled into the waveguides using a single-mode fiber. Waveguide outputs were measured using a 20X lens, pinhole, and infrared detector with calibrated power meter. Output power versus input power was then plotted to check for photorefractive damage.

**Results and Discussion** Table 1 shows the results of temporal stability measurements of waveguides in different regions of the phase diagrams. Sample 1, with the highest proton concentration, is in the  $\delta$  phase of the Z-cut diagram. This sample shows a large index change during the 99 day period over which it was monitored. The magnitude of this change agrees with previously reported data [5], as well as with measured changes in proton-induced strain values  $\epsilon''_{33}$  obtained by rocking curve analysis [4]. Waveguides with this proton concentration are highly unstable and therefore unsuitable for reliable device fabrication.

Sample 2, in the  $\kappa$  phase of the Z-cut diagram, shows improved stability compared to the first sample. The change in index increment for this sample is nearly four times smaller. This confirms previously held notions that stability can be improved by avoiding the presence of high-stress, high-concentration phases. However, even greater stability may be necessary for reliable device operations. Therefore, investigation of waveguides in the  $\alpha$  phase is necessary.

To fabricate  $\alpha$  phase waveguides, we encountered a significant drawback to the APE technique using pyrophosphoric acid. Because of the high proton concentration of this source, proton exchange (PE) leads to very shallow, highly concentrated waveguides which require extensive annealing to reach the  $\kappa$  or  $\alpha$  phase. As a result, their profiles tend to be very graded and mode confinement becomes poor, or extinct. This problem is especially acute in the region of discontinuity between the  $\alpha$  and  $\kappa$  phases, particularly for the Z-cut. APE waveguides supporting a single mode in the  $\kappa$  phase lost this mode by further annealing them to the  $\alpha$  phase because of the large drop in index increment.

In effort to overcome these limitations, we switched to a lower-concentration source, glycerin, expecting the slower rate of surface indiffusion to allow time for diffusion within the sample, thus producing waveguides whose surface concentration never leaves the  $\alpha$  phase during PE and, therefore, would not require annealing. Sample 3 in Table 1 was our first attempt using this approach. This sample was fabricated in glycerin at  $260^\circ\text{C}$  for 24 hours. Rocking curve data for this sample showed it to be near the top of the  $\alpha$  phase, but initial investigation using Raman spectra does indicate the presence of a very shallow region of the  $\kappa$  phase near the surface. Initial stability results show the index of this waveguide to have decreased  $2 \cdot 10^{-4}$  over one week. Examination of samples studied over 3 months or more show that about 40% of the degradation which occurs during the 3 months happens within the first week. Extrapolating the data for sample 3 would suggest

Sample	Cut	$\epsilon''_{33}$	Days	$\delta(\Delta n)$
1	Z	$5.4 \cdot 10^{-3}$	99	$3 \cdot 10^{-3}$
2	Z	$10^{-3}$	98	$8 \cdot 10^{-4}$
3	X	$0.5 \cdot 10^{-3}$	7	$2 \cdot 10^{-4}$

Table 1. Change in index increment  $\delta(\Delta n)$  over time for samples with different proton-induced strain  $\epsilon''_{33}$ .

a change of about  $5 \cdot 10^{-4}$  over the same period as samples 1 and 2. However, as these waveguides were fabricated by only a *one step*, PE technique, they are relatively step-like as compared to their APE counterpart. As a result, mode confinement within the waveguide was significantly improved, leading to an increase in coupling length from about 5mm to about 20mm in couplers with 6.5 $\mu\text{m}$  channel width and an 8 $\mu\text{m}$  gap. Efforts to further reduce surface concentration and improve temporal stability are currently underway.

Fig. 2 shows the results of photorefractive measurements performed on waveguides of similar channel width in LiTaO<sub>3</sub> and LiNbO<sub>3</sub>. As can be seen, the LiTaO<sub>3</sub> sample, with fabrication conditions similar to those of sample 3 above, shows a reasonable degree of linearity between output and input power over the range tested. Therefore, little, if any, degradation to its performance has been caused by photorefractive damage. The LiNbO<sub>3</sub> sample, however, shows some degree of saturation and appears to have already passed its threshold point for photorefractive damage for even the smallest input power tested. Lower levels of input power were not attainable as they are below the lasing threshold of the laser used in this experiment. The significant attenuation of output power relative to input power illustrates the extremely high photoinduced refractive index change in APE:LiNbO<sub>3</sub> waveguides, especially above 100mW.

Initial investigation into the power handling capability of a Mach-Zehnder interferometer fabricated using glycerin in X-cut LiTaO<sub>3</sub> was also performed. Results indicate that the device operates at input power levels as high as 300mW with no photorefractive damage.

**Conclusion** We have presented preliminary results on the improved temporal stability and photorefractive resistance of PE waveguides in LiTaO<sub>3</sub> near 1.5 $\mu\text{m}$  where waveguides in lower-concentration regions of the structural phase diagram exhibited improved temporal stability with far superior photorefractive resistance compared to APE:LiNbO<sub>3</sub>. Added advantages to using a low-concentration PE technique include increased simplicity and improved mode confinement.

## References

- [1] A. M. Glass, G. E. Peterson, and T. J. Negran, "Laser Induced Damage in Optical Materials", A. M. Glass and A. H. Guenter, eds. (Washington, DC, Nat. Bur. Stand., 1972) Spec. Publ 372, pp. 15-26.
- [2] G. T. Harvey, G. Astfalk, A. Y. Feldblum, B. Kassahun, IEEE J. Quantum Electron., v. 22, pp. 939-946, 1986.
- [3] H. Ahlfeldt, J. Webjorn, P. A. Thomas, and S. J. Teat, J. Appl. Phys., v. 77, pp. 4467-4476, 1995.
- [4] D. B. Maring, R. F. Tavlykaev, R. V. Ramaswamy, Yu. N. Korkishko, V. A. Fedorov, and J. M. Zavada, Appl. Phys. Lett., v. 73, pp. 423-425, 1998.
- [5] P. J. Matthews and A. R. Mickelson, J. Appl. Phys., v. 71, pp. 5310-5317, 1992.
- [6] K. El Hadi, P. Baldi, S. Nouh, M. P. De Micheli, A. Leycuras, V. A. Fedorov, and Yu. N. Korkishko, Optics Lett., v. 20, pp. 1698-1700, 1995.

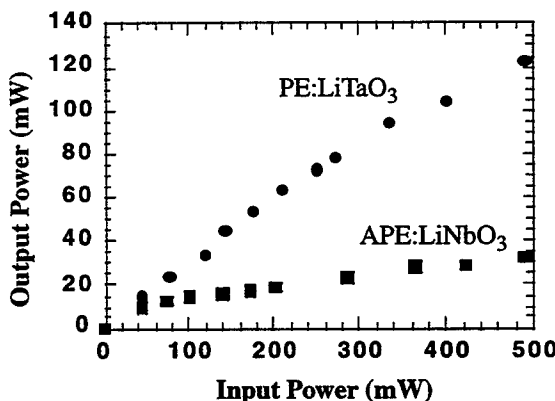


Fig.2. Output power vs. input power for 6 $\mu\text{m}$  wide straight-channel waveguides in PE:LiTaO<sub>3</sub> and APE:LiNbO<sub>3</sub>.

## HIGH SPEED LiNbO<sub>3</sub> MODULATORS FOR TELECOMMUNICATIONS

**Rangaraj Madabhushi**

NEC Corporation, Opto-Electronics & High Frequency Device Research Laboratories  
4-1-1, Miyazaki, Miyamae-Ku, Kawasaki, 216-8555, Japan(rangaraj@oel.cl.nec.co.jp)

High speed and low driving voltage LiNbO<sub>3</sub> optical modulators are the essential components for future optical telecommunication systems of several tens of gigabits per second, due to the advantage of superior chirping characteristics. The bandwidth of the modulator is restricted by the velocity mismatch between the optical and microwaves and the microwave attenuation of the electrode structure. A tradeoff exists between the bandwidth and the driving voltage. A variety of approaches and designs have been reported [1] - [9] to achieve perfect velocity matching. Even if the perfect velocity matching is achieved, the bandwidth is solely controlled by the microwave attenuation. Hence reduction of microwave attenuation of the electrode structure is the key factor to achieve very large bandwidths. We present here the high speed and low driving voltage LiNbO<sub>3</sub> modulators for 40 Gb/s transmission applications.

The main factors influencing the microwave attenuation include the stripline conductor loss (inclusive of stripline tapers and bends) dielectric loss, loss due to mounting and packaging including the connector- stripline pad contact. The conductor loss can be reduced by increasing the surface area (or the width) of the stripline electrode. But, in terms of the velocity matching and characteristic impedance requirements, the gap between the electrodes is to be increased simultaneously. This in turn increases the driving voltage. In order to solve the conflicting requirements of wide signal electrode and narrow gap, we arrived at a novel two stage modified (CPW (coplanar waveguide type) electrode structure [10]. In this structure, the lower portion has normal width and gap values and the upper portions with wider signal electrode width, which reduces the microwave attenuation. The microwave attenuation is improved from 0.5 to 0.34 dB/[cm(GHz)<sup>1/2</sup>]. We realized a bandwidth of 18 GHz (3 dB, electrical) and a driving voltage of 3.4V for an electrode length of 4 cm.

Reduction of buffer layer thickness is one way of decreasing the driving voltage, but this in turn restricts the velocity matching and the characteristic impedance requirements. We arrived at a novel step buffer layer structure [11] where the buffer layer thickness is reduced from the one half of the waveguide to the other half. By suitable optimizing the various parameters, we achieved a bandwidth of 17 GHz (3 dB, electrical) and a driving voltage of 2.25 V for an electrode length of cm.

Another factor that influences the microwave attenuation is the loss due to the tapers and the contact between the connector and signal electrode pad. We arrived through analysis and experimental verifications, that a suitable taper design and a nearly ideal point contact between the connector and the stripline pad reduces the microwave attenuation further [12], [13].

Fig. 1. shows the schematic view (a) and the cross sectional view (b) of the modulator.

We incorporated the step-buffer layer structure and the low microwave attenuation structure as explained above. The modulator is fabricated in z-cut, y-propagation LiNbO<sub>3</sub> substrates, using standard diffusion techniques [13]. SiO<sub>2</sub> buffer layer is then coated and is partially etched so that the thickness is 1.1  $\mu$ m over one half of the waveguide and 0.55  $\mu$ m over the other half. Then the modified electrode structure is then electroplated. The width, gap and the thickness of the electrodes are 7, 28, 15  $\mu$ m (lower part) and 25, 100, 15 (upper part) respectively. The signal electrode of 7  $\mu$ m, is connected to an external K-connector through tapered part and the feeder part. The electrode lengths are 4 cm and 3 cm.

Fig. 2. Shows the electrical response of the fully connectorized modulator with the electrode lengths of 3 and 4 cm. The response follows a nearly root f dependency up to 30 GHz, with a 6 dB value being 32 and 25 GHz respectively.

(Note. The bandwidth, in some cases are represented in dB, optical rather than dB, electrical, with the 3 dB, electrical values corresponding to the 6 dB, optical values. Although in the former case, the bandwidth looks to be larger, but in the actual cases, the bandwidth in dB, electrical is more important, as the eye will open only at the 3dB, electrical and not at 3 dB, optical).

The reflection ( $S_{11}$ ) values are between -10 to -20 up to 30 GHz. Fig. 3 shows the measured optical response for the same with the 3 dB bandwidth (dB, electrical) being 32 and 25 GHz. respectively. The detector response is included in this data. The fiber-to-fiber insertion loss is 4.5 dB, and the driving voltage is 3.3 and 2.5 V (DC) respectively.

In order to verify the capabilities of the modulator for 40 Gb/s applications, we took the eye diagram at 40 Gb/s [13]. Fig. 4 shows the waveform (eye diagram) of the modulator with an electrode length of 4 cm. With the limitations of the available input waveform, it can be said that these modulators are capable of operating at 40 Gb/s applications.

**Acknowledgements:** The author would like to thank Drs. M. Ogawa, T. Uji and M. Fujiwara of Optoelectronics and High Frequency Device Laboratories, NEC Corporation for their encouragement.

#### References

- [1] R.C. Alferness et al., IEEE Trans. Microwave Theory, MT-30, 1121, 1975.
- [2] C.M. Gee et al., Appl. Phys. Lett, 43, 998, 1983.
- [3] R.A. Becker et al., Appl. Phys. Lett., 45, 1168, 1984.
- [4] H. Haga et al., IEEE J. Quantum Electron., QE-22, 902, 1986.
- [5] S. K. Korotky et al., Appl. Phys. Lett., 50, 1631, 1987.
- [6] D. W. Dolfi et al., Electron. Lett., 24, 528, 1988.
- [7] K. Kawano et al., Electron. Lett., 25, 1382, 1989.
- [8] M. Seino et al., Proc. ECOC'90, 999, 1990.
- [9] K. Noguchi et al., Proc. OFC'96, 205, 1996.
- [10] R. Madabhushi et al., Proc. IOOC'95, 105, 1995.

- [11] R. Madabhushi, et al., Proc. OFC'96, 206, 1996..
- [12] R. Madabhushi et al., Proc. ECOC'97, 2-29, 1997.
- [13] R. Madabhushi et al., Proc. ECOC'98, 547 1998.

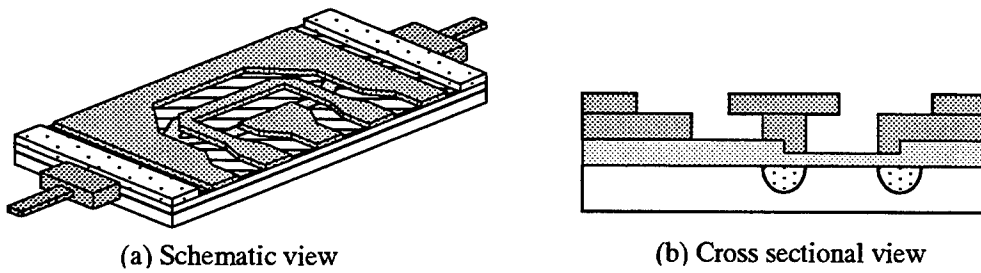


Fig. 1. Optical modulator

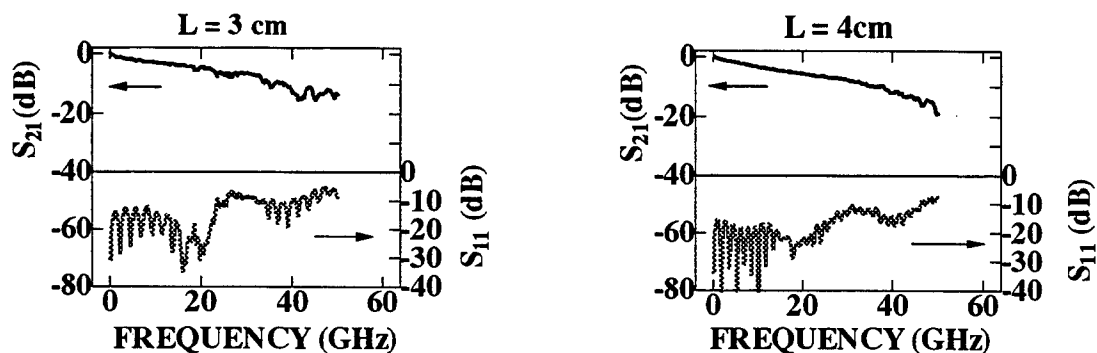


Fig. 2. Electrical response

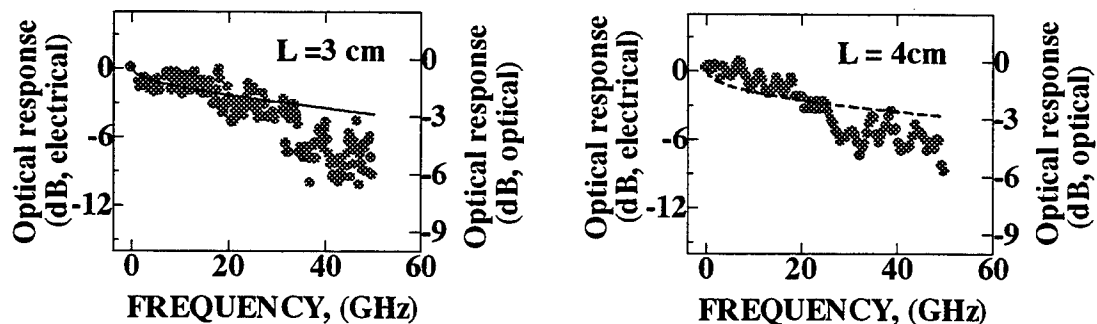


Fig. 3. Optical response

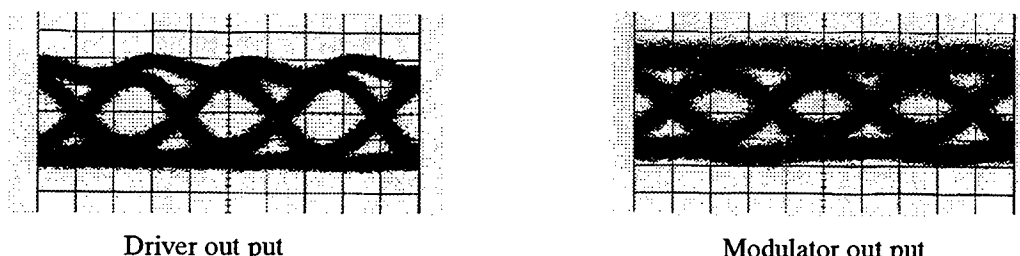


Fig. 4. Eye diagram

**Integrated Photonics Research**

# **Mode Control**

**Tuesday, July 20, 1999**

**Yoshi Nakano, Tokyo Institute of Technology, Japan**  
Presider

**RTuL**  
**3:30pm–5:00pm**  
Anacapa

## Hierarchical Modeling of Semiconductor Distributed-feedback Laser Diodes

Xun Li and Wei-Ping Huang

Department of Electrical and Computer Engineering

University of Waterloo

Waterloo, Ontario, Canada, N2L 3G1

Tel: 519-888-4567 Ext. 5319

Fax: 519-746-3077

E-mail: xli@maxwell.uwaterloo.ca

### Introduction

It has been recognized that modeling and simulation can play an important role in design of advanced laser diodes such as strained layer multiple-quantum-well complex-coupled distributed-feedback lasers. Ideally a simulator should enable a designer to predict the performance of a laser diode for a set of design parameters such as material compositions, doping concentrations and geometrical dimensions. Since the material and geometrical properties and the physical processes involved in the operation of the advanced laser diodes are extremely complex, modeling and simulation of such devices is usually difficult and time-consuming. To achieve a good balance between the accuracy and the efficiency, we have developed a hierarchical model that divides the simulation of a typical laser diode into several levels. At the heart of this simulator is an effective one-dimensional model that takes into the variations of the carrier, photon and temperature distributions along the laser cavity. The cross-sectional properties of the material, the optical field, the carrier and the temperature distributions are also considered by solving the corresponding two-dimensional equations and the results are related to the effective model parameters in the one-dimensional calculations. An overview of this approach and of the capability of the simulator are given in this talk, the calculated results from this approach are compared to those from the comprehensive physics-based three-dimensional simulation and to those from the practical measurements.

### Hierarchical Simulation Model

A schematic diagram for the overall structure, which illustrates the different levels and their relations in the hierarchical simulation model, is shown in Figure 1. The first level modules calculates the electrical, thermal, optical and various material properties for given cross-section structure by solving or using the two-dimensional carrier transport equations, the heat transfer equation, the optical wave equation and the physics-based material model, respectively. The second level module works as a parameter extractor to create the modal parameters for the subsequent level. The carrier, thermal and wavelength dependence of the modal parameters is described by a group of pre-determined analytical formulas with currently fitted coefficients. The third level module computes the static, small signal dynamic and noise related device performances by solving one-dimensional coupled optical, carrier and thermal equations along the cavity

in a self-consistent manner. By incorporating the modal parameters extracted at the above level, the cross-sectional information is also embedded in the calculations at this level.

### Comparisons

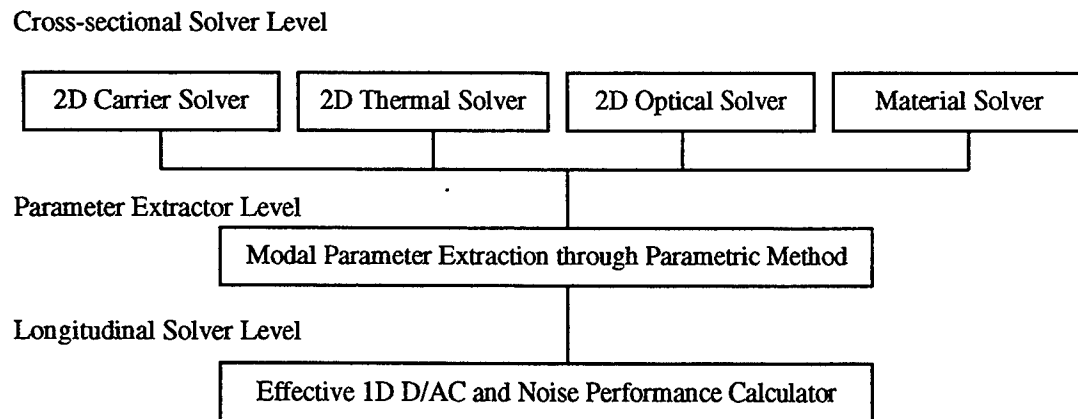
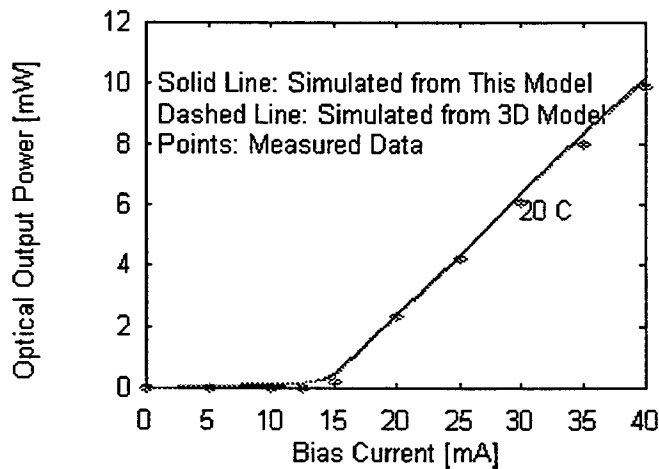
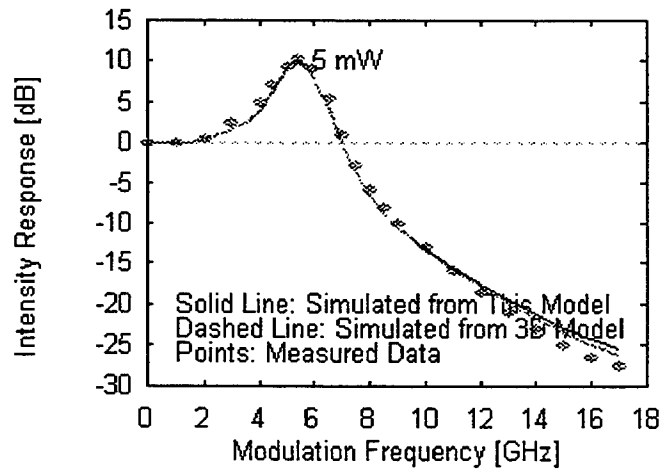
In order to validate this approach, we have calculated the steady-state optical output power as a function of the bias current and the small-signal intensity modulation response taking the corresponding results from a comprehensive physics-based three-dimensional model [1] as benchmarks. The device used is a 1.3  $\mu\text{m}$  InGaAsP-InP DFB laser made by Nortel Networks, the practically measured data are also plotted as shown in Figure 2 and 3. Excellent agreements among different simulation models and the experiments are achieved.

### Conclusion

A hierarchical simulation model for DFB laser diodes is developed and presented. Unlike a simple one-dimensional model along the cavity [2] using fixed modal parameters or a comprehensive three-dimensional model with all physics mixed together, the hierarchical approach treats the cross-sectional and the longitudinal structures separately and differently, namely, parametric treatment for the former and self-consistent treatment for the latter. The calculation and the comparison shows that the discrepancies introduced by the hierarchical approach are negligible. This indicates that the hierarchical approach leads to a significant improvement in computation efficiency comparing with the comprehensive physics-based three-dimensional model without paying many penalties in accuracy comparing with the simple one-dimensional model along the cavity.

### References

1. X. Li, A. D. Sadovnikov, W. -P. Huang and T. Makino, "A physics-based three-dimensional model for distributed feedback laser diodes", *IEEE J. Quantum Electron.*, vol. 34, no. 9, pp. 1545-1553, Sep. 1998.
2. X. Li and W. -P. Huang, "Simulation of DFB semiconductor lasers incorporating thermal effects", *IEEE J. Quantum Electron.*, vol. 31, no. 10, pp. 1848-1855, Oct. 1995.

**Figure 1 Hierarchical Simulation Model Structure****Figure 2 Optical Output Power Comparison****Figure 3 Intensity Modulation Response Comparison**

# An Iterative Bidirectional Beam Propagation Method for Multi-Interface Reflective Photonic Devices

*H. Rao, R. Scarmozzino, M. J. Steel, and R. M. Osgood, Jr.*

*Microelectronics Sciences Laboratories, Columbia University, New York, NY 10027*

*Tel: 1-212-854-8042 Fax: 1-212-860-6182 Email: hongling@cumsl.ctr.columbia.edu*

## I. INTRODUCTION

Since it was first proposed by Kaczmarski [1], the bidirectional beam propagation method (BPM) has been continually improved [2-6] to model an increasing range of reflective guided-wave optical devices, such as waveguide junctions, laser facets and grating structures. As with all beam propagation techniques, its principal advantage over non-BPM bidirectional approaches is efficiency. In contrast, the alternative Finite-Difference Time-Domain (FD-TD) method [7, 8] is accurate and straightforward but is extremely costly in time and memory. Modeling complex structures such as Bragg reflectors with many layers using the FD-TD approach requires intensive computational resources indeed. Hence there is a clear need for a less demanding approach. Previous bidirectional BPM approaches have generally focused either on problems involving a single interface [2, 6], or on limited multi-interface problems, such as problems in which the output field is already known [4], or where the number of discrete index discontinuities is small [5].

In our previous publication [9], we first presented an iterative bidirectional BPM approach, which can deal with structures involving a large number of dielectric interfaces and/or high index contrast. This approach has significantly reduced time and memory requirements compared to the FD-TD method. In this summary, we will begin with a brief review of the formulation and then demonstrate the capability the approach in simulating photonic band gap (PBG) structures through an example. Here, we only consider two dimensional TE cases, although in principle the formulation can be extended to TM and even three dimensional problems.

## II. FORMULATION AND NUMERICAL SCHEME

We consider propagation along the  $z$ -axis. The fields at any fixed position in the propagation direction are represented by a two-component vector consisting of the forward ("+") and backward ("−") fields:  $U(x) = \begin{pmatrix} u^+(x) \\ u^-(x) \end{pmatrix}$ . Propagation through the structure is modeled via two kinds of matrices: a propagation matrix ( $P$ ), which transfers the  $U$  vector from one end of a longitudinally homogeneous region to the other end, and an interface matrix ( $T$ ), which transfers the  $U$  vector from one side of an interface to the other side. Any dielectric structure can be generalized as the alternating product of a series of  $P$ 's and  $T$ 's. The overall transfer matrix  $M$  that relates the fields at the rear of the structure  $U_{out}$  to those at the front  $U_{in}$  is then constructed as:

$$\begin{pmatrix} u_{out}^+ \\ u_{out}^- \end{pmatrix} = M \cdot \begin{pmatrix} u_{in}^+ \\ u_{in}^- \end{pmatrix}; M = P_n T_{n-1,n} \cdots P_2 T_{12} P_1. \quad (1)$$

The matrix  $P_i$  propagates the forward and backward fields independently in region  $i$ , using conventional BPM for  $u^+$  and "time-reversed", conventional BPM for  $u^-$ . Paraxial BPM is sufficient for many cases, but for more difficult problems (e.g. high-index-variation problems) where paraxial BPM fails to yield the correct phase, a wide-angle BPM algorithm must be employed [10].

The interface matrix  $T_{ij}$  for the interface between region  $i$  and region  $j = i + 1$  can be written by analogy with a recently developed Padé-based technique for computing reflection at an interface

[6]. Explicitly, in the TE case, it is:

$$T_{ij} = \frac{1}{2} \begin{pmatrix} 1 + L_j^{-1} L_i & 1 - L_j^{-1} L_i \\ 1 - L_j^{-1} L_i & 1 + L_j^{-1} L_i \end{pmatrix}, \quad (2)$$

where  $L_i = \sqrt{\frac{\partial^2}{\partial x^2} + k_0^2 n_i^2(x)}$ ,  $n_i(x)$  is the refractive index profile in region  $i$ , and  $k_0$  is the wave number in vacuum. The square-root operator  $L_i$  is rationalized by using Padé approximants [6], as is done in wide-angle BPM [10]. Note that the reference wave number employed in the rationalization of operator  $L_i$  must be complex to accomodate evanescent waves generated when guided modes on the high-index side meet the interface to the low-index side. In high-contrast cases, this requirement has the consequence that a single choice of reference wave number does not adequately match either the guided or the evanescent mode behavior, hence a higher-order Padé approximation is required to compensate for the error due to the large distribution of wave numbers in the complex plane.

The formulation above allows us to evaluate  $U_{out}$ , given  $U_{in}$ . However, typically we are given the incident field,  $u_{in}^+$ , and must determine the reflected field,  $u_{in}^-$ , so as to satisfy the boundary condition that no backward field be present at the output, i.e.  $u_{out}^- = 0$ . Thus, precisely, the problem requires the solution of:

$$\begin{pmatrix} u_{out}^+ \\ 0 \end{pmatrix} = M \cdot \begin{pmatrix} u_{in}^+ \\ u_{in}^- \end{pmatrix}. \quad (3)$$

To solve this implicit equation for  $u_{in}^-$ , we rearrange it to the form of a linear system  $A \cdot x = b$ , where  $x$  is the unknown field  $u_{in}^-$ ,  $b = M^{-+} \cdot u_{in}^+$ , and  $A = M^{--}$ . The submatrix  $M^{-+}$  relates  $u_{out}^-$  to  $u_{in}^+$ , and  $M^{--}$  relates  $u_{out}^-$  to  $u_{in}^-$ .

Starting with a given guess, the reflected field,  $u_{in}^-$ , is then obtained by applying a standard iterative matrix algorithm, such as the Bi-Conjugate Gradient (BCG) method, or the Quasi-Minimal Residual (QMR) method [11], or BiCGSTAB method [12]. However, for difficult problems, i.e. complex structures or high index contrast, adequate convergence does not occur unless the matrix equation is preconditioned by applying a matrix  $\tilde{A}^{-1}$ , which approximates  $A^{-1}$ , to the original matrix equation. A suitable preconditioner is obtained by using the matrix  $M^{-1}$  that represents the backward propagation of the forward and backward fields. This preconditioned iterative matrix scheme was found to yield good convergence in most problems.

### III. SIMULATION RESULTS

The efficacy and capability of our approach were first demonstrated in our previous publication [9] through its application to some complex structures, such as high-reflection (HR) coatings and add-drop multiplexer. Here, we extend the capability of our approach to photonic band gap structures. Presently, many of these structures are simulated by FD-TD method, requiring calculation on supercomputers, which greatly constrains the design process. The bidirectional BPM approach allows such structures to be modeled in a matter of hours on a modern PC. The particular structure we examine here is a periodically notched waveguide with a defect in its middle, shown in Fig. 1(a). There are 20 notches on either side of a quarter wave shift. The index contrast is 3.4 : 1. The width of the input waveguide is  $0.13075\mu m$  and the notches are 26% of the waveguide width. The thickness is  $0.14\mu m$  for the fatter waveguide and  $0.16\mu m$  for the thinner one.

We obtain a reflection spectrum, shown in Fig. 1(b), by calculating the reflected field for each wavelength and taking the norm of the overlap integral between the reflected field and the launched fundamental mode field. The example shown used the BiCGSTAB algorithm to solve the linear system with zero initial guess for  $u_{in}^-$ . Convergence was confirmed by repeating the calculation with finer discretization. Compared to the other points, the point at the resonance peak needs a much

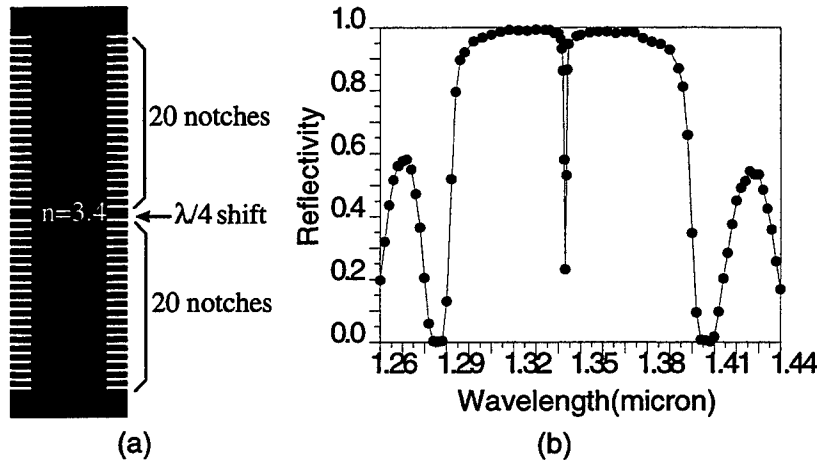


Fig. 1. (a) A periodically notched waveguide with 20 periods on either side of a quarter wave shift. (b) Refelction spectrum simulated with iterative bidirectional BPM

finer propagation step size to reach a consistent answer. Currently our algorithm is implemented using Dirichelet boundary conditions. As a result we are forced to use a broad simulation domain in order to reduce the effect of radiation energy reflecting from the boundary. In future work, we intend to introduce complete non-reflecting boundary conditions. This will allow the use of much smaller domains and increase the speed of our calculation further.

#### IV. CONCLUSIONS

In conclusion, we have developed an iterative bidirectional BPM approach to model optical devices that have multiple dielectric interfaces. An example of its application to simulating photonic band gap structures has been used to demonstrate its capability. Analysis of comparison with FD-TD method indicates its advantage in efficiency.

#### REFERENCES

- [1] P. Kaczmarski and P. E. Lagasse, *Electron. Lett.*, vol. 24, pp. 675–676, 1988.
- [2] C. J. Smartt, T. M. Benson, and P. C. Kendall, *Electron. Lett.*, vol. 29, pp. 1352–1353, 1993.
- [3] R. Pregla and E. Ahlers, *Electron. Lett.*, vol. 29, pp. 1845–1847, 1993.
- [4] Y. Chung and N. Dagli, in *IEEE Antennas and Propagation Society International Symposium, 1992 Digest*, 1992, vol. 1, pp. 248–251.
- [5] G. H. Jin, J. Harari, J. P. Vilcot, and D. Decoster, *Electron. Lett.*, vol. 31, pp. 1867–1869, 1995.
- [6] Y. Chiou and H. Chang, *IEEE Photon. Technol. Lett.*, vol. 9, pp. 964–966, 1997.
- [7] W. P. Huang, S. T. Chu, A. Goss, and S. K. Chaudhuri, *IEEE Photon. Technol. Lett.*, vol. 3, pp. 524–526, 1991.
- [8] J. C. Chen, H. A. Haus, S. Fan, P. R. Villeneuve, and J. D. Joannopoulos, *J. Lightwave Technol.*, vol. 14, pp. 2575–2580, 1996.
- [9] H. Rao, R. Scarmozzino, and R. M. Osgood, *IEEE Photon. Technol. Lett.*, to be published.
- [10] G. R. Hadley, *Opt. Lett.*, vol. 17, pp. 1426–1428, 1992.
- [11] R. W. Freund, *SIAM J. Sci. Stat. Comput.*, vol. 13, pp. 425–448, 1992.
- [12] H. A. Van Der Vorst, *SIAM J. Sci. Stat. Comput.*, vol. 13, pp. 631–644, 1992.

# Large-Signal Regime Nearly Degenerate Four-Wave Mixing in Multi-Section Laser Diodes

J.M.Tang and K.A.Shore

University of Wales, Bangor,

School of Electronic Engineering and Computer Systems,  
BANGOR, LL57 1UT, UK.

Tel: +44(1248)382618; Fax: +44(1248)361429;  
e-mail: alan@sees.bangor.ac.uk

## 1. Introduction

Nearly Degenerate Four-Wave Mixing (NDFWM) in semiconductor laser diodes has been gaining higher degree of interest due to very high conversion efficiency and simple configuration. Both a high conversion efficiency ( $>10\text{dB}$ ) and a large step-tunable frequency detuning over a range ( $> 2.5\text{THz}$ ) can also be achieved by using cavity-enhanced NDFWM in a multimode semiconductor laser [1].

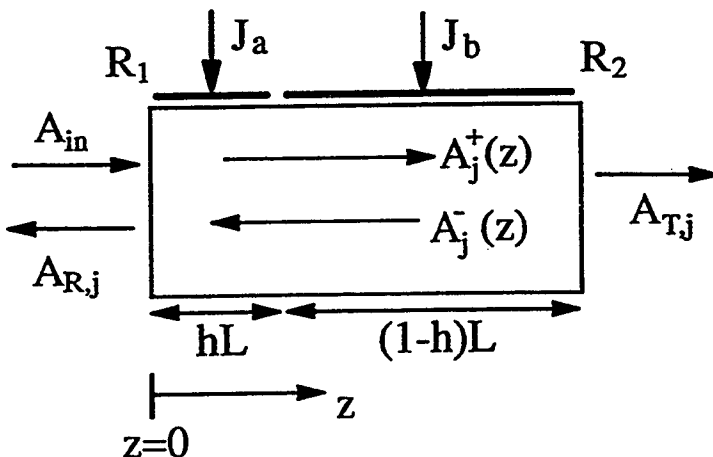


Fig.1 Schematic of NDFWM in a two-section laser diode.

To investigate the properties of NDFWM in semiconductor laser diodes, we presented an advanced theoretical model [2,3], which shows a very good agreement with experimental measurements [4]. The analysis is however performed in conventional single-electrode laser diodes. Multi-section semiconductor laser diodes have been extensively investigated [5]. In spite of the remarkable progress in the development of multi-section DBR and DFB laser diodes, Two-Section Single-Cavity Fabry-Perot (TSSC FP) laser diodes are very attractive light sources for low-cost optical subscriber networks because of their simple structure, which enables easy fabrication and high reproducibility. From fundamental point of view, NDFWM in TSSC FP laser diodes is of great interest. However, it appears that very little attention has been paid to this aspect. This is the motivation of this paper.

## 2. Model Analysis

We consider NDFWM in a TSSC FP laser diode, as shown in Fig.1. The laser is assumed to oscillate in a single transverse and longitudinal mode. A collinear probe wave is injected into the

pump laser through the front facet with power facet reflectivity  $R_1$  at  $z = 0$ .  $h$  is the fraction of the total laser cavity length occupied by the section  $a$ , and is chosen here to be  $h = 0.2$  [6]. The two active sections are pumped differently with injection current densities  $J_a$  and  $J_b$ , respectively, which are normalised to the current density at transparency,  $J_0$ .

Based on the coupled-mode travelling-wave equations obtained in Refs.2,3, the numerical simulations are performed. Note that small-signal gain is a function of  $z$  for TSSC FP laser diode. The probe/conjugate reflectivity is defined as the ratio of the probe /conjugate output power from the front facet (at  $z = 0$ ) to the incident probe power at the same facet.

### 3. Results and Discussions

The parameters used in the calculations are appropriate to GaAs-AlGaAs laser diodes. The injected current corresponding to each section of TSSC FP laser diode satisfies  $hJ_a + (1 - h)J_b = 2.0$  to ensure the output pump power from each facet remaining the same as that of homogeneous pumping condition as discussed in previous work [2,3]. The lasing frequency of the laser diode would vary with different pumping conditions. However, the frequency shift can be neglected if we assume that the probe wavelength is also changed by the same amount.

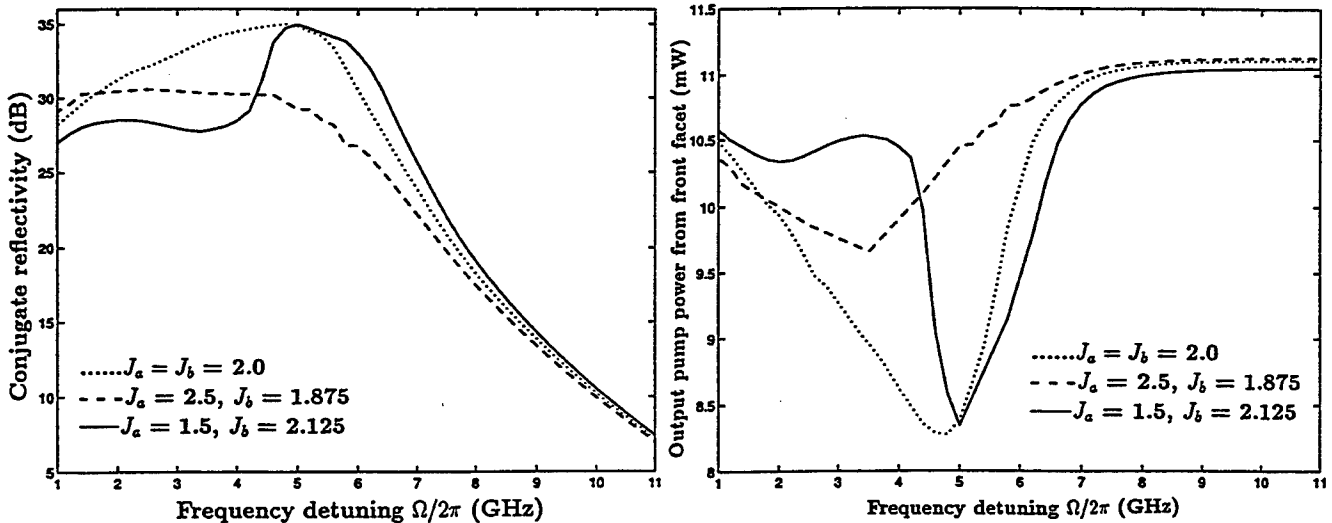


**Fig.2**Conjugate reflectivity versus frequency detuning for three different biasing conditions in a symmetric TSSC FP laser diode with  $R_1 = R_2 = 0.3$ . Input probe power is  $0.5\mu\text{W}$ .

For the injected probe power of  $0.5\mu\text{W}$ , the conjugate reflectivity as a function of frequency detuning is plotted in Fig.2, for different current pumping conditions. The corresponding output pump powers from the front facet are also given in Fig.3. The solid curve shows significantly increased conjugate reflectivity around the relaxation oscillation frequency ( $\sim 5\text{GHz}$ ), and the lowest conjugate reflectivity in the region of  $1\text{GHz} - 4.5\text{GHz}$ , compared with the other curves. Whilst for the dashed curve, no reflectivity peak occurs at the frequency detuning of  $5\text{GHz}$ , and the reflectivity near the resonant frequency is increased, thus resulting in a flatter lineshape. It is interesting to note that for the cases of both weak and strong probe injection power, the influence of carrier diffusion on the NDFWM reflectivity can be controlled by using a TSSC FP laser diode: injecting probe power from

**Fig.3**Output pump power from the front facet of the laser diodes as a function of frequency detuning in symmetric TSSC FP laser structures for three different biasing conditions. Input probe power is  $0.5\mu\text{W}$ .

lower (higher) gain section, the carrier diffusion effect on the NDFWM efficiency can be enhanced (damped).

The evolutions of NDFWM reflectivity can be confirmed by the output pump power versus the frequency detuning, as demonstrated in Fig.3. The output pump power is significantly reduced around the relaxation oscillation frequency where the probe and conjugate reflectivities are considerably increased. Although there is no efficiency peak occurring for the conjugate wave at the frequency detuning of 3.2GHz, as shown by the dashed line, the corresponding output pump power shows a minimum value. This is because the total reflectivity of the probe and conjugate waves exhibits a maximum value at that frequency detuning.

#### 4. Conclusions

The NDFWM behaviours in TSSC FP laser diodes are shown to be significantly dependent on optical probe injection into either section of a TSSC FP laser diode and injected probe power. The influence of carrier diffusion and pump depletion effects on NDFWM processes are also enhanced by this structure. Results suggest that the TSSC FP laser structure may be applied to control the influence of carrier diffusion on NDFWM efficiency.

#### Acknowledgements

This work was supported by EPSRC under grant GR/L03262. J.M.Tang is supported by the Professor Wynn Humphrey Davies Scholarship and the School of Electronic Engineering and Computer Systems, University of Wales, Bangor, UK.

#### References

- 1 J.A.Hudgings and K.Y.Lau, "Step-tunable all-optical wavelength conversion using cavity-enhanced four-wave mixing," *IEEE J. Quantum Electron.*, Vol.34, pp.1349-1355, 1998.
- 2 J.M. Tang and K.A. Shore, "Carrier diffusion and depletion effects on multiwave mixing in semiconductor lasers," *IEEE J. Sel. Top. Quantum Electron.*, Vol.3, pp.1280-1286, 1997.
- 3 J.M.Tang and K.A.Shore, "Nearly degenerate four-wave mixing in laser diodes subject to strong probe injection power," *IEEE J. Lightwave Technol.*, Vol.16, pp.876-883, 1998.
- 4 Y.Hong, J.M.Tang, and K.A.Shore, "Optical phase conjugation in laser diodes subject to strong probe injection power," *Electron. Lett.*, Vol.34, pp.1491-1492, 1998.
- 5 G.Griffel and C.-H.Chen, "Static and dynamic analysis of tunable two-section high-speed distributed feedback laser utilizing the gain lever effect," *IEEE J. Quantum Electron.*, Vol.32, pp.61-68, 1996.
- 6 W.M.Yee and K.A.Shore, "Enhanced uniform phase conjugation in two-section asymmetric laser diodes," *Opt. Lett.*, Vol.19, pp.2128-2130, 1994.

# Fundamental Cavity Mode of a Spot-Size Converted Fabry–Perot Semiconductor Laser

G. Hugh Song\*, Jeong K. Ji†, and Ahn Goo Choo†

\* Kwangju Institute of Science and Technology, Kwangju, 500-712 Republic of Korea, ghsong@kjist.ac.kr

**Abstract**—The fundamental cavity mode of a spot-size converted Fabry–Perot semiconductor laser is analyzed based on coupled local-mode theory. The analysis gives a new guideline on the design of spot-size converter integrated semiconductor lasers.

Reducing packaging costs has become one of the prime objectives in optoelectronics industry owing to massive deployment of optoelectronic components in optical networks. One of such system components is the semiconductor laser in a transmitter module. Tapered-waveguide structures in various designs of laser diodes are widely employed in recent years for the purpose of increasing the spot size of the output beam to directly match the modal beam profile in a single-mode optical fiber to dispense with a cylindrical lens module or with the unreliable lensed fiber.

Such tapered waveguide structures have been conventionally analyzed by the beam-propagation method (BPM) [1]. However, it has been known that the measured far-field patterns hardly match with the results from such simulation even under a well-controlled laboratory environment. Yet, in a small number of measurements, we sometimes observe rather nice-looking far-field patterns which find their way into technical reports. Apart from these few lucky ones, there are just too many samples whose measurements do not match well with predictions made by such BPM simulations. In this paper, for the first time to our knowledge, we present a theory which explains why there exists such a mismatch between the BPM simulation and the actual far-field measurement.

The new theory is hinted by the fact that the length of the straight section of the semiconductor laser with a spot-size converter inside the laser cavity af-

fests the far-field pattern. That is one of the evidences for the fact that building up a resonance state with the tapered structure inherently affects the beam characteristics of such lasers.

To analyze such effects of optical resonance, we have developed a theory as follows: The radiation modes are handled as quasi-guided modes from the artificial boundary of simulation [2]. A sufficient number<sup>1</sup> of coupled-wave equations are then solved to adequately account for the tapered section of the waveguide:

$$\frac{db_\mu(z)}{dz} = -j[\beta_\mu(z) - k_r] b_\mu(z) + \sum_\nu R_{\mu\nu}(z) b_\nu(z), \quad (1)$$

where  $b_\mu(z)$  is the wave amplitude of the  $\mu$ th local mode,  $k_r$  is the reference propagation constant,  $R_{\mu\nu}(z)$  is the coupling coefficient owing to waveguide tapering [3]. Each local propagation constant varies from  $\beta_\mu(0)$  to  $\beta_\mu(L)$  through the tapered waveguide. Consecutive segments of the waveguide within the tapered section are modeled by transmission matrices. Multiplication of such matrices gives a matrix,  $M^{ssc}$ , for the whole section of the tapered waveguide. The straight section of the waveguide is then denoted by a diagonal matrix  $M^{st}$ , whose elements are represented by

$$M_{\mu\nu}^{st} \equiv \delta_{\mu\nu} \exp([\gamma_\mu - j\beta_\mu(0) + jk_r] z), \quad (2)$$

where  $\gamma_\mu$  represents the amplitude gain coefficient of the  $\mu$ th local mode at lasing, and is determined by the facet reflectivities and the cavity length. Then, one round-trip of light is represented by a matrix;

$$M \equiv [M^{ssc} M^{st}] R_f [M^{ssc} M^{st}]^T R_f, \quad (3)$$

where the superscript ‘T’ represents the transpose, and  $R_f$  and  $R_r$  represent the full matrices for the

<sup>1</sup>We solved 40 and 80 equations confirming no significant difference between the two sets of results.

† J. K. J. and A. G. C. are with Samsung Advanced Institute of Technology, Kiheung, 440-600 Korea. This work has been supported in part by the Institute of Information Technology Assessment through the University Basic Research Program and by KOSEF through the UFON ERC Program.

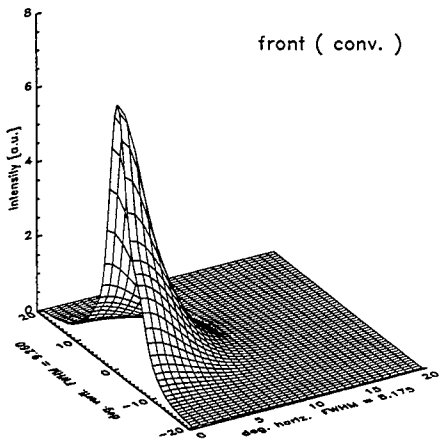


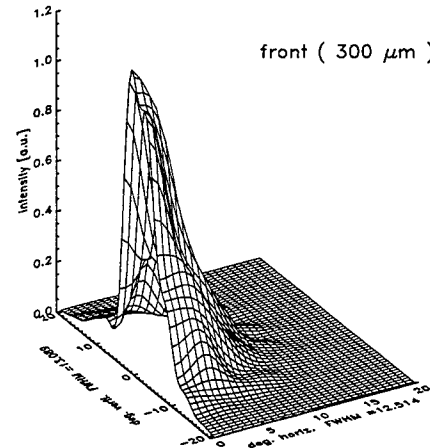
Fig. 1. One-side plot for the symmetric far-field pattern obtained by the conventional method for the beam from a spot-size converted semiconductor laser.

reflection among local modes at the front and rear facets, respectively [4]. Then, the resonance condition for the laser operation can be written by an eigenvalue equation

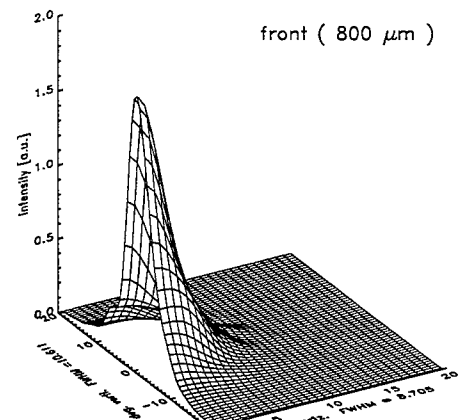
$$\mathbf{M} \begin{pmatrix} b_1(L) \\ b_2(L) \\ \vdots \end{pmatrix} = \lambda \begin{pmatrix} b_1(L) \\ b_2(L) \\ \vdots \end{pmatrix}, \quad (4)$$

where the individual elements,  $b_1(L)$ ,  $b_2(L)$ ,  $\dots$ , for the largest magnitude eigenvalue  $\lambda$ , represent the wave amplitudes of the eigen-field of the fundamental *cavity* mode. These will give information on the true near-field at the front facet of the laser and the corresponding far-field pattern.

In the simplest case of a linearly-shaped taper, Fig. 1 has been obtained from a BPM analysis, thus ignores the effect of the cavity resonance. On the other hand, Fig. 2 has been obtained by the present analysis on the fundamental cavity mode. For this plot, we have assumed down-tapering of the waveguide cross-section for the taper length of 150  $\mu\text{m}$  and the straight section of lengths 300  $\mu\text{m}$  and 800  $\mu\text{m}$  for Fig. 2(a) and (b), respectively, with the common facet reflectivities of 30/80 %. We find that the far-field plots are not as nice as Fig. 1, which conforms to our extensive experience in the laboratory. These figures indicate that when a simple BPM analysis is used, there exists a substantial level of overestimation of the taper performance. In fact, we have



(a)



(b)

Fig. 2. One-side plot for symmetric far-field patterns of the front-side emission from spot-size-converter integrated semiconductor lasers with the straight section of lengths (a) 300  $\mu\text{m}$  and (b) 800  $\mu\text{m}$ .

confirmed in simulation that increase of the facet reflectivities or other disturbances in the waveguide structure during fabrication may affect the far-field pattern quite drastically.

One good manifestation of our theory is provided by the far-field pattern from the rear-side output of the laser. The plots of Fig. 3 are such patterns for the above two cases of Fig. 2. The plots conform to our laboratory experience that the rear-side beam shows rather impure far-field patterns (as shown in Fig. 4(b)) unlike the patterns from the front-side.

In conclusion, the present analysis should give a new dimension in our understanding and new guide-

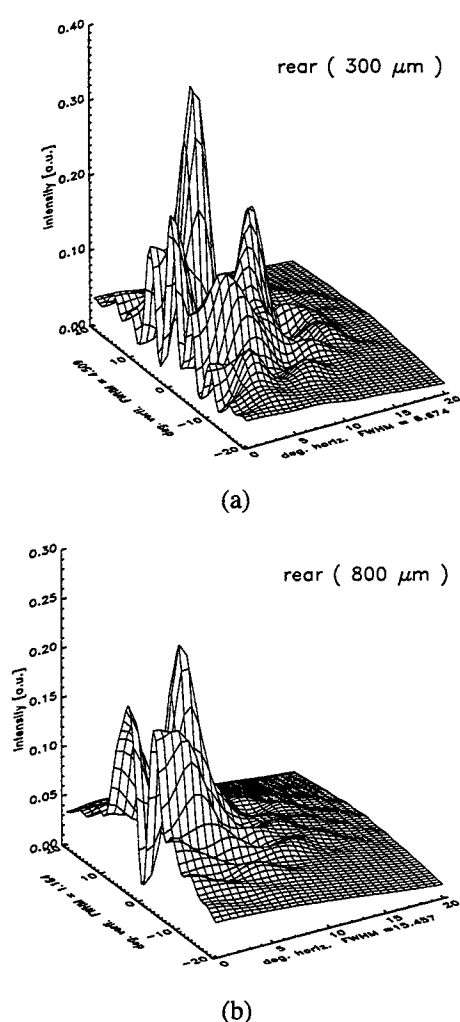


Fig. 3. Far-field patterns of the rear-side emission from the spot-size-converter integrated semiconductor lasers with the straight sections of lengths (a) 300  $\mu\text{m}$  and (b) 800  $\mu\text{m}$ .

lines on the use of the tapered-waveguide design in a simple semiconductor laser of the Fabry-Pérot structure. To avoid mode conversion which degrades the beam characteristics, increasing the internal gain coefficient for the fundamental transverse mode in the straight section of the laser is the most important. To achieve that goal, beside employing the conventional optimization technique on taper shapes [2], one should not design the total length of the laser too short and should not increase the facet reflectivities too high. It is interesting to note that these conditions somewhat contradict to the conditions for an efficient laser.

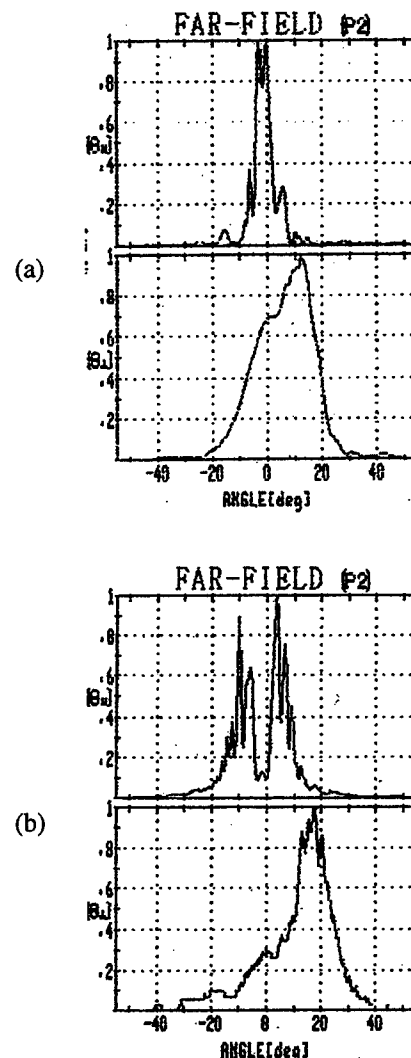


Fig. 4. Far-field patterns obtained by a horizontal scan (upper plots) and a vertical scan (lower plots) of beam from (a) the front facet and (b) rear facet of a typical spot-size converted semiconductor laser.

#### REFERENCES

- [1] K. Yokoyama, N. Sekino, T. Hirono, Y. Tohmori, and Y. Kawaguchi, "Design and fabrication of high-coupling efficiency spot-size converter integrated laser diodes using three-dimensional BMP program," *J. Lightwave Tech.*, vol. 16, pp. 1456–1463, 1998.
- [2] G. H. Song and W. J. Tomlinson, "Fourier analysis and synthesis of adiabatic tapers in integrated optics," *J. Opt. Soc. Am., A*, vol. 9, pp. 1289–1300, 1992.
- [3] D. Marcuse, *Theory of Dielectric Waveguides*, 2nd ed., Academic, New York, NY, 1991.
- [4] G. H. Song, *Principles of Modern Photonics*, class note,

## Transmission, reflection, alignment tolerance, and far-field profiles of spot-size converters

B M A Rahman, T Wongcharoen, M Meyer, M Rajarajan, P K Arasaratnam, and K T V Grattan

City University, London  
 Department of Electrical Electronic and Information Engineering  
 Northampton Square, London EC1V 0HB, UK.  
 Tel: +44-171-477-8123 Fax: +44-171-477-8568 Email: [B.M.A.Rahman@city.ac.uk](mailto:B.M.A.Rahman@city.ac.uk)

### **Introduction:**

Monolithically integrated spot-size converters (SSCs) are increasingly being considered [1-5] to expand the narrow spot-size of an active semiconductor guided-wave device within a Photonic Integrated Circuit (PIC) so that efficient coupling to a single mode fiber (SMF) with a relatively larger spot-size can be made. Over the last 5 years, studies of various system designs incorporating tapered structures, operating very close to their modal cutoff, have shown that improved coupling can be achieved and simultaneously the alignment tolerances can also be relaxed. In this paper, initially important optical parameters are calculated for a 1-dimensional tapered spot-size converter. Although the concept of the tapered SSC approach is gaining popularity, however, the fabrication of such a tapered SSC requires complex material growth and high precision control in lithography and the etching process [1,3]. An alternative approach [6,4] of using two non-identical but phased matched *uniform* coupled waveguides is also considered, to achieve the necessary spot-size conversion and such a system can be easily fabricated by using standard techniques.

### **Theory:**

Analytical techniques are inadequate for the rigorous analysis of different types of PICs incorporating advanced SSC designs. Various numerical approaches have been gaining importance to study such sub-systems and to optimise their performance. It is necessary to find the modal field profiles at each segment of the tapered SSC to estimate the overall expansion of the spot-size. For semiconductor optical waveguides with air-semiconductor interfaces and two-dimensional confinement a rigorous vector approach is necessary, and for such structures the vector H-field finite element method (FEM) [7] has been established as one of the most accurate and efficient techniques. It has been widely used to find modal field profiles of the fundamental modes along the SSCs [3,5].

In order to obtain the evolution of the optical wave in the SSC region, a beam propagation method (BPM) approach may be more useful and has been widely used [2]. A simple one-directional BPM cannot estimate the reflection coefficients at the discontinuity interfaces and also is not best suited to estimate the transmission coefficient from a strong discontinuity interface, such as at the end of a SSC and SMF interface. However, it has been shown that the least squares boundary residual (LSBR) method can be used to estimate this important parameter more accurately [8].

### **Results**

Figure 1 shows the variation of the effective indices,  $n_e = \beta/k_o$ , and spot-size,  $\sigma$ , for the fundamental TE<sub>0</sub> mode with the taper thickness,  $t$ , for an InP based SSC. For this waveguide, the refractive indices of the InGaAsP core and the InP cladding are calculated to be  $n_{g1}=3.367$  and 3.169 at  $\lambda_o=1.55 \mu\text{m}$ . In this work, the spot-size is defined as the distance from the center of the waveguide, where the field intensity is 1/e of its maximum value [3-5]. It can be noted that although a larger spot-size can be obtained by increasing the taper thickness,  $t$ , however, for  $t > 0.95 \mu\text{m}$ , the guide is no longer single moded. It can be observed that as the effective index approaches the slab refractive index, the spot-size starts expanding rapidly for  $t < 0.5 \mu\text{m}$ . This region is considered for the operation of a spot-size converter.

Next, the coupling ( $\tau$ ) to a SMF and the reflection ( $\rho$ ) from the butt-coupling interface are calculated from the modal fields, obtained by the FEM, and by using the LSBR method, as shown in Fig. 2. It can be seen for smaller values of  $t$ , as the spot-size is expanded, the coupling efficiency is also improved and the reflection coefficient is decreased. The far-field from the modal field of the tapered SSC structure is also calculated and the full-width at half-maximum (FWHM) is also shown in Fig.2, which indicates that a narrower beam can be obtained for  $t < 0.2 \mu\text{m}$ .

Figure 3 shows a schematic diagram of the monolithically integrated laser diode (LD) section and the directional coupler-based spot-size converter (SSC) section. The top InGaAsP (1.26Q) waveguide in the SSC section is similar to the active guide in the laser section, so that most of the laser light couples to this waveguide. For this waveguide, the refractive indices of InGaAsP core and InP cladding are calculated to be  $n_{g1}=3.367$  and 3.169 at  $\lambda_0=1.55 \mu\text{m}$ . The width ( $W1$ ) and height ( $H1$ ) are taken as  $1.6 \mu\text{m}$  and  $0.3 \mu\text{m}$ , respectively, as typical of a PIC. Due to the high index difference between the guide and cladding ( $n_{g1}-n_s=0.198$ ), numerically simulated results show small spot-sizes of  $0.85$  and  $0.56 \mu\text{m}$  in the lateral ( $x$ ) and the vertical ( $y$ ) transverse directions, respectively. The FWHM [3-5] far-field beam-width has been calculated as  $28$  and  $35$  degrees in the  $x$  and  $y$  directions. The field profile of an optical fiber with core and cladding indices of  $1.50$  and  $1.45$  respectively and radius  $4.0 \mu\text{m}$  is not only circular, but also much larger than that of the PIC. Numerically simulated results shown here reveal that only  $12\%$  of the optical power can be coupled to the optical fiber and  $38\%$  of the power is reflected, if the laser and fiber are directly butt-coupled.

However, in the approach presented in this work, a lower waveguide is introduced to couple the optical power through the evanescent wave from the top to this lower waveguide. If the lower waveguide is made from a diluted waveguide incorporating multiple thin layers of InAlAs and InP (10:1 thickness ratio), then its core will have a lower refractive index,  $n_{g2} = 3.209$ . Simulated results have shown that the height ( $H2$ ) and the width ( $W2$ ) of this waveguide need to be  $5.0 \mu\text{m}$  and  $8.3 \mu\text{m}$  for this guide to be phase matched to the upper waveguide. The far field profile produced from this expanded modal field is shown in Fig. 4, at  $z = 50 \mu\text{m}$ . The FWHM beam width from this waveguide is  $10.8$  and  $16.6$  degrees in the  $x$  and  $y$ -directions, respectively.

The separation between the two waveguides in the SSC section is taken as  $1.0 \mu\text{m}$  and in this case, the coupling length reaches its maximum value of  $650 \mu\text{m}$  when the guides are phase matched. Since at the end of the SSC section  $98\%$  of the optical power transfers to the lower waveguide with a larger spot-size, the coupling efficiency increases to  $62\%$  (2 dB loss) when butt-coupled to the SMF. In this case only  $20\%$  of the power is reflected back into the SSC section and the remaining  $18\%$  is radiated around the junction. This overall loss compares satisfactorily with the loss values reported in recent work [1-3,5].

Next the effect of the alignment tolerance, a key design parameter, is studied and this is shown in Fig.5, revealing that the power coupling efficiency deteriorates as the distance between the center of the SMF and that of lower waveguide ( $\Delta y$ ) is increased. The  $1 \text{ dB}$  tolerance of  $\pm 1.5 \mu\text{m}$  shown here compares satisfactorily with that for the tapered SSCs, as reported recently [1,3,9]. For the case when the laser-fiber is directly coupled (L-F), the maximum coupling efficiency will drop from  $12\%$  to below  $8\%$  when the guides are misaligned ( $\Delta y$ ) by  $2 \mu\text{m}$ .

Since it has been suggested in this work that one way of achieving the phase matching is by etching the lower waveguide to a correct width, the device performance due to the variation of this parameter ( $W2$ ) has also been studied and is shown in Fig. 6. It can be seen that if the width of the lower guide is changed by  $\pm 0.2 \mu\text{m}$  from the design value of  $8.5 \mu\text{m}$ , the effect on the transmission coefficient is negligible. Since the top waveguide is buried inside the InP cladding, only the effect of the lower waveguide width is studied.

### Conclusions

The enhancement of the coupling efficiency, the reduction of the reflection coefficient, and the production of a narrower FWHM beam width is shown for the tapered spot-size converters. It has also been seen that using evanescent coupling between two non-identical but synchronous uniform waveguides, the spot-size from a laser can be expanded to improve the coupling efficiency to a SMF. In this approach, a more complicated fabrication technique, which is necessary for the SSC incorporating a tapered section, can be avoided. It has been shown that by using a low index contrast waveguide, the laser spot-size can be expanded considerably. In this case the simulated results show that a higher coupling efficiency, with a narrow output divergence beam and with a relaxed fiber alignment tolerance can be achieved without introducing a penalty in laser performance. This approach also yields a reduced reflection coefficient from the SSC-SMF interface.

### References

- [1] I. Moerman *et al.*, *IEEE J. Selected Topics in Quantum Electronics*, vol. 3, pp. 1308-1320, Dec. 1997.
- [2] H. Kobayashi *et al.*, *IEEE J. Selected Topics in Quantum Electronics*, vol. 3, pp. 1384-1391, Dec. 1997.
- [3] G. A. Vawter *et al.*, *IEEE J. Selected Topics in Quantum Electronics*, vol. 3, pp. 1361-1371, Dec. 1997.
- [4] V. Vusirikala *et al.*, *IEEE J. Selected Topics in Quantum Electron.*, vol. 3, pp.1332-1343, Dec. 1997.
- [5] A. Lestra and J.-Y. Emery, *IEEE J. Selected Topics in Quantum Electronics*, vol. 3, pp. 1429-1440, Dec. 1997.
- [6] B. M. A. Rahman *et al.*, *IEEE Photonics Tech. Letters*, vol. 8, pp.557-559, April 1996.
- [7] B. M. A. Rahman and J. B. Davies, *J. Lightwave Technol.*, vol. 2, pp.682-688, Oct. 1984.
- [8] M. Rajarajan *et al.*, *J. Lightwave Technol.*, vol. 14, pp.2078-2084, Sept. 1996.

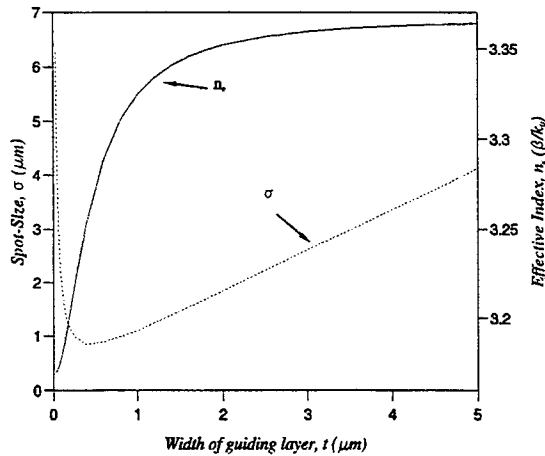
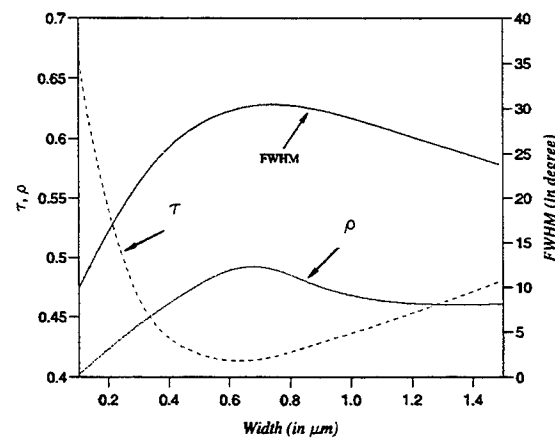
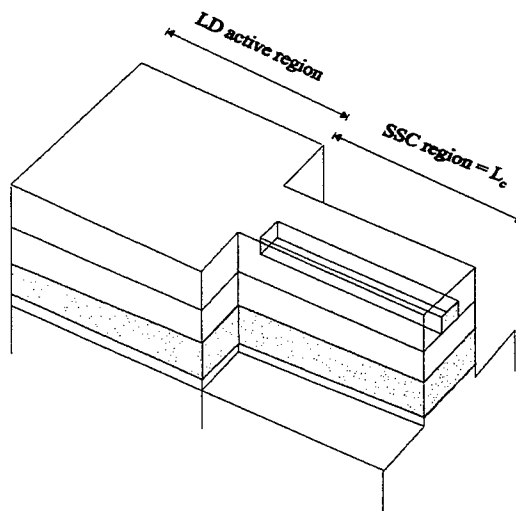
Fig 1. Variation of  $n_e$  and  $\sigma$  with taper thickness,  $t$ .Fig 2. Variation of  $\tau$ ,  $\rho$  and FWHM beam-width with  $t$ .

Fig 3. Schematic diagram of a directional coupler-based spot-size converter.

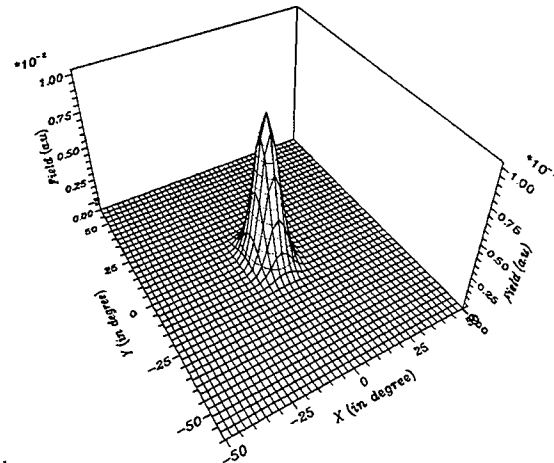
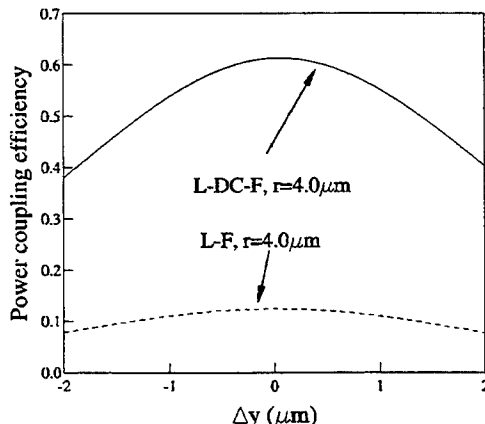
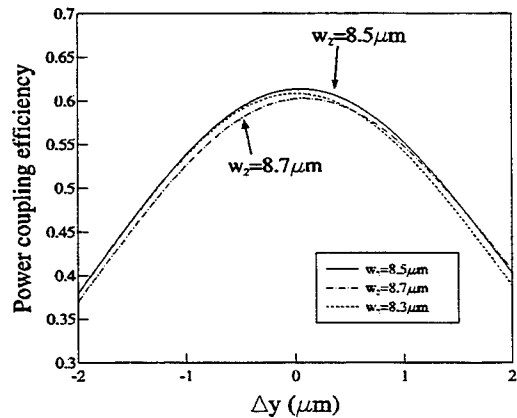


Fig 4. Far-field profile for the expanded modal field profile

Fig 5. Variation of the power coupling efficiency with the alignment tolerance ( $\Delta y$ )Fig 6. Variation of the power coupling efficiency with alignment tolerance for different lower wave-guide widths,  $W_2$ .

**Integrated Photonics Research and Photonics in Switching**

# **Joint Session 1: Technologies for Optical Cross Connects**

**Wednesday, July 21, 1999**

**Julian B. Soole, Bell Laboratories, Lucent Technologies, USA**  
Presider

**JWA**  
**8:45am–10:15am**  
San Rafael

## Micromachined Scalable Fiber-Optic Switch

P.M. Hagelin, U. Krishnamoorthy, C.M. Arft, J.P. Heritage, O. Solgaard

Department of Electrical and Computer Engineering, University of California, Davis CA 95616  
Tel. (530) 752-2522, FAX (530) 752-8428, e-mail: hagelin@ece.ucdavis.edu

### Abstract

In this paper we describe a novel switch architecture for single-mode optical fibers based on micromirror arrays. This architecture allows scaling to a large number of fiber ports and can be integrated directly with free-space wavelength multiplexers (gratings). Using tilt-up surface micromachined polysilicon micromirrors, a 2x2 switch configuration was demonstrated. The measured insertion loss was -4.2 dB and the cross-talk was -50 dB. The mirrors used in the switch design have a maximum optical deflection of 24 degrees and a resonant frequency of 1.9 kHz, leading to a switching time (including settling) of 2 ms. The micromirrors have sufficient resolution to support scaling to 19 channels while maintaining the same low cross-talk.

### Introduction

In recent years, there has been a surge of interest in the area of optical switching for communication networks. All-optical switching has the potential to reduce the need for costly optical-to-electronic and electronic-to-optical conversion in high-speed fiber-optic networks. A number of 2x2 switches have been reported, as well as micromirror-based switches scalable to large fiber-port counts [1, 2]. Our switch combines the scalability of micromachined switches with the potential for WDM (wavelength-division multiplexed) integration [3].

The proposed switch architecture (Fig. 1) requires  $2N$  mirrors for a full  $N \times N$  spatial cross-connect. Two opposing arrays of analog-addressable rotating mirrors make up the switch matrix. The first array directs each optical input beam toward a mirror in the second array, which deflects the switched beams into the output fiber array. Path length variations through the switch are small in the 2x2 configuration, but become an important consideration in larger switches. In comparison with designs requiring a much greater number of mirrors [1, 2] and cascaded 1x2 or 2x2 switches, our design reduces mechanical complexity while maintaining full cross-connect functionality.

An added advantage of our architecture is its scalability in the wavelength dimension. This is shown in Fig. 2, where  $M$  wavelength channels on the input fibers are multiplexed (by gratings) and spatially switched in  $M$  parallel  $N \times N$  cross-connects, providing an independent cross-connect for each wavelength. Each mirror array may be fabricated on a planar substrate with lithographic precision to reduce the complexity of bulk-optical alignment.

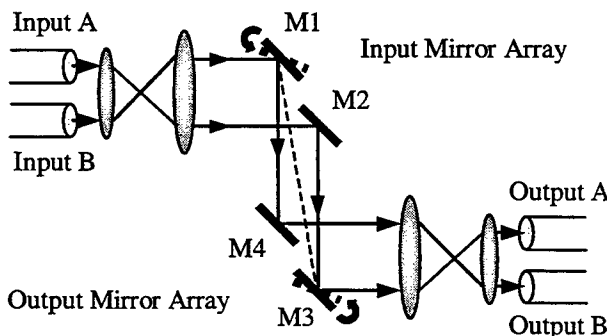


Figure 1. 2x2 Switch Architecture. Mirrors M1 and M2 redirect the input light toward an output mirror. M4 aligns light to the optical fiber at Output B, and M3 aligns light to Output A.

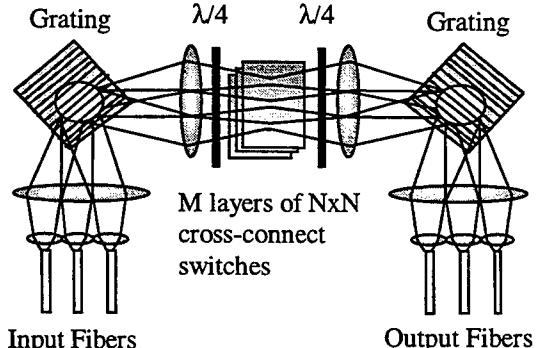


Figure 2. WDM Switch Architecture. Gratings spatially separate the input optical beams by wavelength. Each wavelength channel is routed to a  $N \times N$  cross-connect switch.

### Switch Implementation

Our spatial switch demonstration combines bulk-optical and micromachined components (Fig. 1). The input and output fiber arrays are comprised of single-mode optical fibers with 250  $\mu\text{m}$  center-to-center separation, held in silicon micromachined v-grooves. The optical beams from the input fibers pass through a 10X telescope before reaching the input mirror array (Fig. 3). The mirror positions are staggered to reduce the optical beam separation between the mirror arrays (Fig. 4). The reduced beam separation minimizes the rotational angle required to achieve switching. The optical beams entering and exiting the switch matrix are separated by 2.5 mm, and inside the switch they are separated by 500  $\mu\text{m}$ . The beam waist, located between the two mirror arrays, has a measured  $1/e^2$  radius of 75  $\mu\text{m}$ . The distance between the two arrays is set to the Rayleigh range, which can be shown to be the optimum separation for maximizing the number of addressable channels. The output mirror array and optics are identical to those on the input side.

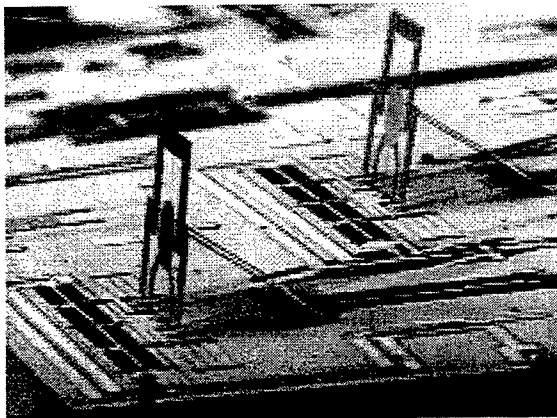


Figure 3. SEM Image of the Switch Micromirrors.

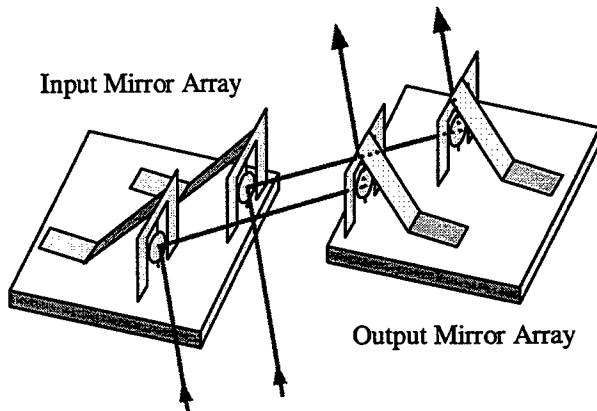


Figure 4. Two-Chip Switch Setup.

### Micromirror Design

The mirror arrays are fabricated using a commercial, three-polysilicon-layer, surface-micromachining process [4]. The mirrors are fabricated flat on the surface of the chip and assembled with a micropositioner. Each micromirror (Fig. 3) is a circular polysilicon plate, 300  $\mu\text{m}$  in diameter and 1.5  $\mu\text{m}$  thick, suspended by two 200  $\mu\text{m}$  long, 3  $\mu\text{m}$  wide, and 1.5  $\mu\text{m}$  thick torsion beams. The mirrors have a 50 nm aluminum coating to enhance reflectivity. The mirrors rotate about an axis perpendicular to the chip surface. The upper torsion beam connects to a supporting tilt-up frame that holds the mirror perpendicular to the chip surface. The lower torsion beam is attached to the substrate by a rotary hinge. Movable hinges, connected by struts to the lower edge of the optical surface, attach the mirror to polysilicon comb-drive actuators that move parallel to the chip surface. There are two banks of comb drives symmetrically connected to each mirror at a distance of 182  $\mu\text{m}$  from the rotational axis. This allows bi-directional operation of the mirrors, maximizing their angular range and the number of switch channels that they may address. In the 2x2 switch, the mirrors need be only actuated in one direction.

### Results

We characterized the switch mirrors by measuring their frequency response and deflection characteristics. The fundamental resonant frequency of the mirrors was measured to be 1.9 kHz, leading to a switching time, including settling, of approximately 2 ms. The optical power in the output channels was measured as a function of mirror actuation using germanium photodetectors and a lock-in amplifier.

The transition of coupled optical power (1550 nm) during switch operation is shown in Fig. 5. The four sections of the figure represent the coupled optical power in the output channels as a single mirror rotates and the others are held stationary. At the far left of Fig. 5, mirrors 1 and 3 are in the cross-state. The insertion loss is measured to be -4.8 dB with -48 dB cross-talk. When mirror 4 is also in the cross-state (not shown), we expect the cross-talk to decrease. Proceeding to the right in Fig. 5, the first section

shows mirror 1 relaxing from the cross-state to the bar-state, with the other mirrors fixed in position. At the beginning of the second section, mirrors 1 and 4 are in the bar-state, but cross-talk is still high because mirror 3 is in the cross-state. By relaxing the voltage on mirror 3, the full-switch bar-state is achieved at the center of the figure, with insertion loss of -4.2 dB and cross-talk of -50 dB. The right half of Fig. 5 represents a re-tracing of the previous mirror states to demonstrate the angular repeatability of the mirror. There is a slight hysteresis in the cross-talk and insertion loss, likely due to friction in the microhinges.

The channel separation inside the switch is 6.7 times the Gaussian-beam radius midway between the mirrors. Our measurements demonstrate that this separation is sufficient to ensure -50 dB cross-talk between channels (Gaussian beam theory would predict a much smaller required separation for this level of cross-talk, but the fiber modes cannot accurately be described as Gaussian down to -50 dB). Based on the current distance between channels and the maximum deflection range of the mirrors (24 degrees optical), our mirror design is, in principle, capable of addressing 19 channels. Measurements with off-center fibers in our present set-up show that this un-optimized configuration allows for arrays of 16 standard fibers without increasing the insertion loss by more than 3 dB. These observations indicate that our switch architecture has the potential to be scaled to 16x16 fibers and beyond. Expansion to M layers of our cross-connect switch with the addition of grating MUX/DEMUX will allow scaling to M wavelength channels (Fig. 2).

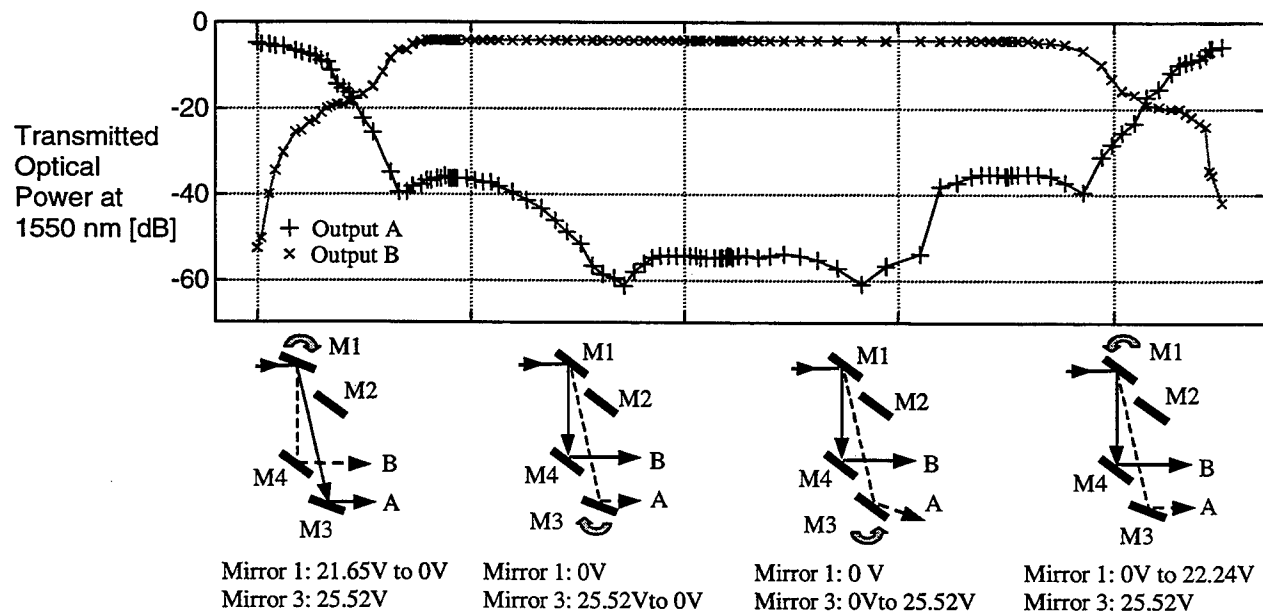


Figure 5. Switch Characterization. The horizontal axis is in units of volts squared.

## Conclusion

We have demonstrated a micromachined all-optical switch with low cross-talk and low insertion loss. The architecture of our switch allows scaling to large numbers of fiber ports and integration with wavelength multiplexers. Fabrication of each mirror array on a single chip has reduced mechanical complexity and increased mirror alignment precision. Additional switch channels may be added by appending a set of input and output mirrors per additional channel up to the maximum channel count.

## References

1. L.Y. Lin, E.L Goldstein, J.M. Simmons, R.W. Tkach, *Photonics Tech. Lett.*, Vol. 10, No. 10, Oct 98, pp. 1425-27.
2. L.Y. Lin, E.L Goldstein, R.W. Tkach, *Photonics Tech. Lett.*, Vol. 10, No. 4, April 98, pp. 525-527.
3. J.S. Patel, Y. Silberberg, *Photonics Tech. Lett.*, Vol. 7, No. 5, May 95, pp. 514-516.
4. K.W. Markus, D.A. Koester, A. Cowen, R. Mahadevan, V.R. Dhuler, D. Robertson, L. Smith, *Proc. SPIE*, Vol. 2639, Oct 95, pp. 54-63.

## A Robust, Low-Crosstalk, InGaAsP/InP Total-Internal-Reflection Switch For Optical Cross-Connect Applications

Ian Betty, Roghieh Rousina-Webb, Chi Wu<sup>1</sup>

Nortel Networks, Box 3511 Station C, Ottawa, Canada, K1Y 4H7

Phone: 01-613-765-2248, Fax: 01-613-765-2471, e-mail: ibetty@nortelnetworks.com

<sup>1</sup>Present Address: Jet Propulsion Laboratory,  
California Institute of Technology, Pasadena, CA 91109, USA  
Phone: 1-818-354-0660, email: Chi.Wu@jpl.nasa.gov

### Introduction

Cross-connect architectures of semiconductor optical switches will be useful in future communication network applications such as packet and/or wavelength switching. Recently, the SOA gate has been the favoured semiconductor switch for its excellent interchannel crosstalk and low insertion loss. However, it generally lacks true system transparency with limitations on the number of WDM channels, and bit rate, polarization, and input power restrictions. It also requires integration with a second switch having low bar-state loss to be useful in scalable architectures [1,2]. An alternative, the total-internal-reflection (TIR) switch, has none of these limitations. Moreover, it still features fully digital operation, compact size and wavelength independence. However, the TIR switch has traditionally required difficult fabrication techniques and suffered from poor crosstalk performance. We propose a robust, InGaAsP/InP TIR switch designed for use within a novel cross-connect architecture that allows for compact, scalable, transparent, and low-crosstalk, NXN optical cross-connects without need for ion implantation or semiconductor regrowth in fabrication.

### TIR Switch Geometry and Cross-connect Architecture

The TIR switch geometry and cross-connect architecture is shown in Figure 1. The TIR switch has an asymmetric waveguide y-junction at an intersection angle of 3° and an optical/electrical interaction length of 450μm. The architectural building block that connects each orthogonal input-to-output waveguide consists of two TIR switches and a 45° optical turning mirror within an area of only 1mm<sup>2</sup> [3]. The orthogonal waveguide architecture minimizes the interchannel crosstalk by cascading the TIR switch performance between any input-to-output waveguide combination, and by limiting the output coupling of input stray light. The digital response of each TIR switch allows a single electrical chip connection in each building block, thus only N<sup>2</sup> connections and only N simultaneous signals are required for the NXN cross-connect operation.

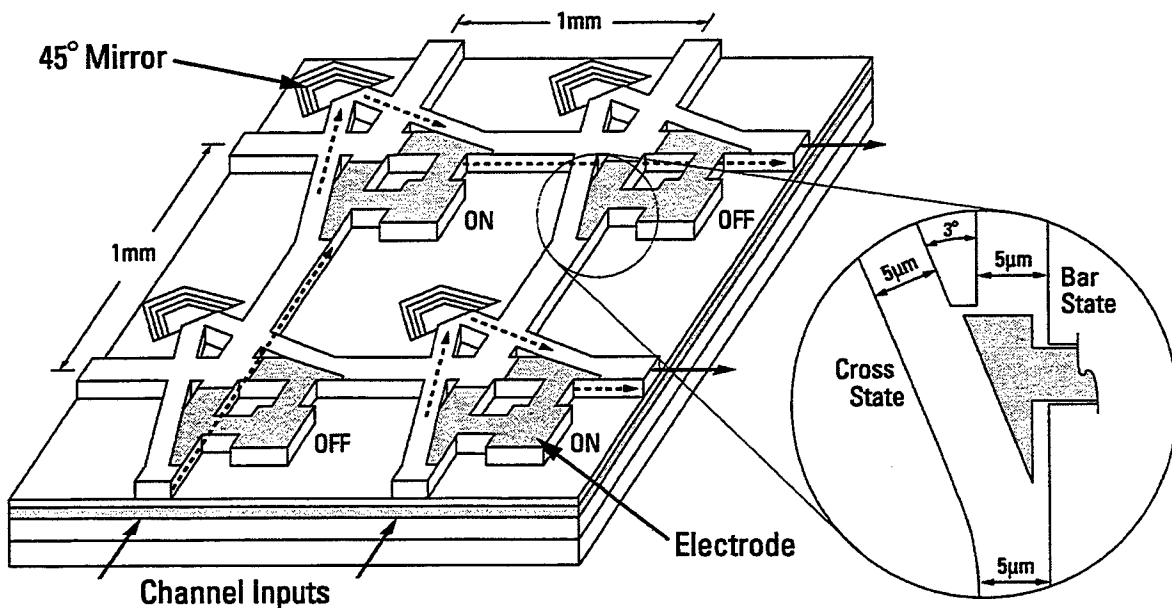


Figure 1: Cross-Connect Architecture and TIR Switch Geometry

### TIR Switch Design and Fabrication

The switch uses single mode,  $5\mu\text{m}$  wide ridge waveguides with weak [ $\Delta n \approx 2 \times 10^{-3}$ ] lateral confinement and a vertical  $Q=1.3\mu\text{m}$  InGaAsP/InP p-i-n heterostructure. Switching is achieved under forward bias using the large, free-carrier-density-induced refractive index change [4]. A guide layer cross-section from a 3D-Semivectorial Beam Propagation simulation of our TIR switch at  $\lambda=1550\text{nm}$  is shown in Figure 2. The bar-state losses and crosstalk are minimized using the waveguide geometry such that a TE bar-state loss of -0.36dB and a bar-state crosstalk of -24.9dB are theoretically expected. Instead of trying to eliminate lateral carrier diffusion using current blocking [5], implant isolation [1,6], or semi-insulating regrowth [2], the carrier gradient has been anticipated and our electrode shaped to minimize the switching losses. This approach is taken to improve the manufacturability of the switch and keep the bar-state loss low since the bar-state loss rather than the switching loss dominates our loss budget. Switching losses of 1.3dB are theoretically expected due to unavoidable free-carrier absorption. The traditional TIR switch limitations of high switching current and poor crosstalk performance have been overcome using single mode operation and low contrast waveguides.

The switch was grown on N+ InP substrates using MOCVD. Ridge waveguides were formed using both CH<sub>4</sub>/Ar RIE and HCl:H<sub>3</sub>PO<sub>4</sub> wet chemical etching. A p-ohmic contact was formed on the top InGaAs contact layer of the device using a lift-off process. After wafer thinning back n-contacts were formed.

### Experimental Results for the TIR Switch

Figure 3 shows the lateral near field profile of an individual AR-coated TIR switch obtained at  $\lambda=1550\text{nm}$  by scanning a  $5\mu\text{m}$  slit across the magnified image of the switch output. Optical coupling to the switch is via cylindrically-lensed single mode fiber with a coupling loss of approximately 2.6dB. Switch performance is shown at 0mA and 40mA injection. An excess cross-state loss (A-C) of 1.6dB is obtained with a cross-state extinction (C-D) of 13.5dB. The bar-state crosstalk (A-D) is -15.2dB with a bar-state extinction (A-B) of 13.7dB. Note, the bar-state crosstalk and cross-state extinction values are pessimistic since the input and output waveguides are not orthogonal and no modal filtering is performed with the integrated power scan measurement. In reverse operation with light input from the cross-state of the switch, the on-off ratio at the single input is 19.6dB. Taken as a whole, this data clearly demonstrates excellent single mode operation for our TIR switch.

Figure 4 shows the normalized TE fiber-to-fiber switch transfer curves. Digital switching performance after 40mA is observed. A bar-state extinction of 13.7dB and a cross-state extinction of 20.7dB are obtained. In our proposed cross-connect architecture the interchannel crosstalk is dominated by twice the cross-state extinction of the individual switch [i.e. 35-40dB interchannel crosstalk is feasible]. This clearly demonstrates that low crosstalk performance is achieved in our TIR switches.

Using the Fabry-Perot cutback method [7], the bar-state loss was measured to be less than our experimental error of 0.5dB for both TE and TM polarization. This low bar-state loss should allow a 16x16 cross-connect to be built with the highest on-chip loss < 12dB. The wavelength performance of the switch was measured using fiber-to-fiber transmission loss measurements from 1528nm to 1561nm normalized against identical straight waveguide measurements. The bar-state loss uniformity was better than 0.2dB, the cross-state uniformity was better than 0.1dB, and the bar-state crosstalk uniformity was better than 0.5dB. This stable wavelength performance confirms true TIR operation for the switch.

In conclusion, we have reported a robust TIR switch designed for a compact, scalable cross-connect architecture that should allow for 35-40dB interchannel crosstalk without the use of SOA gates. The TIR switch has low (<0.5dB) bar state loss and was simple to fabricate since no carrier isolation techniques were needed.

### References

1. Gregory A. Fish et al., *IEEE Photonic Technology Letters*, Vol. 10, No. 9, pp. 1256-58, 1998.
2. T. Kirihara, et al., *IEEE Photonic Technology Letters*, Vol. 6, No. 2, pp. 218-21, 1994.
3. Chi Wu, U.S. Patent No. 5581643, Dec 3<sup>rd</sup> 1996.
4. B. R. Bennett, et al., *Journal of Quantum Electronics*, Vol. 26, No. 1, pp. 113-122, 1990.
5. Kwang-Ryong Oh et al., *IEEE Photonic Technology Letters* Vol. 6, No. 1, pp. 65-67, 1994.
6. Zhuang Wanru et al., *Fiber and Integrated Optics*, Vol. 15, pp. 27-36, 1996.
7. R.G. Walker, *Electronics Letters*, Vol. 21 No. 13 pp. 581-82, 1985.

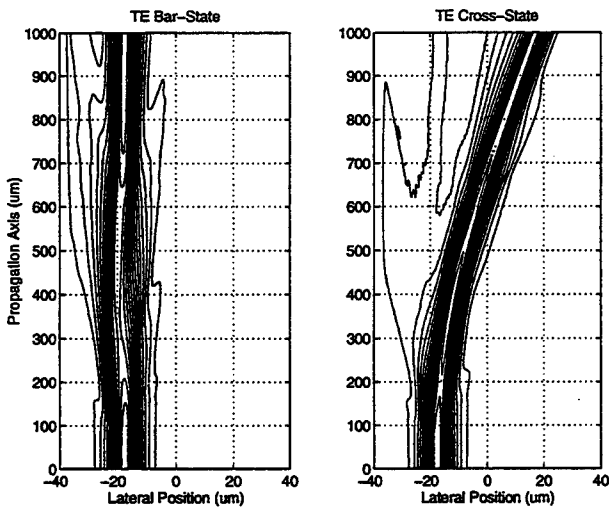


Figure 2: 3D-TE-SVBPM Simulation

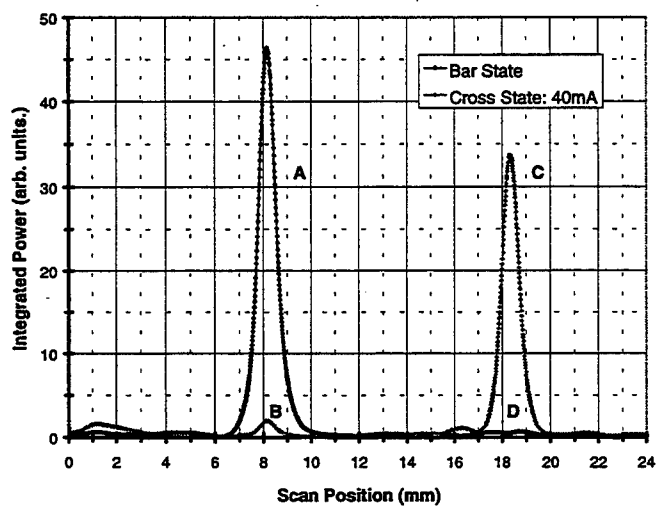


Figure 3: Lateral Near Field Scan of the Switch: TE 1550nm

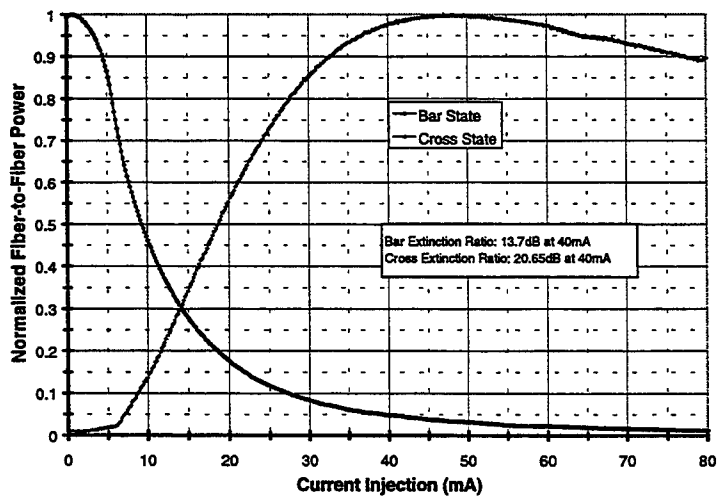


Figure 4: Normalized Switch Fiber-to-Fiber Transfer Curves: TE 1550nm

## Monolithically integrated wavelength selective cross connects

C. R. Doerr

Bell Laboratories, Lucent Technologies

791 Holmdel-Keyport Road, Holmdel, NJ 07733

(732) 888-7067, FAX: (732) 888-7074, e-mail: crdoerr@lucent.com

### 1. Introduction

Integrated wavelength selective cross connects (WSCs), also called wavelength-selective switches, can serve as wavelength add-drops in the field or as elements in large central-office cross connects. The simplest WSC is a two-line by two-line version, and it can have a switch for each wavelength in either a bar or cross state between the lines. We first describe some reported WSCs and then discuss some architectures for the latter application.

### 2. Devices

The first fully integrated WSC was demonstrated by Okamoto, *et. al.* in silica<sup>[1]</sup>. It consists of four waveguide grating routers (WGRs)<sup>[2]</sup> connected by an array of Mach-Zehnder switches. Such a configuration is shown in Fig. 1a. The version in Ref. [1] handles 16 wavelengths. To improve the extinction ratio of the Mach-Zehnder switches, Ref. [1] uses a dilated switch architecture. A dilated switch is a set of switches arranged so that each signal must pass through two switches, providing a net extinction ratio equal to the product of the extinction ratios of the individual switches. Herben, *et. al.* demonstrated the same type of architecture in InP, except for handling 4 wavelengths and employing only single-stage Mach-Zehnder switches<sup>[3]</sup>. These designs can provide excellent switching performance, but they generally require waveguide crossings, hampering their compactness. There are also some reported integrated devices using Mach-Zehnder switches that act as limited WSCs. For example, Ref. [4] demonstrates a WSC that uses WGRs and Mach-Zehnder switches, similar to Fig. 1a, except that it manages to avoid waveguide crossings. However, it pays a price for this by preventing the user from using every other wavelength.

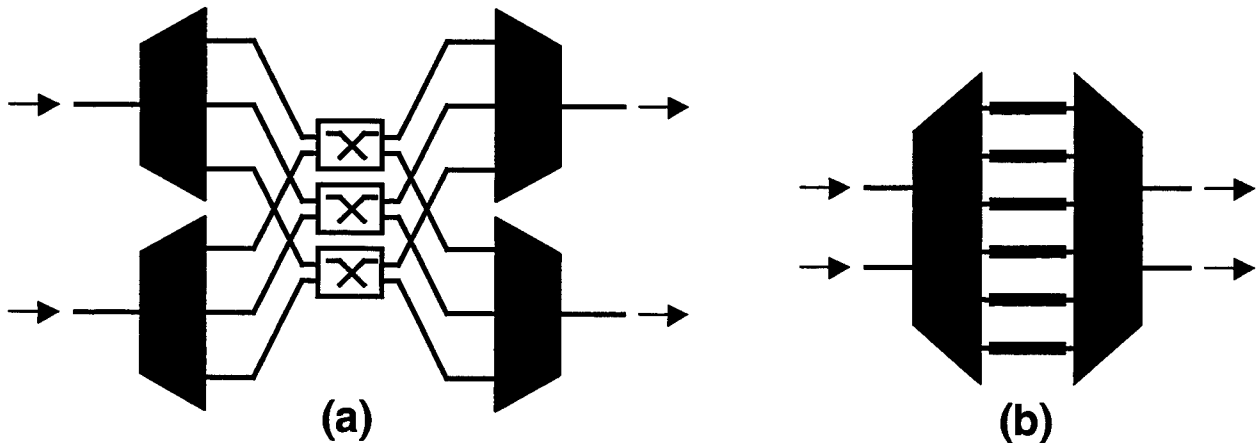


**Figure 1.** Architectures for fully integrated WSCs (3 wavelengths here). The trapezoids represent multi/demultiplexers, and the rectangles in (b) represent phase shifters.

Another approach is to integrate part of the switches and part of the demultiplexer/multiplexer together<sup>[5]</sup>, such as in Fig. 1b. This gives a fully functional WSC with reduced loss and size. It has no waveguide crossings. When the demultiplexer/multiplexers are

WGRs, this device has been called an arrayed-waveguide lens device<sup>[5]</sup>. The WGRs are interleaved chirped so that the WGRs perform both the demultiplexing and splitting/combining functions. While such a device can achieve low loss (6.6-7.7 dB for a 16-channel version in silica<sup>[5]</sup>) and good switching performance, the phase-shifter control is complicated and sensitive.

There are also some integrated WSCs that do not use WGRs at all, such as Ref. [6], which proposes to use (not yet demonstrated) micro ring resonators.

### 3. Application in large cross connects

One can make a large WSC (in terms of number of inlet fibers) from the smaller integrated WSCs. Two example architectures are shown in Fig. 2. These architectures are proposed and analyzed in Ref. [7]. Figure 2a shows a Benes architecture made up of 2 x 2 WSCs. It uses a minimum number of elements, but it is only rearrangeably nonblocking in wavelength. Figure 2b shows a broadcast-and-select architecture made up of 1 x 1 WSCs. It is strict-sense nonblocking in wavelength, and the signals pass through a minimum number of elements; but it uses a large number of elements. The latter architecture was recently demonstrated using 2 x 2 arrayed-waveguide lens WSCs serving as the 1 x 1 WSCs<sup>[8]</sup>.

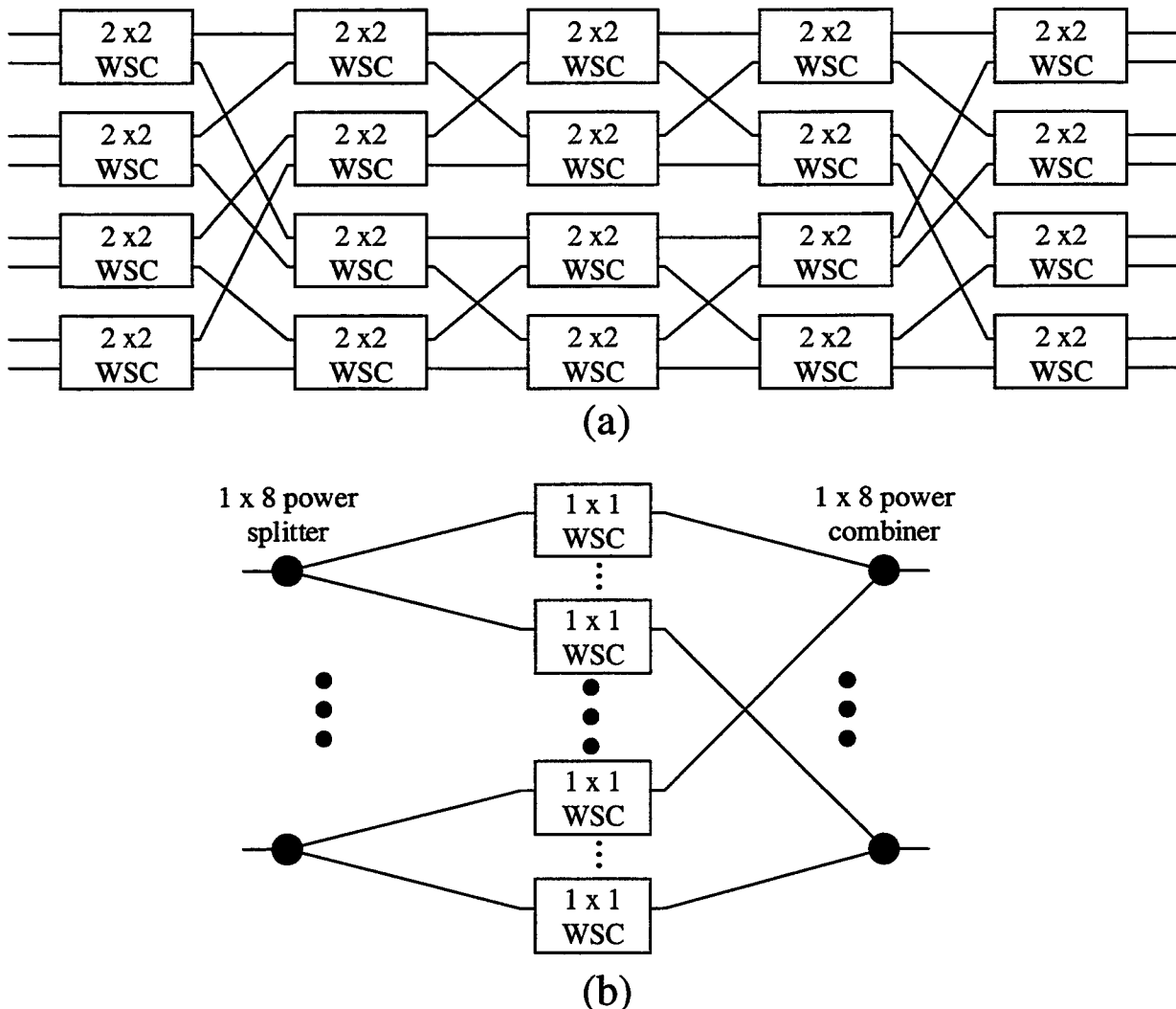


Figure 2. Architectures for large WSCs (8 x 8 here) made up of smaller WSCs.

### Acknowledgments

The author is indebted to L. W. Stulz, C. Dragone, M. Zirngibl, A. White, J. Gates, M. Cappuzzo, E. Laskowski, A. Paunescu, L. Gomez, K. Schwarz, J. Yanchik, and J. Fernandes.

### References

- <sup>1</sup> K. Okamoto, M. Okuno, A. Himeno, and Y. Ohmori, "16-channel optical add/drop multiplexer consisting of arrayed-waveguide gratings and double-gate switches," *Electron. Lett.*, vol. 32, pp. 1471-1472, 1996.
- <sup>2</sup> M. K. Smit and C. van Dam, "Phasar based WDM devices: Principles, design and applications," *IEEE J. Select. Topics Quantum Electron.*, vol. 2, pp. 236-250, 1996; H. Takahashi, S. Suzuki, K. Kato, and I. Nishi, "Arrayed-waveguide grating for wavelength division multi/demultiplexer with nanometer resolution," *Electron. Lett.*, vol. 26, pp. 87-88, 1990; C. Dragone, "An  $N \times N$  optical multiplexer using a planar arrangement of two star couplers," *IEEE Photon. Technol. Lett.*, vol. 3, pp. 812-815, 1991.
- <sup>3</sup> C. G. P. Herben, C. G. M. Vreeburg, D. H. P. Maat, X. J. M. Leijtens, Y. S. Oei, F. H. Groen, J. W. Pedersen, P. Demeester, and M. K. Smit, "A compact integrated InP-based single-phasar optical crossconnect," *IEEE Photon. Technol. Lett.*, vol. 10, pp. 678-680, 1998.
- <sup>4</sup> H. Li, C.-H. Lee, w. Lin, S. Didde, Y.-J. Chen, and D. Stone, "8-wavelength photonic integrated  $2 \times 2$  WDM cross-connect switch using  $2 \times N$  phased-array waveguide grating (PAWG) multi-demultiplexers," *Electron. Lett.*, vol. 33, pp. 592-594, 1997.
- <sup>5</sup> C. R. Doerr, L. W. Stulz, J. Gates, M. Cappuzzo, E. Laskowski, L. Gomez, A. Paunescu, A. White, and C. Narayanan, "Arrayed waveguide lens add-drop in silica," to appear in *IEEE Photon. Technol. Lett.*
- <sup>6</sup> R. A. Soref and B. E. Little, "Proposed N Wavelength M Fiber WDM Crossconnect Switch Using Active Microring Resonators," *IEEE Photon. Technol. Lett.*, vol. 10, pp. 1121-1123, 1998.
- <sup>7</sup> G. Wilfong, B. Mikkelsen, C. R. Doerr, M. Zirngibl, "Non-blocking characteristics of some WDM cross-connects," submitted to *J. Lightwave Technol.*
- <sup>8</sup> C. R. Doerr, B. Mikkelsen, G. Raybon, P. Schiffer, L. W. Stulz, M. Zirngibl, G. Wilfong, M. Cappuzzo, E. Laskowski, A. Paunescu, L. Gomez, and J. Gates, "Wavelength selective cross connect using arrayed waveguide lens multi-wavelength filters," OFC Post Deadline Paper PD34, 1999.

## **Silicon Micromachines for Lightwave Networks**

David Bishop, Bell Laboratories  
Lucent Technologies, Murray Hill, NJ 07974

### **Abstract:**

Silicon micromechanics is an emerging field which is beginning to impact almost every area of science and technology. In areas as diverse as the chemical, automotive, aeronautical, cellular and optical communications industries, Silicon micromachines are becoming the solution of choice for many problems. In my talk I will describe what they are, how they are built and show how they have the potential to revolutionize lightwave systems. Devices such as optical switches, variable attenuators, active equalizers, add/drop multiplexers, optical crossconnects, gain tilt equalizers, data transmitters and many others are beginning to find ubiquitous application in advanced lightwave systems. I will show examples of these devices and describe some of the challenges in attacking the billions of dollars in addressable markets for this technology.

### **What is a MEMS Device?**

MEMS research is an outgrowth of the vast capabilities developed by the semiconductor industry, including deposition, etching, and lithography, as well as an array of chemical processes such as anisotropic and highly selective etches having different etch rates for different crystallographic orientations and materials. These processes, which were originally developed to build microelectronic devices, are also capable of building micromechanical devices—structures capable of motion on a microscopic scale. MEMS devices are built in much the same way as a silicon integrated circuit (see the figure, upper left hand side). Various films such as polysilicon, silicon nitride, silicon dioxide, and gold are deposited and patterned to produce complicated, multilayer three-dimensional structures. However, the major difference is a release step at the end. In a MEMS device, some of the layer materials are removed using a selective etch, leaving a device with moveable elements.

MEMS devices offer a number of advantages to designers. They are made using integrated circuit (IC) batch-processing techniques, so although fabrication may consist of a complicated, multistep process, the devices are economical to produce because many are made simultaneously. In addition, designers and manufacturers can exploit the extensive capabilities of the IC fabrication industry and can profitably use previous-generation equipment. In an era in which an IC factory costs a billion dollars and is obsolete in less than five years, the ability to reuse the equipment for a new class of cutting edge products is very appealing.

IC fabrication techniques also allow designers to integrate micromechanical, analog, and digital microelectronic devices on the same chip, producing multi-functional integrated systems. Contrary to intuition, MEMS devices have proven to be robust and long-lived, especially ones whose parts flex without microscopic wear points. Research in this area has been extremely active over the last decade, producing microscopic versions of most macro-machines. In particular, many of us believe that the size scale at which these machines work well make

them a particularly good match to optics problems where the devices, structures and relevant wavelengths range in size from one to several hundred microns.

### **Where in a Lightwave Network will they be Applied?**

Work at Bell Labs in Optical MEMS has focused on a number of devices such as optical modulators, variable attenuators, switches, add/drop multiplexers, active equalizers and optical crossconnects. Shown in the figure (upper right hand side) is an overview of places in lightwave networks where we see application for MEMS components. Each red dot is a place where MEMS can be the solution of choice. Clearly, there exist many opportunities.

In the figure, LHS center, is a micrograph of our 1x2 MEMS optical switch. The mirror is connected to a see-saw and either reflects the light from the optical fiber on the left to the fiber at right angles to it or moves out of the way to allow the light to go straight into the other fiber. In the figure, RHS center, is a micromirror for use in a variable attenuator. Light from a fiber at right angles to the mirror gets reflected to an output fiber and the coupling between the two can be adjusted by applying a voltage to the electrode to the left of the large mirror. In the figure on the lower LHS is an array of micromirrors for use in an add/drop multiplexer. In operation, each wavelength of light in an optical fiber gets spatially demultiplexed by a grating and lands on its own mirror to be correctly routed to either the output port or the drop port. Finally, shown on the lower RHS is a two axis micromirror for use in a 1xN optical switch. The mirror is doubly gimbaled so that light can be routed in two directions to allow complex switching functions to be accomplished. Clearly, the possibilities for novel optical devices and functions are endless.

### **Summary:**

Although no MEMS device has yet been deployed in an active lightwave network, the wealth of new capabilities presented by MEMS optical devices places them as certain candidates for imminent commercial success. The optical MEMS industry is estimated to become a multi-billion dollar business in five years. Many companies, including Lucent Technologies, identify MEMS as a strategic technology they cannot afford to neglect and we believe it will provide exciting challenges for many years to come.

### **References:**

1. C.R. Giles, B. Barber, V. Aksyuk, R. Ruel, L. Stulz and D. Bishop, "Reconfigurable 16-channel WDM DROP Module using Silicon MEMS Optical Switches," accepted for publication in Photonics Technology Letters, 1998.
2. Randy Giles, Vladimir Aksyuk, Brad Barber, Andrew Dentai, Elles Burrow, Charlie Burrus, Larry Stulz, Joel Hoffman, Brian Moyer, David Bishop, "Highly efficient light-actuated micromechanical photonic switch for enhanced functionality at remote nodes," postdeadline paper PD2, Optical Fiber Conference, San Jose CA, 1998.
3. A.G. Dentai, E.C. Burrow, C.R. Giles, C.A. Burrus, J.C. Centanni, "High-voltage (2.1V) integrated InGaAs photogenerator," Electronics Letters, vol. 33, no. 8. pp 718-719, 1997.

### **Figure Caption:**

Shown in the figure are a schematic MEMS device (ULHS), schematic lightwave network with MEMS applications shown as red dots (URHS), a 1x2 switch (CLHS), a variable attenuator (CRHS), an array of micromirrors (LLHS) and a two axis micromirror (LRHS).

**Integrated Photonics Research**

# **WDM and TDM System Modeling**

**Wednesday, July 21, 1999**

**Curtis R. Menyuk, University of Maryland, Baltimore County, USA**  
Presider

**RWA**  
**8:45am-10:00am**  
Sierra Madre North

# High-speed optical transmission

**John D. Moores**

Lincoln Laboratory  
Massachusetts Institute of Technology  
244 Wood Street  
Lexington, MA 02420-9108  
TEL: (781) 981-6114  
FAX: (781) 981-2874  
Moores@LL.MIT.edu

Numerical simulation using split-step Fourier based algorithms is a widely used tool for modeling the propagation of optical data through fiber-optic telecommunications systems. The algorithm and the application to data transmission systems will be briefly described. Examples of simulations of various high-speed transmission systems will be presented. Examples will include forward-looking 100+ Gb/s time-division multiplexed (TDM) transmission as well as simulations of propagation in an experimental test bed at MIT Lincoln Laboratory. Simulations include both dispersion-managed systems and systems operating near the zero dispersion wavelength. All-optical regeneration will be briefly discussed, and simulations presented demonstrating the utility of optical regeneration. The importance of higher-order dispersion management will be stressed. Two examples are given below.

One example involves of propagation near the zero dispersion wavelength, typically avoided due to phase-matching. Figure 1 shows distortion that is primarily due to uncompensated dispersion slope (third-order dispersion) at 100 Gb/s. Figure 2 shows the improvement possible using all-optical regenerators every 200 km, with 50 km amplifier spacing. The regenerators perform clock recovery to synchronize a local optical clock source to the incoming data. The local clock and the incoming data are fed into an interferometric ultrafast optical switch that acts to gate the local clock pulses based on the incoming data. Figure 3 shows that by using periodic compensation, the regenerator spacing can be increased to 400 km, with 100 km amplifier spacing.

A more forward-looking result is presented in Figure 4. Simulation of 1 Tb/s data was performed, neglecting polarization mode dispersion. With compensation of dispersion and dispersion slope, a 50 km amplifier spacing, and a 200 km regenerator spacing, successful propagation over 2 Mm was achieved.

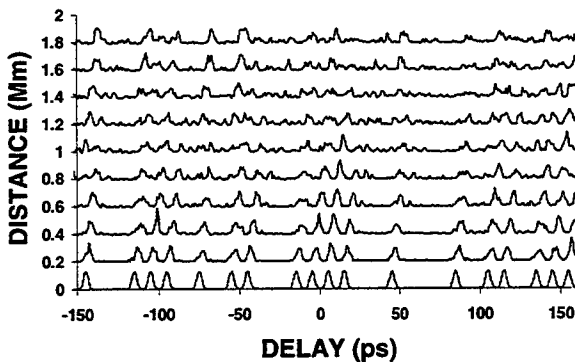


Figure 1. Unregenerated simulation at zero GVD. 100 Gb/s, 3.64 ps raised cosine. Third-order dispersion is uncompensated and is the primary effect that washes out the data pattern.

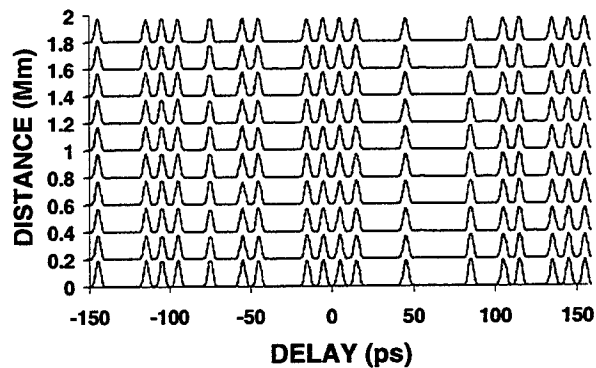


Figure 2. Same as Figure 1, but with interferometric switch based optical regenerators every 200 km, 50 km amplifier spacing.

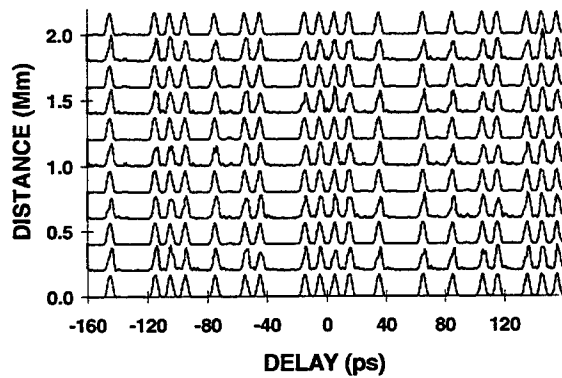


Figure 3. 2 Mm, 100 Gb/s, 3.64 ps raised cosine transmission with 100 km amplifier spacing, 400 km regenerator spacing,  $D=0$ , using lumped third-order dispersion compensation after each amplifier.

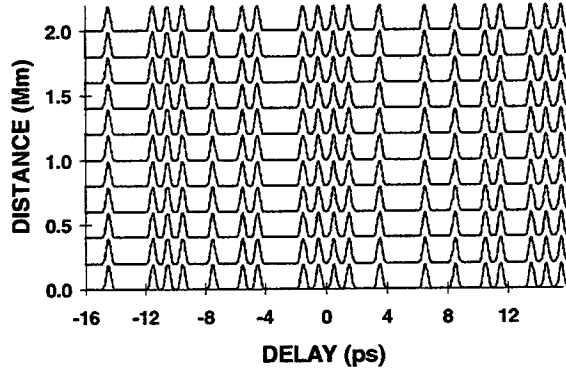


Figure 4. 1 Tb/s transmission over 2 Mm with lumped compensation of dispersion and dispersion slope, 50 km amplifier spacing, 200 km regenerator spacing.

# Modeling of High-Bit Rate TDM and WDM Systems

**Dirk Breuer**

Virtual Photonics Inc., Helmholtzstr. 2-9,  
D-10587 Berlin, Germany

Phone: (++49) 30-347 047 15, Fax: (++49) 30-347 047 17  
Email: d.breuer@virtualphotonics.com

**Klaus Petermann**

TU Berlin, Fachgebiet Hochfrequenztechnik, Einsteinufer 25,  
D-10587 Berlin, Germany  
Email: petermann@tu-berlin.de

**Introduction:** With the introduction of Erbium-Doped Fiber Amplifiers (EDFAs), the fiber loss is no longer a limiting factor in optical communication systems. EDFAs are capable of amplifying a large number of wavelength-division multiplexed (WDM) channels simultaneously over an optical bandwidth of several tens of nanometers. Due to optical amplification an optical transmission system has now many analoglike characteristics since the different effects as cross-talk, amplifier noise, dispersion and nonlinearity *etc.* can accumulate when the signal propagates along the fiber. No signal regeneration like in electronic 3R-regenerators is provided by these fiber amplifiers.

Today point-to-point WDM systems with up to 40 channels at a channel bit rate of 2.5 Gbit/s over transmission length of a few hundreds of kilometers are already in commercial use. Optical transmission systems using high-bit rate WDM techniques are being prototyped in laboratories for use in commercial backbone networks. For example, one research system has a bit rate of 20 Gbit/s per channel and 51 wavelength for transmission over 1000 kilometers of conventional single-mode fiber [1]. In another lab-experiment, the transmission of 19 channels each of 160 Gbit/s, corresponding to a total capacity of 3 Tb/s, over 40 kilometers of dispersion shifted fiber has also been shown [2].

Since the interaction between the impairments due to dispersion, fiber nonlinearity, channel frequency allocation, power per channel, amplifier noise *etc.* is complex, general analytical solutions or simple estimations are difficult or nearly impossible to find. Moreover, building experimental test beds and evaluating multiple technologies experimentally requires considerable time and manpower. Therefore modeling tools for explaining and optimizing experiments, estimating system behavior, and planning future system upgrades on the existing fiber plant or building infrastructure with new developed fibers are necessary. To make these simulation tools more efficient it is important to provide models at different abstraction levels: a simple system-level model allowing a fast performance analysis of communication systems, a more detailed behavioral (black-box) model, that can be fitted with experimentally measured data, down to a very deep physical model which needs a detailed knowledge about device structure and operating conditions *etc.*.

We show excellent qualitative and good quantitative agreement between simulations and experiments for high-capacity TDM and WDM systems. The simulations are particularly useful for comparing transmission schemes, in our example, pre- and post-compensation. In the WDM evaluation the amplifiers are modeled using a black-box model based on measured characteristics to take the amplifier gain shaping into account.

**Numerical Models:** Fig. 1 shows the principle setup of an optical WDM point-to-point system consisting of transmission lasers with external modulators, multiplexer, transmission fiber, optical amplifier, demultiplexer and receiver is depicted in Fig. 1. The electric field propagation in the fiber is modeled by the nonlinear Schrödinger equation, which is mainly solved by the well-known split-step Fourier method,

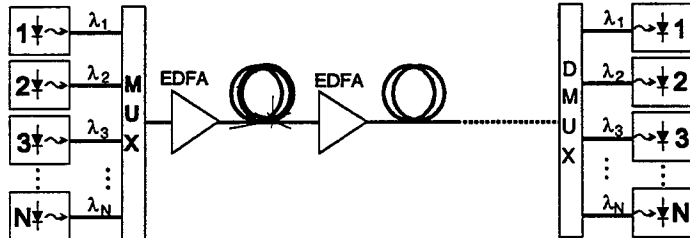


Fig. 1: Schematic of a WDM system

or beam propagation method (BPM) [3]. In the numerical calculations for single channel systems a pseudo-random bit sequence of typically  $2^7\text{-}1$  is used [4]. The number of sampling points is typically in the range of  $2^{14}\text{-}2^{16}$  covering a bandwidth large enough to include new generated frequency components (e.g. due to Four-Wave Mixing). To avoid step-size effects in WDM calculations the maximum step-size for a single step has to be reduced to a few tens of meters [5]. Moreover the step-size in the simulations is controlled by limiting the nonlinear-phase shift in a single-step to a few mrad, typically 1 to 3 mrad [7]. For the EDFA models with different abstraction levels are available.

**40 Gbit/s TDM System:** In a first application we numerically and experimentally investigate the potential of transmitting a 40 Gbit/s signal over already embedded standard single-mode fiber (SMF). The

experiments were performed at the Heinrich-Hertz Institut (HHI) für Nachrichtentechnik Berlin GmbH [6]. The setup is depicted in Fig. 2. The overall link dispersion was fully compensated at  $\lambda=1549.5$  nm by a dispersion compensating fiber (DCF). The DCF ( $\alpha=0.5$  dB/km,  $D_{\text{DCF}} = -90$  ps/km/nm,  $S = -0.15$  ps/km/nm<sup>2</sup>) was placed either at the transmitter (pre-compensating) or at the receiver (post-compensating). The optical power launched into the DCF was always low to ensure operation in the linear regime. The experimentally and theoretically obtained penalty after 150 km SMF transmission is shown in Fig. 3 for the two schemes. Good agreement between experimental and theoretical results has been achieved, as shown in Fig. 3. For low fiber-input powers the system performance is limited by the low signal-to noise ratio (SNR) and for higher fiber-input powers by nonlinear self-phase modulation. The post-compensation allows for an increase in the input-power by about 4 dB compared to the pre-compensation. In the case of single channel transmission the numerical study allows a fast and quite accurate estimation of the system performance, acceptable tolerances or comparison of different fiber types [6].

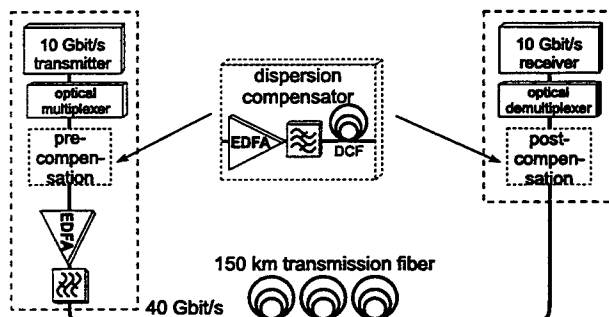


Fig. 2: Schematic Setup

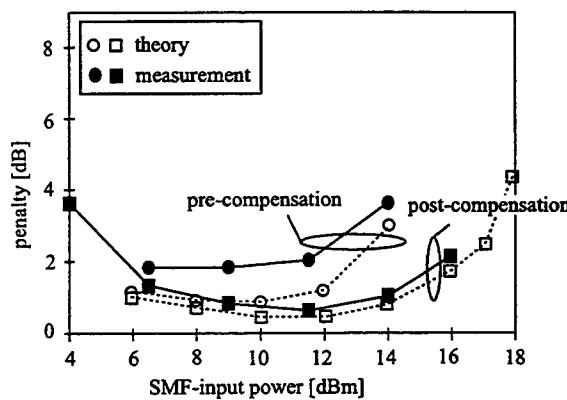


Fig. 3: Penalty for 150 km SMF transmission against fiber-input power for pre- and post-compensation.

**WDM EDFA Simulation and Measurement:** We have also evaluated a commercial available 40 channel WDM system with 50 GHz channel spacing and a total capacity of 100 Gbit/s. The system consists of 5 SMF-spans of nominal 25 dB loss each and 4 in-line amplifiers and one pre-amplifier. The system was modeled using a commercial available tool [9]. Due to the low data rate per channel the system was mainly limited by the ASE-noise of the amplifiers. To estimate the performance of the individual channels, it was necessary to take the amplifier gain shaping properly into account. Therefore a simple

system oriented amplifier model with flat gain could not be used. Since no specific EDFA parameters for a detailed physical model were available, the amplifiers were modeled using a black-box model based on measured gain and ASE noise spectra at two different input power levels [10]. From these characteristics and the saturation characteristic at one wavelength, the EDFA behavior under many operation conditions can be predicted. As shown in Fig. 4, the maximum difference between measured and the predicted (calculated) spectral gain over a large bandwidth was less than 0.2 dB.

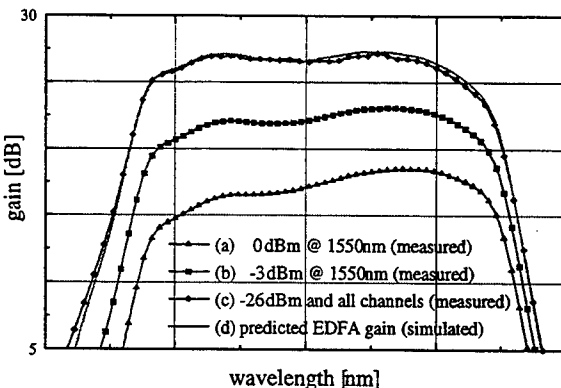


Fig. 4: Measured and simulated EDFA gain characteristics

(OSNR) could be estimated for all 40 channels with a discrepancy between measurement and calculation better than 1 dB. Moreover taking into account the measured filter characteristics at the receiver the Q-factor was found to be in good agreement too.

**Conclusion:** We have shown excellent qualitative and good quantitative agreement between simulations and experiments for high-capacity TDM and WDM systems. In the WDM system the amplifiers were modeled with a black-box model based on measured characteristics to take the gain shaping into account. These confirms the validity of using numerical simulations to predict the performance of advanced optical communication systems.

#### References:

- [1] D. LeGuen, S. DelBurgo, M. L. Moulinard, et al, "Narrow Bank 1.02 Tbit/s (51 x 20 Gbit/s) Soliton DWDM Transmission Over 1000 km of Standard Fiber with 100 km Amplifier Span", Proceeding OFC'99, paper PD4
- [2] S. Kawanishi, H. Takara, K. Uchiyama, I. Shake, and K. Mori, "3 Tb/s (160 Gbit/s x 19ch) OTDM-WDM Transmission Experiment", Proceeding OFC'99, paper PD1
- [3] G. P. Agrawal, "Nonlinear Fiber Optics", Academic Press, 1989
- [4] F. Forghieri, "Modeling the performance of WDM Lightwave systems", Proceeding IPR'96, IthA1, pp. 572-575.
- [5] C. Francia, "Constant Step-Size Analysis in Numerical Simulation for Correct Four-Wave-Mixing Power Evaluation in Optical Transmission Systems", Photonics Technology Letters, 1999, pp. 69-71
- [6] D. Breuer, H. J. Ehrke, F. Küppers, R. Ludwig, and K. Petermann, "Unrepeated 40-Gb/s RZ Single-Channel Transmission at 1.55 μm Using Various Fiber Types", Photonics Technology Letters, 10 (6), 1998, pp. 822-824
- [7] R. W. Tkach, A. R. Chraplyvy, F. Forghieri, et al., "Four Photon Mixing and High-Speed WDM Systems", Journal of Lightwave Technology, 13 (5), 1995, pp. 841-849
- [8] R. Tkach and F. Forghieri, "Lightwave System Limitations of Nonlinear Optical Effects", Proceedings ECOC'96, pp. 6.25-6.63
- [9] BroadNeD and PTDS are a product of Virtual Photonics Incorporated, Berlin, Germany
- [10] D. Bonnedal, "EDFA gain described with a black-box model", OSA Trends in Optics and Photonics Vol. 5 Optical Amplifiers and Their Applications, 1996, pp. 53-6

## Degradation of optical signals caused by opto-electronic transponders in networks: modeling and measurement

C. M. Weinert and L. Molle, Heinrich-Hertz-Institut für Nachrichtentechnik Berlin GmbH  
 Einsteinufer 37, D-10587 Berlin, Germany  
 Tel. + 49 30 31002 255, Fax. + 49 30 31002 241, e-mail: weinert@hhi.de

### Introduction

Optical networks offer the possibility of utilizing the huge bandwidth of the fiber by wavelength division multiplex (WDM) techniques. The WDM data streams in these networks will be transmitted e.g. via dispersion compensated standard single-mode fibre (SMF) links and may be routed by passive wavelength routers, transparent crossconnects (XC) or add/drop multiplexers. Wavelength selective transparent XC's optionally contain all optical or opto-electronic (o-e) frequency converters (FC). For o-e frequency conversion so called transponders can be used, consisting of an optical receiver, electronic amplifier and an optical transmitter. These transponders can be allocated at the borderline of transparent WDM network sections, at interfaces of the input signals, which do not fit the WDM network requirements (e.g. wavelength allocation, chirp, linewidth and stability of the optical carrier). In this case data signals pass typically only one transponder during transmission. On the other hand, transponders can be used as o-e FCs in a wavelength selective XC, and therefore many transponders/FCs are allocated within a typical signal path [1]. Because of their shape and amplitude regenerating (2R: reamplification and reshaping) abilities transponders may be used as o-e repeaters to overcome the limitations caused by chromatic dispersion and nonlinear effects in optical fibers. The regeneration ability which is missing in the transponder is retiming of the signal. In fact, the timing jitter of the signal at the output of the transponder can limit the number of such repeaters in the network [2].

In this work we model and measure the effects of timing jitter produced by a transponder and give an estimate for the signal degradation which can be included in modeling tools for fiber networks. A combined error estimate is given describing the effects of timing jitter and amplitude noise.

### Characteristics of a transponder

Fig. 1a schematically depicts the different opto-electronic components of a typical transponder. The input signal is transformed by a PIN diode into an electrical signal. From the measurement of output power versus input power we find that the electronic decision circuit is set to the average input power  $D$ . Signals below or above  $D$  are determined as a zero or one, respectively. This amplitude regenerated bitstream is fed into an amplifier which drives the transmitter laser. Signal conversion between input and output signals is simulated numerically using the measured  $D$  and pulse shapes. Fig. 1b shows the eye diagrams at the input and output of the transponder. Amplitude noise is introduced at the input of the transponder. The resulting eye diagram at the output shows the regenerated signal with jitter  $\sigma$ .

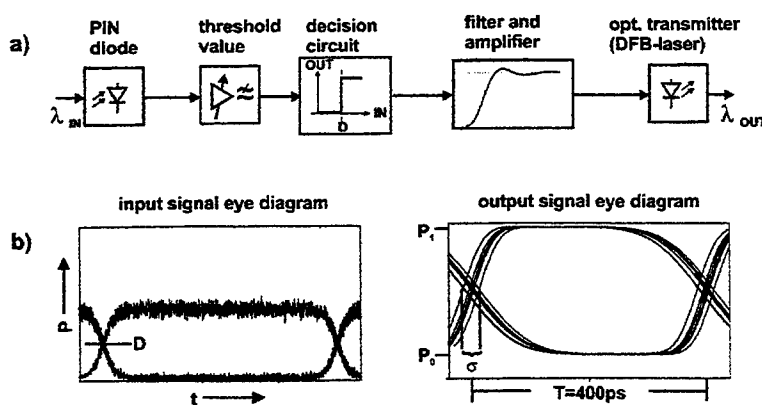


Fig. 1 a) components inside the transponder b) simulated conversion of input signal degraded by amplitude noise into the regenerated output signal with jitter  $\sigma$ .

fluctuations at the input signal flanks are transformed near the decision level D into time fluctuations called jitter (the amplitude noise of the outgoing signal has been omitted in Fig. 1b for better visualization of the jitter). The output pulses are characterized by their rise time  $t_1$  and fall time  $t_2$  and by the extinction ratio  $P_{max}/P_0$ . These parameters can be directly taken from the measured output signal. The rise and fall times are defined by the time intervals between 10% and 90% of  $P_{max}-P_0$ .

### Modeling of the signal degradation due to timing jitter

One of the main problems of numerical network simulation is the necessity to find simple expressions for the bit error rate (BER) estimate. The reason is that Monte-Carlo type of simulations with numerous different network components and including linear and nonlinear effects along the fiber transmission is far too time consuming to simulate error rates of  $10^{-9}$  or even  $10^{-12}$ . The most common way of error estimation is to calculate a small number (typically  $10^4$ ) of randomly arranged bits. Assuming an analytical probability distribution function, the BER can be extrapolated. This method yields confident results if signal degradation is due to white Gaussian noise [3]. In this case the BER is given by the expression

$$BER_N(D_R) = \frac{1}{2} \operatorname{erfc}\left(\frac{D_R - \mu_0}{\sigma_0}\right) + \frac{1}{2} \operatorname{erfc}\left(\frac{\mu_1 - D_R}{\sigma_1}\right) \quad (1)$$

Here  $\operatorname{erfc}$  is the complementary error function and  $D_R$  the decision value at the receiver.  $\mu_0$  and  $\mu_1$  are averages and  $\sigma_0$  and  $\sigma_1$  the standard deviations of the zeros and the ones. Eq. 1 gives the BER in terms of the level position and standard deviation of the zeros and ones, i.e. in terms of the vertical eye closure.

On the other hand, jitter is essentially produced at the flanks of the bits (see Fig. 1b) and its effect on the BER should therefore be included by the temporal eye closure. A measure for timing jitter is the horizontal distribution of the rising and falling flanks of the pulses which can be evaluated at the eye crossing as shown in Fig. 1b. A measure for the amount of jitter is the root mean square jitter (RMS jitter) denoted by  $\sigma_{RJ}$ . In addition, a deterministic jitter  $\sigma_{DJ}$  is present which stems from pattern effects. In analogy to eq. 1 we express the combined error probability  $BER_T$  for a PRBS data stream

$$BER_T(D_R, t) = BER_N(D_R) + BER_J(t) \quad (2a)$$

$$BER_J(t) = p \left\{ \frac{1}{2} \operatorname{erfc}\left((t - \sigma_{DJ})/\sigma_{RJ}\right) + \frac{1}{2} \operatorname{erfc}\left((T - \sigma_{DJ} - t)/\sigma_{RJ}\right) \right\} \quad (2b)$$

$\sigma_{RJ}$  and  $\sigma_{DJ}$  are the RMS and deterministic jitter respectively. The factor  $p$  in eq. 2b depends on the bit sequence. For a 010101 sequence,  $p = 1$  since in this case every bit has length  $T$ . For NRZ PRBS signals the bit duration can be multiples of  $T$ . Due to the rapid decrease of the  $\operatorname{erfc}$  function the error probability of bits larger than  $T$  contribute only with the pulse flank adjacent to the sampling time. The probability of the dominant bits of duration  $T$  is the combined probability of having a 010 pattern or a 101 pattern which is  $1/8$  in both cases. Therefore, only  $1/4$  of the bits contribute with both pulse flanks to the error statistics. In a similar fashion, isolated ones or zeros of length  $2T$  appear with probability  $1/16$  and contribute with a factor of  $1/2$  and so on. Summing over all possible bit lengths gives  $p$

$$p = \sum_{i=1}^{\infty} \frac{1}{i} \frac{1}{2^{i+1}} = 0.3466 \quad (3)$$

Eq. (2) is included as an extended BER estimation formula into the numerical simulation tool for fiber transmission. It accounts for the BER estimation of temporal eye closure effects produced by RMS-jitter in addition to the standard estimation for noise effects. The transponder is simulated as a

device which aside from amplification and pulse shaping adds RMS jitter [2]. For the numerical error analysis, the standard deviation of the jitter is evaluated and is inserted into eq. 2b together with the deterministic jitter  $\sigma_{DJ}$  taken from measurement.

## Experimental

In order to test eq. 2, we perform measurements on a commercially available transponder working at a bitrate of 2.5 Gbit/s and extract the parameter  $\sigma_{DJ}$ . We increase the receiver input power so that signal degradation due to amplitude noise becomes negligible and the BER is only given by  $BER_J$ . Next we measure  $BER_J(t)$  at the optimum decision value for varying sampling time  $t$  across one bit period. In Fig 2 we show the BER measurements of the transponder. Timing jitter was increased by increasing the amplitude noise at the transponder input. The BER is measured while scanning the sampling time from the left hand eye crossing at  $t=0$  ps to the right hand eye crossing at  $t=400$  ps. The resulting bath tub curves shown in Fig. 2 are used to determine the parameters by a fit to eq. 2.

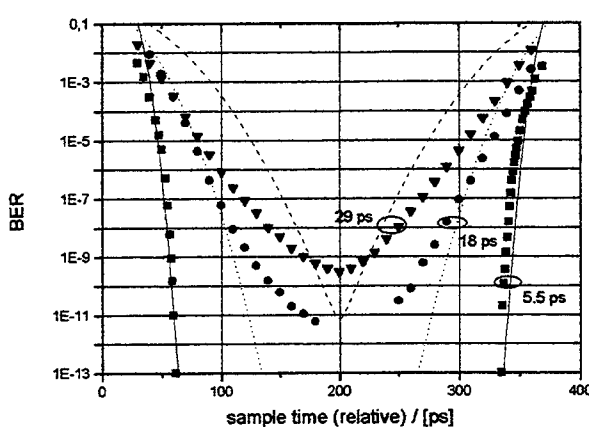


Fig. 2 : measured (symbols) and fitted (lines) curves for NRZ signals with different RMS jitter. Parameter  $\sigma_{RJ}$ .

29 ps (dashed curve). However, it is seen that the fit to eq. 2 becomes less good for increasing jitter. A possible explanation is that jitter distribution for large jitter deviates from the Gaussian statistics.

In conclusion, an improved bit error estimation formula is proposed which includes the effects of timing jitter on signal degradation. The formula is compared with BER measurements of a transponder and shows fair agreement if timing jitter is not too large. The formula is included in the numerical simulation tool for fiber transmission systems.

This work was supported by the ACTS-programme within the project of DEMON.

## References:

- [1] M. Schiess, E. Berglind, A. Karlsson, and L. Thylen, "Pulse shape evolution and noise estimates in concatenated fiber links using analog optoelectronic repeaters", IEEE J. Lightwave Tech., vol 14, pp. 1821-1828, 1996
- [2] C. M. Weinert, L. Molle, C. Caspar and B. Strelle, „Measurement and Modeling of Timing Jitter in Optoelectronic Repeaters and Frequency Converters“, IEEE Photon. Technol. Lett., vol 11, pp. 278-280, 1999.
- [3] N. S. Bergano, F. W. Kerfoot, and C. R. Davidson, „Margin measurements in optical amplifier systems“, IEEE Photon. Technol. Lett., vol. 5, pp.304-306, 1993.

Since the first term of  $BER_J$  (eq. 2b) is dominant for the left hand side branch of the measured data in Fig. 2  $\sigma_{RJ}$  and  $\sigma_{DJ}$  can be extracted from this part of the curve via the inverse erfc function as described in [3].  $\sigma_{DJ}$  essentially causes a rigid shift of the curve. As seen from the solid curve in Fig. 2, a very good description of the jitter function is given for the measurement data given by the squares for  $\sigma_{DJ} = 23$  ps and  $\sigma_{RJ} = 5.5$  ps . The fit to the measured curve given by the filled circles gives  $\sigma_{RJ} = 18$  ps (dotted curve) and the measured curve given by the triangles gives  $\sigma_{RJ} =$



**Integrated Photonics Research**

# **Modulators and Receivers**

**Wednesday, July 21, 1999**

**S. Chandrasekhar, Bell Laboratories, Lucent Technologies, USA**

Presider

**RWB**

**8:45am-10:15am**

Anacapa

## Electroabsorption modulators for ultrafast optical demultiplexing

D. G. Moodie, P. J. Cannard, C. W. Ford, J. Reed, A. D. Ellis, R. T. Moore, and I. D. Phillips.  
 B55 131G, BT Laboratories, Martlesham Heath, Ipswich, Suffolk, IP5 3RE, UK.  
 tel. 44 1473 646797, fax 44 1473 646885, dave.moodie@bt.com

### **Introduction**

The capacity needed in telecommunications networks is rising sharply due to the rapid growth in internet traffic. This trend has led work in many laboratories to address the technologies that will be needed in future ultrafast optically time division multiplexed (OTDM) systems [1] and asynchronous digital optical networks [2]. One technology essential for both is a compact means of demultiplexing an ultrafast optical signal down to the electronic base-rate. We have previously described a batch of high speed polarisation insensitive electroabsorption modulators (EAMs) [3] which were recently used as demultiplexers in a 100 Gbit/s OTDM system [4]. Two of these EAMs connected optically in series and driven synchronously at 20 GHz generated a 4 ps switching window suitable for demultiplexing from 160 Gbit/s to 20 Gbit/s [3]. In this paper a more detailed characterisation of one of these EAMs is presented, including an analysis of how its measured switching window compares against the theoretical requirements for 100 Gbit/s to 10 Gbit/s demultiplexing.

### **Electroabsorption modulator**

The device used in these experiments has a ridged deeply etched buried heterostructure (BH) design as shown in Fig. 1. It employs an InGaAs/InAlAs multiple quantum well (MQW) absorber with 10 nm thick wells of 0.5% tensile strain. As previously described, the 336  $\mu\text{m}$  long EAM has suitable characteristics for high speed demultiplexing. It combines a 19 GHz electrical 3 dB bandwidth with a high modulation depth of  $> 30$  dB, and a low polarisation sensitivity [3]. BH EAMs also have the advantage of being more robust under high voltage and high optical input power than conventional EAMs [5]. A comparison of the absorption spectra of this device for TE and TM polarised light (of -3 dBm input power) is given in Fig. 2. It demonstrates a remarkably low polarisation sensitivity across a wide range of wavelengths and voltages. Because of enhanced quantum well effects, the gradient of these curves is markedly steeper than for previous devices which had an InGaAsP/InGaAsP MQW [6]. These results suggest that when used as a demultiplexer the EAM will be polarisation insensitive and will work over a wide wavelength range, with the optimum wavelength being determined by the DC voltage. The EAMs chirp parameter was measured using the technique of dispersive sideband interference [7] and is plotted in Fig. 3. The chirp parameter also has a low polarisation sensitivity and is quite close to zero at the most important voltages for systems applications. The variation of the DC optical characteristics with the input optical power of a 261  $\mu\text{m}$  long device from the same slice is plotted in Fig. 4. Significant saturation was observed as the power was increased to +18 dBm. This was due to an accumulation of photogenerated electrons and holes in the depletion region at high optical powers, reducing the effective electric field across the MQW. The onset of saturation occurred at higher powers for higher reverse biases due to carriers being swept out more rapidly under higher electric fields. To avoid systems degradations when the EAM acts as a DEMUX it is therefore advisable to restrict the input optical power to  $\leq 6$  dBm with a DC reverse bias of  $> 8$ V. It is also important to assess the EAMs temperature sensitivity. From Fig. 5 it can be seen that increasing the temperature by 20 °C changed the DC absorption characteristic of an unpackaged EAM in approximately the same way as decreasing the wavelength by 10 nm. Thus the band edge of the MQW has a temperature sensitivity of  $\approx 0.5 \text{ nm}/^\circ\text{C}$  and so use of a Peltier cooler is advisable for long-term stable operation.

### **Switching window for 100 Gbit/s to 10 Gbit/s demultiplexing**

The switching windows generated at a 10 GHz repetition rate by the EAM were measured using the experimental configuration shown in Fig. 6. An external cavity laser (ECL) was mode-locked at 10 GHz to give 1.6 ps pulses which were coupled into an EAM that had synchronised 10 GHz and 20 GHz drives. The switching window could then be measured by monitoring the output power as a variable optical delay prior to the EAM was incrementally adjusted. The relative phase and amplitude of the 10 GHz and 20 GHz drives were optimised to minimise the switching window

duration and maximise the extinction ratio. The peak-to-peak amplitude of the optimum combined drive signal measured into  $50\ \Omega$  was  $\approx 13\text{ V}$ . The measured switching windows for both polarisation states at a DC bias of  $-8.5\text{ V}$  are shown in Fig. 7. A low polarisation sensitivity was observed. Furthermore, no secondary switching windows were generated by the  $20\text{ GHz}$  drive midway between the primary switching windows. The measured extinction ratio  $10\text{ ps}$  either side of the switching windows was artificially low due to side pulses from the ECL that were  $\approx 7\text{ ps}$  from the main pulse and  $\approx 24\text{ dB}$  down, so this region was ignored when calculating the minimum extinction ratio.

We have simulated the penalty associated with a  $100\text{ Gbit/s}$  to  $10\text{ Gbit/s}$  DEMUX by considering it as imposing Gaussian switching windows of finite maximum extinction ratio on a random bit-stream of  $2\text{ ps}$  pulses. The measured full width at half maximum intensity switching window durations and minimum extinction ratios are plotted in comparison with contours showing the calculated requirements for a given DEMUX penalty in Fig. 8. Switching windows good enough to have a minimal (i.e.  $< 1\text{ dB}$ ) DEMUX penalty were achieved in both polarisation states and over a relatively wide range of DC bias voltages without adjusting the electrical drive amplitude. This is in agreement with the system results in [4] where a single EAM demultiplexed a  $10\text{ Gbit/s}$  channel from a  $100\text{ Gbit/s}$  signal with a negligible penalty.

### Conclusions

It has been demonstrated that EAMs can generate  $6\text{ ps}$  switching windows with  $> 20\text{ dB}$  extinction ratio at a  $10\text{ GHz}$  repetition rate and that they can be used to form a simple and compact, high performance, high speed, polarisation insensitive demultiplexer. They are suitable for integration and for operation over a wide range of wavelengths.

### References

- [1] S. Kawanishi et al, *IEEE J. of Quantum Electronics*, vol. 34, no. 11, pp. 2064-2079, 1996
- [2] D. Cotter et al, *IEEE J. of Lightwave Technol.*, vol. 16, no. 12, pp. 2068-2080, 1998.
- [3] D. G. Moodie et al., *Electron. Lett.*, vol. 33, no. 24, pp. 2068-2070, 1997.
- [4] A. D. Ellis et al, *Electron. Lett.*, vol. 34, no. 18, pp. 1766-1767, 1998.
- [5] K. Wakita et al, *Jpn. J. Appl. Phys.*, vol. 37, pp. 1432-1435, 1998.
- [6] D. G. Moodie et al, *IEEE J. of Lightwave Technol.*, vol. 14, no. 9, pp. 2035-2043, 1996.
- [7] F. Devaux et al, *IEEE J. Lightwave Technol.*, vol. 11, no. 12, pp. 1937-1940, 1993.

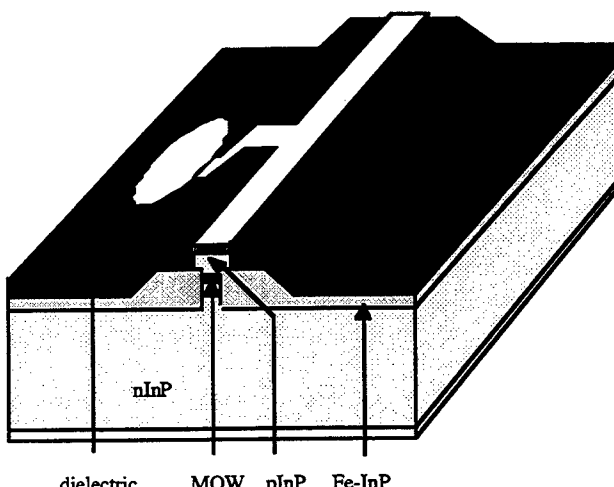


Figure 1. Schematic diagram of ridged deeply etched buried heterostructure EAM.

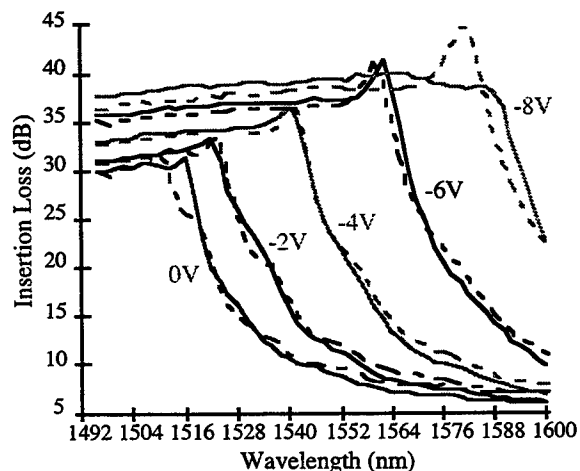


Figure 2. Absorption spectra of EAM module. Solid lines TM, dashed lines TE.

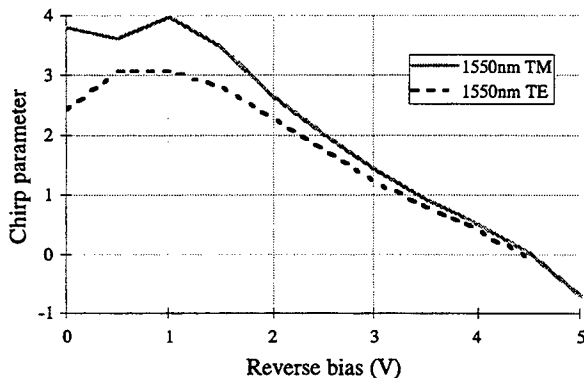


Figure 3. EAM chirp parameter.

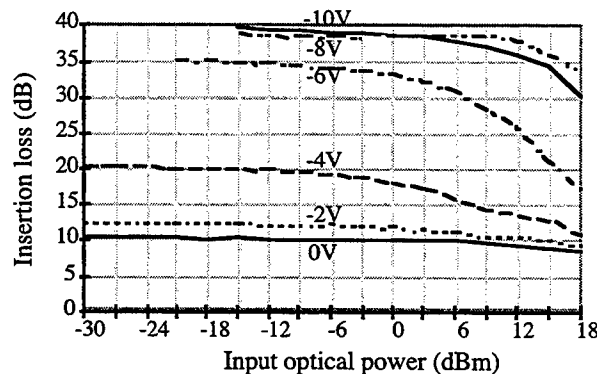


Figure 4. Saturation behaviour for 1550 nm continuous wave TM light.

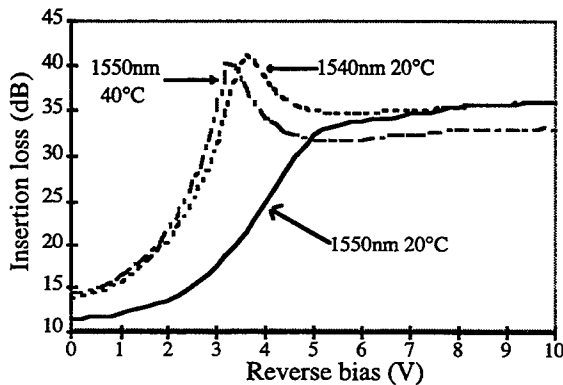


Figure 5. Variation of DC absorption (for 0dBm of TM polarised light) with temperature and wavelength.

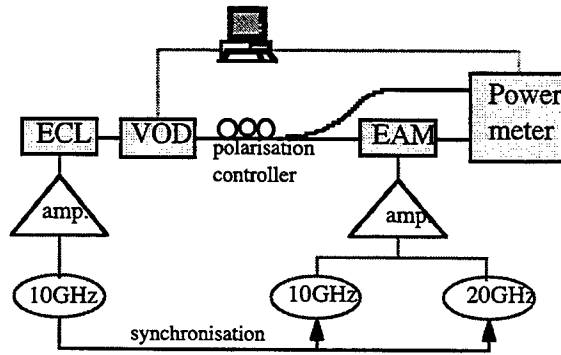


Figure 6. Experimental set-up for measuring switching windows. Key; ECL external cavity laser, VOD variable optical delay.

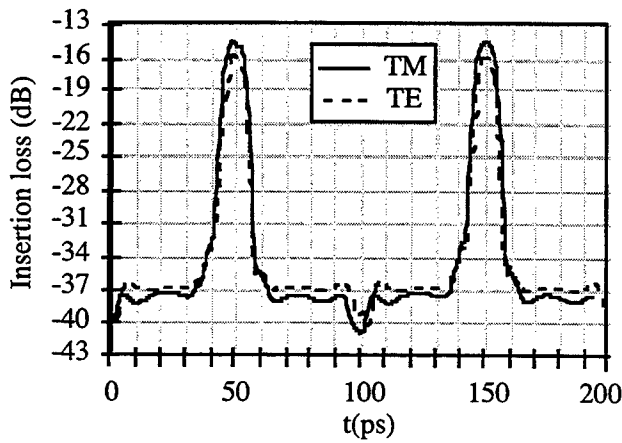


Figure 7. Time resolved switching windows for TE and TM polarisation at -8.5V bias.

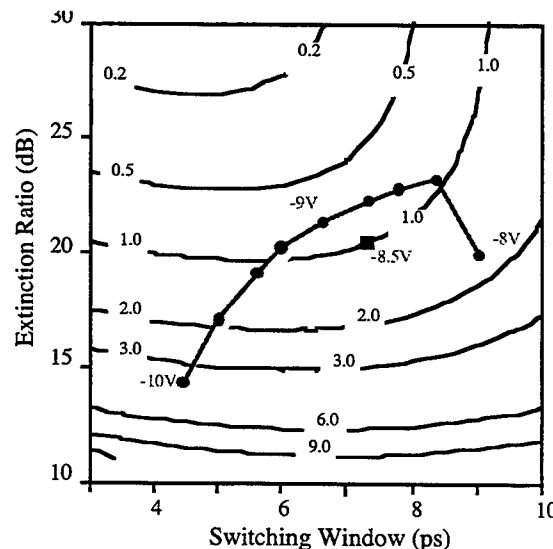


Figure 8. Measured switching window characteristics and required 100Gbit/s DEMUX performance for a given power penalty in dB. Key; ●TM, ■TE.

## Novel Substrate Removed Mach-Zehnder GaAs/AlGaAs Electro-optic Modulators

S. R. Sakamoto, A. Jackson and N. Dagli\*

Electrical and Computer Engineering Department  
University of California, Santa Barbara, CA 93106

\*Phone: (805) 893-4847

Fax: (805) 893-3262

e-mail: dagli@ece.ucsb.edu

### I. Introduction

Ultra-wide bandwidth, low voltage external modulators are essential for digital and analog fiber optic transmission. Previous GaAs/AlGaAs designs utilizing undoped epilayers were able to obtain chirp-free modulation in excess of 40 GHz [1], but at the expense of large drive voltages ( $V_x$  of 16.8 V at 1.55  $\mu\text{m}$ ), mainly due to the poor overlap of the modulating field with the optical mode. Recently, substrate removal techniques enabled processing both sides of epitaxial layers and successful integration of semiconductors and polymers for optoelectronic applications [2]. Here, we present an electro-optic modulator that takes advantage of these new technologies to reduce the drive voltage ( $V_x$ ) by a factor of 2. The device design, processing details, initial measurements, and future design issues will be presented.

### II. Device description

Figures 1(a) and (b) show the top and cross sectional schematics of the modulator. The optical structure is a Mach-Zehnder interferometer. The input and output of the interferometer use 1x2 Multi-Mode Interference (MMI) couplers [3]. The MMI couplers are shorter than large radius of curvature S-bends, resulting in compact devices. The optical waveguides are rib waveguides. The epitaxial structure is an unintentionally doped GaAs/Al<sub>0.3</sub>Ga<sub>0.7</sub>As heterostructure grown by MBE on a semi-insulating (SI) GaAs substrate. There are electrodes at the top and bottom of both arms of the interferometer. These electrodes form Schottky diodes. The electrodes on each arm can be biased independently. At frequencies lower than 100 kHz the voltage across an arm biases two back to back Schottky diodes and makes it possible to apply a vertical electric field component overlapping very well with optical mode in the single mode rib waveguide. Such epilayers are self-depleting due to Fermi level pinning at the surface and the SI substrate interface, hence having very low conductivity. At frequencies over a few 100 kHz they start to behave as slightly lossy dielectrics and the situation becomes very similar to the case of electrodes on a dielectric material. Therefore, push-pull vertical electric fields overlapping very well with the optical mode can be applied. The strength of the field is limited only by the thickness of the epi layer and can be expressed as  $E = V/t$ , where  $V$  is the voltage across an arm, and  $t$  is the overall thickness of the epilayer.  $t$  is 3.6  $\mu\text{m}$  in the present design. These electrodes can be combined with coplanar electrodes in the form of T-rails for high speed traveling wave modulators [4].

### III. Device fabrication

The fabrication begins with the MBE growth of an appropriately designed, unintentionally doped epi layer for single mode waveguide operation at 1.55  $\mu\text{m}$ . Using standard photolithography, the Mach-Zehnder structure is patterned and wet etched using a citric acid solution. The waveguides are 4  $\mu\text{m}$  wide and etched 0.5  $\mu\text{m}$  deep. 2  $\mu\text{m}$  wide metal electrodes are then patterned on top of both 4  $\mu\text{m}$  waveguides in the interaction region using Ti/Pt/Au-Schottky metal liftoff. Each electrode has its own contact pad for independent probing. At this point, the processing of the topside of the epi is complete.

The next step was the transfer of the processed epilayer onto a SI GaAs transfer substrate. To glue the epi layer to the transfer substrate, we used the organic polymer Benzocyclobutene (BCB) [5]. BCB was spun both onto the transfer substrate and on top of the processed epilayer. The sample was then placed epi-side down onto the transfer substrate kept on a hot plate at 160 °C. In this temperature range, the BCB became less viscous and allowed easy sliding of the semiconductors.

This was essential for the manual alignment of the cleavage planes of the transfer and growth substrates and also for the removal of any voids or gas bubbles that may have been trapped. After this alignment the BCB was fully cured at 250 °C for 1 hour in a nitrogen purged oven. A spray etch of an ammonium hydroxide/hydrogen peroxide mixture was used to remove the growth substrate. The etch stopped on an AlAs etch stop layer. Once the AlAs layer was removed, the processing of the backside began.

In the processing of the backside, first the topside alignment marks were exposed through the epi. This was done using a back aligner with infrared (IR) illumination and an IR camera. The epilayer around the topside alignment marks were etched using a citric acid solution. Next, Schottky Ti/Pt/Au backside electrodes were patterned using lift off. These electrodes were aligned directly underneath the topside electrodes. Each of these electrodes had an independent contact pad for probing. The last mask used was to define and etch the areas where the buried topside electrode contact pads were. Finally, the sample was cleaved and mounted.

#### IV. Experimental results

Electrical measurements between two contacts across an arm showed back to back diode characteristics as expected. The reverse breakdown voltage of the diodes was larger than 40 V. The current through an L=0.5 cm long electrode was less than 30  $\mu$ A at 30 V. For optical characterization, the output of a fiber pigtailed 1.55  $\mu$ m distributed-feedback laser was end fire coupled through the cleaved facet. Input polarization was controlled using a three-paddle polarization rotator and was kept at TE polarization during the measurements. At the output facet, the near-field pattern was observed by focusing the image through a microscope objective onto an IR Vidicon camera. Output power was measured by aligning a cleaved fiber to the output port of the modulator and feeding the signal to a Tektronix 11403A Digitizing Oscilloscope via a Tek P6702 Optical/Electric Converter. Since each electrode had its own contact pad, four probes were used to provide a push-pull biasing scheme. A Hewlett-Packard 3325B Synthesizer/Function Generator was used to provide 20 V sinusoidal modulation up to 1 MHz.

The 10 kHz transfer functions of a device with a 1 cm interaction region when driven push-pull and single-arm only are shown in Fig. 2. The transfer functions follow the expected  $\cos^2$  shape. Note how the push-pull nature results in a factor of 2 reduction in  $V_\pi$  (8.7 versus 17.8 V). In addition, the L=1 cm  $V_\pi$  of 8.7 V is about a factor of 2 smaller than the previous ultra high speed traveling wave modulator [1]. This result implies about a 58% overlap between the electrode field and the optical mode. It is possible to increase this overlap to more than 90% by widening the electrode and optimizing the optical waveguide. This should bring  $V_\pi$  to about 5.5 V/cm, which is comparable to existing LiNbO<sub>3</sub> modulators. As described earlier these devices can be combined with coplanar slow wave electrodes to realize ultra wide bandwidth traveling wave modulators.

#### V. Conclusions

Substrate removal techniques enabled us to process both sides of a processed epilayer and integrate it with organic polymers. Using this approach we fabricated novel substrate removed modulators that have 8.7 V/cm drive voltage, which can be further improved to ~ 5.5 V/cm. These modulators can be made ultra high speed using T-rail loaded coplanar slow wave electrodes.

**Acknowledgment:** This work is supported by AFOSR under grant F19628-97-C-0069.

#### VI. References

- [1]. R. Spickermann, S.R. Sakamoto, M.G. Peters and N. Dagli, "GaAs/AlGaAs traveling wave electro-optic modulator with an electrical bandwidth > 40 GHz," *Elec. Lett.*, vol. 32, No. 12, pp. 1095-1096, Jun. 1996.
- [2]. S.R. Sakamoto, C. Ozturk, Y.T. Byun, J. Ko, and N. Dagli, "Low-loss substrate removed (SURE) optical waveguides in GaAs-AlGaAs epitaxial layers embedded in organic polymers," *IEEE Photon. Tech. Lett.*, vol. 10, No. 7, pp. 985-987, Jul. 1998.

- [3]. L.B. Soldano and E.C.M. Pennings, "Optical multi-mode interference devices based on self-imaging: principles and applications," *IEEE J. Light. Tech.*, vol. 13, No. 4, pp. 615-627, Apr. 1995.  
 [4]. S. Sakamoto, R. Spickermann and N. Dagli, "Novel Narrow Gap Coplanar Slow Wave Electrode for Traveling Wave Electrooptic Modulators," *Elec. Lett.*, vol. 31, No. 14, pp. 1183-1185, 6 July 1995.  
 [5]. Form No: 296-01211-493NP&M, Dow Plastics, The Dow Chemical Company, 2040 Dow Center, Midland, MI 48674.

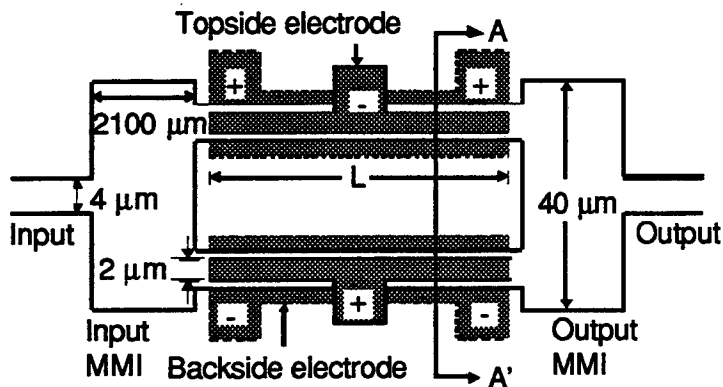


Figure 1(a): Top view of full modulator.

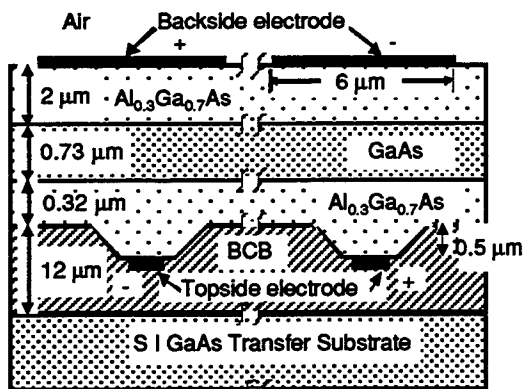


Figure 1(b): Cross section A-A' of full modulator.

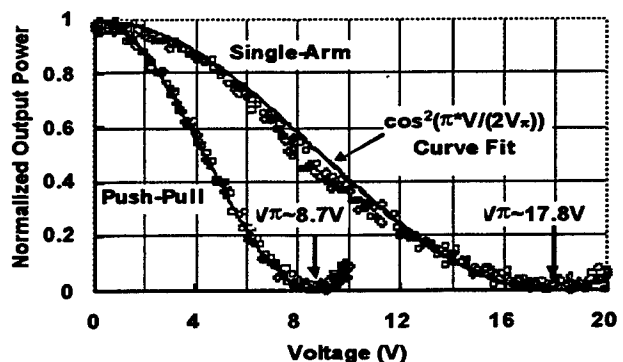


Figure 2: L=1cm 10kHz transfer functions.

## Monolithic OEIC photoreceivers for 40 Gb/s and beyond

H.-G. Bach

Heinrich-Hertz-Institut für Nachrichtentechnik, Einsteinufer 37, D-10587 Berlin, Germany,  
Phone ++49 30 31002-503, FAX ++49 30 31002-551, E-mail: bach@hhi.de

### 1. Introduction

Within the next few years the backbone networks of present photonic-based telecommunication systems will be upgraded to 40 Gb/s data rates [1]. For this aim high-speed photoreceivers, especially for 1.55 μm wavelength, are required, which support RZ as well as NRZ coding. This work presents and discusses recent realizations of 40 Gb/s photoreceivers OEICs (modules) and conceptional extensions to even higher bitrates, to serve forthcoming TDM system applications exceeding a 160 Gb/s single-channel bitrate. OEIC packaging into modules for 1.55 μm TDM system applications is included [2], and essential characteristics of modules are given. The OEICs consist of a monolithical integration of waveguide-integrated [3] or alternatively side-illuminated photodiodes [4] and a traveling wave amplifier (TWA). A conceptional comparison to GaAs-based strain-released GaInAs photodiodes integrated with a PHEMT-based TWA [5] is made.

### 2. Requirements for ultrafast photoreceiver OEICs

In digital communication systems, which are conform to the SDH/SONET transmission protocols, receivers are required, which show a flat gain characteristics down to some 10 kHz to transmit also the STM frame synchronisation. Further they should exhibit a low group delay time scatter (<±15 % of the bit period) and an output reflexion below -10 dB. The transimpedance of the amplifier should be designed to have a Bessel-like low-pass characteristics [6], which satisfies the needs concerning ringing and phase linearity of digital system applications. The main OEIC constituents, i.e. photodiode and amplifier should both provide potential for even higher bandwidth than 60 GHz to allow an upgrade of the photoreceiver concept towards 80 Gb/s and higher.

### 3. Fast photodiodes with 50-100 GHz potential

To overcome the trade-off between carrier transit time and internal quantum efficiency of conventional front- or back-illuminated photodiodes, the perpendicular illumination of the absorbing region is favourably replaced by side-illuminated [7, 8] or evanescent field-coupled configurations [9].

Both concepts show comparable ultra-high bandwidth potential clearly beyond 100 GHz and have been shown to be monolithically integrable with electronics, e.g. MMIC-like amplifiers on InP [3, 4]. The multimode-

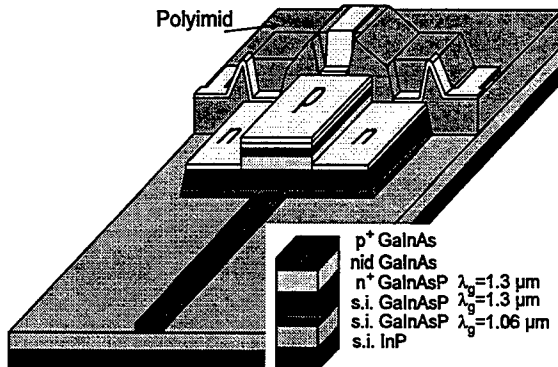


*Fig.1: Waveguide-integrated evanescent-field coupled photodiode [9].*

waveguide photodiode (WGPD) type [8] actually shows some advantage with respect to the very good external quantum efficiency of up to 0.8 A/W; this may be approached applying the waveguide-fed evanescent field-coupled diode, too, if integrated with an on-chip waveguide taper. The latter concept is advantageous for further integration of photodiodes for balanced configurations or for higher-integrated optoelectronic circuits (e.g. with optical pre-amplification, filtering, WDM, ...), applying several photodiodes within optical waveguide interconnections.

### 4. Broadband amplifiers with 100 GHz potential

The demands on broadband receivers, given in section 2, call for a thorough design and subsequent realization scheme of an amplifier with good reproducibility of the complex gain function up to 50 GHz bandwidth and higher. Hence, the inherently broadband distributed amplifier concept, as compared

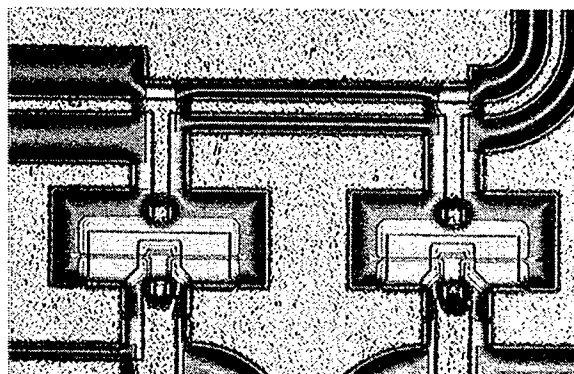


*Fig.2: Microphotograph of HEMTs with e-beam written gates within the distributed amplifier of the InP-based pinTWA OEIC [3].*

to transimpedance amplifiers (suffering from wave propagation effects), appears advantageous for 40 Gb/s and mandatory for higher bitrates. The TWA concept [6] is reproducibly realized in conjunction with coplanar (or microstrip) line MMIC-type technology, based on InP [3, 4], cf. Fig. 2, or GaAs [5]. The potential of the TWA concept extends clearly beyond 100 GHz, based on already realized TWA ICs with 90 GHz bandwidth [10].

### 5. Design of photoreceiver OEICs for 40 Gb/s

An integration scheme of an OEIC (cf. Fig. 3) being composed of a waveguide-integrated photodiode (MOVPE) and a HEMT-based amplifier follows the concept published in [6] and earlier. The monolithical integration of the distributed broadband amplifier, originally started using HEMTs (regrown by MBE)

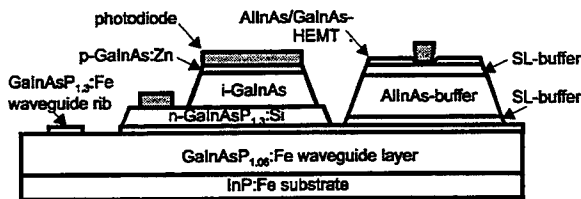


**Fig.3:** Integration scheme of monolithic pinTWA broadband photoreceiver, see e.g. ref. 6.

with optically defined gates of about  $0.6 \mu\text{m}$  length [6], meanwhile was demonstrated using electron-beam direct writing for the HEMT gates ( $0.18 \dots 0.3 \mu\text{m}$ ) [3]. A main aspect of this integration approach is the independent optimisation of the active devices, i.e. photodiode and HEMT, to achieve optimum parameters like internal quantum efficiency of the photodiode ( $> 85\%$ ) or  $f_T/f_{\max}$  ( $100/200 \text{ GHz}$ ) of the HEMTs. The two-step MOVPE/MBE epitaxial process advantageously preserves the properties of photodiode layers during the low-temperature MBE growth of the HEMT layers. Further a quasi-planar surface is achieved by adjustment of the HEMT buffer layer stack. Competitive approaches apply low-pressure MOVPE in a single step to avoid degrading both components during regrowth [4]. In this case the WG photodiode is located on top of the HEMT mesa, establishing a relatively high mesa structure.

### 6. Fabrication of photoreceiver OEIC

The photoreceiver OEICs with waveguide-integrated photodiodes and MBE-regrown HEMTs [3] were fabricated applying MOVPE growth of semi-insulating Fe-doped optical waveguides and subsequent growth of partly  $n^+$ -doped layers for the pin photodiode within the same run.

After definition of the photodiode mesa ( $5 \times 20 \mu\text{m}^2$ ) by selective etching the MBE regrowth of HEMT layers was performed. MIM capacitors and metal film resistors are used as passive devices for the amplifier as well as for the biasing network of the photodiode. Finally coplanar waveguide (CPW) interconnections employing air-bridges are formed by gold electroplating, see Fig. 2.

### 7. Characteristics of photoreceiver OEICs

In the frequency domain integrated photoreceivers are characterized up to 50 GHz by optical heterodyne measurements. The frequency response of the pinTWA photoreceiver of Fig. 3 comprises an amplifier gain of  $\approx 8 \text{ dB}$  with respect to the power delivered from the pin photodiode. The observed 3 dB bandwidth is 37 GHz. The embedded distributed amplifiers show even a transimpedance cut-off frequency up to 42 GHz with an amplitude ripple of only  $\pm 1 \text{ dB}$  within the passband. The output reflection coefficient is less than  $-10 \text{ dB}$  [3].

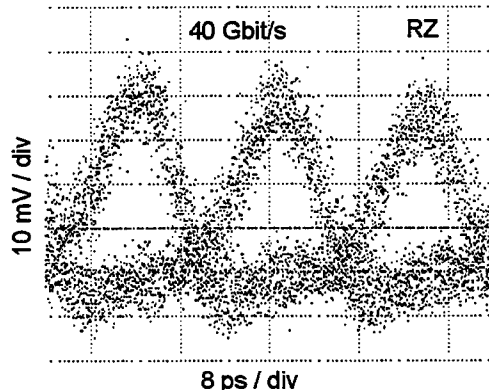


**Fig.4:** 40 Gb/s RZ eye pattern of InP-based pinTWA photoreceiver OEIC (inverted output).

In the time domain characterization was done by optical RZ pulse measurement ( $\text{FWHM} \approx 3 \text{ ps}$ ) with a 40 Gb/s PRBS data stream, cf. Fig. 4 [3]. The electrical RZ signal is modulated to the zero level within the 25 ps bit period and exhibits a well opened eye with approx.  $35 \text{ mV}_p$  output value. This eye pattern quality is maintained up to approx.  $500 \text{ mV}_p$  output voltage so that the receiver OEIC can directly drive any following digital decision circuitry [11].

Good 40 Gb/s NRZ eye pattern quality and  $43.3 \text{ dB}\Omega$  transimpedance was recently achieved with a GaAs-based OEIC, where the top-illuminated pin-InGaAs photodiode was strain-released by a special AlGaInAs buffer technology [4]. However, due to the photodiode concept this integration scheme already appears to be near to its frequency limits, if high responsivity is indispensable.

### 8. OEIC packaging into pig-tailed modules

Our photoreceiver chips were packaged into pig-tailed modules applying a fibertaper-chip coupling using precisely adjustable ferrules [2]. Special care was taken to achieve less than 150  $\mu\text{m}$  bond wire lengths between OEIC and CPW lines of TMM (temperature stable microwave material) interconnection board.

### 9. Photoreceiver module operation in the frequency and time domain

Fig. 5 shows the optoelectronic conversion frequency characteristics for our 1.55  $\mu\text{m}$  photoreceiver module up to 50 GHz. Despite of a dip at 25 GHz, gain within the -3 dB limit is available up to 35 GHz. To estimate the eye pattern behaviour for 40 Gb/s NRZ coded data the procedures described in [2] were applied. Fig. 6 shows the deduced photoreceiver NRZ output eye pattern at 40 Gb/s containing 1024 bit.

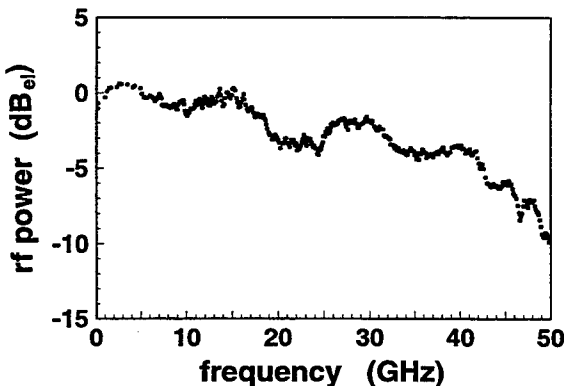


Fig. 5: Frequency characteristics of a 1.55  $\mu\text{m}$  pinTWA photoreceiver module [2].

### 10. Conclusion

Photoreceiver OEIC concepts and packaging were realized for 40-50 Gb/s TDM applications. Actual OEICs/modules comprise additional 8-10 dB gain. Advantageous as compared to single photodiodes is the low output reflection of less than -10 dB with still good conversion efficiency ( $\approx 35$ -40 V/W). The modules are suitable for RZ and NRZ coded applications. The underlying concepts of integrating side- or evanescent field-coupled photodiodes in conjunction with traveling wave amplifiers appear appropriate for 80 Gb/s or even higher data rates.

### References

- [1] A. Bergh, P. Kaiser: **OIDA Communications Roadmap, at "Into the Optical Communications Age"**, A Presentation of European, US and Japanese Roadmaps for the Evolution of Communications Networks using Optical Technologies, 29 May 1998, Brussels, Belgium
- [2] H.-G. Bach, W. Schlaak, G. Unterbörsch, G.G. Mekonnen, G. Jacumeit, R. Ziegler, R. Steingrüber, A. Seeger, Th. Engel, A. Umbach, C. Schramm, and W. Passenberg: **40 Gbit/s Photoreceiver Modules Comprising InP**
- [3] H.-G. Bach, W. Schlaak, G.G. Mekonnen, R. Steingrüber, A. Seeger, Th. Engel, W. Passenberg, A. Umbach, C. Schramm, and G. Unterbörsch: **50 Gbit/s InP-Based Photoreceiver OEIC with Gain Flattened Transfer Characteristics**, Proc. of 24<sup>th</sup> ECOC, Vol. 1, paper MoB01, Sept. 20-24, Madrid (1998).
- [4] K. Takahata, Y. Miyamoto, Y. Muramoto, H. Fukano, and Y. Matsuoka: **50-Gbit/s Operation of Monolithic WGPD/HEMT Receiver OEIC Module**, Proc. of 24<sup>th</sup> ECOC, Vol. 3, pp. 67-69, Sept. 20-24, Madrid (1998).
- [5] V. Hurm, W. Benz, W. Bronner, A. Hülsmann, T. Jakobus, K. Köhler, A. Leven, M. Ludwig, B. Raynor, J. Rosenzweig, M. Schlechtweg, and A. Thiele: **40 Gbit/s 1.55  $\mu\text{m}$  monolithic integrated GaAs-based PIN-HEMT photoreceiver**, Proc. of 24<sup>th</sup> ECOC, Vol. 3, pp. 121-123, Sept. 20-24, Madrid, (1998).
- [6] S. van Waasen, A. Umbach, U. Auer, H.-G. Bach, R.M. Bertenburg, G. Janssen, G.G. Mekonnen, W. Passenberg, R. Reuter, W. Schlaak, C. Schramm, G. Unterbörsch, P. Wolfram, F.J. Tegude: **27 GHz bandwidth high speed monolithic integrated optoelectronic photoreceiver consisting of a waveguide fed photodiode and an InAlAs/InGaAs-HFET-traveling wave amplifier**, IEEE J. Solid State Circuits, vol. 32, no.9, pp. 1394-1401 (1997).
- [7] G. Wanlin, L. Giraudet, J.P. Praseuth, A. Miras, and E. Legros: **High responsivity side illuminated AlGaInAs pin photodiode for 40 Gbit/s – 40 GHz applications**, ECOC'97, vol. 2, pp. 37-40 (1997).
- [8] K. Kato, A. Kozen, Y. Muramoto, Y. Itaya, T. Nagatsuma, and M. Yaita: **110-GHz, 50 %-efficiency mushroom-mesa waveguide p-i-n photodiode for a 1.55-mm wavelength**, IEEE Photon. Technol. Lett., vol. 6, pp. 719-721 (1994).
- [9] G. Unterbörsch, A. Umbach, D. Trommer, G.G. Mekonnen, **"70 GHz long-wavelength photodetector"**, Proc. 23<sup>rd</sup> Europ. Conf. on Optical Communications (ECOC '97), (Edinburgh, U.K.), September 1997, Conf. Publication No. 448 IEE, vol. 2, pp. 25-28 (1997).
- [10] S. Kimura, Y. Imai, Y. Umeda, and T. Enoki: **0-90 GHz InAlAs/InGaAs/InP HEMT distributed baseband amplifier IC**, Electron. Lett., vol. 31, pp. 1430-1431 (1995).
- [11] G.G. Mekonnen, W. Schlaak, H.-G. Bach, R. Steingrüber, A. Seeger, Th. Engel, W. Passenberg, A. Umbach, C. Schramm, G. Unterbörsch, and S. van Waasen: **37-GHz Bandwidth InP-Based Photoreceiver OEIC Suitable for Data Rates up to 50 Gb/s**, IEEE Photon. Technol. Lett., vol. 11, no. 2, pp. 257-259 (1999).

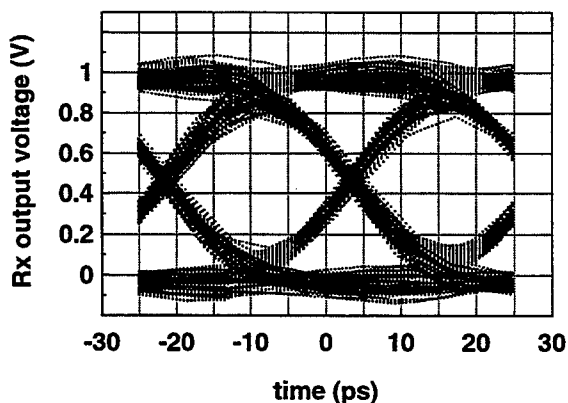


Fig. 6: NRZ eye pattern for a bit rate of 40 Gb/s for photoreceiver module, deduced from measured frequency characteristics (Fig. 5) under "minimum phase" assumption.

OEICs for RZ and NRZ Coded TDM System Applications, OFC/IOC'99, Technical digest, paper Tu15-1, San Diego, CA, USA, Feb. 21-26 (1999).

**Integrated Photonics Research and Photonics in Switching**

# **Joint Session 2: Optical Cross Connects**

**Wednesday, July 21, 1999**

**David Cotter, BT Laboratories, UK**  
Presider

**JWB**  
**10:45am–12:45pm**  
San Rafael

## Progress in optical cross-connects for circuit-switched applications

J.E. Fouquet

Hewlett-Packard Laboratories  
3500 Deer Creek Rd. Palo Alto, CA 94028

The deployment of WDM transmission systems greatly increases the number of communication channels in telecommunications networks. These optical signals need to be switched at both the fiber level and the wavelength level (i.e. before and after demultiplexing the individual wavelengths on a fiber) in order to avoid unnecessary expense and complexity due to using conventional SONET-based switching alone. Furthermore, efficient internet protocol (IP) transmission systems which operate without SONET are expected to occupy the same fibers as SONET-based links, further increasing the need for optical circuit switches. The large numbers of wavelengths being transmitted along each fiber together with large numbers of fibers drive the demand for high port count ( $N$ , with  $N \geq 32$ ) in fiber optic cross-connect ( $N \times N$ ) switches.

Building a scalable single mode optical cross-connect (OXC) switch has proven difficult, leading some workers to pursue an electrical cross-connect (EXC) solution with optoelectronic transducers at the inputs and outputs. However, these approaches lack the highly desirable protocol and bit-rate independence of an OXC. Optical approaches encompass a wide variety of technologies and multiple architectures.  $N \times N$  cross-connect switches can be constructed from  $2N$  each of  $1 \times N$  switches as shown in Fig. 1, with  $N^2$  optical connections between the two columns of  $1 \times N$  switches. Commercial cross-connects constructed with this architecture are available with both opto-mechanical and thermo-optic  $1 \times N$  elements; the former generally have excellent insertion loss and crosstalk but tend to be massive and potentially unreliable, while the latter are compact but suffer from relatively poor optical performance. The  $2N(1 \times N)$  approaches become unwieldy and expensive for large  $N$ , with 1024 fiber connections internal to a  $32 \times 32$  switch, for example. Most can not easily be aggregated into larger switches in a modular architecture because they lack add and drop ports.

True matrix OXCs require better per-crosspoint extinction performance than  $2N(1 \times N)$  approaches, but can be far more compact, inexpensive and convenient since no internal fiber connections are needed (Fig. 2). Many can also be scaled modularly into larger switches (Fig. 3). NTT has constructed large matrix switches using thermo-optic elements. They require more than  $N^2$  switching elements in order to overcome the poor crosstalk performance of the individual switches, which contributes to high insertion loss [1]. A wide variety of silicon-based micro electromechanical systems (MEMS) approaches has been researched. These can provide excellent crosstalk performance, but many have poor reliability due to sliding action of the switches. Other switches achieve higher reliability by utilizing bending rather than sliding motions [2]. Many MEMS approaches utilize free space propagation between mirrors, which does not scale well up to large  $N$  due to beam divergence and alignment issues. Guided wave

propagation, on the other hand, permits low insertion losses in large switches if good alignment can be maintained.

Hewlett-Packard's "Champagne" OXC switch [3] is based on total internal reflection from the sidewalls of trenches etched at the crosspoints of a planar lightwave circuit matrix (Fig. 4). The trenches are normally filled with a refractive index-matching fluid to allow transmission across the trench to the next collinear waveguide segment. The liquid can be displaced using a small bubble generated at the crosspoint by a thermal actuator fabricated on a separate chip (Fig. 5). In this case, light undergoes total internal reflection (Fig. 6). Holes penetrate the actuator chip on either side of each crosspoint (Fig. 7), to accommodate expansion and contraction of the bubble. The crosstalk performance of a switching element is -70 dB for close (but uncontrolled) refractive index match, setting a record for compact optical switch elements orders of magnitude beyond the performance of interference-based switching elements.

Insertion loss is low through the waveguides, which have  $\approx 0.1$  dB/cm loss; the maximum path length in a 32x32 OXC with 250  $\mu\text{m}$  pitch is expected to be only 3.0 cm. The wavefunction diverges during the trench crossings, but at a slower rate in liquid than in free space. Furthermore, the trench widths are far smaller than the crosspoint separations. Thus transmission insertion losses are low compared to those in free space switches with similar, large N. We have experimentally achieved the expected value of 0.2 dB per trench value from fiber-to-fiber losses through a series of 32 nominal 25  $\mu\text{m}$ -wide trenches. We have similarly measured a value of 0.14 dB per trench for 15  $\mu\text{m}$ -wide trenches, which is higher than the theoretical value of 0.09 dB. As a point of reference, NTT's 1x8 thermocapillarity switch, which also uses total internal reflection in 10  $\mu\text{m}$ -wide trenches, has exhibited a loss of 0.1 dB per trench [4]. Insertion loss due to the single reflection point along any input-output path is theoretically expected to be approximately 0.1 dB; to date we have measured a fiber-to-fiber insertion loss of 3.2 dB. Taken together, theoretical insertion loss values for a 32x32 switch with 15  $\mu\text{m}$ -wide trenches imply a worst-path internal insertion loss of  $\leq 6$  dB. Alignment within the switch is set by photolithography and maintained by waveguides, so all inputs are automatically aligned to all outputs. These switches, whose actuators use proven thermal inkjet technology, have survived over  $10^6$  cycles.

Even a one second-long change of state represents a huge improvement over patch panel reconfiguration times. However, for protection applications SONET-like physical changes of state  $\leq 10$  msec are required. Figure 8 shows that these switches change state in  $\sim 1$  msec in both directions.

- [1] T. Goh, A. Hirano, M. Okuno, H. Takahashi and K. Hattori, *IEEE Photonics Technology Letters*, v. 10, n. 3, Mar. 1998.
- [2] Ming Wu, *Proc. Optical Fiber Communications Conf.*, San Diego, Feb. 1999.
- [3] J.E. Fouquet, S. Venkatesh, M. Troll, D. Chen, S. Schiaffino, H.-F. Wong and P.W. Barth, *Proc. IEEE Lasers and Electro-Optics Society Annual Meeting*, Orlando, Dec. 1998.
- [4] M. Sato, F. Shimokawa, S. Inagaki, and Y. Nishida, *Proc. Optical Fiber Communications Conf.*, San Jose, Feb. 1998, pp. 194-5 and private communication.

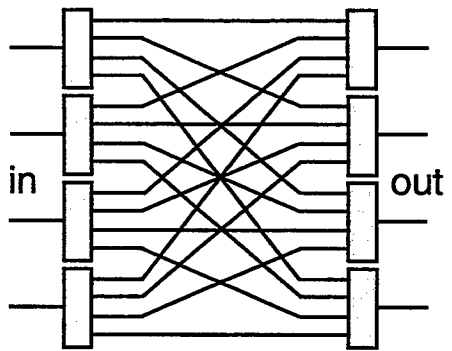


Fig. 1  $2N(1 \times N)$  architecture used to make an  $N \times N$  switch (where  $N=4$ ).

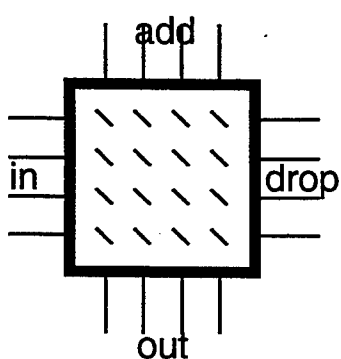


Fig. 2 True  $N^2$  cross-connect architecture (where  $N=4$ ).

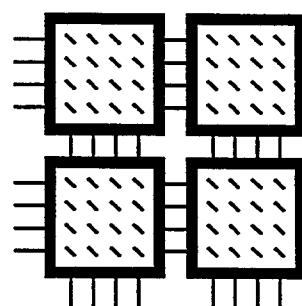


Fig. 3 Modular scalability permits construction of an 8x8 from four 4x4 switches.

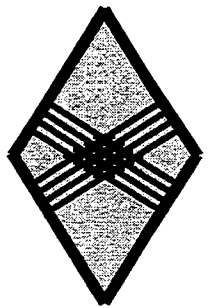


Fig. 4 Planar lightwave circuit matrix for total internal reflection switch.

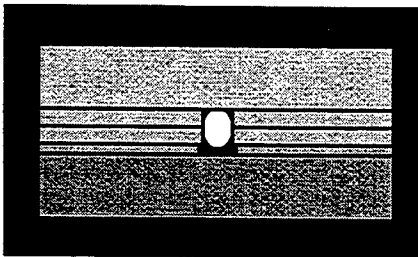


Fig. 5 Thermal actuator is fabricated on separate substrate.

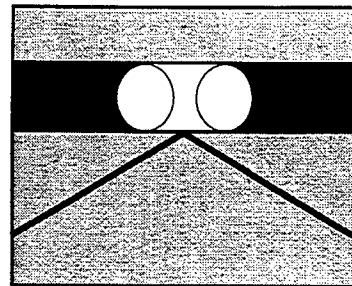


Fig. 6 Bubble in fluid-filled trench causes total internal reflection.

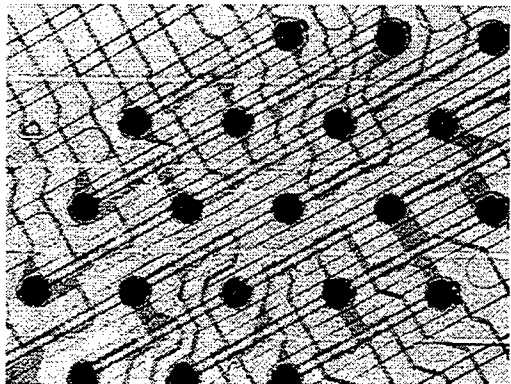


Fig. 7 Waveguides in this 4x4 switch appear as light lines, while trench edges are darker. Fluid fill holes lie to either side of each crosspoint, appearing as dark circles.

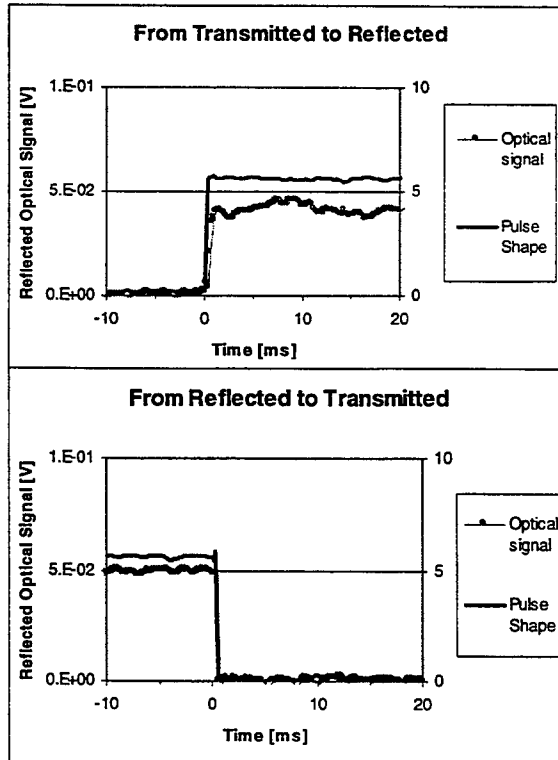


Fig. 8 Switching between states in both directions.

## Monolithic InP Optical Crossconnects: 4 x 4 and Beyond

Gregory A. Fish, B. Mason, Larry A. Coldren, Steven P. DenBaars

*Electrical & Computer Engineering, University of California, Santa Barbara, 93106*

6500fish@ucsbuxa.ucsb.edu,

Phone: (805) 893-8465

Fax: (805) 893-4500

### Introduction

Increasingly, optical crossconnects are being proposed as the basis for various photonic packet switching nodes[1, 2]. Many of these strategies involve using the crossconnects to provide simultaneous packet routing and buffering of multiple input channels through the use of optical fiber delay lines. In addition to the typical optical switching requirements, (e.g. low crosstalk, low insertion loss, and high switching speed) these applications demand crossconnects with a large number of channels, as several buffering channels are usually needed to provide lossless packet routing for relatively few data channels[1].

Crossconnects based upon semiconductor optical amplifiers (SOA) gates are well suited for these applications, as they are compact and have demonstrated lossless, low crosstalk (-50 dB) switching, with speeds sufficient for cell routing (2 ns) [3]. Unfortunately, most SOA gate arrays to date use tree architectures where the loss per channel increases as  $N^2$  ( $N$  being the number of channels), so it is unlikely these strategies can be scaled to significantly larger sizes. Combining optical switches with SOA's has been shown to be a very effective method in creating a more scalable crossconnect which can have lower loss and crosstalk than a simple gate array [4]. Building upon this concept, we demonstrate a very compact 4 x 4 (2 x 2 mm<sup>2</sup>) optical crossconnect using sixteen 1 x 2 Optically Amplified Suppressed Interference Switches (OASIS) [5] elements as shown in Fig. 1 (a). By arranging the sixteen elements in the square array architecture shown in Fig. 1 (b), the average insertion loss reduces to roughly  $N$  times the excess loss of the optical switches (called the Suppressed Modal Interference (SMI) switch) within an OASIS element, which can be made small (~0.5 dB)[6].

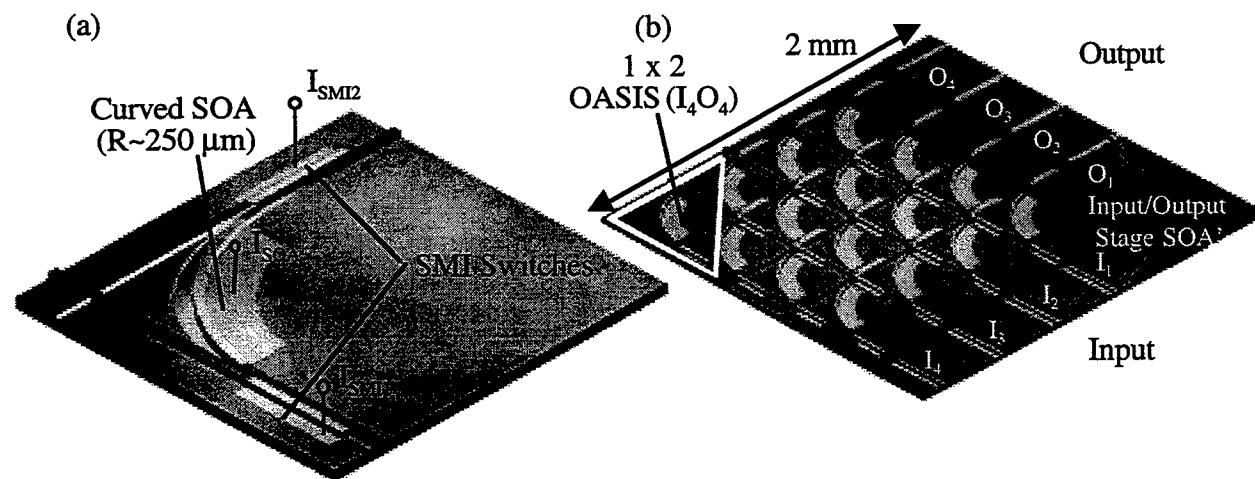


Fig. 1 a) Schematic drawing of an 1x2 OASIS depicting orthogonal inputs and outputs connected by two SMI switches with a 250  $\mu\text{m}$  radius curved amplifier. b) Schematic drawing of a 4x4 crossconnect consisting of 16 OASIS elements.

#### 4x4 Crossconnect Performance

4 x 4 arrays depicted in Fig. 1 b) were characterized using lensed fiber and a lock-in amplifier to measure the transmission of a tunable laser outputting -20 dBm of power over a range of 1500-1570 nm. A multi channel current source was used to drive the two switches and SOA's together to measure the switching response of a particular channel. On/off ratios were measured to be  $33 \pm 4$  dB across the array as shown in Fig. 2 a), and insertion loss as low as 3 dB was measured for channel  $I_1 O_2$ . The optical bandwidth of the device was measured to be 45 nm over which the insertion loss remained within 3 dB of the maximum and the on/off ratio remained above 39 dB.

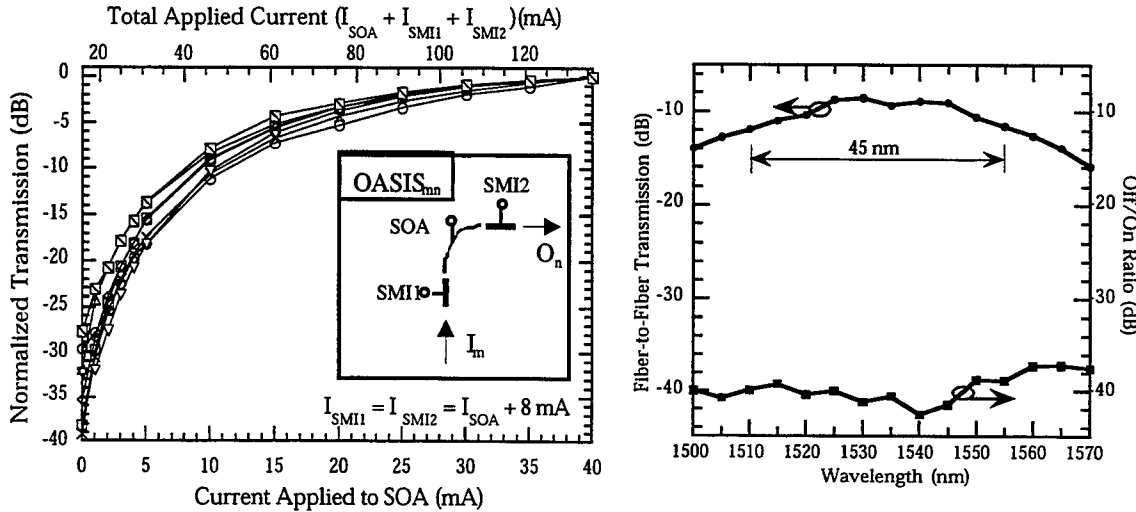


Fig. 2 a)Switching characteristic for multiple OASIS elements in the array. b) Schematic drawing of a 4x4 crossconnect consisting of 16 OASIS elements.

Although good crosstalk performance was measured for the crossconnect, the optical losses were far too high for a practical device, as the additional on-chip amplification stages needed to reduce the fiber-to-fiber loss to -3 dB contributed to a 1.1 dB power penalty for 2.5 GB/s transmission through the switch matrix. The origin of this power penalty is most likely due to the additional noise from amplified spontaneous emission (ASE) created in the SOA.

#### Enhancing the Performance of the Monolithic Crossconnect

The focus of the efforts to improve performance the monolithic optical crossconnect mostly involve reducing the insertion loss. One of the key technologies required to meet this goal is the use of an optical spot-size converter. By simultaneously reducing the coupling loss and increasing the alignment tolerance to optical fibers, spot size converters can dramatically lower the insertion loss and packaging complexity of the switch matrix without introducing additional noise.

There have been several reported methods for producing optical spot size converters, however, they generally involve tapering down the width or thickness of the layer that is providing waveguiding. One of the simplest techniques for producing a high quality, vertically tapered spot-size converter compatible with the switch arrays is selective area etching[7]. Selective area etching involves varying the gap width between two dielectric masks to effect the etch rate of a diffusion limited etchant. Fig 3 a) shows a cross section through the ridge waveguide spot size converter created with selective area etching. The short, ( $<200 \mu\text{m}$ ) cubically tapered converters have exhibited conversion losses below 0.5 dB and coupling efficiencies as high as 75 % to lensed optical fibers.

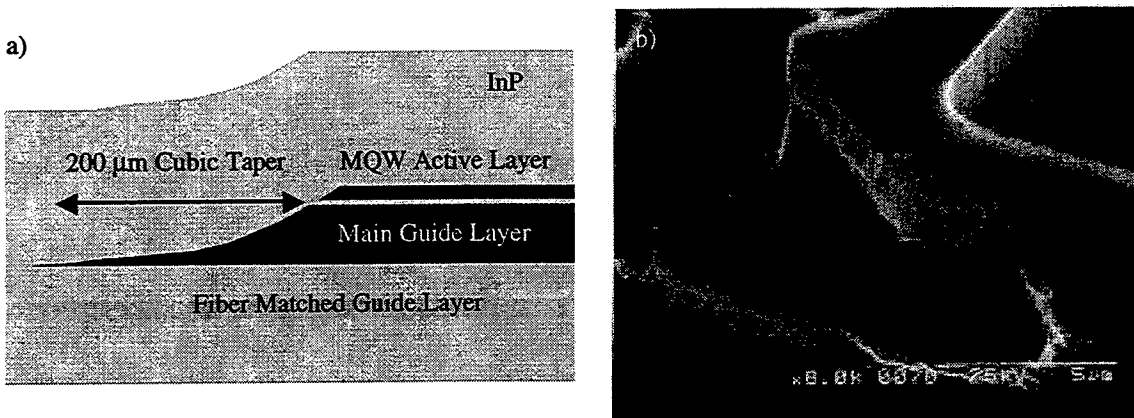


Fig. 3 a) Schematic illustration of a spot-size converter cross section through the center of the ridge waveguide. b) Integrated waveguide turning mirror used to replace the small radius bend (250  $\mu\text{m}$ ) in the cross state SOA.

Another large source of optical loss in the current structure is believed to be the small radius (250  $\mu\text{m}$ ) bend in the cross state SOA. While relatively low loss bends with this radius or smaller have been fabricated in InP, integrating the optical waveguides required for compact, low loss bends with those required by the SMI optical switch is difficult. To eliminate this problem, a waveguide turning mirror (shown in Fig 3 b)) has been fabricated to replace the curved waveguide. The turning mirror uses the same waveguide as the optical switch, so it is much easier to integrate. Mirror reflectivities of 80% have been achieved indicating a smooth facet and good alignment.

## Conclusions

The results of a 4x4 monolithic optical cross connect have been presented. While good crosstalk performance (<-35 dB) was achieved, practical devices will require a reduction of the insertion loss. Two efforts devoted to this goal, namely, the addition of a spot-size converter and a waveguide turning mirror were demonstrated to good effect.

## References

- [1] L. E. Moser and P. M. Melliar-Smith, "Lossless packet switching with small buffers," *IEE Proceedings-Communications*, vol. 143, pp. 335-40, 1996.
- [2] D. A. C. C. Jayasinghe, S. J. Madden, W. L. R. Perera, and P. L. Chu, "Cross-talk effects in fibre feedback buffer memories with single-substrate space switches," in *Proc. LEOS '96 9th Annual Meeting. IEEE Lasers and Electro-Optics Society 1996 Annual Meeting (Cat. No.96CH35895)* Conference Proceedings LEOS'96 9th Annual Meeting IEEE Lasers and Electro-Optics Society, 1996, pp. 320-1.
- [3] R. Krahnenbuhl, R. Kyburz, W. Vogt, M. Bachmann, T. Brenner, E. Gini, and H. Melchior, "Low-loss polarization-insensitive InP-InGaAsP optical space switches for fiber optical communication," *IEEE Photonics Technology Letters*, vol. 8, pp. 632-4, 1996.
- [4] T. Kirihara, M. Ogawa, H. Inoue, H. Kodera, and K. Ishida, "Lossless and low-crosstalk characteristics in an InP-based 4\*4 optical switch with integrated single-stage optical amplifiers," *IEEE Photonics Technology Letters*, vol. 6, pp. 218-21, 1994.
- [5] G. A. Fish, L. A. Coldren, and S. P. DenBaars, "Suppressed modal interference switches with integrated curved amplifiers for scaleable photonic crossconnects," *IEEE Photonics Technology Letters*, vol. 10, pp. 230-2, 1998.
- [6] G. A. Fish, L. A. Coldren, and S. P. DenBaars, "Compact InGaAsP/InP 1\*2 optical switch based on carrier induced suppression of modal interference," *Electronics Letters*, vol. 33, pp. 1898-900, 1997.
- [7] T. Brenner and H. Melchior, "Local etch-rate control of masked InP/InGaAsP by diffusion-limited etching," *Journal of the Electrochemical Society*, vol. 141, pp. 1954-6, 1994.

## Optoelectronic switching in semiconductor waveguides incorporating a resonant tunneling diode

**J. M. L. Figueiredo,<sup>\*</sup> A. R. Boyd, C. R. Stanley, and C. N. Ironside<sup>#</sup>**

Department of Electronics and Electrical Engineering, University of Glasgow, Glasgow G12 8LT, United Kingdom

<sup>#</sup>Telephone: + 44 141 330 4697 Fax: +44 141 330 6002. Electronic mail: ironside@elec.gla.ac.uk.

<sup>\*</sup>Also with the Centro de Física do Porto - ADFCUP, Universidade do Porto, Rua do Campo Alegre 687, 4169-007 PORTO, Portugal. Telephone: + 351 2 6082623 Fax: +351 2 6082622. Electronic mail jlfiguei@fc.up.pt.

### A. M. P. Leite

Centro de Física do Porto - ADFCUP, Universidade do Porto, Rua do Campo Alegre 687, 4169-007 PORTO, Portugal

Telephone: + 351 2 6082623 Fax: +351 2 6082622. Electronic mail apleite@fc.up.pt.

Due to their high-speed response and radio frequency (rf) gain, several groups have proposed the application of resonant tunneling diodes (RTDs) in the optical and infrared regions.<sup>1-3</sup> Embedding a RTD within an optical waveguide core can enhance the interaction length between its active region and the guided light. Our group has successfully integrated a GaAs/AlAs RTD within an unipolar GaAs/AlGaAs optical waveguide, and demonstrated optical modulation of light around 900 nm.<sup>4</sup> The incorporation of a RTD within an optical waveguide introduces large non-linearities into the electric field distribution across the waveguide core, which becomes strongly dependent on the bias voltage, due to accumulation and depletion of electrons in the emitter and collector sides of the RTD, respectively. Depending on the dc bias operating point, a small high frequency ac signal (<1 V) can induce high-speed RTD switching, producing substantial high-speed modulation of the waveguide optical absorption coefficient at a fixed wavelength near the material band-edge via the Franz-Keldysh effect<sup>1</sup>. Therefore, light modulation at photon energies lower than the band-gap energy is possible. The modulation depth can be considerable because, under certain conditions, the RTD operation point switches well into the two positive differential resistance regions of the current-voltage (*I*-*V*) characteristic, with a substantial part of the terminal voltage dropped across the depleted region in the collector side. The advantage of this RTD electroabsorption modulator (RTD-EAM) compared to the conventional *pn* modulators is that, when dc biased in the negative differential resistance (NDR) region, the device behaves as an optical waveguide electro-absorption modulator integrated with a wide bandwidth electrical amplifier. These RTD modulators have been realized in two material systems: GaAs/AlGaAs, operating at around 900nm, and InGaAs/InAlAs, operating at 1550nm. This paper reports the latest results on optoelectronic switching at around 900 nm and 1550 nm.

The RTD optical waveguide structures were grown by Molecular Beam Epitaxy in a Varian Gen II system. Figure 1(a) shows the schematic diagram of the wafer structure for a GaAs based device. The waveguides were defined by reactive ion etching in SiCl<sub>4</sub>.<sup>5</sup> The devices were mounted on packages containing a 50 Ω coplanar waveguide (CPW) transmission line. The packaged RTD optical modulator (RTD-OM) configuration, presented in Fig. 1(b), allows light coupling into the waveguide by a microscope objective end-fire arrangement. The dc and rf signals were applied through an 18 GHz bandwidth connector via a 28 GHz bias tee. A HP 4145 parametric analyzer was used to measure the dc *I*-*V* characteristic of the packaged devices, which shows typical RTD behavior, with peak current densities up to 13 kAcm<sup>-2</sup> (800 μm<sup>2</sup> active area), and peak-to-valley current ratios (PVCRs) around 1.5. Peak voltages were in the range 2.0 - 2.5 V and the valley voltage varied from 2.6 to 3.2 V.

The optical characterization employed light from a Ti:sapphire laser, tuneable in the wavelength region around the absorption edge of the GaAs waveguide (850-950 nm). To measure the change in the optical absorption spectrum induced by the peak-to-valley transition, a rf signal was injected to switch the RTD between the extremes of the NDR region, and a photo-detector was used to measure the transmitted light. The band edge shift was found to be approximately 12 nm.

The high-speed optical response was measured using a streak camera (Hamamatsu C5680) with a minimum time resolution of around 2 ps. The characterization set up is presented in Fig. 1(b). Due to the highly non-linear *I*-*V* characteristic in the NDR region, the RTD is able to generate many high-order harmonics of the injected signal.<sup>6,7</sup>

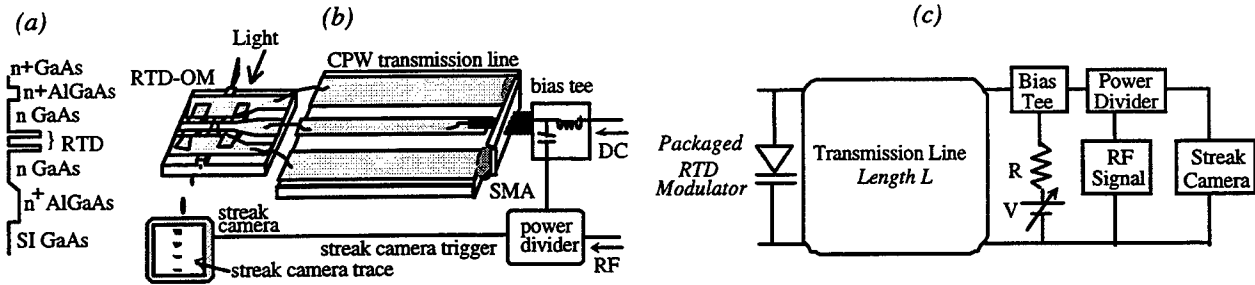


Fig. 1 (a) Schematic diagram of the GaAs/AlGaAs wafer structure. (b) The packaged RTD optical modulator (RTD-OM) and characterization set up configuration. (c) Schematic diagram of the RTD-OM electrical test circuitry.

We have observed optical modulation around 15 GHz in devices packaged with a 5 mm long CPW transmission line, dc biased in the NDR region (2.25 V), when a RF signal of 0.5 V amplitude and frequency around 1 GHz was injected. The 15 GHz modulation frequency corresponds to relaxation oscillation at the fundamental mode of the cavity comprising the RTD and the package CPW line ended with the SMA connector, with the left side of the modulator CPW unterminated, as indicated in the schematic diagram of the RTD-EAM electrical circuitry [Fig. 1(c)].<sup>5</sup> By inserting coaxial transmission lines between the packaged device and the bias tee, we have also observed modulation at the frequencies associated with the fundamental mode of the coaxial transmission lines. The streak camera trace for the 15 GHz optical response is presented in figure 2(a).

Injecting a RF signal around 1V amplitude, we have also found that the RTD modulator produces optical pulses with a full width at half maximum (FWHM) of around 33 ps (approximately the expected intrinsic switching time of the GaAs/AlGaAs device), with repetition rates corresponding to the coaxial fundamental mode frequencies. Figure 2(b) displays the streak camera trace of such optical pulse, for a 680 MHz injected signal. The coaxial transmission line was 15 cm long. The trace shows a modulation depth of 18 dB. On a longer time scale, other streak camera results indicate a pulse repetition rate around 350 MHz, which was confirmed by the waveform on a 2 GHz scope. The modulation efficiency, characterized by the bandwidth-to-drive-voltage ratio (defined as the ratio of the operation bandwidth to the operating voltage for the 10 dB modulation depth), is higher than 35 GHz/V.

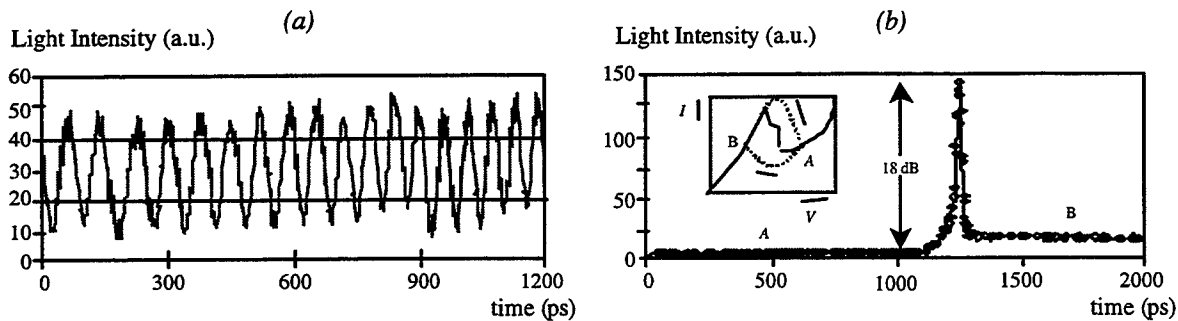


Fig. 2: (a) Streak camera trace of the modulator optical response associated with locking of the RTD oscillation to the fundamental mode of a package with a 5 mm CPW transmission line. (b) Optical response to an applied electrical signal of 1V amplitude at 680MHz: 33 ps FWHM optical pulses, showing modulation up to 18 dB.

The optical modulation associated with locking of the RTD to the frequency of the fundamental mode of a transmission line can be explained by operation of the RTD as a relaxation oscillator.<sup>5-7</sup> The high-speed and large modulation depth characteristics obtained are a direct consequence of the carrier transport across the RTD and the waveguide depletion region. They are closely related to the material system and specific device structure. High-speed performance can be improved by increasing the absolute value of the NDR, or decreasing the device series resistance. The modulation efficiency depends on the electric field strength across the depletion region, which is a function of the peak-to-valley current and voltage differences.

The demonstration and development of this new modulator concept in the quaternary InGaAlAs system lattice-matched to InP, can be of great importance for optical fiber communication, specially in high-speed fiber-radio links as optoelectronic converter (rf-optical and optical-rf). This material system is useful in wavelength range where optical fibers have the lowest loss and chromatic dispersion (1.3 to 1.6  $\mu\text{m}$ ). Fortunately, the material also presents some advantages compared to the GaAs/AlGaAs system, mainly a the larger magnitude of the PVC due to higher peak and lower valley current densities. The device series resistance can also be reduced due to the smaller specific contact resistivity associated with metal to n<sup>+</sup>-InGaAs contact layers.

The dc *I-V* characteristics of the InGaAs/InAlAs based devices, designed to have an absorption band-edge around 1550 nm, show peak voltages in the range 0.6 - 1.5 V and valley voltages between 1.4 and 2.0 V. The peak current densities are as high as 20 kAcm<sup>-2</sup> (400  $\mu\text{m}^2$  active area), with PVCRs up to 7. Figure 3(a) shows a typical InGaAs/InAlAs RTD-OM *I-V* characteristic. Optical characterization of this modulator employed light from a Tunics diode laser tuneable in the wavelength region around the absorption edge of the guiding material (1480-1580 nm). We have observed absorption band-edge shifts as high as 30 nm, and a maximum modulation depth of 28 dB at around 1565 nm (approximately 1.6 times higher than in the GaAs/AlAs device). Figure 2(b) shows the modulation efficiency as a function of the wavelength, for peak-to-valley switching induced by an applied rf signal around 1 V amplitude. The high-speed optoelectronic characterization of this new modulator is under way. From our results with GaAs/AlGaAs and from the improved *I-V* characteristic of the InGaAs/InAlAs devices, we estimate that optimized devices can have operation frequencies well into the millimeter-wave region.

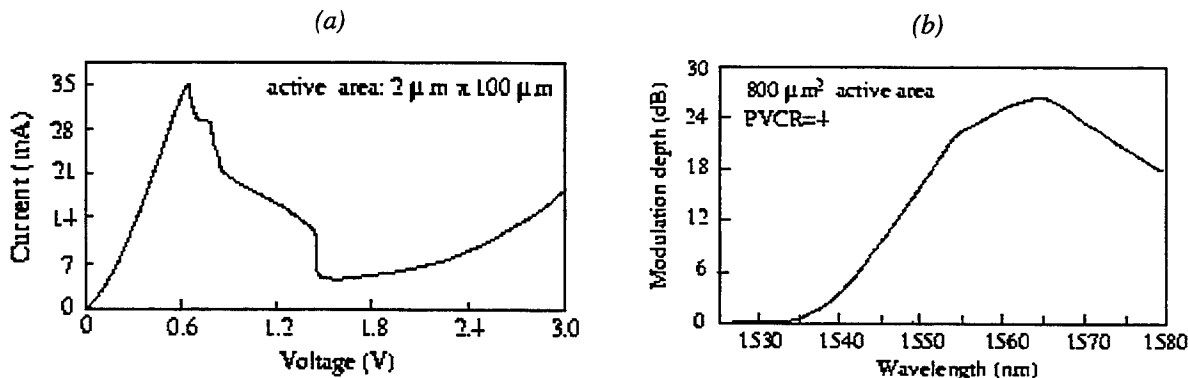


Fig. 3 (a) I-V characteristic of a 2  $\mu\text{m} \times 100 \mu\text{m}$  active area InGaAs/AlAs RTD-OM. (b) Modulation depth as a function of wavelength due to peak-to-valley transition (800  $\mu\text{m}^2$  active area, PVCR=4).

In conclusion, integrating a RTD with an optical waveguide is a relatively easy way of combining a wide bandwidth electrical amplifier with an electro-absorption modulator, opening up the possibility of a variety of operation modes. Optical modulation up to 26 dB in an InGaAlAs optical waveguide containing a InGaAs/AlAs RTD, due to the RTD peak-to-valley switching, has been demonstrated, confirming our results in the GaAs/AlGaAs system. The device appears to be a promising route towards a high speed, low power optoelectronic modulator, operating in the third optical communications window.

<sup>1</sup> A. F. Lann, E. Grumann, A. Gabai, J. E. Golub, and P. England, *Appl. Phys. Lett.* **62**, 13 (1993).

<sup>2</sup> S. C. Kan, S. Wu, S. Sanders, G. Griffel, and A. Yariv, *J. Appl. Phys.* **69**, 3384 (1991); S. C. Kan, P. J. Harshman, K. Y. Lau, Y. Wang, and W. I. Wang, *IEEE Photon. Technol. Lett.* **8**, 641 (1996).

<sup>3</sup> T. S. Moise, Y.-C. Kao, C. L. Goldsmith, C. L. Schow, and J. C. Campbell, *IEEE Photon. Technol. Lett.* **9**, 803 (1997).

<sup>4</sup> S. G. McMeekin, M. R. S. Taylor, B. V'gele, C. R. Stanley, and C. N. Ironside, *Appl. Phys. Lett.*, **65**, 1076 (1994).

<sup>5</sup> J. M. L. Figueiredo, C. R. Stanley, A. R. Boyd, C. N. Ironside, S. G. McMeekin, and A. M. P. Leite, *Appl. Phys. Lett.* **74**, 1197 (1999)

<sup>6</sup> S. Verghese, C. D. Parker, and E. R. Brown, *Appl. Phys. Lett.* **72**, 2550 (1998).

<sup>7</sup> E. R. Brown, C. D. Parker, S. Verghese, M. W. Geis, and J. F. Harvey, *Appl. Phys. Lett.* **70**, 2787 (1997)

## MEMS for Optical Switching

Lih Y. Lin and Evan L. Goldstein

AT&T Labs-Research, 100 Schulz Drive, Red Bank, NJ 07701

Tel: 732-3453249      Fax: 732-3453037      EMail: lylin@research.att.com

As the transmission capacity of WDM networks increases apace with rapidly growing demand, optical switching has attracted strong interest, due chiefly to the fact that its complexity is impervious to steadily rising per-channel bit rate, and its interfaces are inherently simple and inexpensive. Micro-electro-mechanical-systems technology has recently begun to show real promise for achieving high-quality and high-port-count optical switching. This approach has the unique ability to integrate electrical, mechanical, and optical elements on a single chip, and thus promises to offer multiple functionalities in compact, low-cost form. In this paper, we will review various micromachined optical-switching technologies, focusing on the free-space MEMS optical switch we have demonstrated. Emphasis is placed on the ability of this technology to gracefully incorporate the sorts of functionality that become critical in core transport-network settings.

Various MEMS optical switching schemes have been demonstrated, including both waveguide [1] and free-space approaches. The free-space approach possesses the advantage of high interconnection flexibility, and thus has been widely investigated. Both  $2 \times 2$  bypass [2, 3] and  $M \times N$  configurations [4-6] have been demonstrated. The approach we have adopted for free-space micromachined optical switching utilizes free-rotating hinged micromirrors (Fig. 1) [5]. Figure 2 shows an SEM photograph of an  $8 \times 8$  switch. The insertion loss through  $M \times N$  switch configurations has been characterized theoretically and experimentally [7]. Figure 3 shows the results for various mirror radii  $R$ . The corresponding Gaussian beam radius is  $R/1.5$ . The results show that multi-stage switches with the port-counts and loss budgets required by core long-haul networks appear to be feasible.

Figure 4 is an SEM photograph of a free-rotating hinged micromirror. The entire switch is fabricated by surface-micromachining, whose batch processing generates all micro-optical elements from one polysilicon ground layer and two polysilicon structural layers. The design allows effective translation-to-rotation conversion. Switching time less than 1 ms has been demonstrated. This technology achieves low loss and crosstalk, and small dependence on polarization, wavelength, and bit-rate, chiefly through the combination of a free-space interconnection region with high-quality integrated micromirrors. In addition, it has the advantage of integrating various optical-networking functionalities into the switch fabric. These are described below.

**Bridging for optical-layer provisioning and restoration** [8] Bridging signals to both service and protection routes is required for avoiding interruption during optical restoration and maintenance. Since polysilicon material is partially transparent, free-rotating polysilicon plates can be employed at the inputs of the switch fabric as beam-splitters, thus implementing the bridging function with modest incremental complexity. Figure 5 shows an SEM photograph of a free-space MEMS optical switch with bridging.

**Integrated signal-monitoring and fault localization** [9] This is important for facilitating network-management and fast restoration. Such functionality can be realized using a  $45^\circ$  polysilicon beam-splitter and a hybrid-integrated photodetector. Figure 6 shows such a monitor module incorporated in front of each output fiber-collimator. For detection of loss-of-signal, low-

speed photodetectors are sufficient. On the other hand, high-speed photodetectors are required if detection of signal frames and bit-level information are desired.

**Connection symmetry** [10] The connection paths in current telecommunications networks are bi-directionally symmetric. By utilizing the backsides of switch mirrors, raising one switch mirror can set up a pair of connections simultaneously. Exploiting this property can greatly reduce the number of needed switch mirrors. The schematic drawing of a free-space MEMS optical switch with connection-symmetry for nodal degree 3 is shown in Fig. 7.

To summarize, free-space MEMS optical-switching technology, though clearly in its infancy, has begun to show substantial potential for core-transport network applications. The technology's high optical quality and high capacity for integration of advanced network functions have already become clear. Demonstration of long-term reliability and cost-effective packaging appear to be the chief challenges that yet lie between research optical micromachines and their deployment in transport-network switching systems.

#### References:

- [1] J. E. Fouquet, S. Venkatesh, M. Troll, D. Chen, H. F. Wong, and P. W. Barth, "A compact, scalable cross-connect switch using total internal reflection due to thermally-generated bubbles," in *IEEE LEOS Annual Meeting*, Orlando, FL, 1998.
- [2] S.-S. Lee, L.-S. Huang, C.-J. Kim, and M. C. Wu, "Free-space fiber-optic switches based on MEMS vertical torsion mirrors," *J. Lightwave Technol.*, vol. 17, no. 1, pp. 7-13, 1999.
- [3] C. Marxer and N. F. de Rooij, "Micro-opto-mechanical 2 x 2 switch for single-mode fibers based on plasma-etched silicon mirror and electrostatic actuation," *J. Lightwave Technol.*, vol. 17, no. 1, pp. 2-6, 1999.
- [4] H. Toshiyoshi and H. Fujita, "Electrostatic micro torsion mirrors for an optical switch matrix," *J. Microelectromechanical Systems*, vol. 5, no. 4, pp. 231-237, 1996.
- [5] L. Y. Lin, E. L. Goldstein, and R. W. Tkach, "Free-space micromachined optical switches with submillisecond switching time for large-scale optical crossconnects," *IEEE Photonics Technol. Lett.*, vol. 10, no. 4, pp. 525-527, 1998.
- [6] B. Behin, K. Y. Lau, and R. S. Muller, "Magnetically Actuated micromirrors for fiber-optic switching," in *Solid-State Sensor and Actuator Workshop*, Hilton Head Island, SC, June 8-11, 1998.
- [7] L. Y. Lin, E. L. Goldstein, and R. W. Tkach, "Free-space micromachined optical crossconnects: routes to enhanced port-count and reduced loss," in *Conference on Optical Fiber Communication*, San Diego, CA, Feb. 21-26, 1999.
- [8] L. Y. Lin, E. L. Goldstein, and R. W. Tkach, "Free-space micromechanical optical crossconnect with bridging functionality for optical-layer restoration," in *European Conference on Optical Communication*, Madrid, Spain, Sep. 20-24, 1998.
- [9] L. Y. Lin, L. M. Lunardi, and E. L. Goldstein, "Optical cross-connect integrated system (OCCIS): A free-space micromachined module for signal and switching configuration monitoring," in *IEEE LEOS Summer Topical Meeting: Optical MEMS*, Monterey, CA, July 20-22, 1998.
- [10] L. Y. Lin, E. L. Goldstein, J. M. Simmons, and R. W. Tkach, "High-density micromachined polygon optical crossconnects exploiting network connection symmetry," *IEEE Photonics Technol. Lett.*, vol. 10, no. 10, 1998.

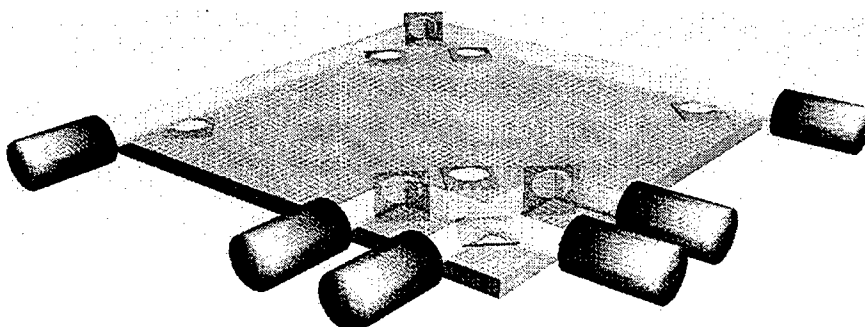


Fig. 1 Free-space MEMS optical switch.

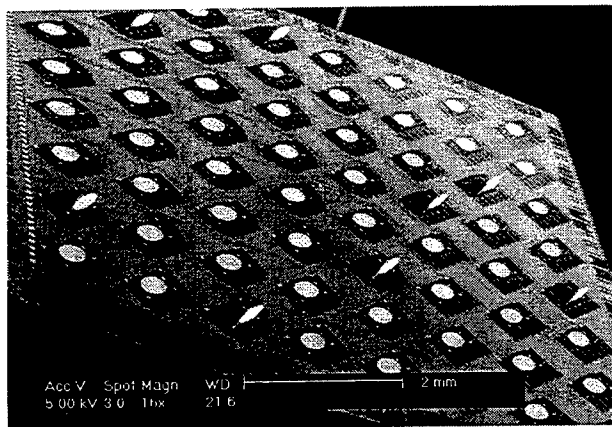
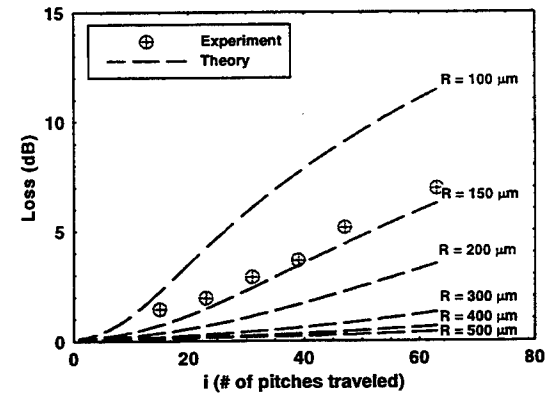
Fig. 2 SEM of an  $8 \times 8$  MEMS optical switch.

Fig. 3 Theoretical and experimental studies of loss versus distance (in pitches between mirrors).

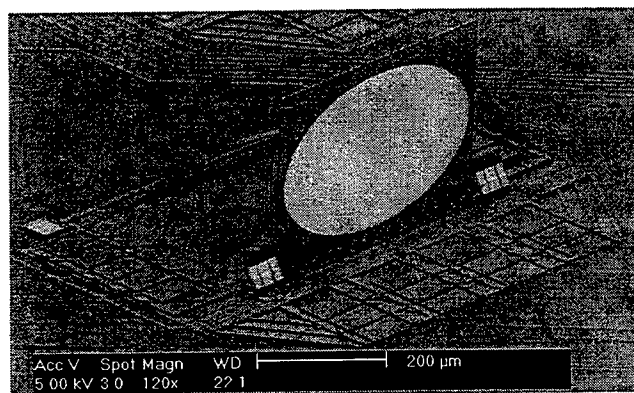


Fig. 4 SEM of a free-rotating switch mirror.

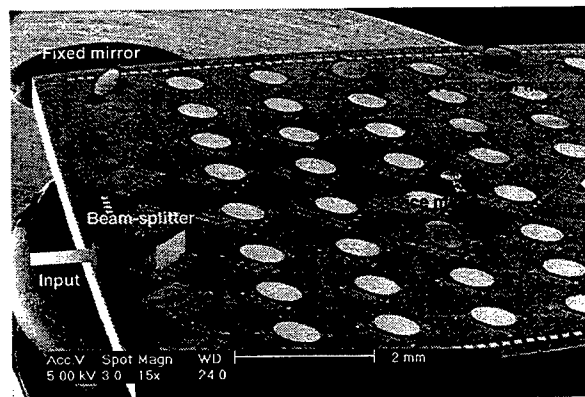


Fig. 5 SEM of the free-space MEMS optical switch with bridging functionality.

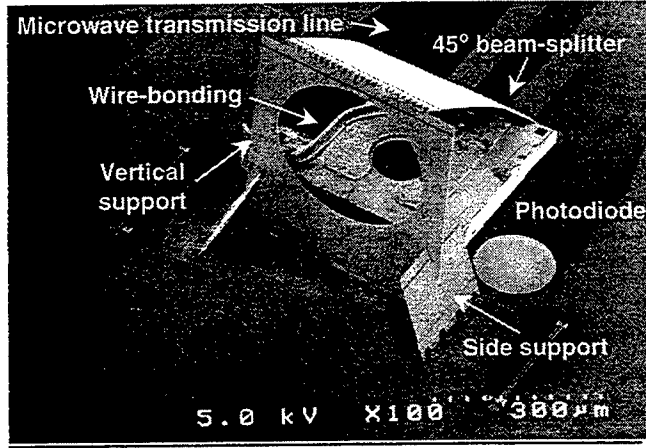


Fig. 6 SEM of a photodetector/beam-splitter monitor module.

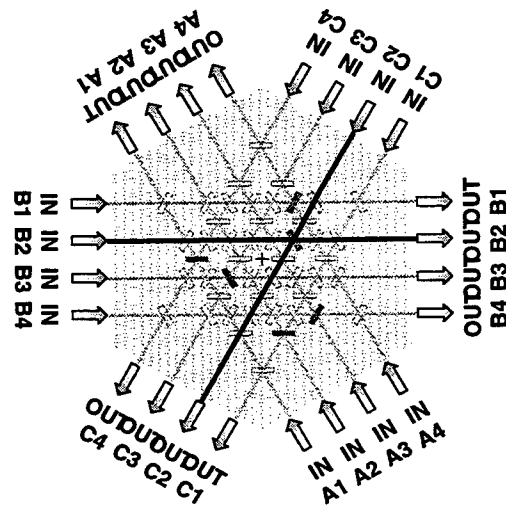


Fig. 7 Schematic drawing of a free-space MEMS optical switch with connection-symmetry.

# IP over Optical Networks: transport and routing

Erik Radius

KPN Research, St. Paulusstraat 4, 2264 XZ Leidschendam, the Netherlands  
e.radius@research.kpn.com

Telecommunication networks are increasingly being used for the transport of IP packets. As IP traffic increases due to the rapid growth of Internet (fueled by the increasing number of users and the bandwidth demands per user), plus the advent of local and wide area networks (LANs and WANs), many indicators predict that IP traffic will become the predominant traffic data type. Therefore, network operators worldwide are seeking solutions for migrating parts of their circuit-switched telecom infrastructure into a high-speed datagram-based IP-backbone.

Optical transport networks can deliver Gigabit/s or even Terabit/s backbone capacity by means of wavelength division multiplexing (WDM) technology. Although only providing static point-to-point links today, the optical layer is expected to gain flexibility and functionality in the coming years as optical networking elements such as optical add-drop multiplexers (OADM)s and optical cross-connects (OXCs) mature. This way, the optical layer will provide some of the routing and switching functionality which currently resides in SDH or ATM. On the other hand, advancements in IP router equipment have resulted in the development of high-speed interfaces operating at 2.5 or 10 Gb/s which may directly interface with individual WDM wavelength channels. An IP-only backbone may render some of the SDH and ATM functionalities obsolete as IP and WDM layers become more and more functional over time. This tendency is depicted in Figure 1.

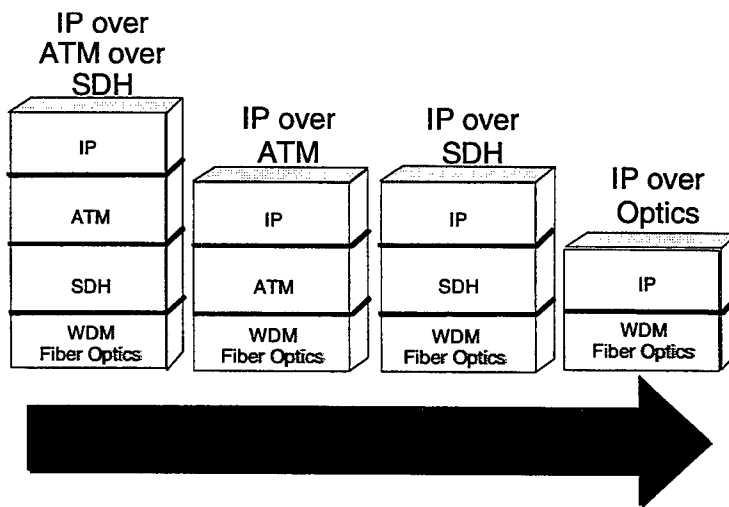


Fig. 1: Layering evolution of IP over WDM

Within the EURESCOM P918 project, titled *Integration of IP over Optical Networks: networking and management*, a group of European telecommunication operators and service providers is studying the integration of IP over optical networks. Project intermediate results will be presented and discussed during the presentation. First project results to be presented will target the points summarised below.

## **WDM bearer service for IP**

Different technologies are proposed to totally or partially meet the IP performance requirements. Several approaches to provide directly IP services over WDM are compared, and an overview is given of available techniques for network operators of the different technical solutions. This overview is based on criteria such as

- scalability
- interoperability with legacy networks
- complexity
- QoS support
- standardisation
- multi-cast support.

Also, methods for mapping IP routing on a cross-connected WDM backbone are assessed.

### *IP protocols and high capacity routers*

Techniques for carrying IP over WDM and particularly possible use of WDM as a way of getting improved functionality into an IP network. The following topics will be addressed: encapsulation of IP over WDM, survey of methods for IP over WDM end-to-end communication, use of wavelengths for bringing QoS for IP, cross-connecting and wavelength routing in the WDM layer and protection and restoration functionalities.

Besides pure data transfer the Internet is used more and more as a platform for multimedia applications like video and audio. From the early seventies, the IP design shows some limitations (scalability problems, missing real-time support etc.). Several approaches exist to solve these problems. An overview is given of state of the art, IP related protocols and software, high speed routers and high speed physical interfaces. Some of the current development tendencies are assessed.

### *IP routing and WDM High Pipe Cross-connection*

Techniques for carrying IP over WDM are investigated and, in particular, the possible use of WDM as a way of getting improved functionality into an IP network. The following topics are addressed:

- encapsulation of IP over WDM
- survey of methods for IP over WDM end-to-end communication
- use of wavelengths for bringing QoS for IP
- cross-connecting and wavelength routing in the WDM layer
- protection and restoration functionalities

This work is part of the EURESCOM P918 project. EURESCOM GmbH (European Institute for Research and Strategic Studies in Telecommunications) is located in the city of Heidelberg, Germany, and was founded in 1991 to organise collaborative research and development in telecommunication related areas of common interest to its Shareholders. EURESCOM Shareholders currently comprise 23 telecommunication Network Operators and Service Providers from 22 European countries.



**Integrated Photonics Research**

# **Photonic Components System Modeling**

**Wednesday, July 21, 1999**

**Joe Donnelly, MIT Lincoln Laboratory, USA**

Presider

**RWC**

**10:45am-12:15pm**

Sierra Madre North

# Integrated Photonic Device and Systems Simulator using Multiple Signal Formats

*Arthur Lowery, Rod Vance,*  
 Virtual Photonics Inc  
 Photonics House  
 129-131 Bouverie Street  
 Carlton VIC 3053 Australia  
 Tel: +61 3 9348 2399  
 Fax: +61 3 9347 4471  
 Email: [australia@virtualphotonics.com](mailto:australia@virtualphotonics.com)

*Olaf Lenzmann, Dirk Breuer, Igor Koltchanov*  
 Virtual Photonics Inc  
 Helmholtzstrasse 2-9  
 D-10587 Berlin Germany  
 Tel: +49 30 3470 4715  
 Fax: +49 30 3470 4717  
[www.virtualphotonics.com](http://www.virtualphotonics.com)

## Abstract

We present a photonic systems simulator which applies the most efficient signal representation to each part of the system, to achieve both efficiency and accuracy.

## Introduction

Photonic systems simulation was once reserved for the research laboratory, and only when prototyping could not be afforded. However, over the last two years, the photonics and telecommunications community has awoken to the benefits of simulation in terms of design time and cost. The demand is for flexible tools that can cover a wide range of scales of problems, from integrated optics to photonic networks. Typically, simulations are built by interconnecting elemental models, such as of waveguides, lasers, modulators, grating and fibers. The key to a flexible simulation environment is detailed consideration of the physics within the models, and the interfaces between the models, that allow the models to interact to form a system simulation [1].

Early tools commercial tools, such as GOLD, OPALS, used a single signal format to pass data between the models [2]. In OPALS, the data format was samples of real optical field, passed in both directions, at each iteration. In GOLD, typical of many simulators, the data format was a complex optical field passed as a block in one direction. The requirement for modeling a large range of scales of problem necessitates the development of simulators that can pass data in many formats, to allow the most efficient (and sufficiently-detailed) models to be applied to each part of the simulation.

This paper describes the advances made at Virtual Photonics Inc. [3] to integrate many data formats within one simulation environment, to give a simulation environment which can cover devices through to networks. We discuss the details of converting from one format to another within a single simulation, and provide examples of multi-domain simulation to show the advantages of multi-domain simulation of photonic systems incorporating complex devices.

### Sample and Block Modes: *Bidirectional and Unidirectional Simulation*

For modeling the details of device performance, and photonic circuits, passing samples of optical fields between devices in both directions allows the compound resonances of the system to be calculated. A good example is a Bragg-grating stabilised laser, that can be modeled by interconnecting a Fabry-Perot laser model with a Bragg grating model [4]. This will exhibit modes due to the laser chip, and the Bragg grating combined with the laser chip. The propagation delay between the laser and the grating must be accurately modeled, as this will determine the modal positions. For generally, this implies that the optical fields must be passed back and forth on an iteration by iteration basis, so that the delay can be an arbitrary length. Indeed, to model a multi-section laser requires that the delay be only a single-iteration.

This form of iteration forms the basis of transmission-line laser models, which split the laser cavity into longitudinal sections in order to represent the effects of spatial hole burning, including laser instabilities. Extending the ‘transmission lines’ (simply one-iteration bidirectional delays), beyond the laser cavity turns the laser model into a photonic circuit model, with many applications. However, passing samples bidirectionally implies that each model of each device is active at every iteration in order to process the samples passing through it, as shown in Fig. 1. This makes the computation task large, and also prevents efficiencies in processing data as blocks. Thus, for systems where the data can be assumed to travel in a single direction (using optical isolators, for example), it is more efficient to pass data in a single direction as blocks, representing a

time-sampled waveform. If the block represents the whole time period to be sampled, then it is only necessary to ‘fire’ each model once during a simulation.

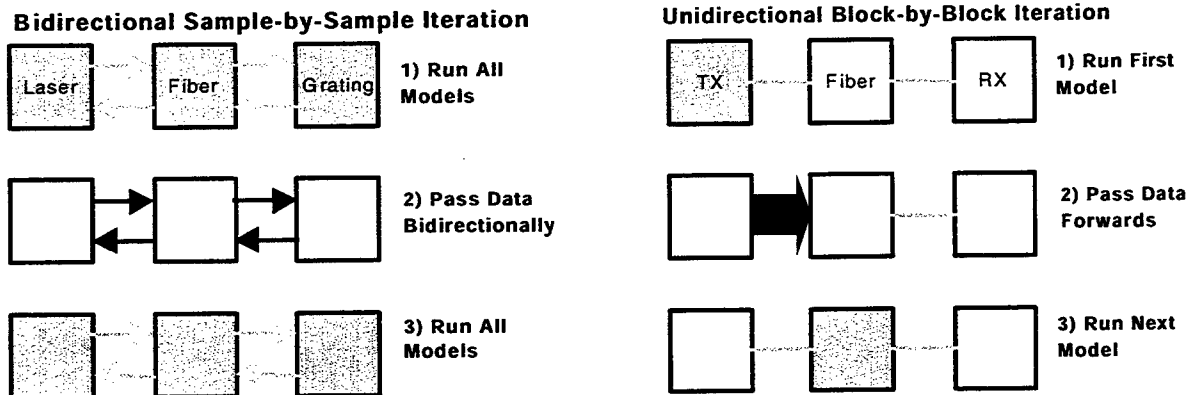


Figure 1: Sample-by-sample and block by block iteration schemes

Because of the interest in all-photonic networks, for example including photonic regeneration and switching, it is now necessary to simulate long-haul networks (with Blocks, for efficiency) which include photonic circuits (with Samples for full bidirectional interaction). We have therefore developed conversion tools between the two modes, and more importantly, a simulation environment that can support both modes simultaneously.

### Other Signal Formats for Block Mode

Early simulators have almost exclusively been based on modeling the ‘total field’ (*Single Frequency Band*) propagating throughout the system. This field is a vector sum of all modulated carriers, including noise sources, and thus requires a sample rate in excess of the total optical bandwidth of the signal and noise. However, this is not be efficient when:

- The spacing of carriers far exceeds their bandwidths when modulated
- The spectrum has groups of channels spaced apart by regions of no signal information
- The spectrum contains CW signals with no information content, such as pump sources in EDFAs.

	Signal Representation		Application Examples		
BLOCK MODE	Noise Bins	Broadband ASE Noise Saturation	Signal to Noise and Crosstalk Analysis		
	Parameterized Signals	Analytical Jitter (RZ-WDM)	EDFA Design		
	Multiple Frequency Bands	Self-Phase Modulation (SPM)	Network Design		
	Single Frequency Band	Four-Wave Mixing (FWM, XPM)	Detailed source and regenerator models (S) with long-haul transmission models (B)		
SAMPLE MODE	Active and Passive Photonic Component Design		Photonic Circuit Design and Evaluation		

Figure 2: Applications mapped onto signal formats.

For the above situations it is more efficient to adapt the simulator signal types to reflect the information content within each part of the spectrum. We have developed techniques to split a spectrum into *Multiple Signal Bands* (MFB), each represented by a sampled data series, and statistical measures of noise spectral density defined using *Noise Bins*, and of CW or RZ channels (*Parameterized Signals*), based on statistical measures of pulse width and jitter. Importantly, we have a series of conversion modules and routines that intelligently adapt the signal representations as the signals propagate through the simulation. For example:

- the spectral resolution of the Noise Bins will increase to maintain a specified amplitude accuracy as the signals pass through filters and amplifiers. Noise bins will be deleted if they are ‘empty’.
- the simulator will multiplex several single channels, represented by multiple sampled bands, into a single sampled band, on demand, or when the bands overlap.

### Mixed signal formats within a simulation

To handle the mixed signal formats, we have developed component modules (models) that will act appropriately on the signals provided by the previous module. Three examples of the mixed signal format are given in Fig. 3.

Arrows of different styles represent the different signal formats, as detailed in the Key of the figure. Modules will generally add new formats if required by the user (for example, put the noise of an EDFA into Noise Bins), and will delete formats if the energy within them falls below a certain level, for example if the pump is filtered out of the EDFA's output. Signal formats can also be merged (for example the noise in Noise Bins converted to random fields then added to the SFB format), for example, if the fiber models rely on total field to estimate four-wave mixing.

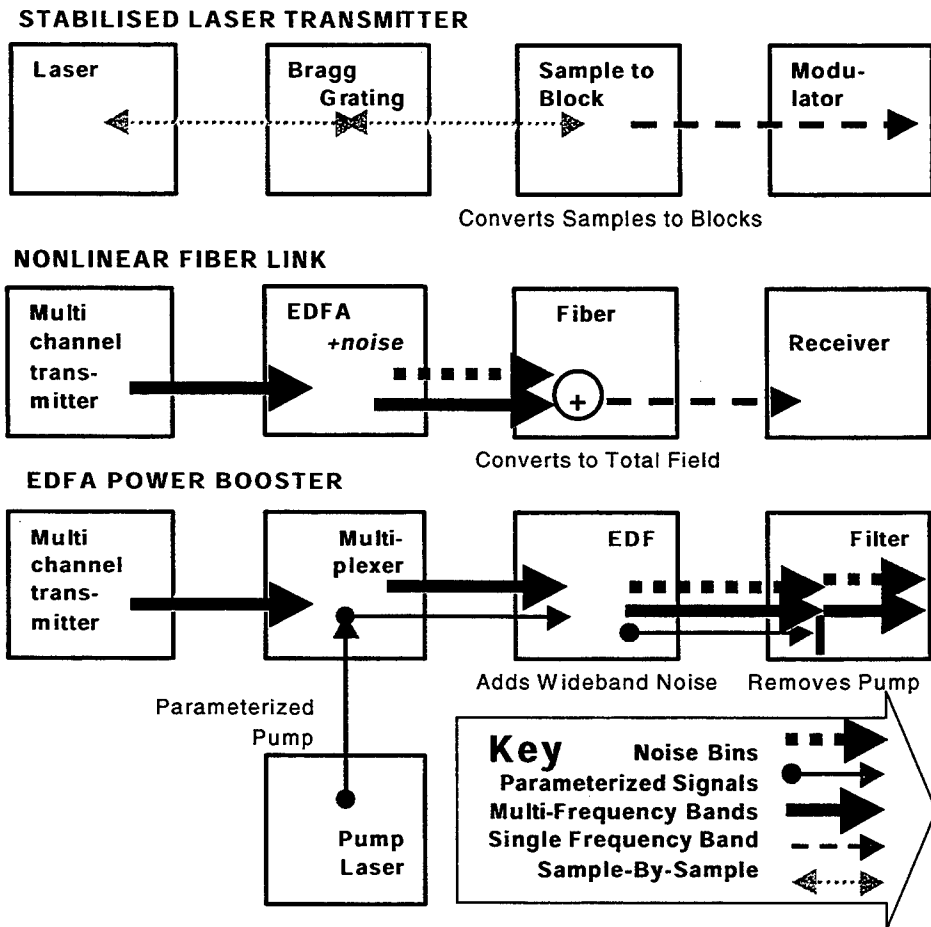


Figure 3: Flow of signal types through typical simulations showing creation and deletion of signal types.

### Conclusions

We have developed a photonic systems simulator that intelligently supports multiple signal formats. This gives the flexibility of previous simulators within one environment, and importantly, allows the most efficient signal representation to be used at each stage of the simulation. The simulator acts intelligently on the signal formats by adjusting bandwidths, spectral resolutions and merging or deleting bands. The models are able to process the signal formats, or convert them to a suitable form for processing. The formats are sufficiently general to allow for future developments in photonic simulation, and importantly, allow efficient simulation over many scales of size and complexity.

### References

- [1] A.J. Lowery, 'Computer-aided photonics design', IEEE Spectrum, vol. 34 (4), pp. 26-31, April 1997
- [2] A.J. Lowery and P.C.R. Gurney, 'Two simulators for photonic computer-aided design', Applied Optics, vol. 37 (26), pp. 6066-6077, September 1998
- [3] Formed in December 1998 by the merger of Virtual Photonics Pty Ltd (Australia) with BNeD GmbH (Germany) and BNeD Inc. (USA). [www.virtualphotonics.com](http://www.virtualphotonics.com)
- [4] M. Premaratne, A.J. Lowery and D. Novak, 'Modelling noise and modulation performance of fiber grating external cavity lasers', IEEE J. Sel. Areas of Quantum Electron., vol.3, pp.290-303, 1997

# Modeling of all optical functional devices for signal processing: 3R-Regenerators

Hans-Peter Nolting, Heinrich-Hertz-Institute Berlin GmbH

(4930) 31002 427 [nolting@hhi.de](mailto:nolting@hhi.de)

## MOTIVATION

Optical signal processing functions are required for implementing future all optical telecommunication networks. Around the world functions such as all optical switching 3R-regeneration, parity checking, wavelength conversion, add-drop multiplexing and header recognition have been demonstrated. Many novel functions have been shown using semiconductor optical amplifiers (SOA) solitary or integrated into interferometers. In this paper we will focus on wavelength conversion and full 3R signal regeneration based on optical clock recovery and clocked decision. For 3R-regeneration a novel device type is presented, which can be used for both clock recovery and for decision unit. It is a multi-section DFB laser, which is modulated by controlling the feedback from an external reflector in phase and amplitude. These components have demonstrated their performance in system experiments at 10 Gbit/s and devices for 40 Gbit/s are presently under investigation.

The switching effects are based on photon-electron interaction in the active layer of the DFB lasers, which will dynamically change the longitudinal carrier and optical field distributions. Often used theoretical approaches are working with a space dependent dynamic equation for the complex field amplitudes (forward and backward travelling) or by using a lumped rate equation for the scalar field energy. Existing dynamic models are based, for example, on the solution of the dynamic coupled wave equation using transfer-matrix method<sup>1,2</sup>, on the transmission-line method<sup>3</sup>, on the power-matrix method<sup>4</sup> or on a single-mode approximation of travelling wave equations<sup>5</sup>. All methods should be equivalent and should yield similar results. They are well suited for understanding the basic effects and making device optimisation. However, for more complex device structures to build enhanced optical circuits a modular working technique able to handle bidirectional propagation is necessary. OPALS (Optoelectronic Photonic, and Advanced Laser Simulator) a commercial available simulation tool offers this possibility. It is basically a bidirectional transmission-line model, thus offering the possibility to model complex laser structures composed of different DFB laser and amplifier sections, passive waveguide sections, couplers, phase shifters and attenuators (see Fig. 1 to 3). Furthermore, complete subsystems like a wavelength converter (see Fig. 3) or a 3R-regenerator (see Fig. 2) and signal transmission on a fibre can be modeled by linking individual components (icons) to a circuit (Fig. 1c). Similar as in electronics, where modeling on technology, physical device, circuit and system level is well known, this tool closes the gap between device, circuit and system level for all optical signal processing. These aspects will be demonstrated with selected examples.

## RESULTS

*Clock recovery.* The optimisation of self-pulsations in three generations of a multi-section DFB laser is shown in Fig. 1: (a) simple 2 section DFB laser with only small parameter range of self-oscillation as is described in [5], (b) three section DFB laser with phase shifter for mode selection and wavelength offset between Bragg and DFB section, leading to large parameter range of self-oscillation, and (c) future device composed of tapered Bragg grating (suppressing unwanted oscillation regions), phase shifter, amplitude control by attenuator and wavelength shifted DFB section. The tapered Bragg grating leads to mainly two very large parameter ranges for self pulsation on both slopes of the reflectivity curve (grey shadowed in Fig. 1d). In contrast simple configurations with uniform gratings show a variety of additional pulsating effects. Modeling with OPALS and with a transfer matrix method<sup>6</sup> similar to [2] show, that - in contrast to earlier results - the self oscillation is present for both signs of the slope<sup>7</sup>. It will be shown, that the small

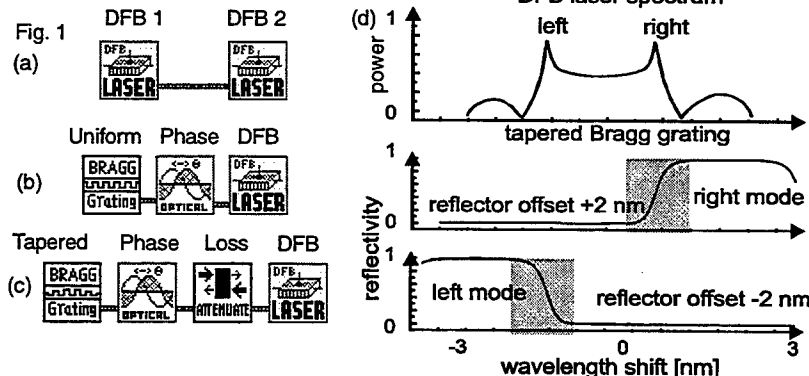


Fig. 1 Evolution of clock recovery: a) 2 section DFB laser, b) uniform Bragg grating + phase shifter + DFB section with wavelength offset c) tapered Bragg grating + phase shifter + attenuator + special DFB section with wavelength offset, d) grey shadowed regions indicate position of Bragg reflector offset with good selfoscillation (mono mode, high extinction ratio, no higher harmonics)

matched feedback from the reflector section is present. The dispersive reflector has to be long to obtain a step-like profile of the dispersive reflectivity. Switching up to 20 Gbit/s has been modelled using the same laser structure as for the clock extraction described above.

**3R-signal regeneration.** A full 3R signal regeneration scheme consists of Reamplification, Retiming, and Reshaping of the signals. The functional blocks for achieving such a regeneration are optical amplifier, optical clock recovery, and clocked decision. Fig. 2 shows the setup of a 3R-regenerator based on Q-switching lasers. To prove the functionality a complete system has to be modeled, starting with the data generation (Tx) at 20 Gbit/s and a wavelength of 1540 nm. This data stream is splitted. One part is injected into the clock recovery circuit via a circulator. The clock recovery is an optical oscillator, which locks in frequency and phase to the injected optical data signals. The output of the clock at a wavelength of 1548 nm is a continuous stream of optical pulses, stable in amplitude and time interval, and synchronised to the data stream. Both the clock and the data signal are injected into the decision element. For proper function the data wavelength has to be suppressed on the clock arm and clock and data signal have to be adjusted by a delay and an attenuator in time and amplitude. The decision element works as a mono flop, generating one pulse if the sum of both signals exceed a certain threshold level. The pulse shape depends mainly on the decision element. All signals have to be controlled in

signal 3 dB frequency limit is extended from 10 to 30 GHz due to the detuned loading of the Q-switched laser. Self-oscillation and locking to a data stream have been modeled for a bitrate up to 30 GHz.

**Decision element.** A decision element based on Q-switching multi section DFB-lasers has been investigated at our laboratory. One can design these lasers as optical oscillators or as mono flops. For decision the laser section has to be short, so that at a high pumping level lasing is achieved only if a phase

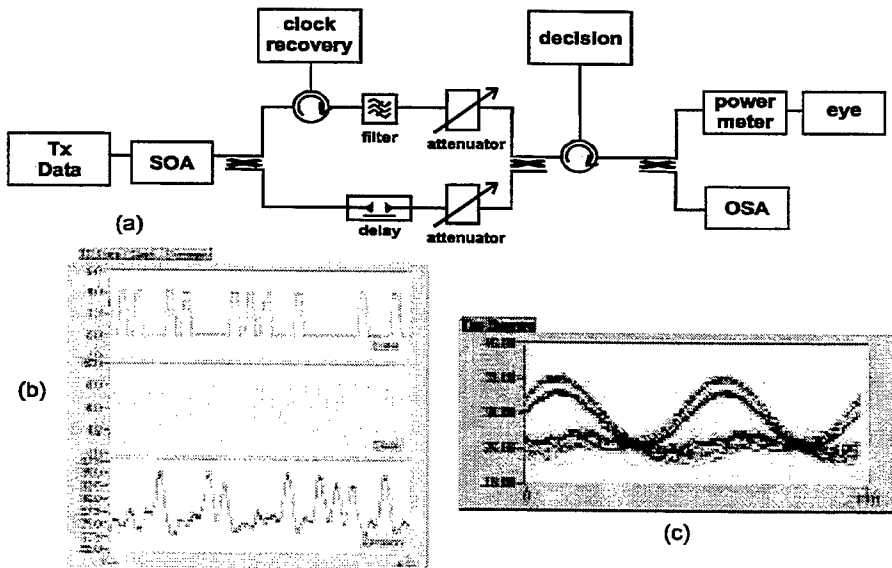


Fig. 2: 3R-regenerator composed of clock recovery and decision unit at 20 Gbit/s a) setup for modelling, b) Data signal in, clock signal and decision out, c) eye diagram

wavelength, bitrate, amplitude and time. Proper function is shown by the time domain signals (data in, extracted clock and decision output in Fig. 2) and the open eye diagram. An open eye with a good Q-factor demonstrates the feasibility of the concept. The experimental verification will be done in the near future.

*Wavelength converter / switching gate.* A wavelength converter consists of a pair of SOAs in a Mach-Zehnder interferometer (Fig. 3). Each optical amplifier has its own additional control input. CW light is injected into the MZ-interferometer and splits into both arms. Data signal(s) coupled to one or both SOAs switch the interferometer by introducing a phase shift due to gain saturation in the amplifier stage(s). Thus the CW light is switched. This can be used as wavelength conversion or as a fast switching gate. Again proper function is proved by the Q-factor of the eye diagram. (Fig. 3b). In a system experiment this fast gate switch has been combined with the clock recovery module based on Q-switched lasers.

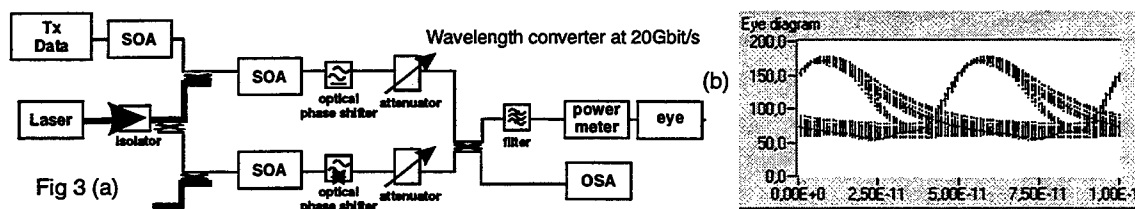


Fig. 3) Wavelength Converter (a) Setup and (b) eye diagram at 20 Gbit/s

## SUMMARY

Modeling allows to optimise the device itself, i. e. Bragg grating shape, length and coupling strength, special laser parameters like modulation bandwidth and threshold current. For special applications optimum operation parameters can be found. Further linking, control and operation of different devices as a subsystem can be studied using OPALS simulation tool. We have found excellent correspondence of our simulation results with our experiments and other laser models.

## ACKNOWLEDGEMENT

I thank B. Sartorius, C. Weinert, O. Brox, H.-J. Wünsche, U. Bandelow, M. Radziunas for fruitful discussions and M. Gravert for assisting in modeling.

<sup>1</sup> M. G. Davies, R. F. O'Dowd, "A new large-signal dynamic model for multielectrode DFB lasers based on the transfer matrix method", IEEE Phot. Techn. Lett., vol.4, pp. 838-840, 1992

<sup>2</sup> D. Marcenac, "Fundamentals of laser modeling", Doctoral dissertation, St. Catherine's College, University of Cambridge, 1993

<sup>3</sup> A. Lowery, A. Keating and C. P. Murtonen, "Modeling the static and dynamic behaviour of quarter-wave shifted DFB lasers", IEEE J. Quantum Electron., vol. 28, pp. 1874-1833, 1992

<sup>4</sup> L. M. Zhang, J. E. Carroll, "Large-signal dynamic model of DFB laser", IEEE J. Quantum Electron., vol. 28, pp. 604-611, 1992

<sup>5</sup> U. Bandelow, H. J. Wünsche, B. Sartorius, M. Möhrle, "Dispersive Self-Q-switching in DFB lasers - Theory versus Experiment", IEEE J. Selected Topics in quantum Electronics, vol. 3, No. 2, pp. 270-278, 1997

<sup>6</sup> M. Radziunas, H.-J. Wünsche, B. Sartorius, H.-P. Nolting, K. Schneider, O. Brox, D. Hoffmann, "Modelling of new grating designs for self-pulsating DFB lasers", submitted to IPR 99

<sup>7</sup> O. Kjebon, R. Schatz, S. Lourdudoss, S. Nisson, B. Stalnacke, L. Bäckbom, "30 GHz Direct Modulation Bandwidth in Detuned Loaded InGaAsP DBR-Lasers at 1.55 um Wavelength", Electron. Lett., vol. 33, no. 6, pp.488-489, 1997

## Modeling of new grating designs for self-pulsating DFB lasers

M. Radziunas<sup>a,b</sup>, H.-J. Wünsche<sup>a</sup>, B. Sartorius<sup>c</sup>, H.-P. Nolting<sup>c</sup>  
 K. Schneider<sup>b</sup>, O. Brox<sup>c</sup>, D. Hoffmann<sup>c</sup>

<sup>a</sup> Institut für Physik der Humboldt-Universität zu Berlin, Invalidenstr. 110, D-10115 Berlin, Germany,

Phone: +49 30 20937649, Fax: +49 30 20937886, email: ede@physik.hu-berlin.de

<sup>b</sup> Weierstraß-Institut für Angewandte Analysis und Stochastik Berlin, Mohrenstr. 39, D-10117 Berlin, Germany

<sup>c</sup> Heinrich-Hertz-Institut für Nachrichtentechnik Berlin, Einsteinufer 37, D-10587 Berlin, Germany

**Introduction:** Multisection DFB lasers showing high-speed self-pulsations (SP) have opened a new field for the optical clock recovery at high bit rates. The basic effect was discovered in 1992 with 2-section devices [1]. Since then, optimization of the devices led to much improvement and the system capability has been demonstrated [2]. The present generation of devices is AR-coated and consists of two DFB sections and one phase section integrated in between (Fig. 1). The two DFB sections are basically identical, only lengths and pump levels are different. The longer one is pumped highly and provides the gain for lasing. The shorter DFB section is driven close to its gain transparency and acts as a dispersive reflector. The center section has neither an  $1.55\mu\text{m}$  active layer nor a grating and serves as a passive phase tuning section.

Devices of this type have not been modeled yet. Our former modeling was based on a single mode approximation and considered devices with the gain section in the center and a reflecting facet adjacent to the phase section [3, 4]. In this paper we describe an improved model that properly takes into account all relevant modes and allows to treat a wider range of operation. Second, it is demonstrated that this model describes well and in good correspondence with the experiments the main features of the new device generation. Third, the model is used for further optimisation of the device structure by individually designing the two DFB-corrugations.

**Mathematical model:** The slowly varying amplitudes  $\Psi^\pm(z, t)$  of forward and backward travelling waves are obtained by numerically solving the travelling wave equations

$$v_{\text{group}}^{-1} \partial_t \Psi^\pm \pm \partial_z \Psi^\pm = -i\beta \Psi^\pm - i\kappa^\mp \Psi^\mp, \quad (1)$$

together with the rate equation for the carrier density in the gain section,

$$\frac{d}{dt} N = \frac{I_g}{eV_g} - (AN + BN^2 + CN^3) - g'(N - N_{tr}) \left\langle |\Psi^+|^2 + |\Psi^-|^2 \right\rangle_g. \quad (2)$$

Here  $\langle \dots \rangle_g$  denotes averaging over the gain section. Other symbols have their usual meaning, the indexes  $g, p, r$  label the section they belong to. No coupling of carriers to the field appears for the phase and reflector sections because they are passive or at transparency, respectively. The relative propagation parameters  $\beta$  are treated as spatially constant within each section. In the reflector section (kept at transparency), only the optical losses contribute,  $\beta_r = -i\alpha_r/2$ . A static detuning  $\delta$  as well as the carrier induced detuning and gain terms appear additionally in the gain section,  $\beta_g = \delta - i\alpha_g/2 + (\alpha_H + i)g' [N - N_{tr}]/2$ . For the phase tuning section we use  $\beta_p = -\varphi/2L_p - i\alpha_p/2$  with the variable phase angle  $\varphi$ . The parameter values of [4] are used except  $\alpha_p = 20 \text{ cm}^{-1}$ ,  $A = 3 \times 10^8 \text{ s}^{-1}$ ,  $B = 10^{-10} \text{ cm}^3/\text{s}$ ,  $C = 10^{-28} \text{ cm}^6/\text{s}$ .

**Evaluation of the model:** We have checked the validity of the new model by comparing

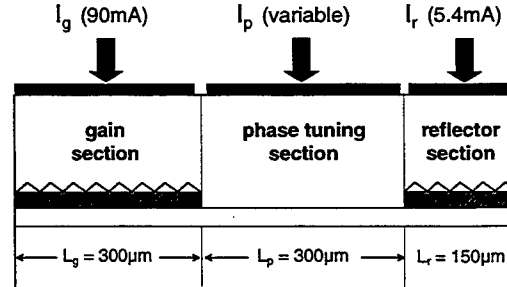
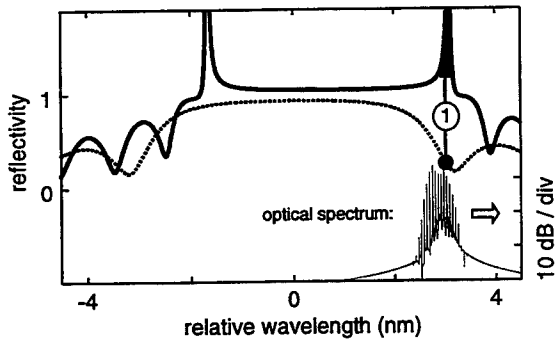
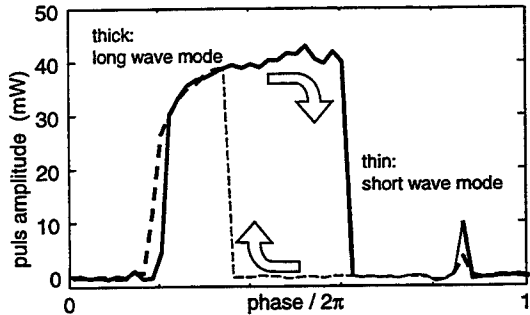


Figure 1: Scheme of a typical device.



**Figure 2:** Reflectivity spectra of the gain section (solid) and the reflector section (dashed) for one moment of a SP. Thin: calculated optical spectrum.



**Figure 3:** Amplitude of the SP calculated for increasing (solid) and decreasing (dashed) phase angle. Thick: long wave mode lasing as ① in Fig. 2, thin: short wave mode lasing.

with measured features of the present device generation as well as with Marcenac's model [5]. SP have been obtained for the same conditions as in the experiment. First, a typical *spectral correlation* is required: the lasing resonance of the gain section has to coincide with the negative reflectivity slope of the reflector section (Fig. 2). The combination of electronic blue and thermal redshift with increasing current allows to adjust to such a position [3]. Second, the SP are switched on and off by *phase current tuning* (Fig. 3).

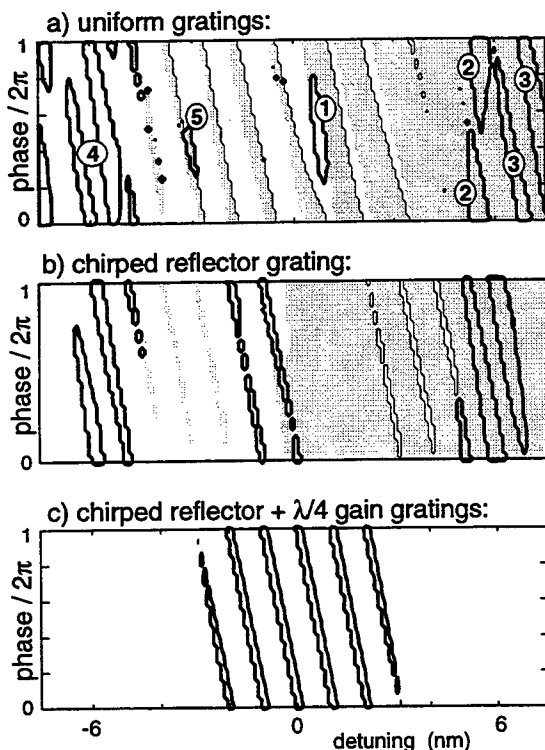


**Figure 4:** Thick: areas of SP in the  $\delta - \varphi$  plane for differently styled DFB gratings. Grey background: short wave mode lasing. White background: long wave mode lasing.

tained are drawn in Fig. 4a as islands with thick black borders. Island ① in the center belongs to the spectral correlation of Fig. 2 and can be addressed by the thermal  $\lambda$ -shift in the present generation of devices discussed above. For larger detunings, several new SP islands appear (note that islands touching the border  $\varphi = 2\pi$  continue at  $\varphi = 0$  and vice versa, due to the

A distinct hysteresis appears at one side of the SP region. In this range, either mode of the gain section may carry the lasing power. The long wave mode shows SP, whereas the short wave mode is stationary. Hysteresis and mode jumps have been observed in the experiments, too, but they appeared less pronounced. We attribute this small difference to neglecting the gain dispersion in the model. The calculated SP frequencies are in the 10 GHz range and depend on the gain current and the phase angle as in the experiments. Summarizing so far, our new model describes well the main features of the self pulsating devices with the reflector section at gain transparency.

**Device optimisation by grating design:** First, we investigated devices with *detuned gratings*, i.e., with different corrugation periods for the gain and reflector sections. The according detuning parameter  $\delta$  of the model has been varied over a 15 nm wide range with steps of 0.1 nm. For every  $\delta$ , the phase angle  $\varphi$  was tuned upwards from 0 to  $2\pi$  in 50 equidistant steps. The SP-regions ob-

phase periodicity). The reflectivity spectra drawn in Fig. 5 for the islands ② to ⑤ show that they belong to other possible combinations of one of the two lasing modes with a negative slope of one of the different lobes of the reflector spectrum. Being larger and less sensitive to mode jumps, these islands are improved compared to island ①. Using first devices with detuned gratings, we could experimentally verify the existence of SP for large detuning.

In a next step, we introduced a tapered grating  $\kappa = \kappa_0 \cos^2(\pi z/L_r)$  in the reflector section ( $z = 0$ : center of the section). This suppresses considerably the side lobes of its reflectivity. As a consequence, all SP islands connected with side lobes disappear (Fig. 4b). The former central island ① reappears a bit short wave shifted in a wider tuning range due to the smaller and smoother stop band of the tapered reflector. The island around 6 nm is the most prominent one. It is a coalescence of the former islands ② and ③, resulting in a much wider continuous tuning range. The sensitivity to mode jumps is not further reduced as indicated by the continuation of the SP islands into mode jump islands. Surprisingly, an additional SP island is situated around -6 nm. Here, the right mode lases on the positive slope of the reflectors stop band. This exception from our usual picture of dispersive self-Q switching [3] was also observed with the simulation tool OPALS [6] and is still under investigation.

Finally, we additionally introduced a quarterwave shift into the gain section. As expected, there is no mode jump in the whole area of calculation. Furthermore, a single distinct SP island appears (Fig. 4c) with SP frequencies also in the 10 GHz range. This island covers an about 6 nm wide region in the center of the tuning range, which seems very useful for the device functionality. The detailed nature of these SP as well as their dependence on parameters have to be further investigated.

**Conclusion:** High-speed self-pulsations can be generated with rather different grating designs. The following possible improvements of the present generation of devices were found: Detuned gratings lead to broader SP regions with less tendency to mode switching. A tapered reflector grating reduces the variety of SP regions to few well pronounced areas. One single extended SP area without mode hopping can be obtained by additionally introducing a quarterwave shift into the gain section.

**Acknowledgement:** We thank D. D. Marcenac to let us have his computer code [5].

## References

- [1] M. Möhrle, U. Feiste, J. Höller, R. Molt, and B. Sartorius, "Gigahertz self-pulsations in 1.5  $\mu\text{m}$  wavelength multisection DFB lasers," *IEEE Photon. Technol. Lett.* **4**, pp. 976-979, 1992.
- [2] B. Sartorius, C. Bornholdt, O. Brox, H. J. Ehrke, D. Hoffmann, R. Ludwig, and M. Möhrle, "All-optical clock recovery module based on a self-pulsating DFB laser," *Electron. Letters* **34**, pp. 1664-65, 1998.
- [3] B. Sartorius, M. Möhrle, S. Reichenbacher, H. Preier, U. Bandelow, and H.J. Wünsche, "Dispersive self Q-switching in self-pulsating DFB lasers", *IEEE Journ. of Quantum Electronics* **33**, pp. 211-18, 1997.
- [4] U. Bandelow, H.J. Wünsche, B. Sartorius and M. Möhrle "Dispersive Self-Q-Switching in DFB Lasers – Theory Versus Experiment", *IEEE J. Selected Topics in Quantum Electronics* **3**, pp. 270-278, 1997.
- [5] D. D. Marcenac, "Fundamentals of laser modelling", *Dissertation, St. Catharine's College, University of Cambridge*, 1993; D. D. Marcenac and J. E. Carroll, "Distinction between multimoded and singlemode self-pulsations in DFB lasers," *Electron. Lett.* **30**, pp. 1137-1138, 1994.
- [6] H.-P. Nolting, "Modeling of all optical functional devices for signal processing: 3R-regenerators", invited to IPR 99.

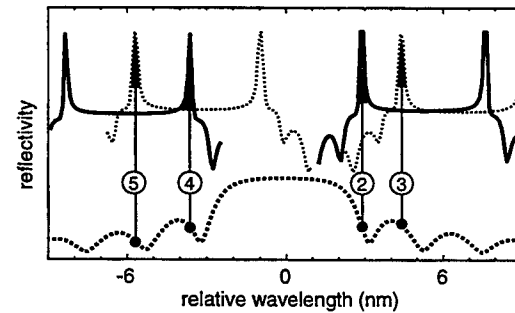


*Figure 5: Spectral correlations for some prominent SP islands of Fig. 4a.*

# Modeling of Lasers with Wavelength dependent Feedback

P. C. Koh, R. G. S. Plumb

University of Cambridge, Department of Engineering, Trumpington St., Cambridge CB2 1PZ, UK.

[pck20@eng.cam.ac.uk](mailto:pck20@eng.cam.ac.uk), [rgsp@eng.cam.ac.uk](mailto:rgsp@eng.cam.ac.uk)

## Introduction

Lasers operating under optical feedback conditions have found widespread applications in various configurations. Some well-known advantages of optical feedback are: narrowing of radiation linewidth, chirp reduction and tuning ability. In addition, external cavity lasers have been directly modulated to generate high efficiency microwave and millimeter-wave modulated light for applications such as optical feeds[1]. More recently, various schemes using external feedback have been used to provide either multi-frequency sources[2] or fixed wavelength sources (using fiber grating) suitable for WDM applications. In these systems, frequency selective elements are employed and are coupled to the gain medium by an AR coating on one of the laser facets.

The steady-state and axial mode stability behaviors of external lasers in the presence of optical feedback have been extensively studied. Interference effects of optical waves due to residual reflections at the coupling facet were first analyzed[3] by adding a time-delayed, external feedback term to the standard electric field rate equation. This method, though effective in predicting the steady-state condition and the criteria for dynamic stability of the system, is only applicable for weak feedback levels. With strong feedback, multiple reflections of the electric fields at the coupling facet must be included[4]. The improved rate equation is effective in predicting the steady-state behavior of the external cavity laser[4][5] and more importantly, it gives the stability condition in terms of parameters like feedback level and residual facet reflectivity. Inspite of its usefulness, there are a few areas in which the above approach is found to be lacking. Firstly, it does not allow full modeling of the laser cavity modes. Secondly, frequency dependent feedback cannot be included with ease. Overcoming these difficulties would require multiple rate equations in which additional parameters like cross-gain and external filter gain detuning for each mode must be determined.

This paper presents a numerical method which overcomes the above-mentioned shortcomings and allows prediction of the dynamic and steady-state characteristics of a laser diode, in the presence of wavelength dependent optical feedback. This method also allows the inclusion of any additional reflections within the extended laser cavity. In order to demonstrate the capability of our approach, a reflection-grating tunable semiconductor laser was simulated and the numerical predictions were compared with experimental measurements.

## Simulation Method

A time-domain method (TDM) was chosen because of its ability to simultaneously simulate all the modes travelling within the laser cavity. In TDM, the laser cavity is divided into N uniform sections with the forward and reverse propagating electric field values stored between sections. A digital filter is used to represent the effects of material gain curve, and a pseudo random number generator is used to add in the "spontaneous emission" from each section. Finally, effects of the linewidth broadening factor,  $\alpha_H$ , are included by making the phase change of the electric fields at each section proportional to the gain in that section[6].

The reflection spectrum of the grating operating in first order Littrow configuration is given by:

$$R(f) = R(f_o) \exp\left\{-2\left(\frac{\Delta f}{c/\pi l_s}\right)^2\right\} \quad (1)$$

where  $l_g = 2w_g \tan \theta$  is the illumination depth,  $f_o$  is the tuned frequency and  $\Delta f$  is the detuning from  $f_o$ . The wavelength dependent feedback of the grating was modeled in the time domain using a digital filter with

a frequency response identical to the reflection spectrum of (1). The filtered electric fields were then feedback into the gain medium as shown in Figure 2. A Finite Impulse Response (FIR) filter design method was employed to obtain the impulse response used in this simulation. This allowed precise simulations of external cavity modes spacing, which is critical in predicting the Side-Mode Suppression Ratio (SMSR) and tuning characteristics of the laser. The spectrum of the laser was obtained by performing Fast Fourier Transform on the fields emerging from the output facet of the laser.

### Experimental Setup

The experimental setup is shown below. It consists of a large-spot amplifier ( $R_{\text{output}} = 0.32$ ,  $R_{\text{coupling}} = 5 \times 10^{-5}$ ), a collimating lens ( $f = 6.5\text{mm}$ ) and a 1200grooves/mm reflection grating. A tapered fiber connected to an optical isolator was used to couple our laser output to the lightwave converter. SMSR of the laser radiation was measured using the RF spectrum analyzer and the optical power meter. The combination of the piezo-electric actuator and the off-axis pivot provides quasi phase-continuous tuning which allowed the onset of multi-moded oscillations to be determined.

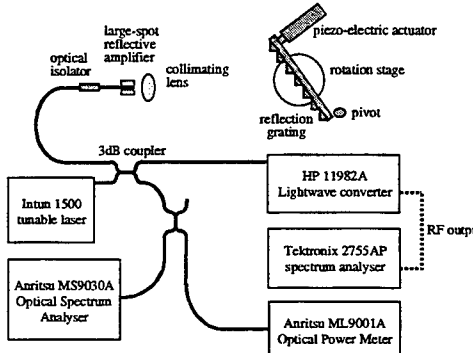


Figure 1. Experimental setup to verify the numerical predictions.

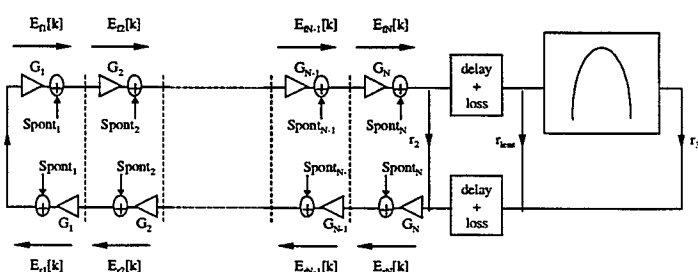


Figure 2. TDM modeling schematic.

### Results and Discussions

The tuning characteristics of our laser were investigated by combining its output with the Intun laser, which was used as a reference. From the RF beat spectrum, our laser was observed to have regions of stable and unstable oscillations. The stable regions have single longitudinal mode oscillations with measured SMSR of  $48 \pm 7\text{dB}$  while the unstable regions have simultaneous oscillations of several cavity modes. Given the limited RF bandwidth of our equipment, no attempts were made to measure the mode profile of individual modes when the output was multi-moded, only the boundaries were identified. It has been found that stable longitudinal oscillations (SMSR>30dB) occur at an *average* frequency spacing of 5.65GHz.

Given the low coupling facet reflectivity and narrow reflection spectrum of the grating (FWHM ~16GHz), the presence of instability regions during tuning was unexpected. Nonetheless, when the reflections at the lens surface was included ( $r_{\text{lens}} = 1 \times 10^{-4}$ ), there was good agreement between our numerical predictions and the experimental measurements, which are plotted in Figure 3. This demonstrates the importance of the inclusion of residual reflections within the laser cavity in predicting stability and frequency-tuning characteristics. The frequency spacing of stable regions shown in Figure 3 are not constant (single mode oscillations at average of 5.5GHz), and this also is consistent with experimental measurements. Finally, Figure 4 shows the microwave spectrum of the RF beat signal at the onset of multi-mode oscillation, while Figure 6 displays the spectrum of our numerical predictions.

A typical simulated output spectrum is plotted in Figure 5. The lasing mode does not coincide with the filter peak. This is due to beating of the electron density at a frequency equal to the cavity mode spacing;

which results in gain suppression for higher frequency modes, and gain enhancement for lower frequency modes[7]. Assuming that the spectrum is Lorentzian, the linewidth can be estimated at ~400kHz. This compares roughly with the measured value of 100kHz (Anritsu MS9602A).

### Conclusion

We present in this paper, a numerical method that allows full modeling of all the cavity modes of a compound cavity laser. This method allows predictions of the characteristics of these lasers in the presence of wavelength dependent feedback as long as the frequency response of the external filter is known. The numerical predictions made using our approach have been shown to agree well with experimental measurements for our tunable grating laser.

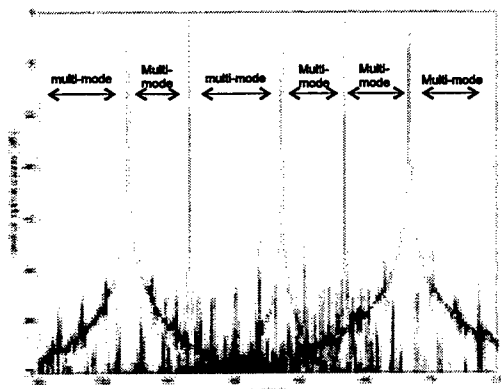


Figure 3. Simulated output spectrum when detuned from  $\lambda = 1.55\mu\text{m}$ .

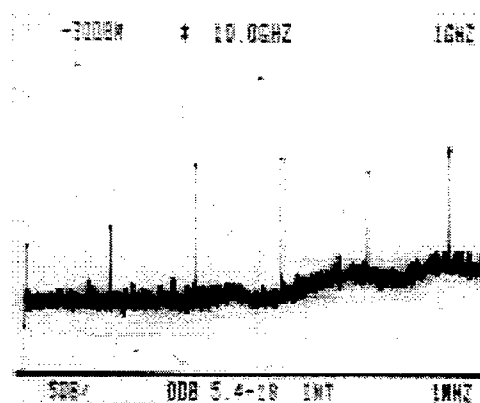


Figure 4. RF beat spectrum indicating onset of multi-mode oscillations.

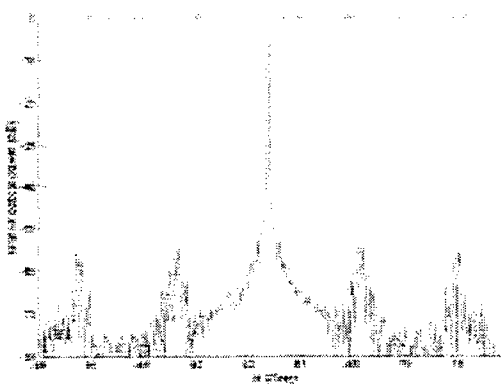


Figure 5. Single mode output spectrum with SMSR~50dB.

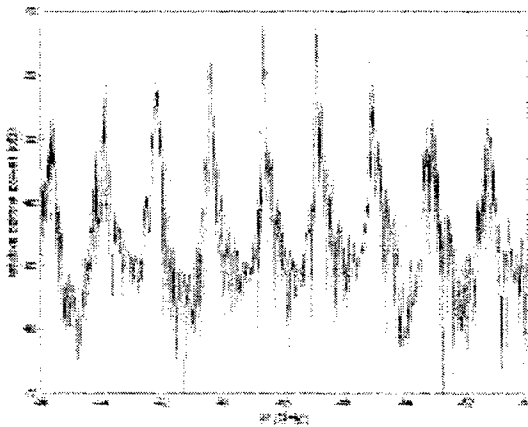


Figure 6. Spectrum of laser output when grating is tuned to unstable regions.

<sup>1</sup> R. Nagarajan., *IEEE Photon. Technol. Lett.*, vol. 5, pp. 4-6, 1993.

<sup>2</sup> K. Lee, *IEEE J. Quantum Electron.*, QE-33, pp.1832-1838, 1997.

<sup>3</sup> R. Lang, *IEEE J. Quantum Electron.*, QE-16, pp. 347-355, 1980.

<sup>4</sup> R-Q Hui, *IEEE J. Quantum Electron.*, QE-25, pp. 1580-1584, 1989.

<sup>5</sup> P. Zorabedian, *IEEE J. Quantum Electron.*, QE-30, pp. 1542-1552, 1994.

<sup>6</sup> J. Carrol, J. Whiteaway and D. Plumb, *Distributed feedback semiconductor lasers*, The Institution of Electrical Engineers, London, U. K., 1998.

<sup>7</sup> A. P. Bogatov, *IEEE J. Quantum Electron.*, QE-11, pp. 510-515, 1975.



**Integrated Photonics Research**

# **Integrated Devices**

**Wednesday, July 21, 1999**

**T. R. Ranganath, Hewlett-Packard Laboratories, USA**  
Presider

**RWD**  
**10:45am–12:15pm**  
Anacapa

## Uncooled and low cost plastic package for high bit rate applications.

Jean-Louis Nicque

Alcatel Optronics, Route de Villejust, F-91625 Nozay, France

Tel : +33 (0) 1 64 49 47 62 Fax : +33 (0) 1 64 49 49 70 e-mail : Jean-Louis.Nicque@alcatel.fr

### Introduction :

Telecommunications is an exponentially growing market for long distance transmission, metropolitan links and local access services. Optical links are now extensively used in telecommunication systems and manufacturers are developing new generations of optical devices for integration in both transport systems and in local area networks. In the following we are first going to define the market environment for optical devices and the technological trends. Then we will focus on Alcatel's new generation of novel products. We will give results obtained on our first uncooled plastic module for SDH/SONET applications.

### Market trends :

Long distance transmission requires more and more capacity due to explosive growth in the worldwide use of Internet<sup>1</sup> (+400% per year) and online services (video on demand, e-commerce, video conferencing). Key requirements for optical components are: more capacity, more integration and cheaper solutions. To increase capacity, DWDM at high bit rates is now widely used. Integration is achieved by increasing the number of optical ports (+23% in 2.5Gbits line per year), by reducing size of components (1/4 per year) and by integrating optical functions (multiplexing with amplification).

Extension of the optical network to the home is still poorly developed, however ambitious projects show high investment efforts in FTTH in the coming years. For example the Japanese optical network extension programs show installation of 10Mkm optical lines installed in 2000 and use of millions of 155Mbps Optical Network Units (ONU) in the next coming years<sup>2</sup>. Here also new requirements for optical devices appear. Integration of passive functions with active devices is needed. For example, wavelength multiplexing must be integrated within the same "black-box" as electronics and opto-electronic devices. In these type of applications, cost/performance factors are still prohibitive (three times more in optical components and installation than current copper solutions<sup>1</sup>). Therefore price reduction in opto-electronic devices is compulsory to challenge conventional solutions. In addition, major improvements in the use and handling of the components must be considered in the technical solutions without limiting the data rate of the products.

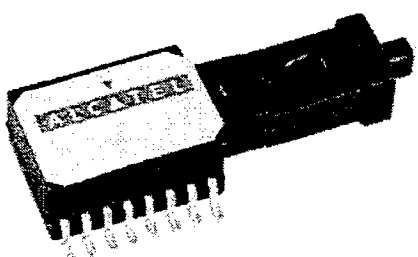


Figure 1 SMT optical device with detachable pigtail

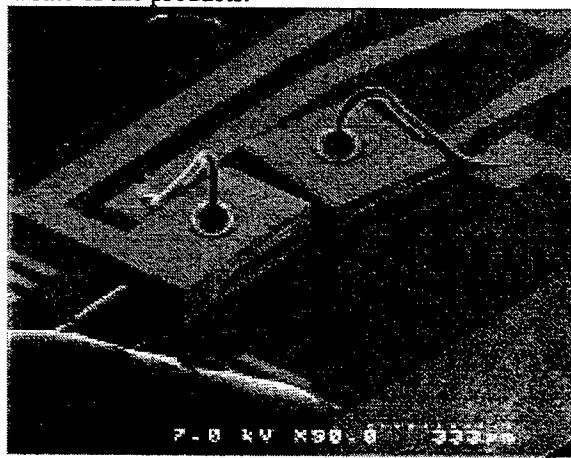


Figure 2 SSLaser and edge illuminated PIN diode on Si submount with passively coupled SMF.

### Technology trends :

Alcatel Optronics and other major telecommunication equipment manufacturers, now use new to increase transmission capacities, to integrate more functions and to reduce costs.<sup>3, 4, 5</sup>

Capacity increase is made by providing higher bit rates; 2.5Gbits/s is becoming a standard bit rate not only in long haul and DWDM applications but also in intra-office applications. Integration of active devices (laser detectors, amplifiers) with passive optical functions is now ready in research centers<sup>6</sup> and universities and can be used in volume manufacturing. Cost reduction that happened years ago in high volume manufacturing and handling of electronics devices is now hitting the opto-electronics field. Until now, most of opto-electronic devices had to be mounted one-by-one on electronic boards because package concepts were incompatible with standard electronics methods. Technology is now ready to manufacture optical surface mounted devices in the

same way as for electronics surface mounted devices (see Figure 1). The need for low profile module for high bit rate applications is driven not only by market but also by the technological evolution of all electronics and opto-electronics world.

Alcatel Optronics chose to develop as a first product to enter this new world an un-cooled and low-cost plastic module for high bit rate applications. This first product will be a starting point to drive a revolutionary technology change in opto-electronic devices. Technology solutions will lead to reduced costs, make the devices easy to use and make it possible to integrate active and passive function into a single product.<sup>7</sup>

#### **Technical solutions :**

Integration and manufacturing cost reduction is achieved through new mechanical approach to handling laser and detector diodes and fibers called "planar Si technology". It uses new types of lasers that integrate spot size converters, detector devices of new generation, and revolutionary package and fiber pigtail concepts.

**Spot-Size Laser :** One of the main cost issues in manufacturing opto-electronic devices comes from the active coupling of a fiber to a laser. Until now, laser dies had beam divergence significantly higher than single mode fibers therefore coupling efficiencies were limited and alignment tolerances were low. As an example, with standard 1.3 $\mu$ m or 1.5 $\mu$ m FP or DFB lasers the coupling efficiency with a standard cleaved SM fiber is about -8 dB with a tolerance of +/-0.5 $\mu$ m for 1 dB loss. New designs of laser die that integrate a "taper" section<sup>8</sup> reduce the beam divergence from 25° to 15° and the coupling efficiency with a standard fiber is -3 dB with a tolerance of +/-1.7 $\mu$ m for 1 dB loss.

Alcatel Optronics uses such lasers in all its new products, and therefore can use passive alignment techniques instead of time consuming and costly active alignments. The internal structure of the laser benefits from years of Alcatel research and manufacturing in this field, the structures are now optimized to achieve up to 2.5Gbits/s transmission capabilities from -40°C to 85°C without the use of a thermoelectric cooler. Figure 3 shows the bit error results of 1.3 $\mu$ m FP lasers at 25°C and 85°C at 2.5Gbits/s. Mean power is 1.5mW, extinction ration is 12dB with -24dB return loss. These results fit the ITU standard requirements for intra-office high bit rate applications.

**Edge illuminated PIN diode :** Until now only surface illuminated diodes were used as monitor diodes behind laser dies. This type of diodes required special mechanical mounting and unitary handling very different from the laser. In the case of edge illuminated diode, mounting and handling can be achieved with the same mechanical references as lasers and with similar equipment. Therefore, cost reduction in manufacturing can be achieved by reducing the mechanical parts in laser modules and by optimizing mounting procedures. (Figure 2)

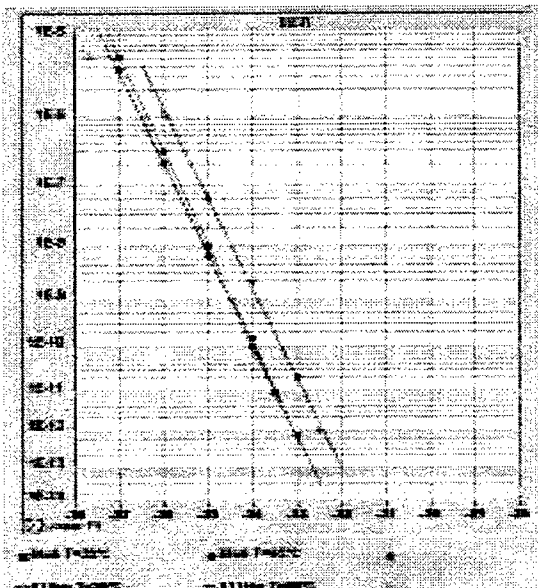


Figure 3 BER results at 2.5Gbits/s at 25°C and 85°C

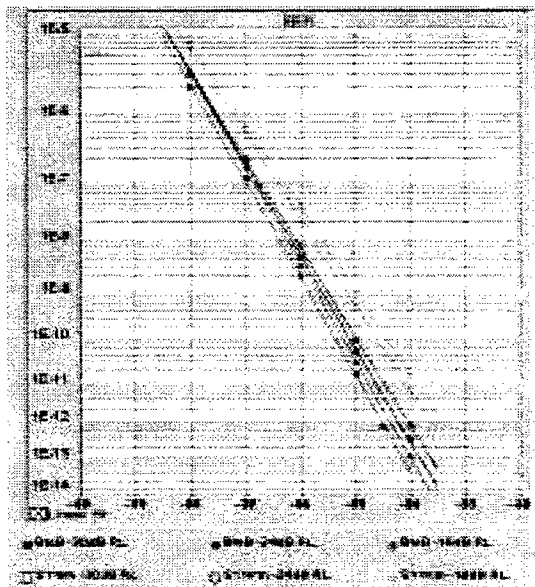


Figure 4 BER results at 2.5Gbits/s on SS laser mounted on Si, under RL= -30dB, -24dB, -19dB.

**Si mother-board :** The heart of novel hybridization techniques in opto-electronic devices is the Si submount. This Si submount is used for mechanical alignment of active devices (laser and detector) and fiber. It can also

integrate  $\text{SiO}_2$  waveguides to achieve passive optical functions such as wavelength multiplexers, splitters, Bragg gratings. Studies to mount also electronic devices on the same Si board are also carried out.

The most complex Si structure will integrate : (1) V grooves for fiber positioning with a tolerance better than  $0.1\mu\text{m}$ . (2) Mechanical structures to accurately align chips on the Si submount. Mechanical stand-off are etched on the Si in the exact alignment of the fiber V grooves therefore passive alignment can be achieved. (3) AuSn bumps for chip soldering and self alignment along the stand-offs<sup>9</sup>. (4) Electrical lines to ensure electrical connection for both DC power and HF line adaptation. (5)  $\text{SiO}_2$  waveguides for passive optical functions<sup>10</sup>. Alcatel Optronics first results in using its own laser dies and Si submounts lead to outstanding results in coupling efficiencies. Results are shown in Figure 4 for 2.5Gbits/s I-16 application. The fiber mean output power is  $-5\text{dBm}$  and extinction ration is 15dB. -30dB, -24dB and -19dB return losses have been tested.

MT optical output : Todays main physical constraint in mounting and handling opto-electronic devices is due to the optical fiber pigtail which can not sustain standard surface mounted device soldering temperatures. Opto-electronics device manufacturers developed their own solution of detachable pigtail to remove the pigtail during mounting process. Many connector types have been proposed<sup>11</sup>. Alcatel Optronics together with Furukawa has chosen MT connector type for its ability to handle multiple fiber applications in the future. Full characterization of the connector characteristics has been carried out and is shown in Figures 5 and 6. Insertion losses remain better than 1dB and refection is always greater than 40dB. These results have been confirmed after temperature cycling and in the  $-40^\circ\text{C}/+85^\circ\text{C}$  temperature range, they are fully compatible with our laser operating conditions.

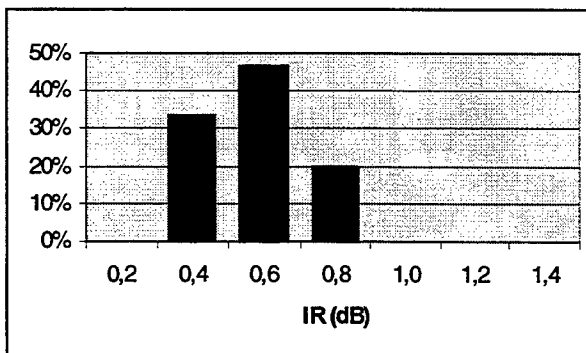


Figure 5 MT1 Insertion Loss

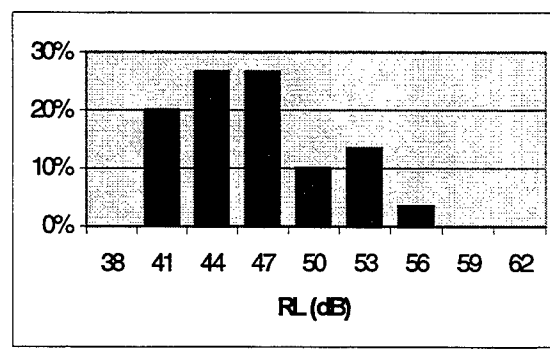


Figure 6 MT1 Return Loss

Plastic package : Until now opto-electronics devices for high speed applications used exclusively metal based packages that include thermoelectric coolers for temperature regulation. Today, new generations of lasers allows the use of plastic packages. The price reduction between standard metal package and plastic package reaches a factor of 6. The HF characteristics of plastic packages have been already optimized in Alcatel to up to 622Mbits/s rate for telecommunication transmission.<sup>12</sup>

### Conclusion :

Alcatel Optronics is ready to support the growing optical telecommunication market with innovative technologies and products. The first products using planar technologies suitable for high bit rate applications are now transferred to mass production. They fulfill market demand by reducing size, reducing costs, making handling easy and allowing 2.5Gbits/s transmissions without using thermoelectric cooling.

The author wants to thank Alcatel Corporate Research Center in Marcoussis, France, and Stuttgart, Germany, for their collaboration and Alcatel Optronics development teams for their contribution.

<sup>1</sup> Photonics Spectra december 1998.

<sup>2</sup> Opto-electronic Industry and Technology Development Association (OITDA) 1998.

<sup>3</sup> R.Cann, SPIE vol.3004, 1997.

<sup>4</sup> J.Gates and al., ECTC 1998.

<sup>5</sup> A.McGhee, Lightwave sept. 1998.

<sup>6</sup> Cl.Artigue and al., OFC 1998.

<sup>7</sup> B.Fernier and al., ECOC 1998.

<sup>8</sup> A.Lestra and al., ECOC 1997.

<sup>9</sup> J.P.Hall, IEE UK 1994.

<sup>10</sup> A.Ambrosy, mst news 1/1998.

<sup>11</sup> J.P.Kilmer, Lightwave, may 1998.

<sup>12</sup> JM.Rainsant and al., NOC 1999.

## Gain and switching measurements of the side-injection light-controlled bistable laser diode

S. I. Pegg and M. J. Adams

Department of Physics, University of Essex, Wivenhoe Park, Colchester, Essex, CO4 3SQ, UK

(S. I. Pegg - Tel: +44 (0)1206 872864 Fax: +44 (0)1206 873598 e-mail: sipegg@essex.ac.uk)

### *Introduction*

The Side-Injection Light-Controlled Bistable Laser Diode (SILC-BLD) has shown itself to have many applications in all-optical switching and processing<sup>1,2</sup>. A saturable absorber is housed between two gain regions of a main laser, which are biased just below threshold (with the absorber inhibiting lasing). When light is injected (via an orthogonal side-waveguide), the absorber changes state and becomes optically transparent, allowing the main laser to switch on strongly. With no input light, the absorber reverts to its original absorbing state, and this provides the mechanism for all-optical switching.

The SILC device's unique orthogonal waveguide configuration (see figure 1) gives it many advantages over more conventional absorptive switching devices. The presence of gain in the side-waveguide (due to it being forward biased) allows for low input switching powers, the tapered side-waveguide allows for a longer absorber (introducing a larger nonlinearity into the cavity), the strongly absorbing region behind the saturable absorber means that there is no resonance of the input signal and the orthogonal waveguides mean there is no leakage of input light into the output (meaning no post-processing filter is required).

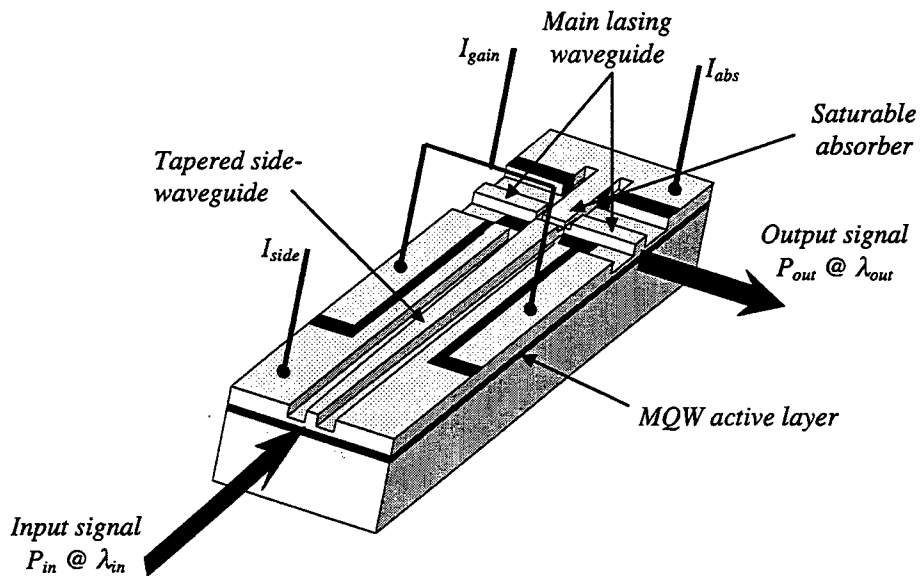


Figure 1. Schematic diagram of SILC-BLD structure.

The device structure and dimensions are as have been earlier reported<sup>3</sup>. This work investigates the spectral properties of the SILC device, and in particular the dependence of the absorptive switching power on injected wavelength. Main lasing waveguide gain spectra have been measured and modelled with strong similarity, and also show good agreement with the spectral switching power dependence. This indicates that it is the side-waveguide gain spectrum that determines the injected light power required to switch the main laser.

### Switching power

The set-on switching power was measured by injecting continuous wave light into the side-waveguide from an external cavity tuneable laser source. The gain regions of the main laser were biased so that the device was 0.5 mA below threshold, with no bias applied to the absorber and 100 mA of forward bias applied to the side waveguide. Example output versus input power plots can be seen in figure 2 for three input wavelengths, and the set-on power is the input power required to change the state of the output. A plot of the spectral dependence of the set-on switching power can be seen in figure 3(a), with a minimum switching power of 13  $\mu\text{W}$  measured, and a 3 dB insensitivity over more than 35 nm observed.

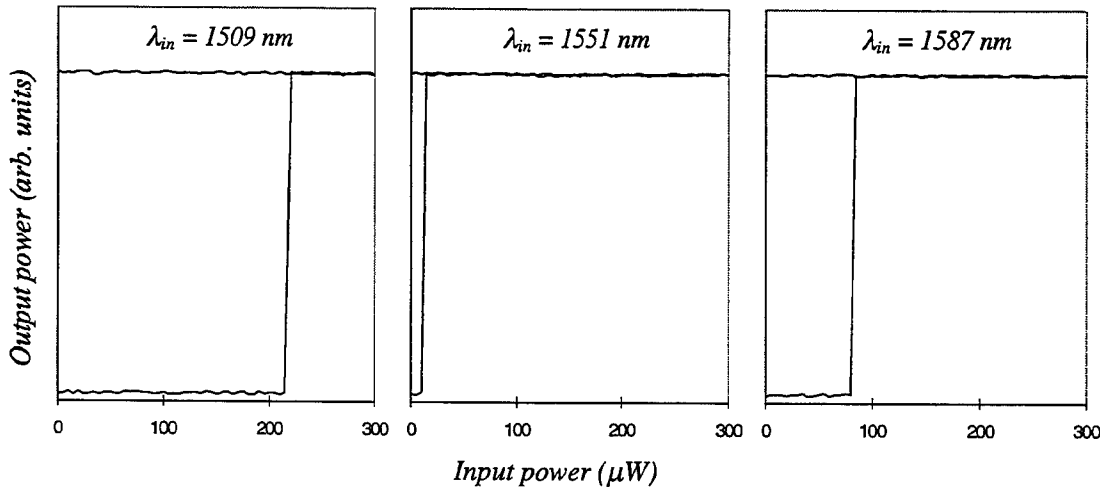


Figure 2. Example output versus input power plotted for three input wavelengths.

### Gain spectra

A gain spectrum was measured with a homogeneous current density applied to the various sections of the main laser, and the device biased 2 mA below threshold. It was measured using the well-known Hakki-Paoli technique<sup>4</sup>, with a cavity length of 300  $\mu\text{m}$  and facet reflectivities of 32 % assumed. Although the spectrum analyser used had a finite resolution of 0.1 nm, clean minima were seen in the emission spectrum, and the gain measured can be seen in figure 3(b).

A quantum-well gain model<sup>5</sup> based upon vertical transitions between conduction and valence band ( $k$ -selection rules), with Lorentzian broadening using an intraband scattering time,  $\tau_{in}$ , was used to calculate a gain spectrum

$$g_m(\omega) = K [f_c(\omega) - f_v(\omega)] \left[ \frac{1}{2} + \frac{1}{\pi} \tan^{-1} \left( \frac{\hbar\omega - E_{tr}}{\hbar/\tau_{in}} \right) \right] \quad (1)$$

where

$$K = \frac{2|M|^2}{m_0} \frac{m_r e^2}{4m_0 v_g \hbar^2 W \omega \epsilon_0 N_s^2} \quad (2)$$

is taken from Coldren and Corzine<sup>6</sup>.  $2|M|^2/m_0$  is the momentum matrix element (24.5 eV),  $m_r$  is the reduced well mass ( $3.41 \times 10^{-31} \text{ kg}$ ),  $v_g$  is the group velocity ( $8 \times 10^9 \text{ cm/s}$ ),  $W$  is the well width (8 nm),  $\omega$  is angular frequency of the light,  $N_s$  is the group refractive index (3.85) and  $E_{tr}$  is the transition

energy (0.79 eV). The carrier concentration was taken to be  $1.59 \times 10^{18} \text{ cm}^{-3}$  (assuming charge neutrality), the internal loss was  $54 \text{ cm}^{-1}$  and  $\tau_{in}$  was 0.045 ps. The calculated spectrum can be seen in figure 3. Comparing this plot with that of figure 3(a) shows good agreement, implying that the spectral dependence of switching power is determined by the gain in the side waveguide.

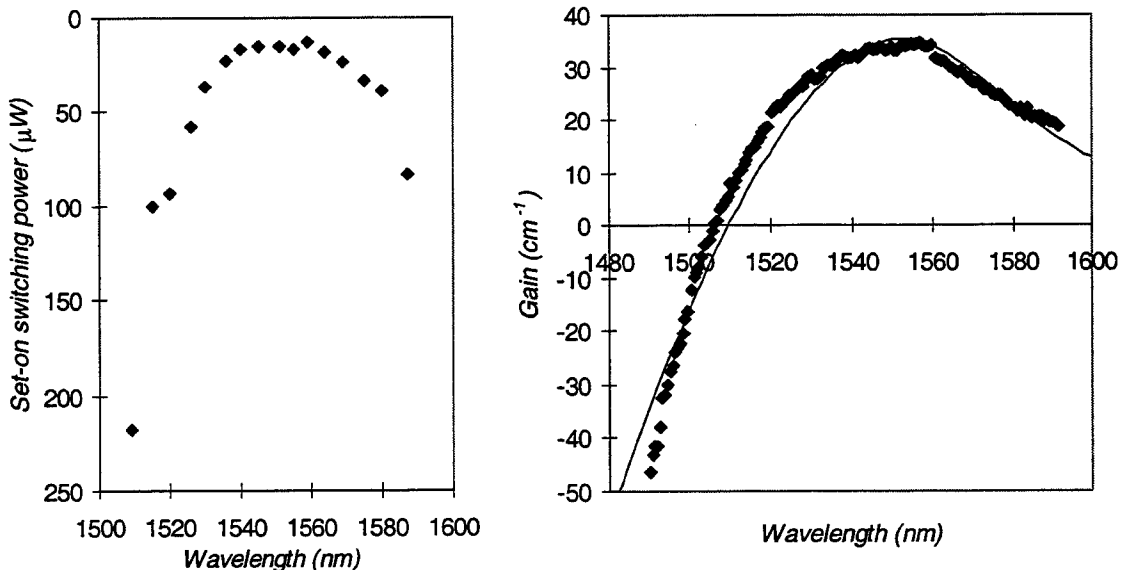


Figure 3. (a) Spectral dependence of set-on power, (b) measured and modelled SILC-BLD gain spectra (points measured, line modelled).

### Conclusions

Set-on powers as low as  $13 \mu\text{W}$  have been measured for the side-injection light-controlled bistable laser diode, and all optical switching has been demonstrated over an almost 80 nm spectral range (this being limited by the tuning range of our input source and not the SILC device operation). Further, the spectral switching dependence has been explained accurately by measuring / modelling the main laser's gain spectrum under similar bias conditions.

### References

1. K. Nonaka, H. Tsuda, H. Uenohara, H. Iwamura, and T. Kurokawa, "Optical nonlinear characteristics of a side-injection light-controlled laser diode with a multiple-quantum-well saturable absorption region", *IEEE Photon. Tech. Lett.*, vol. 5, no. 2, pp. 139-141, 1993.
2. K. Nonaka, Y. Noguchi, H. Tsuda, and T. Kurokawa, "Digital signal regeneration with side-injection light-controlled bistable laser diode as a wavelength converter", *IEEE Photon. Tech. Lett.*, vol. 7, no. 1, pp. 29-31, 1995.
3. S. I. Pegg, M. J. Adams, and K. Poguntke, "Measurements and modelling of the Side-Injection Light-Controlled Bistable Laser Diode (SILC-BLD)", *SPIE Proceedings 3283-78*, pp. 710-720, 1998.
4. B. W. Hakki and T. L. Paoli, "cw degradation at 300 °K of GaAs double-heterostructure junction lasers. II. Electronic gain", *J. Appl. Phys.*, vol. 44, no. 9, pp. 4113-4119, 1973.
5. T. Makino, "Analytical Formulas for the Optical Gain of Quantum Wells", *IEEE J. Quantum Electron.*, vol. 32, no.3, pp. 493-501, 1996.
6. L. A. Coldren and S. W. Corzine, *Diode Lasers and Photonic Integrated Circuits*, Chap. 4, pp. 126-128, Wiley, 1995.

# Novel Ultra-low Voltage Expanded Mode Modulator Monolithically Integrated with a Laser using Single-Epitaxial Growth

S. S. Saini, P. J. S. Heim, R. Grover, and M. Dagenais

Department of Electrical engineering, University of Maryland, College Park, MD 20742  
 saini@eng.umd.edu, heim@eng.umd.edu, rgrover@eng.umd.edu, dage@eng.umd.edu

F. G. Johnson, and D. R. Stone

Laboratory for Physical Sciences, College Park, MD 20740  
 fred@lps.umd.edu, den@lps.umd.edu

H. Shen, J. Pamulapati, and W. Zhou

Army Research Laboratory, Adelphi, College Park, MD 20783  
 paul\_shen@emh3.arl.mil, jpamulapati@arl.mil, wzhou@arl.mil

There is a need for inexpensive laser sources for high-speed optical transmission circuits being deployed today. Direct modulation of semiconductor lasers has a high chirp and, hence, can be used only to moderate speeds. Consequently, very high-speed applications typically require external modulators. This increases the number of optical components required in the transmitter with cumbersome packaging that drives up the cost. There has been considerable interest in monolithically integrating a laser with a modulator on a single substrate [1,2]. These schemes typically involve complex device structure requiring epitaxial regrowth capability. In this paper, we present a compact laser integrated with a modulator that is fabricated using conventional techniques and require only a single epitaxial growth. To reduce the cost of an optoelectronic module, it is important to make the packaging of the devices simple and cost effective. Recently, there has been an increased interest in expanded mode devices [3]. Our proposed device has an inherent expanded mode for ease of coupling into a single-mode fiber.

In our previous work [4], we demonstrated a mode-expanded laser using resonant coupling between two vertically spaced waveguides as shown in Fig. 1. The device used resonance between "supermodes" of a structure consisting of a tightly confined tapered active waveguide and a loosely confined passive waveguide. For efficient and fabrication tolerant mode transformation, a 100  $\mu\text{m}$  long exponential taper was used on the active ridge waveguide followed by a 100  $\mu\text{m}$  long linear taper. From the mode propagation simulation shown in Fig. 1, it can be seen that the region of the taper over which the mode is guided into the underlying waveguide is very small ( $\sim 50 \mu\text{m}$ ). By applying a suitable reverse bias over

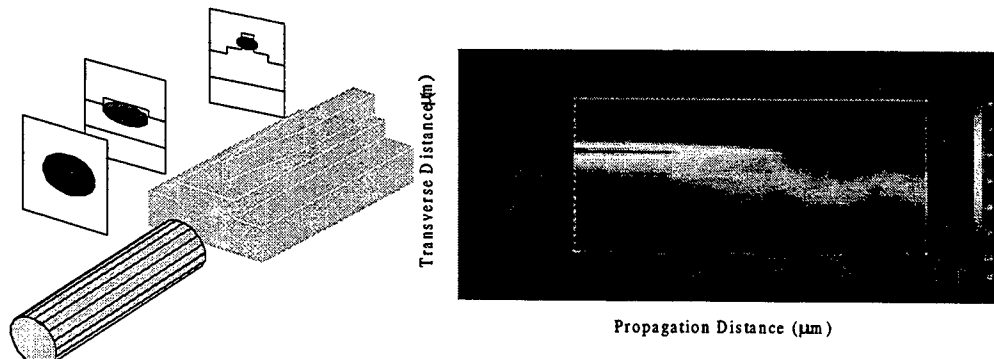


Fig.1. Schematic of the device and simulated light intensity distribution (transverse cut) along the taper.

the coupling region, the refractive index of the quantum well can be changed appreciably [5] and the two waveguides can be made to go off-resonance. In this case, because of the abrupt nature of the taper, the radiation loss during the mode transformation increases appreciably. Thus, by having two electrodes on the active region, the mode-expanded laser can be modified to make a very interesting voltage-controlled optical switch. The first electrode is on the section of the device where the mode is well confined within the active waveguide. This forward biased gain section provides the optical gain needed for lasing. The second electrode is positioned on the section of the taper where the mode couples from the active waveguide to the underlying passive waveguide. By applying an appropriate reverse bias on this electrode, the refractive index of the quantum wells in this region can be increased so that the waveguides go off resonance and the coupling is destroyed. The optical power is now radiated instead of being well coupled into the underlying waveguide and the lasing action is stopped.

The epitaxial structure of the device is the same as described in [4]. The active layer consists of five 1% compressively strained 10 nm thick quantum wells for emission at 1.55  $\mu\text{m}$ , and four lattice matched 10 nm barriers ( $\lambda_g=1.25 \mu\text{m}$ ). The passive waveguide consists of a n-doped ( $5 \times 10^{17} \text{ cm}^{-3}$ ) 20 layer stack of alternating InP and lattice matched quaternary, such that the equivalent refractive index was 3.21 and total thickness was 3  $\mu\text{m}$ . The waveguide width of the active region where phase matching occurs was 1.4  $\mu\text{m}$ . The gain section of the device was 600  $\mu\text{m}$  long with a ridge width of 2.0  $\mu\text{m}$ . The taper on the mode transformation section has been described above. Two electrodes were defined on top of the ridge. The first electrode was 660  $\mu\text{m}$  long and positioned over the straight 2.0  $\mu\text{m}$  ridge and part of the first section of the taper. The second electrode was 130  $\mu\text{m}$  long and positioned over the remaining taper. The top view of the ridge and the electrode position is shown in Fig. 2.

The epitaxial layers were grown using solid source molecular beam epitaxy (MBE) on an InP substrate. The ridge shape was defined using a conventional photoresist and an optical 10x-projection aligner. The ridges were etched just past the active region using Ar:CH<sub>4</sub> chemistry based reactive ion etching (RIE). A 7  $\mu\text{m}$  wide, 1.0  $\mu\text{m}$  high mesa was then dry etched to create the device isolation. Subsequently, a spin-on-glass (SOG) process was used to create the dielectric isolation. The samples were thinned to 100  $\mu\text{m}$  and p-side (TiPtAu) and n-side (AuNiGeNiAu) ohmic contacts deposited. Using negative photoresist and a metal lift-off process, selective p-side metallization was done to create the two electrodes. The InGaAs cap layer between the electrodes was then etched chemically to increase the electrical isolation. The devices were mounted p-side up on copper heatsinks and were tested without any facet coatings.

The typical LI curves for the device with various applied reverse biases on the second electrode are shown in Fig. 3. When no bias is applied on the second electrode, a threshold current of 65 mA is obtained. The threshold current increases by ~20 mA and ~30 mA for reverse bias of 0.2 V and 0.5 V respectively. With a bias of 1.0 V the device does not lase and only spontaneous emission is observed. An on-off contrast ratio of greater than 19 dB is observed at current of 80 mA even with as small a reverse bias as 0.2 V. The contrast ratio increased to 24 dB for a switching voltage of 1 V. The sensitive switching characteristics shown in Fig. 3 should be beneficial for high-speed devices. As the switching is done using reverse bias in absence of carriers, the chirp of the device should be low. Also the low control voltage required make the high-speed electronic driver circuitry simpler and less expensive. The low voltage also makes the device interesting for implementing simple optical microwave links with gain.

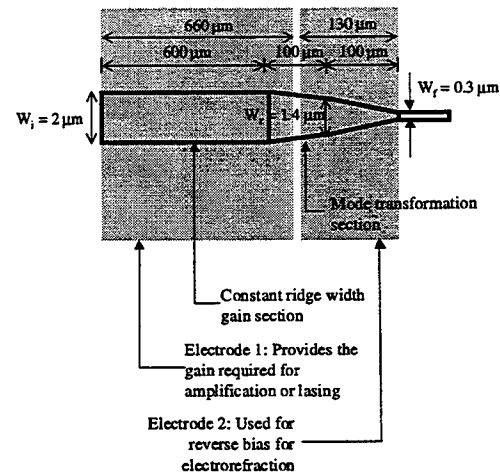


Fig. 2. Schematic of the device with the electrode position shown.

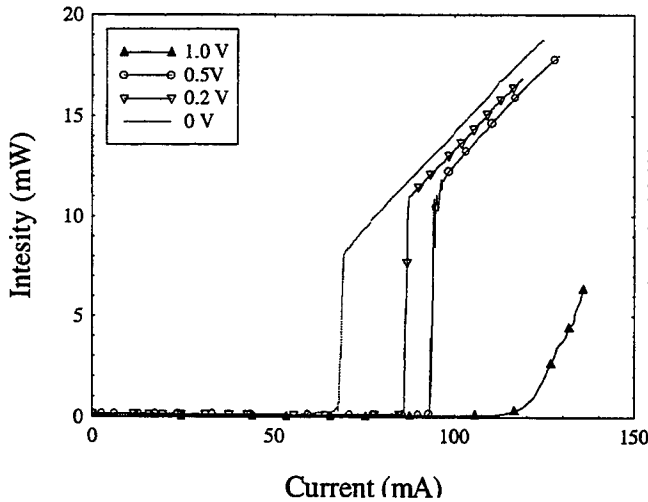


Fig. 3. L-I curves of the device with various reverse bias

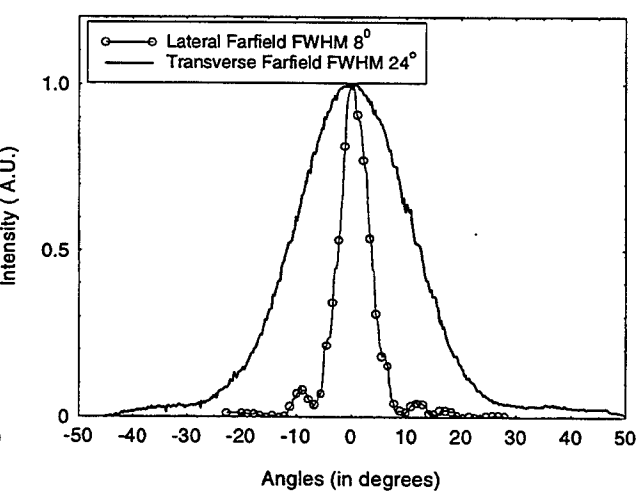


Fig. 4. Farfield plots from the expanded mode side

The transverse and lateral far-field intensity were measured for the expanded mode facet of the device by using a rotating stage and a pin hole detector. These far-field plots are shown in Fig. 4 for zero reverse bias applied control voltage. Reduced far-field full width half-max (FWHM) divergence angles of  $24^\circ \times 8^\circ$  were obtained. These compare well with our previous resonantly coupled mode expanders, which obtained a 3.7 dB fiber coupling loss. The optical switches thus have an expanded mode, which improves the coupling efficiency to single mode fiber.

### Conclusion

In this paper we have proposed and demonstrated a novel optical switch using a resonantly coupled structure. The optical switch shows good on-off ratio (24 dB) at low bias (<1V). Reduced far-field divergence angles of  $8^\circ \times 24^\circ$  (FWHM) were obtained. The expanded mode is expected to improve the coupling efficiency to a single mode fiber. This device can be potentially used as an inexpensive high-speed laser source. As the switching is done using reverse bias in absence of carriers, the chirp of the device should be low. The taper that is used for mode expansion is also used for the switching. Thus, the device is compact. As the device inherently has an expanded mode, fiber coupling has relaxed alignment tolerances. This enables passive packaging of these devices in a batch-processing environment. Also, these devices use conventional fabrication (no e-beam lithography) and growth techniques (no regrowth).

### References

- [1] A. Ramdane et. al., "Monolithic integration of multiple-quantum-well lasers and modulators for high-speed transmission," *IEEE J. Select. Topics Quantum Electron.*, vol. 2, no. 2, pp. 326-335, June 1996.
- [2] S. O'Brien et. al., "Monolithic integration of an (Al)GaAs laser and an intracavity electroabsorption modulator using selective partial interdiffusion," *Apl. Phys. Lett.*, vol. 58, no. 13, pp. 1363-1365, April 1991.
- [3] B. Mersali et. al., "Optical-Mode Transformer: A III-V circuit integration enabler," *IEEE J. Select. Topics Quantum Electron.*, vol. 2, pp. 1332-1343, Dec. 1997.
- [4] S.S. Saini et. al., "Compact mode expanded lasers using resonant coupling between a 1.55-μm InGaAsP Tapered Active Region and an underlying coupling waveguide," *IEEE Photon. Technol. Lett.*, vol. 10, no. 9, pp. 1232-1234, Sept. 1998.
- [5] A. Sneh et.al., "Polarization-insensitive InP-based MQW digital optical switch," *IEEE Photon. Technol. Lett.*, vol. 9, no. 12, pp. 1589-1591, Dec. 1997.

# Compact, 1.55 $\mu\text{m}$ Spot-Size Converters for InP Based Photonic Integrated Circuits

Gregory A. Fish, B. Mason, Larry A. Coldren, Steven P. DenBaars

*Electrical & Computer Engineering, University of California, Santa Barbara, 93106*

6500fish@ucsbuxa.ucsb.edu,

Phone: (805) 893-8465

Fax: (805) 893-4500

## Introduction

Optical spot-size converters are a key enabling technology for photonic integrated circuits. By simultaneously reducing the coupling loss and increasing the alignment tolerance to optical fibers, spot-size converters can dramatically lower the insertion loss and simplify packaging of photonic integrated circuits, especially multiple input/ output devices.

There have been several reported methods for producing optical spot-size converters[1-3], however, they generally involve tapering the width[2] or thickness[3] of the layer that is providing waveguiding. The most flexible methods involve tapering the waveguide layer thickness, as this procedure can be used to create spot-size converters for both ridge and buried heterostructure waveguides. The simplest technique for producing a tapered waveguide layer thickness is selective area etching[4], where the gap between two dielectric masks is varied to effect the etch rate of a diffusion limited etchant. Fig. 1 illustrates a schematic of a spot-size converted laser created using a selective area etch followed by a nonselective regrowth. Fib. 1 b) and c) illustrate the compatibility with a ridge or buried ridge stripe waveguide technology.

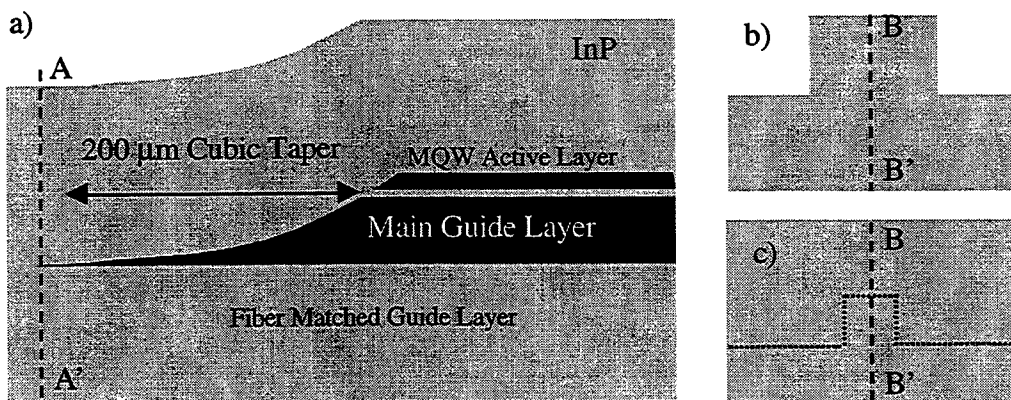


Fig. 1 a) Schematic illustration of an spot-size converted laser cross section through the center of the waveguide, B-B'. b) Cross section through A-A' of the fiber match waveguide using a ridge waveguide technology. c) Cross section through A-A' of the fiber matched waveguide using a buried ridge stripe waveguide technology.

## Compact Selective Area Etched Tapers

Selective area etching has been used to create spot-size converters with high coupling efficiency at 1.55  $\mu\text{m}$  to both lensed[3] and cleaved[5] optical fibers, however, the linear shaped tapers used in these devices were 0.8-1 mm in length. It is highly desirable for a spot-size converter to achieve low loss and high coupling efficiency in the shortest length possible to reduce the overall photonic integrated circuit chip size. To convert the mode shape efficiently in the

shortest length requires a nonlinear thickness taper which reduces the thickness rapidly at the beginning and slowly at the end[6]. Fig 2. illustrates the mask shape and the resulting etch rate enhancement required to produce the cubic thickness taper similar to that shown in Fig 1. a). 3D BPM simulations conducted on spot-size converters using the ridge waveguide technology of Fig. 1 confirm that total conversion plus coupling losses of less than 1 dB to a lensed fiber can be obtained for cubic taper lengths as short as 200  $\mu\text{m}$ .

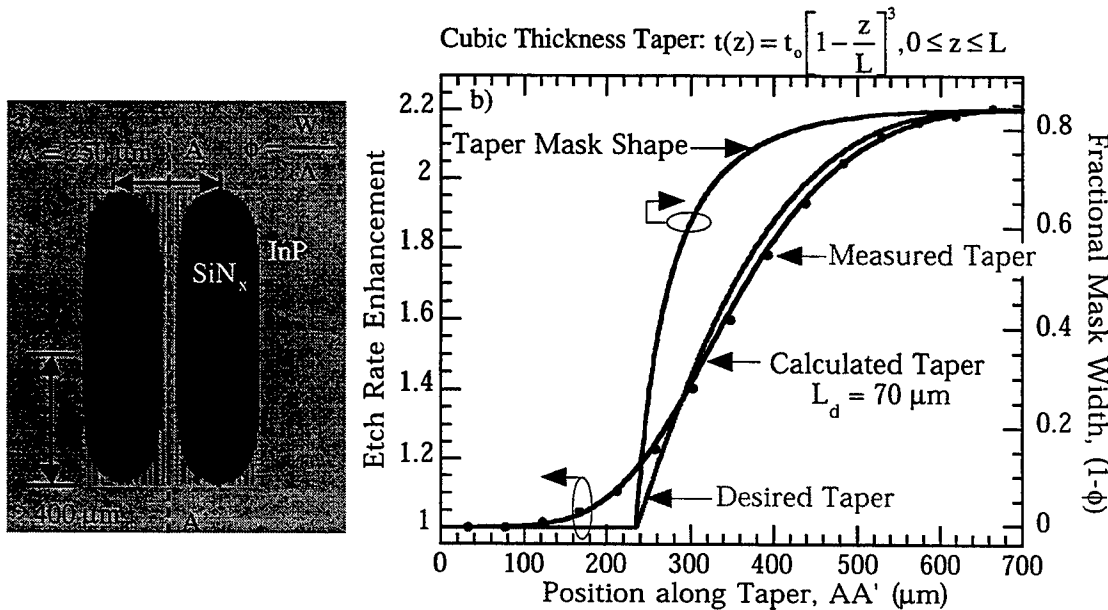


Fig. 2 a) Shape of the dielectric mask and the resulting etch rate enhancement, b), to produce a cubic thickness taper of around 400  $\mu\text{m}$  in length.

### Spot-size Converted Laser Performance

To measure the performance of the selective area etched spot-size converter, MOCVD was used to grow a base structure with the layers illustrated in Fig. 1 a). The active layer consists of six 0.8% compressive InGaAsP quantum wells grown on top of a 0.35  $\mu\text{m}$  thick, InGaAsP ( $\lambda_g = 1.35 \mu\text{m}$ , i.e. 1.35Q) layer that forms the main waveguide. A 0.1  $\mu\text{m}$  layer of 1.1Q is grown 0.3  $\mu\text{m}$  beneath the main waveguide to create the fiber matched waveguide at the end of the spot-size converter.

Processing of the device continues by removing the active region in the spot-size converter region (and any other passive sections of the device) and growing a 1.5  $\mu\text{m}$  p-InP layer to prepare the sample for selective area etching. Selective area etching is conducted using 0.05% Br:Methanol as the etchant with a  $\text{SiN}_x$  mask. The masks are removed and 3  $\mu\text{m}$  p-InP and a contact layer is regrown using MOCVD.

3  $\mu\text{m}$  wide ridge waveguides are then dry etched using  $\text{CH}_4/\text{H}_2/\text{Ar}$  followed by a wet  $\text{H}_3\text{PO}_4/\text{HCl}$  clean up etch to a stop etch layer formed in the first regrowth. The ridge width in the spot-size converter increases to 5.5  $\mu\text{m}$  at the end, also using a cubic taper.

Laser with taper lengths of 200  $\mu\text{m}$ , 300  $\mu\text{m}$ , and 500  $\mu\text{m}$  were fabricated to evaluated the spot-size conversion efficiency. Lasers with no tapering of the waveguide thickness were used to provide a reference. Pulsed LI testing (shown in Fig 3. a)) from the front and the back facet confirmed that the spot-size converters of all lengths had very little (< 0.5 dB) excess loss compared to the control samples. Coupling efficiencies to a lensed fiber as high as 75% (~-1.3 dB) with an average of 65% were measured for all of the lengths fabricated. This represents around a factor of two

improvement compared to the standard laser. At the same time the alignment tolerance was also improved by a factor of two, as shown in Fig 3 b).

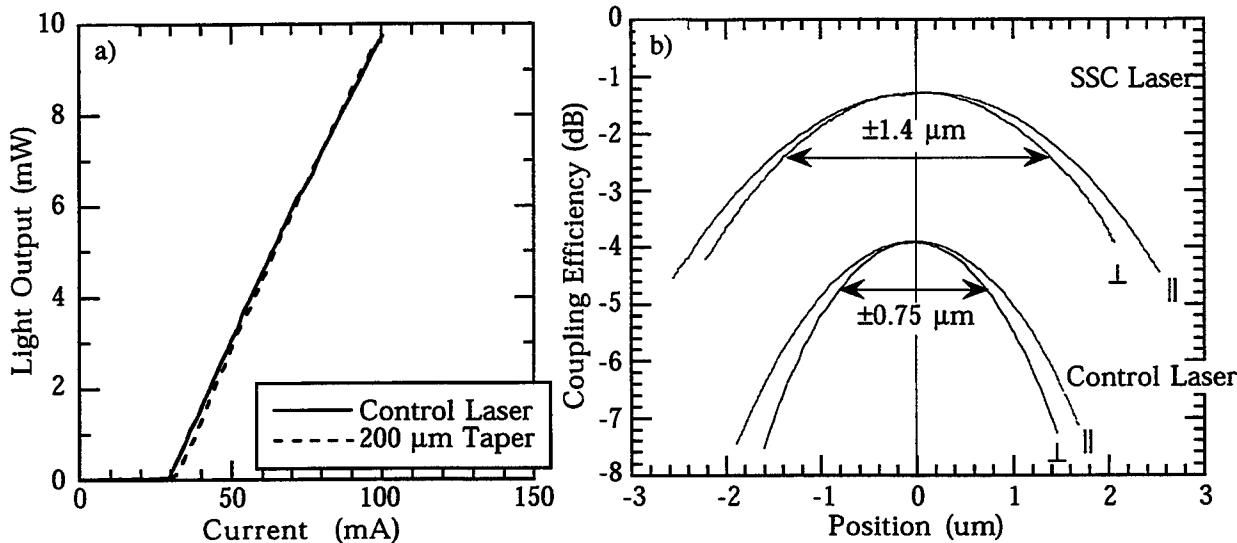


Fig. 3 a) Pulsed LI of the back facet emission from the SSC laser and control laser with 900  $\mu\text{m}$  long gain sections illustrating the very small amount of mode conversion loss. b) Scanning fiber measurements indicating that both the coupling efficiency and alignment tolerance to a lensed fiber ( $\text{MFD} \sim 5 \mu\text{m}$ ) are doubled by the use of a spot-size converter.

## Conclusion

A method for producing compact, 1.55  $\mu\text{m}$  spot-size converter ( $<200 \mu\text{m}$ ) that is compatible with a ridge waveguide or buried heterostructure technology is presented. Lasers made with spot-size converters in the cavity illustrated very low conversion losses ( $<0.5 \text{ dB}$ ) and a coupling efficiency of 75 % to lensed optical fibers ( $\text{MFD } 5 \mu\text{m}$ ).

## References

- [1] H. Bissessur, C. Graver, O. Le Gouezigou, G. Michaud, and F. Gaborit, "Ridge laser with spot-size converter in a single epitaxial step for high coupling efficiency to single-mode fibers," *IEEE Photonics Technology Letters*, vol. 10, pp. 1235-7, 1998.
- [2] R. Ben-Michael, U. Koren, B. I. Muller, G. Young, M. Chien, and G. Raybon, "InP-based multiple quantum well lasers with an integrated tapered beam expander waveguide," *IEEE Photonics Technology Letters*, vol. 6, pp. 1412-14, 1994.
- [3] T. Brenner, M. Bachmann, and H. Melchior, "Low-loss fiber-to-semiconductor waveguide coupling using integrated optical mode expanders," in , 1994, pp. 267-8 vol.2.
- [4] T. Brenner and H. Melchior, "Local etch-rate control of masked InP/InGaAsP by diffusion-limited etching," *Journal of the Electrochemical Society*, vol. 141, pp. 1954-6, 1994.
- [5] T. Brenner, M. Bachmann, and H. Melchior, "Vertically tapered InGaAsP/InP waveguides for highly efficient coupling to flat-end single-mode fibers," *Applied Physics Letters*, vol. 65, pp. 798-800, 1994.
- [6] K. Kawano, M. Kohtoku, H. Okamoto, Y. Itaya, and M. Naganuma, "Coupling and conversion characteristics of spot-size-converter integrated laser diodes," *IEEE Journal of Selected Topics in Quantum Electronics*, vol. 3, pp. 1351-60, 1997.

## All-Active InGaAsP/InP Optical Tapered-Amplifier 1×N Power Splitters\*

S. S. Choi<sup>†‡</sup>, J. P. Donnelly<sup>‡</sup>, S. H. Groves<sup>‡</sup>, R. E. Reeder<sup>‡</sup>, R. J. Bailey<sup>‡</sup>, P. J. Taylor<sup>‡</sup> and W. D. Goodhue<sup>†‡</sup>

<sup>†</sup>Lincoln Laboratory, Massachusetts Institute of Technology  
244 Wood St., Lexington, MA 02420-9108

Tel # (781) 981-4423 Fax # (781)981-0122, E-mail: donnelly@ll.mit.edu

<sup>‡</sup>Department of Physics and Applied Physics Photonics Center, University of Massachusetts Lowell  
One University of Avenue, Lowell, MA 01854  
Tel # (978) 934-3785, E-mail: [Samuel\\_Choi@student.uml.edu](mailto:Samuel_Choi@student.uml.edu)

### Introduction

Photonic and optoelectronic systems require semiconductor optical amplifiers, splitters and switches with high speed, bandwidth, and gain. Various passive and active splitter and combiner designs have been proposed for optoelectronic systems [1-4]. Trees of Y-branches, 2D free-space diffraction region devices with input and output guide coupling and multimode-waveguide imaging devices have all been proposed as passive splitters [1]. Passive power splitters require pre- and/or post-amplification to compensate for the splitting loss. For 1×N splitters with large N, power saturation effects in single-mode amplifiers limit pre-amplification and, therefore, post-amplification is usually also required. Post-amplification, however, only adds more noise and does nothing to alleviate the signal-to-noise ratio degradation that occurs during the 1×N passive splitting process. Amplification during the splitting process can prevent this signal-to-noise ratio degradation and result in signal-to-noise ratios similar to pre-amplification without the power saturation effects inherent in an input single-mode amplifier. All active trees of Y-branches are possible and have been proposed but are difficult to scale to large N. Amplification in a multimode-waveguide splitter turns out to be essentially the same as post-amplification. Extremely tight tolerances on index, geometry and wavelength in multimode devices also limit the robustness of this type of splitter. Tapered-amplifier 2D diffraction splitters, however, are both scalable, robust and preserve most of the signal-to-noise advantages of amplifying during the splitting process. Here we present the design, fabrication and testing of tapered amplifier power splitters.

### Design and Fabrication

A schematic of the 1×8 all-active tapered amplifier power splitter (TAPS) is illustrated in Figure 1. There are three main sections to the tapered amplifier power splitter design. The first section is single-mode ridge-waveguide that serves as a pre-amplifier. The single-mode input section also provides a well define input to the 2D diffracting region and therefore determines the diffraction pattern in this region. A tapered amplifier in the diffraction region that is designed to match the diffracting pattern amplifies the signal during diffraction and keeps the signal intensity high. The active output waveguides are apodized to obtain approximately equal signal powers in each of the output waveguides. This apodization result in a slightly lower signal-to-noise in the outer guides compared to the center guides, but it is still superior to post-amplification. All of the output guides are adiabatically tapered down and the S-bends are used to route the outputs to the straight single-mode output waveguides as indicated in Fig.1. Although the results presented here on an all-active TAPS device is for all sections driven in parallel, the individual sections can be driven separately. In this case the outputs can be used as ON/OFF switches as well as amplifiers.

The material used to fabricate the TAPS devices is a separate-confinement heterostructure with three InGaAsP quantum wells under 1% compressive strain that was grown by organometallic vapor-phase epitaxy. The p-type InP upper cladding layer contains an “etch stop” layer to facilitate the fabrication of the ridge waveguides. A top p<sup>+</sup>-InGaAs layer is provided to facilitate p-type ohmic contact formation. The waveguides are fabricated using a CH<sub>4</sub>/H<sub>2</sub> reactive-ion etching followed by a short selective wet-chemical etch which stops at the stop etch layer. The titanium etch mask used for the reactive ion etching is removed and a dielectric layer deposited.

---

\*This work was sponsored by the Department of the Air Force under AF Contract # F19628-95-C-0002. The opinions, interpretations, conclusions, and recommendations are those of the authors and are not necessarily endorsed by the United States Air Force.

Standard photolithography and etching techniques are then performed to provide contact openings in the dielectric layer. A Ti-Pt-Au metallization is used to form the ohmic contact to the p<sup>+</sup>-InGaAs layer. The top contacts are segmented to allow separate excitation of the input ridge, the 2D horn, and the output splitters in the future. The wafer is thinned and then a backside Ni-Ge-Au contact is applied to the n<sup>+</sup>-InP substrate. The devices are cleaved and mounted junction side down on a Cu package and both facets are anti-reflection coated with a single layer of silicon monoxide.

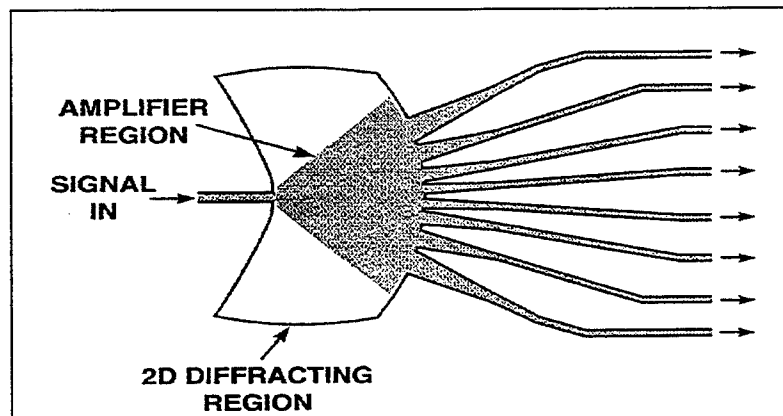


Fig. 1: A schematic of an all active 1×8 TAPS device with the gray area depicting the metallization

In the devices reported here the input and output ridge waveguides are 2.5-μm wide. The 1×8 splitters have a 2-D diffraction region with a radius of 500 μm and an output guide separation of 30 μm. The 1×16 splitters have a 2-D diffraction region with a radius of 1000 μm and an output guide separation of 20 μm.

### Experimental Results

To test the splitter design, passive 1×8 and 1×16 devices were fabricated in a passive waveguide growth to match the active waveguide device characteristics. The 1×16 passive devices have output power uniformity from guide to guide of better than ±4% around the average output power, see figure 2. The 1×8 devices have uniformity of ±9%. The total insertion loss (total output power in all output guides divided by input power) was around -1.8 dB.

The active TAPS devices are mounted on a thermoelectric cooler to keep the temperature at 20 C. For the gain measurement, the chopped input beam from a Fabry-Perot laser diode operating at a wavelength of 1305 nm is coupled into the input ridge of the TAPS device with a 20× objective lens. A reversed-bias photocurrent measurement is used to determine the power coupled into the device. The output of the device was magnified so each output waveguide could be imaged individually on a calibrated photodiode. Chopping the input signal facilitates separating the amplified signal from the amplified spontaneous emission.

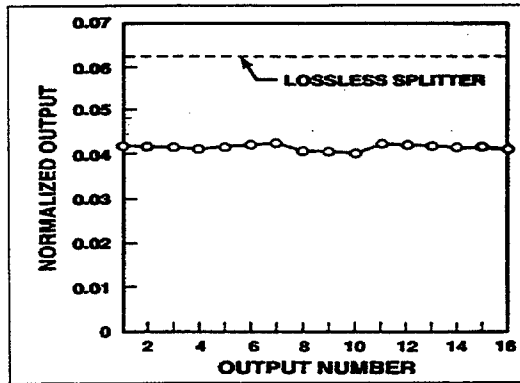


Fig. 2: Normalized output power out of each guide of a 1×16 passive splitter

The measured output powers of a  $1 \times 8$  TAPS device with an input coupled power of  $350 \mu\text{W}$  along with a photograph of the output near-field pattern are shown in Figure 3. In this case, all sections are driven in parallel at a current of  $1.85\text{A}$ . Gain in the output guides ranged from  $9.5 \text{ dB}$  for the center guides to  $3.5 \text{ dB}$  for the lowest outside guide. The uniformity is not as good as obtained on the passive splitters. The outputs of guides 1 and 2 in particular are substantially less than the center guides. Uniformity appeared better at lower drive currents and under pulsed conditions indicating some of the problem may be associated with inhomogeneous soldering resulting in a non-uniform current distribution and junction temperature.

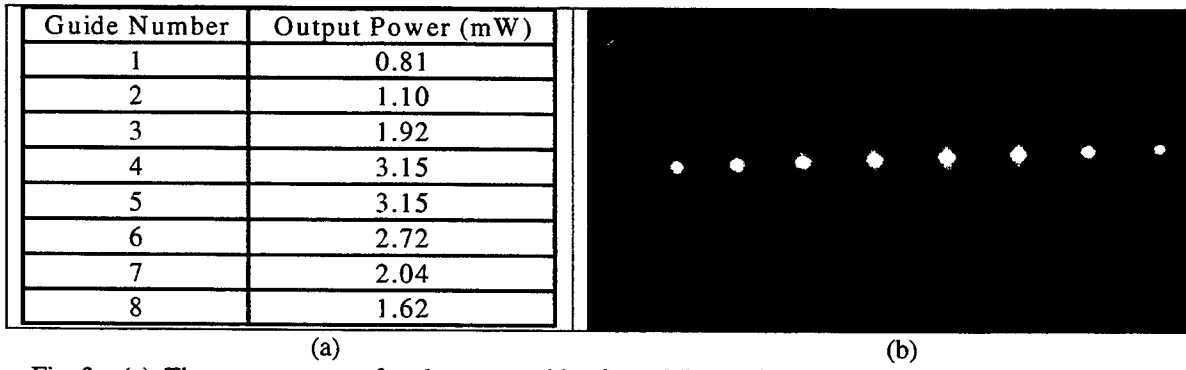


Fig. 3: (a) The output power of each output guide of a  $1 \times 8$  Power Splitter with  $350 \mu\text{W}$  of coupled input power. (b) A photograph of the near-field pattern of the output of the splitter.

## Discussion

We have presented initial results on all active tapered amplifier power splitters. Gains in each output guide ranged from  $3.5$  to  $9.5 \text{ dB}$  at a drive current of  $1.85\text{A}$ . Uniformity of the outputs can be improved by increasing the input guide's lateral confinement. This will decrease the input mode width and increase the diffraction angle to better fill the taper section. Uniformity should also be improved with better soldering and mounting. Operating currents can be decreased by material improvements and by driving the individual sections independently. The devices reported here were fabricated from material that has a transparency current density of  $270 \text{ A/cm}^2$ . This is substantially higher than our more typical laser material, which with the same structure has a transparency current density in the  $150 \text{ A/cm}^2$  range. Both  $1 \times 8$  and  $1 \times 16$  devices are currently being fabricated with higher quality material. Improvements are also expected by operating at a wavelength that more optimally matches the gain spectra of the devices and by improvements in the antireflective coatings.

- [1] F. Ratovelomanana, N. Vodjdani, A. Enard, G. Glastre, D. Rondi, R. Blondeau, "Active Lossless Monolithic One-by-Four Splitters/Combiners Using Optical Gates on InP," *IEEE Photonics Tech. Lett.*, vol. 7, pp. 511-513 (1995).
- [2] M. Zirngibl, C. Dragone, C. H. Joyner, M. Kuznetsov, U. Koren, "Efficient  $1 \times 16$  Optical Power Splitter Based on InP," *Electronics Lett.*, vol. 28, pp. 1212-1213 (1992).
- [3] U. Koren, M. G. Young, B. I. Miller, M. A. Newkirk, M. Chien, M. Zirngibl, C. Dragone, B. Glance, T. L. Koch, B. Tell, K. Brown-Goeble, G. Raybon, " $1 \times 16$  photonic switch operating at  $1.55 \mu\text{m}$  wavelength based on optical amplifiers and a passive optical splitter," *Appl. Phys. Lett.* **61**, pp. 1613-1615 (1992).
- [4] M. G. Young, U. Koren, B. I. Miller, M. A. Newkirk, M. Chien, M. Zirngibl, C. Dragone, B. Tell, H. M. Presby, G. Raybon, "A  $16 \times 1$  Wavelength Division Multiplexer with Integrated Distributed Bragg Reflector Lasers and Electroabsorption Modulators," *IEEE Photonics Tech. Lett.*, vol. 5, pp. 908-910, (1993).

# Key to Authors and Presiders

- Abraham, Patrick ■ RMH9  
 Adams, M. J. ■ RWD2  
 Ahmad, R. U. ■ RMF5  
 Amin, Jaymin ■ RTuD  
 Antoniades, N. ■ RTuJ2  
 Arasaratnam, P. K. ■ RTuL5  
 Arft, Carl M. ■ JWA1  
 Arnold, S. ■ RTuH3  
 Baba, Toshihiko ■ RTuB2,  
     RTuE3  
 Bach, H.-G. ■ RWB3  
 Bailey, R. J. ■ RWD5  
 Bakhrus, H. ■ RTuG2  
 Benisty, H. ■ RTuE1  
 Benson, O. ■ RMC1  
 Berglund, W. ■ RMD4  
 Betty, Ian ■ RMH5, JWA2  
 Bishop, David ■ JWA4  
 Blood, Peter ■ RTuC4  
 Blumenthal, Daniel J. ■  
     RMB5  
 Boggess, T. F. ■ RTuC3  
 Bowers, John E. ■ RMH9  
 Boyd, A.R. ■ JWB3  
 Bremberg, Dan ■ RMF3,  
     RMF4  
 Breuer, Dirk ■ RWA2,  
     RWC1  
 Brox, O. ■ RWC3  
 Bruce, A. J. ■ RTuA1  
 Bulutay, C. ■ RTuF3  
 Cannard, P. J. ■ RWB1  
 Cappuzzo, M. A. ■ RTuA1  
 Chan, K. S. ■ RMH3  
 Chandrasekhar, Shandra ■  
     RWB  
 Chaudhuri, Sujeet K. ■  
     RTuI2  
 Choi, S. S. ■ RWD5  
 Choo, Ahn Goo ■ RTuL4  
 Chow, W. W. ■ RTuF1  
 Chu, Sai T. ■ RMB3, RMF6,  
     RTuB4  
 Chuang, Shun Lien ■ RMC  
 Chung, K. B. ■ RMH10  
 Chung, P. S. ■ RMF2  
 Chung, Youngchul ■ RMG3,  
     RTuI  
 Cibinetto, Lucio ■ RTuG1  
 Clayton, Rick D. ■ RME
- Cohen, A. D. ■ RMB2  
 Coldren, Larry A. ■ RME2,  
     JWB2, RWD4  
 Cotter, David ■ JWB  
 Csutak, S. ■ RMG1  
 Cyr, Michel ■ RME3  
 Dagenais, Mario ■ RWD3  
 Dagli, Nadir ■ RMA, RTuF3,  
     RWB2  
 Day, Stephen ■ RTuA3  
 De La Rue, Richard ■ RTuE1  
 DenBaars, Steven P. ■  
     RME2, JWB2, RWD4  
 Deppe, D. G. ■ RMG1,  
     RTuC  
 Doerr, Christopher R. ■  
     JWA3  
 Doi, M. ■ RMB1  
 Dong, Xuesong ■ RMH11  
 Donnelly, J. P. ■ RWC,  
     RWD5  
 Dorren, B. H. P. ■ RTuD1  
 Dridi, Kim H. ■ RTuI4  
 Ellis, A. D. ■ RWB1  
 El-Mikati, H. A. ■ RMD5  
 El-Refaei, Hatem ■ RMH5  
 Fan, Li ■ RTuD3  
 Feng, Dazeng ■ RTuE5  
 Feng, Hao ■ RTuG4  
 Fielding, Alan ■ RTuA3  
 Figueiredo, J.M.L. ■ JWB3  
 Fish, Gregory A. ■ RME2,  
     JWB2, RWD4  
 Flatté, Michael E. ■ RTuC3  
 Fleck, J. A., Jr. ■ RMD1  
 Fludger, C. R. S. ■ RMB2  
 Ford, C. W. ■ RWB1  
 Fouquet, J.E. ■ JWB1  
 Franken, H. J. ■ RTuD1  
 Fujita, J. ■ RMF5  
 Fujiwara, Takumi ■ RMF1,  
     RTuK3  
 Fukaya, Naoyuki ■ RTuE3  
 Furukawa, Yasunori ■  
     RTuK3  
 Goddard, N.L. ■ RTuH3  
 Goh, Takashi ■ RTuD5  
 Goldstein, Evan L. ■ JWB4  
 Gomez, L. T. ■ RTuA1  
 Goodhue, W. D. ■ RWD5  
 Goorjian, Peter M. ■ RMG2,  
     RMH2  
 Gopinath, A. ■ RMD,  
     RMD4, RTuK1  
 Grattan, K. T. V. ■ RMD5,  
     RTuL5  
 Grein, C. H. ■ RTuC3  
 Groen, F. H. ■ RTuD1  
 Grover, R. ■ RWD3  
 Groves, S. H. ■ RWD5  
 Gutierrez, C. ■ RMF5  
 Hadley, G. Ronald ■ RTuI1  
 Hagelin, Paul M. ■ JWA1  
 Han, Dongkyoon ■ RTuA2  
 Harmsma, Peter ■ RMB4  
 Hasenberg, T. C. ■ RTuC3  
 Hashimoto, N. ■ RMB1  
 Hauffe, R. ■ RMH8  
 Haus, Hermann A. ■ RTuB1,  
     RTuH4  
 Heim, P. J. S. ■ RWD3  
 Helfert, Stefan ■ RTuI5  
 Helmfrid, S. ■ RMF3, RMF4  
 Herben, C. G. ■ RTuD1  
 Heritage, J. P. ■ JWA1  
 Hernández-Figueroa, H. E.  
     ■ RMD2  
 Hesthaven, Jan S. ■ RTuI4  
 Himeno, Akira ■ RTuD5  
 Ho, H. P. ■ RMH3  
 Hoffmann, D. ■ RWC3  
 Houdré, R. ■ RTuE1  
 Huang, Wei-Ping ■ RTuL1  
 Huffaker, D. L. ■ RMG1  
 Hyun, Kyung-Sook ■ RTuA6  
 Ichikawa, Tadashi ■ RTuK2  
 Ikegami, Tetsuhiko ■ RMA3  
 Ikushima, Akira J. ■ RMF1,  
     RTuK3  
 Ilchenko, V. S. ■ RTuH2  
 Illegems, M. ■ RTuE1  
 Imamoğlu, A. ■ RMC2,  
     RTuF3  
 Ippen, Erich P. ■ RMA1  
 Ironside, C.N. ■ JWB3  
 Ito, Hiroshi ■ RTuK2  
 Itoh, Mikitaka ■ RTuD5  
 Jackel, J. L. ■ RTuJ2  
 Jackson, A. ■ RWB2  
 Jakubczyk, Z. Jan ■ RTuE5  
 Jalali, Bahram ■ RTuA  
 Jaskorzynska, B. ■ RMF3,  
     RMF4  
 Jeong, Jong Sool ■ RTuA6  
 Ji, Jeong K. ■ RTuL4  
 Jiang, Hongtao ■ RTuF2  
 Jin, Yong-Sung ■ RTuD4  
 Johnson, F. G. ■ RWD3  
 Jones, N. J. ■ RMB2  
 Jung, Jae-Hoon ■ RTuD4  
 Kagami, Manabu ■ RTuK2  
 Kaneko, Taro ■ RMB3,  
     RTuB4  
 Kaspi, Ron ■ RMH11  
 Khaled, Jabri ■ RMF1  
 Kim, Boo-Gyoun ■ RTuG5  
 Kim, Byoung-Sung ■ RMG3  
 Kim, Hong-Kuk ■ RTuG5  
 Kim, Hyoun-Soo ■ RTuA2  
 Kim, J. ■ RMC1  
 Kitamura, Kenji ■ RTuK3  
 Koh, P. C. ■ RWC4  
 Kokubun, Yasuo ■ RMB3,  
     RMF6, RTuB4  
 Koltschanov, Igor ■ RWC1  
 Kostritskii, S. M. ■ RTuK4  
 Kostrzewska, C. ■ RMH8  
 Krauss, T.F. ■ RTuE1  
 Krishnamoorthy, Uma ■  
     JWA1  
 Kumar, A. ■ RTuG2  
 Labilloy, D. ■ RTuE1  
 Laine, J. P. ■ RTuH4  
 Laliew, Chanin ■ RTuK1  
 Lavrova, Olga A. ■ RMB5  
 Lee, Byoung-ho ■ RTuG5  
 Lee, Hong-Seok ■ RTuG5  
 Lee, Sang-Shin ■ RTuD4  
 Lee, Yeong-Gyu ■ RTuA2  
 Leite, A. M. P. ■ JWB3  
 Lenz, G. ■ RTuA1  
 Lenzi, Maurizio ■ RTuG1  
 Lenzmann, Olaf ■ RWC1  
 Levy, M. ■ RMF5, RTuG2  
 Ley, Maarten R. ■ RMB4  
 Li, Xun ■ RTuL1

- LiKamWa, Patrick ■ RMH11  
 Lim, D. ■ RTuH4  
 Lin, Lih Y. ■ JWB4  
 Little, Brent E. ■ RMB3, RMF6, RTuA5, RTuB, RTuB3, RTuB4, RTuE, RTuH4  
 Liu, Ansheng ■ RTuC1  
 Loehr, John ■ RMH11  
 Lowery, Arthur J. ■ RWC1  
 Maat, D. H. P. ■ RTuD1  
 Madabhushi, Rangaraj ■ RTuK5  
 Madsen, C. K. ■ RTuA1, RTuA4  
 Magliocco, Massimo ■ RTuG1  
 Maleki, L. ■ RTuH2  
 Man, S. Q. ■ RMF2  
 Maring, D. B. ■ RTuK4  
 Mason, Beck ■ RME2, JWB2, RWD4  
 Mears, R. J. ■ RMB2, RTuJ4  
 Meichenin, D. ■ RME1  
 Menyuk, Curtis R. ■ RTuJ1, RWA  
 Meyer, J. R. ■ RTuC2  
 Meyer, M. ■ RTuL5  
 Molle, L. ■ RWA3  
 Molloy, Catherine ■ RTuC4  
 Moodie, D. G. ■ RWB1  
 Moore, R. T. ■ RWB1  
 Moores, John D. ■ RWA1  
 Moriwaki, Kazuyuki ■ RTuD5  
 Murphy, Thomas E. ■ RTuA5  
 Na, Ki-Woon ■ RTuD4  
 Nakamura, Shu ■ RMH4  
 Nakano, Hisamatsu ■ RMH4, RTuI3  
 Nakano, Yoshi ■ RTuL  
 Nakazawa, Tadao ■ RMB1  
 Nicque, Jean-Louis ■ RWD1  
 Nikonov, D. ■ RMC2  
 Ning, C.-Z. ■ RMG2, RMH2, RTuC1  
 Nolting, Hans-Peter ■ RWC2, RWC3  
 Obayya, S. S. A. ■ RMD5  
 Oei, Y. Siang ■ RMB4  
 Oesterle, U. ■ RTuE1  
 Oh, Tae-Won ■ RTuD2  
 Ohmori, Yasuji ■ RTuD5  
 Okamoto, K. ■ RMA3  
 Okuno, Masayuki ■ RTuD5  
 Olesberg, J. T. ■ RTuC3  
 Osgood, R. M., Jr. ■ RMF5, RTuG2, RTuL2  
 Ougazzaden, A. ■ RME1  
 Pamulapati, J. ■ RWD3  
 Pan, Wugen ■ RMB3, RMF6, RTuB4  
 Parker, Michael C. ■ RMB2, RTuJ3, RTuJ4  
 Patterson, S. G. ■ RMH6  
 Pegg, S. I. ■ RWD2  
 Petermann, Klaus ■ RMH8, RWA2  
 Philipsen, J. L. ■ RMF3, RMF4  
 Phillips, I. D. ■ RWB1  
 Pierce, Iestyn ■ RMH7  
 Pinheiro, Helder F. ■ RMD2  
 Piprek, Joachim ■ RMH9  
 Piyawattanametha, Wibool ■ RTuD3  
 Plumb, R. G. S. ■ RWC4  
 Pregla, Reinhold ■ RMD3, RTuI5  
 Pun, E. Y. B. ■ RMF2, RMH3  
 Radius, Erik ■ JWB5  
 Radojevic, A. M. ■ RTuG2  
 Radziunas, M. ■ RWC3  
 Rahman, B. M. A. ■ RMD5, RTuL5  
 Rahmat-Samii, Yahya ■ RTuE4  
 Rajarajan, M. ■ RMD5, RTuL5  
 Ram, R. J. ■ RMH6  
 Ramaswamy, Ramu V. ■ RTuG, RTuG4, RTuK4  
 Ramdane, A. ■ RME1  
 Rana, F. ■ RMH6  
 Randles, M. ■ RMF5  
 Ranganath, T. R. ■ RWD  
 Rao, H. ■ RTuL2  
 Reed, J. ■ RWB1  
 Reeder, R. E. ■ RWD5  
 Rees, Paul ■ RMH7  
 Richards, D. H. ■ RTuJ2  
 Rivera, Michael ■ RMH1  
 Rollier, Raphael ■ RTuD3  
 Roudas, I. ■ RTuJ2  
 Rousina-Webb, Roghieh ■ JWA2  
 Saini, S. S. ■ RWD3  
 Sakamoto, S. R. ■ RWB2  
 Santori, C. ■ RMC1  
 Sartorius, B. ■ RWC3  
 Sato, Shinya ■ RMF6  
 Scarmozzino, R. ■ RTuL2  
 Scherer, Axel ■ RTuH1  
 Schmidt, H. ■ RMC2  
 Schneider, K. ■ RWC3  
 Scotti, R. E. ■ RTuA1  
 Seino, M. ■ RMB1  
 Seki, S. ■ RTuF  
 Shen, H. ■ RWD3  
 Shibayama, Jun ■ RTuI2  
 Shin, Sang-Yung ■ RTuD2  
 Shore, K. Alan ■ RMG, RMH7, RTuL3  
 Siebel, U. ■ RMH8  
 Sik, H. ■ RME1  
 Singh, Jasprit ■ RTuF2  
 Smit, Meint K. ■ RMA2, RMB, RMB4  
 Smith, C.J.M. ■ RTuE1  
 Smith, Henry I. ■ RTuA5  
 Sohler, Wolfgang ■ RTuK  
 Solgaard, Olav ■ JWA1  
 Son, Yung-Sung ■ RTuD4  
 Song, G. Hugh ■ RTuL4  
 Song, Hyung-Seung ■ RTuA2  
 Soole, Julian B. ■ JWA  
 Spencer, Paul S. ■ RMH7  
 Stanley, C.R. ■ JWB3  
 Steel, M. J. ■ RTuL2  
 Steier, Bill ■ RMF  
 Stone, D. R. ■ RWD3  
 Su, Guo-Dung J. ■ RTuD3  
 Suche, Hubertus ■ RTuG3  
 Suzuki, Shuichi ■ RMF6  
 Swillo, Marcin ■ RMF4  
 Takahashi, Tomokazu ■ RTuI3  
 Takasu, Y. ■ RMB1  
 Takeuchi, Hiroaki ■ RME4  
 Tanaka, Masahiro ■ RTuE2  
 Tanev, Stoyan ■ RTuE5  
 Tang, J. M. ■ RTuL3  
 Taniguchi, S. ■ RMB1  
 Tavlykaev, Robert F. ■ RTuG4, RTuK4  
 Taylor, P. J. ■ RWD5  
 Tolstikhin, Valery I. ■ RTuC5  
 Tzolov, Velko P. ■ RTuE5  
 Van, Vien ■ RTuB3, RTuI2  
 van Brug, H. ■ RTuD1  
 Vance, Rod ■ RWC1  
 Vergnol, E. ■ RME1  
 Verschuren, Coen A. ■ RMB4  
 Villareal, R. ■ RMP5  
 Vonk, Hilbert ■ RMB4  
 Vurgaftman, I. ■ RTuC2  
 Wagner, R. E. ■ RTuJ2  
 Walker, Stuart D. ■ RTuJ3  
 Weinert, Carl M. ■ RTuJ, RWA3  
 Weisbuch, C. ■ RTuE1  
 Whiteaway, James ■ RTuA3  
 Wilkinson, C.D.W. ■ RTuE1  
 Wongcharoen, T. ■ RTuL5  
 Wood, Scott ■ RTuC4  
 Wu, Chi ■ JWA2  
 Wu, Ming C. ■ RTuD3  
 Wünsche, Hans ■ RWC3  
 Yamamoto, Y. ■ RMC1  
 Yamauchi, Junji ■ RMH4, RTuI3  
 Yao, X. S. ■ RTuH2  
 Yevick, David ■ RMH5  
 Yi, Jong Chang ■ RMC3  
 Yiptong, A. ■ RTuJ4  
 Yonekura, Jun ■ RTuE3  
 Yoo, Byueng-Su ■ RTuA6  
 Zhan, L. ■ RMH3  
 Zhang, Xiaobo ■ RTuK1  
 Zhang, Yifei ■ RTuF2  
 Zhou, W. ■ RWD3  
 Ziolkowski, Richard W. ■ RTuB, RTuE, RTuE2, RTuH  
 Zou, Z. ■ RMG1

**Integrated Photonics Research**

# **Postdeadline Paper Session**

**Tuesday, July 20, 1999**

**Fred Heismann, Qtera Corporation, USA**  
**Presider**

**PD**  
**5:30pm**  
**Sierra Madre**

## Novel device for CW probe “recovery” from a modulated optical signal with wavelength and polarisation conservation

C. Janz, B. Dagens & F. Devaux

OPTO+, Groupement d’Intérêt Economique

Route de Nozay, 91460 Marcoussis, France (Alcatel Corporate Research Centre)

Tel.: +33 (0)1 69 63 15 61; Fax: +33 (0)1 69 63 14 22; e-mail: Christopher.Janz@alcatel.fr

**Introduction:** Coherent optical receivers require a local optical oscillator which must have the same wavelength and polarisation as the incoming signal. Since the polarisation of an optical signal following fibre transmission is, as a rule, unknown, polarisation-diversity schemes have generally been employed in coherent optical receivers [1]. However, the implementation of such schemes in integrated form is invariably complex. Furthermore, in a coherent WDM system, a network of local oscillator lasers would be required in the receiver. A device which would allow the recovery of a CW “probe” from an incoming signal of arbitrary wavelength and polarisation, such that the wavelength and polarisation of the probe rigorously matched that of the signal, would therefore be of great interest. The same device might also be used in non-coherent transponder applications: in future optical networks, periodic partial (2R) or full (3R) signal regeneration might be required to maintain signal quality over long transmission distances or in high-order cascades of crossconnects or switching nodes. Since the wavelengths assigned to optical channels are expected to become managed network resources in their own right in future WDM network layers [2], transponders might often be required to conserve wavelength in the regeneration process. A wavelength recovery device such as we propose here would ensure the matching of input and output wavelengths with a “generic” implementation.

To ensure rigorous conservation of wavelength and polarisation, the device we propose recovers an optical probe directly from an incoming amplitude-modulated digital optical signal, where the signal might be degraded by various transmission impairments. The device must, as a general matter, perform three operations: erasure of the amplitude modulation on the signal, spectral “cleaning” of the signal (full or partial elimination of amplified spontaneous emission), and erasure of phase modulation (that already present on the signal as well as any added during the amplitude de-modulation process). With this in mind, the “generic” wavelength recovery device shown in Figure 1.(a) can be imagined. In the first stage, the high-frequency content of the signal is filtered using a narrow-band optical filter (typically  $<\sim 1\text{GHz}$ ); this filtering also enhances the real optical signal-to-noise ratio (OSNR) by filtering ASE well within the signal bandwidth (high bit rate signals are envisaged). The second block is used to cancel the remaining, low-frequency intensity modulation (optical amplification is inserted to maintain the power level and OSNR). Finally, the third stage eliminates any phase modulation imposed by the second stage or present on the input signal; the final probe linewidth should then depend on the magnitude of “delay 3.” Note that the amplitude and phase modulators used must be polarisation-independent.

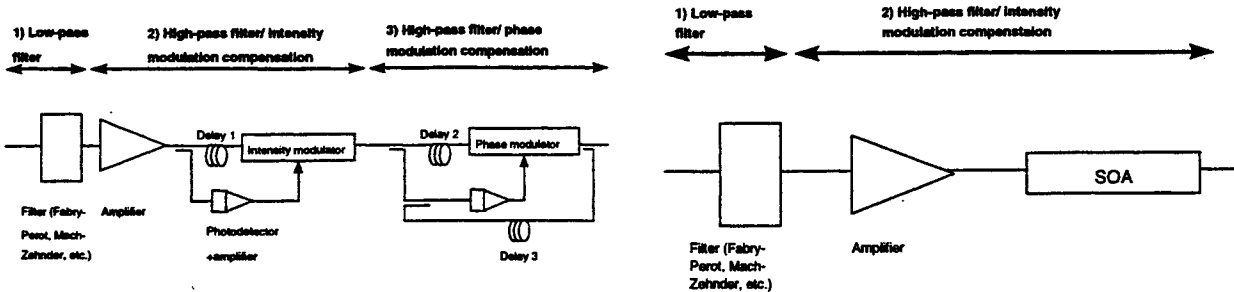


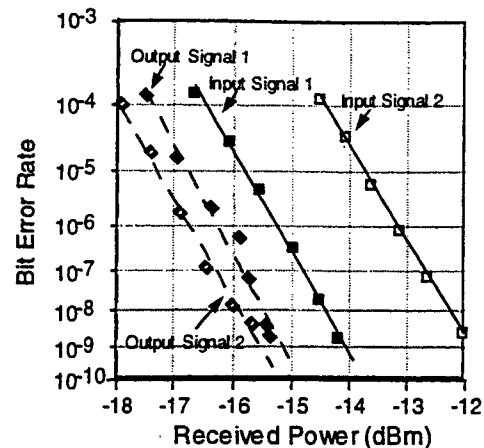
**Figure 1.(a) (left):** “Generic” system for wavelength recovery from a modulated optical signal; the terms “low-pass” and “high-pass” refer to the baseband signal modulation. The all-optical implementation of **Figure 1.(b)** (right) is studied here.

In this paper, we demonstrate an equivalent all-optical implementation of, at least, the first two stages of the generic device in Figure 1.(a), by replacing the second stage by a semiconductor optical amplifier (SOA); see Figure 1.(b). Operated in saturation, the SOA tends to cancel the amplitude modulation remaining after the filter; as the SOA gain-modulation bandwidth is typically on the order of a few GHz, its high-pass characteristic (with respect to the input signal) overlaps neatly with the low-pass characteristic of the filter, and of course the SOA does not block the intensity at DC. For the first stage, we have used a commercial Fabry-Perot (FP) filter; such filters are ideal for the present application, as they can be realised with narrow bandwidths, are periodic and hence can be chosen to correspond to a typical WDM channel allocation grid, and furthermore are, generally, easily tunable, with simple feedback control, to compensate for variations of the channel wavelengths with respect to the defined grid. In the following, we experimentally demonstrate this FP filter-SOA device in a transponder application at 10Gb/s, and furthermore we discuss the optimisation of the various filter and SOA parameters, which were studied by detailed numerical simulations.

**Experiment:** The following experiment was carried out to experimentally evaluate the proposed device. A 10Gb/s,  $2^7$ -1 PRBS intensity modulated signal, generated using a LiNbO<sub>3</sub> modulator, was amplified by an EDFA following variable attenuation (to control the resulting OSNR). This “input” signal was then injected into the wavelength recovery device: a FP filter (bandwidth ~1GHz), followed by an EDFA, and finally a polarisation-independent SOA (length 800μm, confinement factor 0.45, bias current 300mA). The EDFA was required to ensure a sufficiently high power level at the input to the SOA. The output of the SOA was then modulated using a second LiNbO<sub>3</sub> modulator (“output” signal), following several metres of fibre propagation and polarisation control. BER measurements were conducted on both the “input” signal and the “output” signal following the second modulator, where the “recovered” wavelength was used as the CW probe. The results are shown in Figure 2. “Input signal 1” had an extinction ratio (ER) of 7dB and an OSNR of 44dB in 0.1nm, while “input signal 2” also had an extinction ratio of 7dB, but a degraded OSNR (25dB in 0.1nm). In both cases, the FP filter and SOA provided a CW probe of sufficient quality to allow negative penalties, and essentially normal sensitivities, at the output of the second modulator. In our experiment, we observed an onset of BER penalty on the “output” signal when either the “input” signal ER was increased beyond 7dB, or the PRBS length was increased beyond  $2^7$ -1. On the other hand, higher ER’s could be tolerated with short, programmed words, and longer PRBS patterns could be accommodated with lower input ER’s.

The observed limitations are therefore not fundamental but rather determined by the filter bandwidth.

**Figure 2.** Measured BER characteristics (10Gb/s, PRBS=2<sup>7</sup>-1). The "input signals" were those injected into the wavelength recovery device (FP filter+EDFA+SOA); in each case, the input signal ER was 7dB, while the OSNR's were 44dB in 0.1nm (1) and 25dB in 0.1nm (2), respectively. In both cases, the signal generated by a second LiNbO<sub>3</sub> modulator using the recovered probe has a "normal" sensitivity of about -15.5dBm at 10<sup>-9</sup>.



This was confirmed by numerical simulations, carried out using an advanced in-house modelling tool. In these simulations we assumed a 40Gb/s, PRBS=2<sup>7</sup>-1 NRZ signal pattern, with an ER of 10dB and a high OSNR. In Figure 3, we show the ER of the detected "probe," following the SOA, as a function of the FP filter bandwidth. The SOA parameters/current are the same as those used in the experiment, the input signal power to the filter is 5dBm, and no amplifier is used between the filter and the SOA. The influence of the filter bandwidth, which varies from 125GHz to 125MHz, is clearly evident. The simulations also revealed that the input signal power must be maintained at a fairly high level to properly saturate the SOA; as shown in Figure 4 (the same SOA parameters are assumed), powers above -5dBm are needed. This indicates a general need for optical amplification in the device; however, a properly optimised SOA could conceivably be used for this, rather than an EDFA as in our experiment. As expected, long, high confinement factor SOA's were found to be best suited to the present application.

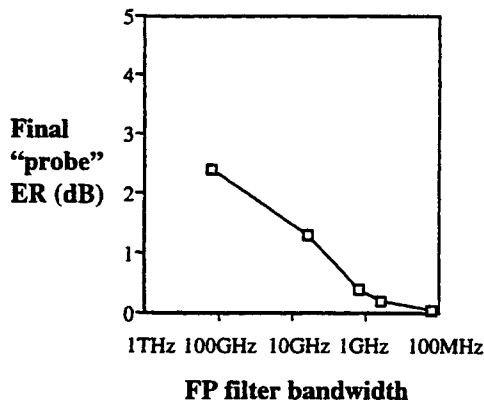


**Figure 3.** Final probe ER as a function of filter bandwidth (fixed signal & SOA parameters).

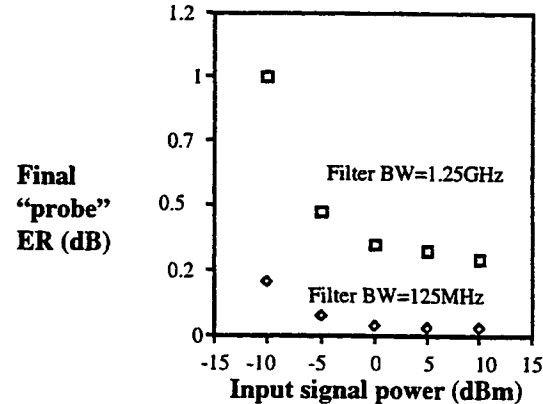


**Figure 4.** Final probe ER as a function of input signal power.

**Conclusions:** We have demonstrated an all-optical device which allows recovery of a spectrally-cleaned, CW probe from a modulated optical signal. The device could find application in coherent receivers or in optical transponder applications.

#### References:

- [1] Kaiser et al., Electron. Lett., vol. 30, no. 77, 1994, pp. 1446-1447
- [2] Jourdan et al., J. Lightwave Technol., vol. 14, no. 6, 1996, pp. 1198-1206

## **KEY TO AUTHORS**

Dagens, B., RPDPI

Devaux, F., RPDPI

Janz, C., RPDPI

# Integrated Photonics Research Technical Program Committee

## **Research Organizing Committee**

**Nadir Dagli**, *General Chair, University of California, Santa Barbara, USA*

**Sujeet Chaudhuri**, *Program Chair, University of Waterloo, Canada*

**Fred Heismann**, *Program Chair, Qtera Corporation, USA*

## **International Liaison Group Chairs**

### **Asia/Pacific Rim**

**Yasuo Kokubun**, *Yokohama National University, Japan*

### **Europe**

**Gunnar Arvidsson**, *Institute of Optical Research, Sweden*

## **OSA Technical Council Representative**

**Tso Yee Fan**, *MIT Lincoln Laboratory, USA*

## **Subcommittee I: Active and Compound Semiconductor Devices**

**S. Chandrasekhar**, *Chair, Bell Laboratories, Lucent Technologies, USA*

**T.R. Ranganath**, *Hewlett-Packard Laboratories, USA*

**Akihiko Kasukawa**, *Furukawa Electric Company Ltd., Japan*

**Kazutoshi Kato**, *NTT Opto-Electronics Laboratories, Japan*

**Jean-Francois Vinchant**, *Alcatel Optronics, France*

**Claude Rolland**, *Nortel Networks, Canada*

**M.K. Smit**, *Delft University of Technology, The Netherlands*

**Julian Soole**, *Bell Laboratories, Lucent Technologies, USA*

## **Subcommittee II: Dielectric Waveguides and Waveguides Devices**

**Ramu V. Ramaswamy**, *Chair, University of Florida, USA*

**Jaymin Amin**, *Corning Inc., USA*

**Bahram Jalali**, *University of California, Los Angeles, USA*

**Yasuo Kokubun**, *Yokohama National University, Japan*

**Takashi Mizuuchi**, *Mitsubishi Electric Corporation, Japan*

**Kazuhito Noguchi**, *NTT Opto-Electronics Laboratory, Japan*

**Wolfgang Sohler**, *University of Paderborn, Germany*

**William Steier**, *University of Southern California, Los Angeles, USA*

## **Subcommittee III: Modeling, Numerical Simulation and Theory**

**Joseph P. Donnelly**, *Chair, MIT Lincoln Laboratory, USA*

**Shun-Lien Chuang**, *University of Illinois, USA*

**Youngchul Chung**, *Kwangwoon University, South Korea*

**Gregory Dente**, *GCD Associates, USA*

**Wei Ping Huang**, *University of Waterloo, Canada*

**Brent Little**, *Massachusetts Institute of Technology, USA*

**Jerry Meyer**, *Naval Research Laboratory, USA*

**Shuji Seki**, *NTT Opto-Electronics Laboratory, Japan*

**K. Alan Shore**, *University of Wales, UK*

**C. W. Weinert**, *Heinrich-Hertz-Institute, Germany*

**Junji Yamauchi**, *Hosei University, Japan*

**Richard W. Ziolkowski**, *University of Arizona, USA*

## **IPR Advisory Committee**

**Bob Deri**, *Lawrence Livermore National Laboratories, USA*

**Anand Gopinath**, *University of Minnesota, USA*

**David Smith**, *Case Western Reserve University, USA*

**David Yevick**, *Queen's University at Kingston, Canada*

**Jane Zucker**, *Bell Laboratories, Lucent Technologies, USA*